HYDRODYNAMICS – OPTIMIZING METHODS AND TOOLS

Edited by **Harry Edmar Schulz, André Luiz Andrade Simões** and **Raquel Jahara Lobosco**

INTECHWEB.ORG

Hydrodynamics – Optimizing Methods and Tools
Edited by Harry Edmar Schulz, André Luiz Andrade Simões and Raquel Jahara Lobosco

Published by InTech
Janeza Trdine 9, 51000 Rijeka, Croatia

Publishing Process Manager Bojana Zelenika
Technical Editor Teodora Smiljanic
Cover Designer Jan Hyrat
Image Copyright André Luiz Andrade Simões, 2011.

First published September, 2011
Printed in Croatia

A free online edition of this book is available at www.intechopen.com
Additional hard copies can be obtained from orders@intechweb.org

Hydrodynamics – Optimizing Methods and Tools, Edited by Harry Edmar Schulz, André Luiz Andrade Simões and Raquel Jahara Lobosco
p. cm.
ISBN 978-953-307-712-3

Contents

Preface

The Presence of Hydrodynamics in Modern Sciences: Optimizing Methods and Tools

"Water is the beginning of everything" (Tales of Mileto)
"Air is the beginning of everything" (Anaxímenes of Mileto)

Why is it important to study Hydrodynamics? The answer may be strictly technical, but it may also involve some kind of human feeling about our environment, and our (eventual) limitations to deal with its fluidic constituents.

As teachers, when talking to our students about the importance of quantifying fluids, we (authors) go to the blackboard and draw, in blue color, a small circumference in the center of the board, and add the obvious name "Earth". Some words are then said, in the sense that Hydrodynamics is important, because we are beings strictly adapted to live immersed in a fluidic environment (air), and because we are beings composed basically by simple fluidic solutions (water solutions), encapsulated in fine carbon membranes. Then, with a red chalk, we draw two crosses: one inside and the other outside the circumference, explaining: "our environment is very limited. We can only survive in the space covered by the blue line. No one of us can survive in the inner part of this sphere, or in the outer space. Despite all films, games, and books about contacts with aliens, and endless journeys across the universe, our present knowledge only allows to suggest that it is much most probable that the human being will extinct while in this fine fluid membrane, than to create sustainable artificial environments in the cosmos".

Sometimes, to add some dramaticism, we project the known image of the earth on a wall (the image of the blue sphere), and then we blow a soap bubble, explaining that the image gives the false impression that the entire sphere is our home. But our "home" is better represented by the liquid film of the soap bubble (only the film) and then we touch the bubble, exploding it, showing its fragility.

In the sequence, we explain that a first reason to understand fluids would be, then, to guarantee the maintenance of the fluidic environment (the film), so that we could also guarantee our survival as much as possible. Further, as we move ourselves and produce our things immersed in fluid, it is interesting to optimize such operations, in order to facilitate our survival. Still further, because our organisms interchange heat

and mass in cellular and corporal scales between different fluids, the understanding of these transports permits to understand the spreading of diseases, the delivering of medicines to cells, and the use of physical properties of fluids in internal treatments, allowing to improve our quality of life. Finally, the observation of the inner part of the sphere, the outer space and its constituents, shows that many "highly energetic" phenomena behave like the fluids around us, giving us the hope that the knowledge of fluids can help, in the future, to quantify, reproduce, control and use energy sources similar to those of the stars, allowing to "move through the cosmos", and (only then) also to create sustainable artificial environments, and to leave this "limited film" when necessary. Of course, this "speech" may be viewed as a sort of escapism, related to a fiction of the future. In fact, the day-by-day activities show that we are spending our time with "more important" things, like the fighting among us for the dividends of the next fashion wave (or the next technical wave), the hierarchy among nations, or the hierarchy of the cultures of the different nations. So, fighters, warriors, or generals, still seem to be the agents that write our history. But global survival, or, in other words, the guarantee of any future history, will need other agents, devoted to other activities. The hope lies on the generation of knowledge, in which the knowledge about fluids is vital.

Context of the present book "Hydrodynamics - Optimizing Methods and Tools"

A quick search in virtual book stores may result in more than hundred titles involving the word "Hydrodynamics". Considering the superposition existing with Fluid Mechanics, the number of titles grows much more. Considering all these titles, why to organize another book on Hydrodynamics? One answer could be: because the researchers always try new points of view to understand and treat the problems related to Hydrodynamics. Even a much known phenomenon may be re-explained from a point of view that introduces different tools (conceptual, numerical or practical) into the discussion of fluids. And eventually a detail shows to be useful, or even very relevant. So, it is necessary to give the opportunity to the different authors to expose their points of view.

Among the historically relevant books on Hydrodynamics, some should be mentioned here. For example, the volumes "Hydrodynamics" and "Hydraulics", by Daniel Bernoulli (1738) and his father, Johann Bernoulli (1743), respectively, present many interesting sketches and the analyses that converged to the so called "Bernoulli equation", later deduced more properly by Leonhard Euler. Although there are unpleasant questions about the authorship of the main ideas, as pointed out by Rouse (1967) and Calero (2008), both books are placed in a "prominent position" in the history, because of their significant contributions. The volume written by Sir Horace Lamb (1879), now named "Hydrodynamics", considers the basic equations, the vortex motion, tidal waves, among other interesting topics. Considering the classical equations and procedures followed to study fluid motion, the books "Fundamentals of Hydro and Aerodynamics" and "Applied Hydro and Aerodynamics" by Prandtl and Tietjens (1934) present the theory and its practical

applications in a comprehensive way, influencing the experimental procedures for several decades. Over fifty years, the classical volume of Landau and Lifschitz (1959) remains as an extremely valuable work for researchers in fluid mechanics. In addition to the usual themes, like the basic equations and turbulence, the book also covers themes like the relativistic fluid dynamics and the dynamics of superfluids. Each of the major topics considered in the studies of fluid mechanics can be widely discussed, generating specific texts and books. An example is the theory of boundary layers, in which the book of Schlichting (1951) has been considered an indispensable reference, because it condenses most of the basic concepts on this subject. Further, still considering specific topics, Stoker (1957) and Lighthill (1978) wrote about waves in fluids, while Chandrasekhar (1961) and Drazin and Reid (1981) considered hydrodynamic and hydromagnetic stability. It is also necessary to mention the books of Batchelor (1953), Hinze (1958), and Monin and Yaglom (1965), which are notable examples of texts on turbulence and statistical fluid mechanics, showing basic concepts and comparative studies between theory and experimental data. A more recent example may be the volume written by Kundu e Cohen (2008), which furnishes a chapter on "biofluid mechanics" The list of the "relevant books" is obviously not complete, and grows continuously, because new ideas are continuously added to the existing knowledge.

The present book is one of the results of a project that generated three volumes, in which recent studies on Hydrodynamics are described. The remaining two titles are "Hydrodynamics - Natural Water Bodies", and "Hydrodynamics - Advanced Topics". In the present volume, efforts to improve different methods that allow to understand and optimize different processes and operations involving fluids are presented and discussed. The editors thank all authors for their efforts in presenting their chapters and conclusions, and hope that this effort will be welcomed by the professionals dealing with Hydrodynamics.

The book "Hydrodynamics - Optimizing Methods and Tools" is organized in the following manner:

Part 1: Smoothed Spheres
Part 2: Models and Codes in Fluid Dynamics
Part 3: Complex Hydraulic Engineering Applications
Part 4: Hydrodynamics and Heat/Mass Transfer

Hydrodynamics is a very rich area of study, involving some of the most intriguing theoretical problems, considering our present level of knowledge. General nonlinear solutions, closed statistical equations, explanation of sudden changes, for example, are wanted in different areas of research, being also matter of study in Hydromechanics. Further, any solution in this field depends on many factors, or many "boundary conditions". The changing of the boundary conditions is one of the ways through which the human being affects its fluidic environment. Changes in a specific site can impose catastrophic consequences in a whole region. For example, the permanent leakage of petroleum in one point in the ocean may affect the life along the entire

region covered by the marine currents that transport this oil. Gases or liquids, the changes in the quality of the fluids in which we live certainly affect our quality of life. The knowledge about fluids, their movements, and their ability to transport physical properties and compounds is thus recognized as important for life. As a consequence, thinking about new solutions for general or specific problems in Hydromechanics may help to attain a sustainable relationship with our environment. Re-contextualizing the classical discussion about the truth, in which it was suggested that the "thinking" is the guarantee of our "existence" (St. Augustine, 386a, b, 400), we can say that we agree that thinking guarantees the human existence, and that there are too many warriors, and too few thinkers. Following this re-contextualized sense, it was also said that the man is a bridge between the "animal" and "something beyond the man" (Nietzsche, 1883). This is an interesting metaphor, because bridges are built crossing fluids (even abysms are filled with fluids). Considering all possible interpretations of this phrase, let us study and understand the fluids, and let us help to build the bridge.

Harry Edmar Schulz, André Luiz Andrade Simões and Raquel Jahara Lobosco
University of São Paulo
Brazil

References

Batchelor, G.K. (1953), The theory of homogeneous turbulence. First published in the Cambridge Monographs on Mechanics and Applied Mathematics series 1953. Reissued in the Cambridge Science Classics series 1982 (ISBN: 0 521 04117 1).

Bernoulli, D. (1738), Hydrodynamics. Dover Publications, Inc., Mineola, New York, 1968 (first publication) and reissued in 2005, ISBN-10: 0486441857. Hydrodynamica, by Daniel Bernoulli, as published by Johann Reinhold Dulsecker at Strassburg in 1738.

Bernoulli, J. (1743), Hydraulics. Dover Publications, Inc., Mineola, New York, 1968 (first publication) and reissued in 2005, ISBN-10: 0486441857. Hydraulica, by Johann Bernoulli, as published by Marc-Michel Bousquet et Cie. at Lausanne and Geneva in 1743.

Calero, J.S. (2008), The genesis of fluid mechanics (1640-1780). Springer, ISBN 978-1-4020-6413-5. Original title: La génesis de la Mecánica de los Fluidos (1640–1780), UNED, Madrid, 1996.

Chandrasekhar, S. (1961), Hydrodynamic and Hydromagnetic Stability. Clarendon Press edition, 1961. Dover edition, first published in 1981 (ISBN: 0-486-64071-X).

Drazin, P.G. & Reid, W.H. (1981), Hydrodynamic stability. Cambridge University Press (second edition 2004). (ISBN: 0 521 52541 1).

Hinze, J.O. (1959), Turbulence. McGraw-Hill, Inc. second edition, 1975 (ISBN:0-07-029037-7).

Kundu, P.K. & Cohen, I.M. (2008), Fluid Mechanics. 4th ed. With contributions by P.S. Ayyaswamy and H.H. Hu. Elsevier/Academic Press (ISBN 978-0-12-373735-9).

Lamb, H. (1879), Hydrodynamics (Regarded as the sixth edition of a *Treatise on the Mathematical Theory of the Motion of Fluids*, published in 1879). Dover Publications, New York., sixth edition, 1993 (ISBN-10: 0486602567).

Landau, L.D.; Lifschitz, E.M. (1959), Fluid Mechanics. Course of theoretical Physics, Volume 6. Second edition 1987 (Reprint with corrections 2006). Elsevier (ISBN-10: 0750627670).

Lighthill, J. (1978), Waves in Fluids. Cambridge University Press, Reissued in the Cambridge Mathematical Library series 2001, Third printing 2005 (ISBN-10: 0521010454).

Monin, A.S. & Yaglom, A.M. (1965), Statistical fluid mechanics: mechanics of turbulence. Originally published in 1965 by Nauka Press, Moscow, under the title Statisticheskaya Gidromekhanika-Mekhanika Turbulentnosti. Dover edition, first published in 2007. Volume 1 and Volume 2.

St. Augustine (386a), Contra Academicos, in Abbagnano, N. (2007), Dictionary of Philosophy, "Cogito", Martins Fontes, Brasil (Text in Portuguese).

St. Augustine (386b), Soliloquia, in Abbagnano, N. (2007), Dictionary of Philosophy, "Cogito", Martins Fontes, Brasil (Text in Portuguese).

St. Augustine (400-416), De Trinitate, in Abbagnano, N. (2007), Dictionary of Philosophy, "Cogito", Martins Fontes, Brasil (Text in Portuguese).

Nietzsche, F. (1883), Also sprach Zarathustra, Publicações Europa-América, Portugal (Text in Portuguese, Ed. 1978).

Rouse, H. (1967). Preface to the english translation of the books Hydrodynamics and Hydraulics, already mentioned in this list. Dover Publications, Inc.

Prandtl, L. & Tietjens, O.G. (1934) Fundamentals of Hydro & Aeromechanics, Dover Publications, Inc. Ed. 1957.

Prandtl, L. & Tietjens, O.G. (1934) Applied Hydro & Aeromechanics, Dover Publications, Inc. Ed. 1957.

Schlichting, H. (1951), Grenzschicht-Theorie. Karlsruhe: Verlag und Druck.

Stoker, J.J. (1957). Water waves: the mathematical theory with applications. Interscience Publishers, New York (ISBN-10: 0471570346).

Part 1

Smoothed Spheres

1

SmoothViz: Visualization of Smoothed Particles Hydrodynamics Data

Lars Linsen[1], Vladimir Molchanov[1], Petar Dobrev[1], Stephan Rosswog[1], Paul Rosenthal[2] and Tran Van Long[3]
[1]*Jacobs University, Bremen*
[2]*Chemnitz University of Technology*
[3]*University of Transport and Communication, Hanoi*
[1,2]*Germany*
[3]*Vietnam*

1. Introduction

Smoothed particle hydrodynamics (SPH) is a completely mesh-free method to simulate fluid flow (Gingold & Monaghan, 1977; Lucy, 1977). Rather than representing the physical variables on a fixed grid, the fluid is represented by freely moving interpolation centers ("particles"). Apart from their position and velocity these particles carry information about the physical quantities of the considered fluid, such as temperature, composition, chemical potentials, etc. As the method is completely Lagrangian and particles follow the motion of the flow, the particles represent an unstructured data set at each point in time, i.e., the particles do not exhibit a regular spatial arrangement nor a fixed connectivity. For a recent detailed review of modern formulations of the SPH method see Rosswog (2009).

For the analysis of the simulation results, data visualization plays an important role. However, visualization methods need to account for the highly adaptive, unstructured data representation in SPH simulations. Reconstructing the entire data field over a regular grid is not an option, as it would either use grids of immense sizes that cannot be handled efficiently anymore or it inevitably would introduce significant interpolation errors. Such errors should be avoided, especially as they would occur most prominently in areas of high particle density, i.e., areas of highest importance are undersampled. Adaptive grids may be an option as interpolation errors can be kept low, but the adaptivity requires special treatments during the visualization process.

In this chapter, we introduce visualization methods that operate directly on the particle data, i.e., on unstructured point-based volumetric data. Section 3 introduces an approach to directly extract isosurfaces from a scalar field of the SPH simulation. Isosurfaces extraction is a common visualization concept and is suitable for SPH data visualization, as one is often interested in seeing boundaries of certain features.

Because of the use of radial kernel functions in SPH computations (which is crucial for exact conservation of energy, momentum, and angular momentum) together with a poor a resolution, one can observe that the extracted isosurfaces may be bumpy, especially in regions of low particle density. We approach this issue by introducing level-set methods for

scalar field segmentation that include a smoothing term and extracting isosurfaces from the smooth level-set function. Again, the level-set method is only operating on the positions of the particles and does not use any auxiliary grid to perform the computations. In Section 4, we describe the general approach of smooth isosurface extraction from SPH data based on level-set segmentation and in Section 5, we detail methods for improving the speed of the level-set approach narrow-band processing, a local isosurface extraction approach based on variational level sets, and a non-iterative second-order approximation of the signed distance function which is needed throughout the level-set processing.
The surfaces that are extracted from particle data are in form of a point cloud representation. Point-based rendering methods that display such surfaces without the necessity to first generate a triangular mesh from the point clouds have become popular in computer graphics within the last decades. We have developed an approach that uses image-space operations to create desired renderings of large point clouds at interactive rates without any pre-computations, i.e., not even computing neighborhoods of points. This property is desirable, as we want to interactively extract different surfaces and display them immediately. Section 6 provides the description of our approach including rendering features such as transparency and shadows.
Since SPH simulations include a multitude of fields, it is of interest to investigate them simultaneously and to explore their correlations. In Section 7, we investigate how multi-field features can be detected and visualized. Detection is based on a clustering in the multi-dimensional attribute space. The hierarchy of density clusters can be investigated using coordinated views of the cluster tree, parallel coordinates of the multi-dimensional attribute space, and a visualization of the volumetric physical space. The features are displayed in physical space using surface extraction and rendering.
Finally, in Section 8, we explain how multiple scalar and volume fields can be explored interactively using a visual system based on the methods described in this chapter. In addition to the methods already mentioned, we support some further common visualization functionality for scalar and vector fields.

2. Related work

In the astrophysics SPH community, visualization of slices through the volume, isosurface extraction, direct volume rendering techniques, and particle rendering as color-mapped points are most commonly used for the display of single scalar fields (Navratil et al., 2007; Walker et al., 2005). A tool that provides such functionality (except for isosurfaces) is the freely available visualization tool SPLASH (Price, 2007). The direct volume rendering is executed by a ray casting approach, where integration along the rays is performed by integrating the SPH kernel function. The high adaptivity of the SPH data forces one to use many rays to not lose details in densely populated regions, which makes this purely software-based direct volume rendering approach slow. Rotation, zooming, and similar desired features cannot be achieved at interactive framerates (requiring about 20 frames per second). Navratil et al. (2007) apply an inverse-distance-based interpolation for resampling the data to a regular grid prior to isosurface extraction. Also, volume rendering approaches tend to resample over a regular grid (Cha et al., 2009). However, due to the highly varying particle density (commonly ten orders of magnitude), the precision of these approaches that resample over a static grid is limited.

The generation of tetrahedral meshes from particle data also has a long tradition. Du & Wang (2006) give an overview over various approaches. Widely accepted are the results given by Delaunay tetrahedrization (Delaunay, 1934), whose implementation is also included into the Computational Geometry Algorithms Library (CGAL, 2011). More recent approaches try to improve existing Delaunay tetrahedrization algorithms with respect to robustness, quality, and efficiency. Robustness against numerical errors during Delaunay insertion (Pav & Walkington, 2004) or for boundary recovery (Sapidis & Perucchio, 1991) is desired. Quality criteria with respect to some design goals are often ensured by post-processing steps (Maur & Kolingerová, 2001). The incremental insertion method (Borouchaki et al., 1995; George et al., 1991) is one of the most efficient implementations. Still, computational costs are high. Co & Joy (2005) presented an approach for isosurface extraction from point-based volume data that uses local Delaunay triangulations, which keeps the number of points for each Delaunay triangulation step low and thus improves the overall performance. An approach that also operates locally, but is not based on tetrahedral meshes is given by Rosenberg & Birdwell (2008). They presented an approach based on extracting isosurfaces while marching through slices, which works at interactive rates for smaller number of particles. Our approach (Rosenthal & Linsen, 2006) was the first to extract isosurfaces directly from SPH data, which still outperforms the algorithms listed above.

In terms of volume rendering approaches, splatting of transparent particle sprites is a popular technique (Fraedrich et al., 2009; Hopf & Ertl, 2003; Hopf et al., 2004). A slice-based approach was presented by Biddiscombe et al. (2008). The approach that is closest to the volume rendering approach we propose in here is the work by Fraedrich et al. (2010). Instead of reconstructing the field on a static grid, they use a view-dependent grid. Hence, when the viewing parameters change, the reconstruction is recomputed, which allows for application to the highly adaptive structure of SPH data.

For the visualization of flow fields, direct and 2D streamline visualization methods are supported by the SPH data visualization tool SPLASH (Price, 2007). Other flow visualization methods for SPH data rely on reconstructing over a grid or on extracting and displaying integral lines using the SPH kernel. Schindler et al. (2009) make use of the SPH kernel by presenting a method for vortex core line extraction which operates directly on the SPH representation. It generates smoother and more spatially and temporally coherent results. The underlying predictor-corrector scheme is specialized for several variants of vortex core line definitions.

3. Direct isosurface extraction

Isosurface extraction is a standard visualization method for scalar volume data and has been subject to research for decades. We proposed a method that directly extracts surfaces from SPH simulation data without 3D mesh generation or reconstruction over a structured grid (Rosenthal, 2009; Rosenthal & Linsen, 2006; Rosenthal et al., 2007). It is based on spatial domain partitioning using a kd-tree and an indexing scheme for efficient neighbor search.

In every point in time, the result of an SPH simulation is an unstructured point-based volume data set. More precisely, it is a set of trivariate scalar fields $f : \mathbb{R}^3 \rightarrow \mathbb{R}$, whose values are given for a large, finite set of sample points $\mathbf{x}_i$, whose positions are unstructured, i.e., they are not arranged in a structured way, nor are any connectivity or neighborhood informations known for the sample point locations. To visualize such a scalar field, our intention is to extract an

isosurface $\Gamma_{\text{iso}} = \{\mathbf{x} \in \mathbb{R}^3 \ : \ f(\mathbf{x}) = v_{\text{iso}}\}$ with respect to a real isovalue v_{iso} out of the range of f.

Our approach consists of a geometry extraction and a rendering step. The geometry extraction step computes points $\mathbf{p}_k \in \mathbb{R}^3$ on the isosurface, i.e., $f(\mathbf{p}_k) = v_{\text{iso}}$, by linearly interpolating between neighbored pairs of samples. The neighbor information is retrieved by partitioning the 3D domain into cells using a *k*d-tree. The cells are merely described by their index and bit-wise index operations allow for a fast determination of potential neighbors. We use an angle criterion to select appropriate neighbors from the small set of candidates. The output of the geometry step is a point cloud representation of the isosurface. The final rendering step uses point-based rendering techniques to visualize the point cloud.

In the following, all integers indexed with d, such as a_{d} or 100_{d} denote binary numbers. The operator $\oplus$ denotes the bitwise Boolean exclusive-or operator. Finally, the operators $\ll$ and $\gg$ denote the bit-shift operators, which are recursively defined by

0. $a_{\text{d}} \ll 0 \ = \ a_{\text{d}} \quad \text{and} \quad a_{\text{d}} \gg 0 \ = \ a_{\text{d}}$.
1. $a_{\text{d}} \ll j \ = \ (a_{\text{d}} \ll (j-1)) * 2$.
2. $a_{\text{d}} \gg j \ = \ (a_{\text{d}} \gg (j-1)) \operatorname{div} 2$.

The indexing scheme of the *k*d-tree represents its construction. The father of node with binary index b_{d} has index $b_{\text{d}} \gg 1$ and its children have indices $b_{\text{d}} \ll 1$ and $(b_{\text{d}} \ll 1) \oplus 1_{\text{d}}$. Figure 1 shows a 2D example. Thus, we can navigate through the tree using fast binary operations. Moreover, qualitative propositions about the locations of cells can be made. For instance the cells with index 1111_{d} and 1000_{d} lie in diagonally distant corners of the *k*d-tree. Thus, most information is implicitly saved in the indexing scheme. We exploit this property for fast neighbor search.

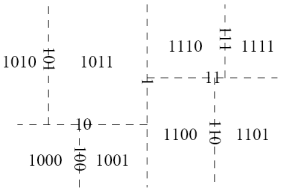

Fig. 1. Indexing scheme for two-dimensional *k*d-tree.

For validation, we have applied our approach to a sphere data set, which consists of randomly distributed sample points in a $200 \times 200 \times 200$ cube. The sample values describe the distance to the center of a sphere. We extract an isosurface from the distance field using isovalue 70. The generated and rendered sphere can be seen in Figure 2. Our direct isosurface extraction algorithm for scattered data produces results of quality close to the results from standard isosurface extraction algorithms for gridded data (like marching cubes). In comparison to 3D mesh generation algorithms (like Delaunay tetrahedrization), our algorithm is about one order of magnitude faster for our examples.

4. Smooth isosurface extraction

SPH uses radial smoothing kernels since they ensure the exact conservation of the physically conserved quantities (Rosswog, 2009). This has as a side effect that the particles are constantly re-adjusting their positions which can lead to "noise" in the particle velocities. Moreover,

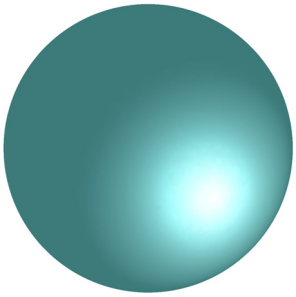

Fig. 2. Isosurface extracted from an example 16M particles.

in particular in sparsely sampled regions the radial kernels can produce some "bumpiness" when direct isosurface extraction from SPH scalar fields is applied. Figure 3(a) shows the result of direct isosurface extraction from SPH data. Here, points on the extracted isosurface are rendered as circular splats to show the noise issue. Hence, it is desirable to add a controllable smoothing term to the isosurface extraction procedure. Smooth surface extraction using partial differential equations (PDEs) is a well-known and widely used technique for visualizing volume data. Existing approaches operate on gridded data and mainly on regular structured grids. When considering unstructured point-based volume data, where sample points do not form regular patterns nor are they connected in any form, one would typically resample the data over a grid prior to applying the known PDE-based methods. We proposed an approach that directly extracts smooth surfaces from unstructured point-based volume data without prior resampling or mesh generation (Rosenthal & Linsen, 2008b).
When operating on unstructured data one needs to quickly derive neighborhood information, which we retrieve from the *k*d-tree. We exploit neighborhood information to estimate gradients and mean curvature at every sample point using a four-dimensional least-squares fitting approach. This procedure finally results in a closed formula for the gradient approximation. For a one-dimensional function φ, represented through the points $(x_1, \varphi_1), \ldots, (x_n, \varphi_n)$, we get

$$\frac{\mathrm{d}\varphi}{\mathrm{d}x} = \frac{n\sum_{i=1}^{n} x_i\varphi_i - \sum_{i=1}^{n} x_i \sum_{i=1}^{n} \varphi_i}{n\sum_{i=1}^{n} x_i^2 - \left(\sum_{i=1}^{n} x_i\right)^2} \,. \tag{1}$$

It can be shown that this scheme is a generalization of common finite differencing schemes. Having gradients $\nabla\varphi$ of the level-set function φ and mean curvature κ_φ computed, one can apply a PDE-based method that combines hyperbolic advection to an isovalue of a given scalar field and mean curvature flow. A time step is performed with respect to the equation

$$\frac{\partial\varphi}{\partial t} = \left(a\left(f - f_{\mathrm{iso}} - \varphi\right) + b\kappa_\varphi\right)\left|\nabla\varphi\right| \,, \tag{2}$$

which models hyperbolic normal advection, weighted with factor $a > 0$, and mean curvature flow, weighted with factor $b > 0$. This leads to a level-set segmentation algorithm. Since we are solving a partial differential equation by means of an explicit time integration scheme, the

time step is restricted by the Courant-Friedrichs-Lewy (CFL) stability criterion Courant et al. (1928). Due to different conditions in different parts of the fluid, the allowed time steps can vary considerably between different particles. In order to avoid the computational burden of advancing all particles globally on the shortest allowed time step, one can also advance different elements on their own individual time steps, a technique that is commonly used in expensive SPH simulations.

We extract a smooth surface by successively fitting a smooth level-set function to the data set. This level-set function is initialized as a signed distance function. For each sample and for every time step we compute the respective gradient, the mean curvature, and a stable time step. With this information the level-set function is manipulated using an explicit Euler time integration. The process successively continues with the next sample point in time. If the norm of the level-set function gradient in a sample exceeds a given threshold at some time, the level-set function is reinitialized to a signed distance function. After convergence of the evolution, the resulting smooth surface is obtained by extracting the zero isosurface from the level-set function using direct isosurface extraction from unstructured point-based volume data (as described above) and rendering the extracted surface using point-based rendering methods. Figure 3(b) shows the result of our smooth isosurface extraction for the same data set as in Figure 3(a) and using the same splat-based rendering method. It can be observed that the objective of extracting a smooth version of an isosurface has been achieved (especially in the zoomed-in view).

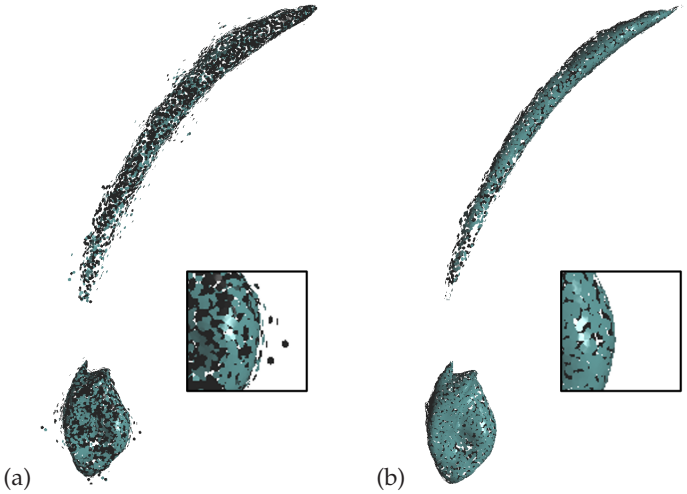

Fig. 3. Comparison between (a) direct isosurface extraction and (b) smooth isosurface extraction for an SPH simulation data set.

5. Acceleration of smooth isosurface extraction

5.1 Narrow-band processing

The global processing of the level-set function can be slow when dealing with unstructured point-based volume data sets containing several million data points. We developed an improved level-set approach that performs the process of the level-set function locally

(Rosenthal et al., 2010). Since for isosurface extraction we are only interested in the zero level set, values are only updated in regions close to the zero level set. In each iteration of the level-set process, the zero level set is extracted using direct isosurface extraction from unstructured point-based volume data and a narrow band around the zero level set is constructed. The band consists of two parts: an inner and an outer band. The inner band contains all data points within a small area around the zero level set. These points are updated when executing the level-set step. The outer band encloses the inner band providing all those neighbors of the points of the inner band that are necessary to approximate gradients and mean curvature. As before, neighborhood information is obtained using an efficient kd-tree scheme, gradients and mean curvature are estimated using a four-dimensional least-squares fitting approach.

The construction of the two-layer band around the zero level set is shown in Figure 4. The zero level set (colored blue) is extracted in form of a point cloud representation. Then, all sample points with distance to the zero level set less than a distance d_α are marked as belonging to the inner layer of the band (green). Thereafter, all additional sample points needed for the gradient computations within the level-set process are marked as belonging to the outer layer of the band (red points). All other sample points (grey) are not used for the current level-set step. The distance d_α can be estimated using the CFL condition that bounds the level-set step.

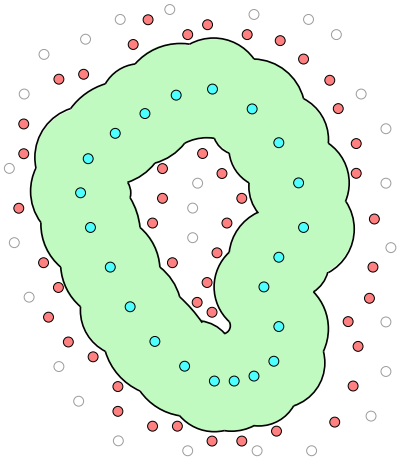

Fig. 4. Narrow-band construction for more efficient level-set processing.

How the level-set function is updated after having executed a level-set iteration on the narrow band with size d_α is shown in Figure 5: Points (green) with minimum distance to the zero-level-set points (blue) smaller than $\frac{d_\alpha}{4}$ have been in the α-band in the preceding time step and, thus, their level-set function values have been updated in the level-set iteration step. Points (red) in the outer band or with distance to the zero level set greater than $\frac{d_\alpha}{2}$ might have not be included in the computations of the last level-set iteration step. We assign their level-set function value to the signed distance to the zero-level-set points. For all points in the α-band with a distance to the zero level set in the range $\left[\frac{d_\alpha}{4}, \frac{d_\alpha}{2}\right]$, the new level-set function value is interpolated between the level-set function value from the preceding level-set step and their signed distance to the zero-level-set points.

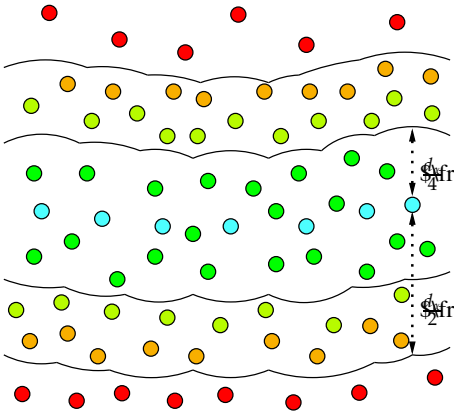

Fig. 5. Narrow-band update during level-set procedure (d_α denotes the size of the narrow band).

For performance analysis we applied it to an unstructured point-based volume data set with eight million randomly distributed samples. The data set was generated by resampling the regular Hydrogen data set of size $128 \times 128 \times 128$ to the random points. Illustrations of the evolution process for this data set are shown in Figure 6 (Data set courtesy of Peter Fassbinder and Wolfgang Schweizer, SFB 382 University Tübingen.). For each time step, a splat-based ray tracing of the zero level set is shown on the right-hand side. On the left-hand side, a point rendering of a slab of the data set is shown illustrating the narrow band. Extracted surface points of the zero level set are colored black, sample points in the α-band are colored green, and sample points in the outer band are colored red. Sample points not belonging to the narrow band are not rendered.
The whole local level-set process for extracting a smooth isosurface from the Hydrogen data set with eight million sample points and given nearest neighbors needed 24 steps and was performed in 6 minutes. For the four million version of the data set, the overall computation time for the entire level-set approach including pre-computations dropped to 84 seconds. This is a significant speed-up in comparison to the time of 13 minutes needed without the narrow-band processing. Still, it produces equivalent results in terms of quality and correctness.

5.2 Variational level-set detection of local isosurfaces

Another acceleration of the level-set approach can be achieved by only operating locally on a region of interest. We derived a variational formulation for smooth local isosurface extraction using an implicit surface representation in form of a level-set approach, deploying a moving least-squares (MLS) approximation, and operating on a kd-tree (Molchanov et al., 2011). The locality of our approach has two aspects: First, our algorithm extracts only those components of the isosurface, which intersect a subdomain of interest. Second, the action of the main term in the governing equation is concentrated near the current isosurface position. Both aspects reduce the computation times per level-set iteration. As for most level-set methods a reinitialization procedure is needed, but we also consider a modified algorithm where this step is eliminated. The final isosurface is extracted in form of a point cloud representation.

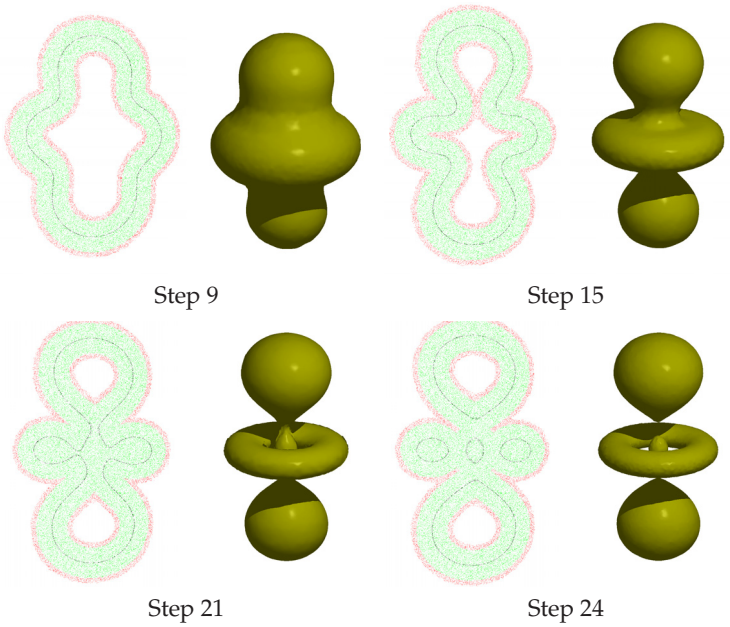

Fig. 6. Narrow-band level-set evolution.

We also presented a novel point completion scheme that allows us to handle highly adaptive point sample distributions.
A variational approach is used to derive the local level-set updates. We start with a construction of an error functional E, which is the target function that we want to minimize. The error depends on the given data f, the constant f_{iso} representing the isovalue, and a level-set function φ together with its derivatives of first order, i.e., $E = E(\varphi, \nabla\varphi; f, f_{\text{iso}})$. The total error consists of two weighted terms

$$E = E_1 + \lambda E_2, \tag{3}$$

measuring accuracy and smoothness of the solution, respectively. We propose to use

$$E_1 = \frac{1}{4}\int_D (\operatorname{sgn}(\varphi(\mathbf{x})) - \operatorname{sgn}(f(\mathbf{x}) - f_{\text{iso}}))^2 \,\mathrm{d}\mathbf{x}, \tag{4}$$

and

$$E_2 = \int_D \delta(\varphi(\mathbf{x}))\,|\nabla\varphi(\mathbf{x})|\,\mathrm{d}\mathbf{x}. \tag{5}$$

Here, we use the standard definitions of the sign function $\operatorname{sgn}(x)$ and the Dirac function $\delta(x)$ and the derivative is used in the sense of distributions.
A function φ_∞ minimizing some functional of the form $\int L(\varphi, \nabla\varphi)\,\mathrm{d}\mathbf{x}$ should satisfy the Euler-Lagrange equation

$$\left(\frac{\partial L}{\partial \varphi} - \sum_i \frac{\partial}{\partial x_i}\frac{\partial L}{\partial \varphi_i}\right)\Bigg|_{\varphi=\varphi_\infty} = 0, \tag{6}$$

where φ_i is the i-th component of $\nabla\varphi$. We derive the Euler-Lagrange equations for functionals E_1 and E_2. The idea of a level-set approach is to detect φ_∞ as a fixed point of an evolution equation for $\varphi = \varphi(\mathbf{x}, t)$ minimizing E. Here, t is an artificial time parameterizing the minimization process $\varphi(\mathbf{x}, t) \rightarrow \varphi_\infty(\mathbf{x})$ as $t \rightarrow \infty$. To construct the PDE, one equates the left-hand side of Euler-Lagrange Equation with $-\partial\varphi/\partial t$. For the functional E, it reads

$$\frac{\partial\varphi}{\partial t} = \delta(\varphi)\,(\mathrm{sgn}(f - f_{\mathrm{iso}}) - \mathrm{sgn}(\varphi)) + \lambda\,\delta(\varphi)\,\nabla\cdot\left(\frac{\nabla\varphi}{|\nabla\varphi|}\right). \tag{7}$$

Subsequently, this equation is regularized and discretized in space and time leading to an iterative process for the value of φ at each sample point. Using an explicit Euler time integration, we obtain the iteration step

$$\varphi^{k+1} = \varphi^k + \Delta t\left[\delta_\epsilon(\varphi^k)\,(\mathrm{sgn}(f - f_{\mathrm{iso}}) - \mathrm{sgn}_\epsilon(\varphi^k)) + \lambda\,\delta_{\epsilon'}(\varphi^k)\,\nabla\cdot\left(\frac{\nabla\varphi^k}{|\nabla\varphi^k|}\right)\right] \tag{8}$$

which is applied to all sample points $\mathbf{x}_i$, where the upper index k stands for the k-th layer in time. This update rule can be applied locally. Figure 7 shows how smooth isosurface components are extracted locally within a given region of interest.

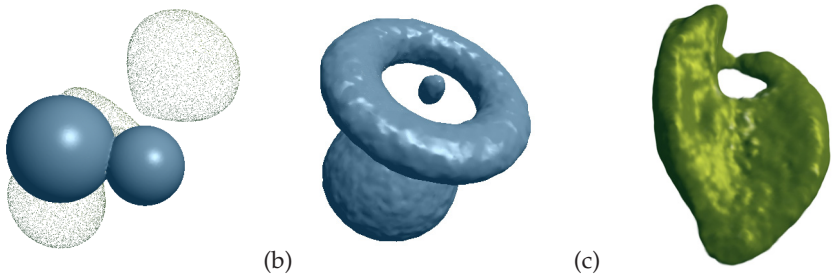

(a) (b) (c)

Fig. 7. Local level-set evolution of isosurfaces within a region of interest for multi-component data sets: (a) selecting region of interest; (b) extracted isosurface components; (c) same procedure applied to extract one component of an isosurface from the density field of an SPH simulation of a white dwarf.

5.3 Non-iterative second-order approximation of signed distance function

Signed distance functions are an obligatory ingredient to the level-set methods. When assuming that the underlying function is a signed distance function, several simplifications and speed-ups of the level set approach can be achieved. Usual approaches for the construction of signed distance functions to a surface are either based on iterative solutions of a special partial differential equation or on marching algorithms involving a polygonization of the surface. We propose a novel method for a non-iterative approximation of a signed distance function and its derivatives in a vicinity of a manifold. We use a second-order scheme to ensure higher accuracy of the approximation (Molchanov et al., 2010).

The manifold is defined (explicitly or implicitly) as an isosurface of a given scalar field, which may be sampled at a set of irregular and unstructured points. We use a spatial subdivision in form of a fast kd-tree implementation to access the samples and perform transformations on

the data. We derive a novel moving least-squares (MLS) approach for a second-order algebraic fitting to locally reconstruct the isosurface. Stability and reliability of the algorithm is achieved by a proper scaling of the MLS weights, accurate choices of neighbors, and appropriate handling of degenerate cases. We obtain the solution in an explicit form, such that no iterative solving is necessary, which makes our approach fast. The accuracy relies on second-order algebraic fitting.

We propose to perform the following steps to construct a signed distance field around an implicitly given isosurface:

1. Given a scalar field $f(\mathbf{x})$ on samples $\mathbf{x}_i$, extract a set of isopoints $\mathbf{p}_j$ corresponding to the isovalue f_{iso}; estimate normals on isopoints $\mathbf{n}_j$ using kd-tree and MLS technique. Skip this step if the isosurface is given explicitly.
2. For a given $\alpha > 0$ mark all samples $\mathbf{x}_i$ lying in α-neighborhood of the isosurface; jointly establish lists of neighboring isopoints for the marked samples.
3. For each sample $\mathbf{y}_k$ in the band find its neighbors and check two angles to detect a layer sheet.
4. If the sample lies between isosurface components, compute the distances to both of them as in the next step, compare the values found and take the minimal one.
5. If the criterion for a layer is not fulfilled:
   - perform a local sphere fitting to reconstruct a part of the isosurface close to $\mathbf{y}_k$,
   - if the sphere degenerates to a plane, compute a distance between the sample and the surface (taking into consideration its orientation),
   - if the sphere is not degenerated, use the isopoint normals to analyse its convexity and compute the distance between the sample and the sphere.

An accurate computation of the distance between a sample and an isosurface is hard if the isosurface is represented as a sparse set of isopoints. Therefore a (local) reconstruction of the smooth surface is required. In our approach we find an implicit algebraic surface to fit the discrete data which includes isopoints positions and associated normals. We consider algebraic spheres of the form

$$s(\mathbf{x}) = a_0 + \mathbf{a} \cdot \mathbf{x} + a_4 \mathbf{x} \cdot \mathbf{x}, \tag{9}$$

where $\mathbf{a} = (a_1, a_2, a_3)$ and $\mathbf{x} = (x_1, x_2, x_3)$. The solution may naturally degenerate to a plane as a_4 vanishes and therefore is exact for flat surfaces. However, a direct enrichment of the class is problematic: there exist no analytic formula for distance to algebraic ellipsoids. We utilize an approach of algebraic sphere fitting using positional and derivative constraints. First, we find $m+1$ isopoints nearest to the point of interest $\mathbf{y}$. Let h be the distance from $\mathbf{y}$ to the farthest neighbor. This parameter will define the support size of the weighting function

$$\omega_{\mathbf{y}}(\mathbf{p}) = \max\left\{ \left(1 - \frac{\|\mathbf{y}-\mathbf{p}\|^2}{h^2}\right)^4,\ 0 \right\}. \tag{10}$$

Now we look for the optimal algebraic sphere, whose zero-isosurface $\{\mathbf{x} \in \mathbb{R}^3 : s(\mathbf{x}) = 0\}$ optimally fits the positions of the isopoints, i.e., $s(\mathbf{p}_j) = 0$, and their normals, i.e., $\nabla s(\mathbf{p}_j) = \mathbf{n}_j$. The best fit is defined by parameters $a_0, \ldots, a_4$ minimizing the cost function

$$E(a_0, \ldots, a_4) = \sum_{j=1}^{m} \omega_j \left[|s(\mathbf{p}_j)|^2 + \beta \|\nabla s(\mathbf{p}_j) - \mathbf{n}_j\|^2 \right] \tag{11}$$

with $\omega_j = \omega_{\mathbf{y}}(\mathbf{p}_j)$. The minimization problem

$$s_{\text{opt}}(\mathbf{x};\, a_0, \ldots, a_4) = \arg\min E \tag{12}$$

has the following explicit solution

$$a_4 = \frac{\beta}{2} \frac{\sum \omega_j \mathbf{p}_j \cdot \mathbf{n}_j - \sum \omega_j \mathbf{p}_j \cdot \sum \omega_j \mathbf{n}_j / \Omega}{\sum \omega_j \mathbf{p}_j \cdot \mathbf{p}_j - \sum \omega_j \mathbf{p}_j \cdot \sum \omega_j \mathbf{p}_j / \Omega}, \tag{13}$$

$$\mathbf{a} = \sum \omega_j \mathbf{n}_j / \Omega - 2a_4 \sum \omega_j \mathbf{p}_j / \Omega, \tag{14}$$

$$a_0 = \mathbf{a} \cdot \sum \omega_j \mathbf{p}_j / \Omega - a_4 \sum \omega_j \mathbf{p}_j \cdot \mathbf{p}_j / \Omega, \tag{15}$$

where $\Omega = \sum \omega_j$.
Figure 8 shows the result when extracting different isosurfaces from a signed distance field to a surface in explicit point cloud representation. Isosurfaces for different isovalues f_{iso} of the signed distance function field constructed for the bunny data set with $35k$ surface points, (Data set courtesy of the Stanford University Computer Graphics Laboratory.).

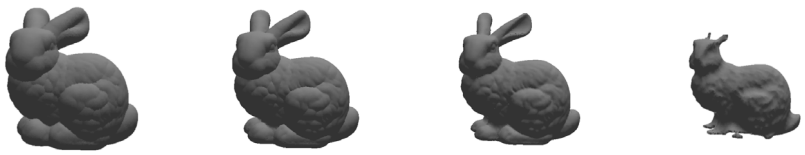

$f_{\text{iso}} = 4.0$ $f_{\text{iso}} = 2.0$ $f_{\text{iso}} = 0.0$ $f_{\text{iso}} = -3.5$

Fig. 8. Isosurfaces extracted from a non-iterative second-order approximation of the signed distance function to a surface in point cloud representation.

We proposed a novel method for the efficient computation of a signed distance function to a surface in point cloud representation. This allows us to develop a fast level-set approach for extracting smooth isosurfaces from point-based volume data, as we can use any point cloud surface as initial zero level set. Since for most applications a rough estimate of the desired surface can be obtained quickly, the overall level-set process can be shortened significantly. Additionally, we can avoid the computational overhead and numerical difficulties of PDE-based reinitialization.
In summary, putting all acceleration methods together we achieved to reduce the computation costs for the entire level-set approach including all components by about two orders of magnitude. For data sets with 16 million particles, the processing time dropped from tenths of minutes to tenths of seconds.

6. Image-space point cloud surface rendering

The extracted surfaces are given in point cloud surface representation, i.e., points on the surfaces with no structure or neighborhood known. Reconstructing a triangular mesh from

these point clouds can be very time consuming. Instead, point-based rendering approaches have gained a major interest in recent years, basically replacing global surface reconstruction with local surface estimations using, for example, splats or implicit functions. Crucial to their performance in terms of rendering quality and speed is the representation of the local surface patches. We presented a novel approach that goes back to the original ideas of Grossman & Dally (1998) to avoid any object-space operations and compute high-quality renderings by only applying image-space operations (Rosenthal & Linsen, 2008a).
Starting from a point cloud including normals (obtained from gradients of the underlying scalar field), we render a lit point cloud to a texture with color, depth, and normal information. Subsequently, we apply several filter operations. In a first step, we use a mask to fill background pixels with the color and normal of the adjacent pixel with smallest depth. The mask assures that only the desired pixels are filled. We use the eight masks shown in Figure 9, where the white pixels indicate background pixels and the dark pixels could be both background or non-background pixels. For each background pixel, we test whether the 3×3 neighborhood of that pixel matches any of the cases. In case it does, the pixel is not filled. Otherwise, it is filled with the color and depth information of the pixel with smallest depth out of the 3×3 neighborhood.

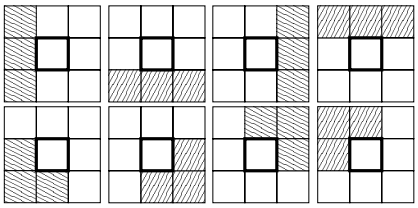

Fig. 9. Filters with size 3×3 for detecting whether a background pixel is beyond the projected silhouette of the object. If one of the eight masks matches the neighborhood of a background fragment, it is not filled. White cells indicate background pixels, dark cells may be background or non-background pixels.

Similarly, in a second pass, we fill the pixels that display occluded surface parts. The resulting piecewise constant surface representation does not exhibit holes anymore and is smoothed by a standard smoothing filter in a third step. The same three steps can also be applied to the depth channel and the normal map such that a subsequent edge detection and curvature filtering leads to a texture that exhibits silhouettes and feature lines. Anti-aliasing along the silhouettes and feature lines can be obtained by blending the textures. When highlighting the silhouette and feature lines during blending, one obtains illustrative renderings of the 3D objects. The GPU implementation of our approach achieves interactive rates for point cloud renderings without any pre-computation. Figure 10 shows the individual steps of the proposed pipeline including illustrative rendering. Figure 13(a) shows such another rendering result for a data set with 883k surface points. The rendering is performed at 52 frames per second (fps).
For a realistic visualization of the models, transparency and shadows are essential features. We propose extensions to our method for point cloud rendering with transparency and shadows at interactive rates (Dobrev et al., 2010a;b). Again, our approach does not require any global or local surface reconstruction method, but operates directly on the point cloud. All passes are executed in image space and no pre-computation steps are required. The

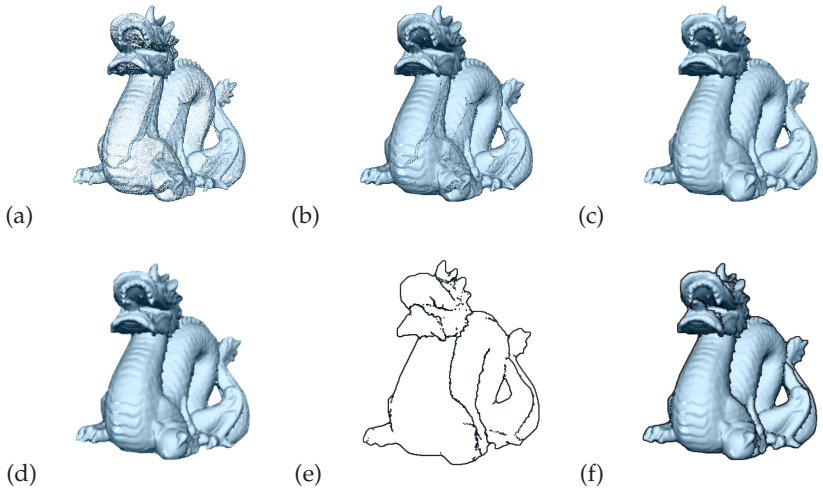

Fig. 10. Image-space point cloud surface rendering pipeline applied to the Dragon data set (Data set courtesy of Stanford University Computer Graphics Lab.): (a) Lit points; (b) after filling background pixel; (c) after filling occluded pixels; (d) after smoothing; (e) extracted feature lines; (f) illustrative rendering.

underlying technique for our approach is a depth peeling method for point cloud surface representations. The idea of depth peeling is to successively remove the front layer to extract hidden layers. Hence, one virtually renders the object and all visible parts represent the first layer. This is removed and the process is iterated to successively extract all hidden layers. For surfaces in point cloud representation, another challenge arises, as shown in Figure 11. When projecting the first layer (blue) in point cloud representation to the screen, the layer exhibits holes such that hidden layers (red) or the background (grey) become visible. To overcome the problem we use, again, the image-space masks presented above to produce layers without holes. Figure 12 shows four different layers of the Blade data set that are extracted using depth peeling.

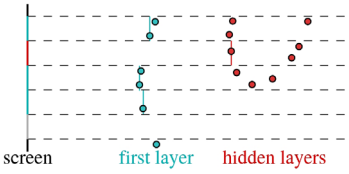

Fig. 11. Depth peeling for point cloud surfaces.

Having detected a sorted sequence of surface layers, they can be blended front to back with given opacity values to obtain renderings with transparency. These computation steps achieve interactive frame rates. Figure 13(b) shows a rendering with transparency. The rendering is performed at 17.5 fps.

To determine which parts of a surface are directly lit by a light source and which parts fall into the shadow of the light source, we determine and mark all points that are visible from the light

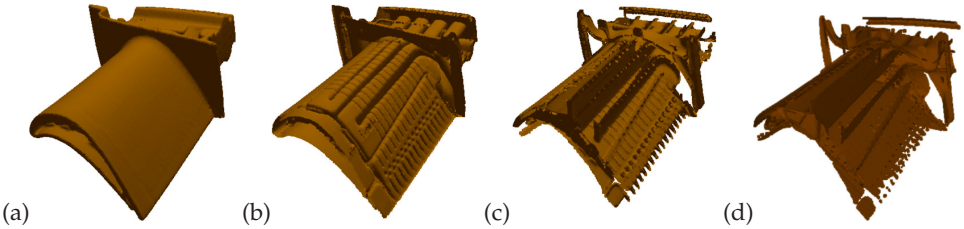

Fig. 12. Four successive layers extracted using depth peeling on point cloud surface representations.

source similar to "pre-baking" irradiance textures for polygonal mesh scenes. We use point cloud shadow textures, which are basically Boolean arrays that store which points are lit. Once the shadow texture is determined, lit points are drawn properly illuminated with ambient, diffuse, and specular reflection components using Phong's illumination model (Phong, 1975), while unlit points are only drawn using the ambient reflection component. This illumination creates the effect of shadows, as only those points are marked unlit where the light source is occluded by other surface parts.

To determine which points are visible from the light source, we render the scene with the light source's position being the viewpoint with depth testing enabled. All visible points are marked in an array. However, we observe that, due to the high point density, it is not unusual that several adjacent points of one surface layer project to the same fragment position. The suggested procedure would only mark the closest point for each fragment as lit, which would lead to an inconsistent shadow textures. Again, depth peeling is the key to solve this problem, but we apply it differently. While for transparent surface rendering our goal was to extract different surface layers, now we use it to find all the points that belong to a single surface layer, namely the closest one.

For the shadow texture computation, we also apply a Monte-Carlo integration method to approximate light from an area light source, leading to soft shadows. Shadow computations for point light sources are executed at interactive frame rates. Shadow computations for area light sources are performed at interactive or near-interactive frame rates depending on the approximation quality. Figure 13(c) shows a rendering with shadows using the Monte-Carlo approach. The rendering with 5 Monte Carlo samples is performed at 9 fps, while the rendering without Monte-Carlo sampling, i.e., with 1 sample, is performed at 25 fps.

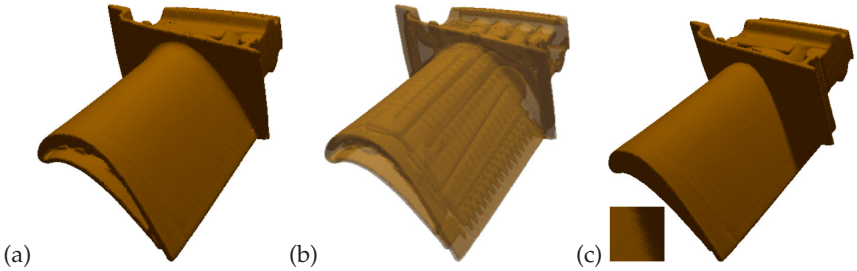

Fig. 13. (a) Image-space point cloud surface rendering applied to the Blade data set (courtesy of Visualization Toolkit). (b) Rendering with transparency using depth-peeling approach. (c) Rendering with shadows using Monte-Carlo integration.

We also investigated the use of ray tracing techniques for high-quality rendering based on splat representations, but the complexity of this approach impedes interactivity (Linsen et al., 2007).

7. Surface extraction from multiple fields

As the data sets resulting from SPH simulations typically contain a multitude of physical variables, it is desirable that visualization methods take into account the entire multi-field volume data rather than concentrating on one variable. We presented a visualization approach based on surface extraction from multi-field particle volume data (Linsen et al., 2008). The surfaces segment the data with respect to the underlying multi-variate function. Decisions on segmentation properties are based on the analysis of the multi-dimensional attribute space. The attribute space exploration is performed by an automated multi-dimensional hierarchical clustering method, whose resulting density clusters are shown in the form of density level sets in a 3D star coordinate layout (Long, 2010; Long & Linsen, 2011). In the star coordinate layout, the user can select clusters of interest. A selected cluster in attribute space corresponds to a segmenting surface in object space. Based on the segmentation property induced by the cluster membership, we extract a surface from the volume data. We directly extract our surfaces from the SPH data without prior resampling or grid generation. The surface extraction computes individual points on the surface, which is supported by an efficient neighborhood computation. The extracted surface points are, again, rendered using point-based rendering operations. Our approach combines methods in scientific visualization for object-space operations with methods in information visualization for attribute-space operations.

7.1 Attribute space visualization

Given the multi-dimensional attribute space with a large number of d-dimensional points lying in that attribute space, each point corresponds to one sample of the volumetric data field and each dimension represents one data attribute (typically one scalar value) stored at that sample. In order to understand the distribution of the points in attribute space, we propose to compute a density function and to determine the number of clusters as well as the high density region of each cluster. Given a multivariate density function $f(x)$ in d dimensions, modes of $f(x)$ are positions where $f(x)$ has local maxima. Thus, a mode of a given distribution is more dense than its surrounding area. We want to find the attraction regions of modes. To do so, we choose various values for constants λ $(0 < \lambda < \sup_x f(x))$ and consider regions of the particle space where values of $f(x)$ are greater than or equal to λ. The λ-level set of the density function $f(x)$ denotes a set $S(f,\lambda) = \{x \in \mathbb{R}^d : \ f(x) \geq \lambda\}$. The set $S(f,\lambda)$ consists of a number q of connected components $S_i(f,\lambda)$ that are pairwise disjoint. The subsets $S_i(f,\lambda)$ are called λ-density clusters (λ-clusters for short). A cluster can contain one or more modes of the respective density function. Let the domain of the data set be given in the form of a d-dimensional hypercube, i. e., a d-dimensional bounding box. To derive the density function, we spatially subdivide the domain of the data set into cells of equal shape and size. Thus, the spatial subdivision provides a binning into d-dimensional cells. For each cell we count the number of points lying inside. The multivariate density function $f(x)$ is given by the number of points per cell divided by the cell's area and the overall number of data points. As the area is equal for all cells, the density of each cell is proportional to the number of data points lying inside the cell. The cell should be small enough such that local changes of the density

function can be detected but also large enough to contain a large number of points such that averaging among points is effective. Because of the curse of dimensionality, there will be many empty cells. We do not need to store empty cells such that the amount of cells we are storing and dealing with is (significantly) smaller than the number of the d-dimensional points. The λ-clusters can be computed by detecting regions of connected cells with densities larger than λ. As we identify density with point counts, the densities are integer values. Hence, we start by computing density clusters for $\lambda = 1$. Subsequently, we process each detected λ-cluster individually by iteratively removing those cells with minimum density, where the minimum density increases in steps of 1. If this process causes a cluster to fall into two subclusters, the subclusters represent higher-density clusters within the original cluster. If a cluster does not fall into subclusters during the process, it is a mode cluster. This process generates a hierarchical structure, which is summarized by the high density cluster tree (short: cluster tree). The root of the cluster tree represents all points. Figure 14(a) shows a cluster tree with 4 mode clusters represented by the tree's leaves. Cluster tree visualization provides a method to understand the distribution of data by displaying the attraction regions of modes of the multivariate density function. Each cluster contains at least one mode.

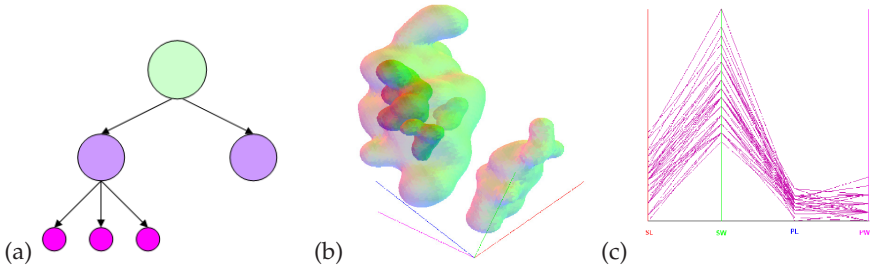

Fig. 14. (a) Cluster tree of density visualization with four modes shown as leaves of the tree. (b) Nested density cluster visualization based on cluster tree using 3D star coordinates. (c) Right-most cluster in (b) is selected and its homogeneity is evaluated using parallel coordinates.

Having computed the d-dimensional high density clusters, we need to project them into a three-dimensional space for visualization purposes. In order to visualize the high density clusters in a way that allows clusters to be correlated with the d dimensions, we need to use a coordinate system that incorporates all d dimensions. Such a coordinate system can be obtained by using star coordinates. When projecting the d-dimensional high density clusters into a three-dimensional star coordinate representation, clusters should remain clusters. Thus, points that are close to each other in the d-dimensional feature space should not be further apart after projection into the three-dimensional space. Let O be the origin of the $3D$ star coordinate system and $(a_1, \ldots, a_d)$ be a sequence of d three-dimensional vectors representing the axes. The mapping of a d-dimensional data point $x = (x_1, \ldots, x_d)$ to a three-dimensional data point $\Pi(x)$ is determined by the average sum of vectors a_k of the $3D$ star coordinate system multiplied with its attributes x_k for $k = 1, \ldots, d$, i.e.,

$$\Pi(x) = O + \frac{1}{d} \sum_{k=1}^{d} x_k a_k. \tag{16}$$

Since it can be shown that

$$||\Pi(x) - \Pi(y)||_1 \leq ||x - y||_1 \tag{17}$$

for any d-dimensional points x and y, the distance of the images of two d-dimensional points is lower than or equal to the distance of the points with respect to the L_1-norm. Therefore, two points in the multi-dimensional space are projected to $3D$ star coordinates preserving the similarity properties of clusters (at least with respect to the L_1-norm). In other words, the mapping of d-dimensional data to the 3D visual space does not break clusters. The second property that our projection from multi-dimensional feature space into three-dimensional star coordinate systems should fulfill is that separated clusters should not be projected into the same region. The projection into star coordinates may cause severe cluttering of clusters when not carefully choosing the axes $(a_1, \ldots, a_d)$. To alleviate the problem of overlapping clusters we introduce a method which chooses a "good" coordinate system. Assume that a hierarchy of high density clusters have q mode clusters, which do not contain any higher level densities. Let m_i be the barycenter of the points within the ith cluster, $i = 1, \ldots, q$. We want to choose a projection that maintains best the distances between clusters. Let $\{v_1, v_2, v_3\}$ be an orthonormal basis of the candidate three-dimensional space of projections. The desired choice of a $3D$ star coordinate layout is to maximize the distance of the q projected barycenters $V^T m_i$ with $V = [v_1, v_2, v_3]^T$, i.e. to maximize the objective function

$$\sum_{i<j} ||V^T m_i - V^T m_j||^2 = \text{trace}(V^T S V) \tag{18}$$

with

$$S = \sum_{i<j} (m_i - m_j)(m_i - m_j)^T . \tag{19}$$

Thus, the three vectors v_1, v_2, v_3 are the three unit eigenvectors corresponding to the three largest eigenvalues of matrix S. This step is a principal component analysis (PCA) applied to the barycenters of the clusters. As a result, we choose the d three-dimensional axes of the $3D$ star coordinate system as $a_i = (v_{1i}, v_{2i}, v_{3i})$, $i = 1, \ldots, d$.

Obviously, we can also project into 2D coordinates in the same way. However, when comparing and evaluating projections to 2D and 3D visual space (Poco et al., 2011), a quantitative analysis confirms that 3D projections outperform 2D projections in terms of precision. Moreover, a user study indicates that certain tasks can be more reliably and confidently answered with 3D projections. Nonetheless, as 3D projections are displayed on 2D screens, interaction is more difficult.

After having computed the projected clusters, we can display them using star coordinates by rendering a point primitive for each projected data point. A less cluttered and more beautiful display is to render the boundary of the clusters. Considering the cluster that is described by the set of points $\{p_i = (x_i, y_i, z_i) : i = 1, \ldots, m\}$ after being projected into the 3D space. In order to compute the boundary of this group of points,we need to have a continuous representation of the group. Therefore, we consider the function

$$f_h(p) = \sum_{i=1}^{m} K\left(\frac{p - p_i}{h}\right), \; p \in \mathbb{R}^3 , \tag{20}$$

where K is a kernel function and h is the bandwidth. Then, we can reconstruct the field over a regular grid and render the boundary set of the points by using standard isosurface extraction

methods to extract the boundary surface of the set $S(h,c) = \{p \in \mathbb{R}^3 : f_h(p) \geq c\}$, where c is an isovalue. We choose parameter h and c to guarantee that $S(h,c)$ is connected and has a volume of minimum extension. The kernel function should be sufficiently smooth and have a small compact support. For example, we can choose $K(p) = (1 - ||p||^2)^2$ for $||p|| \leq 1$ and $K(p) = 0$ otherwise and the bandwidth h to be equal to the longest length of the minimum spanning tree of these m points. In Figure 14(b) we show the visualization of the clusters by rendering such boundary surfaces, where it can be shown that for the chosen kernel isovalue $c = \frac{9}{16}$ is appropriate. In order to visualize all clusters of the cluster tree, we render the surfaces in a semi-transparent fashion. The resulting visualization shows sequences of nested surfaces, where the inner surfaces represent higher density levels. Figure 14(b) shows the nested density cluster visualization with respect to the cluster tree in Figure 14(a).

7.2 Coordinated views

Generating all clusters and displaying them in star coordinates allows for further analysis of the detected clusters. The simplest interaction method is to select individual clusters by just clicking at the boundary surface. When a cluster is selected, intra-cluster variability is visualized using parallel coordinates, see Figure 14(b) and (c). In both pictures the relation between the selected cluster with the dimension can be observed.

Moreover, we visualize the coordinated view in physical space, which exhibits the spatial location of the selected feature. The rendering in physical space can be preformed by just plotting all particles that belong to the selected feature or by extracting a boundary surface of that feature, i.e., a surface that separates all particles that belong to the feature from all particles that do not belong to the feature. Figure 15 shows an attribute-space rendering of the detected clusters in 3D optimized star coordinates (a), a color-coded object-space rendering of the clustered particles (b), and a separation surface of clusters in object space (c). The underlying SPH simulation is that of tidal disruption and ignition of a white dwarf by a moderately massive black hole (Rosswog et al., 2009).

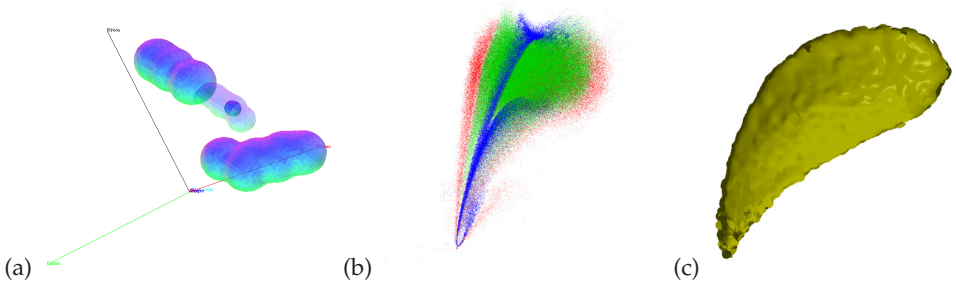

(a) (b) (c)

Fig. 15. (a) Seven-dimensional attribute space visualization of SPH data set using optimized 3D star coordinates. (b) Object space visualization of cluster distribution. (c) Object space visualization of a separating surface.

For the visualization of enclosing surfaces in attribute as well as in object space, we looked into an alternative approach of enclosing surfaces for point clusters using 3D discrete Voronoi diagrams (Rosenthal & Linsen, 2009). Our system provides three different types of enclosing surfaces. By generating a discrete distance field to the point cluster and extracting an isosurface from the field, an enclosing surface with any distance to the point cluster can be

generated. As a second type of enclosing surfaces, a hull of the point cluster is extracted. The generation of the hull uses a projection of the discrete Voronoi diagram of the point cluster to an isosurface to generate a polygonal surface. Generated hulls of non-convex clusters are also non-convex. The third type of enclosing surfaces can be created by computing a distance field to the hull and extracting an isosurface from the distance field. This method exhibits reduced bumpiness and can extract surfaces arbitrarily close to the point cluster without losing connectedness. Figure 16 shows the idea of the different approaches starting from an isosurface from the distance field to the point cluster (a), connecting the neighbors that contribute to the surface in (a) to form a non-convex hull (b), and computing surfaces that are equidistant to the computed non-convex hull (b). Figure 17 shows a comparison of the different enclosing surfaces when applied to a cluster of points when projected into optimized star coordinates.

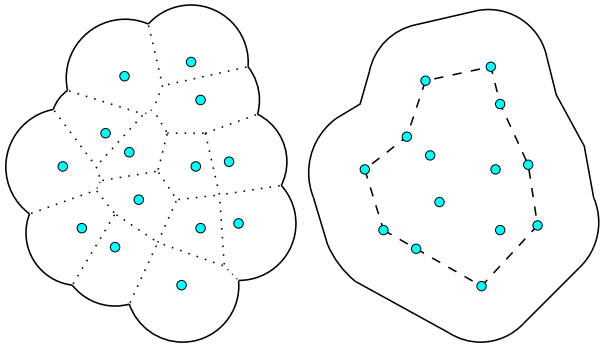

Fig. 16. (a) Extracting an isosurface from the distance field to the point cluster. Voronoi regions on the isosurface induce neighborhoods. (b) Neighbors are connected to form a hull. The image also shows an isosurface extracted from the distance field to the hull.

We extended our work on interactivity by explicitly encoding the cluster hierarchy in a tree that is visually encoded in a radial layout. Coordinated views between cluster tree visualization and parallel coordinates as well as object-space visualizations allow for an interactive analysis of multi-field SPH data (Linsen et al., 2009). The cluster tree allows for the selection of detected clusters, the parallel coordinate plots show the properties of the selected clusters, and object-space visualizations in form of extracted surfaces or particle distributions exhibit the location of the respective clusters in physical space. Figure 18 shows such a visual analysis set-up when applied to the IEEE Visualization Contest data (Rosenthal et al., 2008).
We also proposed a method to integrate the parallel coordinates into the cluster tree visualization. The MultiClusterTree approach (Long & Linsen, 2011) uses circular parallel coordinates for the embedding into the radial hierarchical cluster tree layout, which allows for the analysis of the overall cluster distribution. This visual representation supports the comprehension of the relations between clusters and the original attributes. The combination of the 2D radial layout and the circular parallel coordinates is used to overcome the overplotting problem of parallel coordinates when looking into data sets with many records. Figure 19 shows how integrated circular coordinates can provide a good overview of the cluster distribution.

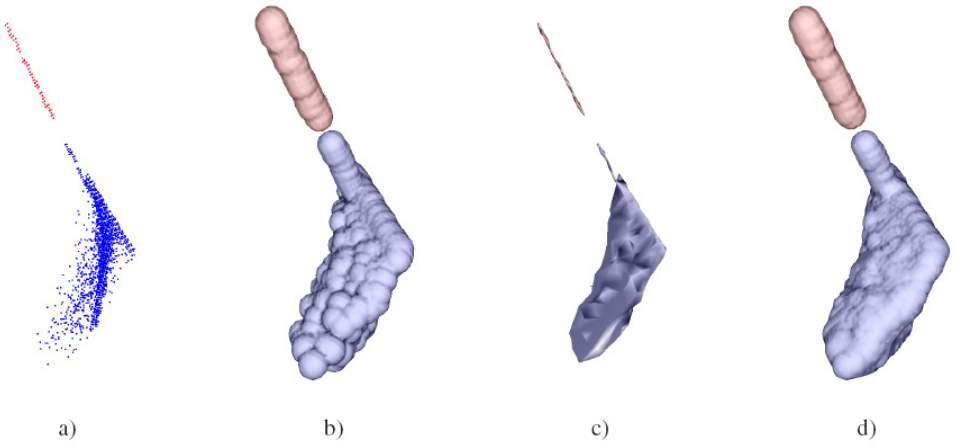

Fig. 17. Different visualizations of two point clusters (colored red and blue) from the 2008 IEEE Visualization Design Contest data. The clusters were found using density-based clustering of multidimensional feature space and were projected to a 3D visual space using a linear projection. Additionally to the cluster points (a), three types of enclosing surfaces are shown. (b) Isosurface extraction from distance field computed using a 3D discrete Voronoi diagram of resolution $256 \times 256 \times 256$. (c) Hull of the cluster computed from the isosurface of the distance field. (d) Isosurface extraction from distance field to hull.

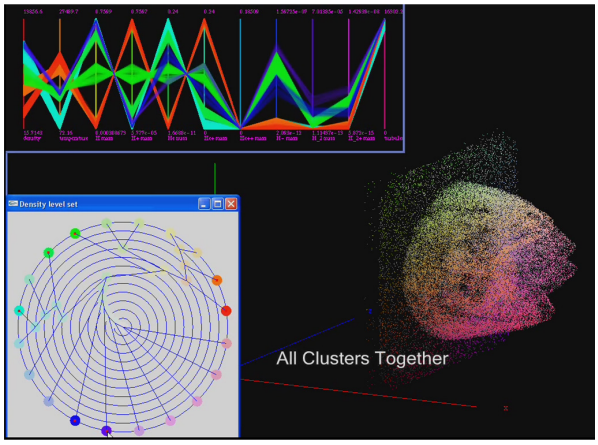

Fig. 18. Coordinated views allow for selecting clusters in cluster tree and investigating properties in attribute space (using parallel coordinates) as well as locations in physical space.

8. Interactive visual system for exploration of multiple scalar and flow fields

Our research results are combined in the SmoothViz software system that is offered to the SPH community via our website (http://vcgl.jacobs-university.de/software). Not all presented features are included yet. Currently, the system consists of three modules responsible

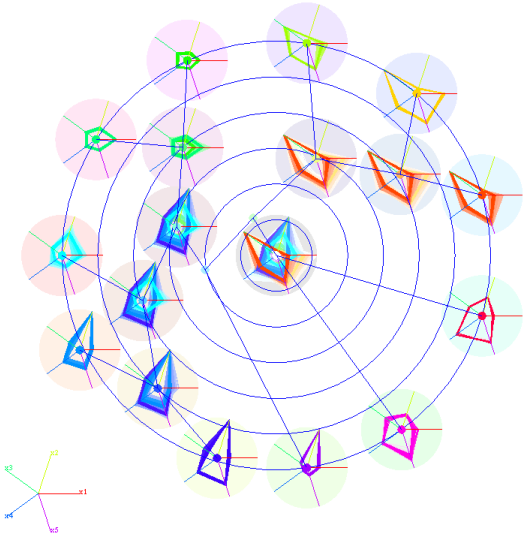

Fig. 19. Integrated circular parallel coordinates in clusters tree visualization for data set with hierarchical clusters.

for time-varying data manipulation, scalar field exploration, and flow field visualization. An intuitive graphical user interface (GUI) allows for easy processing and interaction. Additional functionalities and visualizations that are common in the SPH community have been included.

First, the user can load SPH data containing time-varying particle positions and time-varying multiple scalar and vector field values sampled at the particles. A 3D view of the particle distribution at a chosen time step allows the user to adjust the viewing parameters using arbitrary rotation and translation of camera. Loading of successive or preceding time steps from the time-varying series of data sets is as easy as play or rewind in a standard media player. Extracted pathlines can show evolution in time of an individual particle or sets of particles. Figure 20(a) shows the GUI and a particle distribution plot for a chosen time step.

There are two options to represent the structure of a selected scalar field: Maximal intensity projection plots can render any of the scalar fields using one of the build-in color maps and allowing for manually modifying the transfer function. Figure 20(b) shows the GUI for the transfer function modification and the respective maximum intensity plot of a chosen scalar field. Alternatively, isosurfaces can be extracted for interactively selected isovalues and shown using a point splatting technique or a dense point cloud rendering. Figure 20(c) shows a number of nested isosurfaces using point cloud renderings.

Finally, a specified number of streamlines can be computed with respect to the vector field chosen by the user. Combined views are possible to explore multiple fields simultaneously, e.g. multiple isosurfaces together with stream- or pathlines. Figure 20(d) shows an isosurface rendering using point splatting combined with a rendering of selected streamlines. For more details on the system, we refer to the user manual that comes with the SmoothViz software package.

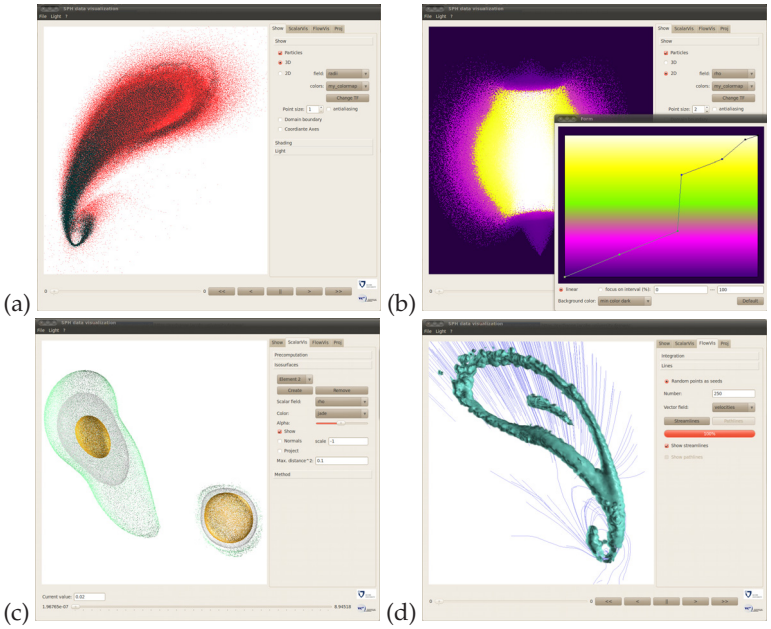

Fig. 20. Screenshots of SmoothViz software system for SPH data exploration: (a) Three-dimensional particle distribution modeling a White Dwarf passing close to a Black Hole. (b) Maximal intensity projection plot of the density field of a White Dwarf with user defined transfer function; (c) Several density isosurfaces of two White Dwarfs in point-based representation. (d) Interplay of a velocity field (shown with streamlines) and a temperature field (shown as splatted isosurface).

9. Conclusion

We have presented approaches for visualization of SPH data. All methods operate directly on the particles that are distributed in a highly adaptive and irregular manner and that do not have any connectivity. Operating on the particles avoids the introduction of errors that occur when resampling to a grid. Our visualizations focus on surface extractions from such data. We first presented an isosurface extraction from any scalar field of the SPH data. It exploits a fast navigation through a *k*d-tree via an indexing structure and allows for fast isosurface extraction of high quality. Because of approximations made during simulation, it is desirable to add a smoothing term to the isosurface extraction method. This is achieved by the use of level-set methods. Again, the method operates on the particles only. We have presented several ways on how to accelerate the computations including a narrow-band approach, a local variational approach, and a signed distance function computation to any isosurface representation. Extracted isosurfaces are given in form of point clouds. We presented how they can be rendered using an image-space point cloud rendering approach that avoids any pre-computation and thus can immediately applied to any extracted surface. Shadows and transparency are supported at interactive rates. We further extended the work to the extraction of boundary surfaces of features in multi-field data. The attribute space of the multi-field data is being explored using clustering and cluster visualization

methods. Coordinated or integrated views to parallel or circular coordinates, respectively, allow for further visual analysis of the properties of the extracted clusters. Coordinated views to object space allow for the investigation of the spatial distribution of detected features. Enclosing surfaces show the cluster boundaries. The presented functionality has partially been incorporated into the SmoothViz software package including further features such as geometric flow visualization. It allows for interactive exploration and integrated analysis of multiple fields of SPH data.

10. Acknowledgments

This work was supported by the German Research Foundation (DFG) under grant number LI 1530/6-1.

11. References

Biddiscombe, J., Graham, D. & Maruzewski, P. (2008). Visualization and analysis of SPH data, *ERCOFTAC Bulletin* 76(9-12).

Borouchaki, H., Hecht, F., Saltel, E. & George, P. (1995). Reasonably efficient delaunay based mesh generator in 3 dimensions, *4th International Meshing Roundtable*, Sandia National Laboratories, pp. 3–14.

CGAL (2011). Computational geometry algorithms library (CGAL), http://www.cgal.org/.

Cha, D., Son, S. & Ihm, I. (2009). Gpu-assisted high quality particle rendering, *Computer Graphics Forum* 28(4): 1247–1255.

Co, C. S. & Joy, K. I. (2005). Isosurface Generation for Large-Scale Scattered Data Visualization, *in* G. Greiner, J. Hornegger, H. Niemann & M. Stamminger (eds), *Proceedings of Vision, Modeling, and Visualization 2005*, Akademische Verlagsgesellschaft Aka GmbH, pp. 233–240.

Courant, R., Friedrichs, K. & Lewy, H. (1928). Über die partiellen differenzengleichungen der mathematischen physik, *Mathematische Annalen* 100(1): 32 – 74.

Delaunay, B. N. (1934). Sur la sphere vide, *Bull. Acad. Sci. USSR* 7: 793–800.

Dobrev, P., Rosenthal, P. & Linsen, L. (2010a). An image-space approach to interactive point cloud rendering including shadows and transparency, *Computer Graphics and Geometry* 12(3): 2–25.

Dobrev, P., Rosenthal, P. & Linsen, L. (2010b). Interactive image-space point cloud rendering with transparency and shadows, *in* V. Skala (ed.), *Communication Papers Proceedings of WSCG, The 18th International Conference on Computer Graphics, Visualization and Computer Vision*, UNION Agency – Science Press, Plzen, Czech Republic, pp. 101–108.

Du, Q. & Wang, D. (2006). Recent progress in robust and quality delaunay mesh generation, *J. Comput. Appl. Math.* 195(1): 8–23.

Fraedrich, R., Auer, S. & Westermann, R. (2010). Efficient high-quality volume rendering of sph data, *IEEE Transactions on Visualization and Computer Graphics* 16: 1533–1540.

Fraedrich, R., Schneider, J. & Westermann, R. (2009). Exploring the "millennium run" - scalable rendering of large-scale cosmological datasets, *IEEE Transactions on Visualization and Computer Graphics* 15(6): 1251–1258.

George, P. L., Hecht, F. & Saltel, E. (1991). Automatic mesh generator with specified boundary, *Comput. Methods Appl. Mech. Eng.* 92(3): 269–288.

Gingold, R. A. & Monaghan, J. J. (1977). Smoothed particle hydrodynamics - Theory and application to non-spherical stars, *Monthly Notices of the Royal Astronomical Society* 181: 375–389.

Grossman, J. P. & Dally, W. J. (1998). Point sample rendering, *Proceedings of 9th Eurographics Workshop on Rendering*, pp. 181–192.

Hopf, M. & Ertl, T. (2003). Hierarchical splatting of scattered data, *Visualization Conference, IEEE* .

Hopf, M., Luttenberger, M. & Ertl, T. (2004). Hierarchical splatting of scattered 4d data, *IEEE Computer Graphics and Applications* 24: 64–72.

Linsen, L., Long, T. V. & Rosenthal, P. (2009). Linking multi-dimensional feature space cluster visualization to surface extraction from multi-field volume data, *IEEE Computer Graphics and Applications* 29(3): 85–89.

Linsen, L., Long, T. V., Rosenthal, P. & Rosswog, S. (2008). Surface extraction from multi-field particle volume data using multi-dimensional cluster visualization, *IEEE Transactions on Visualization and Computer Graphics* 14(6): 1483–1490.

Linsen, L., Müller, K. & Rosenthal, P. (2007). Splat-based ray tracing of point clouds, *Journal of WSCG* 15(1–3): 51–58.

Long, T. V. (2010). *Visualizing High Density Clusters in Multidimensional Data*, PhD thesis, Jacobs University.

Long, T. V. & Linsen, L. (2011). Visualizing high density clusters in multidimensional data using optimized star coordinates, *Journal of Computational Statistics (to appear)* .

Lucy, L. B. (1977). A numerical approach to the testing of the fission hypothesis, *Astronomical Journal* 82: 1013–1024.

Maur, P. & Kolingerová, I. (2001). Post-optimization of delaunay tetrahedrization, *SCCG '01: Proceedings of the 17th Spring conference on Computer graphics*, IEEE Computer Society, Washington, DC, USA, p. 31.

Molchanov, V., Rosenthal, P. & Linsen, L. (2010). Non-iterative second-order approximation of signed distance function for any isosurface representation, *Computer Graphics Forum* 29(3): 1211–1220.

Molchanov, V., Rosenthal, P. & Linsen, L. (2011). Variational level-set detection of local isosurfaces from unstructured point-based volume data, *Schloss Dagstuhl Scientific Visualization Workshop 2009 Follow-up, to appear*.

Navratil, P. A., Johnson, J. L. & Bromm, V. (2007). Visualization of cosmological particle-based datasets, 13(6): 1712–1718.

Pav, S. E. & Walkington, N. J. (2004). Robust three dimensional delaunay refinement, *13th International Meshing Roundtable*, Sandia National Laboratories, SAND 2004-3765C, pp. 145–156.

Phong, B. T. (1975). Illumination for computer generated pictures, *Commun. ACM* 18: 311–317.

Poco, J., Etemadpour, R., Paulovich, F. V., Long, T. V., Rosenthal, P., de Oliveira, M. C. F., Linsen, L. & Minghim, R. (2011). A framework for exploring multidimensional data with 3d projections, *Computer Graphics Forum* 30(3): 1111–1120.

Price, D. (2007). SPLASH: An interactive visualisation tool for smoothed particle hydrodynamics simulations, *Publications of the Astronomical Society of Australia* 24: 159–173.

Rosenberg, I. D. & Birdwell, K. (2008). Real-time particle isosurface extraction, *Proceedings of the 2008 symposium on Interactive 3D graphics and games*, I3D '08, ACM, New York, NY, USA, pp. 35–43.

Rosenthal, P. (2009). *Direct Surface Extraction from Unstructured Point-based Volume Data*, Shaker Verlag, Aachen, Germany (Ph.D. Thesis Jacobs University, Bremen, Germany).

Rosenthal, P. & Linsen, L. (2006). Direct isosurface extraction from scattered volume data, *in* B. S. Santos, T. Ertl & K. I. Joy (eds), *Eurographics / IEEE VGTC Symposium on Visualization - EuroVis 2006*, pp. 99–106,367.

Rosenthal, P. & Linsen, L. (2008a). Image-space point cloud rendering, *Proceedings of Computer Graphics International*, pp. 136–143.

Rosenthal, P. & Linsen, L. (2008b). Smooth surface extraction from unstructured point-based volume data using PDEs, *IEEE Transactions on Visualization and Computer Graphics* 14(6): 1531–1546.

Rosenthal, P. & Linsen, L. (2009). Enclosing surfaces for point clusters using 3d discrete voronoi diagrams, *Computer Graphics Forum* 28(3): 999–1006.

Rosenthal, P., Long, T. V. & Linsen, L. (2008). "Shadow Clustering": Surface extraction from non-equidistantly sampled multi-field 3D scalar data using multi-dimensional cluster visualization, VisWeek 08 Conference Compendium, Winner of IEEE Visualization Design Contest.

Rosenthal, P., Molchanov, V. & Linsen, L. (2010). A narrow band level set method for surface extraction from unstructured point-based volume data, *in* V. Skala (ed.), *Proceedings of WSCG, The 18th International Conference on Computer Graphics, Visualization and Computer Vision*, UNION Agency – Science Press, Plzen, Czech Republic, pp. 73–80.

Rosenthal, P., Rosswog, S. & Linsen, L. (2007). Direct surface extraction from smoothed particle hydrodynamics simulation data, *Proceedings of the 4th High-End Visualization Workshop*, Lehmanns Media - LOB, pp. 50–61.

Rosswog, S. (2009). Astrophysical smooth particle hydrodynamics, *New Astronomy Reviews* 53(4-6): 78 – 104.

Rosswog, S., Ramirez-Ruiz, E. & Hix, W. R. (2009). Tidal Disruption and Ignition of White Dwarfs by Moderately Massive Black Holes, *Astrophysical Journal* 695: 404–419.

Sapidis, N. S. & Perucchio, R. (1991). Domain delaunay tetrahedrization of arbitrarily shaped curved polyhedra defined in a solid modeling system, *SMA '91: Proceedings of the first ACM symposium on Solid modeling foundations and CAD/CAM applications*, ACM Press, New York, NY, USA, pp. 465–480.

Schindler, B., Fuchs, R., Biddiscombe, J. & Peikert, R. (2009). Predictor-corrector schemes for visualization ofsmoothed particle hydrodynamics data, *IEEE Transactions on Visualization and Computer Graphics* 15: 1243–1250.

Walker, R., Kenny, P. & Miao, J. (2005). Visualization of Smoothed Particle Hydrodynamics for Astrophysics, *in* L. Lever & M. McDerby (eds), *Theory and Practice of Computer Graphics 2005*, Eurographics Association, University of Kent, UK, pp. 133–138. (Electronic version http://diglib.eg.org).
URL: *http://www.cs.kent.ac.uk/pubs/2005/2230*

2

Using DEM in Particulate Flow Simulations

Donghong Gao[1] and Jin Sun[2]

[1]*Optimization Services, Metso Minerals, Colorado Springs, CO 80903*
[2]*Institute for Infrastructure and Environment, School of Engineering, The University of Edinburgh, Edinburgh EH9 3JL, Scotland*
[1]*USA*
[2]*UK*

1. Introduction

There is no doubt that the dynamics of solid particles is the center of interest in the mineral processing industry, including crushing, grinding, classification, mineral separation, and leaching, just to name a few. But most processes involve fluid as a carrier and/or media, making the study of fluid dynamics and coupling between fluid dynamics and particle motion essential part for such a particulate flow. Various modeling and coupling approaches capable of considering particle behaviors, fluid dynamics and coupling effects, have been actively pursued, researched and developed in recent years.

By name, particulate flows usually include one or more continuous fluid phase, and one or more type of particles, or say generally, discrete phases. The discrete particles/bubbles/droplets are often dispersed in a continuous phase, so a discrete phase is also called a disperse phase in continuum multiphase modeling. There may be strong interactions between discrete phases and continuous phase, and strong interactions among discrete phases for dense particulate flows. The coupling physics pose a huge challenge to researchers, since coupling physics between fluid dynamics and particle motion requires coupling numerical modeling approaches. There is no one-fits-all solution for all applications especially after considering limitations, accuracy, computational costs of various numerical models.

As computer technology for hardware and software advances so rapidly, it also push scientific and engineering simulations to high standards of requirement with respects to accuracy, fidelity, efficiency. There is increasing research activity of using Discrete Element Method (DEM) in particulate flow simulations.

Discrete Element Method (DEM) (Cundall & Strack, 1979; Landry et al., 2003; Walton, 1992) is a Lagrangian model and is well accepted nowadays to model solid particle behavior. In principle, the DEM is based on the concept that individual particles, each of which is usually assumed to be semi-rigid, are considered to be separate and are connected at boundaries by appropriate contact laws. DEM naturally captures characteristics of each particle, therefore further dynamics like breakage and wear can be modeled locally at the small scale. Using DEM to track dynamics of particles, although the computing cost is high, eliminates the need of modeling fluid dynamics of particle phase, therefore improves fidelity of simulations. Interactions among discrete phases can be addressed more accurately inside DEM, thank to that microscopic physics has been clearly understood and described at most times.

For fluid dynamics modeling, the terminology Computational Fluid Dynamics (CFD) is well-known dedicated to it. A conventional CFD is usually based on continuum mechanics principles and control volume methods. After decades of intensive research, conventional CFD is a well-developed technology with a series of mature well-defined numerical and physical models for single phase, turbulence and multiphase flows. It is basically a grid-based Eulerian model and is usually computationally efficient, especially for single phase flows.
In practice, using CFD is not as easy as expected, since most mineral processing applications involve complex geometry and free surface flows. Generating appropriate volume mesh for complex geometry is a challenge even with help of commercial programs. Free surface flow also adds cost and difficulty to simulations. In the commonly used VOF method, the entire possible physical domain, even the space that is to be occupied by fluid occasionally, has to be meshed, and interface capturing and reconstruction scheme have to be implemented (Gao et al., 2003).
Among CFD approaches, the one named Eulerian–Eulerian model, or say, multi-fluid model, has been extensively studied, implemented in MFIX (Syamlal, 1998; Syamlal et al., 1993), CFX, and FLUENT, and applied to simulations of fluidized beds (Gera et al., 2004; Sun & Battaglia, 2006a). The formulation of this model is essentially based on the continuum fluid dynamics. It considers both the fluid phase and solid particles to be interpenetrating continua whose dynamics are governed by the Navier-Stokes equations (Goldhirsch, 2003; Huilin et al., 2003; Savage, 1998). The particle mixture can be divided into several disperse phases with different properties. Closure of the model requires formulation of constitutive equations for each phases and inter-phase momentum transfer models, where often the most difficulties are encountered and approximations are made (Jenkins & Savage, 1983; Srivastava & Sundaresan, 2003). From the difficulty of building continuum models for granular flows (Gao et al., 2006; Savage, 1998), people realized that many of the physics–based governing equations work well at small scale, but non-linear physics makes derivations of those equations at a larger scale based on simplifications and assumptions no longer valid. For particulate flows with a wide property distribution, modeling errors are easily accumulated and computation costs are largely amplified.
The major drawback of the Eulerian–Eulerian approach is that it cannot capture essential characteristics of individual solid particles regarding size and shape, and thus cannot effectively identify influence of these characteristics on process performances. Contact of individual particles with structure is often the major source of wear and erosion. Size- and shape-change processes, such as breakage and chemical reaction of individual particles, usually are core features of the mineral processing industry.
However, the extensive Eulerian–Eulerian research laid solid foundation for coupling DEM with CFD. Lots of ideas and equations can be adopted in DEM-CFD full coupling. DEM-CFD assumes the high theoretical fidelity, since each phase is kept to have its natural properties. We treat fluid as continuous continuum, and particles as discrete entities. The basic concepts of interpenetrating phases for multiphase flows still hold, although we only need to model and compute fluid phase. Instead of modeling several disperse particle phases in kinetic theory (Savage, 1998), we derive particle motions directly from DEM, therefore improves modeling accuracy.
Smooth Particle Hydrodynamics (SPH) has been used to simulate fluid dynamics for years (Monaghan, 1988; 1994; Morris et al., 1997). In SPH, a fluid field is represented by particles, each of which is associated with a mass, density, velocity, viscosity, pressure and position. Particles are moved by averaging (smoothing) their interaction with spatial

neighbors based on the theory of integral interpolants using kernel functions which can be differentiated without use of the grid. SPH, as a Lagrangian particle–based method, has its particular characteristics. It has some special advantages over conventional grid–based CFD. The most significant one is the meshfree feature. SPH does not require a pre-defined mesh to provide connections between particles when solving the governing equations. The SPH particles themselves are adaptive to geometry and free surface confinement.

From a numerical implementation point of view, DEM–SPH, a Lagrangian–Lagrangian model, is the best incorporation for particulate flows because it can totally eliminate the need for a volume mesh. The meshfree feature is very attractive to the mineral processing industry, where geometry is complex and free surface flow is typical in many applications.

However, SPH is not without problems. While Eulerian–Eulerian approaches, modeling naturally discrete particles as continua, have difficulty to give correct constitutive equations, similarly, SPH, modeling naturally continuous media as particles, compromises accuracy in some aspects. It resolves the dissipative term poorly in comparison with grid–based methods. SPH has a limited ability to deal with steep density gradient or other large property changes. Boundary conditions do not fit naturally in the particle approach, so they are difficult to implement in SPH. It is hard to capture fluid dynamics where complex boundary conditions are of critical importance.

In summary, there is no single one-fits-all solution. Every model has strengths on some aspects and weaknesses on others, especially considering accuracy and cost factors. People have to be able to, based on preliminary understanding of the physical characteristics of a system of interest, pick up the right models, combine them together, and develop/use appropriate models for the specific system to capture major phenomena to discover and investigate the controlling mechanisms behind them. In this work we present three numerical coupling approaches to capture the physics of interest: one-way coupling with CFD, DEM-CFD coupling, DEM-SPH coupling.

A one-way coupling is basically to run fluid dynamic solver separately from DEM, then import fluid flow solution to DEM, where the fluid effect on particles is considered. The one-way approach is practically important for industry applications, because at complex situations full coupling modelings are hard to converge, if not impossible. It has the advantages of using commercial package. This advantage may become very attractive in industry applications where the flow condition is very complex and density of particles is not very high. A one-way coupling can be extended to so-called 1.5-way coupling if multiphase fluid solver is used instead of single phase solver. We applied one-way coupling to a slurry pump, where solid particles and fluid are well mixed so that it is appropriate to treat slurry as a kind of single phase mixture, and the FLUENT is used to solve the flow field. But the CFD solver cannot give direct answers to our concerns: wear effect of particles on pump structure and particle breaking probability, therefore CFD results are imported into our DEM code to simulate the detailed behavior of individual particles.

For the strong coupling physics, the full coupling of DEM-CFD or DEM-SPH is necessary. In the DEM-CFD coupling, we employ a lot of widely accepted Eulerian–Eulerian multi-fluid models that have been intensively studied in the continuum multiphase fluid dynamics. Convergence of the coupling models is usually a huge challenge. The numerical methods are discussed in each section of model descriptions. The segregation of different sizes of particles in a fluidization bed is controlled by both particles motion and fluid dynamics. Due to the simple geometry of a bed, DEM-CFD is the best candidate for this application.

In the DEM-SPH coupling, a multiphase DEM-SPH model is proposed and described in detail. The coupling between the solid particles and the fluid phase are considered via volume fraction, pressure and drag force. In mills, particles are so dense that the behaviors of solid particles dominate the overall physics, and separation of solid particles from fluid is apparent. But fluid dynamics cannot be neglected because fluid damping/drag may change particle–particle contacts and particle–boundary contacts. Furthermore, the rotating nature, presence of a free surface flow, and liner geometry make CFD simulations of mills prohibitively expensive. Numerical scheme is simple at this stage, time stepping scheme could be either explicit Euler or lower order Runge-Kutta for more accuracy. The DEM-SPH is applied to a preliminary study of a mill.

2. DEM model with flow effect

The DEM simulation is based on a 3D soft particle model (Cundall & Strack, 1979; Silbert et al., 2001; Walton & Braun, 1986) where small deformations and multiple contacts on a particle are allowed, and friction and rotation are also taken into account. Each particle has six degrees of freedom of motion. For simplification of the description of the DEM model, spherical particles are assumed, although in our real application and implementation, we use spherical, tetrahedral and irregular convex shape particles together. The complex shapes definitely add difficulty to the computational geometric and solving for particle rotation, but the basic theory behind it is the same as for all spherical particles. Although our program is fully parallelized for a distributive memory machine, this work is not intended to cover the parallelization scheme and readers who are interested are referred to Plimpton (1995), which is the framework we follow.

The movement of a particle with mass m, moment of inertia I can be described by Newton's law and the kinematic relation:

$$m_i \frac{\mathrm{d}\,\mathbf{u}_i}{\mathrm{d}\,t} = \sum_j \mathbf{F}_{\mathrm{c},ij} + \mathbf{F}_{\mathrm{sf},i} + m_i\,\mathbf{g}\,, \tag{1}$$

$$I_i \frac{\mathrm{d}\,\boldsymbol{\omega}_i}{\mathrm{d}\,t} = -\sum_j R_i\,\mathbf{n}_{ij} \times \mathbf{F}_{\mathrm{c},ij}\,, \tag{2}$$

$$\frac{\mathrm{d}\,\mathbf{r}_i}{\mathrm{d}\,t} = \mathbf{u}_i\,, \tag{3}$$

where subscripts i and j are for identifying particles, $\mathbf{u}$ is the velocity of the mass center, $\boldsymbol{\omega}$ the angular velocity, $\mathbf{r}$ the position, R the radius of the particle, $\mathbf{F}_{\mathrm{c},ij}$ the contact force of particle j acting on i, $\mathbf{F}_{\mathrm{sf},i}$ the fluid–solid interaction which is assumed to act at the mass center of particles, and $\mathbf{n}_{ij}$ the normal direction of the contact pointing to particle i from j.

The governing equations are simply ordinary differential equations in time. Each particle is evolved by integrating the governing equations and applying the initial condition. The major task of modeling and simulation thus becomes actually formulating and calculating the force terms.

The implementation of contact forces is essentially a reduced version of that employed by Walton & Braun (1986), developed earlier by Cundall & Strack (1979). Contact force $\mathbf{F}_{\mathrm{c},ij} = \{\mathbf{F}_{\mathrm{n},ij}, \mathbf{F}_{\mathrm{t},ij}\}$ is first calculated from the deformation through the spring-dashpot model,

assuming soft particles:

$$\mathbf{F}_{\mathrm{n},ij} = k_{\mathrm{n}}\boldsymbol{\delta}_{\mathrm{n},ij} - \lambda_{\mathrm{n}}\, m_{\mathrm{eff}}\, \mathbf{u}_{\mathrm{n},ij}\,, \tag{4}$$

$$\mathbf{F}_{\mathrm{t},ij} = k_{\mathrm{t}}\boldsymbol{\delta}_{\mathrm{t},ij} - \lambda_{\mathrm{t}}\, m_{\mathrm{eff}}\, \mathbf{u}_{\mathrm{t},ij}\,, \tag{5}$$

where $m_{\mathrm{eff}} = (m_i\, m_j)/(m_i + m_j)$, subscript n denotes the normal direction and t the tangential direction, k is the spring coefficient, λ the damping coefficient, and $\boldsymbol{\delta}$ the elastic displacement for a contact, respectively. The damping effect in the tangential direction can be neglected. The tangential displacement $\boldsymbol{\delta}_{\mathrm{t}}$ between particles is obtained by integrating surface relative velocities over time during deformation of the contact. Actually just this history dependent feature makes the computation, especially parallel computation, more expensive. The magnitude of $\boldsymbol{\delta}_{\mathrm{t}}$ is truncated as necessary to satisfy a local Coulomb yield criterion $|\mathbf{F}_{\mathrm{t}}| \leq \mu|\mathbf{F}_{\mathrm{n}}|$.
In the above DEM model, the normal compression between two particles is easily written as:

$$\boldsymbol{\delta}_{\mathrm{n,ij}} = [(R_i + R_j) - r_{ij}]\mathbf{n}_{ij}, \tag{6}$$

here,

$$\mathbf{r}_{ij} = \mathbf{r}_i - \mathbf{r}_j, \qquad r_{ij} = |\mathbf{r}_{ij}|\,, \tag{7}$$

The normal direction and tangential direction are defined as:

$$\mathbf{n}_{ij} = \mathbf{r}_{ij}/r_{ij}\,, \tag{8}$$

$$\mathbf{n}_{ij} \times \mathbf{t}_{ij} = 1\,. \tag{9}$$

The value of the spring constant should be large enough to avoid particle interpenetration, but not too large to require an unreasonably small time step Δt, since an accurate simulation typically requires $\Delta t \sim t_{\mathrm{c}}/50$, here t_{c} is the characteristic contact time during a collision process between particles. The amount of energy lost in collisions is characterized by the inelasticity through the coefficient of restitution e. For the linear spring-dashpot model, the following relations can be taken as guidance to find the damping coefficient λ_{n}

$$e_{\mathrm{n}} = \exp(-\lambda_{\mathrm{n}} t_{\mathrm{c}}/2)\,, \tag{10}$$

$$t_{\mathrm{c}} = \pi(k_{\mathrm{n}}/m_{\mathrm{eff}} - \lambda_{\mathrm{n}}^2/4)^{-1/2}\,. \tag{11}$$

After contact force is calculated, the equations of motion, which are ordinary differential equations, can be numerically integrated to get the particle trajectories. The boundary surfaces are represented by triangles. Any meshing tool generating surface triangles can be used here. In comparison with particle–particle contact, the only difference is the geometry resolution for the particle–triangle contact. The overlap δ_{n} is equal to a particle radius minus the distance to a triangle.
The advantage of DEM is that it can capture behaviors of individual particles, and collect detailed contact information, such as velocity, contact force, shear and impact energy spectrum, so that it can model wear more accurately. Most severe wear happens in particulate flows when solid particles collide on a surface. We model the particle wear effect on a boundary triangle as:

$$\Delta h\, A = \sum_i C_{\mathrm{wr},i} E_{\mathrm{sh},i}, \tag{12}$$

where subscript i denotes the particle groups, Δh is the thickness to be worn off the surface, A is the triangle area, $E_{\mathrm{sh},i}$ is the cumulative shear energy over the time period of interest, and $C_{\mathrm{wr},i}$ is the wear coefficient that is a function of the triangle and particle material properties and the particle size.
Similarly, we model the particle breakage as

$$B\mathrm{r}_i = C_{\mathrm{br},i} E_{\mathrm{imp},i} / m_i, \tag{13}$$

where $B\mathrm{r}_i$ is the breakage percentage (probability) of the group i of particles when passing through a process, $E_{\mathrm{imp},i}$ is the cumulative impact energy over the retention time of the process, and $C_{\mathrm{br},i}$ is the breakage coefficient that is a function of the material properties and the particle size. The constants $C_{\mathrm{wr},i}$ and $C_{\mathrm{br},i}$ are to be determined from the calibration with experiment or operational data in this work. See the reference for details and recent developments about the wear model (Hollow & Herbst, 2006; Qiu et al., 2001) and particle breakage model (Herbst & Potapov, 2004; Potapov et al., 2007).

3. CFD coupling with DEM

The basic conceptual theory for CFD coupling with DEM comes from the Eulerian–Eulerian multi-fluid model, where the fluid phase and the solid particle mixture are described as interpenetrating continua. The particle mixture can be divided into a discrete number of phases, each of which can have different physical properties. Generally, n sets of governing equations have to be solved for a multiphase flow with n phases, and an exponentially increasing number of constitutive equations are required for closure of the model.
The approach of CFD coupling with DEM is proposed to overcome the closure difficulty. The Eulerian control-volume multiphase CFD governing equation is used to describe the fluid dynamics, while the DEM is used to model the solid mixture dynamic behaviors.
The governing equations for incompressible flow, continuity and momentum equations, for the fluid phase, are:

$$\frac{\partial}{\partial t}(\rho\theta_{\mathrm{f}}) + \boldsymbol{\nabla}\cdot\rho\theta_{\mathrm{f}}\mathbf{u}_{\mathrm{f}} = 0\,, \tag{14}$$

$$\frac{\partial}{\partial t}(\rho\theta_{\mathrm{f}})\mathbf{u}_{\mathrm{f}} + \boldsymbol{\nabla}\cdot(\rho\theta_{\mathrm{f}}\mathbf{u}_{\mathrm{f}}\mathbf{u}_{\mathrm{f}}) = -\rho\boldsymbol{\nabla}P + \mathbf{F}_{\mathrm{d}} + \boldsymbol{\nabla}\cdot\mathbf{T} + \rho\theta_{\mathrm{f}}\mathbf{g}\,, \tag{15}$$

where ρ is the fluid density, $\mathbf{u}_{\mathrm{f}}$ the fluid velocity, θ_{f} the fluid volume fraction, and P the pressure, and F_{d} the drag force, and $\mathbf{T}$ the viscous stress tensor.
The drag force $\mathbf{F}_{\mathrm{d}}$ between particles and fluid phase is generally defined as

$$\mathbf{F}_{\mathrm{d}} = \beta(\mathbf{u}_{\mathrm{s}} - \mathbf{u}_{\mathrm{f}}), \tag{16}$$

where β is the drag force coefficient, $\mathbf{u}_{\mathrm{s}}$ the velocity vector of solid particles, and $(\mathbf{u}_{\mathrm{s}} - \mathbf{u}_{\mathrm{f}})$ is the slip velocity between the two phases. The volume fraction θ_{s} and velocity fields $\mathbf{u}_{\mathrm{s}}$ of the solid phase are obtained through averaging particle data from DEM simulation, thus θ_{f} can be obtained from $\theta_{\mathrm{f}} = 1 - \theta_{\mathrm{s}}$.
Without losing generality, in the DEM-CFD coupling, the drag correlation by Syamlal et al. (1993) is adopted:

$$\beta = \frac{3}{4}\frac{C_{\mathrm{d}}}{V_r^2}\frac{\rho|\mathbf{u}_{\mathrm{s}} - \mathbf{u}_{\mathrm{f}}|}{d_p}\theta_{\mathrm{s}}\theta_{\mathrm{f}}\,, \tag{17}$$

$$C_{\mathrm{d}} = \left(0.63 + 4.8\sqrt{V_{\mathrm{r}}/\mathrm{Re}}\right)^2, \tag{18}$$

where C_d is drag coefficient, and the particle Reynolds number Re is defined as

$$\mathrm{Re} = \frac{\bar{d}_\mathrm{p}|\mathbf{u}_\mathrm{s} - \mathbf{u}_\mathrm{f}|\rho}{\mu}, \tag{19}$$

where $\bar{d}_\mathrm{p}$ is the average diameter of particles, and V_r is the ratio of the falling velocity to the terminal velocity of a single particle. The following form for V_r is used

$$V_\mathrm{r} = 0.5\left(A - 0.06\,\mathrm{Re} + \sqrt{(0.06\,\mathrm{Re})^2 + 0.12\,\mathrm{Re}(2\mathrm{B} - \mathrm{A}) + \mathrm{A}^2}\right), \tag{20}$$

$$A = \theta_\mathrm{f}^{4.14} \tag{21}$$

$$B = \begin{cases} 0.8\,\theta_\mathrm{f}^{1.28} & \text{if} \quad \theta_\mathrm{f} \leq 0.85 \\ \theta_\mathrm{f}^{2.65} & \text{if} \quad \theta_\mathrm{f} > 0.85. \end{cases} \tag{22}$$

From the above governing equations and drag force calculation, we can see volume fractions appear allover everywhere. This is the core modeling concept for interpenetrating disperse flow, whereas the exact particle shape has not been followed, rather the volume/mass conservation must be maintained. This multiphase modeling approach is a perfect compromise for large scale particulate flows with a huge number of small (relative to flow characteristic length) particles.

The volume fraction and velocity of the solid phase are needed for each cell. It sounds simple at the first glance. It may be simple for regular mesh, not for irregular mesh and irregular particles. As we mentioned, particle shape is not of importance at modeling particle fluid interaction, nor should be mesh geometry. We compromise the geometry details for the efficiency of numerical calculation. Many researchers use kernel function to calculate the volume fraction to avoid handling complex mesh and particle geometry. The volume fraction of each cell is obtained from the particle spatial distribution and the volume of each particle through the averaging processes:

$$\theta_\mathrm{s} = \frac{1}{V_\mathrm{c}} \frac{\sum_{i=1}^{N_p} K(|\mathbf{x}_i - \mathbf{x}_\mathrm{c}|)V_i}{\sum_{i=1}^{N_p} K(|\mathbf{x}_i - \mathbf{x}_\mathrm{c}|)} \tag{23}$$

where the subscript c denotes a cell and i denotes a particle. N_p is the total number of particles in the system. K is a kernel function, which should be bell-shape function with local support, such as Gaussian function $K(\xi) = \exp[-(\xi/w)^2]$, where $\xi = (|\mathbf{x}_i - \mathbf{x}_\mathrm{c}|)/w$ and w is the bandwidth. In this study, the following kernel function is used:

$$K(\xi) = \begin{cases} \left[1 - \xi^2\right]^4 & \text{if } |\xi| < 1 \\ 0 & \text{if } |\xi| \geq 1 \end{cases} \tag{24}$$

This function is very close to Gaussian function (with scaled bandwidth $w = 0.45$), and it is more efficient to compute than Gaussian function, because it only requires to loop over the particles in the neighbor cells. Recently, Xiao & Sun (2011) dedicated a big portion of their paper to the particle volume fraction calculation. Please refer to that for details.

Similarly, the solid phase velocity is obtained via the following coarse-graining procedure:

$$\mathbf{u}_\mathrm{s} = \frac{\sum_{i=1}^{N_p} K(|\mathbf{x}_i - \mathbf{x}_\mathrm{c}|) V_i \mathbf{u}_i}{\sum_{i=1}^{N_p} K(|\mathbf{x}_i - \mathbf{x}_\mathrm{c}|) V_i} \tag{25}$$

On the DEM side, two major solid–fluid interaction terms acts on a particle. In Equation 1 force $F_{\mathrm{sf},i}$ equals the sum of buoyancy force and drag force acting on particle i:

$$\mathbf{F}_{\mathrm{sf},i} = -V_i \boldsymbol{\nabla} P - F_{\mathrm{d,i}}\,, \tag{26}$$

The drag of Equation 16 is the aggregate drag force acting on all the particles in a cell. For the motion equation 1 of a solid particle, the drag force on each particle is needed. There are many ways of redistributing the aggregate force back to individual particles. This can be obtained from the cell whose center is nearest to the particle, or from the neighboring cells whose contribution portion is determined by distances between particles and cell centers. Each particle shares the drag force proportional to its surface area, or proportional to its volume, or as functions of other properties. The uncertainty also occurs with buoyancy force. There is no sure answer to the question of where pressure values are used in calculation of buoyancy force on a particle. Here in the application of DEM-CFD full coupling, we take the simple scheme by distributing the nearest cell force according to surface areas of particles.
For the one-way coupling applications, particles are small and well mixed with fluid phase, so that one-way coupling is justified, and Wen-Yu drag relation (Li & Kuipers, 2002; Rong & Horio, 1999) is used. Thus, the drag force calculation can be as simple as:

$$\mathbf{F}_{\mathrm{sf},i} = -V_i \boldsymbol{\nabla} P - \frac{3}{4} \frac{C_d |\mathbf{u}_i - \mathbf{u}_\mathrm{f}| \rho \theta_\mathrm{f}^{-1.65} V_i}{D_i} \left(\mathbf{u}_i - \mathbf{u}_\mathrm{f}\right), \tag{27}$$

where V_i is the volume, and D_i the hydraulic diameter of particle i. For the drag coefficient C_d, please refer to DEM–SPH coupling section.
For DEM-CFD coupling, the fluid equations are solved using a solver provided by a library in the OpenFOAM (Open Field Operation and Manipulation) toolbox (Rusche, 2002). This solver is used in the current study with modifications to accommodate the fact that only the fluid phase is solved and the disperse phase is tracked in the Lagrangian framework. Finite volume method is used to discretize the equations on an unstructured mesh. For the time integration, Euler implicit scheme is used, which has only first order accuracy but is unconditionally stable. The convection and diffusion terms are discretized with a blender of central differencing (second-order accurate) and upwind differencing (first order accurate). The advantage of blended differencing is that high accuracy is achieved while the boundness of the solution is ensured. A sophisticate stepping control and interpolation over time was brought up by (Xiao & Sun, 2011) to enhance accuracy and convergence of the DEM–CFD coupling solver.
The velocity-pressure coupling is handled with the modified PISO algorithm (Rhie & Chow, 1983). In this algorithm, momentum equation is first solved to get a predicted velocity field, and then the pressure equation (obtained by combining momentum equation into continuity equation) is solved for a corrected velocity field. This process is repeated until the velocity field satisfies continuity equation. The PISO algorithm prevents from the decoupling of pressure-velocity and the oscillation in the solution, eliminating the necessity of a stagger grid. Therefore, a collocated grid is used in the models, where all the variables are stored in the cell centers, thus it is a significant simplification over a stagger grid.

4. SPH coupling with DEM

SPH equations are obtained by interpolating fluid dynamics governing equations over disordered mass points in the influence range of an interpolation kernel function (Monaghan, 1988). The kernels are analytical functions which can be differentiated without using a mesh. Although control volume CFD can be tuned to get accurate solutions of physical problems, it requires tremendous work, including generating the mesh, in order to couple with DEM to account for the multiphase flows. On the other hand, SPH is a method which gives reasonable accuracy and couples well with the particle method DEM without requiring a mesh.
Monaghan & Kocharyan (1995) originally built SPH multiphase models for interpenetrating multi-fluids. In the later work, Monaghan (1997) improved the multiphase SPH solver by using an implicit drag technique. In this work, we will modify the interpenetrating multiphase SPH model to couple SPH for fluid dynamics with DEM for solid particles. SPH is only used to model fluid phase, and particles are represented and evolved by DEM
The governing equations, continuity and momentum equations, for the fluid phase are:

$$\frac{\mathrm{d}\,\hat{\rho}}{\mathrm{d}\,t} = -\hat{\rho}\,\boldsymbol{\nabla}\cdot\mathbf{u}\,, \tag{28}$$

$$\frac{\mathrm{d}\,\mathbf{u}}{\mathrm{d}\,t} = -\frac{\boldsymbol{\nabla}\,P}{\rho} + \frac{\beta}{\hat{\rho}}(\mathbf{u}_\mathrm{s}-\mathbf{u}) + \frac{\boldsymbol{\nabla}\cdot\mathbf{T}}{\hat{\rho}} + \mathbf{g}\,, \tag{29}$$

where β is the drag force coefficient, $\mathbf{u}_\mathrm{s}$ the velocity vector of solid particles and $\mathbf{T}$ the viscous stress tensor. The fluid density $\hat{\rho}$ in the multiphase model is related to the fluid volume fraction θ and actual fluid density ρ by

$$\hat{\rho} = \rho\,\theta\,. \tag{30}$$

The equation of state has to be defined in order to fully describe the dynamics of the fluid. The actual equation of state of incompressible flow is very stiff, requiring extremely small time steps. In SPH, the fluid pressure is an explicit function of local fluid density. Therefore, it is necessary to use a quasi-compressible equation of state and an artificial speed of sound as a reference value. Monaghan (2000) used the equation of state similar to that defined for water:

$$P = \frac{\rho_0 c_0^2}{\gamma}\left[\left(\frac{\rho}{\rho_0}\right)^\gamma - 1\right] \tag{31}$$

$$\approx c_0^2\,(\rho-\rho_0)\,, \tag{32}$$

where ρ_0 is the reference density, c_0 the speed of sound at ρ_0, and γ a constant with physical meaning of the ratio of specific heat for ideal gases. Monaghan (2000) took $\gamma = 7$ for incompressible flows. The choice $\gamma = 7$ results in large changes in pressure from small changes or perturbations in density. We confirmed that Equation 31 works well for single phase flow SPH. However, in this work considering multiphase free surface flow, the density changes could also be exaggerated by changes or errors in calculation of volume fraction (see below). We also follow suggestions of Morris et al. (1997) regarding choosing appropriate values of γ and c_0. The speed of sound is:

$$c = \sqrt{\frac{\gamma P}{\rho}} \tag{33}$$

SPH is based on the theory of integral interpolants. If the kernel functions are some types of delta functions, then a field variable $A(\mathbf{r})$ can be approximated by the weighted averaging over a limited range of neighboring particles as:

$$A(\mathbf{r}) = \int A(\mathbf{r}')W(\mathbf{r}-\mathbf{r}', h)\mathrm{d}\,\mathbf{r}' \simeq \sum_a A_a \frac{m_a}{\rho_a} W(\mathbf{r}-\mathbf{r}_a, h)\,, \tag{34}$$

where m_a denotes mass of SPH particle a at the position $\mathbf{r}_a$, and similar notations for ρ_a, A_a. $W(\mathbf{r}-\mathbf{r}_a, h)$ is the kernel which is a function of smoothing length h and distance between positions $\mathbf{r}$ and $\mathbf{r}_a$.
For clarification of the description, the subscripts a and b are used for the SPH fluid particles, and i and j for the DEM solid particles. Integrating the governing equations and simplifying the integrals as above, we can get the overall SPH governing equations:

$$\frac{\mathrm{d}\,\hat{\rho}}{\mathrm{d}\,t} = \sum_b m_b \mathbf{u}_{ab}\cdot\boldsymbol{\nabla}_a W_{ab} \tag{35}$$

$$\begin{aligned}\frac{\mathrm{d}\,\mathbf{u}_a}{\mathrm{d}\,t} = &-\sum_b m_b\left(\frac{P_a\theta_a}{\hat{\rho}_a^2}+\frac{P_b\theta_b}{\hat{\rho}_b^2}\right)\boldsymbol{\nabla}_a W_{ab}\\ &-\sum_j \frac{P_a\,V_j}{\hat{\rho}_a}\boldsymbol{\nabla}_a W_{aj}\\ &+\frac{1}{3}\sum_j \frac{\beta_{aj}V_j}{\hat{\rho}_a\theta_j}\left(\frac{\mathbf{u}_{ja}\cdot\mathbf{r}_{ja}}{r_{ja}}\right)W_{ja}\frac{\mathbf{r}_{ja}}{r_{ja}}\\ &+\boldsymbol{\tau}_{ab}+\mathbf{g}_a\,,\end{aligned} \tag{36}$$

where V_j is the volume of DEM particle j, θ_j the solid phase volume fraction at the position of DEM particle j, θ_a the fluid phase volume fraction at the position of SPH particle a, and $\boldsymbol{\tau}_{ab}$ the viscous term. The solid–fluid inter-phase interaction force is represented by the second and third group of terms on the right hand side of Equation 36. The second term is the pressure gradient on a solid particle, and third term is the drag force. The drag force between two particles acts along their center line, working like dashpot damping in the DEM models. Thus the inter-phase interaction in Equation 1 can be written as:

$$\mathbf{F}_{\mathrm{sf},j} = -\sum_a m_a \frac{P_a\,V_j}{\hat{\rho}_a}\boldsymbol{\nabla}_j W_{ja} - \frac{1}{3}\sum_a m_a \frac{\beta_{aj}V_j}{\hat{\rho}_a\theta_j}\left(\frac{\mathbf{u}_{ja}\cdot\mathbf{r}_{ja}}{r_{ja}}\right)W_{ja}\frac{\mathbf{r}_{ja}}{r_{ja}}. \tag{37}$$

In the above equations, we have used the notation

$$\mathbf{u}_{aj} = \mathbf{u}_a - \mathbf{u}_j\,,$$

for a vector, and

$$\begin{aligned} W_{ab} &= W(r_{ab})\,,\\ \boldsymbol{\nabla}_a W_{ab} &= \frac{\mathbf{r}_{ab}}{r_{ab}}\frac{\mathrm{d}\,W}{\mathrm{d}\,r}(r_{ab}) = \frac{\mathbf{r}_{ab}}{r_{ab}}\left(\frac{\mathrm{d}\,W}{\mathrm{d}\,r}\right)_{ab}\,,\end{aligned}$$

for a kernel and a kernel derivative, where r_{ab} is the distance between particle a and b. Similar notation is used for other terms.

The kernel function is the commonly used cubic spline function

$$W(r,h) = \frac{1}{\pi h^3} \begin{cases} 1 - \frac{3}{2}q^2 + \frac{3}{4}q^3 & \text{if} \quad 0 \le q < 1 \\ \frac{1}{4}(2-q)^3 & \text{if} \quad 1 \le q < 2 \\ 0 & \text{otherwise} \end{cases} \tag{38}$$

where $q = r/h$ and r is the distance between particles.
The Gidaspow drag correlation, which combines the Wen-Yu relation and the Ergun equation, is commonly used in CFD multiphase modeling (Gera et al., 1998; 2004; Li & Kuipers, 2002; Rong & Horio, 1999) and it is used here:

$$\beta_{aj} = \begin{cases} \frac{3}{4} \frac{|\mathbf{u}_a - \mathbf{u}_j| C_\mathrm{d} \theta_a^{-2.65}}{D_j} \rho_a \theta_a \theta_j & \theta_j \le 0.2 \\ \left[\frac{150(1-\theta_a)\mu_a}{\theta_a^2 \rho_a D_j^2} + \frac{1.75|\mathbf{u}_a - \mathbf{u}_j|}{\theta_a D_j} \right] \rho_a \theta_a \theta_j & \theta_j > 0.2 \end{cases} \tag{39}$$

$$C_\mathrm{d} = \begin{cases} \frac{24}{\mathrm{Re}}(1 + 0.15 Re^{0.687}) & 10^{-4} < Re < 1000 \\ 0.44 & \mathrm{Re} \ge 1000 \end{cases} \tag{40}$$

$$\mathrm{Re} = \frac{\rho_a \theta_a |\mathbf{u}_a - \mathbf{u}_j| D_j}{\mu_a} \tag{41}$$

where D_j is solid particle effective hydraulic diameter. The ρ_a, θ_a and θ_j terms are intentionally grouped together as factors, because these terms will be canceled when β_{aj} is substituted back to Equations 36 and 37.
From the comparison of governing equations of DEM–CFD to those of DEM–SPH, one apparent difference is that DEM–CFD calculates aggregate coupling force first, and distributes back to particles, while the DEM–SPH calculates coupling force for individual particles and collects the total force on SPH particle. Due to the high cost the drag force calculation, the cost of DEM–SPH may be much higher than DEM–CFD. Further modification to the DEM–SPH by adopting DEM–CFD approach is the future work of authors.
No matter which way of coupling, we have to obtain the collective volume fractions θ_j and θ_a. Using kernel function for volume fraction calculation is the most natural way in the SPH framework. Please refer to Monaghan (1997); Monaghan & Kocharyan (1995) for more theory support. The most simple form of fluid fraction in the SPH type of kernel functions can be defined as follows:

$$\theta_a = 1 - \sum_j V_j W_{aj}^* \tag{42}$$

where W^* is a kernel function that can be different from W, and a different smoothing length should be used. The smoothing length should be at least twice the maximum particle size. After that, θ_j can be obtained by smoothing over SPH particles and using the same smoothing length as in SPH equations.
One can use the same way as in the above DEM–CFD, Equation 23, for volume fraction calculation, however, using a imaginary sphere as V_c, because there is no real mesh in SPH. The imaginary sphere radius should be at least twice the maximum particle size. In this work,

we use a combination of both approaches. We first obtain the intermediate volume fraction in a way like Equation 23, then smooth it over SPH particles in the normal way as

$$\theta_b = \sum_a \theta_a \frac{m_a}{\hat{\rho}_a} W_{ab} \,. \tag{43}$$

We have to go back to formulate the viscous term in order to complete the set of modeling equations. This work employs a SPH viscous diffusion model used by Morris et al. (1997):

$$\begin{aligned} \boldsymbol{\tau}_{ab} &= \sum_b \frac{m_b(\mu_a + \mu_b)\mathbf{r}_{ab} \cdot \boldsymbol{\nabla}_a W_{ab}}{\rho_a \rho_b \, r_{ab}^2} \mathbf{u}_{ab} \\ &= \sum_b \frac{m_b(\mu_a + \mu_b)\mathbf{u}_{ab}}{\rho_a \rho_b \, r_{ab}} \left(\frac{\mathrm{d}\, W}{\mathrm{d}\, r} \right)_{ab} \end{aligned} \tag{44}$$

where μ is the dynamic viscosity. This expression uses only the first order kernel derivative. It conserves translation momentum accurately, while angular momentum is only approximately conserved. For applications with low fluid velocities like in this work, this formulation is appropriate.

In this work, several practical approaches suggested in a series of SPH publications by Monaghan (1989; 1994; 2000) are employed in order to build a stable, robust solver. First, the so-called XSPH velocity correction is employed:

$$\frac{\mathrm{d}\, \mathbf{r}_a}{\mathrm{d}\, t} = \mathbf{u}_{\mathrm{xsph},a} = \mathbf{u}_a - 0.5 \sum_b \frac{m_b}{0.5(\rho_a + \rho_b)} W_{ab} \mathbf{u}_{ab} \,. \tag{45}$$

The XSPH variant is used to move the particles and also in the continuity equation for consistency. The adjustment is important for free surface flows and useful for high speed flows. It basically keeps the particles more ordered and moves particles in a velocity similar to the average velocity in their neighborhood to prevent fluid penetration. Second, artificial pressure is introduced into the momentum equation to avoid SPH particle clustering. See Monaghan (2000) for details.

The overall time advancing scheme for a DEM and SPH coupling system is: 1) calculate the solid and fluid coupling terms based on the old field values, 2) calculate the fluid–fluid interactions and integrating SPH particles. 3) calculate the solid–solid contact forces and move solid particles.

Two different time stepping schemes for SPH particle integration have been applied and tested in this work. One scheme is analogous to the explicit method of control volume CFD for incompressible flow, where the source term of pressure and force terms are calculated based on the old velocity field at t^n, then the pressure equation is solved, and finally the new pressure field is used to update the velocity to t^{n+1}. Similarly in the SPH solver, at the first sweep, the density changes and force terms are calculated based on fields at t^n; at the second sweep, the pressure and density are updated; at the third sweep, the velocity fields are updated and the particles are moved. The method is enhanced by incorporation of the leap-frog approach: velocities are updated at intervals midway, $t^{n+1/2}$, between time steps t^n and t^{n+1}.

The other scheme is the simple predictor-corrector (Monaghan & Kocharyan, 1995), or, the second order Runge-Kutta method. First, values (velocity, density, position) at $t^{n+1/2}$ are predicted from t^n and $t^{n-1/2}$. Then, force and other changes under the predicted conditions are calculated. After that, field values at $t^{n+1/2}$ are corrected using the new changes. Finally,

values at t^{n+1} can be obtained using the trapezoidal rule. This method can achieve second order accuracy.
Boundary conditions for SPH particles are similar to that for solid DEM particles: spring-dashpot contact models are applied to the particles assuming spherical particles with diameter equal to the initial separation distance. The contact coefficients are taken from DEM parameters for the same size of DEM particle.

5. Applications

5.1 One-way coupling for a pump

For slurry in pump operation, solid particles are well mixed with fluid, the particle volume fraction is usually not very high, velocity is high but streamlines do not interweave together, so that the particle–particle collision probability is low, thus the particle–boundary collision is the main interest here since particle–boundary interaction is the major source of wear and the reason for particle breakage under these conditions. DEM simulations were also performed to estimate the breakage percentage and liberation percentage of the particles during the operation of the pump at different conditions. The commercial software FLUENT is used to obtain the fluid dynamics solutions assuming single phase mixture flow.
The CFD simulation of a pump is not easy and straightforward like pipe flow. First of all, for high fidelity we use the manufacturer's geometry files in IGES format. These geometry files need a lot of cleaning, merging, and smoothing work in Gambit before appropriate CFD meshes can be generated. Moreover, due to the rotating part, the multiple reference frame technique has been used. Due to the unsymmetrical geometry, time dependent solutions have to be pursued, thus the sliding mesh method has been used.
Fluid field solutions including pressure and velocity fields are imported into our DEM program, where DEM tracer particles are created and evolved as described above. During the simulations, particles are first set at the inlet segment of the pump, then particles flow along with fluid to enter the pump. Particles leaving the pump from the outlet are re-inserted at the inlet as in semi-periodic boundary condition, so that particle dynamics gradually reaches steady state. Once steady state is reached, shear and impact energy data are collected and recorded for at least three revolutions of the pump.
We performed the wear study on the Metso slurry pump HM300. Ultrasonic measurements of lining thickness as a function of location number is marked on Fig. 1. One hundred thousand (100,000) ore particles from size 0.5 mm to 3 mm are generated for DEM. Shear energy spectra are used in wear analysis as described by Equation 12. The prediction error was found to be less than 4%. The comparison of the wear prediction with measurements is shown in Fig. 2.
We performed the ore breakage and valuable particle liberation study on Metso slurry pump MM300. We employed 5 different sizes (1.4 mm, 5.2 mm, 8.17 mm, 10.6 mm and 15 mm) of DEM particles to represent valuable particles, respectively. There are a total of 400,000 particles for ore, and 1000 particles for each of the 5 groups of valuable particles. Based on the impact energy spectra, the particle breakage percentage can be calculated according to Equation 13. The liberation percentage is proportional to be the breakage rate of the ores. The valuable particle breakage percentages and liberation percentages are estimated as shown in Table 1. The valuable particle liberation percentages are under 5% and the valuable particle breakage percentages are very small ($< 0.1\%$) at the pump conditions under consideration. The trend of liberation percentages changing with flow rate and with solid concentration meet the qualitative expectation. As the volume flowrate increases, although the increased velocity enhances the collision of particles, but the retention time decreases, therefore, the liberation

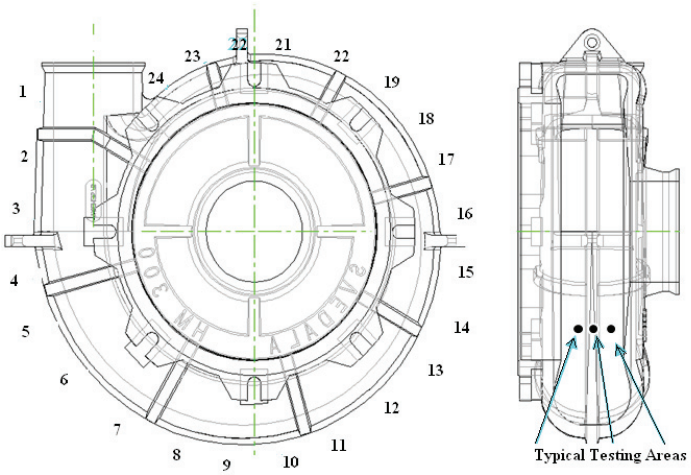

Fig. 1. The slurry pump with location numbers marked.

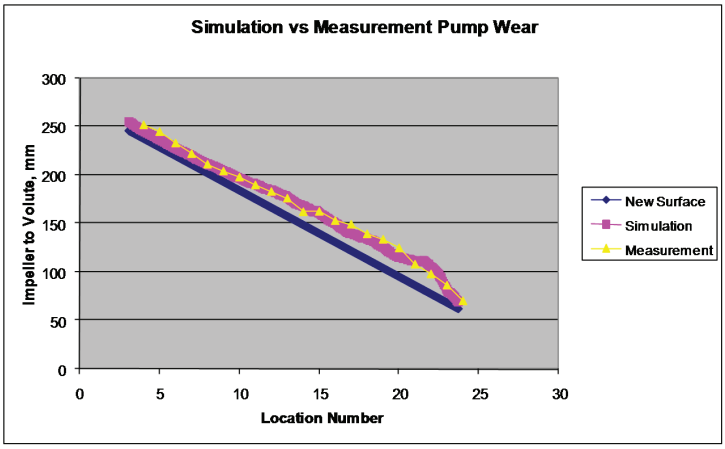

Fig. 2. Wear study result for the pump.

percentage decreases from the combination of two effects. This result may show us that the probability of collision, which increases with retention time, outweighs the collision strength increase with velocity at the current conditions.

5.2 DEM-CFD coupling for a fluidization bed

The DEM-CFD coupling has been applied to a study of particle segregation due to size. Here, we simulated and presented the segregation of two different sizes of particles in a model fluidization bed with inlet velocity of 1.5 m/s, which is larger than the minimum fluidization of the large particles reported in the experiments (Goldschmidt, 2001).

Solid mass fraction in slurry	Flowrate m^3/s	valuable-part liberate-%	valuable-part break-%
64%	0.278	3.79%	0.06%
72%	0.278	3.68%	0.06%
80%	0.278	3.62%	0.07%
72%	0.250	4.64%	0.06%
72%	0.278	3.68%	0.06%
72%	0.306	2.97%	0.06%

Table 1. Valuable particle liberation and breaking analysis in slurry pump.

To quantify the bed expansion, an average particle height is defined as

$$< h_{\mathrm{p}} >= \frac{\sum_i^{N_{\mathrm{p}}} m_i h_i}{\sum_i^{N_{\mathrm{p}}} m_i}, \tag{46}$$

here, m_i is the mass of particle i.
To reduce computational cost while still keeping the essential physics of the process, a smaller bed as shown in Fig. 3, thus a smaller number of particles, is used, while the aspect ratio of the bed is kept the same as in the experiment (Goldschmidt, 2001).
Two types of particles with the same density but different sizes were perfectly mixed initially. The simulation was conducted for 10 seconds. The results in Fig. 4 show the close to zero segregation percentages, which agrees with the experimental results.
The initial bed configuration as well as those at $t = 6$ s are presented in Fig. 5. The left panel shows that initially the particles are perfectly mixed and randomly packed. At $t = 6$ s, the two types of particles are still well mixed without visible segregation. The results are better than the multi-fluid modeling results (Sun & Battaglia, 2006b).

5.3 DEM–SPH coupling for a mill

We applied the DEM–SPH coupling multiphase solver described in section 2 and 3 to the modeling of a SAG mill. The mill operating conditions are: mill diameter 10 m; mill effective length 4 m; mill volume 386 m^3; total filling 31.7%; ball filling 15.4%; ore density 2700 kg/m^3; ball density 7850 kg/m^3; rotation speed 10.1 RPM; solid feed 1977 mt/h (mt = metric tons); solid mass percentage in feed 70%. We first ran the PBM model (Herbst & Pate, 2001) to estimate the size distribution under steady operation conditions. Due to the high cost of the particle methods, we use a truncated size distribution list that cuts the PBM size range to keep only the 5 coarsest sizes. We also assume that 25% solid fine particles are totally mixed with water to form a dilute slurry. The slurry has density 1380 kg/m^3 and dynamics viscosity 5.0E-3 kg/m s. Based on these practical treatments, we employ 6 groups of ore particles: 43 mm (in diameter) sphere, and 43 mm, 62 mm, 88 mm, 124 mm, 176 mm tetrahedron, and 4 groups of balls with diameter equal to 78 mm, 100 mm, 125 mm. At initialization, a total of 750,024 ore particles from the 6 ore groups according to the truncated size distribution are generated in the mill, and a total of 48,000 balls, 12,000 in each ball group, are set in the mill. Assuming 0.4 voidage of dense packing, we set up 868,158 SPH particles, with spacing distance 50 mm to make the fluid charge level about the same as that of the solid particles. Fig. 6 shows the initial setup of the particles in the mill. Due to the high density, all particles are initially packed regularly at the mill belly part.

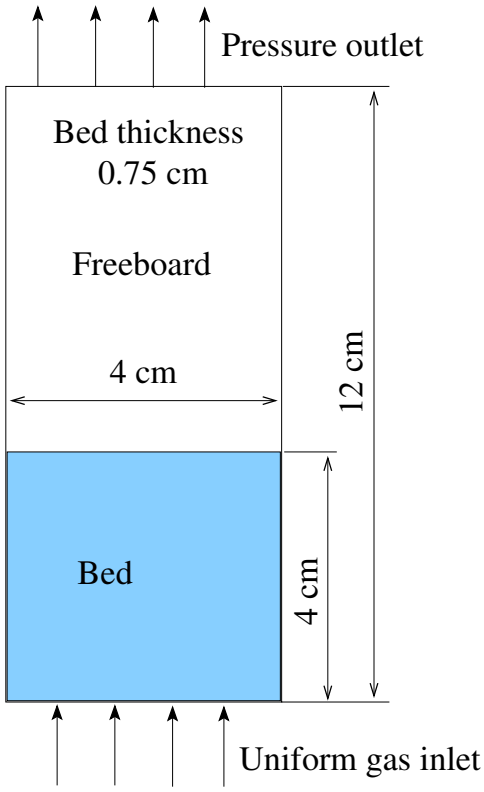

Fig. 3. Geometry of the pseudo 3D computational domain and boundary conditions.

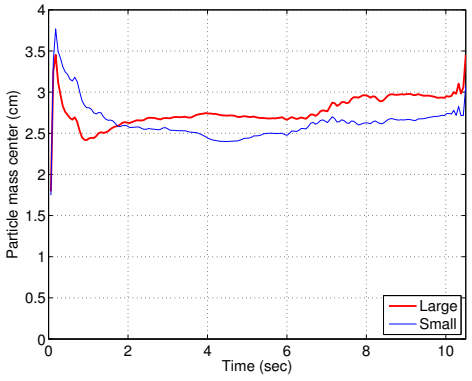

Fig. 4. Average bed heights for small and large particles as a function of time.

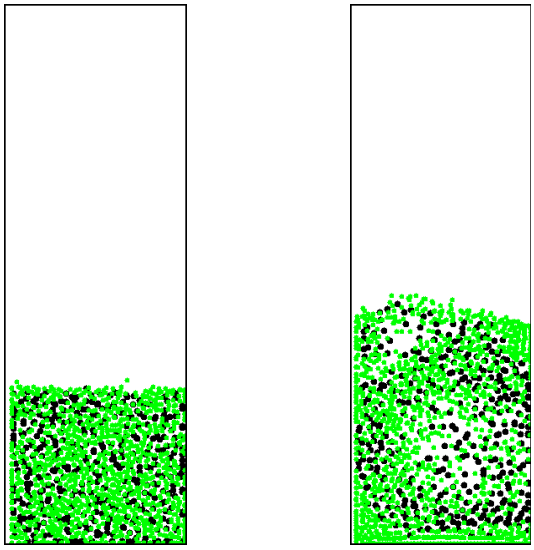

Fig. 5. Two-dimensional snapshots of particle mixtures. Dark dots denote large particles and light ones denote small particles. Left: Initial configuration. Right: configuration after 6 seconds.

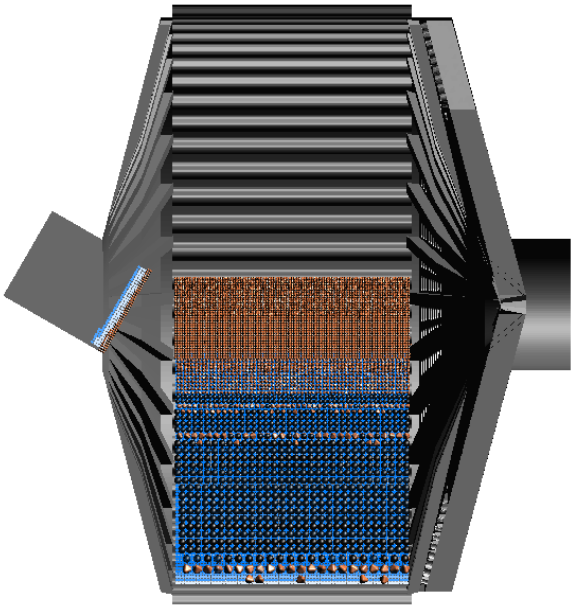

Fig. 6. The initial setting of the particles

The computation is expensive. The case has been running for 20 days using 16 processes but it only simulates 6 seconds of physical time, still not reaching steady state. We also realized the simulation is unstable due to explicit particle stepping, so time-step need to be controlled to be small. Here, we only can present some preliminary results.

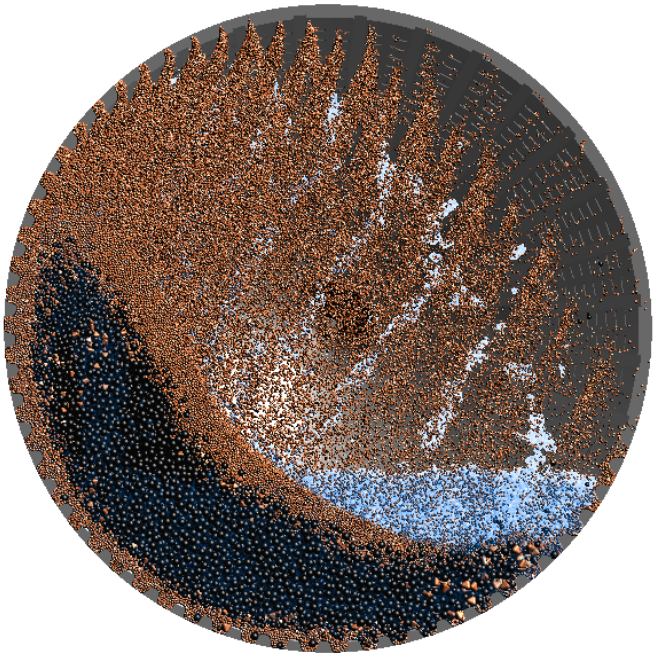

Fig. 7. A view with particle shapes at the mill center cross section.

Figure 7 shows the DEM and SPH particles at 5.68 seconds after the mill starts rotating from the initial setup. The light blue color represents SPH particles, red or brown denotes DEM ore particles, and black demotes steel balls. We can see the profiles of DEM and SPH particles spatial distribution that meet our expectation. In the figure DEM particles overshadow the SPH particles, so that it creates false impression that there are no SPH particles in most area. The initial setup as shown in Fig. 6 may cause the segregation shown in Fig. 7. Please note at 5.68 seconds, the mill has finished less than one revolution.
The potential power draw can be calculated as $\sum_{i,a} \mathbf{g} \times \mathbf{r}$, where the sum is over all DEM and SPH particles. The change of this potential power with time is shown in Fig. 8, reflecting how close a mill is reaching the steady–state. The fluid power draw is less than 10% of the total power draw. It is understandable, at the first half revolution, potential power draw increases to its highest value because particles have to be lifted up by a mill. Unfortunately we do not have operational data to compare with. In another way, the power draw is calculated by $\sum \mathbf{F} \cdot \mathbf{u}$, where the sum is over all contact work acting on the boundary. At the time 5.68 seconds, power draw calculated in the second way is 9.18 MW. This value can be thought to be gross power draw, because it includes energy loss between inelastic contacts and viscous dissipation.

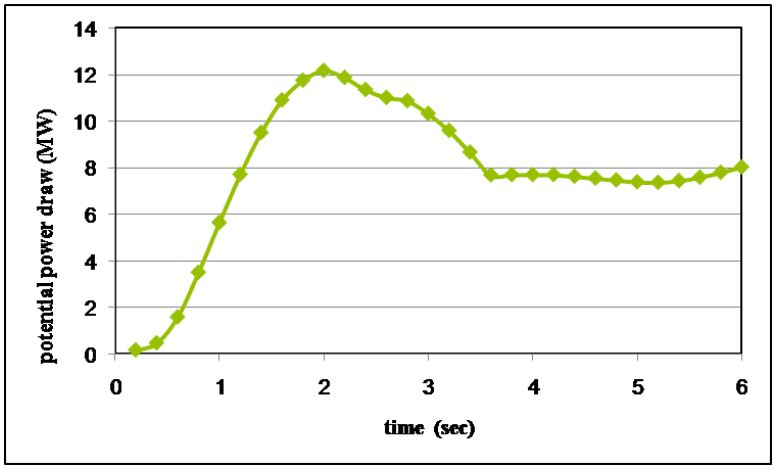

Fig. 8. The calculated power draw variation with time

The advantage of the DEM–SPH solver, a total particle method, can be shown in Fig. 9, where small solid and SPH particles pass through the grid. We can imagine the difficulty of meshing a mill with a grid for a conventional CFD solver, considering the multi-scale challenge here:

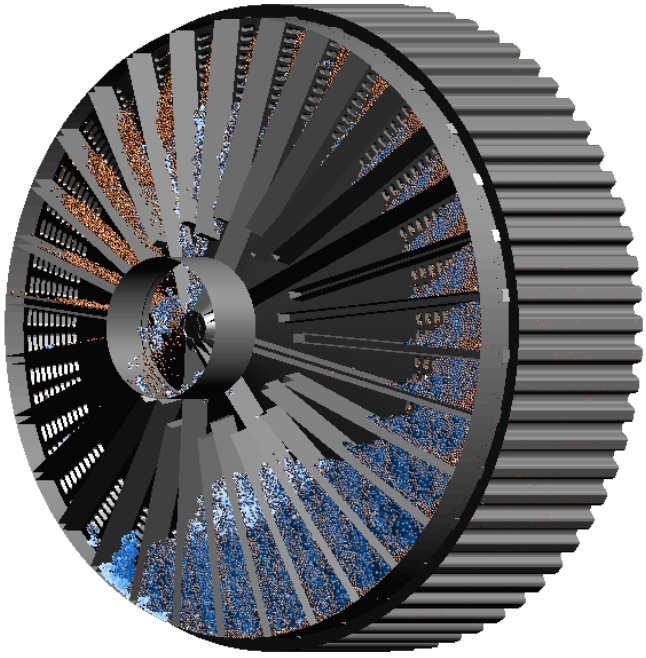

Fig. 9. A view of the mill discharge end.

the mill main body diameter is 10 m while grid size is 75 mm. But with SPH, it is flexible to control the solver by assigning SPH particle probability of passing through, or by applying different sets of triangles to SPH and DEM particles.

6. Conclusions

Three approaches to couple solid particle behavior with fluid dynamics have been described and three applications have been provided. For full coupling approaches DEM-CFD and DEM-SPH, they are physically equivalent, but may appear in different forms of equations. The governing equations have been carefully formulated. Numerical methods, difficulties and possible problems have been discussed in detail. The one-way coupling of CFD with DEM has been used in analysis of wear on lining structure and particle breaking probability during a pump operation. The DEM–CFD coupling has been applied to modeling fluidization bed. The multiphase DEM–SPH solver has been used in a wet grinding mill simulation. Each numerical approach has its strength and weakness with respect to modeling accuracy and computation cost. The final choice of best models should be made by application specialists on a case by case basis based on dominant features of physical phenomena and numerical models.

7. References

Cundall, P. A. & Strack, O. D. L. (1979). Discrete numerical model for granular assemblies, *Géotechnique* 29: 47–64.

Gao, D., Fan, R., Subramaniam, S., Fox, R. O. & Hoffman, D. (2006). Momentum transfer between polydisperse particles in dense granular flow, *J. Fluids Engineering* 128.

Gao, D., Morley, N. B. & Dhir, V. (2003). Numerical simulation of wavy falling film flows using VOF method, *J. Comput. Phys.* 192(10): 624–642.

Gera, D., Gautam, M., Tsuji, Y., Kawaguchi, T. & Tanaka, T. (1998). Computer simulation of bubbles in large-particle fluidized beds, *Powder Technology* 98: 38–47.

Gera, D., Syamlal, M. & O'Brien, T. J. (2004). Hydrodynamics of particle segregation in fluidized beds, *International Journal of Multiphase Flow* 30: 419–428.

Goldhirsch, I. (2003). Rapid granular flows, *Annu. Rev. Fluid Mech.* 35: 267–293.

Goldschmidt, M. (2001). *Hydrodynamic Modelling of Fluidised Bed Spray Granulation*, Ph.D. Thesis, Twente University, Netherlands.

Herbst, J. A. & Pate, W. T. (2001). Dynamic modeling and simulation of SAG/AG circuits with MinOOcad: Off-line and on-line applications, *in* D. Barratt, M. Allan & A. Mular (eds), *Proceedings of International Autogenous and Semiautogenous Grinding Technology, Volume IV*, Pacific Advertising Printing & Graphics, Canada, pp. 58–70.

Herbst, J. A. & Potapov, A. V. (2004). Making a discrete grain breakage model practical for comminution equipment performance simulation, *Powder Technology* 143-144: 144–150.

Hollow, J. & Herbst, J. (2006). Attempting to quantify improvements in SAG liner performance in a constantly changing ore environment, *in* M. Allan, K. Major, B. Flintoff, B. Klein & A. Mular (eds), *Proceedings of International Autogenous and Semiautogenous Grinding Technology, Volume I*, pp. 359–372.

Huilin, L., Yurong, H. & Gidaspow, D. (2003). Hydrodynamics modelling of binary mixture in a gas bubbling fluidized bed using the kinetic theory of granular flow, *Chemical Engineering Science* 58: 1197–1205.

Jenkins, J. T. & Savage, S. B. (1983). A theory for the rapid flow of identical, smooth, nearly elastic, spherical particles, *J. Fluid Mech.* 130: 187–202.

Landry, J. W., Grest, G. S., Silbert, L. E. & Plimpton, S. J. (2003). Confined granular packings: Structure, stress, and forces, *Phys. Rev. E* 67: 041303.

Li, J. & Kuipers, J. A. M. (2002). Effect of pressure on gas-solid flow behavior in dense gas-fluidized study, *Powder Tech.* 127: 173–184.

Monaghan, J. (1988). An introduction to SPH, *Computer Physics Communications* 48: 89–96.

Monaghan, J. (1989). On the problem of penetration in particle methods, *Journal of Computational Physics* 82: 1–15.

Monaghan, J. (1994). Simulating free surface flows with SPH, *Journal of Computational Physics* 110: 399–406.

Monaghan, J. (1997). Implicit SPH drag and dusty gas dynamics, *Journal of Computational Physics* 138: 801–820.

Monaghan, J. (2000). SPH without a tensile instability, *Journal of Computational Physics* 159: 290–311.

Monaghan, J. & Kocharyan, A. (1995). SPH simulation of multi-phase flow, *Computer Physics Communications* 87: 225–235.

Morris, J. P., Fox, P. J. & Zhu, Y. (1997). Modeling low reynolds number incompressible flows using SPH, *Journal of Computational Physics* 136: 214–226.

Plimpton, S. (1995). Fast parallel algorithms for short-range molecular dynamics, *J. Comput. Phys.* 117: 1–19.

Potapov, A., Herbst, J., Song, M. & Pate, W. (2007). A dem-pbm fast breakage model for simulation of comminution process, *in* UNKNOWN (ed.), *Proceedings of Discrete Element Methods*, Brisbane, Australia.

Qiu, X., Potapov, A., Song, M. & Nordell, L. (2001). Prediction of wear of mill lifters using discrete element methods, *in* D. Barratt, M. Allan & A. Mular (eds), *Proceedings of International Autogenous and Semiautogenous Grinding Technology, Volume IV*, Pacific Advertising Printing & Graphics, Canada, pp. 260–265.

Rhie, C. & Chow, W. (1983). A numerical study of the turbulent flow past an isolated airfoil with trailing edge separation, *AIAA* 21(11): 1525–1532.

Rong, D. & Horio, M. (1999). DEM simulation of char combustion in a fluidized bed, *in* M. Schwarz, M. Davidson, A. Easton, P. Witt & M. Sawley (eds), *Proceedings of Second International Conference on CFD in the Minerals and Process Industry*, CSIRO Australia, CSIRO, Melbourne, Australia, pp. 65–70.

Rusche, H. (2002). *Computational fluid dynamics of dispersed two-phase flows at high phase fractions*, Ph.D. Thesis, Imperial College London, UK.

Savage, S. B. (1998). Analyses of slow high-concentration flows of granular materials, *J. Fluid Mech.* 377: 1–26.

Silbert, L. E., Ertas, D., Grest, G. S. & et al. (2001). Granular flow down an inclined plane: Bagnold scaling and rheology, *Phys. Rev. E* 64: 051302.

Srivastava, A. & Sundaresan, S. (2003). Analysis of a frictional-kinetic model for gas-particle flow, *Powder Tech.* 129: 72–85.

Sun, J. & Battaglia, F. (2006a). Hydrodynamic modeling of particle rotation for segregation in bubbling gas-fluidized beds, *Chemical Engineering Science* 61: 1470–1479.

Sun, J. & Battaglia, F. (2006b). Hydrodynamic modeling of particle rotation for segregation in bubbling gas-fluidized beds, *Chemical Engineering Science* 61(5): 1470–1479.
URL: *http://dx.doi.org/10.1016/j.ces.2005.09.003*

Syamlal, M. (1998). MFIX documentation: Numerical technique, *Technical Note DOE/MC31346-5824, NTIS/DE98002029*, National Energy Technology Laboratory, Department of Energy, Morgantown, West Virginia. See also URL `http://www.mfix.org`.

Syamlal, M., Rogers, W. & O'Brien, T. (1993). MFIX documentation: Theory guide, *Technical Note DOE/METC-95/1013, NTIS/DE95000031*, National Energy Technology Laboratory, Department of Energy. See also URL `http://www.mfix.org`.

Walton, O. R. (1992). Numeical simulation of inelastic, frictional particle–particle interaction, *in* M. C. Roco (ed.), *Particulate Two-phase Flow*, Butterworth-Heinemann, London, pp. 1249–1253.

Walton, O. R. & Braun, R. L. (1986). Viscosity, granular-temperature, and stress calculations for shearing assemblies of inelastic, frictional disks, *J. Rheol.* 30: 949.

Xiao, H. & Sun, J. (2011). Algorithms in a robust hybrid CFD-DEM solver for particle-laden flows, *Communications in Computational Physics* 9: 297–323.

3

Hydrodynamic Loads Computation Using the Smoothed Particle Methods

Konstantin Afanasiev, Roman Makarchuk and Andrey Popov
Kemerovo State University
Russia

1. Introduction

The study of wave fluid flows is now under special consideration in view of serious effects, caused by dams breaking and consequent formation of moving waves, their interaction with solids and structures, uprush on shore, etc. Thereby solving the problem of hydrodynamic loads estimation is important for designing the shape and stiffness of the structures, interacting with oncoming waves. Such problems, due to large deformations of free surfaces, are very complex, and meshless methods proved to be the most suitable for numerical simulation of them.

Particle methods form the special class of meshless methods, which mainly based on the strong form of governing equations of gas dynamics and fluid dynamics. The peculiar representatives of particle methods are Smoothed Particle Hydrodynamics (SPH) (Lucy, 1977; Gingold & Monaghan, 1977) and Incompressible SPH (ISPH) (Cummins & Rudman, 1999; Shao & Lo, 2003; Lee et al., 2008).

Large amount of papers, devoted to numerical simulations of free surface flows using SPH or ISPH, demonstrated a high degree of efficiency of both methods in obtaining the kinematic characteristics of flows, though it has been revealed, that ISPH shows a larger particle scattering at the stages, following the water impact, in comparison with the classic SPH, where particles are more ordered. However, dynamic characteristics of flows are still hard to compute, especially it concerns the classic SPH.

The objective of the chapter is to analyze the capacity of the methods to compute pressure fields and hydrodynamic loads subsequently.

2. Governing equations

The governing equations of fluid dynamics, including the Navier-Stokes equations and the continuity equation, in the case of the Newtonian viscous compressible fluids, are of the following form:

$$\frac{dv^a}{dt} = F^a - \frac{1}{\rho}\frac{\partial p}{\partial x^a} + \frac{1}{\rho}\frac{\partial}{\partial x^b}(T^{ab}); \tag{1}$$

$$\frac{d\rho}{dt} = -\rho\frac{\partial v^a}{\partial x^a}, \tag{2}$$

where $a,b=1,2,3$ – numerical indices of coordinates, v^a – components of the velocity vector, F^a – components of the vector of volumetric forces density, δ_{ab} – Kronecker symbols, p and ρ – pressure and density of the fluid, correspondingly. Here the Einstein summation convention is assumed. The viscous stress tensor components are calculated by the formula (μ - dynamic viscosity):

$$T^{ab}=\mu\left(\frac{\partial v^a}{\partial x^b}+\frac{\partial v^b}{\partial x^a}-\frac{2}{3}\frac{\partial v^c}{\partial x^c}\cdot\delta^{ab}\right) \tag{3}$$

For enclosing the system (1)-(3) one should make some assumptions about fluid properties. The original SPH method assumes the fluid to be weakly compressible, and therefore is applied to the system (1)-(3) with certain equation of state for enclosure. The most often used equation of state is the Theta form equation for barotropic processes (Monaghan et al., 1994):

$$p=B\left[\left(\frac{\rho}{\rho_0}\right)^{\gamma}-1\right] \tag{4}$$

Selecting the coefficient of volume expansion B one can obtain the effect of incompressible fluid.

The ISPH method in contrast to the original SPH uses the model of incompressible fluid, what means $d\rho/dt=0$. In that case the equation of state shouldn't be considered and the enclosed system of governing equations takes the following form:

$$\frac{dv^a}{dt}=F^a-\frac{1}{\rho}\frac{\partial p}{\partial x^a}+\frac{\mu}{\rho}\frac{\partial}{\partial x^b}\left(\frac{\partial v^a}{\partial x^b}\right) \tag{5}$$

$$\frac{\partial v^a}{\partial x^a}=0; \tag{6}$$

3. Smoothed particle methods

3.1 The basis of the methods

The key idea of smoothed particle methods lies in discretization of the problem domain into a set of Lagrangian particles, which play the role of nodes in function approximation. For construction of approximation formulas in smoothed particle methods the exact integral representation with the Dirac δ-function is used:

$$f(\mathbf{r})=\int_{-\infty}^{\infty} f(\mathbf{r}')\delta(\mathbf{r}-\mathbf{r}')d\mathbf{r}', \tag{7}$$

The Dirac δ-function is changed here by a compactly supported function W, called the kernel function, what allows to obtain the integral formula about the bounded domain:

$$f(\mathbf{r})=\int_{D} f(\mathbf{r}')W(\mathbf{r}-\mathbf{r}',h)d\mathbf{r}', \tag{8}$$

The value h determines a size of support domain D of the function W and is called a smoothing length. Having a set of particles scattered about the problem domain Ω we

can estimate the value of the above integral with the quadrature (Lucy, 1977; Gingold & Monaghan, 1977):

$$f_s(\mathbf{r}_i) = \sum_{j=1}^{n} f(\mathbf{r}_j)\frac{m_j}{\rho_j} W(\mathbf{r}_i - \mathbf{r}_j, h), \tag{9}$$

where n is a number of particles, determined as "nearest neighbours" of the i-th particle within the support domain D. Two particles i and j are called neighbouring or interacting particles, if the distance between their centers does not exceed kh, where k depends on the type of kernel function and $h = (h_i + h_j)/2$. $\mathbf{r}_j, m_j, \rho_j$ - radius-vector, mass and density of the j-th particle, correspondingly. A simple formula for the gradient of a function has the form:

$$\nabla f_s(\mathbf{r}_i) = \sum_{j=1}^{n} f(\mathbf{r}_j)\frac{m_j}{\rho_j} \nabla W(\mathbf{r}_i - \mathbf{r}_j, h) \tag{10}$$

3.2 Kernel function

As kernel function is a keystone of smoothed particle methods a great attention is paid to construction of new types of kernels. Till now a large amount of different types of kernel functions have been developed. All of them should satisfy the following basic conditions:

- $W(\mathbf{r} - \mathbf{r}', h) = 0, \|\mathbf{r} - \mathbf{r}'\| > kh;$
- $\int_{\Omega} W(\mathbf{r} - \mathbf{r}', h) d\mathbf{r}' = 1;$
- $\lim_{h \to 0} W(\mathbf{r} - \mathbf{r}', h) = \delta(\mathbf{r} - \mathbf{r}').$

Here for the problems, simulated with SPH, the original Monaghan's cubic spline is utilized (Monaghan et al., 1994):

$$W(\mathbf{r} - \mathbf{r}', h) = \frac{15}{7\pi h^2} \begin{cases} 2/3 - q^2 + q^3/2, 0 \le q \le 1; \\ (2-q)^3/6, 1 < q \le 2; \\ 0, q > 2, \end{cases} \tag{11}$$

where $q = \dfrac{\|\mathbf{r} - \mathbf{r}'\|}{h}$.

As it was pointed out (G.R. Liu & M.B. Liu, 2008) the approximations of functions based on the kernels that haven't smooth second derivative are too sensitive to particle scattering. It plays a crucial role for the ISPH method as elliptic Poisson equation is solved for obtaining a pressure field. That is why in numerical simulations using ISPH the fourth-order spline has been used (Morris, 1996; Lee et al., 2008):

$$W(\mathbf{r} - \mathbf{r}', h) = \frac{96}{1199\pi h^2} \begin{cases} (5/2 - q)^4 - 5(3/2 - q)^4 + 10(1/2 - q)^4, \ 0 \le q \le 1/2 \\ (5/2 - q)^4 - 5(3/2 - q)^4, \ 1/2 < q \le 3/2 \\ (5/2 - q)^4, \ 3/2 < q \le 5/2 \\ 0, \ q > 5/2 \end{cases} \tag{12}$$

3.3 Approximation of governing equations

For approximation of gradient terms in equations (1) or (5) the original formula (10) may be applied. However, it is usually implemented for derivation of new forms of gradient approximations. In numerical simulations the following form is commonly used:

$$-\frac{1}{\rho}\nabla p_i = -\sum_{j=1}^{n} m_j \left(\frac{p_i}{\rho_i^2} + \frac{p_j}{\rho_j^2} \right) \nabla_i W(\mathbf{r}_i - \mathbf{r}_j, h) \tag{13}$$

This formula has an advantage of being symmetric in relation to interacting particles and thus conserves total momentum of a system of particles, representing the problem domain. Besides it gives more stable results of numerical simulations in comparison to (10).
For a divergence of a velocity field in the continuity equation (2) the following expression is usually applied:

$$\nabla \cdot \mathbf{v}_i = -\frac{1}{\rho_i} \sum_{j=1}^{n} m_j (\mathbf{v}_i - \mathbf{v}_j) \cdot \nabla_i W(\mathbf{r}_i - \mathbf{r}_j, h) \tag{14}$$

The above form gives a zero-valued first derivatives for a constant field.
Using (13) for approximation of gradient of a function one can obtain the following discrete representation for viscous term in equation (1):

$$\left(\frac{1}{\rho} \nabla \cdot \mathbf{T} \right)_i = \sum_{j=1}^{n} m_j \left(\frac{\mathbf{T}_i}{\rho_i^2} + \frac{\mathbf{T}_j}{\rho_j^2} \right) \cdot \nabla_i W(\mathbf{r}_i - \mathbf{r}_j, h) \tag{15}$$

Normal and tangent components of viscous stress tensor T_i are defined by following expressions similar to (14) (G.R. Liu & M.B. Liu, 2008):

$$\begin{aligned} T_i^{ab} = \mu \sum_{j=1}^{n} \frac{m_j}{\rho_j} \Big[(v_j^a - v_i^a) \nabla_i^b W(\mathbf{r}_i - \mathbf{r}_j, h) + (v_j^b - v_i^b) \nabla_i^a W(\mathbf{r}_i - \mathbf{r}_j, h) \Big] - \\ - \left(\frac{2}{3} \mu \sum_{j=1}^{n} \frac{m_j}{\rho_j} (\mathbf{v}_j - \mathbf{v}_i) \cdot \nabla_i W(\mathbf{r}_i - \mathbf{r}_j, h) \right) \delta^{ab} \end{aligned} \tag{16}$$

As it will be pointed out in section 3.4 the pressure Poisson equation need to be solved in the ISPH method. There are some ways to obtain the approximations of second derivatives in smoothed particle methods. One way consists in directly deriving the formula in a similar manner as for first derivative (10). The idea of the other is in subsequent implementation of a gradient formula (13) and a divergence of vector field (14). However these ways proved to be too sensitive to inhomogeneous particle distribution and result in non-physical oscillations of pressure field. So the approximation of the first derivative in terms of the SPH method and its finite difference analogue are usually applied together according to Brookshaw's idea (Brookshaw, 1985). Based on it some different forms of Laplacian operator were derived (Cummins & Rudman, 1999; Shao & Lo, 2003; Lee et al., 2008). Here for numerical simulations the form of Lee (Lee et al., 2008) is used:

$$\Delta p_i = \frac{2}{\rho_i} \sum_{j=1}^{n} m_j \frac{\left(p_i - p_j \right) \left(\mathbf{r}_i - \mathbf{r}_j \right) \cdot \nabla_i W(\mathbf{r}_i - \mathbf{r}_j, h)}{\left\| \mathbf{r}_i - \mathbf{r}_j \right\|^2} \tag{17}$$

The approximation formulas for viscous forces in ISPH are obtained in a similar way and may take different forms (Cleary & Monaghan, 1999; Shao & Lo, 2003). Here for numerical simulations the following viscous term by Morris (Morris et al., 1997) is utilized:

$$\nabla\cdot\left(\frac{\mu}{\rho}\nabla\mathbf{v}\right)_i=\sum_{j=1}^{n}m_j\frac{\left(\mu_i+\mu_j\right)}{\rho_i\rho_j}\frac{\left(\mathbf{r}_i-\mathbf{r}_j\right)\cdot\nabla_i W(\mathbf{r}_i-\mathbf{r}_j,h)}{\left\|\mathbf{r}_i-\mathbf{r}_j\right\|^2}\left(\mathbf{v}_i-\mathbf{v}_j\right) \tag{18}$$

3.4 Time integration

In the original SPH method for time integration the "predictor-corrector" scheme is commonly used:
"*predictor*":

$$\begin{cases}\rho_i^n=\rho_i^{n-1/2}+(\Delta t/2)(d\rho_i^{n-1}/dt);\\ \mathbf{v}_i^n=\mathbf{v}_i^{n-1/2}+(\Delta t/2)(d\mathbf{v}_i^{n-1}/dt).\end{cases} \tag{19}$$

"*corrector*":

$$\begin{cases}\rho_i^{n+1/2}=\rho_i^{n-1/2}+\Delta t(d\rho_i^n/dt);\\ \mathbf{v}_i^{n+1/2}=\mathbf{v}_i^{n-1/2}+\Delta t(d\mathbf{v}_i^n/dt).\end{cases} \tag{20}$$

The new radius-vectors of particles on $(n+1)$-th time step are calculated using the Euler integration scheme:

$$\mathbf{r}_i^{n+1}=\mathbf{r}_i^n+\Delta t(\mathbf{v}_i^{n+1/2}/dt). \tag{21}$$

For time integration of motion equations in the ISPH method the split step scheme is applied (Yanenko, 1960; Chorin, 1968). According to its idea time integration process is splitted into convection-diffusion and pressure contribution. So the first step of the scheme for preliminary velocity values takes the from:

$$\mathbf{v}_i^*=\mathbf{v}^n+\left(\mathbf{g}+\nabla\cdot\left(\frac{\mu}{\rho}\nabla\mathbf{v}\right)\right)\Delta t \tag{22}$$

Projecting the preliminary velocity values onto a null-divergence field one can obtain:

$$\mathbf{v}_i^{n+1}=\mathbf{v}_i^*-\frac{1}{\rho}\nabla p^{n+1}\Delta t, \tag{23}$$

provided the pressure field on $(n+1)$-th time step is calculated through the pressure Poisson equation (Lee et al., 2008):

$$\Delta p_i^{n+1}=\frac{\rho\nabla\cdot\mathbf{v}_i^*}{\Delta t}, \tag{24}$$

where the velocity divergence at right hand side of above equation is calculated using formula (14). The radius-vectors of particles on $(n+1)$ -th time step can be get out of the following formula according to Euler explicit integration scheme:

$$\mathbf{r}_i^{n+1} = \mathbf{r}_i^n + \mathbf{v}_i^{n+1}\Delta t \tag{25}$$

The equation (24) is reduced to the system of linear algebraic equations with symmetric matrix. For solving this system the preconditioned generalized minimum residual method (PGMRES) is applied (Saad, 2003).

3.5 Free surface

For identification of particles on the free surface, one can apply some different ways. One of such ways is using the geometrical Dilts algorithm (Dilts, 2000), based on the fact, that each particle has its size, commonly determined by the smoothing length.
The other way is detection of particles, satisfying the inequality (Lee et al., 2008):

$$\sum_{j=1}^{n} \frac{m_j}{\rho_j}\left(\mathbf{r}_i - \mathbf{r}_j\right)\cdot\nabla_i W(\mathbf{r}_i - \mathbf{r}_j, h) < 2\beta \tag{26}$$

as free surface particles have less nearest neighbors in comparison with the inner ones.
Here the Dilts algorithm is used for the original SPH method and the formula (26) for ISPH. For free surface particles the Dirichlet condition is imposed: $p = 0$. For the original SPH it means that free surface particles has the zero pressure, not the pressure obtained out of the equation of state as for inner fluid particles. As the pressure Poisson equation (PPE) is solved in the ISPH method for obtaining pressure field, the Dirichlet condition is embedded into the matrix of the system of linear algebraic equations (SLAE), which is the discrete representation of PPE. This procedure conserves the symmetry of matrix of SLAE.

3.6 Solid boundary

In smoothed particle methods the most commonly way of imposing conditions at solid boundaries is the virtual particle method, divided into two basic types.
The first type – Monaghan virtual particles method (Monaghan et al., 1994). The virtual particles are located along the solid boundary in a single line, don't change their characteristics in time, and effect on the fluid particles by means of a repulsive force, based on certain interaction potential. The most popular among researchers is the Lennard-Jones potential.
The second type – Morris virtual particles (Morris et al., 1997). These particles are located along the solid boundary in several lines. The number of the lines depends on the smoothing length of particles of the fluid. This allows solving one of the main problems of the SPH method – asymmetry of the kernel function near the boundaries. The effect of the Morris particles on the fluid ones differs from the effect of Monaghan particles by the fact, that there is no need in using any interaction potential. Instead of this, values of the characteristics in the Morris particles are calculated on the basis of their values in particles of the fluid. Here for imposing solid boundary conditions on velocity the Morris virtual particles are used for both methods. In ISPH the Morris virtual particles are also implemented for imposition of Neumann boundary conditions on solid walls, that is $\partial p / \partial n = 0$ (Koshizuka et al., 1998; Lee et al., 2008). The procedure of embedding these conditions into the matrix of SLAE breaks its symmetry. Therefore, as it was mentioned in section 3.4, the PGMRES solver is utilized.

3.7 Pressure field in the original SPH method

In the SPH method barotropic condition for pressure $p = p(\rho)$ is supposed . For the first time Monaghan (Monaghan et al., 1994) applied equation for pressure in the Theta form:

$$p = B\left[\left(\frac{\rho}{\rho_0}\right)^{\gamma} - 1\right] \tag{27}$$

where $B = 200\rho gH / \gamma$ – gravitational constant, ρ - density, ρ_0 - initial density, H – initial height of fluid, $\gamma = 7$.

Monaghan applied this equation for free surface flow simulations, such as breaking dam problems. But research of the calculation of pressure by (27) shows that pressure field in fluid has a significant oscillations.

To reduce pressure oscillations we smooth density field. For free surface problems in the case of the system being at rest under the action of gravity force at the initial time the hydrostatic pressure distribution is true: $p_0 = \rho_0 g(H - y)$. Then we can define the corrected value for the initial density from equation of state (27):

$$\rho_0^* = \rho_0\left[1 + \frac{\rho_0 g(H - y)}{B}\right]^{\frac{1}{\gamma}} \tag{28}$$

Besides in time integration scheme for density computation the equation for density smoothing is added based on the formula (9) following Chen's idea (Chen et al., 2001):

$$\rho_i^{smooth} = \frac{\sum_{j=1}^{n} m_j \rho_j W(\mathbf{r}_i - \mathbf{r}_j, h)}{\sum_{j=1}^{n} m_j W(\mathbf{r}_i - \mathbf{r}_j, h)} \tag{29}$$

Using (27) and (29), we can obtain smoothed pressure field $p^{smooth} = p(\rho^{smooth})$. The pressure at solid boundary particles can be determined out of the following expression:

$$p_i = \sum_{j=1}^{n} \frac{m_j}{\rho_j} p_j W(\mathbf{r}_i - \mathbf{r}_j, h) \tag{30}$$

Thus the pressure at solid boundary particles is calculated using the values of the pressure at neighbouring fluid particles by formula (9).

4. Hydrodynamic loads

Hydrodynamic loads onto the solid boundary Γ is the integral characteristic of the wave pressure. Here the following formula is used (Afanasiev & Berezin, 2004):

$$P_s = \int_{\Gamma} \left[p(T) - p(0)\right] d\Gamma, \tag{31}$$

where $p(0)$ is initial pressure and $p(T)$ is the pressure at any other moment T .

In the numerical computations the value of the integral (31) is estimated by the formula:

$$P_s \approx \sum_{j \in P_B} p_j(T) - p_j(0), \tag{32}$$

where P_b is a set of solid boundary particles.

5. Nearest neighbour search

In numerical simulations using the smoothed particle methods it is necessary to determine for every particle j its interacting particles, as all physical characteristics of the fluid are estimated over the values at neighbouring particles according to the formula (9). For each fluid particle j its smoothing length h_j is set, determining the radius of interaction with neighbours. As it is clear from section 3.1 in smoothed particle methods if particle i interacts with particle j then particle j interacts with particle i too, so forming the interacting pair. Thus it is necessary to solve a geometrical problem of determination of points which are in the circle of radius kh with the center at the point j (fig. 1 a).

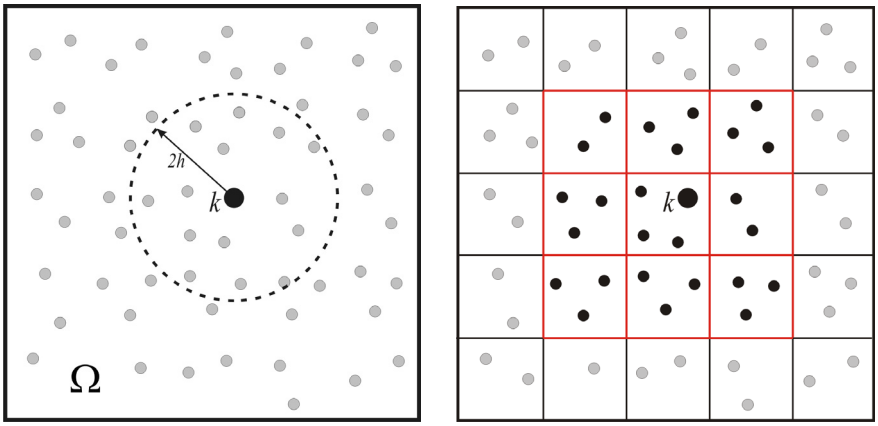

a) b)

Fig. 1. Nearest neighbour search: a) search area, b) cells for search

Direct search algorithm has time complexity about $O(N^2)$ operations for procedure of determination of all interacting pairs, where N is the total number of particles in problem domain. Here the efficient algorithm, based on rectangular grid construction is implemented.

The idea of the method consists in construction of a grid on each time step which fully covers the problem domain. The linear size of grid cells is constant and equals to:

$$l = kh(1 + \varepsilon) \tag{33}$$

where $\varepsilon > 0$ and $\varepsilon << 1$. At next step for each particle its belonging to one of the cells of a grid is defined. Then nearest neighbours for particle j are determined using direct search algorithm but only within the adjacent cells (fig. 1 b).

In fig. 2 the results of testing the speed of both algorithms are presented (X-axis corresponds to total number of particles and Y-axis corresponds to full time search procedure).
Test calculations were carried out on uniprocessor system: AMD Athlon 2000+, 512 Mb RAM. Time of nearest neighbour particle search depending on number of particles for 1000 time steps was measured. It can be noted that grid algorithm is very efficient and, for example, calculations with 8000 fluid particles gives acceleration of about 100.

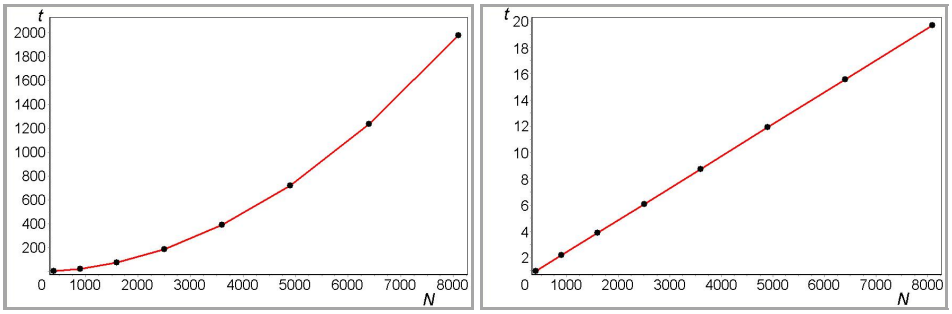

a) b)

Fig. 2. Search time for: a) direct search, b) grid algorithm

For the grid algorithm it is shown that its analytic time complexity is about $O(N)$ operations (Afanasiev et al., 2008) that agrees well with obtained numerical data (see fig. 2 b).

6. Testing the methods

6.1 Poiseuille flow

This problem is one of the classical tests for viscous fluid flows, because of well-known analytical solution for velocity profile. Here two-dimensional non-stationary viscous fluid flow between two parallel solid walls is considered. Initially the fluid in the infinite channel, bounded with solid walls Γ_2 and Γ_4, is at rest. Motion of fluid particles occurs in rectangular domain Ω, representing the infinite channel, due to difference of pressure at opposite open boundaries Γ_1 and Γ_3 (fig. 3). On horizontal solid walls Γ_2 and Γ_4 the slip condition is set (the zero-valued velocity vector).

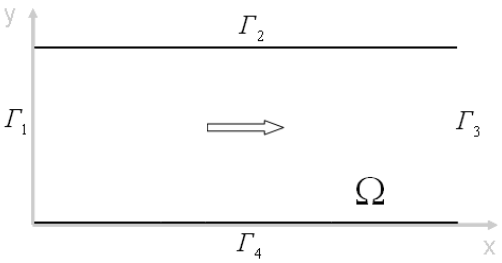

Fig. 3. Problem domain for Poiseuille flow

Within the problem domain Ω the fluid motion is described with the simplified momentum equation:

$$\frac{dv}{dt} = -\frac{P_{out} - P_{in}}{\rho L} + \frac{\mu}{\rho}\frac{d^2 v}{dy^2} \tag{34}$$

where P_{in}, P_{out} - the pressure at Γ_1 and Γ_3 accordingly; ρ, μ, L are the density, dynamic viscosity and the channel length, H is the height of the channel. The infinity of the channel is simulated by cyclic returning of particles, passed through the right open boundary Γ_3, on left boundary Γ_1 with the obtained physical characteristics. Pressure difference is simulated by the horizontal volumetric force F, directed from Γ_1 to Γ_3:

$$\frac{dv}{dt} = F + \frac{\mu}{\rho}\frac{d^2 v}{dy^2} \tag{35}$$

The analytical solution of above ordinary differential equation with slip boundary conditions takes the form (Leonardo et al., 2003):

$$v(y,t) = -\frac{F}{2\upsilon}(y^2 - d^2) + \sum_{n=0}^{\infty} \frac{16(-1)^{n+1} d^2 F}{\upsilon \pi^3 (2n+1)^3} \cos\left(\frac{(2n+1)\pi y}{2d}\right) \exp\left(-\frac{(2n+1)^2 \pi^2 \upsilon t}{4d^2}\right) \tag{36}$$

where $d = H/2$ is the half-height of the channel, $\upsilon = \mu/\rho$ is the kinematic viscosity and the first term in the right hand side is the stationary velocity in the channel when $t \to \infty$.
For simulations the following values of parameters have been used: $L = H = 2d$, $d = 5 \times 10^{-4}\ m$, the fluid density $\rho = 1000\ kg/m^3$, the kinematic viscosity $\upsilon = 10^{-6}\ m^2/s$ (that corresponds to the real viscosity of water $\mu = 10^{-3}$ kg/(m·s)) and external horizontal force $F = 10^{-4}\ m/s^2$.
As the velocity profiles for Poisseuille flow obtained with the original SPH method and ISPH are very similar, the results are presented only for the original SPH method. In fig. 4 the velocity profiles for two moments of time are given, where line describes the analytic solution (36) and the points show the results by SPH for 2500 fluid particles. Approximately at $t = 0.6\ s$ (fig. 4 b) flow within the channel becomes stationary. In table 1 the numerical errors by SPH and ISPH are compared.

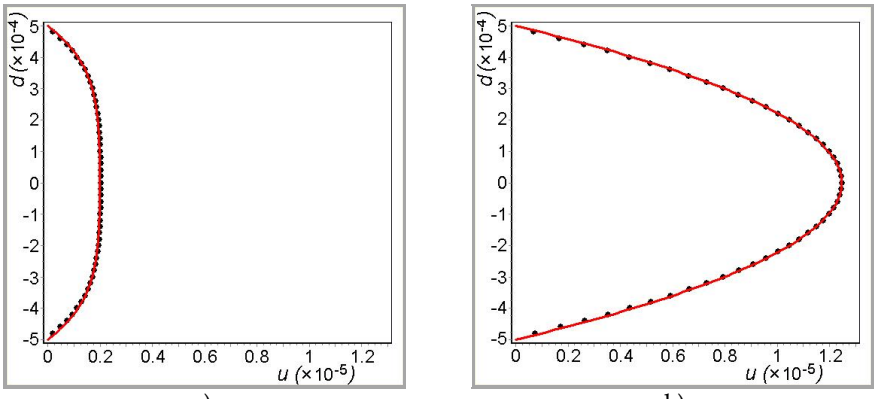

a) b)

Fig. 4. Velocity profile for Poiseuille flow: a) $t = 0.02\ s$, b) $t = 0.6\ s$

N	225	400	625	900	1600	2500	3600
Numerical error by SPH (%)	12.9	6.9	5.0	3.3	1.4	0.85	0.71
Numerical error by ISPH (%)	2.12	1.67	1.38	1.01	0.86	0.7	0.62

Table 1. Numerical errors by SPH and ISPH for different sets of particles

6.2 Laminar fluid flow along the infinite inclined plane

The problem is of special interest because it is one of few problems for viscous free surface flows, that have an analytic solution. The problem domain is shown in fig. 5 a. The fluid flow takes place in a rectangular infinite region Ω, bounded with solid wall Γ_1 inclined at an angle α to the horizontal surface. Γ_2 is free surface and initially fluid flow is at rest. Fluid flow occurs under gravity force, directed vertically to the horizontal surface. On solid boundary Γ_1 the slip condition is set.

The formulation can be simplified by performing rotation of the coordinate axes by angle α so that the X-axis coincides with the horizontal surface. Considering that the velocity of the fluid depends only on the vertical coordinate y: $v = v_x(y)$, the action of gravity can be replaced by volumetric horizontal force F, which is the projection of gravity onto X-axis. Thus, the problem domain is changed to shown in fig. 5 b.

For numerical simulations the problem domain has a finite length L along the X-axis and finite height H along the Y-axis.

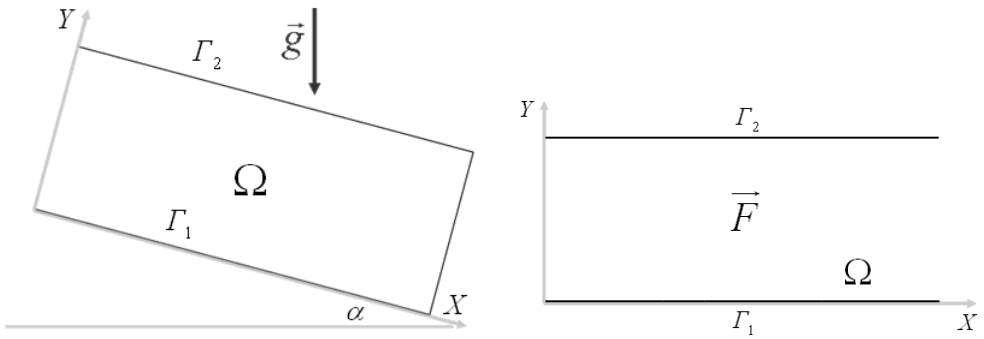

Fig. 5. Problem domain: a) initial, b) simplified

The infinity of the channel is modeled by the algorithm described for Poiseuille flow in section 6.1. Provided $F_x = g\sin\alpha$, equation of motion with slip boundary conditions is written as:

$$0 = \upsilon\frac{\partial^2 v}{\partial y^2} + g\sin\alpha \tag{37}$$

$$v|_{\Gamma_1} = 0 \tag{38}$$

As was mentioned above the problem has stationary analytic solution, that has the following form (Slezkin, 1995):

$$v(y) = g(H - \frac{y}{2})y\frac{\sin\alpha}{\upsilon} \tag{39}$$

In simulations by the smoothed particle methods the non-stationary equations were used and the convergence of the non-stationary solutions obtained by SPH and ISPH methods to the stationary analytic solution (39) are considered. Parameters used in numerical simulations: $L = H = 10^{-3}\ m$, density of the fluid $\rho = 1000\ kg/m^3$, kinematic viscosity $\upsilon = 10^{-6}\ m^2/s$, volumetric horizontal force $F_x = 10^{-4}\ m/s^2$. As for previous problem the velocity profiles are provided only for the original SPH method (see fig. 6) , where line represents the analytic solution and points by SPH for 2500 fluid particles. As it can be seen from fig. 6 b the flow becomes stationary approximately at $t = 4\ s$. The comparison of numerical errors given by SPH and ISPH is presented in table 2 for $t = 4\ s$.

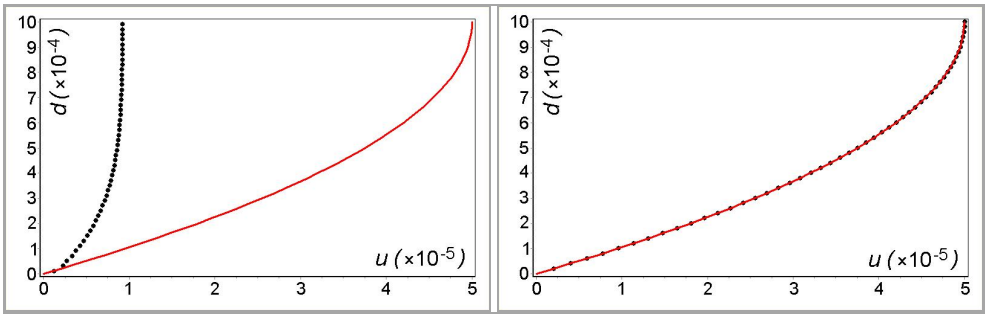

a) b)

Fig. 6. Velocity profiles for laminar flow along the incline plane: a) $t = 0.075\ s$, b) $t = 4\ s$

N	225	400	625	900	1600	2500	3600
Numerical error by SPH (%)	11.45	6.28	4.34	2.08	1.11	0.82	0.75
Numerical error by ISPH (%)	6.89	5.73	4.46	3.62	2.76	2.12	1.79

Table 2. Numerical errors by SPH and ISPH for different sets of particles

6.3 Droplet problem

At initial moment of time the problem domain Ω is a circle of incompressible fluid with radius $r = 1$ and with center located at the origin of the coordinates (Ovsyannikov, 1967). Deformation of a circle into ellipse with semi-axes $a(t)$ (along $y = 0$) and $b(t)$ (along $x = 0$) is initiated by the non-zero velocity field:

$$u(\mathbf{x},t) = a'(t)/a(t)\cdot x, v(\mathbf{x},t) = -a'(t)/a(t)\cdot y. \tag{40}$$

Incompressibility is provided by constancy of ellipse's square for any moment of time, that is $a(t)\cdot b(t) = 1$. So at any moment of time the form of ellipse is described with the following equation:

$$\frac{x^2}{a^2(t)} + a^2(t)y^2 = 1, \tag{41}$$

where $a(t)$ is taking from the system of ordinary differential equations:

$$\begin{cases} a' = c; \\ c' = 2c^2/(a^5 + a), \end{cases} \tag{42}$$

with appropriate initial conditions:

$$a(t)|_{t=0} = 1, c(t)|_{t=0} = 1. \tag{43}$$

In simulations using the ISPH method parameter β (in free surface detecting algorithm, see section 3.5) and parameter h/dx were varied. The best results were obtained for $h/dx = 1.1$ and $\beta = 0.75$. The results are provided for these values of mentioned parameters.
Fourth-order Runge-Kutta method was used for obtaining sample results. The results of numerical simulations are provided only for the ISPH method as the results of the original SPH are very similar (Afanasiev et al., 2006). The comparison with solution by Runge-Kutta is presented on fig. 7. Thin points represent the result by ISPH, thick points – by Runge-Kutta method. Table 3 shows the comparison of numerical errors by the original SPH method and by ISPH for $t = 0.8\ s$ with different numbers of fluid particles, which corresponds to the moment of time for the relation of semi-axes of ellipse 1:2.

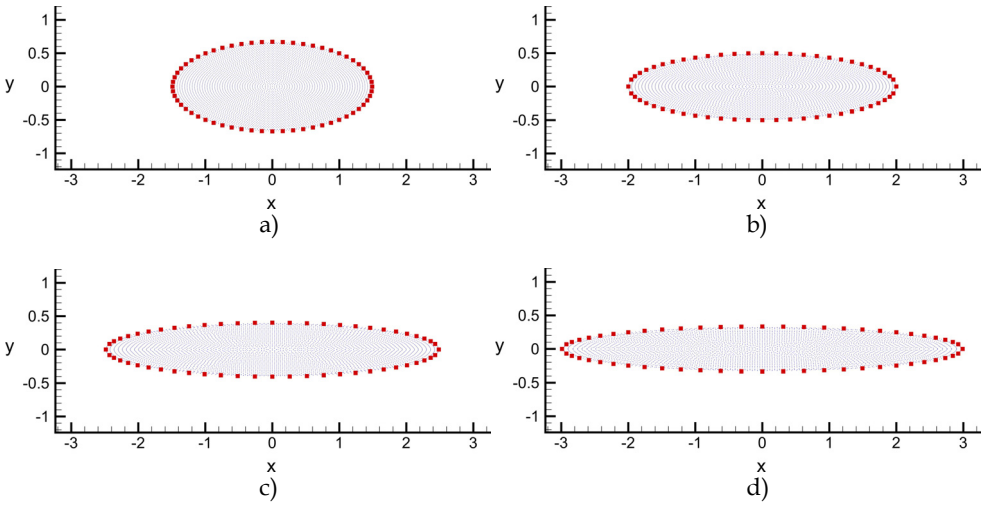

Fig. 7. Droplet problem: a) $t = 0.43\ s$, b) $t = 0.8\ s$, c) $t = 1.16\ s$, $t = 1.51\ s$

N	721	1261	2791	4921	7651
Numerical error by SPH (%)	1.56	0.69	0.21	0.17	0.15
Numerical error by ISPH (%)	0.56	0.42	0.3	0.22	0.17

Table 3. Numerical errors by SPH and ISPH for different sets of particles

7. Dam breaking problem

Dam breaking problem is a classical test for benchmarking the meshless methods. The equations (1)-(2) or (5)-(6) are solved depending on the method. The formulation of the problem is following (see fig. 8).

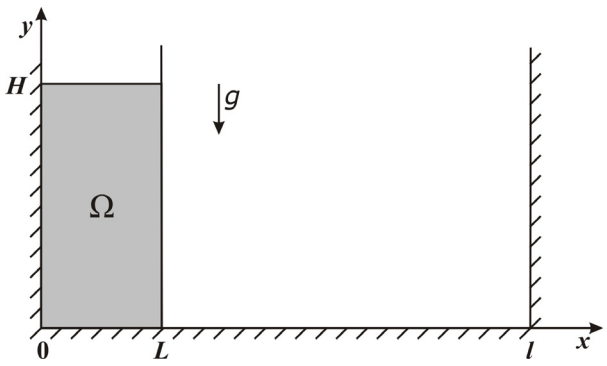

Fig. 8. The problem domain for dam breaking

At the initial moment of time viscous fluid column gets broken under gravity force and starts its motion towards the opposite solid wall of the basin. When the fluid flow reaches the wall the wave is forming at the backoff and at a certain moment of time it breaks. For numerical simulation of the problem the following values of physical characteristics were used: $\rho = 1000\ kg/m^3$ – the fluid density, $\nu = 10^{-6}\ \mathrm{m}^2/\mathrm{s}$ – the kinematic viscosity. Fig. 9 presents flow charts, colored by pressure field and obtained using SPH (a, c, e) and ISPH (b, d, f) at different moments of time: $t = 0.195\ s$ (a, b), $t = 0.278\ s$ (c, d) and $t = 0.593\ s$ (e, f). The obtained smooth pressure field allows to estimate the hydrodynamic loads on the left and right solid walls of the basin, the time charts of which are shown in fig. 10. In the simulations by the ISPH method the turbulent viscous forces were taken into account. As it is pointed out by Lee (Lee et al., 2008), the additional turbulent viscosity makes pressure field smoother. Here the Boussinesq assumption for enclosure Reynolds-averaged Navier-Stokes equations was used along with mixing length model of Prandtl for the turbulent viscosity coefficient (Lee et al., 2008). Stability of calculations by the original SPH method

are provided by the additional artificial viscosity. Smooth pressure field is a result of utilizing the special techniques, proposed in section 3.7. The difference between the time charts of hydrodynamic loads obtained by SPH and ISPH may be explained probably by the effect of turbulence in the ISPH method. However this is the subject for future work.

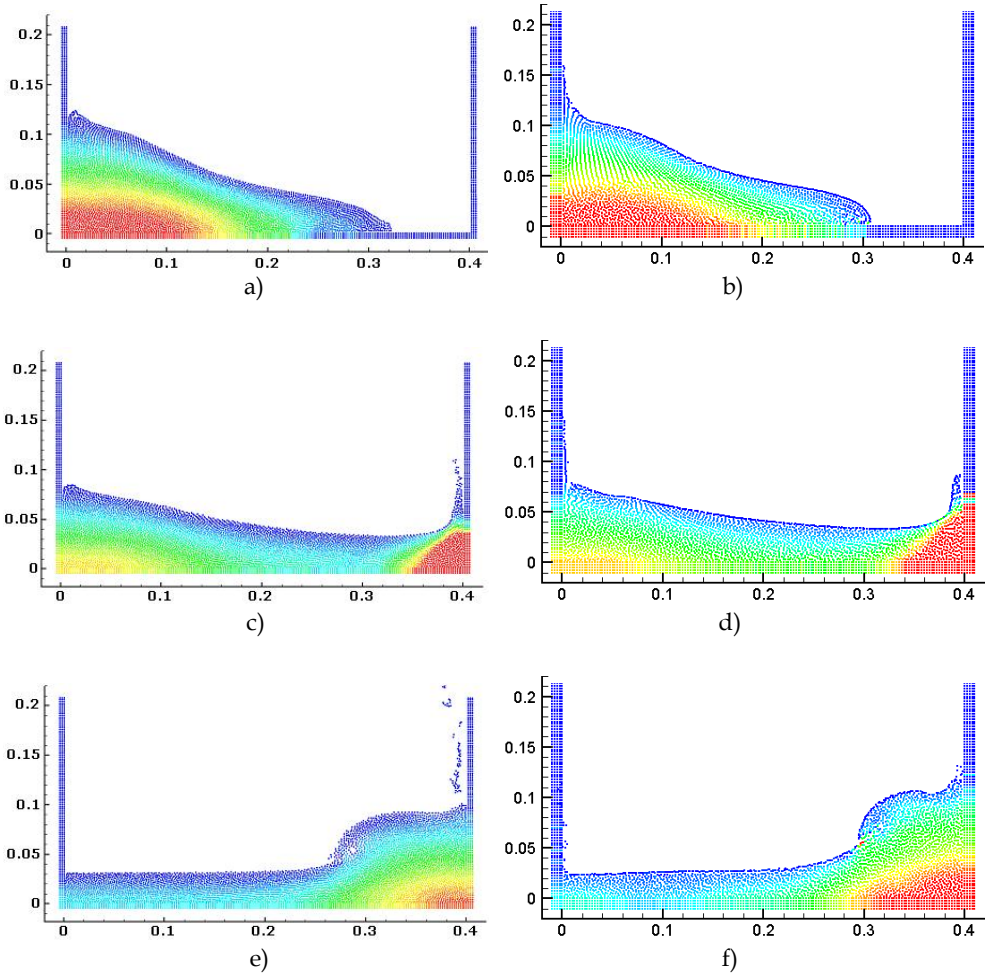

Fig. 9. Flow charts colored by pressure field: a, c, e) by SPH; b, d, f) by ISPH

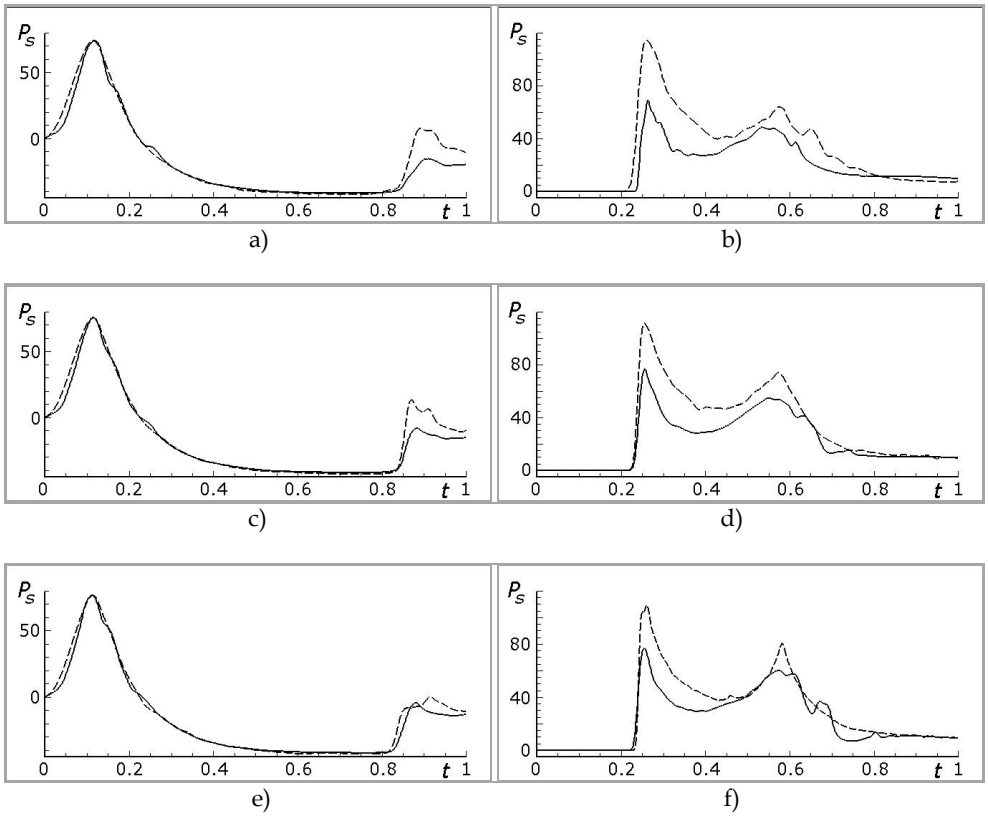

Fig. 10. Time charts of hydrodynamic loads: a, c, e) on the left wall; b, d, f) on the right wall

8. Conclusion

As it follows from the results of simulation of dam breaking problem using SPH and ISPH, the both methods demonstrate good results in pressure field calculation. The time charts of hydrodynamic loads on the solid walls of the basin show good agreement, what proves their correctness. It can be concluded that the smoothed particle methods allow obtaining correct hydrodynamic loads in the case of large deformations of free surface and can be used for problems of that type. As some differences between hydrodynamic loads obtained on one side by SPH and on the other side by the ISPH method is observed, explanation of this fact becomes a subject for future work. It is also planned to analyse the influence of turbulent forces onto the hydrodynamic loads.

9. References

Afanasiev, K.E. & Berezin, E.N. (2004). Dynamic characteristics analysis in the problem of solitary wave interaction with an obstacle [in Russian]. *Computational Technologies*, Vol. 9, No. 3, pp. 22-37.

Afanasiev, K.E.; Iliasov, A.E.; Makarchuk, R.S. & Popov, A.Yu. (2006). Numerical simulation of free surface flows using SPH and MPS [in Russian]. *Computational technologies,* Vol. 11, special issue, pp. 26-44.

Afanasiev, K.E.; Makarchuk, R.S. & Popov A.Yu. (2008). Nearest neighbor search algorithm in the smooth particle method and its parallel implementation [in Russian]. *Computational technologies*, Vol. 13, special issue, pp. 9-13.

Brookshaw, L.A. (1985) Method of Calculating Radiative Heat Diffusion in Particle Simulation. *Proc. ASA,* Vol. 6, pp. 207-210.

Chen, J.K.; Beraun, J.E. & Jih, C.J. (2001) A corrective smoothed particle method for transient elastoplastic dynamics. Computational Mechanics, Vol.27, pp. 177-187.

Chorin, A.J. (1968). Numerical solution of the Navier-Stokes equations. *Math. Comput.*, Vol. 22, pp. 745-762.

Cleary, P.W. & Monaghan, J.J. (1999) Conduction modelling using smoothed particle hydrodynamics. *Journal of Computational Physics*, Vol. 148, pp. 227–264.

Cummins, S.J. & Rudman, M. (1999). An SPH projection method. *Journal of Computational Physics,* Vol. 152, pp. 584-607.

Dilts, G.A. (2000) Moving-least-squares-particle hydrodynamics ii: Conservation and boundaries. *International Journal for Numerical Methods in Engineering,* Vol. 48, pp. 1503 – 1524.

Gingold, R.A. & Monaghan, J.J. (1977). Smoothed particle hydrodynamics: theory and application to non-spherical stars. *Monthly Notices of the Royal Astronomical Society,* Vol. 181, pp. 375-389.

Koshizuka, S; Nobe, A & Oka, Y. (1998) Numerical analysis of breaking waves using the moving particle semi-implicit method. International Journal for Numerical Methods in Fluids, Vol. 26, pp. 751–769.

Lee, E.-S.; Moulinec, C.; Xu, R.; Violeau, D.; Laurence, D. & Stansby, P. (2008). Comparisons of weakly compressible and truly incompressible algorithms for the SPH mesh free particle method. *Journal of Computational Physics*, Vol. 227, pp. 8417–8436.

Leonardo, Di G.S.; Jaime, K.; Eloy, S.; Yasmin, M. & Anwar, H. (2003). SPH simulations of time-dependent Poiseuille flow at low Reynolds numbers. *Journal of computational physics*, Vol. 191, No. 2, pp. 622-638.

Liu, G.R. & Liu, M.B. (2003) *Smoothed particle hydrodynamics: a meshfree particle method*, World Scientific, ISBN 981-238-456-1, Singapore.

Lucy, L.B. (1977). A numerical approach to the testing of fusion process. *The Astronomical Journal,* Vol. 82, No.12, pp. 1013-1024.

Monaghan, J.J.; Thompson, M.C. & Hourigan, K. (1994). Simulation of free surface flows with SPH. *Journal of computational physics*, Vol. 110, pp. 399-406.

Morris, J.P. (1996). A study of the stability properties of smooth particle hydrodynamics. *Publications Astronomical Society of Australia,* Vol. 13, No. 1, pp. 97-102.

Morris, J.P.; Fox, P.J. & Zhu, Y. (1997) Modeling low Reynolds number incompressible flows using SPH. *Journal of computational physics*, Vol. 136, pp. 214-226.

Ovsyannikov, L.V. (1967). General equations and examples [in Russian]. *Non-stationary free surface problems*, pp. 5-75.

Saad, Y. (2003) Iterative methods for sparse linear systems. Society for Industrial and Applied Mathematics, 10.09.2011, Available from http://www-users.cs.umn.edu/~saad/books.html

Shao, S. & Lo, E.Y.M. (2003). Incompressible SPH method for simulating Newtonian and non-Newtonian flows with a free surface. *Advances in Water Resources*, Vol. 26, pp. 787–800.

Slezkin, N.A. (1995). *The dynamics of a viscous incompressible fluid*, Technical and theoretical literature, Russia.

Yanenko, N.N. (1960). On efficient implicit schemes (fractional step method) [in Russian]. *Report of AS USSR*, Vol. 134, 5 p.

4

Simulating Flows with SPH: Recent Developments and Applications

Giacomo Viccione[1], Vittorio Bovolin[1] and Eugenio Pugliese Carratelli[2]
[1]*University of Salerno, Dept. of Civil Engineering*
[2]*University Centre for the Prediction and Prevention of Great Hazards, C.U.G.Ri*
Italy

1. Introduction

Fluid motion is often numerically reproduced by means of grid-based methods such as Finite Difference Methods (FDMs) and Finite Elements Methods (FEMs). However, these techniques exhibit difficulties, mainly related to the presence of time-dependent boundaries, large domain deformations or mesh generation. This chapter describes a relatively recent meshfree and pure Lagrangian technique, the Smoothed Particle Hydrodynamics (SPH) method, which overcomes the above mentioned limitations. Its original frame has been developed in 1977 by (Gingold and Monaghan, 1977) and independently by (Lucy, 1977) for astrophysical applications. Since then, a number of modifications to ensure completeness and accuracy have been yielded, in order to solve the main drawbacks of the primitive form of the method.
Because a calculation is based on short-range particle interactions, it is essential to limit the computational costs related to the neighbourhood definition. Available searching algorithms are then presented and discussed.
Finally, some practical applications are presented, primarily concerning free surface flows. The capability to easily handle large deformations is shown.

2. Basic formulation of the SPH method

Governing equations describing the motion of fluids, are usually given as a set of Partial Differential Equations (PDEs). These are discretized by replacing the derivative operators with equivalent integral operators (the so called integral representation or kernel approximation) that are in turn approximated on the particle location (particle approximation).
Next paragraph 2.1 gives further details about these two steps, with reference to a generic field $f(\vec{\mathbf{x}})$ depending on the location point $\vec{\mathbf{x}} \in \Re^{n_d}$, whereas paragraph 2.2 provides more specific details concerning the treatment of Navier-Stokes equations.

2.1 Approximation of a field f(x) and its spatial gradient

Following the concept of integral representation, any generic continuous function $f(\vec{\mathbf{x}})$ can be obtained using the Dirac delta functional δ, centered at the point $\vec{\mathbf{x}}$ (Fig. 1) as

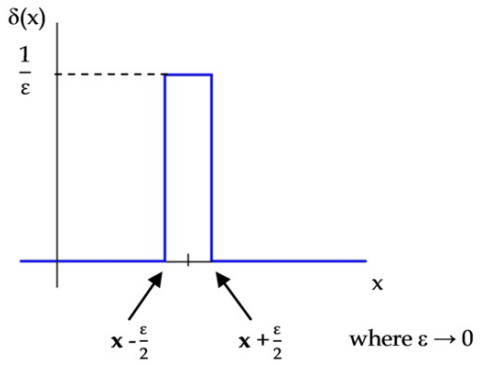

Fig. 1. Dirac delta function centered at the point **x** (for one dimensional problems).

$$f(\vec{\mathbf{x}}) = \int_{\Omega} f(\vec{\mathbf{y}})\,\delta(\vec{\mathbf{x}} - \vec{\mathbf{y}})\,d\Omega_y \tag{1}$$

where Ω represents the domain of definition of f and $\mathbf{x},\mathbf{y} \in \Omega$. Replacing δ with a smoothing function W(**x** - **y**, h), eq. (1) can be approximated as

$$f_I(\vec{\mathbf{x}}) = \int_{\Omega} f(\vec{\mathbf{y}})\,W(\vec{\mathbf{x}} - \vec{\mathbf{y}}, h)\,d\Omega_y \tag{2}$$

in which W is the so called smoothing kernel function or simply kernel and h, acting as spatial scale, is the smoothing length defining the influence area where W is not zero. While eq. (1) yields an exact formulation for the function $f(\vec{\mathbf{x}})$, eq. (2) is only an approximation. The definition of W is a key point in the SPH method since it establishes the accuracy of the approximating function $f(\vec{\mathbf{x}})$ as well as the efficiency of the calculation. Note that the kernel approximation operator is marked by the index I.

The kernel function W has to satisfy several properties (Monaghan, 1988; Vila, 1999). The following condition

$$\int_{\Omega} W(\vec{\mathbf{x}} - \vec{\mathbf{y}}, h)\,d\Omega_y = 1 \tag{3}$$

is known as partition of unity (or the zero-order consistency) as the integration of the smoothing function must yield the unity. Since W mimics the delta function, eq. (3) can be rewritten as a limit condition in which the smoothing length tends to zero

$$\lim_{h\to 0} W(\vec{\mathbf{x}} - \vec{\mathbf{y}}, h) \to \delta(\vec{\mathbf{x}} - \vec{\mathbf{y}}) \tag{4}$$

Still, W has to be defined even, positive and radial symmetric on the compact support (Fig. 2)

$$W(\vec{\mathbf{x}} - \vec{\mathbf{y}}, h) = W(\vec{\mathbf{y}} - \vec{\mathbf{x}}, h) = W(|\vec{\mathbf{x}} - \vec{\mathbf{y}}|, h) > 0 \quad |\vec{\mathbf{x}} - \vec{\mathbf{y}}| < \varphi \cdot h \tag{5a}$$

$$W(\vec{\mathbf{x}} - \vec{\mathbf{y}}, h) = 0 \quad \text{otherwhise} \tag{5b}$$

where φ is a positive quantity. A large number of kernel functions are examined in literature, e.g. quadratic to quintic polynomials, Gaussian etc. Among the others (Liu & Liu, 2003), a smoothing function satisfying the above condition is the cubic spline based kernel (Monaghan & Lattanzio, 1985) defined as:

$$\begin{aligned} W &= A(n_d)\left(\tfrac{2}{3}-q^2+\tfrac{q^3}{3}\right) && 0 \le q < 1 \\ W &= A(n_d)(2-q)^3 && 1 \le q < 2 \\ W &= 0 && \text{otherwise} \end{aligned} \tag{6}$$

where $\varphi = 2$, $A(n_d)$, depending on the number of dimensions n_d, denotes a scaling factor that ensures the consistency of eq. (3) whereas q denotes the dimensionless distance $|\vec{x}-\vec{y}|/h$.

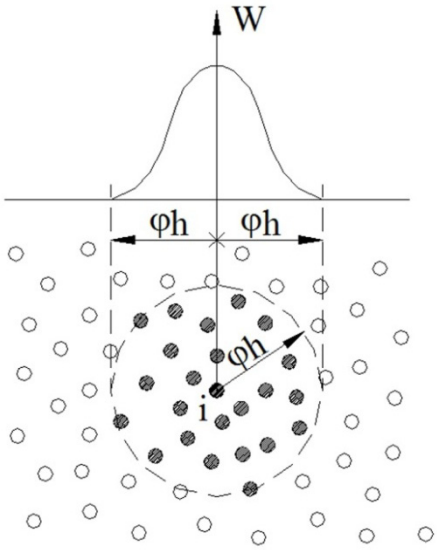

Fig. 2. Typical shape of the smoothing function W

Knowing the function f carried by a collection of moving particles, the integral representation given by eq. (2) can be converted into a discretized summation over all particle N within the compact support (Fig. 2), yielding the particle approximation

$$f_a(\vec{x}) = \sum_{k=1}^{N} \frac{m_k}{\rho_k} f(\vec{x}_k) W(\vec{x}-\vec{x}_k, h) \tag{7}$$

where the index k refers to particles within the compact support (see bold ones in Fig. 2), with mass m_k and density ρ_k being carried. Note that in this case the particle approximation is marked by the index a. The subscript will be avoided from now on.
The presence of these two variables allows SPH to be easily and conveniently applied to hydrodynamics problems. The smooth estimate eq. (7) can be referred to a generic particle occupying the position $\vec{x}_i$, as follow

$$f(\vec{x}_i) = f_i = \sum_{k=1}^{N} \frac{m_k}{\rho_k} f_k W_{ik} \tag{8}$$

where W_{ik} is the abbreviation of $W(\vec{x}_i - \vec{x}_k, h)$. Particle approximation of spatial derivatives of a field function, such as divergence and gradient, is determined using the gradient of the kernel function rather than from the derivatives of the function itself

$$\vec{\nabla} \cdot \vec{f}_i = \sum_{k=1}^{N} \frac{m_k}{\rho_k} \vec{f}_k \cdot \vec{\nabla}_i W_{ik} \tag{9}$$

$$\vec{\nabla} f(\vec{x}_i) = \vec{\nabla} f_i = \sum_{k=1}^{N} \frac{m_k}{\rho_k} f_k \vec{\nabla}_i W_{ik} \tag{10}$$

where the nabla operator is referred to the location of particle I. The symbol "·" denotes the dot product. Eqs. (9)-(10) offer the great advantage of estimating their left hand side in term of the kernel gradient, i.e. allowing no special hypotheses on the particular field function (vector in the first case, scalar in the latter).
A different formulation of the spatial derivative in eq. (9) can be achieved introducing the following identity (Liu and Liu, 2003)

$$\vec{\nabla} \cdot \vec{f}(\vec{x}) = \frac{1}{\rho}\left\{\vec{\nabla} \cdot \left[\rho \vec{f}(\vec{x})\right] - \vec{f}(\vec{x}) \cdot \vec{\nabla}\rho\right\} \tag{11}$$

inside the integral in eq. (2), yielding in this case

$$\vec{\nabla} \cdot \vec{f}_i = \frac{1}{\rho_i} \sum_{k=1}^{N} m_k \left(\vec{f}_k - \vec{f}_i\right) \cdot \vec{\nabla}_i W_{ik} \tag{12}$$

Likewise the divergence, another particle approximation of the gradient can be derived, taking into account the following equation

$$\vec{\nabla} f(\vec{x}) = \rho\left\{\vec{\nabla}\frac{f(\vec{x})}{\rho} + \frac{f(\vec{x})}{\rho^2}\vec{\nabla}\rho\right\} \tag{13}$$

yielding

$$\vec{\nabla} f_i = \rho_i \sum_{k=1}^{N} m_j \left(\frac{f_k}{\rho_k^2} + \frac{f_i}{\rho_i^2}\right) \vec{\nabla}_i W_{ik} \tag{14}$$

Since the field function on the right hand side of Eqs. (12) and (14) appears in the form of paired particles, such equations are conveniently employed in fluid dynamics, allowing the conservation of linear and angular momentum.

2.2 SPH-form of governing equations

The mostly used governing laws ruling fluid motion are the Navier-Stokes equations, which specify that mass and linear momentum (also expressed in Newton's second law which state that the rate of change of the momentum of a particle is proportional to the resultant force acting on the particle) are preserved. Conservation laws in Lagrangian form are in the following provided

$$\frac{d\rho}{dt} = -\rho\vec{\nabla}\cdot\vec{\mathbf{v}} \tag{15a}$$

$$\frac{d\vec{\mathbf{v}}}{dt} = -\frac{\vec{\nabla}p}{\rho} + \nu\Delta\vec{\mathbf{v}} + \vec{\mathbf{f}} \tag{15b}$$

in which ρ and $\vec{\mathbf{v}}$ are respectively the density and velocity field, p is the isotropic pressure, ν the laminar kinematic viscosity and $\vec{\mathbf{f}}$ the external force.
Different approaches (Monaghan, 1994; Liu and Liu, 2003; Oger et al., 2007) are available in order to derive the density particle approximation of the continuity equation (15.a) and momentum equation (15.b). For instance, referring to eq. (12), the density rate at particle i can be approximated as follows

$$\frac{d\rho_i}{dt} = -\sum_{k=1}^{N} m_k\left(\vec{\mathbf{v}}_k - \vec{\mathbf{v}}_i\right)\cdot\vec{\nabla}_i W_{ik} \tag{16}$$

The SPH formulation of the velocity variation can be deduced from eq. (14)

$$\frac{d\vec{\mathbf{v}}_i}{dt} = -\sum_{k=1}^{N} m_k\left(\frac{p_k}{\rho_k^2} + \frac{p_i}{\rho_i^2}\right)\vec{\nabla}_i W_{ik} + \vec{\mathbf{f}} \tag{17}$$

An artificial viscosity term (Monaghan & Gingold, 1983) can be added in eq. (14), allowing shock waves to be properly simulated (Liu et al., 2003a), damping spurious oscillation near the fronts

$$\frac{d\vec{\mathbf{v}}_i}{dt} = -\sum_{k=1}^{N} m_k\left(\frac{p_k}{\rho_k^2} + \frac{p_i}{\rho_i^2} + \Pi_{ik}\right)\vec{\nabla}_i W_{ik} + \vec{\mathbf{f}} \tag{18}$$

The dissipative term above introduced is the most general viscosity used in SPH computations, since it provides good results when modelling shock fronts and prevents interparticle penetration (β term in eq. (19)). It is defined as

$$\begin{aligned} \Pi_{ik} &= \frac{-\alpha\,\bar{c}_{ik}\,\vartheta_{ik} + \beta\,\vartheta_{ik}^2}{\bar{\rho}_{ik}} \quad \text{when}\ \vec{\mathbf{v}}_{ik}\cdot\vec{\mathbf{x}}_{ik} < 0 \\ \Pi_{ik} &= 0 \qquad\qquad\qquad\quad \text{otherwise} \end{aligned} \tag{19}$$

where

$$\vartheta_{ik} = \frac{-h\,\vec{\mathbf{v}}_{ik}\cdot\vec{\mathbf{x}}_{ik}}{\vec{\mathbf{x}}_{ik}^2 + \eta^2} \tag{20}$$

The notation $\bar{a}_{ik} = (a_i + a_k)/2$, $b_{ik} = b_i - b_k$ is introduced above. Term c refers to the speed of sound which magnitude has conveniently to be at least ten times greater than the maximum estimate of the scalar velocity field (Monaghan, 1994), $\eta = 0.1h$ is employed to prevent numerical divergences when two particle are approaching. α typically ranges from 0 to 0.01, depending on how viscous is the fluid. When other approaches for reproducing shear stresses are taking in, e.g. (Cleary, 1998), then it is not necessary to employ the first term inside eq. (19).

Problem closure is achieved by combining conservation equations in discrete form (16), (18) with an equation of state, when the weakly compressible scheme is adopted (Lee et al., 2010). A relationship between pressure and density is given by (Dymond & Malhotra, 1988)

$$p_i = \frac{c_0^2 \rho_0}{\gamma}\left[\left(\frac{\rho_i}{\rho_0}\right)^{\gamma} - 1\right] \tag{21}$$

where c_0 is the reference speed of sound, large enough to guarantee Mach numbers lower than $0.1 \div 0.01$, $\gamma = 7$, $\rho_0 = 1000 kg/m^3$, if the liquid is water.

3. Completeness and accuracy of the SPH method

In SPH the consistency order of a function (or more properly completeness or reproducing conditions) means the order of a polynomial required to evaluate the function exactly, when using values carried by particles. Next section 3.1 deals with how restoring consistency to j-th order, while section 3.2 provides some aspects related to the spatial scale h, which has a strong influence on the accuracy.

3.1 J-th order consistency

Zero-order consistency for particle approximation is attained when the smoothing kernel satisfies eq. (3) in discrete form

$$\sum_{k=1}^{N} \frac{m_k}{\rho_k} W(\vec{\mathbf{x}} - \vec{\mathbf{x}}_k, h) = 1 \tag{22}$$

together with

$$\sum_{k=1}^{N} \frac{m_k}{\rho_k} \vec{\nabla}_i W(\vec{\mathbf{x}} - \vec{\mathbf{x}}_k, h) = 0 \tag{23}$$

Eqs. (22), (23) are satisfied when a corrected smoothing function, e.g. the Shepard function (Bonet et al., 2004) is adopted.

$$W^S = S(\vec{x}) W(\vec{\mathbf{x}} - \vec{\mathbf{x}}_k, h) \tag{24}$$

where $S^{-1}(\vec{\mathbf{x}}) = \sum_{k=1}^{N} \frac{m_k}{\rho_k} W(\vec{\mathbf{x}} - \vec{\mathbf{x}}_k, h)$. Still, Eqs. (22), (23) are not satisfied in the case of the evaluation near the boundaries, where kernel truncation yields a lack of interpolation or when particles are exceedingly disordered.

There are several ways to restore higher order consistency conditions. j-th order consistency ($j \geq 1$) is achieved with updated versions of the original SPH method, e.g. Reproducing Kernel Particle Method (Chen et al., 2000; Liu et. al., 1995), Element Free Galerkin Mehod (Belytschko et. al., 1994; Krongauz & Belytschko 1997), Moving Least Square Particle Hydrodynamics (Dilts, 1999). An interesting method to ensure j-th order consistency has been proposed by (Liu et al., 2003b). Using the Taylor series expansion for the kernel

$$W\left(\vec{\mathbf{x}}-\vec{\mathbf{x}}_k,h\right)=G_0\left(\vec{\mathbf{x}},h\right)+G_1\left(\vec{\mathbf{x}},h\right)\frac{\vec{\mathbf{x}}-\vec{\mathbf{x}}_k}{h}+G_1\left(\vec{\mathbf{x}},h\right)\frac{\vec{\mathbf{x}}-\vec{\mathbf{x}}_k}{h}$$
$$+G_2\left(\vec{\mathbf{x}},h\right)\left(\frac{\vec{\mathbf{x}}-\vec{\mathbf{x}}_k}{h}\right)^2+\ldots=\sum_{p=1}^{j}G_p\left(\vec{\mathbf{x}},h\right)\left(\frac{\vec{\mathbf{x}}-\vec{\mathbf{x}}_k}{h}\right)^p \tag{25}$$

and introducing the above equation in the following set, representing the reproducing condition of a function to the j-th accuracy in integral form (Liu and Liu, 2003)

$$\begin{aligned}
M_0&=\int_\Omega W\left(\vec{\mathbf{x}}-\vec{y},\,h\right)d\Omega_y=1\\
M_1&=\int_\Omega\left(\vec{\mathbf{x}}-\vec{y}\right)W\left(\vec{\mathbf{x}}-\vec{y},\,h\right)d\Omega_y=0\\
M_2&=\int_\Omega\left(\vec{\mathbf{x}}-\vec{y}\right)^2W\left(\vec{\mathbf{x}}-\vec{y},\,h\right)d\Omega_y=0\\
&\vdots\\
M_j&=\int_\Omega\left(\vec{\mathbf{x}}-\vec{y}\right)^jW\left(\vec{\mathbf{x}}-\vec{y},\,h\right)d\Omega_y=0
\end{aligned} \tag{26}$$

a discretized consistency condition to j-th order is ensured by the resulting set

$$\begin{aligned}
&\sum_{p=1}^{j}G_p\left(\vec{\mathbf{x}},h\right)\sum_{k=1}^{N}\left(\frac{\vec{\mathbf{x}}-\vec{\mathbf{x}}_k}{h}\right)^p\frac{m_k}{\rho_k}=1\\
&\sum_{p=1}^{j}G_p\left(\vec{\mathbf{x}},h\right)\sum_{k=1}^{N}\left(\frac{\vec{\mathbf{x}}-\vec{\mathbf{x}}_k}{h}\right)^{p+1}\frac{m_k}{\rho_k}=0\\
&\qquad\vdots\\
&\sum_{p=1}^{j}G_p\left(\vec{\mathbf{x}},h\right)\sum_{k=1}^{N}\left(\frac{\vec{\mathbf{x}}-\vec{\mathbf{x}}_k}{h}\right)^{p+j}\frac{m_k}{\rho_k}=0
\end{aligned} \tag{27}$$

posing

$$\sum_{k=1}^{N}\left(\frac{\vec{\mathbf{x}}-\vec{\mathbf{x}}_k}{h}\right)^j\frac{m_k}{\rho_k}=U_j\left(\vec{\mathbf{x}},h\right) \tag{28}$$

eqs. (27) can be rewritten in a matrix fashion, such as

$$\begin{pmatrix}U_0\left(\vec{\mathbf{x}},h\right)&\cdots&U_k\left(\vec{\mathbf{x}},h\right)\\ \vdots&\ddots&\vdots\\ U_j\left(\vec{\mathbf{x}},h\right)&\cdots&U_{j+j}\left(\vec{\mathbf{x}},h\right)\end{pmatrix}\begin{pmatrix}G_0\left(\vec{\mathbf{x}},h\right)\\ \vdots\\ G_j\left(\vec{\mathbf{x}},h\right)\end{pmatrix}=\begin{pmatrix}1\\ \vdots\\ 0\end{pmatrix} \tag{29}$$

which solution yields the j+1 coefficients $G_j(\vec{\mathbf{x}},h)$. While the restoring condition to j-th order is ensured by eqs. (27), still some open issues arise. First of all, the corrected kernel may not be symmetric, in contrast with the requirements stated in eq. (5.a). Second, it

might be negative somewhere, which may produce unphysical field results (e.g. non positive density). Finally, it might show secondary peaks aside the central (see Fig. 2), hence affecting the internal force between two approaching particles. Consequently, special care has to be taken when simulating flows with corrected version of SPH. Concerning the stability of SPH, a pioneering work is given by (Swegle et al., 1994), whose results have then been confirmed by (Randles et al., 1999) and independently by (Belytschko, & Xiao, 2002).

3.2 Variable smoothing length

The introduced smoothing length h is crucial for the accuracy of the particle approximation. When h is too large, carried particle properties are excessively smoothed out in space, affecting the accuracy. Vice versa, too small values determine a little number of computing particles inside the compact support, determining a lack of interpolation. In SPH computations, h may be kept fixed or variable in time and space. Since the carried particle's mass is usually constant, the number of neighbouring particles inside the support domain should not vary, according to the following

$$h = h_0 \left(\frac{\rho_0}{\rho} \right)^{1/n_d} \tag{30}$$

where h_0 and ρ_0 are respectively the reference smoothing length and density. When h is chosen to be variable, special concern must be taken with reference to the third law of Newton (action – reaction principle). Indeed, if computing particles a and b have different h_a and h_b, then their compact supports are not the same, causing different exerting forces between such pairs. Symmetry of particle interactions must then be preserved. This condition can be achieved, taking into account a symmetrised smoothing length, as proposed by (Benz, 1989)

$$h_{ab} = \frac{h_a + h_b}{2} \tag{31}$$

Others approaches exist to ensure symmetry (e.g. the geometric average instead of the arithmetic average).

4. Neighbouring search methods

A limitation of SPH is that a single computation becomes very demanding in terms of running time as the number of particle increases. For each particle, since the integration of the governing equations is carried out on a limited number of adjacent particles located inside a cut-off distance $r_c = \varphi h$, a large part of the computational burden depends on the actual searching procedure of the neighbouring particles. It is therefore crucial that efficient methods are adopted for such a search. The cut-off radius is indeed much lower than the typical domain's spatial dimension, hence the number of neighbouring particles N is a little fraction of the total number N_{tot}. Straightforward determination of which particles are inside the interaction range would require the calculation of all pair-wise distances, a procedure whose computational burden would be of the order $O(N_{tot}^2)$, and therefore unpractical or totally impossible for large problems.

Two main approaches have been developed in the past in order to reduce the unnecessary computation of distances: the first based on dynamically storing each particle's neighborhood list, namely the Verlet list (Verlet L, 1967), and the second based on a framework of fixed cells (Allen and Tildesley, 2000). The first dataset gathers the $N_{V,i}$, i = 1,…,N, neighbours contained in a range r_v slightly greater than the cut off distance r_c (Fig. 3).

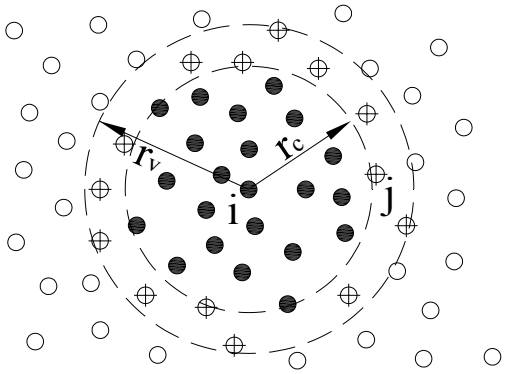

Fig. 3. Verlet list definition for the fluid particle "i"; particles marked with a cross between r_c and r_v, are included in the list but they do not give any contribution to the hydrodynamics properties of the targered particle.

The condition $N_{V,i} << N_{tot}$, will still hold, as long as r_v is small enough, even though – obviously – the number of neighbouring particles stored in the list is greater than those strictly required. The difference $r_v - r_c = V_{skin}$ represents a sort of safety "skin" around the cut-off distance r_c and contains some elements which are initially unnecessary for the definition of the i_{th} particle's properties, as shown by particles marked with a cross in Fig. 3. This takes into account the possibility that some or all of them will cross the interaction sphere and thus become part of the neighbourhood in the following time steps.
With this approach the list is kept unchanged for some time steps, till a "refresh condition" is established. A number of criteria have evolved over the years as a condition to activate the list refresh operation, mostly based on the maximum possible distance traveled by the particle (Chialvo & Debenedetti, 1983; Blink and Hoover, 1985). The latter approach sets a partition of the physical space into fixed cells so that, for each particle, the neighbouring search only has to be performed within the surrounding particles, i.e. those inside the cell where the current particle is located and in the 8 (for 2D problems) or 26 (3D) adjoining ones. In order to define the neighbourhood, a data structure must be created so that each moving particle is connected to the grid cell it is located in; such a structure (linked-cell list) must be renewed at each time step, a relatively straightforward operation of $O(N_{tot})$ complexity.
For this approach, as for the Verlet list method, the overall efficiency depends very much on the choice of parameters, balancing the size of the cells against their total number. Large cells imply a longer neighborhood search, while a greater number requires a longer data structure reconstruction. (Viccione et al., 2008) carried a numerical sensitivity analysis on the efficiency of the two procedures as function of the key spatial parameters, that is the Verlet list skin and the cell size. The most relevant results are shown in the following figures

$\alpha=r_v/r_c$	τ_s	$\tau_s/\tau_{s,b}$	τ_{tot}	$\tau_{tot}/\tau_{tot,b}$
1	16.36	1.00	18.23	1
1.1	14.75	0.90	16.65	0.91
1.2	12.43	0.76	14.36	0.79
1.3	**11.57**	**0.71**	**13.48**	**0.74**
1.4	13.74	0.84	15.63	0.86
1.5	15.23	0.93	17.17	0.94

Fig. 4.a

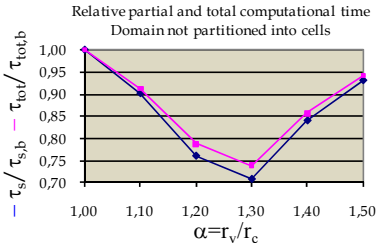

$\alpha=r_v/r_c$	τ_s	$\tau_s/\tau_{s,b}$	τ_{tot}	$\tau_{tot}/\tau_{tot,b}$
1	9.45	0.58	11.27	0.62
1.1	8.23	0.50	10.07	0.55
1.2	7.65	0.47	9.48	0.52
1.3	**6.84**	**0.42**	**8.69**	**0.48**
1.4	7.85	0.48	9.61	0.53
1.5	8.98	0.55	10.83	0.59

Fig. 4.b

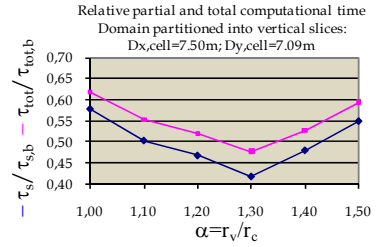

$\alpha=r_v/r_c$	τ_s	$\tau_s/\tau_{s,b}$	τ_{tot}	$\tau_{tot}/\tau_{tot,b}$
1	4.78	0.29	6.57	0.36
1.1	4.38	0.27	6.23	0.34
1.2	3.66	0.22	5.5	0.30
1.3	**3.19**	**0.19**	**5.03**	**0.28**
1.4	3.86	0.24	5.71	0.31
1.5	4.55	0.28	6.39	0.35

Fig. 4.c

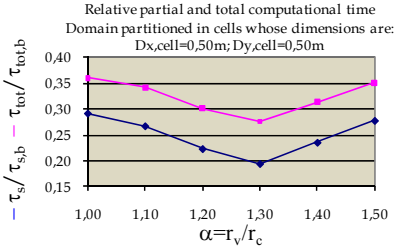

$\alpha=r_v/r_c$	τ_s	$\tau_s/\tau_{s,b}$	τ_{tot}	$\tau_{tot}/\tau_{tot,b}$
1	3.11	0.19	4.94	0.27
1.1	2.99	0.18	4.81	0.26
1.2	2.78	0.17	4.62	0.25
1.3	**2.64**	**0.16**	**4.47**	**0.25**
1.4	2.85	0.17	4.68	0.26
1.5	3.05	0.19	4.89	0.27

Fig. 4.d

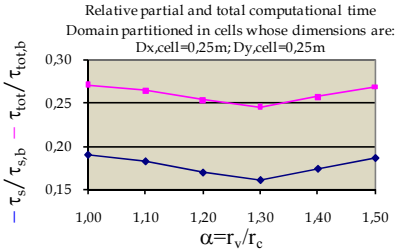

Fig. 4.a. refers to the case with no fixed cell structure. Here obviously the "Verlet list" procedure is highly beneficial, even though it appears that the size of the list must be carefully chosen, in order to fully exploit it effects. Figs. 4.b to 4.d show different computational times, depending on the cell size. Figure 5, gives a better insight of the results, showing the non-dimensional running cost trend $\tau_s/\tau_{s,b}$. As can be seen, minimum is achieved for a certain grid size.

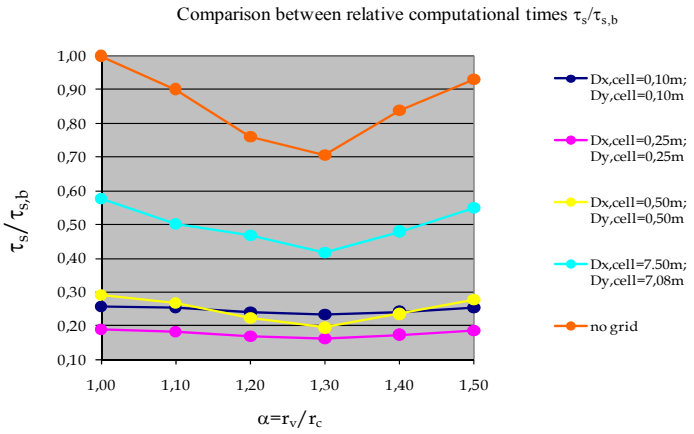

Fig. 5. Comparison among different cell sizes.

It appears that while both the linked cell list and the Verlet list do relieve the computational time, the comparative advantage of the linked cell increases to the point where it is practically of no use whatsoever.
Later on, (Domínguez et. al., 2010) proposed an innovative searching algorithm based on a dynamic updating of the Verlet list yielding more satisfying results in term of computational time and memory requirements.

5. Applications of the SPH method

Smoothed Particle Hydrodynamics has been applied to a number of cases involving free surfaces flows.

5.1 Slamming loads on a vertical structure

The case of a sudden fluid impact on a vertical wall (Peregrine, 2003) has been examinated on a geometrically simple set up. (Viccione et al., 2009) shown how such kind of phenomenon is strongly affected by fluid compressibility, especially during the first stages. A fluid mass, 0.50m high and 4.00m long, moving with an initial velocity v_0 = 10m/s is discretized into a collection of 20.000 particles whith an interparticle distance d_0 = 0.01m. The resulting mass is at a close distance to the vertical wall, so the impact process takes place after few timesteps (Fig. 6). Timestep is automatically adjusted to satisfy the Courant limit of stability.

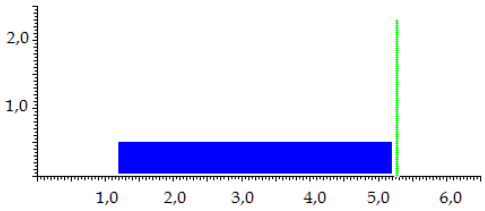

Fig. 6. Initial conditions with fluid particles (blue dots) approaching the wall (green dots)

The following Fig. 7 shows the results in terms of pressure at different times.

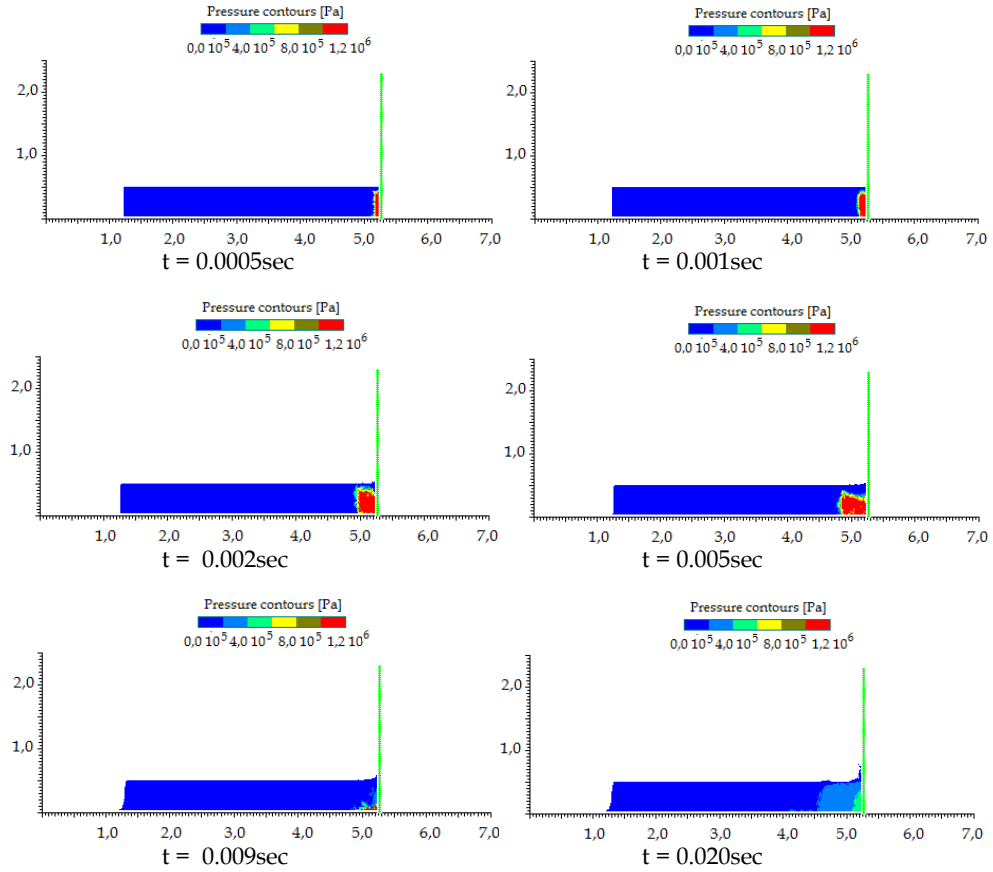

Fig. 7. Pressure contour as the impact progress takes place.

The rising and the following evolution of high pressure values is clearly evident. The order of magnitude is about 10^6 Pa, as it would be expected according to the Jokowski formula $\Delta p = \rho C_0 \Delta v$, with $\Delta v = v_0 = 10$m/s. After about 1/100 seconds most of the Jokowsky like pressure peak, generated by the sudden impact with the surface, disappeared, following that, the pressure starts building up again at a slower rate.

5.2 Simulating triggering and evolution of debris-flows with SPH

The capability into simulating debris-flow initiation and following movement with the Smoothed Particle Hydrodynamics is here investigated. The available domain taken from an existing slope, has been discretized with a reference distance being d_0=2.5m and particles forming triangles as equilateral as possible. A single layer of moving particles has been laid on the upper part of the slope (blue region in Fig. 8).

Triggering is here settled randomly, releasing a particle located in the upper part of a slope, while all the remaining ones are initially frozen. Motion is then related to the achievement of a pressure threshold p_{lim} (Fig. 9). The resulting process is like a domino effect or a cascading failure. While some particles are moving, they may approach others initially still, to the

point for which the relative distance yields a pressure greater than the threshold value. Once reached such point, those neighbouring particles, previously fixed, are then set free to move. Runout velocity is instead controlled by handling the shear stress τ_{bed} with the fixed bed.

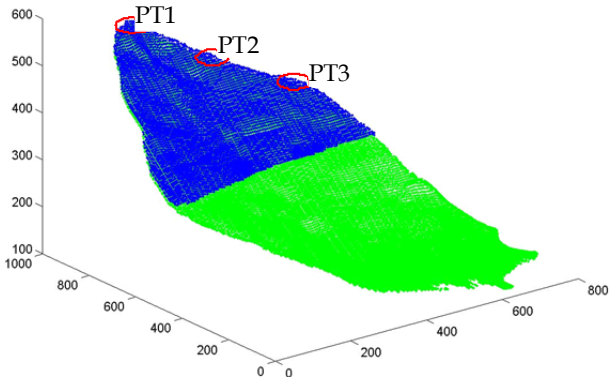

Fig. 8. Spatial discretization. Red circles represent the area where local triggering is imposed.

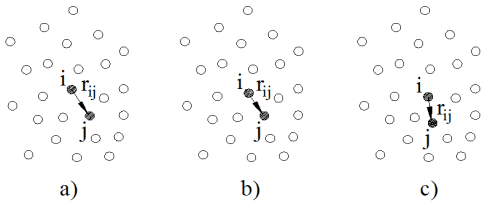

Fig. 9. Neighbour particle destabilization. a) Particle "i" is approaching the neighbour particle "j". b) Despite the relative distance "$|r_{ij}|$" is decreased, particle "j" is still fixed because $p_{ij} < p_{lim}$. c) Particle "j" is set free to move because the pressure "p_{ij}" has reached the threshold value "p_{lim}".

Next Figures show three instants for each SPH based simulation, with the indication of the volume mobilized.

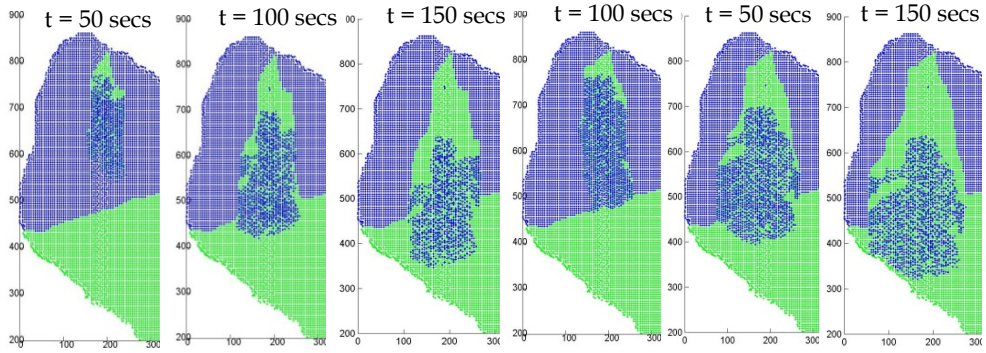

Fig. 10. PT1 Particle triggered zone, limit pressure p_{lim} = 300kg_f /cm^2(left side), p_{lim} = 200kg_f /cm^2 (right side), viscosity coefficient α_{bed}=0.1.

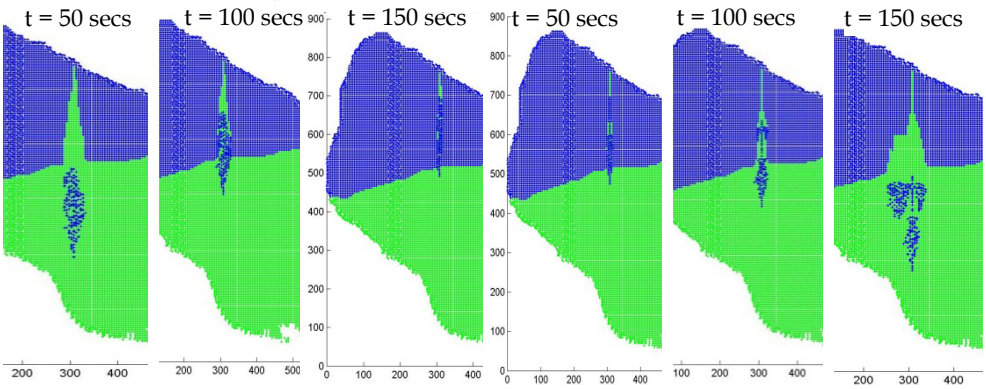

Fig. 11. PT2 Particle triggered zone, limit pressure p_{lim} = 300kg$_f$ /cm^2(left side), p_{lim} = 200kg$_f$ /cm^2 (right side), viscosity coefficient α_{bed}=0.1.

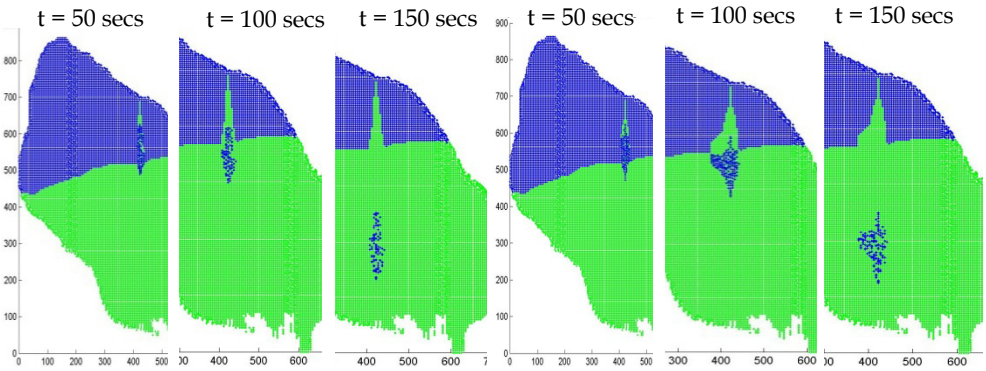

Fig. 12. PT3 Particle triggered zone, limit pressure p_{lim} = 300kg$_f$ /cm^2(left side), p_{lim} = 200kg$_f$ /cm^2 (right side), viscosity coefficient α_{bed}=0.1.

As can been seen from the above Figures 10 to 12, by varying the location of the triggering area and the limit pressure p_{lim}, the condition of motion are quite different. More specifically, the mobilized area increases when the isotropic pressure p_{lim} decreases.

6. Conclusion

Recent theoretical developments and practical applications of the Smoothed Particle Hydrodynamics (SPH) method have been discussed, with specific concern to liquids. The main advantage is the capability of simulating the computational domain with large deformations and high discontinuities, bearing no numerical diffusion because advection terms are directly evaluated.

Recent achievements of SPH have been presented, concerning (1) numerical schemes for approximating Navier Stokes governing equations, (2) smoothing or kernel function properties needed to perform the function approximation to the Nth order, (3) restoring consistency of kernel and particle approximation, yielding the SPH approximation accuracy.

Also, computation aspects related to the neighbourhood definition have been discussed. Field variables, such as particle velocity or density, have been evaluated by smoothing interpolation of the corresponding values over the nearest neighbour particles located inside a cut-off radius "r_c" The generation of a neighbour list at each time step takes a considerable portion of CPU time. Straightforward determination of which particles are inside the interaction range requires the computation of all pair-wise distances, a procedure whose computational time would be of the order $O(N^2)$, and therefore unpractical for large domains.
Lastly, applications of SPH in fluid hydrodynamics concerning wave slamming and propagation of debris flows have been discussed. These phenomena – involving complex geometries and rapidly-varied free surfaces - are of great importance in science and technology.

7. Acknowledgment

The work has been equally shared among the authors. Special thanks to the C.U.G.Ri. (University Centre for the Prediction and Prevention of Great Hazards), center, for allowing all the computations here presented on the Opteron quad processor machine.

8. References

Allen M.P. & Tildesley D.J. (1987). Computer Simulation of Liquids; *Clarendon Press*; Oxford.

Belytschko T.; Lu Y.Y. & Gu L. (1994). Element-free Galerkin methods. *International Journal for Numerical methods in Engineering*, Vol. 37, pp. 229 - 256.

Belytschko, T. & Xiao, S. (2002). Stability analysis of particle methods with corrected derivatives, *Computers and Mathematics with Applications*, Vol. 43, pp. 329-350.

Benz W. (1990). Smoothed Particle Hydrodynamics: a review, in numerical modellying of Non-Linear Stellar Pulsation: Problems and Prospects, Kluwer Academic, Boston.

Blink J.A. & Hoover WG. (1985). Fragmentation of suddenly heated liquids, *Phys Rev A*; Vol. 32, No. 2, pp. 1027-1035.

Bonet, J.; Kulasegaram S.; Rodriguez-Paz M.X. & Profit M. (2004). Variational formulation for the smooth particle hydrodynamics (SPH) simulation of fluid and solid problems, *Computer Methods in Applied Mechanics and Engineering*, Vol. 193, No. 12, pp. 1245–1257.

Chialvo A.A. & Debenedetti P.G. (1983). On the use of the Verlet neighbour list in molecular dynamics, *Comp. Ph. Comm*, Vol. 60, pp. 215-224.

Cleary, P.W. (1998). Modelling confined multi-material heat and mass flows using SPH, *Appl. Math. Modelling*, Vol. 22, pp. 981–993.

Dilts G. A. (1999). Moving –least squares-particle hydrodynamics I, consistency and stability. *International Journal for Numerical Methods in Engineering*, Vol. 44, No. 8, pp. 1115–1155.

Domínguez, J. M.; Crespo, A. J. C. ; Gómez-Gesteira, M. & Marongiu, J. C. (2011). Neighbour lists in smoothed particle hydrodynamics. International Journal for Numerical Methods in Fluids, 66: n/a. doi: 10.1002/fld.2481.

Dymond, J. H. & Malhotra, R. (1988). The Tait equation: 100 years on, International Journal of Thermophysics, *Vol*. 9, No. 6, pp. 941-951, doi: 10.1007/bf01133262.

Gingold, R.A. & Monaghan, J.J. (1977). Smoothed Particle hydrodynamics: theory and application to non-spherical stars. *Mon. Not. R. Astr. Soc.*, Vol. 181, pp. 375-389.

Krongauz Y. & Belytschko T. (1997). Consistent pseudo derivatives in meshless methods. *Computer methods in applied mechanics and engineering*, Vol. 146, pp. 371-386.

Lee, E.S.; Violeau, D.; Issa, R. & Ploix, S. (2010) Application of weakly compressible and truly incompressible SPH to 3-D water collapse in waterworks, *Journal of Hydraulic Research*, Vol. 48(Extra Issue), pp. 50–60, doi:10.3826/jhr.2010.0003.

Liu M. B.; Liu G. R. & Lam K. Y. (2003a). A one dimensional meshfree particle formulation for simulating shock waves, *Shock Waves*, Vol. 13, No. 3, pp.201 – 211.

Liu M. B.; Liu G. R. & Lam K. Y. (2003b). Constructing smoothing functions in smoothed particle hydrodynamics with applications, *Journal of Computational and Applied Mathematics*, Vol. 155, No. 2, pp. 263-284.

Liu, G. R. & Liu, M. B. (2003). *Smoothed particle hydrodynamics: a meshfree particle method*, World Scientific, ISBN 981-238-456-1, Singapore.

Liu W. L.; Jun S., Li S. ; Adee J. & Belytschko T. (1995). Reproducing kernel particle methods for structural dynamics. *International Journal for Numerical Methods in Engineering*, Vol. 38, pp. 1655-1679.

Chen, J. S.; Yoon, S.; Wang, H. P. & Liu, W. K. (2000). An Improved Reproducing Kernel Particle Method for Nearly Incompressible Hyperelastic Solids, *Computer Methods in Applied Mechanics and Engineering*, Vol. 181, No. 1-3, pp. 117-145.

Lucy, L.B. (1977). A numerical approach to the testing of the fission hypothesis. *Astronomical Journal*, Vol. 82, pp. 1013–1024.

Monaghan, J.J. (1988). Introduction to SPH. *Computer Physics Communication*, Vol.48, pp. 89 –96.

Monaghan, J.J. (1994). Smoothed particle hydrodynamics, *Annual Review of Astronomy and Astrophysics*, Vol. 30, pp. 543–574.

Monaghan, J.J. & Gingold, R.A. (1983). Shock simulation by the particle method SPH, *Journ. of Comp. Physics*, Vol. 82, pp. 374-389.

Monaghan, J.J. & Lattanzio J.C. (1985). A refined particle method for astrophysical problems. *Astronomy and Astrophysics*, Vol. 149, pp. 135-143.

Oger, G.; Doring, M.; Alessandrini, B.; & Ferrant, P. (2007). An improved SPH method: Towards higher order convergence. *Journal of Computational Physics*, Vol. 225, No.2, pp. 1472-1492.

Peregrine, D.H. (2003). Water wave impact on walls. *Ann. Rev. Fluid Mech*, Vol. 35, pp. 23-43.

Randles, P. W.; Libersky, L. D. & Petschek, A. G. (1999). On neighbors, derivatives, and viscosity in particle codes, *Proceedings of ECCM Conference*, Munich, Germany.

Swegle, J. W.; Attaway, S. W.; Heinstein, M. W.; Mello, F. J. & Hicks, D. L. (1994). An analysis of smooth particle hydrodynamics. *Sandia Report* SAND93-2513.

Verlet L. (1967). Computer Experiments on Classical Fluids. *Phys. Rev.* Vol. 159, No. 1, pp. 98-103.

Vila, J.P. (1999). On particle weighted methods and smooth particle hydrodynamics. *Mathematical Models and Methods in Applied Sciences*, Vol.9, No.2, pp. 191–209.

Viccione, G., Bovolin, V. & Carratelli, E. P. (2008). Defining and optimizing algorithms for neighbouring particle identification in SPH fluid simulations, *International Journal for Numerical Methods in Fluids*, Vol. 58 pp. 625–638. doi: 10.1002/fld.1761.

Viccione G.; Bovolin, V. & Pugliese Carratelli E. (2009). Influence of the compressibility in Fluid - Structure interaction Using Weakly Compressible SPH. 4rd ERCOFTAC SPHERIC workshop on SPH applications. Nantes.

5

3D Coalescence Collision of Liquid Drops Using Smoothed Particle Hydrodynamics

Alejandro Acevedo-Malavé and Máximo García-Sucre
Venezuelan Institute for Scientific Research (IVIC)
Venezuela

1. Introduction

The importance of modeling liquid drops collisions (see figure 1) is due to the existence of natural and engineering process where it is useful to understand the droplets dynamics in specific phenomena. Examples of applications are the combustion of fuel sprays, spray coating, emulsification, waste treatment and raindrop formation (Bozzano & Dente, 2010; Bradley & Stow, 1978;Park & Blair, 1975; Rourke & Bracco, 1980; Shah et al., 1972).
In this study we apply the Smoothed Particle Hydrodynamics method (SPH) to simulate for the first time the hydrodynamic collision of liquid drops on a vacuum environment in a three-dimensional space. When two drops collide a circular flat film is formed, and for sufficiently energetic collisions the evolution of the dynamics leads to a broken interface and to a bigger drop as a result of coalescence. We have shown that the SPH method can be useful to simulate in 3D this kind of process. As a result of the collision between the droplets the formation of a circular flat film is observed and depending on the approach velocity between the droplets different scenarios may arise: (i) if the film formed on the droplets collision is stable, then flocks of attached drops can appear; (ii) if the attractive interaction across the interfacial film is predominant, then the film is unstable and ruptures may occur leading to the formation of a bigger drop (permanent coalescence); (iii) under certain conditions the drops can rebound and the emulsion will be stable. Another possible scenario when two drops collide in a vacuum environment is the fragmentation of the drops.
Many studies has been proposed for the numerical simulation of the coalescence and break up of droplets (Azizi & Al Taweel, 2010; Cristini et al., 2001; Decent et al., 2006; Eggers et al., 1999; Foote ,1974; Jia et al., 2006; Mashayek et al., 2003; Narsimhan, 2004; Nobari et al., 1996; Pan & Suga, 2005; Roisman, 2004; Roisman et al., 2009; Sun et al., 2009; Xing et al., 2007; Yoon et al., 2007). In these studies, the authors propose different methods to approach the dynamics of liquid drops by a numerical integration of the Navier-Stokes equations. These examine the motion of droplets and the dynamics that it follows in time and study the liquid bridge that arises when two drops collide. The effects of parameters such as Reynolds number, impact velocity, drop size ratio and internal circulation are investigated and different regimes for droplets collisions are simulated. In some cases, those calculations yield results corresponding to four regimes of binary collisions: bouncing, coalescence, reflexive separation and stretching separation. These numerical simulations suggest that the collisions that lead to rebound between the drops are governed by macroscopic dynamics. In these simulations the mechanism of formation of satellite drops was also studied,

confirming that the principal cause of the formation of satellite drops is the "end pinching" while the capillary wave instabilities are the dominant feature in cases where a large value of the parameter impact is employed.

Experimental studies on the coalescence process involving the production of satellite droplets has been reported in the literature (Ashgriz & Givi, 1987, 1989; Brenn & Frohn, 1989; Brenn & Kolobaric, 2006; Zhang et al., 2009). These authors found out that when the Weber number increases, the collision takes the form of a high-energy one and results of different type may arise. In these references the results show that the collision of the droplets can be bouncing, grazing and generating satellite drops. Based on data from experiments on the formation and breaking up of ligaments, the process of satellite droplets formation is modeled by these authors and the experiments are carried out using various liquid streams. On the other hand, for Weber numbers corresponding to a high-energy collision, permanent coalescence occurs and the bigger drop is deformed producing satellite drops. Experimental studies on the binary collision of droplets for a wide range of Weber numbers and impact parameters have been carried out and reported in the literature (Ashgriz & Poo, 1990; Gotaas et al., 2007b; Menchaca-Rocha et al., 1997; Qian & Law, 1997). These authors identified two types of collisions leading to drops separation, which can be reflexive or stretching separation. It was found that the reflexive separation occurs for head-on collisions, while stretching separation occurs for high values of the impact parameter. Carrying out Experiments, the authors reported the transition between two types of separation, and also collisions that lead to coalescence. In these references experimental investigations of the transition between different regimes of collisions were reported. The authors analyzed the results using photographic images, which showed the evolution of the dynamics exhibited by the droplets. As a result of these experiments were proposed five different regimes governing the collision between droplets: (i) coalescence after a small deformation, (ii) bouncing, (iii) coalescence after substantial deformation, (iv) coalescence followed by separation for head-on collisions, and (v) coalescence followed by separation for off-center collisions.

Li (1994) and Chen (1985) studied the coalescence of two small bubbles or drops using a model for the dynamics of the thinning film in which both, London-van der Waals and electrostatic double layer forces, are taken into account. Li (1994) proposes a general expression for the coalescence time in the absence of the electrostatic double layer forces. The model proposed by Chen (1985), depending on the radius of the drops and the physical properties of the fluids and surfaces, describes the film profile evolution and predicts the film stability, time scale and film thickness.

The dynamics of collision between equal-sized liquid drops of organic substances has also been reported in the literature (Ashgriz & Givi, 1987, 1989; Gotaas et al., 2007a; Jiang et al., 1992; Podgorska, 2007). They reported the experimental results of the collision of water and normal-alkane droplets in the radius range of 150 μm. These results showed that for the studied range of Weber numbers, the behavior of hydrocarbon droplets is more complex than the observed for water droplets. For water droplets head-on collisions, permanent coalescence always result. Experimental studies on the different ways in which may occur the coalescence of drops, have been performed by different authors (Gokhale et al., 2004; Leal, 2004; Menchaca-Rocha et al., 2001; Mohamed-Kassim & Longmire, 2004; Thoroddsen et al., 2007; Wang et al., 2009; Wu et al., 2004). In these studies are reported the evolution in time of the surface shape as well as a broad view of the contact region between the droplets.

Tartakovsky & Meakin (2005) have shown that the artificial surface tension that emerge from the standard formulation of the Smoothed Particle Hydrodynamics (SPH) method (Gingold & Monaghan, 1977) could be eliminated by using SPH equations based on the number density of particles instead of the density of particles in the fluid. The contribution of Tartakovsky & Meakin (2005) could be very useful when modeling the hydrodynamic interaction of drops in liquid emulsions. Combining these schemes with some continuous-discrete hybrid approach (Cui et al., 2006; Koumoutsakos, 2005; Li et al., 1998; Nie et al., 2004; O'Connell & Thompson, 1995) it could be constructed an interesting model to discuss the collapse and disappearance of the interfacial film in emulsion media (Bibette et al., 1992; Ivanov & Dimitrov, 1988; Ivanov & Kralchevsky, 1997; Kabalnov & Wennerström, 1996; Sharma & Ruckenstein, 1987). Ivanov & Kralchevsky (1997) conducted a study on the possible outcomes for the collision of liquid droplets in emulsions. According to this study, when the collision between two drops occurs, an interfacial film of flat circular section is formed, and coalescence or flocculation may arise (Ivanov & Kralchevsky, 1997). These authors did not carry out the hydrodynamical modeling of collision between drops. Instead, they discuss thermodynamics and hydrodynamics aspects of the problem and raise some possible outcomes when two liquid droplets collide.
In this work we apply the SPH method to simulate for the first time in three-dimensional space the hydrodynamic coalescence collision of liquid drops in a vacuum environment. This method is employed in order to obtaining approximate numerical solutions of the equations of fluid dynamics by replacing the fluid with a set of particles. These particles may be interpreted as corresponding to interpolation points from which properties of the fluid can be determined. Each SPH particle can be considered as a system of smaller particles. The SPH method is particularly useful when the fluid motion produce big deformations and a large velocity of the whole fluid.
All our calculations were performed defining inside the SPH code two drops composed by 4700 SPH particles, running on a Dell Work Station with 8 processors Intel Xeon of 3.33 Ghz with 32.0 GB of RAM memory.

2. Smoothed particle hydrodynamics method

The SPH method was invented first and simultaneously by Lucy, (1977) and Gingold & Monaghan (1977) to solve astrophysical problems. This method has been used to study a range of astrophysical topics including formation of galaxies, formation of stars, supernovas, stellar collisions, and so on. This method has the advantage that if you want to model more than one material, the interface problems arising can be modeled easily, while they are hard to model using other methods based on finite differences. An additional advantage is that SPH method can be considered as a bridge between continuous and fragmented material, which makes it one of the best method to study problems of fragmentation in solids (Benz & Asphaug, 1994, 1995). Another feature that makes the SPH method attractive is that it yields solutions depending on space and time, making it versatile for treating a wide variety of problems in physics. Furthermore, given the similarity between SPH and molecular dynamics, combination of these two methods can be used to treat complex problems in systems that differ considerably in their length scales. The easiness of the method to be adaptable and their Lagrangian character make of SPH one of the most popular among existing numerical methods used for modeling fluids. On the other hand, the SPH method can be used to describe the dynamics of deformable bodies (Desbrun

& Gascuel, 1996). Currently there are several applications of SPH in different areas related to fluid dynamics, such as: incompressible flows, elastic flows, multiphase flows, supersonic flows, shock wave simulation, heat transfer, explosive phenomena, and so on (Liu & Liu, 2003; Monaghan, 1992). A major advantage of SPH is that their physical interpretation is relatively simple.

In the SPH model, the fluid is represented by a discrete set of N particles. The position of the ith particle is denoted by the vector r_i, i=1,…, N. We start introducing the function $A_s(r)$, that is the smoothed representation of any arbitrary function A(r) (the function A(r) is any physical quantity of the hydrodynamical model and $A_s(r)$ is the smoothed version of this quantity). The SPH scheme is based on the idea of a smoothed representation $A_s(r)$ of the continuous function A(r) that can be obtained from the convolution integral

$$A_S(\mathbf{r}) = \int A(\mathbf{r}')W(\mathbf{r}-\mathbf{r}',h)d\mathbf{r}'. \tag{1}$$

Here h is the smoothing length, and the smoothing function W satisfies the normalization condition

$$\int W(\mathbf{r}-\mathbf{r}',h)d\mathbf{r}' = 1. \tag{2}$$

The integration is performed over the whole space. In the limit of h tending to zero, the smoothing function W becomes a Dirac delta function, and the smoothed representation $A_s(r)$ tends to A(r).

In the SPH scheme, the properties associated with particle i, are calculated by approximating the integral in eq. (1) by the sum

$$\begin{aligned} A_i &= \sum_j \Delta V_j A_j W(\mathbf{r}_i - \mathbf{r}_j, h) \\ &= \sum_j m_j \frac{A_j}{\rho_j} W(\mathbf{r}_i - \mathbf{r}_j, h). \end{aligned} \tag{3}$$

Here ΔV_j is the fluid volume associated with particle j, and m_j and ρ_j are the mass and density of the jth particle, respectively. In equation (3), A_j is the value of a physical field A(r) on the particle j, and the sum is performed over all particles. Furthermore, the gradient of A is calculated using the expression

$$\nabla A_i = \sum_j m_j \frac{A_j}{\rho_j} \nabla_i W(\mathbf{r}_i - \mathbf{r}_j, h). \tag{4}$$

In the equation (3), ρ_i/m_i can be replaced by the particle number density $n_i=\rho_i/m_i$, so that

$$A_i = \sum_j \frac{A_j}{n_j} W(\mathbf{r}_i - \mathbf{r}_j, h). \tag{5}$$

The particle number density can be calculated using the expression

$$n_i = \sum_j W(\mathbf{r}_i - \mathbf{r}_j, h). \tag{6}$$

The mass density is given by

$$\rho_i = \sum_j m_j W(\mathbf{r}_i - \mathbf{r}_j, h). \tag{7}$$

Similarly, the gradient can be calculated using the expression

$$\nabla A_i = \sum_j \frac{A_j}{n_j} \nabla_i W(\mathbf{r}_i - \mathbf{r}_j, h). \tag{8}$$

The SPH discretization reduces the Navier-Stokes equation to a system of ordinary differential equations having the form of Newton's second law of motion for each particle. This simplicity allows taking into account a variety of chemical effects with relatively little effort in the development of computational codes. Also, since the number of particles remains constant in the simulation and the interactions are symmetrical, the mass, momentum and energy are conserved exactly, and the systems like dynamic boundaries and interfaces can be modeled without too much difficulty. Hoover (1998), and Colagrossi & Landrini (2003), used the SPH method to model immiscible flows and found that the standard formulation of SPH proposed by Gingold & Monaghan (1977) creates an artificial surface tension on the border between the two fluids. Colagrossi & Landrini (2003) put forward an SPH formulation for the simulation of interfacial flows, that is, flow fields of different fluids separated by interfaces. The scheme proposed for the simulation of interfacial flows starts considering that the fluid field is represented by a collection of N particles interacting with each other according to evolution equations of the general form

$$\begin{aligned} \frac{d\rho_i}{dt} &= -\rho_i \sum_j M_{ij}, \\ \frac{d\mathbf{u}_i}{dt} &= -\frac{1}{\rho_i} \sum_j \mathrm{F}_{ij} + f_i, \\ \frac{d\mathbf{x}_i}{dt} &= \mathbf{u}_i. \end{aligned} \tag{9}$$

The terms M_{ij} and F_{ij} arise from the mass and momentum conservation equations. In the equations (9) appear the density ρ_i, the velocity u_i of the particles, and the force f_i can be any body force. When there are fluid regions with a sharp density gradient (interfaces), the SPH standard formulations must be modified in order to be applied to treat such systems. This difficulty can be circumvented using the following discrete approximations

$$\begin{aligned} div(\mathbf{u}_i) &= \sum_j (\mathbf{u}_j - \mathbf{u}_i) \cdot \nabla W_{ji} \frac{m_j}{\rho_j}, \\ \nabla A_i &= \sum_j (A_j - A_i) \nabla W_{ji} \frac{m_j}{\rho_j}. \end{aligned} \tag{10}$$

Here W is the Kernel or Smoothing Function and A can be any scalar field or continuous function. The small difference between the equation (10) and the standard equation that uses

m_j/ρ_i instead m_j/ρ_j is important for the treatment of the case of small density ratios. On the other hand, it can be shown that the pressure gradient can be written as

$$\nabla p_i = \sum_j (p_j + p_i)\nabla W_{ji} dV_j. \tag{11}$$

The equation (11) is variationally consistent with eq. (10). In this scheme the terms M_{ij} and F_{ij} appearing in eq. (9) are given by the expressions

$$\begin{aligned} M_{ij} &= (u_j - u_i)\cdot \nabla W_{ji} \frac{m_j}{\rho_j}, \\ F_{ij} &= (p_j + p_i)\nabla W_{ji} \frac{m_j}{\rho_j}. \end{aligned} \tag{12}$$

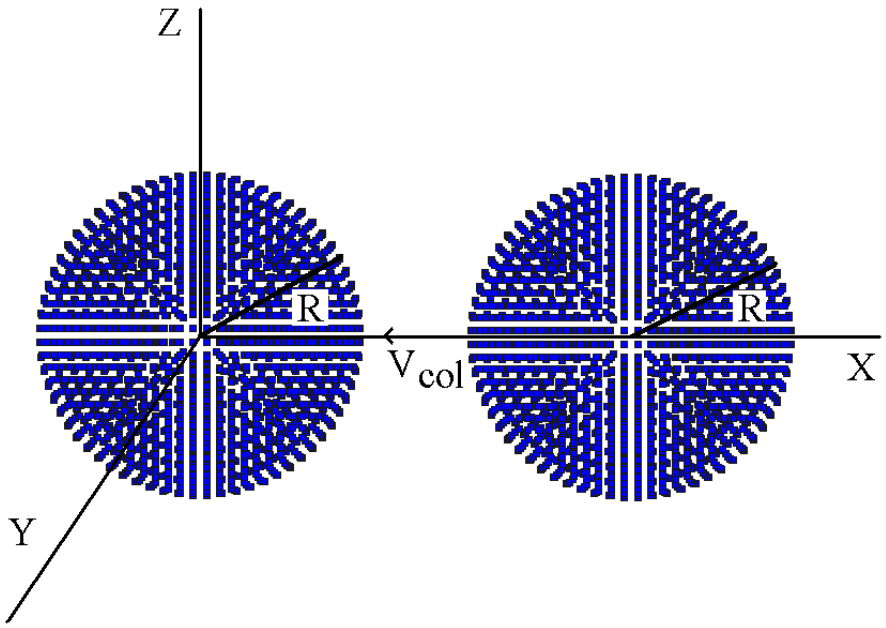

Fig. 1. Definition of the problem: head-on coalescence collision in three dimensions between two drops of equal size approaching with a velocity of collision V_{col} and radius R in empty space. Each drop is composed by 4700 SPH particles.

A density re-initialization is needed when each particle has a fixed mass, and when the number of particles is constant the mass conservation is satisfied. Yet if one uses eq. (9) for the density, the consistency between mass, density and occupied area is not satisfied. To solve this problem, the density is periodically re-initialized applying the expression

$$\rho_i = \sum_j m_j W_{ij}. \tag{13}$$

In this formulation special attention must be paid to the kernel. In fact depending on which kernel is used, eq. (13) could introduce additional errors. For this reason a first-order interpolation scheme is suitable to re-initialize the density field by using the equation

$$\left\langle \rho_i \right\rangle = \sum_j \rho_j W_j^{MLS}(x_i) dV_j = \sum_j m_j W_j^{MLS}(x_i), \tag{14}$$

Where W_j^{MLS} is the moving-least-square kernel.

The XSPH (Extended Smoothed Particle Hydrodynamics, which is a variant of the SPH method for the modeling of free surface flows (Monaghan, 1994)) velocity correction Δu_i is introduced to prevent particles inter-penetration (Colagrossi & Landrini, 2003), which takes into account the velocity of the neighbor particles using a mean value of the velocity, according to the equations

$$\left\langle \mathbf{u}_i \right\rangle = u_i + \Delta u_i, \quad \Delta u_i = \frac{\varepsilon'}{2} \sum_j \frac{m_j}{\bar{\rho}_{ij}} (u_j - u_i) W_{ji}, \tag{15}$$

where $\bar{\rho}_{ij}$ is the mean value of density between the ith and jth particle, and ε' is the relative change of an arbitrary quantity between simulations (Colagrossi & Landrini, 2003).
The velocity and acceleration fields are (Liu & Liu, 2003)

$$\begin{aligned} \frac{d\mathbf{r}_i}{dt} &= \mathbf{v}_i, \\ \frac{d\mathbf{v}_i^{\alpha}}{dt} &= \sum_{j=1}^{N} m_j \left(\frac{\sigma_i^{\alpha\beta}}{\rho_i^2} + \frac{\sigma_j^{\alpha\beta}}{\rho_j^2} \right) \cdot \nabla W_{ij}^h, \end{aligned} \tag{16}$$

where σ is the total stress tensor.
The internal energy evolution is given by the expression (Liu & Liu, 2003) :

$$\frac{dE_i}{dt} = \frac{1}{2} \sum_{j=1}^{N} m_j \left(\frac{p_i}{\rho_i^2} + \frac{p_j}{\rho_j^2} \right) \left(\mathrm{v}_i^{\beta} - \mathrm{v}_j^{\beta} \right) \frac{\partial W_{ij}}{\partial x_i^{\beta}} + \frac{\mu_i}{2\rho_i} \varepsilon_i^{\alpha\beta} \varepsilon_i^{\alpha\beta}, \tag{17}$$

In the above equation p is the pressure, μ is the dynamic viscosity and ε is the shear strain rate.
In the present work, our calculations are performed in three dimensions and we use the cubic B-spline kernel (Monaghan, 1985). We consider water drops, and the equation of state that we use in the hydrodynamical code was a general Mie-Gruneisen form of equation of state with different analytic forms for states of compression $(\rho/\rho_0\text{-}1)>0$ and tension $(\rho/\rho_0\text{-}1)<0$ (Liu & Liu, 2003). This equation has several parameters, namely the density ρ, the reference density ρ_0, and the constants A_1, A_2, A_3, C_1 and C_2. The pressure P is

$$P = A_1 \left(\frac{\rho}{\rho_0} - 1 \right) + A_2 \left(\frac{\rho}{\rho_0} - 1 \right)^2 + A_3 \left(\frac{\rho}{\rho_0} - 1 \right)^3 \quad if \quad \left(\frac{\rho}{\rho_0} - 1 \right) > 0 \tag{18}$$

and

$$P = C_1\left(\frac{\rho}{\rho_0}-1\right)+C_2\left(\frac{\rho}{\rho_0}-1\right) \quad if \quad \left(\frac{\rho}{\rho_0}-1\right)<0. \tag{19}$$

In all our calculations we use the following values for the constants: A_1=2.20x10^6 kPa, A_2=9.54x10^6 kPa, A_3=1.46x10^7 kPa, C_1=2.20x10^6 kPa, C_2=0.00 kPa, and ρ_0=1000.0 Kg/m^3.

3. Coalescence, fragmentation and flocculation of liquid drops in three dimensions

In order to model the collision of liquid drops several calculations were carried out. We have varied the velocity of collision for modeling the permanent coalescence of droplets in the three dimensional space (3D) in a vacuum environment using the SPH method. In order to proceed we have defined drops with diameter of 30μm and 4700 SPH particles for each drop with a collision velocity of 1.0 mm/ms.

In figure 2 is illustrated a sequence of times showing the evolution of the collision between two drops (permanent coalescence) with V_{col} = 1.0 mm/ms and We= 4.5. The evolution of time is shown in milliseconds. It can be seen in this figure that at t=0.0009 ms a flat circular section appears (Ivanov & Kralchevsky, 1997), which increases its diameter as dynamics progresses. The appearance of this flat circular section has been reported for the case of collision of drops in emulsion media (Ivanov & Kralchevsky, 1997), yet in this reference the hydrodynamic modeling of the collision of liquid drops is not considered. In the dynamics we observe that at t = 0.0053 ms a bridge structure between the two drops appears in the region of contact (this bridge is the structure that joins the drops through their flat circular interfaces placed in the center of the droplets coalescence), which disappears at a later time due to the penetration of particles of one drop into the other. After that, a process of coalescence occurs (see figure 2 at t=0.0069 ms) and a bigger drop is formed (see figure 2 at t=0.0077ms).

Figure 3 shows the velocity vector field inside the droplets and in the region of contact between them at t=0.004ms. Notice that inside the drops, the fluid tends to a velocity value lower than the initial velocity of 1.00 mm/ms, while in the area of contact between the drops we observe an increase in the fluid velocity to a value of 1.436 mm/ms. Once the coalescence process occurs, the velocity of the fluid inside the drops tends to zero, i.e. the largest drop size that is formed after some time tends to equilibrium. This can be seen in figure 4 where it is illustrated the time evolution of the kinetic and internal energy of the bigger drop. When two drops collide the possible results of the collision (coalescence, flocculation or fragmentation of drops) depends only on the kinetic energy and the Weber number (We) (Foote, 1974), which is given by

$$We = \frac{\rho V_r^2 d}{\sigma}. \tag{20}$$

Here Vr is the difference between the velocities of the drops, d the diameter of the drop, and σ the surface tension.

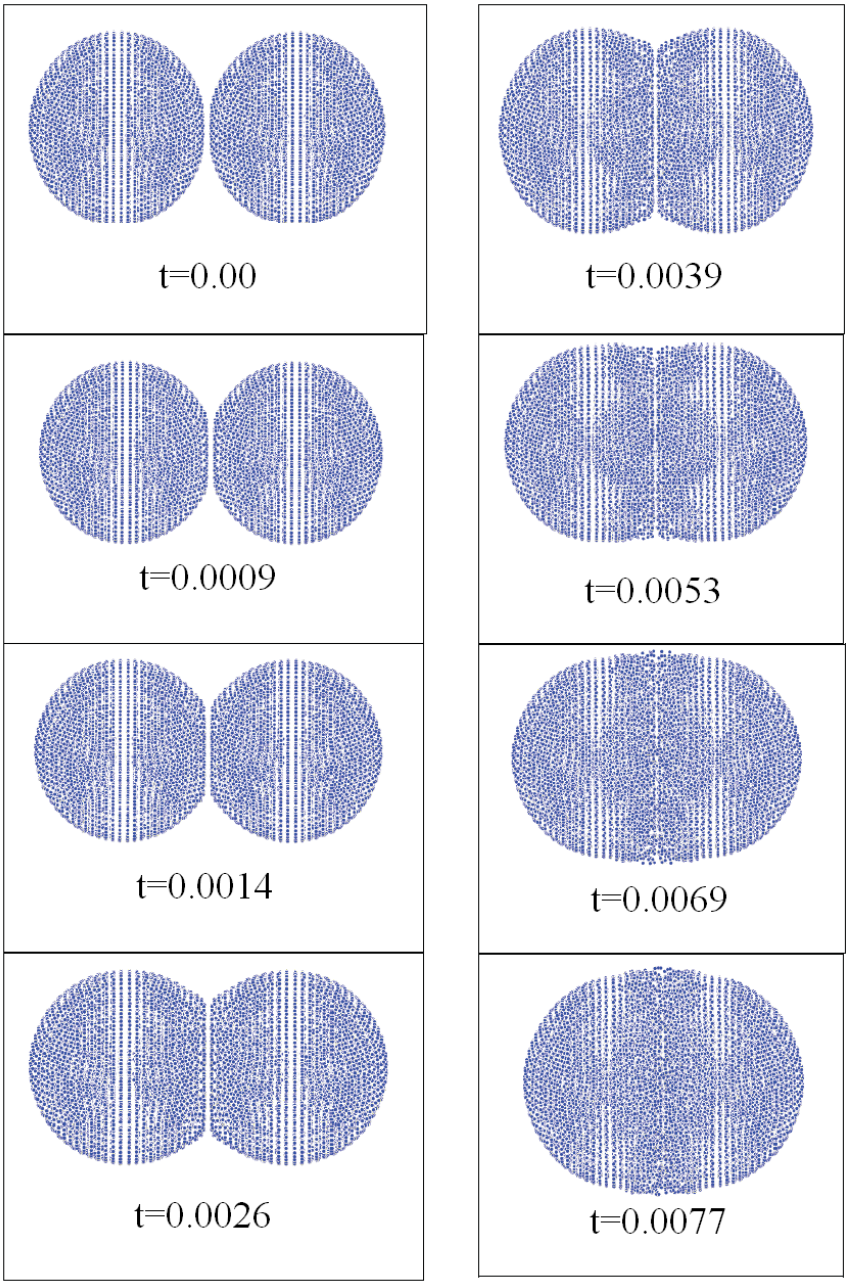

Fig. 2. Sequence of times showing the evolution of the collision between two drops (permanent coalescence) with V_{col} = 1.0 mm/ms and We = 4.5. The time scale is given in milliseconds.

From the values of density, relative velocity, droplet diameter and surface tension we obtain the Weber number. The Surface tension σ is determined using the Laplace equation

$$\left[p(r=0) - p(r\to\infty)\right] = \frac{\sigma}{R}. \tag{21}$$

The first term p (r = 0) on the left side of the equation (21) is determined at the drop center and the second term p (r → ∞) is taken as the vanishing pressure far away from the drop. The calculations were made in a vacuum environment and only head-on collisions were considered. The value of the pressure at the drop center is 1.78kPa and the Weber number for the coalescence collision is We=4.5. Values of the Weber number in the range 1≤We≤19 have been chosen, which corresponds to the range reported by Ashgriz & Poo (1990) for experimental head-on collisions and coalescence of water drops.

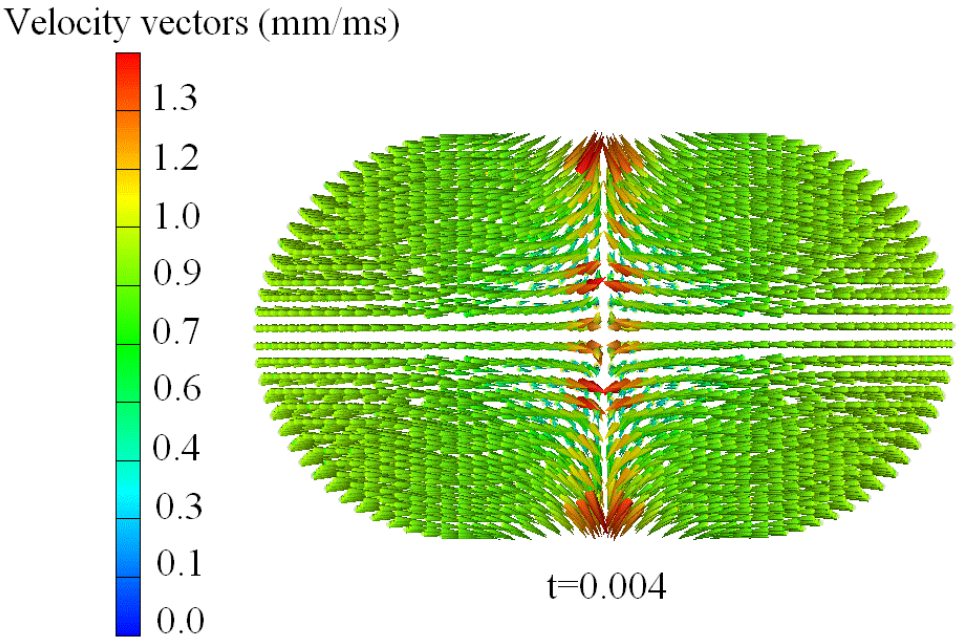

Fig. 3. Velocity vector field for the collision between two drops at t=0.004 ms (permanent coalescence process) with V_{col} = 1.0 mm/ms and We = 4.5. The time scale is given in milliseconds.

The coalescence processes occurring in droplets collision at low Weber numbers illustrated in the figures 1, 2 and 3 are governed by the competition between stretching and drop drainage. This drainage occurs when the liquid flows from the high-pressure drop region toward the point of contact to form a liquid bridge.

For larger values of We, the initially merged droplets would subsequently split apart, with the simultaneous production of smaller satellite droplets. It can be observed in our simulations (see figure 2) that the circular flat section disappears. Also, due to the effect of the surface tension a structure having the form of bridge is observed at t=0.0053ms and the

permanent coalescence occurs. The outcomes reported by Qian & Law (1997) are in good agreement with our results. In our SPH calculation, the relative velocity is not enough to produce fragmentation of the bigger drop and subsequently to produce small satellite droplets. In this calculation, the coalescence is permanent and the bigger drop that is formed reaches the equilibrium (see figure 4). On the other hand, the experiments of Qian & Law (1997) do not have a sufficient resolution to show in detail the deformation of the drops just before the formation of the bridge. However, the appearance of the flat circular section shown in figure 2 is in good agreement with the experimental and theoretical outcomes reported in the literature (Bibette et al., 1992; Ivanov & Dimitrov, 1988; Ivanov & Kralchevsky, 1997; Kabalnov & Wennerström, 1996; Sharma & Ruckenstein, 1987).

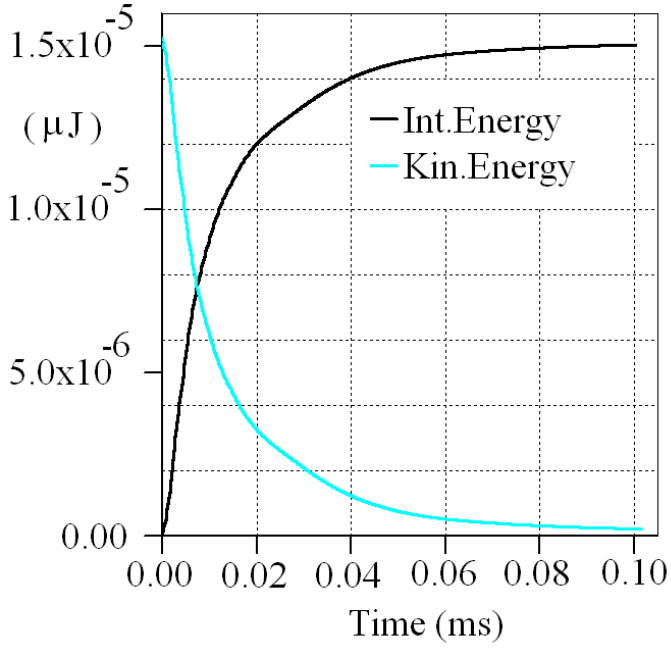

Fig. 4. Evolution of the Kinetic and Internal energy for the collision between two equal-sized drops with V_{col} = 1.0 mm/ms and We = 4.5.

On the other hand, it is observed that if we choose a Weber number for the collision greater than the range of values producing permanent coalescence, the phenomenon of fragmentation arises, i.e. the regime 2 reported by Qian & Law (1997) occurs giving rise to coalescence followed by separation into small satellite drops. The following calculations were performed for droplets with 30μm of diameter, 4700 SPH particles for each drop, and a collision velocity of 10.0 mm/ms (We=450) which is a characteristic velocity for the elements of a liquid spray (Choo & Kang, 2003). In the first stage of the calculation at t=2.0x10^{-4}ms the collision of the two droplets is shown in figure 5. It can be seen the formation of a flat circular section between the drops (Ivanov & Kralchevsky, 1997). This circular section vanishes completely at t = 5.6 x10^{-4}ms. At this time a portion of fluid appears to form a wave front propagating in the plane x = 0.

This wave front begins to form little satellite drops and increases its amplitude until $t=1.8x10^{-3}$ms. There is no substantial growth of these satellite drops and the structure tends to a flatten form as the dynamic runs. Figure 6 shows the velocity vector field (seen from the plane y = 0) after the fragmentation of the drops has taken place. As shown in figure 6, the fluid velocity at the center of the structure is 8.7 mm/ms, which is less than the initial rate of collision, while the fluid that is spread to the edges is accelerated reaching a speed of 15.0 mm/ms. A longer stretched ligament is produced and the amount of satellite droplets increases with the evolution of dynamics. Figure 5 illustrates that a portion of the fluid begins to separate, stretching away from the bigger drop, and a non-uniform pressure field is created inside the ligament. This is related to the value in the velocity vector field differences, and due to this pressure differential a flow parallel to the plane x=0 is produced. The fragmentation phenomena and the subsequent formation of satellites drops may be analyzed following the conjectures made by Qian & Law (1997).

Once the ligament begins to form (see figure 5), a flow is generated directed in the opposite direction to the vector field shown in figure 6. This motion transform this portion of the ligament in a bulbous due to the accumulation of mass in this volume, and this change in geometry implies the appearance of a local minimum in the pressure field which is located between the bulbous and its neighboring region.

As a result of this pressure difference a local flow is generated through the point of minimum pressure that opposes to the flow that is coming from the bulbous. This fluid motion causes a local reduction of mass and therefore the ligament between the bulbous and the neighboring region starts to decrease its radius (at the point of minimal pressure). Because of this local decrease of the ligament radius the pressure rises, which creates a flow with the same direction of the flow that comes from the end of the bulbous and other flow in the opposite direction from the point of local reduction of mass. Given these opposing flows emerging from this point, the radius of the ligament decreases even more. Then the system tends to relax this unstable situation reducing the radius of this region to zero, giving rise to a division of the fluid and so producing a satellite drop (see figure 5). Subsequently, this process is repeated in the other regions of the ligament, producing more satellites drops. These shattering collisions occur only at high velocities making the surface tension forces of secondary importance (the phenomenon is inertial dominated).

When the Weber number for the collision is decreased below the range corresponding to the permanent coalescence regime, then flocculation occurs. These calculations were performed for droplets with 30μm of diameter, 4700 SPH particles for each drop, and a collision velocity of 0.2mm/ms (We=0.18). At the beginning of the calculation one observes at t=0.29ms (see figure 7) that a flat circular section appears between the two droplets (Ivanov & Kralchevsky, 1997), which has already increased in diameter at t=1.0ms. Then, there is a stretching of the surface of the drop as can be seen at t=1.77ms. This stretch is deforming the drops until t=3.76 ms, and after that the drop shape remains constant. The chosen collision velocity cannot produce coalescence between the droplets. In fact no penetration was observed through the plane x=0. In this case, only the drops stay together, interacting through their surfaces, giving rise to flocs (Ivanov & Kralchevsky, 1997).

It has been reported that these flocs are formed in emulsions when the interfacial film between drops is very stable or the drops approach each other with a very small kinetic energy (Ivanov & Dimitrov, 1988; and Ivanov & Kralchevsky, 1997). In this case, the wave front that appears in the plane x=0 of figure 5 was not observed. Figure 8 shows the velocity vector field at t = 1.78ms. It can be seen in this figure that the value of the fluid velocity

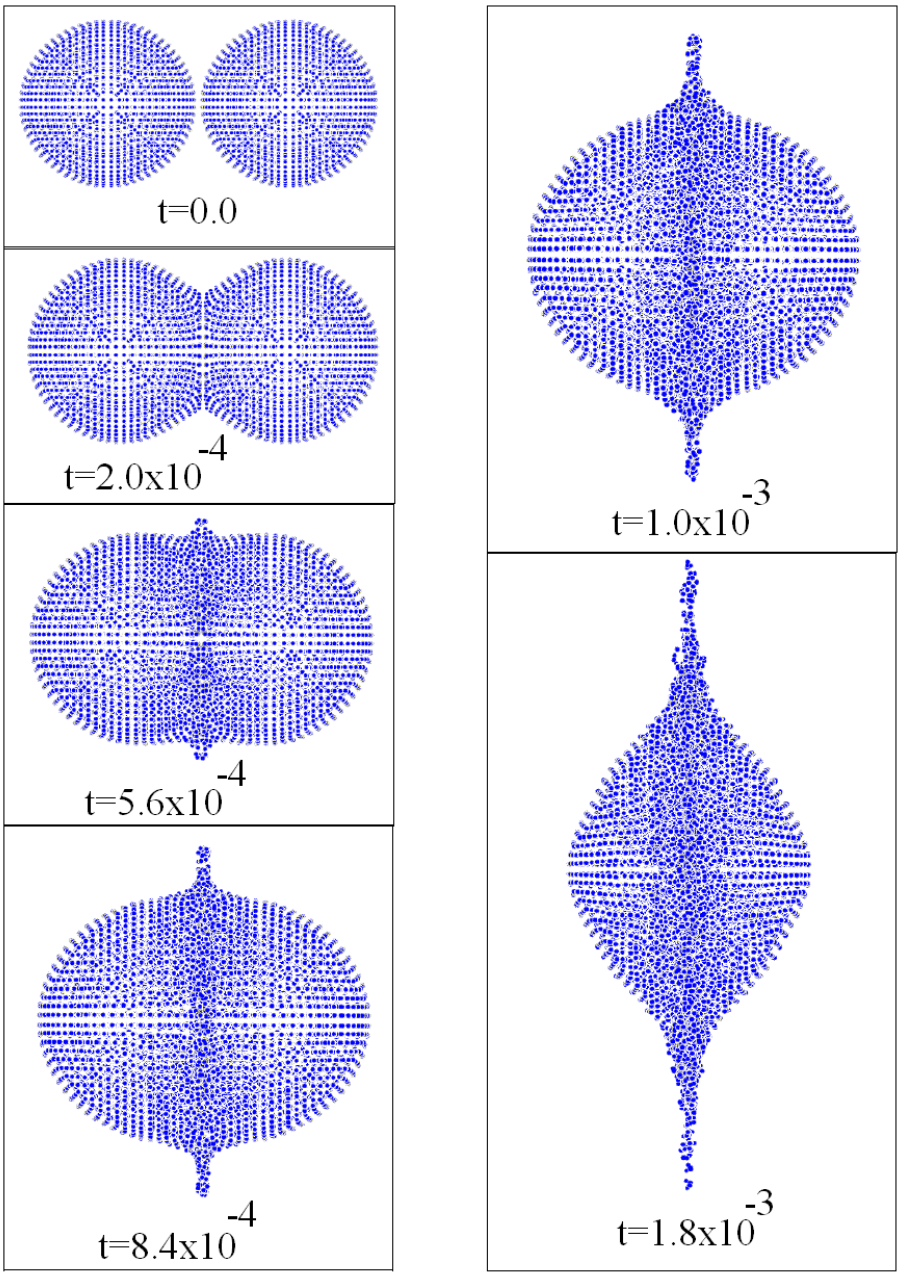

Fig. 5. Sequence of times showing the evolution of the collision between two drops with V_{col} = 10.0 mm/ms and We = 450. This figure illustrates the formation of small satellite droplets. The time scale is given in milliseconds.

decreases from the border to the center of the drop. In this case, the velocity has decreased below its initial value, which is 0.2mm/ms in all zones of the fluid. As is shown in figure 9, after an elapsed time of 3.76ms, the fluid velocities decrease even more, reaching a value of $2.24x10^{-2}$ mm/ms in the zone of interaction between the two drops and $4.48x10^{-2}$ mm/ms near the border.

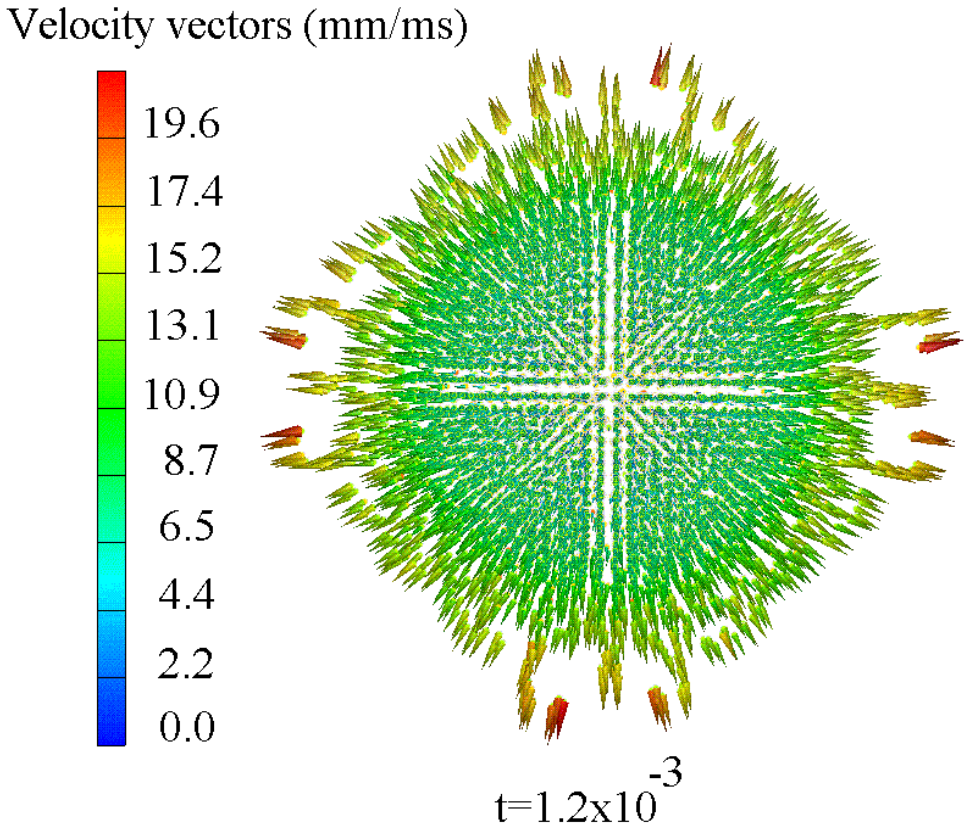

Fig. 6. Velocity vector field showing the fragmentation of two colliding drops at $t=1.2x10^{-3}$ms (see from the plane z-x) with V_{col}=10.0 mm/ms and We = 450. The time scale is given in milliseconds.

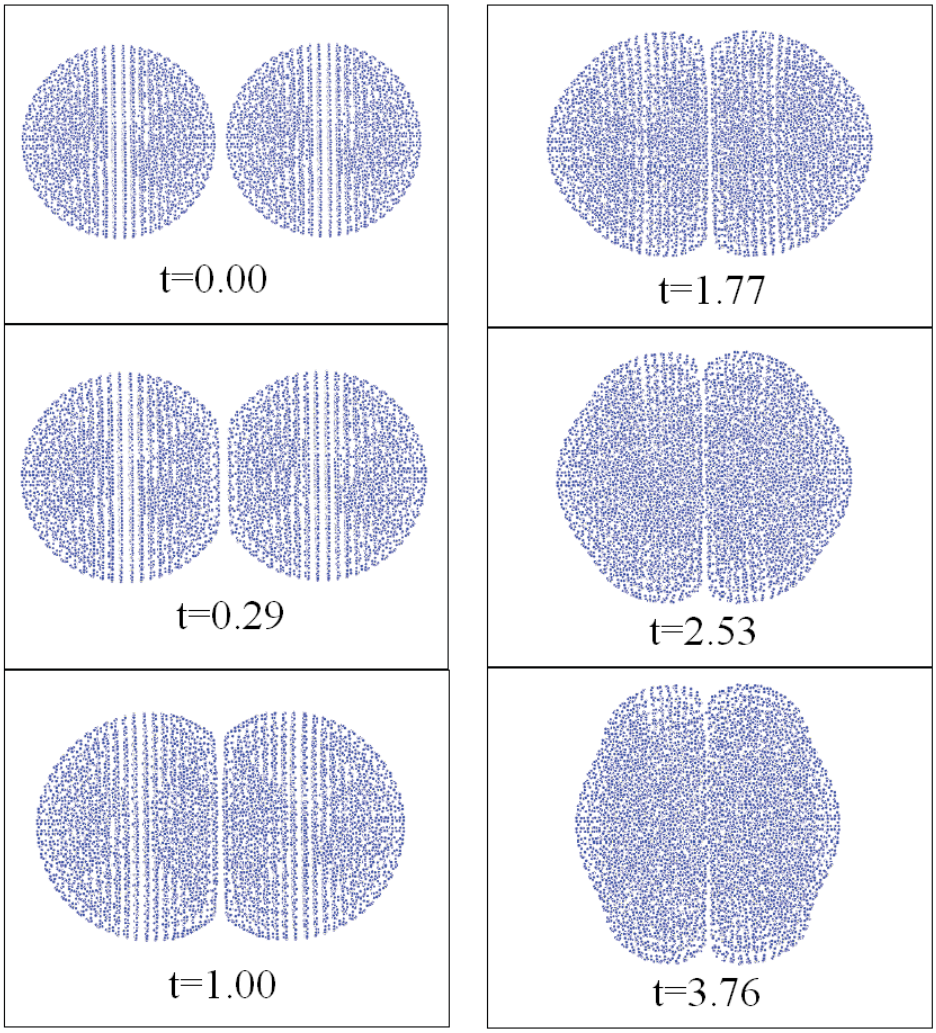

Fig. 7. Sequence of times showing the evolution of the collision between two drops (flocculation) with V_{col} = 0.2 mm/ms and We = 0.18. The time scale is given in milliseconds.

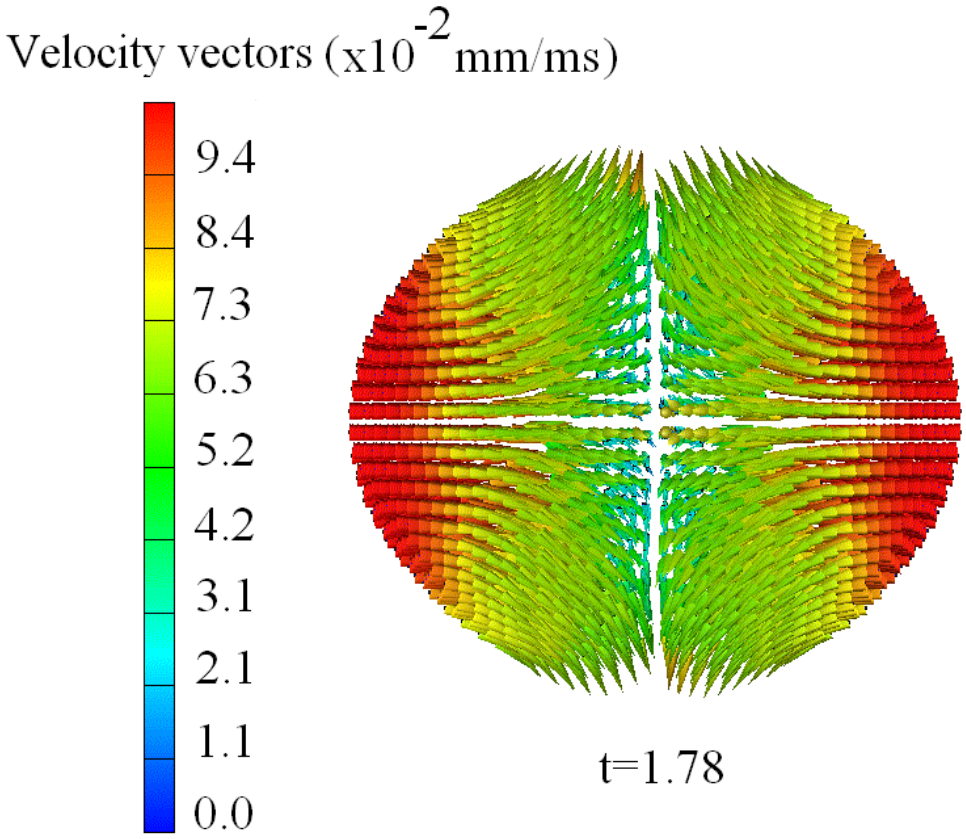

Fig. 8. Velocity vector field showing the flocculation of two liquid drops at t=1.78 ms with V_{col} = 0.2mm/ms and We = 0.18. The time scale is given in milliseconds.

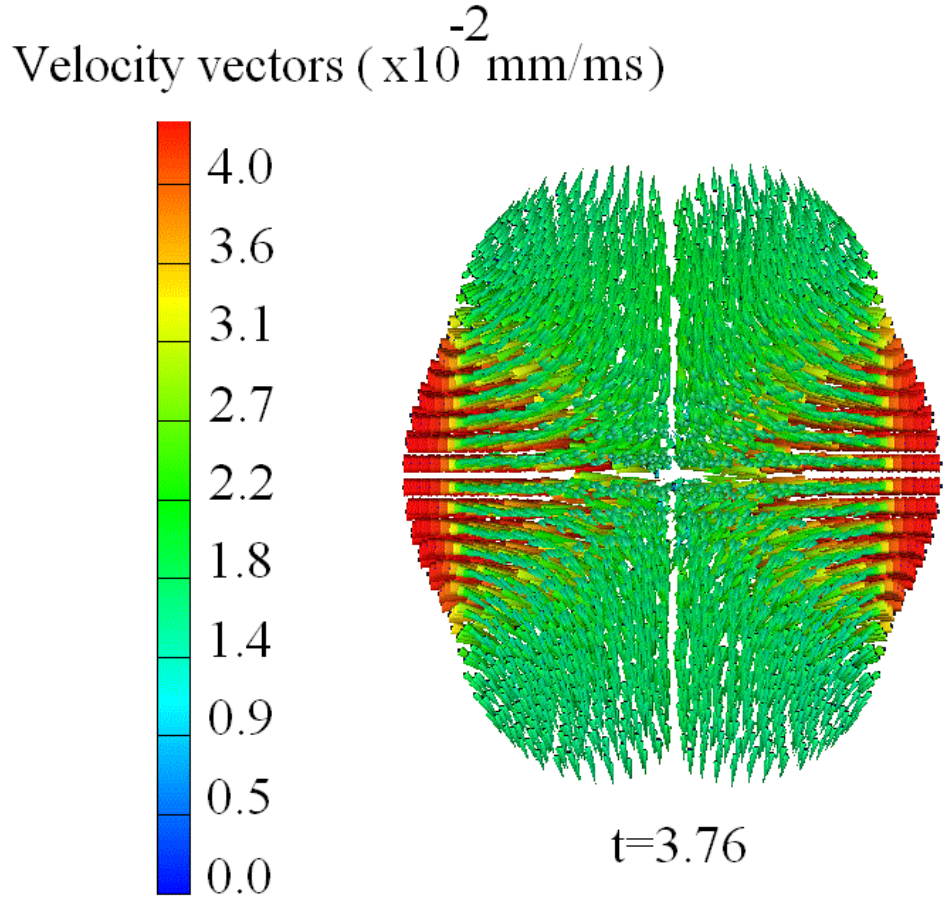

Fig. 9. Velocity vector field showing the flocculation of two liquid drops at t=3.76 ms with V_{col} = 0.2mm/ms and We = 0.18. The time scale is given in milliseconds.

4. Conclusions

An adequate methodology using the SPH method in three-dimensional space was presented for the calculation of hydrodynamic collisions of liquid drops in a vacuum environment. Several features of binary collisions in three dimensions have been observed in our calculations. As a result of the collision between droplets the formation of a circular flat film was obtained for a range of values of the Weber number. We have found three possible outcomes for the collision: permanent coalescence, fragmentation and flocculation of drops. We have ascribed a range of Weber number values for the three possible outcomes of the collisions.

Inside the drops, the fluid tends to a velocity value lower than the initial velocity of collision, while in the area of contact between the drops, we observed an increase in the fluid velocity. When the Weber number of the drops is larger than the range of values corresponding to coalescence, a fragmentation phenomenon is observed. Otherwise, when the Weber number is below this range, we obtained drop flocculation. In the case of drop fragmentation, we have observed the formation of satellite droplets emerging from the contact zone between the two drops. The mechanism of formation of these satellite droplets has been discussed.

We can see in the velocity vector field that after the fragmentation of the drops has taken place, the fluid velocity at the center of the structure is less than the initial rate of collision, while the fluid that is spread to the edges is accelerated producing a long stretched ligament and several satellite droplets. In the SPH dynamics that the drops follow when flocculation occurs, we have obtained that the system tends to a state of equilibrium in which the kinetic energy remains constant and the drops interact mainly through their deformed surfaces. On the velocity vector fields can be seen that in this case the value of the fluid velocity decreases from the border to the center of the drops. In all zones of the fluid the velocity has decreased below its initial value. After an elapsed time the fluid velocities decrease even more in the zone of interaction between the two drops near the border.

5. References

Ashgriz, N. & Givi, P. (1987). Binary collision dynamics of fuel droplets. *Int. J. Heat Fluid Flow,* 8, 1987, pp. 205-208;

Ashgriz, N. & Givi, P. (1989). Coalescence efficiencies of fuel droplets in binary collisions. *Int. Commun. Heat Mass Transfer,* 16, 1989, pp. 11-17;

Ashgriz, N. & Poo, J.Y. (1990). Coalescence and separation of binary collisions of liquid drops. *J. Fluid Mech.,* 221, 1990, pp. 183-204;

Azizi, F. & Al Taweel, A.M. (2010). Algorithm for the accurate numerical solution of PBE for drop breakup and coalescence under high shear rates. *Chem. Eng. Sci.*, 65, 2010, pp. 6112-6127;

Benz, W. & Asphaug. (1994). Impact simulations with fracture: I. Method and tests. *Icarus*, 1233, 1994, pp. 98-116.

Benz, W. & Asphaug. (1995). Simulations of brittle solids using smoothed particle hydrodynamics. *Comput. Phys. Commun.,* 87, 1995, pp. 253-265;

Bibette, J., Morse, D.C., Witten, T.A. & Weitz, D.A. (1992). Stability criteria for emulsions. *Phys. Rev. Lett.*, 69, 1992, pp. 2439-2443;

Bozzano, G. & Dente, M. (2010). Mechanism of drop coalescence at the interface of two immiscible liquids. 20th European Symposium on Computer Aided Process Engineering – ESCAPE20, 28, 2010, pp. 55-60;

Bradley, S.G. & Stow, C.D. (1978). Collision between liquid drops. *Philos. Trans. R. Soc. London Ser. A*, 287, 1978, pp. 635-642;

Brenn, G. & Frohn, A. (1989). Collision and merging of two equal droplets of propanol. *Exp. Fluids*, 7, 1989, pp. 441-446;

Brenn, G. & Kolobaric, V. (2006). Satellite droplet formation by unstable binary drop collisions. *Phys. Fluids*, 18, 2006, pp. 1-18;

Chen, J.D. (1985). A model of coalescence between two equal-sized spherical drops or bubbles. *J. Colloid Interface Sci.*, 107, 1985, pp. 209-220;

Choo, Y.J. & Kang, B.S. (2003). A study on the velocity characteristics of the liquid elements produced by two impinging jets. *Exp. in Fluids*, 34, 2003, pp. 655-661;

Colagrossi, A. & Landrini, M. (2003). Numerical simulation of interfacial flows by smoothed particle hydrodynamics. *J. Comput. Phys.*, 191, 2003, pp. 448-475;

Cristini, V., Bawzdziewicz, J. & Loewenberg, M. (2001). An Adaptive Mesh Algorithm for Evolving Surfaces: Simulations of Drop Breakup and Coalescence. *J. Comput. Phys.*, 168, 2001, pp. 445-463;

Cui, J., He, G.W. & Qi, D.W. (2006). A constrained particle dynamics for continuum-particle hybrid method in micro- and nano fluidics. Acta Mechanica Sinica, 22, 2006, pp. 503-508;

Decent, S.P., Sharpe, G., Shaw, A.J. & Suckling, P.M. (2006). The formation of a liquid bridge during the coalescence of drops. Int. J. *Multi-phase Flow*, 32, 2006, pp. 717-738;

Desbrun, M. & Gascuel, M.P. (1996). Smoothed Particles: a new paradigm for animating highly deformable bodies. *Proceedings of Eurographics Workshop on animation and simulation*, 1996.

Duchemin, L., Eggers, J. & Josserand, C. (2003). Inviscid coalescence of drops. *J. Fluid Mech.*, 487, 2003, pp. 167-180;

Eggers, J., Lister, J.R. & Stone, H.A. (1999). Coalescence of liquid drops. *J. Fluid Mech.,* 401, 1999, pp. 293-310;

Foote, G.B. (1974). The water drop rebound problem: Dynamics of collision. *J. Atmos. Sci.*, 32, 1974, pp. 390-401;

Gingold, R.A. & Monaghan, J.J. (1977). Smoothed particle hydrodynamics: theory and application to non-spherical stars. *Roy. Astronom. Soc.*, 181, 1977, pp. 375-389;

Gokhale, S.J., Dasgupta, S., Plawsky, J.L. & Wayner, P.C. (2004). Reflectivity-based evaluation of the coalescence of two condensing drops and shape evolution of the coalesced drop. *Phys. Rev. E.*, 70, 2004, pp. 1-12;

Gotaas, C., Havelka, P., Jakobsen, H., Svendsen, H., Hase, M., Roth, N. & Weigand, B. (2007, a). Effect of viscosity on droplet-droplet collision outcome: Experimental study and numerical comparison. *Phys. Fluids*, 19, 2007, pp. 1-17;

Gotaas, C., Havelka, P., Jakobsen, H. & Svendsen, H. (2007, b). Evaluation of the impact parameter in droplet-droplet collision experiments by the aliasing method. *Phys. Fluids*, 19, 2007, pp. 1-14;

Hoover, W.G. (1998). Isomorphism linking smooth particles and embedded atoms. *Physica A*, 260, 1998, pp. 244-255;

Ivanov, I.B. & Dimitrov, D.S. (1988). Thin Liquid Films Fundamentals and Applications. Dekker, 1988.

Ivanov, I.B. & Kralchevsky, P.A. (1997). Stability of emulsions under equilibrium and dynamic conditions. *Coll. Surf. A*, 128, 1997, pp. 155-175;

Jia, X., McLaughlin, J.B. & Kontomaris, K. (2006). Lattice Boltzmann simulations of drop coalescence and chemical mixing. *Physica A*, 362, 2006, pp. 62-67;

Jiang, Y.J., Umemura, A. & Law, C.K. (1992). An experimental investigation on the collision behaviour of hydrocarbon droplets. *J. Fluid Mech.*, 234, 1992, pp. 171-190;

Kabalnov, A. & Wennerström, H. (1996). Macroemulsion stability: The oriented wedge theory revisited. *Langmuir*, 12, 1996, pp. 276-292;

Koumoutsakos, P. (2005). Multiscale flow simulation using particle. *Ann. Rev. Fluid Mech.*, 37, 2005, pp. 457-487.

Leal, L.G. (2004). Flow induced coalescence of drops in a viscous fluid. *Phys. Fluids*, 16, 2004, pp. 1833-1851;

Li, D. (1994). Coalescence between two small bubbles or drops. *J. Colloid Interface Sci*., 163, 1994, pp. 108-119;

Li, J., Liao, D. & Yip, S. (1998). Coupling continuum to molecular-dynamics simulation: reflecting particle method and the field estimator. *Phys. Rev. E,* 57, 1998, pp. 7259-7267;

Liu, G.R. & Liu, M.B. (2003). Smoothed Particle Hydrodynamics – A Meshfree Particle Method. World Scientific, 2003;

Lucy, L.B. (1977). A numerical approach to the testing of the fission hypothesis. *Astron. J.,* 82, 1977, pp. 1013-1024;

Mashayek, F., Ashgriz, N., Minkowycz, W.J. & Shotorban, B. (2003). Coalescence collision of liquid drops. *Int. J. Heat Mass Trans.,* 46, 2003, pp. 77-89;

Menchaca-Rocha, A., Huidobro, F., Martinez-Davalos, A., Michaelian, K., Perez, A., Rodriguez, V. & Carjan, N. (1997). Coalescence and fragmentation of colliding mercury drops. *J. Fluid Mech.,* 346, 1997, pp. 291-318;

Menchaca-Rocha, A., Martinez-Davalos, A., Nuñez, R. (2001). Coalescence of liquid drops by surface tension. *Phys. Rev. E.,* 63, 2001, pp. 1-5;

Mohamed-Kassim, Z. & Longmire, E.K. (2004). Drop coalescence through a liquid/liquid interface. *Phys. Fluids*, 2004, pp. 1-47;

Monaghan, J.J. (1994). Simulating Free Surface Flows with SPH. *J. Comput. Phys.,* 110, 1994, pp. 399-406;

Monaghan, J.J. (1992). Smoothed particle hydrodynamics. *Annu. Rev. Astron. Astrophys,* 1992, pp. 543-574;

Monaghan, J.J. (1985). Extrapolating B splines for interpolation. *J. Comput. Phys.,* 60, 1985, pp. 253-262;

Narsimhan, G. (2004). Model for drop coalescence in a locally isotropic turbulent flow field. *J. Coll. Interf. Sci*., 272, 2004, pp. 197-209;

Nie, X.B., Chen, S.Y., WN, E. & Robbins, M.O. (2004). A continuum and molecular dynamics hybrid method for micro- and nano-fluid flow. *J. Fluid Mech.*, 500, 2004, pp. 55-64.

Nobari, M.R., Jan, Y.J. & Tryggvason, G. (1996). Head-on collision of drops-A numerical investigation. Phys. Fluids, 8, 1996, pp. 29-42;

O'Connell, S.T. & Thompson, P.A. (1995). Molecular dynamics-continuum hybrid computations: a tool for studying complex fluid flows. *Phys. Rev. E,* 52, 1995, pp. 5792-5795.

Pan, Y. & Suga, K. (2005). Numerical simulation of binary liquid droplet collision. *Phys. Fluids,* 17, 2005, pp. 1-14;

Park, J.Y. & Blair, L.M. (1975). The effect of coalescence on drop size distribution in an agitated liquid–liquid dispersion. *Chem. Eng. Sci.,* 30, 1975, pp. 1057-1064;

Podgorska, W. (2007). Influence of Dispersed Phase Viscosity on Drop Coalescence in Turbulent Flow. *Chem. Eng. Res. Design,* 85, 2007, pp. 721-729;

Qian, J. & Law, C.K. (1997). Regimes of coalescence and separation in droplet collision. *J. Fluid Mech*., 331, 1997, pp. 59-80.

Roisman, L. (2004). Dynamics of inertia dominated binary drops collisions. *Phys. Fluids,* 16, 2004, pp. 3438-3449;

Roisman, L., Berberovic, E. & Tropea, C. (2009). Inertia dominated drops collisions. I. On the universal flow in the lamella. *Phys. Fluids*, 21, 2009, pp. 1-10;

Rourke, P.J. & Bracco, F.V. (1980). Modelling of drop interactions in thick sprays and a comparison with experiments, in: Stratified Charged Auto Engineering Conference. *Institute of Mechanical Engineering Publications*, 1980, pp. 101-116;

Shah, P.S., Fan, L.T., Kao, I.C. & Erickson, L.E. (1972). Modeling of growth processes with two liquid phases: a review of drop phenomena, mixing, and growth. *Adv. Appl. Microbiol.,* 15, 1972, pp. 367-414;

Sharma, A. & Ruckenstein, E. (1987). Stability, critical thickness, and the time of rupture of thinning foam and emulsion films. *Langmuir*, 3, 1987, pp. 760-768;

Sun, Z., Xi, G. & Chen, X. (2009). Mechanism study of deformation and mass transfer for binary droplet collisions with particle method. *Phys. Fluids*, 21, 2009, pp. 1-13;

Tartakovsky, A.M. & Meakin, P.A. (2005). Smoothed particle hydrodynamics model for miscible flow in three-dimensional fractures and the two-dimensional Rayleigh–Taylor instability. *J. Comput. Phys*., 207, 2005, pp. 610-624.

Thoroddsen, S.T., Qian, B., Etoh, T.G. & Takehara, K. (2007). The initial coalescence of miscible drops. *Phys. Fluids*, 19, 2007, 1-21;

Wang, W., Gong, J., Ngan, K.H. & Angeli, P. (2009). Effect of glycerol on the binary coalescence of water drops in stagnant oil phase. *Chem. Eng. Res. Design*, 87, 2009, pp. 1640-1648;

Wu, M., Cubaud, T. & Ho, C. (2004). Scaling law in liquid drop coalescence driven by surface tension. *Phys. Fluids*, 16, 2004, pp. 51-54;

Xing, X.Q., Butler, D.L., Ng, S.H., Wang, Z., Danyluk, S. & Yang, C. (2007). Simulation of droplet formation and coalescence using lattice Boltzmann-based single-phase model. *J. Coll. Interf. Sci*., 311, 2007, pp. 609-618;

Yiantsios, S.G. & Davis, R.H. (1991). Close approach and deformation of two viscous drops due to gravity and van der Waals forces. *J. Colloid Interface Sci*., 144, 1991, pp. 412-433;

Yoon, Y., Baldessari, F., Ceniceros, H.D. & Leal, L.G. (2007). Coalescence of two equal-sized deformable drops in an axisymmetric flow. *Phys. Fluids*, 19, 2007, pp. 1-24;

Zhang, F.H., Li, E.Q. & Thoroddsen, S.T. (2009). Satellite formation during coalescence of unequal size drops. *Phys. Rev. Lett.*, 102, 2009, pp. 1-4;

Part 2

Models and Codes in Fluid Dynamics

6

Eulerian-Lagrangian Formulation for Compressible Navier-Stokes Equations

Carlos Cartes and Orazio Descalzi
Complex Systems Group, Universidad de los Andes
Chile

1. Introduction

The Eulerian-Lagrangian formulation of the (inviscid) Euler dynamics in terms of advected Weber-Clebsch potentials (Lamb, 1932), was extended by Constantin to cover the viscous Navier-Stokes dynamics (Constantin, 2001). Numerical studies (Ohkitani & Constantin, 2003), of this formulation of the Navier-Stokes equations concluded that the diffusive Lagrangian map becomes non-invertible under time evolution and requires resetting for its calculation. They proposed the observed sharp increase of the frequency of resettings as a new diagnostic of vortex reconnection.
In previous work we were able (Cartes et al., 2007; 2009) to complement these results, using an approach that is based on a generalised set of equations of motion for the Weber-Clebsch potentials, that turned out to depend on a parameter τ, which has the unit of time for the Navier-Stokes case. Also to extend our formulation to magnetohydrodynamics, and thereby obtain a new diagnostic for magnetic reconnection.
In this work we present a generalisation of the Weber-Clebsch variables in order to describe the compressible Navier-Stokes dynamics. Our main result is a good agreement between the dynamics for the velocity and density fields that come from the dynamics of Weber-Clebsch variables and direct numerical simulations of the compressible Navier-Stokes equations.
We first present the inviscid Eulerian-Lagrangian theory, then Constantin's extension to viscous fluids and derive our equations of motion for the Weber-Clebsch potentials that describe the compressible Navier-Stokes dynamics. Then, performing direct numerical simulations of the Taylor-Green vortex, we check that our formulation reproduces the compressible dynamics.

2. Eulerian-Lagrangian theory

2.1 Euler equations and Clebsch variables

Let us consider the incompressible Euler equations with constant density, fixed to one, for the velocity field $\mathbf{u}$

$$\begin{aligned} \partial_t \mathbf{u} + \mathbf{u} \cdot \nabla \mathbf{u} &= -\nabla p \\ \nabla \cdot \mathbf{u} &= 0\,, \end{aligned} \tag{1}$$

here p is the pressure field. Now the equations for evolution of the vorticity $\boldsymbol{\omega} = \nabla \times \mathbf{u}$ field

$$D_t \boldsymbol{\omega} = \boldsymbol{\omega} \cdot \nabla \mathbf{u}\,, \tag{2}$$

where D_t is the convective derivative

$$D_t = \partial_t + \mathbf{u} \cdot \nabla\,. \tag{3}$$

A well known consequence of this equation is the preservation of vorticity lines (Helmholtz's theorem).
Here we introduce Clebsch variables (Lamb, 1932). They can be considered as a representation of vorticity lines. In fact from this transformation, which defines the velocity field in terms of scalar variables (λ, μ, ϕ)

$$\mathbf{u} = \lambda \nabla \mu - \nabla \phi, \tag{4}$$

we can write the vorticity field as

$$\boldsymbol{\omega} = \nabla \times \mathbf{u} = \nabla \lambda \times \nabla \mu. \tag{5}$$

Vorticity lines $\mathbf{r}(s)$ are defined as the solutions of

$$\frac{d\mathbf{r}}{ds} = \boldsymbol{\omega}(\mathbf{r}(s))\,, \tag{6}$$

which admits integrals

$$\begin{aligned} \lambda(\mathbf{r}(s)) &= \text{const.} \\ \mu(\mathbf{r}(s)) &= \text{const.} \end{aligned} \tag{7}$$

In other words the intersections of surfaces λ =const. and μ =const. are the vorticity lines. If vorticity lines follow Euler equations and are preserved, then the fields λ and μ follow the fluid.
Clebsch variables can also be used to find a variational principle for Euler equations. We can write a Lagrangian density for Euler equations

$$\mathcal{L} = \frac{|\mathbf{u}|^2}{2} + \lambda \partial_t \mu\,, \tag{8}$$

and the variations of $\mathcal{L}$ in function of the fields λ, μ and ϕ give us the system equations

$$\begin{aligned} \frac{\delta \mathcal{L}}{\delta \mu} &= -D_t \lambda = 0 \\ \frac{\delta \mathcal{L}}{\delta \lambda} &= \ D_t \mu \ = 0 \\ \frac{\delta \mathcal{L}}{\delta \phi} &= \ \nabla \cdot \mathbf{u} \ = 0\,. \end{aligned} \tag{9}$$

From this system and the identity

$$[\nabla, D_t] \equiv (\nabla \mathbf{u}) \cdot \nabla, \tag{10}$$

we can obtain the evolution equation for $\mathbf{u}$

$$D_t \mathbf{u} = -\nabla \left(D_t \phi + \frac{1}{2} \mathbf{u}^2 \right) . \tag{11}$$

2.2 Weber transformation

Let us note a^i as the initial coordinate (at $t = 0$) of a fluid element and $X^i(a,t)$ its position at time t and note $A^i(x,t)$ the inverse application: $a^i \equiv A^i(X^i(a,t),t)$.
At time t Eulerian coordinates are by definition the variables $x^i = X^i(a,t)$ then the Lagrangian velocity of a fluid element is

$$\tilde{u}^i(a,t) = \frac{\partial X^i}{\partial t}(a,t) \tag{12}$$

and its acceleration

$$\frac{\partial \tilde{u}^i}{\partial t}(a,t) = \frac{\partial^2 X^i}{\partial t^2}(a,t) . \tag{13}$$

Newton equations for the fluid element are

$$\frac{\partial^2 X^i}{\partial t^2}(a,t) = F_X^i(a,t) , \tag{14}$$

where the forces $F_X^i(a,t)$ are given by

$$F_X^i(a,t) = -\frac{\partial p}{\partial x^i}(X(a,t),t) \tag{15}$$

and $p(X(a,t))$ is the pressure field in Eulerian coordinates.
Therefore the movement equations for the fluid elements are

$$\frac{\partial^2 X^i}{\partial t^2}(a,t) = -\frac{\partial p}{\partial x^i}(X(a,t),t) . \tag{16}$$

For an incompressible fluid, the transformation matrix, between Lagrangian and Eulerian coordinates, verifies

$$\det\left(\frac{\partial X^i}{\partial a^j}\right) = 1 , \tag{17}$$

this value is fixed from the relation between the volume elements in the two coordinate systems. We also note that this transformation is always invertible.
From Eq. (16) we perform a coordinate transformation for the derivatives of p using

$$\begin{aligned} \frac{\partial}{\partial x^i} &= \frac{\partial A^j}{\partial x^i}\frac{\partial}{\partial a^j} \\ \frac{\partial}{\partial a^i} &= \frac{\partial X^j}{\partial a^i}\frac{\partial}{\partial x^j} \end{aligned} \tag{18}$$

to obtain

$$\frac{\partial^2 X^i}{\partial t^2}(a,t) = -\frac{\partial A^j}{\partial x^i}\frac{\partial \tilde{p}}{\partial a^j}(a,t) \tag{19}$$

where $\tilde{p}(a,t)$ is the pressure field in Lagrangian coordinates.
We multiply Eq. (19) with the inverse coordinate transformation $\frac{\partial X^i}{\partial a^j}$ in order to obtain

$$\frac{\partial^2 X^i}{\partial t^2}(a,t)\frac{\partial X^i}{\partial a^j}(a,t) = -\frac{\partial \tilde{p}}{\partial a^j}(a,t) \tag{20}$$

which is the *Lagrangian form* for the dynamic equations.
The left hand side of this equation can be written as

$$\frac{\partial^2 X^i}{\partial t^2}(a,t)\frac{\partial X^i}{\partial a^j}(a,t) = \frac{\partial}{\partial t}\left(\frac{\partial X^i}{\partial t}(a,t)\frac{\partial X^i}{\partial a^j}(a,t)\right) - \frac{1}{2}\frac{\partial}{\partial a^j}\left|\frac{\partial X^i}{\partial t}(a,t)\right|^2 \tag{21}$$

and Eq. (20) becomes

$$\frac{\partial}{\partial t}\left(\frac{\partial X^i}{\partial t}(a,t)\frac{\partial X^i}{\partial a^j}(a,t)\right) = -\frac{\partial \tilde{q}}{\partial a^j}(a,t) \tag{22}$$

where the term $\tilde{q}(a,t)$ is given by

$$\tilde{q}(a,t) = \tilde{p}(a,t) - \frac{1}{2}\left|\frac{\partial X^i}{\partial t}(a,t)\right|^2 . \tag{23}$$

Now let us integrate Eq. (22) over t, maintaining a^i fixed

$$\left[\frac{\partial X^i}{\partial t}(a,t)\frac{\partial X^i}{\partial a^j}(a,t)\right]_0^t = \frac{\partial X^i}{\partial t}(a,t)\frac{\partial X^i}{\partial a^j}(a,t) - \tilde{u}_0^j(a)$$

to obtain

$$\frac{\partial X^i}{\partial t}(a,t)\frac{\partial X^i}{\partial a^j}(a,t) - \tilde{u}_0^j(a) = -\frac{\partial \tilde{\phi}}{\partial a^j}(a,t)\ , \tag{24}$$

where $\tilde{\phi}$ is written as

$$\tilde{\phi}(a,t) = \int_0^t \left(\tilde{p}(a,s) - \frac{1}{2}\left|\frac{\partial X^i}{\partial t}(a,s)\right|^2\right) ds\,. \tag{25}$$

This equation system (24) is called *Weber transformation* (Lamb, 1932).
Now we perform a coordinate transformation

$$\frac{\partial X^i}{\partial t}(a,t) = \tilde{u}_0^j(a)\frac{\partial A^j}{\partial x^i} - \frac{\partial A^j}{\partial x^i}\frac{\partial \tilde{\phi}}{\partial a^j}(a,t)\ . \tag{26}$$

identifying $\tilde{\mu}^i(a,t) = a^i$ and the initial velocity $\tilde{\lambda}^i(a,t) = \tilde{u}_0^i(a)$ we obtain the evolution equations for the fields in Lagrangian coordinates

$$\begin{aligned}
\frac{\partial \tilde{\lambda}^i}{\partial t}(a,t) &= 0 \\
\frac{\partial \tilde{\mu}^i}{\partial t}(a,t) &= 0 \\
\frac{\partial \tilde{\phi}}{\partial t}(a,t) &= \tilde{p}\,(a,t) - \frac{1}{2}\left|\frac{\partial X^i}{\partial t}\,(a,t)\right|^2 .
\end{aligned} \tag{27}$$

If we now go to the Eulerian coordinates, identifying $\mu^i(x,t) = A^i(x,t)$ and $\lambda^i(x,t) = u_0^i\,(\mu(x,t))$, we obtain the *Weber-Clebsch transformation*

$$u^i(x,t) = \sum_{j=1}^{3} \lambda^j \frac{\partial \mu^j}{\partial x^i} - \frac{\partial \phi}{\partial x^i}\,. \tag{28}$$

Using the convective derivative, the dynamic equations for the Clebsch variables Eq. (27) can be written in Eulerian coordinates as

$$\begin{aligned}
D_t \lambda^i(x,t) &= 0 \\
D_t \mu^i(x,t) &= 0 \\
D_t \phi(x,t) &= p(x,t) - \frac{1}{2}\left|u^i(x,t)\right|^2 .
\end{aligned} \tag{29}$$

The Weber-Clebsch transformation Eq. (28) and its evolution laws Eq. (29) are very similar to Clebsch variables Eq. (4) and the system (9). An important difference is the number of potential pairs.
If we use Clebsch variables Eq. (4) to represent the velocity field $\mathbf{u}$

$$\mathbf{u} = \lambda \nabla \mu - \nabla \phi\,, \tag{30}$$

we have the problem that $\mathbf{u}$ is restricted to fields with mean helicity

$$h = \int_V \mathbf{u} \cdot \boldsymbol{\omega} d^3x \tag{31}$$

of value zero (Grossmann, 1975). In fact, writing h in terms of Clebsch variables

$$h = \int_V (\lambda \nabla \mu - \nabla \phi) \cdot (\nabla \lambda \times \nabla \mu)\, d^3x = -\int_V \nabla \phi \cdot (\nabla \lambda \times \nabla \mu)\, d^3x\,, \tag{32}$$

the term $\lambda \nabla \mu$ is perpendicular to $\nabla \lambda \times \nabla \mu$ and then their scalar product is zero. For the other terms, we integrate by parts

$$\int_V \nabla \phi \cdot (\nabla \lambda \times \nabla \mu)\, d^3x = \oint_{\partial V} \phi\, (\nabla \lambda \times \nabla \mu) \cdot d\mathbf{s} - \int_V \phi \nabla \cdot (\nabla \lambda \times \nabla \mu) \tag{33}$$

but in a periodic domain the first term in the right hand side is zero. We also know that $\nabla \cdot \boldsymbol{\omega} = 0$ and therefore we have

$$\nabla \cdot (\nabla\lambda \times \nabla\mu) = 0 \tag{34}$$

and we finally get

$$h = \int_V \mathbf{u} \cdot \boldsymbol{\omega} d^3x = 0. \tag{35}$$

If we consider now two pairs of Clebsch variables, for each component of the velocity field, we have

$$u^j = \sum_{i=1}^{2} \lambda^i \frac{\partial \mu^i}{\partial x^j} - \frac{\partial \phi}{\partial x^j}, \tag{36}$$

and we arrive to a system of equations of second degree in its unknowns, this system does not have an analytic solution and we don't have a systematic way to find λ^i and μ^i for an arbitrary velocity field $\mathbf{u}$.
If we use now the same number of pairs as spatial variables (three in this case), we get the Weber-Clebsch transformation

$$\mathbf{u} = \sum_{i=1}^{3} \lambda^i \nabla \mu^i - \nabla \phi, \tag{37}$$

with this representation we can write an arbitrary velocity field defining, at $t = 0$:

$$\begin{aligned} \lambda^i(x,0) &= u^i(x,0) \\ \mu^i(x,0) &= x^i \\ \phi(x,0) &= 0 \end{aligned} \tag{38}$$

which is completely equivalent to the Weber transformation.

2.3 Constantin's formulation of Navier-Stokes equations

Here we will recall Constantin's extension for the Eulerian-Lagrangian formulation of Navier-Stokes equations.
The departing point (Constantin, 2001), is the expression for the Eulerian velocity $\mathbf{u} = \left(u^1, u^2, u^3\right)$ from the Weber-Clebsch transformation

$$u^i = \sum_{m=1}^{3} \lambda^m \frac{\partial \mu^m}{\partial x^i} - \frac{\partial \phi}{\partial x^i}. \tag{39}$$

The fields in this equation admit the same interpretation as in the Weber transformation: λ^m are the Lagrangian velocity components, μ^m are the Lagrangian coordinates and ϕ fixes the incompressibility condition for the velocity field.
In a way similar to the Weber transformation, we have the Lagrangian coordinates $a^i = \mu^i(x,t)$ and the Eulerian coordinates $x^i = X^i(a,t)$.
If we now consider the first term of the right hand side in Eq. (39) as a coordinate transformation, it is possible to write their derivatives in Lagrangian coordinates, as in Eq. (18)

$$\frac{\partial}{\partial a^i} = \sum_{m=1}^{3} \frac{\partial X^m}{\partial a^i} \frac{\partial}{\partial x^m} \,. \tag{40}$$

In the same way it is possible to write the derivatives of the Eulerian coordinate in terms of Lagrangian coordinates

$$\frac{\partial}{\partial x^i} = \sum_{m=1}^{3} \frac{\partial \mu^m}{\partial x^i} \frac{\partial}{\partial a^m} \,. \tag{41}$$

We also have the relation for the commutators

$$\begin{aligned} \left[\frac{\partial}{\partial x^i} , \frac{\partial}{\partial x^k} \right] &= 0 \\ \left[\frac{\partial}{\partial a^i} , \frac{\partial}{\partial a^k} \right] &= 0 \,. \end{aligned} \tag{42}$$

Using relations Eq. (40), Eq. (41) and Eq. (42) we can compute the commutators between ∂_x and ∂_a

$$\left[\frac{\partial}{\partial a^i} , \frac{\partial}{\partial x^k} \right] = \left[\frac{\partial}{\partial a^i} , \frac{\partial \mu^m}{\partial x^k} \frac{\partial}{\partial a^m} \right] = \frac{\partial}{\partial a^i} \left(\frac{\partial \mu^m}{\partial x^k} \right) \frac{\partial}{\partial a^m} \,. \tag{43}$$

Introducing the displacement vector $\ell^m = \mu^m - x^m$ which relates the Eulerian position x to the original Lagrangian position μ, we can express the commutator Eq. (43) as

$$\left[\frac{\partial}{\partial a^i} , \frac{\partial}{\partial x^k} \right] = \frac{\partial}{\partial a^i} \left(\frac{\partial \ell^m}{\partial x^k} \right) \frac{\partial}{\partial a^m} = C_{m,k;i} \frac{\partial}{\partial a^m} \,. \tag{44}$$

The term $C_{m,k;i}$ is related to the Christoffel coefficients Γ_{ij}^m of the flat connection in $\mathbb{R}^3$ by the formula

$$\Gamma_{ij}^m = -\frac{\partial X^k}{\partial a^j} C_{m,k;i} \,. \tag{45}$$

We consider now the diffusive evolution of our fields, with that goal in mind we define the operator

$$\Gamma = \partial_t + \mathbf{u} \cdot \nabla - \nu \triangle \,, \tag{46}$$

where ν is the viscosity and $\mathbf{u}$ is the Eulerian velocity. When the operator Eq. (46) is applied over a vector or a matrix each component is taken in an independent way.
Constantin imposes that the coordinates μ^i are advected and diffused so they follow

$$\Gamma \mu^i = 0. \tag{47}$$

We also need a coordinate transformation that can be invertible at any time t, that condition is always satisfied when the diffusion is zero ($\nu = 0$) and the fluid is incompressible, because the fluid element volume is preserved by the coordinate transformation, and therefore

$$\mathrm{Det} \left(\nabla \boldsymbol{\mu} \right) = 1 \,, \tag{48}$$

where

$$(\nabla \boldsymbol{\mu})_{jk} = \frac{\partial \mu^j}{\partial x^k}\,. \tag{49}$$

In order to get the evolution for the λ^i fields we apply D_t on Eq. (39), and using the relation

$$\left[D_t\,, \frac{\partial}{\partial x^i}\right] = -\frac{\partial u^l}{\partial x^i}\frac{\partial}{\partial x^l} \tag{50}$$

we obtain

$$D_t u^i = \sum_{m=1}^{3}\left(D_t\lambda^m \frac{\partial \mu^m}{\partial x^i} + \lambda^m \frac{\partial}{\partial x^i} D_t \mu^m\right) - \frac{\partial}{\partial x^i}\left(D_t\phi + \frac{1}{2}\mathbf{u}^2\right)\,. \tag{51}$$

We also have, from Navier-Stokes equations:

$$D_t u^i = \nu \triangle u^i - \frac{\partial}{\partial x^i} p\,. \tag{52}$$

We compute the term $\triangle u^i$ with the transformation Eq. (39), using Eq. (47) and regrouping the terms we obtain

$$\frac{\partial}{\partial x^i}\left(\Gamma\phi + \frac{1}{2}\mathbf{u}^2 - p\right) = \sum_{m=1}^{3}\left(\Gamma\lambda^m \frac{\partial \mu^m}{\partial x^i} - 2\nu \frac{\partial \lambda^m}{\partial x^k}\frac{\partial}{\partial x^k}\frac{\partial \mu^m}{\partial x^i}\right)\,. \tag{53}$$

Now we split the ϕ field to obtain the pressure equation

$$\Gamma\phi + \frac{1}{2}\mathbf{u}^2 - p = c\,. \tag{54}$$

where c is a constant.
To obtain the λ^l dynamics we have to invert the transformation matrix

$$\frac{\partial \mu^m}{\partial x^i} \tag{55}$$

in Eq. (53) if the determinant of the transformation matrix follows

$$\det\left(\frac{\partial \mu^m}{\partial x^i}\right) = 0. \tag{56}$$

then it will be impossible to perform a coordinate transformation.
Therefore, if the matrix is invertible, the λ^l dynamics is written as

$$\Gamma\lambda^l = 2\nu \frac{\partial \lambda^m}{\partial x^k} C_{m,k;l}\,. \tag{57}$$

We have to remark that the dynamics of $\mathbf{u}$ is completely described by Eq. (47), (57) and the incompressibility condition for $\mathbf{u}$, thus Eq. (54) becomes an identity.

3. Generalisation of Constantin's formulation

We begin with the Weber-Clebsch transformation for the velocity field $\mathbf{u}$

$$\mathbf{u} = \sum_{i=1}^{3} \lambda^i \nabla \mu^i - \nabla \phi \tag{58}$$

and perform a variation on the Weber-Clebsch transformation Eq. (58) to obtain the relation (Cartes et al., 2007)

$$\delta \mathbf{u} = \sum_{i=1}^{3} \left(\delta \lambda^i \nabla \mu^i - \delta \mu^i \nabla \lambda^i \right) - \nabla \left(\delta \phi - \sum_{i=1}^{3} \delta \mu^i \lambda^i \right) \tag{59}$$

here δ represents a spatial or temporal variation. In the system (59) it is already possible to see that we have three equations ($\delta \mathbf{u}$) and six unknowns to find ($\delta \lambda^i$ and $\delta \mu^i$, $\delta \phi$ is fixed by the continuity equation).
In order to write the temporal evolution of $\mathbf{u}$, in terms of Weber-Clebsch potentials, we use the convective derivative D_t and the identity

$$[\nabla, D_t] \equiv (\nabla \mathbf{u}) \cdot \nabla \,. \tag{60}$$

We compute now the convective derivative for $\mathbf{u}$, which can be written as a function of the potentials

$$D_t \mathbf{u} = \sum_{i=1}^{3} \left(D_t \lambda^i \nabla \mu^i + \lambda^i \nabla D_t \mu^i - \lambda^i \left(\nabla \mathbf{u} \right) \cdot \nabla \mu^i \right) - \nabla D_t \phi + \left(\nabla \mathbf{u} \right) \cdot \nabla \phi \,. \tag{61}$$

For that purpose we write in gradient form

$$\sum_{i=1}^{3} \lambda^i \nabla D_t \mu^i = \sum_{i=1}^{3} \left(\nabla \left(\lambda^i D_t \mu^i \right) - D_t \mu^i \nabla \lambda^i \right) \tag{62}$$

and noting that

$$\sum_{i=1}^{3} \left(\lambda^i \left(\nabla \mathbf{u} \right) \cdot \nabla \mu^i \right) - \left(\nabla \mathbf{u} \right) \cdot \nabla \phi = \frac{1}{2} \nabla \mathbf{u}^2 \,. \tag{63}$$

Finally we regroup the gradients

$$D_t \mathbf{u} = \sum_{i=1}^{3} \left(D_t \lambda^i \nabla \mu^i - D_t \mu^i \nabla \lambda^i \right) - \nabla \left(D_t \phi + \frac{1}{2} \mathbf{u}^2 - \sum_{i=1}^{3} D_t \mu^i \lambda^i \right) \,. \tag{64}$$

We must note that this expression is very similar to Eq. (59), the only difference is given by the term $\frac{1}{2}\mathbf{u}^2$, that comes from the commutator between the gradient and the convective derivative.

3.1 General formulation for the compressible Navier-Stokes equations

We now consider the compressible Navier-Stokes equations with a general forcing term $\mathbf{f}$

$$\begin{aligned} D_t \mathbf{u} &= -\nabla w + \mathbf{f} \left[\mathbf{u}, x, t \right] \\ \partial_t \rho &= -\nabla \cdot \left(\rho \mathbf{u} \right) . \end{aligned} \tag{65}$$

where w is the enthalpy and ρ the density field.
For this work we will consider, for simplicity and without loss of generality, a barotropic fluid, then the relation for the enthalpy w is

$$w = \frac{(\rho - 1)}{Ma^2}, \tag{66}$$

where Ma is the Mach number for a flow of density $\rho_0 = 1$ and velocity $\mathbf{u} \sim 1$. In this approximation we suppose the density field ρ is very near to the uniformity state and consequently the Mach number is small.
The usual compressible Navier-Stokes equations are obtained when the forcing term $\mathbf{f}$ is the viscous dissipation

$$\mathbf{f} = \nu \triangle \mathbf{u}. \tag{67}$$

The idea is to find the evolution equations, in the most general way, for the potentials Eq. (58), now we replace D_t, in the equations of motion Eq. (65), by its expression Eq. (64) and we define

$$\begin{aligned} D_t \lambda^i &= L^i[\lambda, \mu] \\ D_t \mu^i &= M^i[\lambda, \mu]\,. \end{aligned} \tag{68}$$

To wit we made the separation in Eq. (64) and Eq. (65) between gradient and non-gradient terms

$$D_t \phi + \frac{1}{2}|\mathbf{u}|^2 - \sum_{i=1}^{3} M^i \lambda^i = w + G \tag{69}$$

$$\sum_{i=1}^{3} \left(L^i \nabla \mu^i - M^i \nabla \lambda^i \right) = \mathbf{f} - \nabla G \tag{70}$$

here G is an arbitrary gauge function, which comes from the fact that the separation in gradient and non-gradient terms is not unique.
The equation system (70) has 3 linear equations and 6 unknowns L^i, M^i. In order to solve this system with $\mathbf{f}$ we must remark that, when $\nu = 0$, the fields λ^i and μ^i follow Euler dynamics

$$\begin{aligned} D_t \lambda^i &= 0 \\ D_t \mu^i &= 0 \end{aligned} \tag{71}$$

If we are in the overdetermined case (more equations than unknowns), in general, equation (70) has no solution. Then we consider only the under determined case (more unknowns than equations).
In order to obtain evolution equations in the same way as (Constantin, 2001) we look for advection diffusion equations. With that goal in mind we introduce $\widetilde{L^i}$ and $\widetilde{M^i}$, defined by

$$\begin{aligned} D_t\lambda^i &= L^i[\lambda,\mu] = \nu\triangle\lambda^i + \widetilde{L^i}[\lambda,\mu] \\ D_t\mu^i &= M^i[\lambda,\mu] = \nu\triangle\mu^i + \widetilde{M^i}[\lambda,\mu]\,. \end{aligned} \tag{72}$$

The terms $\widetilde{L^i}$ and $\widetilde{M^i}$ must verify

$$\sum_{i=1}^{3}\left(\widetilde{L^i}\nabla\mu^i - \widetilde{M^i}\nabla\lambda^i\right) = \tilde{\mathbf{f}} - \nabla\widetilde{G} \tag{73}$$

where $\widetilde{G}$ is an arbitrary scalar function, linked to the old function G, by the relation $G = \widetilde{G} - \nu\triangle\phi + \nu\lambda^i\triangle\mu^i$, and

$$\tilde{\mathbf{f}} = 2\nu\sum_{i=1}^{3}\sum_{\alpha=1}^{3}\partial_\alpha\lambda^i\partial_\alpha\nabla\mu^i. \tag{74}$$

The process used to obtain $\widetilde{L^i}$ and $\widetilde{M^i}$ consists in solving the linear system (73).

3.2 Moore-Penrose solution

As the system (73) is under determined, we must impose additional restrictions to solve it.

The most straightforward way is to force the coefficients $\widetilde{M^i} = 0$ as in Constantin's formulation then we will have 3 equations for the 3 unknowns.

Another, more general, method relies in the imposition of additional conditions on the solution's length.

For that purpose we use the Moore-Penrose algorithm (Ben-Israel & Greville, 1974; Moore, 1920; Penrose, 1955), which produces 3 additional conditions that allow us to solve this more general system (73).

For the under determined case, the Moore-Penrose general solution consists in finding the solution to the linear system (73) with the imposition that the norm

$$\sum_{i=1}^{3}\left(\widetilde{L^i}\widetilde{L^i} + \tau^{-2}\widetilde{M^i}\widetilde{M^i}\right) \tag{75}$$

is minimal.

The constant τ is introduced here because λ^i and μ^i have different dimensions. In fact, the Weber-Clebsch transformation Eq. (58) means that the dimensions for λ^i and μ^i are

$$\begin{aligned} \left[\lambda^i\right] &= \frac{L}{T} \\ \left[\mu^i\right] &= L \end{aligned} \tag{76}$$

because the product $\lambda\nabla\mu$ has the same dimensions as the velocity and the fields μ^i have the dimensions of L they are the Lagrangian coordinates of the system. Then, from equations (72), it is straightforward that the dimensions of $\widetilde{L^i}$ and $\widetilde{M^i}$ are

$$\widetilde{L}^i = \frac{L}{T^2} \tag{77}$$
$$\widetilde{M}^i = \frac{L}{T}$$

and the parameter τ in Eq. (75) has the dimension of time.
The Moore-Penrose general solution which minimises the norm Eq. (75) (Cartes et al., 2007), is given by Eq. (78) and Eq. (79)

$$\widetilde{L}^i = \nabla\mu^i \cdot \mathbb{H}^{-1} \cdot \left(\widetilde{\mathbf{f}} - \nabla\widetilde{G}\right) \tag{78}$$
$$\widetilde{M}^i = -\tau^2 \nabla\lambda^i \cdot \mathbb{H}^{-1} \cdot \left(\widetilde{\mathbf{f}} - \nabla\widetilde{G}\right) . \tag{79}$$

where $\mathbb{H}$ represents the squared symmetric matrix

$$\mathbb{H}_{\alpha\beta} \equiv \sum_{i=1}^{3} \left(\tau^2\, \partial_\alpha\lambda^i \partial_\beta\lambda^i + \partial_\alpha\mu^i \partial_\beta\mu^i\right) \tag{80}$$

and the arbitrary function $\widetilde{G}$ is given by

$$\widetilde{G} = \triangle^{-1}\nabla \cdot \widetilde{\mathbf{f}} \tag{81}$$

in order to minimise the general norm Eq. (82)

$$S[\widetilde{G}] = \frac{1}{2}\int_\Omega \left(\widetilde{\mathbf{f}} - \nabla\widetilde{G}\right) \cdot \mathbb{H}^{-1} \cdot \left(\widetilde{\mathbf{f}} - \nabla\widetilde{G}\right) W(x^\alpha) d^d x. \tag{82}$$

with the objective to achieve numerical stability in our simulations.
Replacing these solutions $\widetilde{L}^i$ and $\widetilde{M}^i$ in Eq. (72) we arrive to the explicit evolution equations

$$D_t\lambda^i = \nu\triangle\lambda^i + \nabla\mu^i \cdot \mathbb{H}^{-1} \cdot \left(\widetilde{\mathbf{f}} - \nabla\widetilde{G}\right) \tag{83}$$
$$D_t\mu^i = \nu\triangle\mu^i + -\tau^2 \nabla\lambda^i \cdot \mathbb{H}^{-1} \cdot \left(\widetilde{\mathbf{f}} - \nabla\widetilde{G}\right) .$$

3.2.1 Comparison of the invertibility conditions

Constantin's method will have problems when the determinant $\det(\nabla\boldsymbol{\mu}) = 0$ which is the case in a manifold of codimension 1. In three dimensional space the generic situation becomes that, for any point in the space (x^1, x^2, x^3), there is a time t^* for which the determinant becomes zero.
In our more general formulation, with three equations and six unknowns, the inversibility of

$$\mathbb{H} = \nabla(\boldsymbol{\mu}) \cdot \nabla(\boldsymbol{\mu})^T + \tau^2 \nabla(\boldsymbol{\lambda}) \cdot \nabla(\boldsymbol{\lambda})^T \tag{84}$$

which corresponds to isolated points in a manifold of codimension 4 in space-time.
In consequence the condition $\det(\nabla\boldsymbol{\mu}) = 0$ will arrive more frequently because of its lower codimension, than the condition with a higher codimension, for $\det(\mathbb{H})$ and $\tau \to 0$ is a *singular limit*.

3.3 Resettings

As we saw, when the determinant $\det(\mathbb{H})$ is zero the Weber-Clebsch potential evolution equations (83) are no longer defined.
In order to avoid this situation, we follow (Ohkitani & Constantin, 2003) and we perform a *resetting*. More precisely, when the spatial minimum of the determinant

$$\text{Min}\left(\det(\mathbb{H})\right) \leq \epsilon^2 \tag{85}$$

where ϵ is a pre defined lower limit. We *reset* the fields in the following way

$$\begin{aligned} \mu_p^i &= 0 \\ \lambda^i &= u^i(t_0) \\ \phi &= 0\,, \end{aligned} \tag{86}$$

where $u^i(t_0)$ are the components of the velocity field obtained from Eq. (58) in the instant t_0, when the resetting is performed, and the fields λ^i, μ^i and ϕ^i are generated in the same way as in section 4.2.
It was already pointed (Cartes et al., 2007; Ohkitani & Constantin, 2003), that the vanishing of $\det(\mathbb{H})$ is related to intense particle diffusion that takes place near reconnection of vorticity lines in the case of incompressible fluids, that means the spatial position of the minima of $\det(\mathbb{H})$ are the places where the reconnections take place.

4. Numerical results

In this section we will show the results from numerical simulations of our formulation for compressible Navier-Stokes equations. We used pseudo-spectral methods because they are easy to implement and their high precision. The technical details of the implementation are described in section 6.

4.1 Taylor-Green flow

The Taylor-Green flow is an standard flow used in the study of turbulence (Taylor & Green, 1937). Its advantages are the existence of numerous studies, see for instance (Brachet et al., 1983) and references therein, which allow us to perform comparisons, at the same time we can economise memory and computation resources by using its symmetries (Cartes et al., 2007).
The initial Taylor-Green condition is:

$$\begin{aligned} u^1 &= \sin x \cos y \cos z \\ u^2 &= -\cos x \sin y \cos z \\ u^3 &= 0\,. \end{aligned} \tag{87}$$

As the length and the initial velocity are of order 1, the Reynolds number is defined as $R = 1/\nu$.

4.2 Periodic field generation

Periodic fields are generated from the Weber-Clebsch representation Eq. (58) as

$$\mu^i = x^i + \mu_p^i \,, \tag{88}$$

we also impose that μ_p^i and the other fields λ^i and ϕ in Eq. (58) are periodic. In order to generate an arbitrary velocity field $\mathbf{u}$ we can use

$$\begin{aligned} \mu_p^i &= 0 \\ \lambda^i &= u^i \\ \phi &= 0 \,. \end{aligned} \tag{89}$$

We note that the non-periodic part of μ^i in Eq. (88) is made in a way that μ^i *gradients* are periodic.
The initial ρ is given by imposing the incompressibility condition over w at $t = 0$

$$w_0 = -\triangle^{-1} \nabla \cdot (\mathbf{u} \cdot \nabla \mathbf{u}) \tag{90}$$

and the relation Eq. (66).

4.3 Simulation results

The following simulations were made using a spatial resolution of 128^3 points, a Reynolds number of 200 and a Mach number of 0.3.
We will compare the velocity field which comes from simulations made with the Weber-Clebsch potentials with the velocity field that comes from a direct numerical simulation of Navier-Stokes equations.
Navier-Stokes equations are integrated using standard pseudo-spectral methods (Gottlieb & Orszag, 1977). The temporal scheme is Adams-Bashforth of order 2 (for details see section 6.3).
In order to characterise and measure the precision of our algorithm for the Weber-Clebsch potentials, we compute the associated *enstrophy* which is defined as

$$\Omega(t) = \sum_k k^2 E(k,t) \tag{91}$$

where $E(k,t)$ is the energy spectrum and can be described from the velocity field in Fourier space $\hat{\mathbf{u}}(\mathbf{k},t)$ as

$$E(k,t) = \frac{1}{2} \sum_{k-\frac{\triangle k}{2} < |\mathbf{k}'| < k+\frac{\triangle k}{2}} \left| \hat{\mathbf{u}}(\mathbf{k}',t) \right|^2 . \tag{92}$$

Then $E(k,t)$ is obtained as the mean value over spherical shells with thickness $\triangle k = 1$. This enstrophy is computed from the velocity field which comes from the Weber-Clebsch and direct Navier-Stokes simulations.
Fig. (1) shows the temporal evolution of the enstrophy for different values of the parameter τ. We found good agreement between our formulation and the direct Navier-Stokes simulations. The spatial mean of the quantity $\rho^2/2$, which represents the density field, can be seen in Fig. (2).

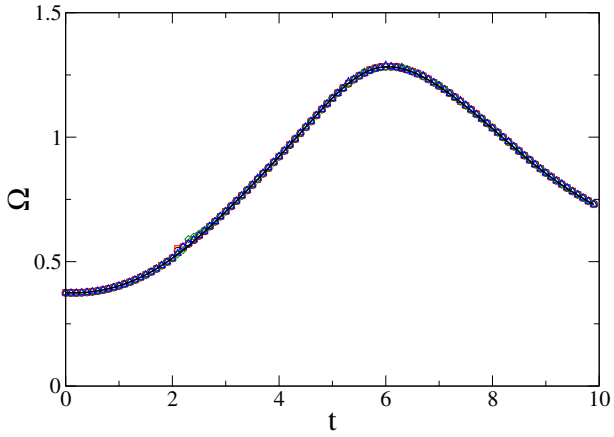

Fig. 1. Temporal evolution of the enstrophy Ω for a Reynolds number of 200 and a Mach number of $Ma = 0.3$ with $\tau = 0$, 0.01, 0.1 and 1 ($\circ$, $\square$, $\Diamond$ and $\triangle$), the continuous line represents the direct compressible Navier-Stokes simulation.

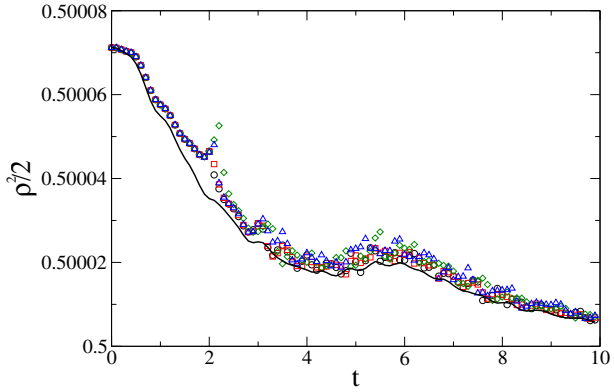

Fig. 2. Temporal evolution of the quantity $\rho^2/2$ for a Reynolds number of 200 and a Mach number of $Ma = 0.3$ with $\tau = 0$, 0.01, 0.1 and 1 ($\circ$, $\square$, $\Diamond$ and $\triangle$), the continuous line represents the direct compressible Navier-Stokes simulation.

As our λ and μ fields evolved in time we had to reset them to be able to continue the simulation as the coordinate transformation becomes non-invertible. The temporal evolution of the interval between resettings is characterised by

$$\triangle t_j = t_j - t_{j-1} \tag{93}$$

where t_j is the resetting time, we fixed the value for the lower limit of $\det(\mathbb{H})$ as $\epsilon^2 = 0.01$, is shown in Fig. (3). We can see that, for a given time, the interval is a growing function of τ. However the shape of $\triangle t$ is well preserved even when the range of τ goes through several orders of magnitude.

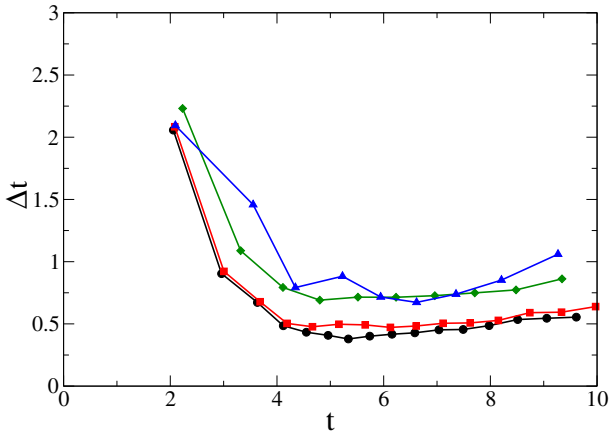

Fig. 3. Temporal evolution of the interval between resettings $\triangle t_j$ versus the resetting time t_j for a Reynolds number of 200 and a Mach number of $Ma = 0.3$ with $\tau = 0$, 0.01, 0.1 and 1 ($\circ$, $\square$, $\Diamond$ and $\triangle$).

5. Conclusions and perspectives

We arrived to a good agreement between the derived generalised equations of motion for the Weber-Clebsch potentials that implying that the velocity field follows the compressible Navier-Stokes equations. These new equations were shown to depend on a parameter with the dimension of time, τ. Direct numerical simulations of the Taylor-Green vortex were performed in order to validate this new formulation.

This Eulerian-Lagrangian formulation of compressible Navier-Stokes equations, allows us to study in detail the reconnection process, the turbulence generated by such process and the sound generated by those moving fluids using for example the two antiparallel vortex approach (Virk et al., 1995). This subject is known as aeroacoustics (Lighthill, 1952), which is relevant for aerodynamic noise production, and is a key issue in the design of air planes, turbines, etc.

6. Appendix – Numerical methods

The simulated equations are nonlinear partial differential equations solved by the pseudo-spectral methods. The flows in this work are periodic because we work in a periodic box.

A periodic field f verifies: $f(x + L) = f(x)$ where L is the box periodicity length. In our simulations we choose $L = 2\pi$. In this representation a continuous function can be expressed by the infinite Fourier series

$$f(x) = \sum_{-\infty}^{\infty} \hat{f}_k e^{ikx} \,. \tag{94}$$

Then we can define the scalar product by

$$\langle g, h \rangle = \frac{1}{2\pi} \int_0^{2\pi} \bar{g}(x) h(x) dx \,, \tag{95}$$

where the Fourier series coefficients are

$$\begin{aligned}\hat{f}_k &= \langle e^{ikx}, f(x)\rangle \\ &= \frac{1}{2\pi}\int_0^{2\pi} e^{-ikx} f(x)dx\,. \end{aligned} \tag{96}$$

In a numerical simulation f is known by its values in a finite number of points over L

$$f_j = f(x_j)\,, \tag{97}$$

with

$$x_j = j\triangle x \; j = 0, 1, \ldots, N-1\,, \tag{98}$$

in a way that the distance between the points is

$$\triangle x = \frac{2\pi}{N}\,. \tag{99}$$

The discretisation points are supposed to capture the shape of $f(x)$. The x variable is defined in *physical space* and the points $j = 0, 1, \ldots, N-1$ are called *collocation points*. Then the Fourier coefficients Eq. (96) become

$$\hat{f}_N(k) = \frac{1}{N}\sum_{k=-\frac{N}{2}}^{\frac{N}{2}-1} f_N(x_n)e^{-ikx_n}\,, \tag{100}$$

with

$$x_n = \frac{2\pi n}{N}\; n = 0, 1, \ldots, N-1\,. \tag{101}$$

This is the discrete Fourier transformation (DFT). We projected f over a base formed by N sine and cosine functions. Then we can find an approximation for f ,f_N, by inverting Eq. (100) in the following way

$$f_N(x_n) = \sum_{k=-\frac{N}{2}}^{\frac{N}{2}-1} \hat{f}_N(k)e^{ikx_n}\,. \tag{102}$$

The points $k = -\frac{N}{2}, \ldots, \frac{N}{2} - 1$ form the discrete *spectral space*. They characterise the functions from our projection base. We must note that the functions Eq. (100) and Eq. (102) are written in a more symmetric way than Eq. (94) and Eq. (96).

A priori, to perform the summations Eq. (100) and Eq. (102) we must perform a number of operations of order $\mathcal{O}\left(N^2\right)$. This requirement was a handicap in the use of this method, until the introduction of Cooley and Turkey algorithm for the fast Fourier transformation (FFT) in 1965 (Cooley & Tukey, 1965). This FFT algorithm allows us to reduce the number of operations to $\mathcal{O}\left(N \log_2 N\right)$.

The use of spectral methods is justified by their convergence which is better than the convergence obtained with finite differences. That comes from the fact that, in a finite differences computation of order p, the approximation coefficients of a field f in a Taylor expansion of $p+1$ points have an error of order $\mathcal{O}\left(\triangle x^p\right)$. On the other hand with spectral

methods we compute the coefficients $\hat{f}_N(k)$, of its approximation of f, using the N points from the chosen resolution, then the order of the pseudo-spectral methods grows with the resolution. If the distance between the collocation points is $\triangle x = \mathcal{O}\left(\frac{1}{N}\right)$ the error has an order of $\mathcal{O}\left(\left(\frac{1}{N}\right)^N\right)$. In consequence the errors decay faster than any finite power of N, that is what we call an exponential convergence. From this point of view, the spectral methods gave us a considerable gain in memory use from a fixed precision.

6.1 Pseudo-spectral methods

The pseudo-spectral methods are based in the computation of the approximation of a determined function interpolating over a collocation point set, that means the differential equation will be exactly solved over the collocation points.

We chose this method in order to compute the convolutions in physical space. As base we use the DFT from trigonometric functions which corresponds to the collocation points. In the case of non-linear terms we use two inverse FFT ($\mathcal{O}(N \log_2 N)$ operations) in order to have these terms in physical space. Then we compute the product (N operations) and we perform one FFT ($\mathcal{O}(N \log_2 N)$ operations) in order to go back into the spectral space. For example, if we compute

$$w(k) = \mathrm{DFT}\left(\lambda(x_n)\, \partial_x \mu(x_n)\right) \tag{103}$$

we have

$$\begin{aligned}
\mathrm{DFT}\left(\lambda(x_n)\, \partial_x \mu(x_n)\right) &= \frac{1}{N} \sum_{n=-\frac{N}{2}}^{\frac{N}{2}-1} \lambda(x_n)\, \partial_x \mu(x_n)\, e^{-ikx_n} \qquad (104)\\
&= \frac{1}{N} \sum_{n=-\frac{N}{2}}^{\frac{N}{2}-1} e^{-ikx_n} \sum_{p=-\frac{N}{2}}^{\frac{N}{2}-1} \hat{\lambda}(p)\, e^{ipx_n} \sum_{q=-\frac{N}{2}}^{\frac{N}{2}-1} \widehat{\partial_x \mu}(q)\, e^{iqx_n}\\
&= \frac{1}{N} \sum_{n=-\frac{N}{2}}^{\frac{N}{2}-1} \sum_{p=-\frac{N}{2}}^{\frac{N}{2}-1} \sum_{q=-\frac{N}{2}}^{\frac{N}{2}-1} e^{ix_n(p+q-k)} \hat{\lambda}(p)\, \widehat{\partial_x \mu}(q)\ .
\end{aligned}$$

The summation over n includes all the terms where $p + q - k \equiv O[N]$. Then the approximated coefficients for the term $w(k)$ are composed by all the exact coefficients plus other terms for which the correspondent function $e^{ikx_n}[N]$ can not be distinguished from the function e^{ikx_n}, this phenomena is called *aliasing*, the Fourier modes with higher wave numbers are taken for modes with lower wave numbers.

Even with these defects the pseudo-spectral methods have interesting properties, for example when we have to deal with multiple dimensions. In fact the DFT in 3D can be factorised as $e^{i\vec{k}\cdot\vec{x}} = e^{ik_x x} e^{ik_y y} e^{ik_z z}$. Moreover a DFT in 3D can be computed as a succession of DFT in 1D, so for N^3 point we have to perform $3N^2$ DFT in 1D over N points and then $3N^3 \log_2 N$ operations, on the other hand if we compute the products as convolutions in spectral space we need to perform N^6 operations.

This passage by physical space and the use of pseudo-spectral methods allow us to gain in computation time but generates the problem of *aliasing*.

6.2 *Aliasing correction*

The only way to correct the *aliasing* error over the convoluted term is eliminating the aliased terms which, in spectral space, belong to $|k| \leq N/2$.
Over a grid of N points, working modulo N, the values of k will belong to the interval $\left[-\frac{N}{2}, \frac{N}{2}\right]$. The method which allows us to solve the problem implies the elimination of the part of the spectrum which lays outside the interval $]-k_{max}, k_{max}[$, with the condition (for nonlinearities of order 2) $2k_{max} - N < -k_{max}$, this means $k_{max} < \frac{N}{3}$. We remove then all the values from the spectrum whose wave numbers are bigger than $\frac{N}{3}$ and smaller than $-\frac{N}{3}$. In this way all the replicated values are fixed to zero in each time step and they are no longer a problem.
The *aliasing* correction is very expensive, because we lose one third of, otherwise, useful modes, but these computations are completely equivalent to the Galerkin truncation.

6.2.1 Integration by parts and conservation of energy

Let us suppose for a moment that our product computation is not *dealiased*. We consider the product of the quantity f by $\partial_x g$ and perform an integration by parts in spectral space. We perform the summation in the interval $]-N/2, N/2[$

$$\mathrm{DFT}\left(f\partial_x g\right)(n) = \sum_{j+k=n[N]} ik\hat{f}_N(j)\hat{g}_N(k) = \sum_{j+k=n[N]} i(n-j)_{[N]}\hat{f}_N(j)\hat{g}_N(k)\,. \tag{105}$$

The term which forbids us to integrate by parts in an exact way is $(n-j)_{[N]}$. If we do a *dealiasing* over the term the summation is now over the interval $]-k_{max}, k_{max}[$ and

$$\begin{aligned}\mathrm{DFT}\left(f\partial_x g\right)(n) = \sum_{j+k=n} ik\hat{f}_N(j)\hat{g}_N(k) &= \sum_{j+k=n} i(n-j)\hat{f}_N(j)\hat{g}_N(k) \\ &= in\sum_{j+k=n}\hat{f}_N(j)\hat{g}_N(k) - \sum_{j+k=n} ij\hat{f}_N(j)\hat{g}_N(k) \\ &= \mathrm{DFT}\left(\partial_x(fg)\right)(n) - DFT\left(g\partial_x f\right)(n)\,.\end{aligned} \tag{106}$$

Let us remember that the integration by parts is a necessary step in the computation of the amount of energy present in our system, and it must be preserved if there is not diffusion. This physical requirement is satisfied by the *dealiased* spectral methods.

6.3 Temporal scheme

We made a pseudo-spectral solver for the equations, with periodic boundary conditions and a FFT base which allows us to integrate the partial differential equations

$$\partial_t a = L(a) + N(a)\,, \tag{107}$$

where we call L the linear operator in Fourier space and N the nonlinear term.
The resolution method is a second order finite difference. The time step is made by the explicit Adam-Bashforth method

$$a_{t+\triangle t} = \frac{\left(1 - \nu\frac{k^2}{2}\triangle t\right)a_t + \triangle t\left(\frac{3}{2}N(a_t) - \frac{1}{2}N(a_{t-\triangle t})\right)}{1 + \nu\frac{k^2}{2}\triangle t}\,. \tag{108}$$

To begin with the temporal integration we did an Euler time step in the following way

$$a_{\triangle t} = \frac{a_0 + \triangle t N(a_0)}{1 + \nu k^2 \triangle t}, \tag{109}$$

where a_0 is the initial condition.

7. Acknowledgments

The authors wish to thank Marc–Etienne Brachet and Jaime Cisternas for valuable comments. We acknowledge the financial support of FONDECYT (Projects No. 3110028 and No. 1110360) and Universidad de los Andes through FAI initiatives.

8. References

Ben-Israel, A. & Greville, T. N. E. (1974). *Generalized Inverses: Theory and Applications*, Wiley-Interscience [John Wiley & Sons], New York. (reprinted by Robert E. Krieger Publishing Co. Inc., Huntington, NY, 1980.).

Brachet, M. E., Meiron, D. I., Orszag, S. A., Nickel, B. G., Morf, R. H. & Frisch, U. (1983). Small–scale structure of the Taylor–Green vortex, *J. Fluid Mech.* 130: 411–452.

Cartes, C., Bustamante, M.-D. & Brachet, M.-E. (2007). Generalized Eulerian-Lagrangian description of Navier-Stokes dynamics.

Cartes, C., Bustamante, M.-D., Pouquet, A. & Brachet, M.-E. (2009). Capturing reconnection phenomena using generalized Eulerian–Lagrangian description in Navier–Stokes and resistive MHD, *Fluid Dynamics Research* 41.

Constantin, P. (2001). An Eulerian–Lagrangian approach to the Navier–Stokes equations, *Commun. Math. Phys.* 216: 663–686.

Cooley, J. W. & Tukey, J. W. (1965). An algorithm for the machine calculation of complex Fourier series, *Math. Comput.* 19: 297–301.

Gottlieb, D. & Orszag, S. A. (1977). *Numerical Analysis of Spectral Methods*, SIAM, Philadelphia.

Grossmann, S. (1975). An order-parameter field theory for turbulent fluctuations, *Physical Review A* 11(6): 2165–2172.

Lamb, H. (1932). *Hydrodynamics*, Cambridge University Press, Cambridge.

Lighthill, M. J. (1952). On sound generated aerodynamically. i. general theory, *Proceedings of The Royal Society A: Mathematical, Physical and Engineering Sciences* 211: 564–587.

Moore, E. H. (1920). On the reciprocal of the general algebraic matrix, *Bulletin of the American Mathematical Society* 26: 394–395.

Ohkitani, K. & Constantin, P. (2003). Numerical study of the Eulerian–Lagrangian formulation of the Navier–Stokes equations, *Physics of Fluids* 15(10): 3251–3254.

Penrose, R. (1955). A generalized inverse for matrices, *Proceedings of the Cambridge Philosophical Society* 51: 406–413.

Taylor, G. I. & Green, A. E. (1937). Mechanism of the production of small eddies from large ones, *Proc. Roy. Soc. Lond. A* 158: 499–521.

Virk, D., Hussain, F. & Kerr, R. M. (1995). Compressible vortex reconnection, *Journal of Fluid Mechanics* 304.

7

Lattice Boltzmann Modeling for Melting/Solidification Processes

Dipankar Chatterjee
CSIR-Central Mechanical Engineering Research Institute
India

1. Introduction

The phenomena of melting and solidification are associated with many practical applications, such as metal processing, castings, environmental engineering, thermal energy storage system in space station and many more. In these processes, matter is subject to a change of phase and consequently, a boundary separating two different phases evolves and moves within the matter. Mathematical modeling of such 'moving boundary problems' are always a challenging task because of the dynamic evolution of the phase separating boundary, complex boundary conditions as well as varying thermophysical properties. Many macroscopic mathematical modeling strategies for the solidification/melting problems can be found in the contemporary literatures. An excellent review in this regard can be found in Hu & Argyropoulos (1996). Early efforts in melting/solidification modeling initiated with a moving/deforming grid approach (Rubinsky & Cravahlo, 1981; Voller & Cross, 1981; Voller & Cross, 1983; Weaver & Viskanta, 1986; Askar, 1987), in which independent conservation equations for each phase need to be initially formulated, and are to be subsequently coupled with appropriate boundary conditions at the inter-phase interfaces. However, such multiple region solutions require the existence of discrete interfaces between the respective phases. In fact, a major difficulty with regard to their implementation is associated with tracking of the phase interfaces (which are generally unknown functions of space and time). The need for moving numerical grids and/or coordinate mapping procedures complicates the application of this technique further, and generally, simplifying assumptions regarding the geometric regularity of the interfaces are made. Additionally, a serious limitation exists for modeling phase change behavior of multi-component systems, since, unlike pure substances; such systems do not exhibit a sharp interface between solid and liquid phases, in a macroscopic sense. The phase-change behavior of such systems depends on many factors including the phase-change environment, composition, and thermodynamic descriptions of specific phase transformations. Moreover, solidification occurs over extended temperature ranges and solid formation often occurs as a permeable crystalline-like matrix which coexists with the liquid phase. In such cases, it would be virtually impossible to track a morphologically complex zone in a macroscopic framework, using any moving grid technique. In contrast, in fixed-grid mathematical models of phase change (Comini et al., 1974; Morgan et al., 1978; Roose & Storrer, 1984; Dalhuijsen & Segal, 1986; Pham, 1986; Dhatt et al., 1989; Comini et al., 1990; Voller et al., 1990), transport equations for individual phases are volume-averaged to

come up with equivalent single-phase conservation equations that are valid over the entire domain, irrespective of the constituent phases locally present. A separate equation for evolution of liquid fraction is solved in conjunction with the above set of conservation equations, which implicitly specifies and updates the interfacial locations with respect to space and time.

It can be noted at this point that although simulation strategies mentioned as above have become somewhat standardized over the past few decades, solution of phase-change problems over multiple length scales still poses serious challenges, primarily because of the disparate and coupled length scales characterizing the entire sequence of transport processes. To overcome such difficulties, phase-field models of dendritic solidification have been developed and proposed by several researchers (Mikheev & Chernov, 1991; Kim et al., 1999; Harrowell & Oxtoby, 1987; Khachaturyan, 1996; Beckermann et al., 1999; Tong et al., 2001). Advantage of the phase field models lies in the fact that computational difficulties associated with front tracking are eliminated by introducing an auxiliary order parameter (the so-called phase field) that couples with the evolution of the thermal field. Dynamics of the phase field are designed to follow the evolving solidification front, thereby eliminating the necessity of any explicit front tracking.

Recently, the multiscale mesoscopic lattice Boltzmann (LB) (Kendon et al., 2001; Sankaranarayanan et al., 2002; Barrios et al., 2005) method has emerged to offer huge potentials for solving complex thermofluidic problems involving morphological development of complicated phase boundaries such as the problem of phase separation of two immiscible fluids (Chen & Doolen, 1998). Such a method, typically, considers volume elements of fluid comprising of a collection of particles that are represented by characteristic particle velocity distribution functions defined at discrete grid points. The rules governing the collisions and subsequent relaxations are designed such that the time-averaged motion of fluid particles becomes consistent with that predicted by the Navier-Stokes equation. Further advancements in LB modeling of fluid flow enabled the research community to explore more complicated problems addressing flow through porous medium and a few generic cases of multi-phase flow (Gunstensen et al., 1991; Shan & Chen, 1993; Ferreol & Rothman, 1995). In this context, it can be mentioned here that a distinct advantage of the LB method for modeling solid-liquid phase transitions, in comparison to a classical continuum based formulation, lies in the fact that the LB method is fundamentally based on microscopic particle models and mesoscopic kinetic equations, which means that micro and meso-scale physics of phase transitions can elegantly be incorporated. Another important advantage is that it does not require an immediate explicit calculation of fluid pressure, leading to time-efficient computational simulations. Further, LB models are inherently parallelizable, which renders their suitability to address phase change processes over large-scale computational domains.

The LB approaches proposed so far for modeling solid-liquid phase transition problems can broadly be categorized into two major groups, *viz*. (a) phase field based methods following the Ginzburg-Landau theory and (b) enthalpy based methods. De Fabritiis et al. (1998) developed a thermal LB model for such problems by employing two types of quasiparticles for solid and liquid phases, respectively. Miller et al. (2001) proposed a simple reaction LB model with enhanced collisions, using a single type of quasiparticle and a phase field approach. Further work proceeded along similar lines (Miller & Schroder, 2001; Miller, 2001; Miller & Succi, 2002; Miller et al., 2004; Rasin et al., 2005; Medvedev & Kassner, 2005), with

the phase-field model acting as a pivotal basis for determining the evolution of respective phase fractions. It needs to be emphasized that one of the major problems in implementing the phase field based methods in the context of solid-liquid phase transition problems is the requirement of limitlingly finer grid spacing for resolving the interfacial region to reproduce the dynamics of the sharp interface equations. Consequently, adaptive mesh refinement strategies involving computationally involved data structures are required for problems subjected to small undercooling. On the other hand, enthalpy-based models have been extensively used to solve complex solidification problems over macroscopic and mesoscopic length scales. An extended LB methodology, in conjunction with an enthalpy formulation for treatment of solid–liquid phase change aspects in case of diffusion dominated problems, was first introduced by Jiaung et al. (2001). Subsequently, taking the computational advantage of the enthalpy-based technique, Chatterjee & Chakraborty (2005, 2006, 2008), Chakraborty & Chatterjee (2007) and Chatterjee (2009, 2010) proposed a series of LB models primarily applicable to a wide range of melting-solidification problems. It was started with an enthalpy based LB model for diffusion dominated phase transition problems, followed by a hybrid LB method for generalized convection-diffusion transport processes pertinent to melting/solidification problems. In the diffusion models, the temperature field was obtained from an evolution equation of a single particle density distribution function (DF), whereas in the convection-diffusion models the thermal field is described by a novel enthalpy density DF through a kinetic equation based on the total enthalpy of the phase changing system or alternatively from an evolution equation of temperature. The analysis of solidification in a semitransparent material using the enthalpy based LB method was performed by Raj et al. (2006). The radiative component of the energy equation in the LB formulation was computed using the discrete transfer method in their model. Recently, Huber et al. (2008) developed a multiple DF LB model for coupled thermal convection and pure-substance melting, where the two DFs were interrelated through the buoyancy term and the equilibrium DF of the temperature kinetic equation.

In this chapter, we describe a straightforward technique for simulating solid-liquid phase transition, by coupling a passive scalar based thermal LB model with a fixed-grid enthalpy-porosity approach (Brent et al., 1988) that is consistent with the microscopic solvability theory. The macroscopic density and velocity fields are simulated using a single particle density DF through a kinetic equation, while the macroscopic temperature field is obtained from a separate temperature DF through another kinetic equation (Chatterjee, 2010). The phase change aspect is numerically handled by the enthalpy-porosity technique with an adapted enthalpy-updating scheme. The source terms originating out of the physical situation are incorporated into the respective kinetic equations by the most formal technique following the extended Boltzmann equation. Test cases for one and two-dimensional solidification problems are presented and compared with the analytical and available numerical solutions. Finally, simulation results for a popular solid-liquid phase change problem, such as the Bridgman crystal growth in a square crucible are also shown to establish the capability of the model.

2. Model formulation

In this section we first present the generalized convection-diffusion macroscopic conservation equations governing the transport processes occurring during phase change, followed by the corresponding lattice Boltzmann formulation.

2.1 Macroscopic conservation equations

The equivalent single phase volume-averaged macro-scale continuity, momentum and energy conservation equations for a nonparticipating phase changing system, assuming a laminar, incompressible and Newtonian flow, can be presented as:

$$\nabla \cdot \mathbf{u} = 0 \tag{1}$$

$$\rho\left[\partial_t \mathbf{u} + \mathbf{u}.\nabla\mathbf{u}\right] = -\nabla p + \nabla \cdot \boldsymbol{\sigma} + \rho \mathbf{F} \tag{2}$$

$$\rho c_p\left[\partial_t T + \mathbf{u}.\nabla T\right] = \nabla \cdot \left(\kappa \nabla T\right) + \boldsymbol{\sigma} : \nabla\mathbf{u} + \dot{q} \tag{3}$$

where $\mathbf{u}$, p and T denote the macroscopic velocity, pressure and temperature, $\boldsymbol{\sigma} = \rho\nu\left[\left(\nabla\mathbf{u} + \nabla\mathbf{u}^T\right) - 2/3(\nabla.\mathbf{u})\mathbf{I}\right]$ is the viscous stress tensor, ρ, ν, c_p and κ are the density, kinematic viscosity, specific heat and thermal conductivity, $\mathbf{F} = \mathbf{G} + \mathbf{S}$ is the body force per unit mass which incorporates a combined contribution form the buoyancy force $\mathbf{G} = \mathbf{g}_a \beta\left(T - T_{ref}\right)$, assuming the Boussinesq approximation to be valid, where $\mathbf{g}_a$ is the acceleration due to gravity, β is the volumetric thermal expansion coefficient and T_{ref} is the reference temperature and a porous medium frictional resistance force $\mathbf{S} = -\left(\nu/\mathbf{K}\right)\cdot\mathbf{u}$, where $\mathbf{K}$ represents the permeability tensor. Components of the tensor $\mathbf{K}$ depend on the specific morphology of the phase changing domain, for which any appropriate formulation for flow through a porous medium can be effectively invoked. A common approach followed in the literature is to adopt the celebrated Darcy model (or some of its variants) for flow through a porous medium, in association with the Cozeny-Karman equation (Voller & Prakash, 1987) as $\mu/\mathbf{K} = M\left(1 - f_l\right)^2 \Big/ \left(f_l^3 + \varepsilon\right)$, where μ is the dynamic viscosity, $M\left(\sim O\left(10^8\right)\right)$ is a morphological constant and $\varepsilon\left(\sim O\left(10^{-3}\right)\right)$ is a computational constant introduced to avoid division by zero. Further, f_l is the liquid fraction, given as $f_l = \Delta h / L$, where L is the latent heat of phase change and Δh is the latent enthalpy content of a computational cell undergoing phase change and can be given by,

$$\begin{aligned} \Delta h = f(T) &= L \quad &: T > T_l \\ &= f_l L \quad &: T_s \le T \le T_l \\ &= 0 \quad &: T < T_s \end{aligned} \tag{4}$$

where T_s and T_l are the solidus and liquidus temperatures respectively.

The above formulation effectively ensures that in the phase changing cells, the porous medium resistance term dominates over the transient, convective and diffusive effects manifested by molecular interaction mechanisms, thereby forcing the velocity field to imitate the Cozeny-Karman law. On the other hand, in totally solid elements $\left(f_l = 0\right)$, the high porous medium resistance forces any velocity predictions effectively to zero. In a fully liquid element $\left(f_l = 1\right)$, however, this term has no consequence, and the usual form of the Navier Stokes equation can be retrieved.

The latent-heat evolution is accounted for by introducing a source term in the macroscopic energy conservation equation (final term on the right-hand side of Eq. (3)) as, $\dot{q} = -\left[\partial_t\left(\rho\Delta h\right) + \nabla.\left(\rho\mathbf{u}\Delta h\right)\right]$. For pure material phase change the term $\nabla.\left(\rho\mathbf{u}\Delta h\right)$ vanishes and the energy source term becomes $\dot{q} = -\partial_t\left(\rho\Delta h\right)$.

2.2 The lattice Boltzmann model

A statistical description of a fluid system can be made in terms of a particle density DF, which satisfies the continuous Boltzmann equation with a single-relaxation-time BGK (Bhatnagar-Gross-Krook) model (Bhatnagar et al., 1954) as:

$$\partial_t f + \boldsymbol{\xi} \cdot \nabla f = -\left(f - f^{eq}\right)\big/\lambda_f + F \tag{5}$$

where $f(\mathbf{x},\boldsymbol{\xi},t)$ is a single particle density DF from which the macroscopic properties of the fluid can be obtained, $\boldsymbol{\xi}$ is the microscopic velocity, λ_f is the relaxation time, F and $f^{eq}(\mathbf{x},\boldsymbol{\xi},t)$ are the external forcing parameter and the Maxwell-Boltzmann type equilibrium DF, given by,

$$F = \frac{\mathbf{F}.(\boldsymbol{\xi}-\mathbf{u})}{RT} f^{eq}\ ,\ f^{eq} = \frac{\rho}{(2\pi RT)^{D/2}} \exp\left[-\frac{(\boldsymbol{\xi}-\mathbf{u})^2}{2RT}\right] \tag{6}$$

where R is the gas constant and D is the dimensionality. The macroscopic variables are obtained by taking (microscopic velocity) moments of the density DF f as: $\rho = \int f\, d\boldsymbol{\xi}$, $\rho\mathbf{u} = \int f\boldsymbol{\xi}\, d\boldsymbol{\xi} + \rho\mathbf{F}$. However, it is a well known fact that the temperature field obtained from the second moment of the DF f yields a fixed Prandtl number, implying that the thermal diffusivity cannot be adjusted independent of the kinematic viscosity (He et al., 1998), which restricts its applicability to a limited class of problems only.

To this end, we define a new temperature DF $g(\mathbf{x},\boldsymbol{\xi},t)$ following the passive scalar approach of He et al. (1998), which obeys a kinetic equation of the form:

$$\partial_t g + \boldsymbol{\xi} \cdot \nabla g = -\left(g - g^{eq}\right)\big/\lambda_g + \Re + Q \tag{7}$$

where λ_g is the relaxation time, $g^{eq}(\mathbf{x},\boldsymbol{\xi},t)$ is the is the Maxwell-Boltzmann type equilibrium DF, given by,

$$g^{eq} = \frac{\rho c_p T}{(2\pi RT)^{D/2}} \exp\left[-\frac{(\boldsymbol{\xi}-\mathbf{u})^2}{2RT}\right] = c_p T f^{eq} \tag{8}$$

Here $\Re = \Re^I + \Re^{II} + \Re^{III}$ accounts for the viscous heating ($\Re^I$), compression work ($\Re^{II}$) and kinetic energy ($\Re^{III}$) contributions given as (Shi et al., 2004):

$$\Re^I = -\left(f - f^{eq}\right)\left[(\boldsymbol{\xi}-\mathbf{u})(\boldsymbol{\xi}-\mathbf{u}) : \nabla\mathbf{u}\right]\big/R \tag{9a}$$

$$\Re^{II} = -f^{eq}\left[(\boldsymbol{\xi}-\mathbf{u})(\boldsymbol{\xi}-\mathbf{u}) : \nabla\mathbf{u}\right]\big/R \tag{9b}$$

$$\Re^{III} = -f(\boldsymbol{\xi}-\mathbf{u}).\left[\partial_t\mathbf{u} + (\mathbf{u}.\nabla)\mathbf{u}\right]\big/R \tag{9c}$$

It should be mentioned that in the incompressible limit (which is the limit of small Mach number, $Ma \to 0$), $\Re^{II}$ and $\Re^{III}$ become negligible and hence $\Re = \Re^I$. In Eq. (7), Q is the

energy source term that features out of the physical situation within the participating fluid media. The macroscopic temperature can be obtained from the temperature DF g as: $\rho c_p T = \int g d\boldsymbol{\xi} + \int (\Re + Q) d\boldsymbol{\xi}$. Since two separate kinetic equations with corresponding DFs are used to describe the flow and thermal fields respectively, the kinematic viscosity and thermal diffusivity can be independently adjusted, which makes the model suitable for varying Prandtl number flows.

Eqs. (5) and (7) can now be represented by the following generic discrete-velocity form:

$$\partial_t \psi_i + \boldsymbol{\xi}_i \cdot \nabla \psi_i = -\left(\psi_i - \psi_i^{eq}\right) \Big/ \lambda + \Phi_i \tag{10}$$

where $\psi = f$ or g, $\lambda = \lambda_f$ or λ_g, $\Phi = F$ or $\Re + Q$ for the respective kinetic equations and $i \in \{1, b\}$ stands for the b base vectors of the underlying lattice type. Eq. (10) is subsequently integrated along its characteristic using the second order trapezoidal rule (He et al., 1998) to yield the discrete evolution equation:

$$\begin{aligned} &\psi_i(\mathbf{x} + \boldsymbol{\xi}_i \delta t, \boldsymbol{\xi}_i, t + \delta t) - \psi_i(\mathbf{x}, \boldsymbol{\xi}_i, t) = -\frac{\delta t}{2\lambda}\left[\psi_i(\mathbf{x} + \boldsymbol{\xi}_i \delta t, \boldsymbol{\xi}_i, t + \delta t) - \psi_i^{eq}(\mathbf{x} + \boldsymbol{\xi}_i \delta t, \boldsymbol{\xi}_i, t + \delta t)\right] \\ &-\frac{\delta t}{2\lambda}\left[\psi_i(\mathbf{x}, \boldsymbol{\xi}_i, t) - \psi_i^{eq}(\mathbf{x}, \boldsymbol{\xi}_i, t)\right] + \frac{\delta t}{2}\Phi_i(\mathbf{x} + \boldsymbol{\xi}_i \delta t, \boldsymbol{\xi}_i, t + \delta t) + \frac{\delta t}{2}\Phi_i(\mathbf{x}, \boldsymbol{\xi}_i, t) \end{aligned} \tag{11}$$

where δt denotes the time step. The forcing parameter and the discrete equilibrium DFs can be constructed as:

$$F_i = w_i \rho \left[\frac{\boldsymbol{\xi}_i - \mathbf{u}}{c_s^2} + \frac{(\boldsymbol{\xi}_i \cdot \mathbf{u})}{c_s^4}\boldsymbol{\xi}_i\right] \cdot \mathbf{F} \tag{12}$$

$$f_i^{eq} = w_i \rho \left[1 + \frac{(\boldsymbol{\xi}_i \cdot \mathbf{u})}{c_s^2} + \frac{\mathbf{uu} : (\boldsymbol{\xi}_i \boldsymbol{\xi}_i - c_s^2 \mathbf{I})}{2c_s^4}\right], \; g_i^{eq} = c_p T f_i^{eq} \tag{13}$$

Finally, the energy sources can be formulated as:

$$\Re_i = \Re_i^I = -T\left(f_i - f_i^{eq}\right)\frac{(\boldsymbol{\xi}_i - \mathbf{u})(\boldsymbol{\xi}_i - \mathbf{u}) : \nabla \mathbf{u}}{c_s^2}, \; Q_i = w_i \dot{q}\left[1 + \frac{(\boldsymbol{\xi}_i \cdot \mathbf{u})}{c_s^2}\right] \tag{14}$$

The weights w_i and the discrete velocities $\boldsymbol{\xi}_i$ correspond to the D2Q9 configuration (He et al., 1998) (refer to Fig. 1) as:

$$w_i = \begin{cases} 4/9 & i = 0 \\ 1/9 & i = 1,2,3,4 \\ 1/36 & i = 5,6,7,8 \end{cases} \tag{15}$$

$$\boldsymbol{\xi}_i = \begin{cases} \mathbf{0} & i = 0 \\ \left(\cos\left[(i-1)\pi/2\right], \sin\left[(i-1)\pi/2\right]\right)c & i = 1,2,3,4 \\ \sqrt{2}\left(\cos\left[(i-5)\pi/2 + \pi/4\right], \sin\left[(i-5)\pi/2 + \pi/4\right]\right)c & i = 5,6,7,8 \end{cases} \tag{16}$$

where $c\left(=\sqrt{3RT}\right)$ is the characteristic speed, and the sound speed of the model is chosen as $c_s=\sqrt{RT}=1/\sqrt{3}$.

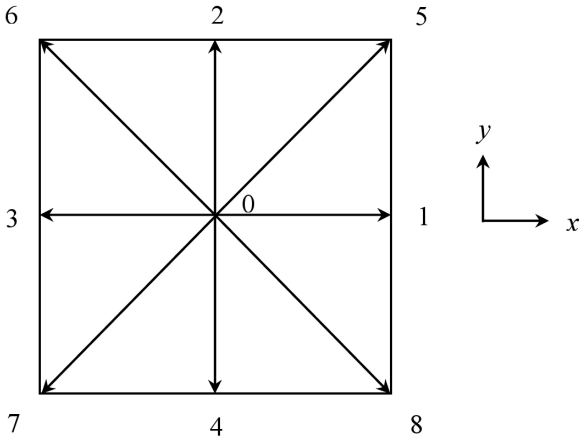

Fig. 1. Discretized 2D velocity space (D2Q9)

By using the Chapman-Enskog multiscale expansion, Eq. (11) correctly recovers the macroscopic conservation equations in the incompressible limit by setting the kinematic viscosity as $\nu=c_s^2\left(\lambda_f^*-0.5\right)\delta t$, where $\lambda_f^*=0.5+\left(\lambda_f-0.5\right)/\rho(\mathbf{x},t,T)$ is the modified relaxation time for the non-isothermal flows (Chatterjee & Chakraborty, 2006) with $\rho(\mathbf{x},t,T)=\sum_i f_i(\mathbf{x},t,T)$ being the local particle density and the thermal diffusivity as $\alpha=\kappa/\rho c_p=c_s^2\left(\lambda_g-0.5\right)\delta t$. Accordingly, the approach offers the possibility of varying the Prandtl number by adjusting the relaxation times of the respective kinetic equations as: $\mathrm{Pr}=\nu/\alpha=\left(\lambda_f^*-0.5\right)/\left(\lambda_g-0.5\right)$.

In order to avoid implicitness of Eq. (11), we further introduce (He et al., 1998) $\overline{\psi}_i=\psi_i+\frac{\delta t}{2\lambda}\left[\psi_i-\psi_i^{eq}\right]-\frac{\delta t}{2}\Phi_i$. Consequently, the discretized evolution equations for $\overline{\psi}_i$ become

$$\overline{\psi}_i\left(\mathbf{x}+\boldsymbol{\xi}_i\delta t,\boldsymbol{\xi}_i,t+\delta t\right)=\overline{\psi}_i\left(\mathbf{x},\boldsymbol{\xi}_i,t\right)-\frac{\delta t}{\left(\lambda+0.5\delta t\right)}\left[\overline{\psi}_i\left(\mathbf{x},\boldsymbol{\xi}_i,t\right)-\psi_i^{eq}\left(\mathbf{x},\boldsymbol{\xi}_i,t\right)\right]+ \\ +\frac{\lambda\delta t}{\left(\lambda+0.5\,\delta t\right)}\Phi_i\left(\mathbf{x},\boldsymbol{\xi}_i,t\right) \tag{17}$$

The macroscopic flow and thermal quantities are obtained from $\overline{f}_i$ and $\overline{g}_i$ as: $\rho=\sum_i\overline{f}_i$, $\rho\mathbf{u}=\sum_i\boldsymbol{\xi}_i\overline{f}_i+\left(\delta t/2\right)\rho\mathbf{F}$, $\rho c_pT=\sum_i\overline{g}_i+\left(\delta t/2\right)\sum_i\left(\Re_i+Q_i\right)$.

3. Numerical implementation

3.1 Enthalpy update

For accurate prediction of the liquid fraction, the latent enthalpy content of each computational cell needs to be updated according to the predicted macroscopic value of temperature each iteration within a time step. For that purpose, an enthalpy updating scheme in accordance with the formulation of Brent et al. (1988) is used, which is of the form, $\left[\Delta h\right]_{n+1} = \left[\Delta h\right]_n + \eta\left\{\left[h_s\right]_n - F^{-1}\left[\Delta h\right]_n\right\}$, where n is the iteration level characterizing the updation stage, h_s is the sensible enthalpy of the concerned cell, Δh is the latent heat contained by the cell, and η is a suitable relaxation factor to smoothen convergence. In the above formulation, $F^{-1}\left[\Delta h\right]$ is an appropriate mathematical function, which needs to be constituted in consistency with microscopic phase change considerations. A detailed guideline in this regard can be found in Chakraborty & Dutta (2001). For the case of pure material phase change an appropriate choice of the function can be $F^{-1}\left[\Delta h\right] = c_p T_m$, where T_m is the equilibrium freezing temperature in presence of a flat interface. With the updated Δh, nodal values of sensible heat, and hence the temperature can be obtained as:

$$\left[h_s\right]_{n+1} = \left[h\right]_{n+1} - \left[\Delta h\right]_{n+1} = c_p\left[T\right]_{n+1} \tag{18}$$

3.2 Boundary conditions

A no-slip hydrodynamic boundary condition and both Neumann and Dirichlet type thermal boundary conditions at the walls can be used. The non-equilibrium extrapolation method (Guo et al., 2002), which has a good numerical accuracy and stability, can be adopted to implement the above mentioned boundary conditions in the LB framework. According to this method, the non-equilibrium part of the DF at a boundary node can be well approximated by the same at the nearest neighboring node in the fluid region along the discrete velocity. As an example, if $\mathbf{x}_b$ represents a boundary node and $\mathbf{x}_f$ its nearest neighboring fluid node, then $f_i^{neq}\left(\mathbf{x}_b\right) = f_i^{neq}\left(\mathbf{x}_f\right)$ and $g_i^{neq}\left(\mathbf{x}_b\right) = g_i^{neq}\left(\mathbf{x}_f\right)$, and the total DF at $\mathbf{x}_b$ can be given as:

$$f_i\left(\mathbf{x}_b\right) = f_i^{eq}\left[\rho^*\left(\mathbf{x}_b\right), \mathbf{u}^*\left(\mathbf{x}_b\right)\right] + \left[f_i\left(\mathbf{x}_f\right) - f_i^{eq}\left(\mathbf{x}_f\right)\right] \tag{19}$$

$$g_i\left(\mathbf{x}_b\right) = g_i^{eq}\left[\rho^*\left(\mathbf{x}_b\right), \mathbf{u}^*\left(\mathbf{x}_b\right), T^*\left(\mathbf{x}_b\right)\right] + \left[g_i\left(\mathbf{x}_f\right) - g_i^{eq}\left(\mathbf{x}_f\right)\right] \tag{20}$$

where the equilibrium part of the DF is determined by imposing the macroscopic boundary conditions through the auxiliary density ρ^*, velocity $\mathbf{u}^*$ or temperature T^*. For example, if velocity $\mathbf{u}\left(\mathbf{x}_b\right)$ and temperature $T\left(\mathbf{x}_b\right)$ are known but $\rho\left(\mathbf{x}_b\right)$ is unknown, we may use $\rho^*\left(\mathbf{x}_b\right) = \rho\left(\mathbf{x}_f\right)$ or $\rho^*\left(\mathbf{x}_b\right) = 2\rho\left(\mathbf{x}_f\right) - \rho\left(\mathbf{x}_{ff}\right)$ with $\mathbf{x}_{ff}$ as the next neighboring fluid node of $\mathbf{x}_b$ in the same direction, and $\mathbf{u}^*\left(\mathbf{x}_b\right) = \mathbf{u}\left(\mathbf{x}_b\right)$, $T^*\left(\mathbf{x}_b\right) = T\left(\mathbf{x}_b\right)$. $\mathbf{u}^*$ and T^* are specified according to the given boundary conditions for $\mathbf{u}$ and T.

A Neumann boundary condition can be implemented by transferring it to the Dirichlet type boundary condition by using a conventional second order finite difference approximation to obtain the boundary temperatures (Shu et al., 2002), in an iterated manner. Regarding interface conditions, it is apparent that the solid/liquid interface in phase change problems

acts as a wall, and the same needs to be treated appropriately. However, according to the enthalpy-porosity formulation, one does not need to track the interface separately and impose hydrodynamic or thermal boundary conditions on the same, since the interface comes out as a natural outcome of the solution procedure itself.

3.3 Numerical scheme

The simulation starts with the prescribed initial values of the temperature $T(\mathbf{x},0)$, velocity $\mathbf{u}(\mathbf{x},0)$ and liquid-fraction $f_l(\mathbf{x},0)$. The sensible enthalpy $h_s(\mathbf{x},0)$ and latent enthalpy $\Delta h(\mathbf{x},0)$ values are obtained from the prescribed initial conditions. Thereafter, the initial DFs $\overline{f}_i(\mathbf{x},0)$ and $\overline{g}_i(\mathbf{x},0)$ are computed using one term in their respective Knudsen expansions, i.e., $\overline{f}_i(\mathbf{x},0)=f_i^{eq}(\mathbf{x},0)$ and $\overline{g}_i(\mathbf{x},0)=g_i^{eq}(\mathbf{x},0)$. Distribution functions are then evolved according to Eq. (17). The overall solution algorithm is as follows:

i. Read the geometry
ii. Set initial conditions $\mathbf{u}(\mathbf{x},0)$, $T(\mathbf{x},0)$ and $f_l(\mathbf{x},0)$
iii. Calculate sensible and latent enthalpy $h_s(\mathbf{x},0)$ and $\Delta h(\mathbf{x},0)$
iv. Calculate initial equilibrium DFs $f_i^{eq}(\mathbf{x},0)$ and $g_i^{eq}(\mathbf{x},0)$
v. Set the initial DFs $\overline{f}_i(\mathbf{x},0)=f_i^{eq}(\mathbf{x},0)$ and $\overline{g}_i(\mathbf{x},0)=g_i^{eq}(\mathbf{x},0)$

Time loop
{
1. Impose boundary conditions
2. Propagate fluid particles (Streaming)
3. Calculate equilibrium DFs f_i^{eq} and g_i^{eq}
4. Calculate relaxation
5. Obtain velocity, temperature and liquid fraction fields
6. Update nodal enthalpy
7. Go back to step 1 until convergence

}
vi. Obtain macroscopic variables

The convergence is declared if the following criterion is satisfied:

$$\min\left(\left|\frac{\mathbf{u}^{n+1}-\mathbf{u}^{n}}{\mathbf{u}^{n}}\right|,\left|\frac{T^{n+1}-T^{n}}{T^{n}}\right|,\left|\frac{\Delta h^{n+1}-\Delta h^{n}}{\Delta h^{n}}\right|\right)\le 10^{-8} \tag{21}$$

The relaxation parameters should lie in the range $0.5<\lambda_i<1$, $i=f,g$ such that positive distribution functions can be obtained close to the local equilibrium, thereby ensuring non-linear stability of the numerical scheme (Higuera et al., 1989). It should be emphasized here that a rigorous, exact, theoretical analysis of nonlinear stability of the scheme is impossible, for it would amount to solving the lattice Boltzmann equations (LBE) itself. However, a number of general guiding criteria prove fairly useful. One of these criteria is the conservativeness of the scheme. The streaming operators in the LBE are perfectly conservative and the collision operators are also conservative. This makes the method an

exactly conserving numerical scheme which automatically protect against numerical blow-ups in the actual simulation (Chatterjee, 2009).

4. Case studies

We present here some case studies such as 1-D and 2-D solidification/melting problems for which analytical solutions are available and some other benchmark problems in melting and solidification.

4.1 1-D directional solidification

A one-dimensional (1-D) directional solidification problem is solved for which analytical solution is available. The schematic of the problem is shown in Fig. 2. Initially, the material is kept in a molten state at a temperature T_i (= 1) higher than the melting point T_m (= 0.5). Heat is removed from the left at a temperature T_0, which is scaled to be zero. The one-dimensional infinite domain is simulated by a finite domain (considering a domain extent of 4). The analytical solutions for the interface position $\xi(t)$, the solid (T_s) and liquid (T_l) temperatures are given by (Voller, 1997; Palle & Dantzig, 1996):

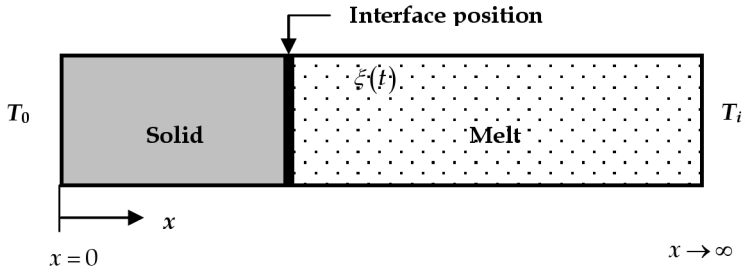

Fig. 2. Schematic of the one-dimensional solidification problem (Chatterjee, 2010)

$$\xi(t) = 2\gamma\sqrt{t}\ ,\ T_s = \frac{T_m}{erf(\gamma)} erf\left(x/\sqrt{4t}\right),\ T_l = 1 + \frac{T_m - 1}{erf(\gamma)} erf\left(x/\sqrt{4t}\right) \tag{22}$$

where γ is a constant and can be obtained implicitly from the transcendental equation,

$$T_m = erf(\gamma)\left(1 + \frac{\sqrt{\pi}}{St}\gamma \exp\left(\gamma^2\right) erfc(\gamma)\right) \tag{23}$$

Numerical simulation is performed by considering 40 uniform lattices in total in the computational range from x = 0 to 4. The dimensionless time, position and temperature are defined as $\bar{t} = \alpha t/Y^2$, $\bar{x} = x/Y$ and $\bar{T} = (T - T_0)/(T_i - T_0)$ respectively and the numerical value of Y is set as unity. The calculated isotherms at different times and the interface positions at different Stefan numbers ($St = c_p \Delta T/L$, where $\Delta T = T_i - T_0$) are shown in Fig. 3 (a, b). An excellent agreement is found between the present simulation and the analytical solution which in turn demonstrates the effectiveness of the proposed method.

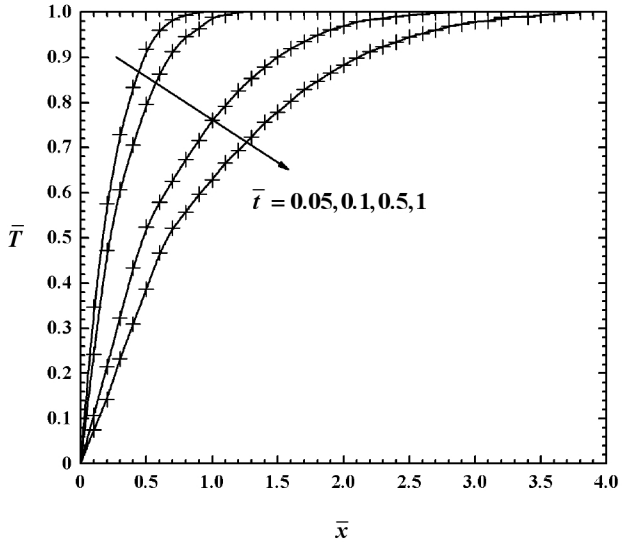

(a)

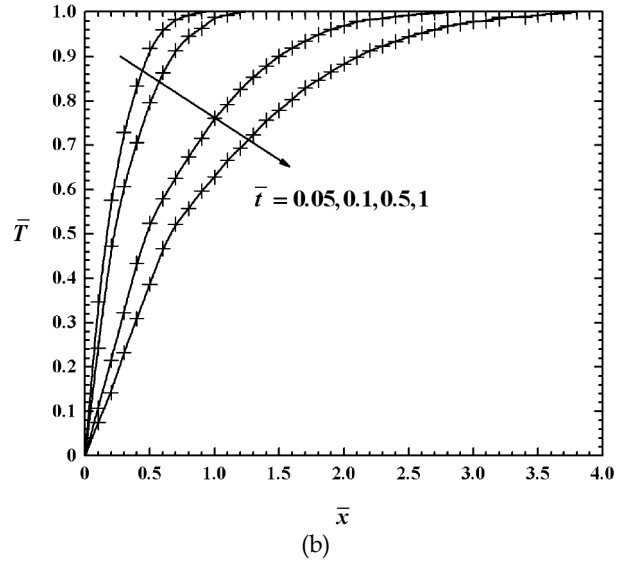

(b)

Fig. 3. Comparison of calculated (symbol) (a) isotherms for St = 1 at different times, and (b) interface position at different Stefan numbers with analytical solutions (solid lines) for the one-dimensional solidification problem (Chatterjee, 2010)

4.2 2-D solidification problem

A two-dimensional (2-D) solidification problem for which analytical (Rathjen & Jiji, 1971) and numerical (LB) (Jiaung et al., 2001; Lin & Chen, 1997) solutions are available in the

literature is now presented. Fig. 4 shows the schematic diagram of the problem with the boundary conditions. The material is kept initially at a uniform temperature T_i which is higher than or equal to the melting temperature $T_{m.}$ The left (x = 0) and bottom (y = 0) boundaries are lowered to some fixed temperature $T_0 (< T_m)$ and consequently, solidification begins from these surfaces and proceeds into the material. Setting the scaled temperatures $T_i = 0.3$, $T_0 = -1$ and $T_m = 0$ as considered in Jiaung et al. (2001) and Rathjen & Jiji (1971) and assuming constant material properties, we obtain the LB simulation results following the proposed methodology. Fig. 5a and b depict the interface position and isotherms respectively at a normalized time $\bar{t} = 0.25$ and $St = c_p (T_m - T_0)/L = 4$. The interval between the isotherm lines is 0.2 units (dimensionless). The agreement with the available analytical and numerical results is quiet satisfactory. This in turn demonstrates the accuracy and usefulness of the proposed method.

4.3 Melting of pure gallium

Melting of pure gallium in a rectangular cavity is a standard benchmark problem for validation of phase change modeling strategies, since reliable experiments in this regard (particularly, flow visualization and temperature measurements) have been well-documented in the literature (Gau & Viskanta, 1986). Brent et al. (1988) solved this problem numerically with a first order finite volume scheme, coupled with an enthalpy-porosity approach, and observed an unicellular flow pattern, in consistency with experimental findings reported in Gau & Viskanta (1986), whereas Dantzig (1989) obtained a multicellular flow pattern, by employing a second order finite element enthalpy-porosity model. Miller et al. (2001), again, obtained a multicellular flow patterns while simulating the above problem,

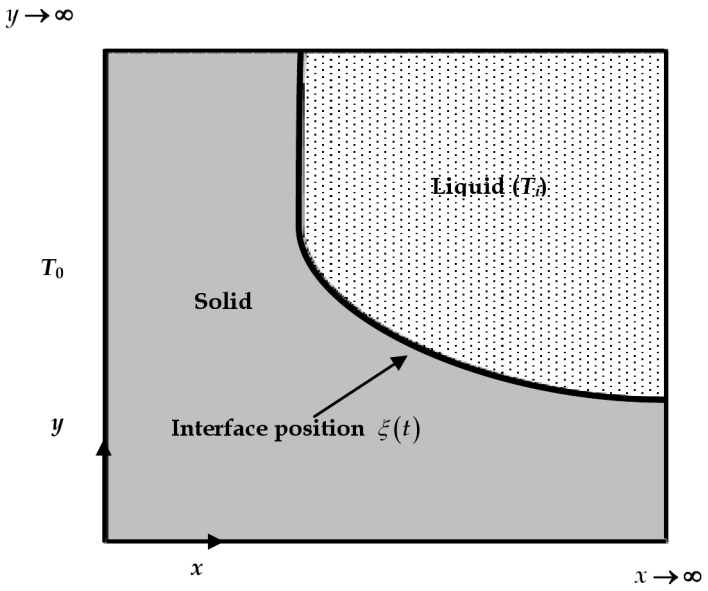

Fig. 4. Schematic of the two-dimensional solidification problem (Chatterjee, 2010)

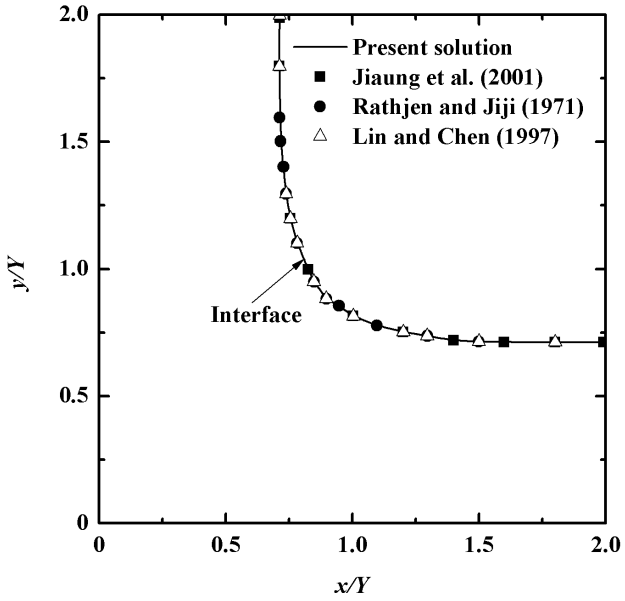

(a)

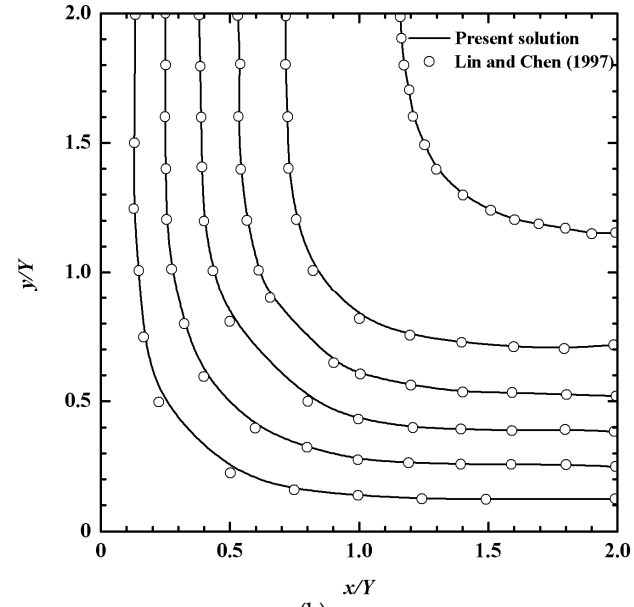

(b)

Fig. 5. Comparison of (a) interface position and (b) isotherm at $\bar{t} = 0.25$ for the two-dimensional solidification problem (Chatterjee, 2010)

by employing a LB model in conjunction with the phase field method. In all the above cases, nature of the flow field was observed to be extremely sensitive to problem data employed for numerical simulations. Here, simulation results (Chakraborty & Chatterjee, 2007) are shown with the same set of physical and geometrical parameters, as adopted in Brent et al. (1988). The study essentially examines a two-dimensional melting of pure gallium in a rectangular cavity, initially kept at its melting temperature, with the top and bottom walls maintained as insulated. Melting initiates from the left wall with a small thermal disturbance, and continues to propagate towards the right. The characteristic physical parameters are as follows: Prandtl number (Pr) = 0.0216, Stefan number (St) = 0.039 and Raleigh number (Ra) = 6×10^5. Numerical simulations are performed with a (56 × 40) uniform grid system, keeping the aspect ratio 1.4 in a 9 speed square lattice (D2Q9) over 6×10^5 time steps (corresponding to 1 min of physical time). The results show excellent agreements with the findings of Brent et al. (1988). For a visual appreciation of flow behavior during the melting process, Fig. 6 is plotted, which shows the streamlines and melt front location at time instants of 6, 10 and 19 min, respectively. The melting front remains virtually planar at initial times, as the natural convection field begins to develop. Subsequently, the natural convection intensifies enough to have a pronounced influence on overall energy transport in front of the heated wall. Morphology of the melt front is subsequently dictated by the fact that fluid rising at the heated wall travels across the cavity and impinges on the upper section of the solid front, thereby resulting in this area to melt back beyond the mean position of the front. After 19 min, the shape of the melting front is governed primarily by advection. Overall, a nice agreement can be seen between numerically obtained melt front positions reported in a benchmark study executed by Brent et al. (1988) and the present simulation. Slight discrepancies between the computed results

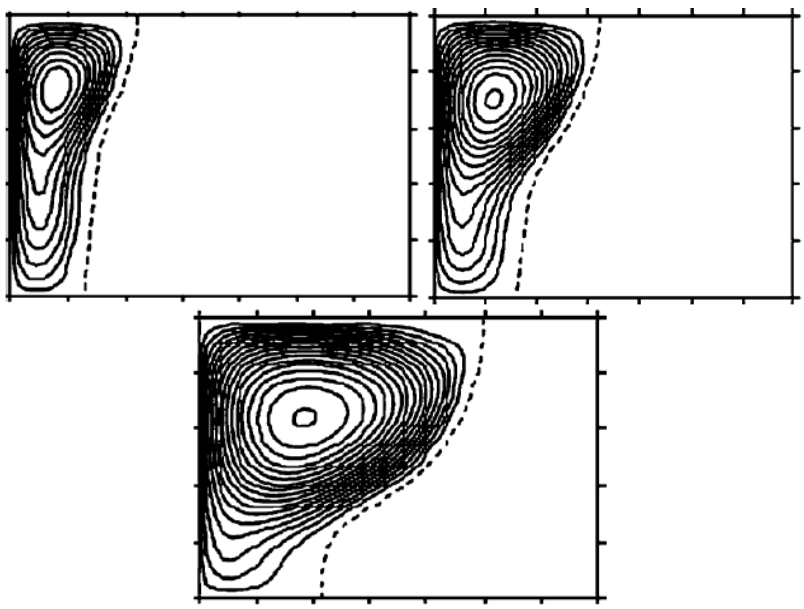

Fig. 6. Melting of pure gallium in a rectangular cavity (Chakraborty & Chatterjee, 2007)

(both in benchmark numerical work reported earlier and the present computations) and observed experimental findings (Gau & Viskanta, 1986) can be attributed to three-dimensional effects in experimental apparatus to determine front locations, experimental uncertainties and variations in thermo-fluid properties. However, from a comparison of the calculated and experimental (Gau & Viskanta, 1986) melt fronts at different times (refer to Fig. 7), it is found that both the qualitative behavior and actual morphology of the experimental melt fronts are realistically manifested in the present numerical simulation.

4.4 Bridgman crystal growth

Results are presented for simulation of transport processes in a macroscopic solidification problem such as the Bridgman crystal growth in a square crucible (Chatterjee, 2010). The Bridgman crystal growth is a popular process for growing compound semiconductor crystals and this problem has been solved extensively as a benchmark problem. The typical problem domain along with the boundary condition is shown schematically in Fig. 8. Initially, the material is kept in a molten state at a temperature T_i (= 1) higher than the melting point T_m. Since initially there is no thermal gradient, consequently, there is no convection. At $t = 0^+$, the left, right and the bottom walls are set to the temperature T_0, which is scaled to be zero, while the top wall is assumed to be insulated. This will lead to a new phase formation (solidification) at the walls with simultaneous melt convection. The characteristic physical parameters (arbitrary choice) for the problem are the Prandtl number Pr = 1, Stefan number St = 1 and Raleigh number $Ra = g_a \beta \Delta T A^3 / (\nu \alpha) = 10^5$, with A being

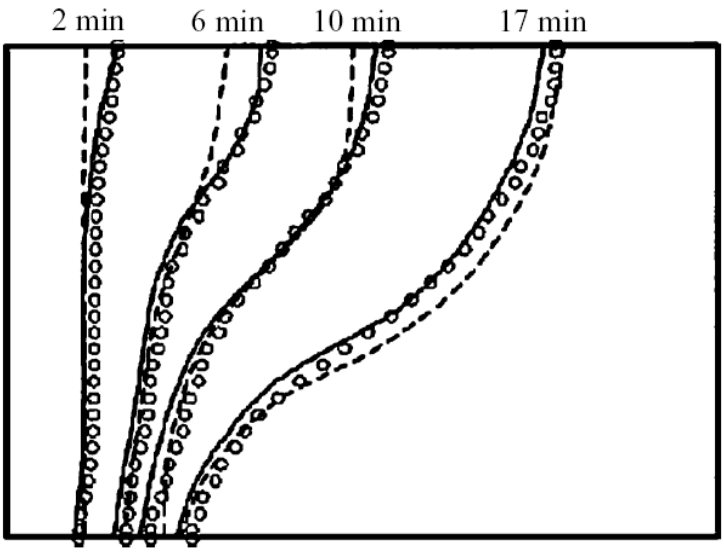

Fig. 7. Melting of pure gallium in a rectangular cavity: comparisons of the interfacial locations as obtained from the LB model (circles) with the corresponding experimental (Gau & Viskanta, 1986) results (dotted line) and continuum based numerical simulation (Brent et al., 1988) predictions (solid line) (Chakraborty & Chatterjee, 2007)

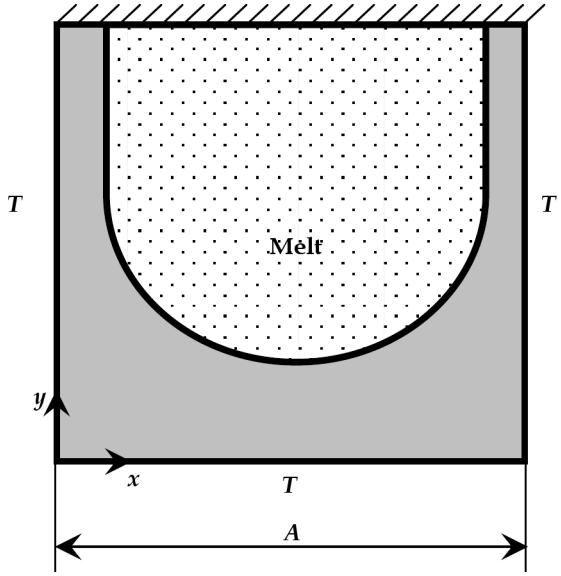

Fig. 8. Schematic of the Bridgman crystal growth in a square crucible (Chatterjee, 2010)

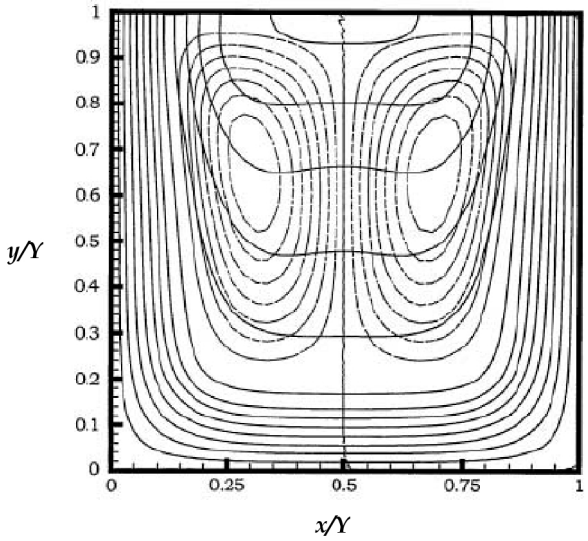

Fig. 9. Isotherm (continuous line) and flow pattern (dashed lines) at $\bar{t} = 0.25$ for the Bridgman crystal growth process (Chatterjee, 2010)

the characteristic dimension of the simulation domain. Numerical simulations are performed on a (80 × 80) uniform grid systems with an aspect ratio of 1, in a 9 speed square lattice (D2Q9) over 6×10^5 time steps corresponding to 1 min of physical time. For a visual appreciation of the overall evolution of the transport quantities in this case, Fig. 9 is plotted, which shows the representative flow pattern and isotherms at a normalized time instant of $\bar{t} = 0.05$. The interval between the contour lines is 0.05 units (dimensionless). Larger isotherm spacing is observed in the melt which is a consequence of the heat of fusion released from the melt as well as a subsequent convection effect. The isotherms are normal to the top surface since the top surface is an adiabatic wall. Two counter rotating symmetric cells are observed in the flow pattern which is consistent with the flow physics. The melt convection will become weaker as the solidification progresses since there is very little space for convection. Also the thermal gradient will become small at this juncture. The calculation continues until the melt completely disappears and the temperature of the entire domain eventually reaches T_0.

In order to demonstrate the capability of the proposed method in capturing the interfacial region without further grid refinement as normally required for the phase field based method or any other adaptive methods, Fig. 10 is plotted in which the comparison of the isotherm obtained from the present simulation for the Bridgman crystal growth and from an adaptive finite volume method (Lan et al., 2002) is shown. Virtually there is no deviation of

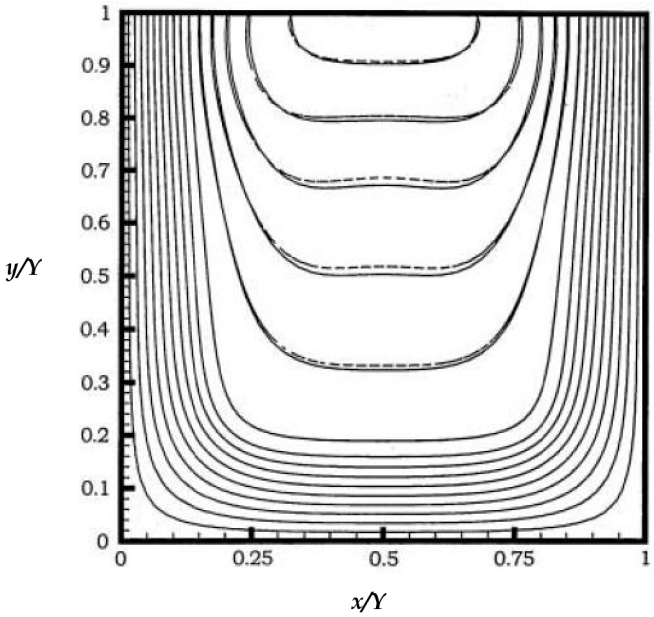

Fig. 10. Comparison of isotherm from the present calculation (solid lines) and from an adaptive finite volume method (dashed lines) (Lan et al., 2002) (Chatterjee, 2010)

the calculated isotherm form that obtained from the adaptive finite volume method (Lan et al., 2002) has been observed. This proves that the present method is quiet capable of capturing the interfacial region without further grid resolution.

4.5 Crystal growth during solidification

In this section, the problem of crystal growth during solidification of an undercooled melt is discussed (Chatterjee & Chakraborty, 2006). Special care is taken to model the effects of curvature undercooling, anisotropy of surface energy at the interface and the influence of thermal noise, borrowing principles from cellular automaton based dendritic growth models (Sasikumar & Sreenivasan, 1994; Sasikumar & Jacob, 1996), in the framework of a generalized enthalpy updating scheme adopted here. Numerical experiments are performed to study the effect of melt convection on equiaxed dendrite growth. Since flow due to natural convection (present in a macroscopic domain) can be simulated as a forced flow over microscopic scales, a uniform flow is introduced through one side of the computational domain, and its effect on dendrite growth morphology is investigated. Computations are carried out in a square domain (50 × 50 uniform grid-system) containing initially a seed crystal at the center, while the remaining portion of the domain is filled with a supercooled melt. The physical parameters come from the following normalization of length (W) and time (τ) units: $W = \sqrt{2}\delta$ and $\tau = 2\delta^2 / \mu_k \varphi_g$, where δ is the interfacial length scale (typically O (10^{-9} m)), μ_k is a kinetic coefficient (typically O (10^{-1} m/s.K)) and φ_g is the Gibbs-Thompson coefficient (typically O (10^{-7} m.K)). Exact values of the above parameters have been taken from Beckermann et al. (1999). The degree of undercooling corresponds to 0.515 K. Fig. 11 demonstrates the computed evolution of dendritic arms under the above conditions. In absence of fluid flow, the dendrite arms grow in an identical manner

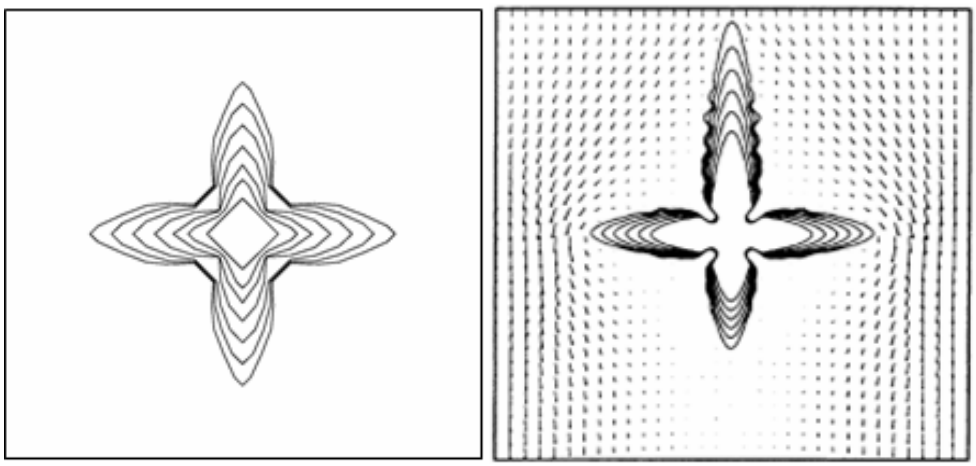

Fig. 11. Effect of fluid flow on evolution of dendrite (Pr = 0.002) (0.4, 0.8, 1.2, 1.6, 2, 2.4 and 2.8 s) (a) with only diffusion (b) in presence of fluid flow. The interval between solid fraction contour lines is 0.05 units (dimensionless) (Chatterjee & Chakraborty, 2006)

(Fig. 11a), simply because of isotropic heat extraction through all four boundaries. Fig. 11(b) illustrates the effect of convection on the above dendritic growth. In the upstream side (top), convection opposes heat diffusion, which subsequently reduces the thermal boundary layer thickness and increases local temperature gradients, eventually, leading to a faster growth of the upper dendritic arm. Evolution of the downstream arm (bottom), on the other hand, is relatively retarded, for identical reasons.

For a more comprehensive validation of the quantitative capabilities of the present LB model to simulate dendritic growth in presence of fluid flow, results predicted by the present model are compared with those reported in Beckermann et al. (1999), and a visual appreciation of the same is depicted in Fig. 12. It is revealed from Fig. 12 that the solid fraction contours and isotherms based on the present model match excellently with the dendritic envelopes depicted in Beckermann et al. (1999). These results, further, indicate excellent convergence properties of the present LB based method, over a wide range of Reynolds and Prandtl numbers.

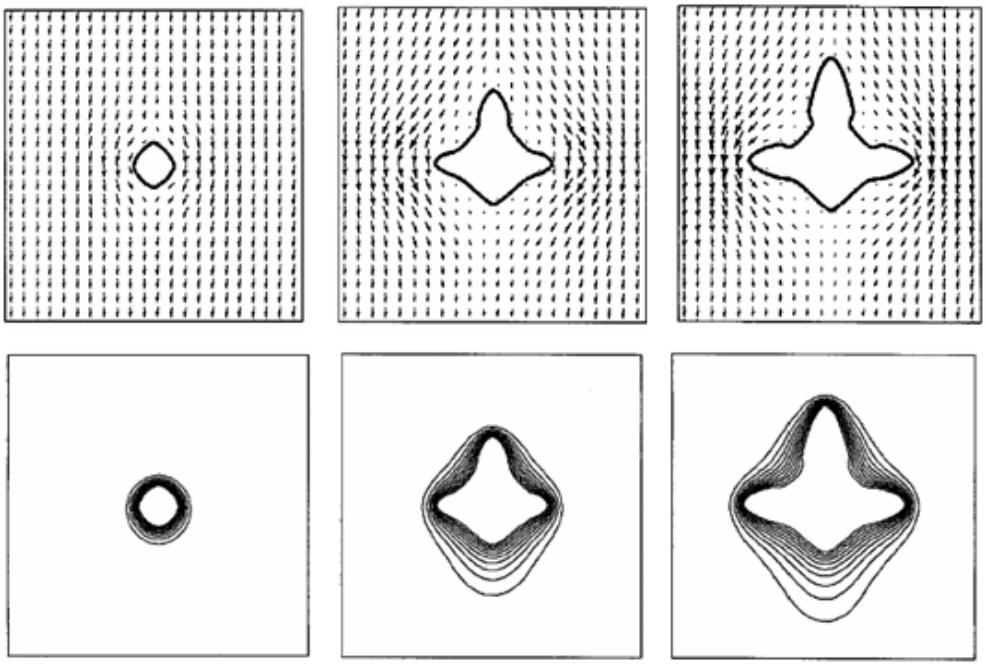

Fig. 12. LB Simulation of dendritic growth by employing problem data reported in Beckermann *et al*. (1999), solid fraction contour with velocity vectors (top panel) and isotherms (bottom panel), a) t = 2 s (b) t = 8 s (c) t = 12 s. The interval between isotherms is 0.05 units (dimensionless) (Chatterjee & Chakraborty, 2006)

5. Summary

This chapter briefly summarizes the development of a passive scalar based thermal LB model to simulate the transport processes during melting/freezing of pure substances. The model incorporates the macroscopic phase changing aspects in an elegant and straightforward manner into the LB equations. Although the model is developed for two-dimensional phase change problems, it can be easily extended to three-dimension. These features make the model attractive for simulating generalized convection-diffusion melting/solidification problems. Because of its inherent simplicity in implementation, stability, accuracy, as well as its parallel nature, the proposed method might be a potentially powerful tool for solving complex phase change problems in physics and engineering, characterized by complicated interfacial topologies. Compared with the phase field based LB models, the present scheme is much simpler to implement, since extremely refined meshes are not required here to resolve a minimum length scale over the interfacial regions. Although a finer mesh would definitely results in a better-resolved interface and a more accurate capturing of gradients of field variables, the mesh size for the present model merely plays the role of a synthetic microscope to visualize topological features of the interface morphology.

6. Acknowledgment

The author gratefully acknowledge Dr. Bittagopal Mondal (Scientist, Simulation & Modeling Laboratory, CSIR-Central Mechanical Engineering Research Institute, India) for reading the chapter and suggesting some modifications/corrections.

7. References

Askar, H.G. (1987). The front tracking scheme for the one-dimensional freezing problem. *International Journal for Numerical Methods in Engineering*, Vol. 24, pp. 859-869

Barrios, G.; Rechtman, R.; Rojas, J. & Tovar, R. (2005). The lattice Boltzmann equation for natural convection in a two-dimensional cavity with a partially heated wall. *Journal of Fluid Mechanics*, Vol. 522, pp. 91-100.

Beckermann, C.; Diepers, H.-J.; Steinbach, I.; Karma, A. & Tong, X. (1999). Modeling melt convection in phase-field simulations of solidification. *Journal of Computational Physics*, Vol. 154, pp. 468-496

Bhatnagar, P.L.; Gross, E.P. & Krook, M. (1954). A model for collision processes in charged and neutral one-component system. *Physical Review*, Vol. 94, pp. 511-525

Brent, A.D.; Voller, V.R. & Reid, K. (1988). Enthalpy-porosity technique for modeling convection–diffusion phase change: application to the melting of a pure metal. *Numerical Heat Transfer*, Vol. 13, pp. 297-318

Chakraborty, S. & Chatterjee, D. (2007). An enthalpy-based hybrid lattice-Boltzmann method for modelling solid–liquid phase transition in the presence of convective transport. *Journal of Fluid Mechanics*, Vol. 592, pp. 155-175

Chakraborty, S. & Dutta, P. (2001). A generalized formulation for evaluation of latent heat functions in enthalpy-based macroscopic models for convection–diffusion phase change process. *Metallurgical Transactions B*, Vol. 32, pp. 562-564

Chatterjee, D. & Chakraborty, S. (2005). An enthalpy-based lattice Boltzmann model for diffusion dominated solid–liquid phase transformation. *Physics Letters A*, Vol. 341, pp. 320-330

Chatterjee, D. & Chakraborty, S. (2006). A hybrid lattice Boltzmann model for solid–liquid phase transition in presence of fluid flow. *Physics Letters A*, vol. 351, pp. 359-367

Chatterjee, D. & Chakraborty, S. (2008). An enthalpy-source based lattice Boltzmann model for conduction dominated phase change of pure substances. *International Journal of Thermal Sciences*, Vol. 47, pp. 552-559

Chatterjee, D. (2009). An enthalpy-based thermal lattice Boltzmann model for non-isothermal systems. *Euro physics Letters*, Vol. 86, pp. 14004

Chatterjee, D. (2010). Lattice Boltzmann simulation of incompressible transport phenomena in macroscopic solidification processes. *Numerical Heat Transfer B*, Vol. 58, pp. 55-72

Chen, S. & Doolen, G.D. (1998). Lattice Boltzmann method for fluid flows, *Annual Review of Fluid Mechanics*, Vol. 30, pp. 329-364

Comini, G.; Guidice, S.D. & Saro, O. (1990). A conservative algorithm for multidimensional conduction phase change. *International Journal for Numerical Methods in Engineering*, Vol. 30, pp. 697-709

Comini, G.; Guidice, S.D.; Lewis, R.W. & Zienkiewicz, O.C. (1974). Finite element solution of non-linear heat conduction problems with special reference to phase change. *International Journal for Numerical Methods in Engineering*, Vol. 8, pp. 613-624

Dalhuijsen, A.J. & Segal, A. (1986). Comparison of finite element techniques for solidification problems. *International Journal for Numerical Methods in Engineering*, Vol. 23, pp. 1807- 1829

Dantzig, J.A. (1989). Modeling liquid-solid phase changes with melt convection. *International Journal for Numerical Methods in Engineering*, Vol. 28, pp.1769-1785

De Fabritiis, G.; Mancini, A.; Mansutti, D. & Succi, S. (1998). Mesoscopic models of liquid/solid phase transitions. *International Journal of Modern Physics C*, Vol. 9, pp. 1405-1415

Dhatt, G.; Song, R. & Cheikh, A.N. (1989). Direct enthalpy method for solidification calculation, In: Gruber *et al*. (Ed.), *Proceedings of the Fifth International Symposium on Numerical Methods in Engineering*, pp. 487-494, Boston,

Ferreol, B. & Rothman, D.H. (1995). Lattice Boltzmann simulations of flow through fontainebleau sandstone. *Transport in Porous Media,* Vol. 20, pp. 3-20

Gau, C. & Viskanta, R. (1986). Melting and solidification of a pure metal on a vertical wall. *Journal of Heat Transfer*, Vol. 108, pp. 174-181

Gunstensen, A.K.; Rothman, D.H.; Zaleski, S. & Zanetti, G. (1991). A lattice-Boltzmann model of immiscible fluids, *Physical Review A,* Vol. 43, pp. 4320-4327

Guo, Z.; Zheng, C. & Shi, B. (2002). An extrapolation method for boundary conditions in lattice Boltzmann method. *Physics of Fluids*, Vol. 14, pp. 2007-2010

Harrowell, P.R. & Oxtoby, D.W. (1987). On the interaction between order and a moving interface: Dynamical disordering and anisotropic growth rates. *Journal of Chemical Physics*, Vol. 86, pp. 2932-2942

He, X.; Chen, S. & Doolen, G.D. (1998). A novel thermal model for the lattice Boltzmann method incompressible limit. *Journal of Computational Physics*, Vol. 146, pp. 282-300

Higuera, F.J.; Succi, S. & Benzi, R. (1989). Lattice gas-dynamics with enhanced collisions. *Euro physics Letters*, Vol. 9, pp. 345-349

Huber, C.; Parmigiani, A.; Chopard, B.; Manga, M. & Bachmann, O. (2008). Lattice Boltzmann model for melting with natural convection. *International Journal of Heat and Fluid Flow*, Vol. 29, pp. 1469-1480

Hu, H. & Argyropoulos, S.A. (1996). Mathematical modeling of solidification and melting: a review. *Modeling Simulation Material Science Engineering*, Vol. 4, pp. 371–396

Jiaung, W.-S.; Ho, J.-R. & Kuo, C.-P. (2001). Lattice-Boltzmann method for the heat conduction problem with phase change. *Numerical Heat Transfer B*, Vol. 39, pp. 167-187

Kendon, V.M.; Cates, M.E.; Pagonabarraga, I.; Desplat, J.-C. & Bladon, P. (2001). Inertial effects in three-dimensional spinodal decomposition of a symmetric binary fluid mixture: a lattice Boltzmann study. *Journal of Fluid Mechanics*, Vol. 440, pp. 147-203

Khachaturyan, A.G. (1996). Long-range order parameter in field model of solidification. *Philosophical Magazine A*, Vol. 74, pp. 3-14

Kim, Y-T.; Provatas, N.; Goldenfeld, N. & Dantzig, J.A. (1999). Universal dynamics of phase-field models for dendritic growth. *Physical Review E*, Vol. 59, pp. R2546-R2549

Lan, C.W.; Liu, C.C. & Hsu, C.M. (2002). An Adaptive Finite Volume Method for Incompressible Heat Flow Problems in Solidification. *Journal of Computational Physics*, Vol. 178, pp. 464-497

Lin, J.-Y. & Chen, H.-T. (1997). Hybrid Numerical Scheme for Nonlinear Two-Dimensional Phase-change Problems with the Irregular Geometry. *Heat and Mass Transfer*, Vol. 33, pp. 51-58

Medvedev, D. & Kassner, K. (2005). Lattice Boltzmann scheme for crystal growth in external flows. *Physical Review E*, Vol. 72, pp. 056703

Mikheev, L.V. & Chernov, A.A. (1991). Mobility of a diffuse simple crystal melt interface. *Journal of Crystal Growth*, Vol. 112, pp. 591-596

Miller, W. & Succi, S. (2002). A Lattice Boltzmann model for anisotropic crystal growth from melt. *Journal of Statistical Physics*, Vol. 107, pp. 173-186

Miller, W. (2001). The lattice Boltzmann method: a new tool for numerical simulation of the interaction of growth kinetics and melt flow. *Journal of Crystal Growth*, Vol. 230, pp. 263-269

Miller, W., & Schroder, W. (2001). Numerical modeling at the IKZ: an overview and outlook. *Journal of Crystal Growth*, Vol. 230, pp. 1-9

Miller, W.; Rasin, I. & Pimentel, F. (2004). Growth kinetics and melt convection. *Journal of Crystal Growth*, Vol. 266, pp. 283-288

Miller, W.; Succi, S. & Manutti, D. (2001). Lattice Boltzmann Model for Anisotropic Liquid-Solid Phase Transition. *Physical Review Letters*, Vol. 86, pp. 3578-3581

Morgan, K.; Lewis, R.W. & Zienkiewicz, O.C. (1978) An improved algorithm for heat conduction problems with phase change. *International Journal for Numerical Methods in Engineering*, Vol. 12, pp. 1191-1195

Palle, N. & Dantzig, J.A. (1996). An adaptive mesh refinement scheme for solidification problems. *Metallurgical Transactions A*, Vol. 27, pp. 707-718

Pham, Q.T. (1986). The use of lumped capacitance in the finite-element solution of heat conduction problems with phase change. *International Journal of Heat and Mass Transfer*, Vol. 29, pp. 285-291

Raj, R.; Prasad, A.; Parida, P.R. & Mishra, S.C. (2006). Analysis of solidification of a semitransparent planar layer using the lattice Boltzmann method and the discrete transfer method. *Numerical Heat Transfer A*, Vol. 49, pp. 279–299

Rasin, I.; Miller, W. & Succi, S. (2005). Phase-field lattice kinetic scheme for the numerical simulation of dendritic growth. *Physical Review E*, Vol. 72, pp. 066705

Rathjen, K.A. & Jiji, L.M. (1971). Heat Conduction with Melting or Freezing in a Corner. *Journal of Heat Transfer*, Vol. 93, pp. 101-109

Roose, J. & Storrer, O. (1984). Modelization of phase changes by fictitious heat flow. *International Journal for Numerical Methods in Engineering*, Vol. 20, pp. 217-225

Rubinsky, B. & Cravahlo, E.G. (1981). A finite element method for the solution of one-dimensional phase change problems. *International Journal of Heat and Mass Transfer*, Vol. 24, pp. 1987-1989

Sankaranarayanan, K.; Shan, X.; Kevrekidis, I.G. & Sundaresan, S. (2002). Analysis of drag and virtual mass forces in bubbly suspensions using an implicit formulation of the lattice Boltzmann method. *Journal of Fluid Mechanics*, Vol. 452, pp. 61-96

Sasikumar, R. & Jacob, E. (1996). Simulation of side branch evolution in thermal dendritic grains. *Scripta Materialia*, Vol. 35, pp. 505-510

Sasikumar, R. & Sreenivasan, R. (1994). Two dimensional simulation of dendrite morphology. *Acta Metallurgica et Materialia*, Vol. 42, pp. 2381-2386

Shan, X. & Chen, H. (1993). Lattice Boltzmann model for simulating flows with multiple phase and components, *Physical Review E,* Vol. 47, pp. 1815-1819

Shi, Y., Zhao; T.S. & Guo, Z.L. (2004). Thermal lattice Bhatnagar-Gross-Krook model for flows with viscous heat dissipation in the incompressible limit. *Physical Review E*, Vol. 70, pp. 066310

Shu, C.; Peng, Y. & Chew, Y.T. (2002). Simulation of natural convection in a square cavity by Taylor series expansion and least square based lattice Boltzmann method. *International Journal of Modern Physics C*, Vol. 13, pp. 1399-1414

Tong, X.; Beckermann, C.; Karma, A. & Li, Q. (2001). Phase-field simulations of dendritic crystal growth in a forced flow. *Physical Review E*, Vol. 63, pp. 061601-(1-16)

Voller, V. & Cross, M. (1981). Accurate solutions of moving boundary problems using the enthalpy method. *International Journal of Heat and Mass Transfer*, Vol. 24, pp. 545-556

Voller, V. & Cross, M. (1983). An explicit numerical method to track a moving phase change front. *International Journal of Heat and Mass Transfer*, Vol. 26, pp. 147-150

Voller, V.; Swaminathan, C.R. & Thomas, B.G. (1990). Fixed grid techniques for phase change problems: a review. *International Journal for Numerical Methods in Engineering*, Vol. 30, pp. 875- 898

Voller, V.R. & Prakash, C. (1987). A fixed grid numerical modeling methodology for convection–diffusion mushy region phase change problems. *International Journal of Heat and Mass Transfer*, Vol. 30, pp. 1709-1719

Voller, V.R. (1997). A similarity solution for the solidification of multicomponent alloys. *International Journal of Heat and Mass Transfer*, Vol. 40, pp. 2869-2877

Weaver, J.A. & Viskanta, R. (1986). Freezing of liquid saturated porous media. *International Journal of Heat and Mass Transfer*, Vol. 33, pp. 2721-2734

8

Lattice Boltzmann Computations of Transport Processes in Complex Hydrodynamics Systems

Zhiqiang Dong[1], Weizhong Li[2], Yongchen Song[2] and Fangming Jiang[1]
[1]*CAS Key Laboratory of Renewable Energy and Gas Hydrate, Guangzhou Institute of Energy Conversion, Chinese Academy of Sciences, Guangzhou*
[2]*Key Laboratory of Ocean Energy Utilization and Energy Conservation of Ministry of Education, Dalian University of Technology, Dalian*
China

1. Introduction

Lattice Boltzmann method (LBM) has recently been receiving considerable attention as a possible alternative to conventional computational fluid dynamics (CFD) approaches in many areas related to complex fluid flows. It is of great promise for simulating flows in topologically complicated geometries, such as those encountered in porous media, and for simulations of multi-component and/or multiphase flow conjugated with heat and mass transfer. In these particular areas, there are few viable conventional CFD methods for using. The present chapter deals with LBM numerical investigation to heat and mass transfer in flows with multiple components and/or phases encountered in the rotating packed-bed or nucleate pool boiling.

In the following section 2 the LB multi-component model is adapted for simulating the mixing process in a rotating packed-bed with a serial competitive reaction (A+B→R, B+R→S; A, B, R, and S denote different components.) occurred inside. The serial competitive reaction in the main filling area of a rotating packed-bed is simulated and the mass transfer with forced convection caused by a cylindrical filler (to mimic the packing material) is studied as well. The obtained results provide some guidance for further studying the forced mass-transfer in and for the design of the real rotating packed-bed in industries.

In section 3, a hybrid LBM model is constructed. In combination with a lattice Boltzmann thermal model, the lattice Boltzmann multiphase model being capable of handling a large density ratio between phases is extended to describe the phenomenon of phase change with mass and heat transferring through the interface. Based on the Stefan boundary condition, the phase change is considered as change of the phase order parameter and is treated as a source term in the Cahn-Hilliard(C-H) equation. The evolution of the interfacial position is thereby tracked. With an improved Briant's treatment to the partial wetting boundaries, this hybrid model is used to simulate the growth of a single vapour bubble on and its departure from a heated wall. Numerical results exhibit similar parametric dependence of the bubble departure diameter in comparison with the experimental correlation available in recent literatures. Furthermore, parametric studies on the growth, coalescence and departure of a pair of twin-bubbles on a heated wall are conducted as well.

2. LBM mass transfer model

In practical engineering, the fluid flow is commonly multiphase and/or multi-component flow. The interface between phases or components changes randomly with time and the boundary surfaces between fluid and solid are sometimes very topologically-complicate. These factors make the corresponding numerical study being of great challenge. Based on the lattice gas method (Frish et al., 1986) since 1992, LBM has been developed and employed in the area of computational fluid dynamics, particularly, for the simulations of multi-component flows. Alexander et al. (1993) first used the LBM work to study component delivery problems, but the model was limited to a fixed Prandtl number. Chen et al. (1997) introduced a matrix instead of the Bhatnagar-Gross-Krook (BGK) collision factor to overcome this limitation, but their method is subjected to some computational instability (Soe et al., 1998; Vahala et al., 1998; Vahala et al., 2000). Bartoloni et al. (1993) and Shan (1997) employed two distribution functions to enhance the stability of the calculation. Inamuro et al. (2002) further simplified the distribution function. Because non-linear first-order error term presents in the macroscopic diffusion equation, the LBM multi-component model has only first-order accuracy.

Via comparison with the analytical solution, this section firstly analyzes the truncation error and accuracy of LBM. Secondly, we build up the serial competitive reaction LBM and use this model to simulate the mass transfer process in a rotating packed-bed.

In a rotating packed bed, the extremely high rotation speed forms super large centrifugal body force, which can be hundreds times of the gravity. Multiphase and/or multi-component fluids flowing inside the porous packed-bed will be torn into micro- or even nano- sized fragments, leading to greatly elongated interfaces between phases or components and hence making the mixing process around 1 - 3 orders of magnitude more efficient than in the traditional mixing towers. In this section, mixing process with a serial competitive reaction in a simplified rotating packed-bed will be simulated using an improved LBM mass transport model.

2.1 Mathematical formulation and model validation

2.1.1 Mathematical formulation

Continuity and Navier-Stokes equations

We assume the fluid system contains fluid phase of n-components. The D2Q9 BGK model is applied and the equilibrium distribution function (f) of component n is formulated as follows,

$$f_a^{eq}(\mathbf{x},t,n) = c_n\omega_a(1+3\mathbf{e}_a\cdot\mathbf{u}+\frac{9}{2}(\mathbf{e}_a\cdot\mathbf{u})^2-\frac{3}{2}u^2) \tag{1}$$

The term on the left hand side denotes the probability that component n is present at position x, at time t along the direction a. The $\boldsymbol{e_a}$ is the particle velocity，e_0=0；$e=\Delta\mathbf{x}/\Delta t$，$\Delta\mathbf{x}$ is the space step, Δt is the time step, $\omega_a=\begin{cases}4/9, & a=0;\\ 1/9, & a=1,3,5,7;\\ 1/36, & a=2,4,6,8.\end{cases}$ c_n is the concentration of component n, $\mathbf{u}$ is the velocity vector of fluid flow. The corresponding LBM equation of component n is

$$f_a(\mathbf{x}+\mathbf{e}_a\varepsilon,t+\varepsilon,n)-f_a^{eq}(\mathbf{x},t,n)=-\frac{f_a(\mathbf{x},t,n)-f_a^{eq}(\mathbf{x},t,n)}{\tau} \tag{2}$$

with τ being the relaxation parameter and ε the time step. We define the macroscopic variables as

$$c_n = \sum_a f_a^{eq}(\mathbf{x}, t, n) \tag{3}$$

$$c_n \mathbf{u}_i = \sum_a \mathbf{e}_{ia} f_a = \sum_a \mathbf{e}_{ia} f_a^{eq} \tag{4}$$

$$c(\mathbf{x}, t) = \sum_n c_n(\mathbf{x}, t, n) \tag{5}$$

By virtue of the Chanman-Enskog expansion and multiscale analysis, the corresponding continuity and Navier-Stokes equations yield

$$\frac{\partial c}{\partial t} + \frac{\partial c u_j}{\partial x_j} = 0 \tag{6}$$

$$\frac{\partial c u_i}{\partial t} + \frac{\partial c u_i u_j}{\partial x_j} = -\frac{\partial p \delta_{ij}}{\partial x_j} + \mu \frac{\partial^2 c u_i}{\partial x_j \partial x_j} + \eta \frac{\partial^2 c u_k}{\partial x_k \partial x_i} + o(\varepsilon^2) \tag{7}$$

where, the viscosity is calculated with μ=(2τ-1)ε/6.0=η/2.0, the pressure **p**=c/3. Eqs. (6) and (7) ensure the multi-component system being of the general flow characteristics.

Mass transport equations of fluid components

Applying the Taylor series expansion and using the Chapman-Enskog approximation to Eq. (2), we get the following second order LB mass transport equation,

$$\frac{\partial}{\partial t} \sum_\alpha f_\alpha^{(0)} + \frac{\partial}{\partial x_i} \sum_\alpha \mathbf{e}_{i\alpha} f_a^{(0)} + \varepsilon \left(\frac{1}{2} - \tau\right) \sum_\alpha \left(\frac{\partial}{\partial t_0} + \mathbf{e}_{i\alpha} \frac{\partial}{\partial x_i}\right)^2 f_\alpha^{(0)} + o(\varepsilon^2) = 0 \tag{8}$$

Combined with Eqs.(3)and (4), Eq.(8) can be expressed as

$$\frac{\partial c_n}{\partial t} + \frac{\partial c_n u_i}{\partial x_i} = \mu \frac{\partial^2 c_n}{\partial^2 x_i} + \mu \frac{\partial^2 c_n u_i}{\partial t \partial x_i} + o(\varepsilon^2) \tag{9}$$

where, μ=(2τ-1)ε/6.0 is the diffusion coefficient. A perturbation term $\mu \frac{\partial^2 c_n u_i}{\partial t \partial x_i}$ of first-order accuracy is present in the convection-diffusion equation. The dimensionless velocity u is very small, so the perturbation term only has little influence on the precision of Eq. (9). The difference between LBM and the traditional convection-diffusion equation is that the series truncation error term appears in the diffusion term of the corresponding macroscopic equation (9). This section focuses firstly on the truncation error term and the perturbation term to investigate their influence on the LBM diffusion behavior.

Mass transport with serial competitive reaction

We consider a serial competitive reaction: A+B→R；B+R→S. The corresponding convection -diffusion equation is formulated as

$$\frac{\partial c_n}{\partial t}+\frac{\partial c_n u_i}{\partial x_i}=D\frac{\partial^2 c_n}{\partial {x_i}^2}-r_i \tag{10}$$

where, u_i is the x_i-direction velocity; c_n is the concentration of component n; D is molecular diffusion coefficient; r_i is the source or sink term due to chemical reaction.

$$\begin{aligned} r_A &= k_1 c_A c_B \\ r_B &= k_1 c_A c_B + k_2 c_B c_R \\ r_R &= -k_1 c_A c_B + k_2 c_B c_R \\ r_S &= -k_2 c_B c_R \end{aligned} \tag{11}$$

where, k_1 and k_2 are rate constants.
Based on D2Q9 BGK model, the equilibrium distribution function of component n is set as follows.

$$f^{eq}{}_a(\mathbf{r},t,n)=c_n\omega_a(1+3\mathbf{e}_a\cdot\mathbf{u}+\frac{9}{2}(\mathbf{e}_a\cdot\mathbf{u})^2-\frac{3}{2}\mathbf{u}^2) \tag{12}$$

$$\mathbf{e}_a=e\left[\mathbf{i}\cos\frac{(\alpha-1)}{2}+\mathbf{j}\sin\frac{(\alpha-1)}{2}\right] \tag{13}$$

where, $1\le\alpha\le 4, \mathbf{e}_0=0$, $\omega_a=\begin{cases}4/9, & a=0;\\ 1/9, & a=1,3,5,7;\\ 1/36, & a=2,4,6,8.\end{cases}$ $\mathbf{i}$、$\mathbf{j}$ are the unit vector in the x, y direction, respectively; $\mathbf{e}_a$ is the particle velocity. The distribution function $f^{eq}{}_a(\mathbf{r},t,n)$ denotes the mass fraction probability of component n presented at location **r**, at time t and along the a direction. Using r_{na} toi denote the corresponding chemical reaction term, the equation of LBM is thus obtained as

$$f_a(\mathbf{r}+\mathbf{e}_a\varepsilon,t+\varepsilon,n)-f^{eq}{}_a(\mathbf{r},t,n)=-\frac{f_a(\mathbf{r},t,n)-f_a{}^{eq}(\mathbf{r},t,n)}{\tau}+r_{na} \tag{14}$$

Likewise, we define macroscopic variables:

The node mass fraction of the component **n:** $c_n=\sum_a f_a{}^{eq}(\mathbf{r},t,n)$ (15)

The total mass fraction of nodes: $c(\mathbf{r},t)=\sum_n c_n(\mathbf{r},t,n)$ (16)

Node momentum of component n： $c\mathbf{u}=\sum_a \mathbf{e}_a\sum_n f_a(r,t,n)=\sum_a \mathbf{e}_a\sum_n f_a^{eq}(r,t,n)$ (17)

Node chemical reaction term of composition **n**: $r_n=\sum_a r_{na}$ (18)

Applying the Taylor series expansion and Chapman-Enskog expansion to Eq. (14), we can get a different time scale LBM equation. Bonded with the multi-scale equations, the following equation yields

$$\frac{\partial}{\partial t}\sum_{\alpha} f_{\alpha}^{(0)} + \frac{\partial}{\partial r}\sum_{\alpha} \mathbf{e}_{\alpha} f_{\alpha}^{(0)} + \varepsilon(\frac{1}{2}-\tau)\sum_{\alpha}(\frac{\partial}{\partial t_0} + \mathbf{e}_{\alpha}\frac{\partial}{\partial r})^2 f_{\alpha}^{(0)} - \sum_{a} r_{na} + o(\varepsilon^2) \tag{19}$$

Introducing Eqs. (15), (16), (17) and (18) into the Eq. (19), we get

$$\frac{\partial c_n}{\partial t} + \frac{\partial c_n u_i}{\partial x_i} = D\frac{\partial^2 c_n}{\partial x_i^2} - r_i + o(\varepsilon^2) \tag{20}$$

where, D=(τ-0.5)ε/3is the diffusion coefficient.

2.1.2 Model validation

In order to validate the model prediction we consider a transient diffusion case, which is described with:

$$\frac{\partial c}{\partial t} = \kappa\frac{\partial^2 c}{\partial x^2}, 0 < x < 1, \ t > 0 \tag{21}$$

The boundary and initial conditions are,

$$c(0,t) = 1 \ , \ \frac{\partial c(1,t)}{\partial x} = 0 \ , (t > 0); \ c(x,0) = 0 \ , (0 \le x \le 1) \tag{22}$$

It has an analytical solution,

$$c(x,t) = 1 - \sum_{j=0}^{\infty}\frac{4}{(2j-1)\pi}\exp\left[-\frac{1}{4}\pi^2(j-1)^2\kappa t\right]\sin\left[\frac{1}{2}\pi(2j-1)x\right] \tag{23}$$

As shown by Fig. 1, the LBM simulated results are in good agreement with the analytical solutions. No initial value fluctuation occurs in the LBM computation.

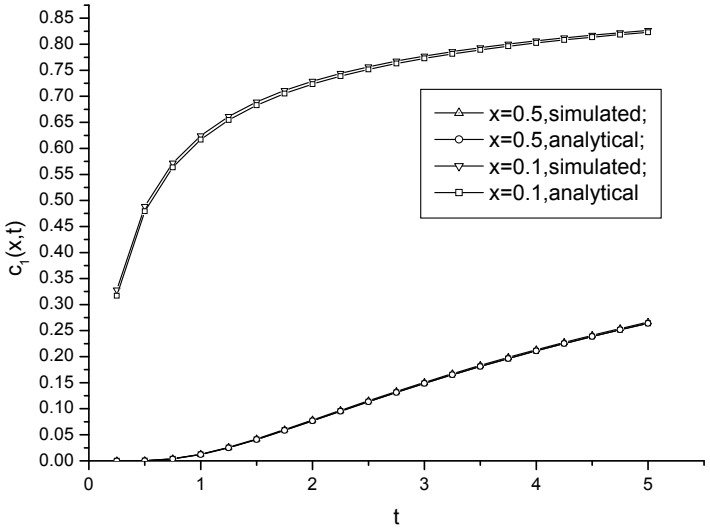

Fig. 1. Diffusion behavior without convection effect

The above test case verifies that the perturbation term $\mu \frac{\partial^2 c_n u_i}{\partial t \partial x_i}$ in Eq. (9) can be safely omitted. Hereby we validate the reliability and accuracy of the LBM diffusion transport model.

2.2 Mixing process with serial competitive reaction

2.2.1 Laminar diffusion and reaction model

Experimental results of TV camera image and stroboscopic photography show that the liquid flow in rotating packed-bed is mainly in the form of film flow (Liu, 2000). Due to the strong centrifugal force, the liquid film is very thin, thinner than tens of microns. Therefore, the Reynolds number is small (approximately less than 30) and thus the liquid flow falls in the laminar flow regime. To this understanding, we perform the LB modeling to the laminar diffusion and reaction process.

We consider a case that two liquid films meet and bond together and then move at the same speed with no tangential movement due to shear force. The diffusion is across the interface of two liquid films and the reaction is added: A+B→R；B+R→S. Analyzing this serial competitive reaction and comparing the first product R and second product S, we can quantify the reactive mass transport.

Fig.2 displays the concentration profile of each component of reactants and products, at position i=75 and at time t=50000 time steps, which corroborates the process follows the laminar diffusion and reaction regime. More simulation results about temporal variation of the total amount of each component ($c = \sum_{i,j} c(i,j)$) are shown in Fig. 3.

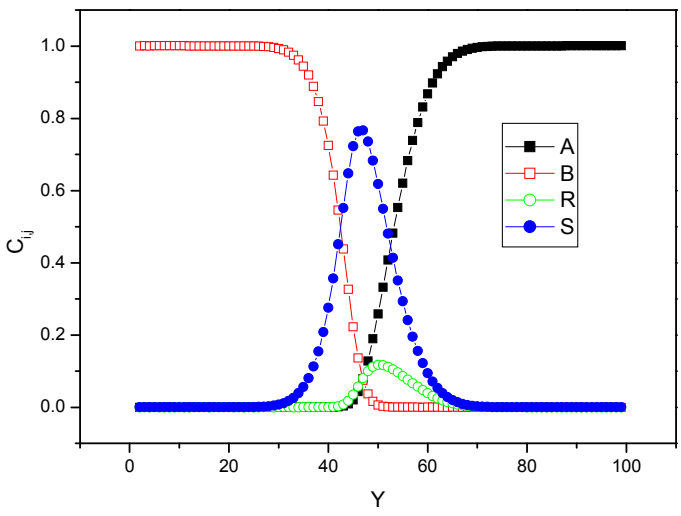

Fig. 2. Component concentration at i=75 and at t=50000 time steps

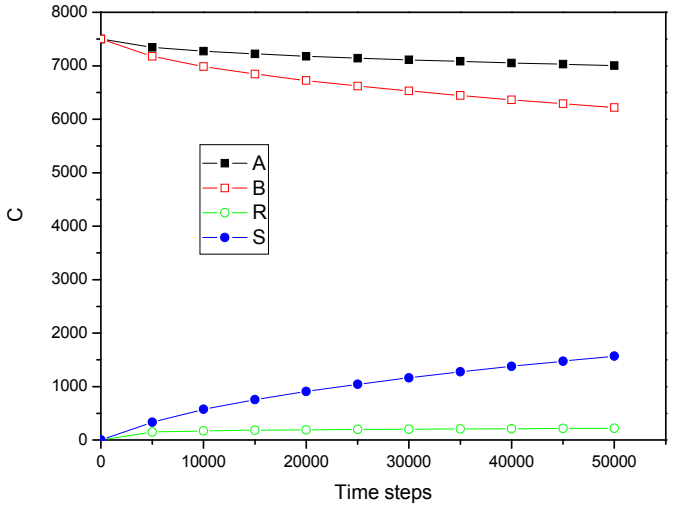

Fig. 3. Temporal variation of the total amount of each component

2.2.2 Forced convection and reaction model

To introduce convection disturbance to the mixing process, a cylindrical pillar is put at the entry section of the simulated geometry. The cylindrical pillar mimics one packed- filler in a rotating packed-bed. With the LBM, the mixing with serial competitive reaction at the end-effect regions of the rotating packed-bed is simulated and some hints about the convective mixing in the packed-bed are obtained. Typical results are shown in Figs. 4 and 5. The inserted pillar induces disturbance to fluid flow, deforming the interface of different components and hence enhancing the mixing process.

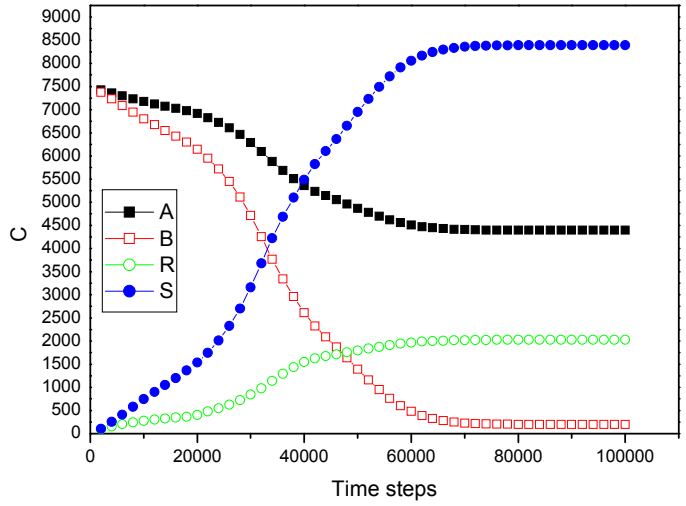

Fig. 4. Temporal variation of the total amount of each component

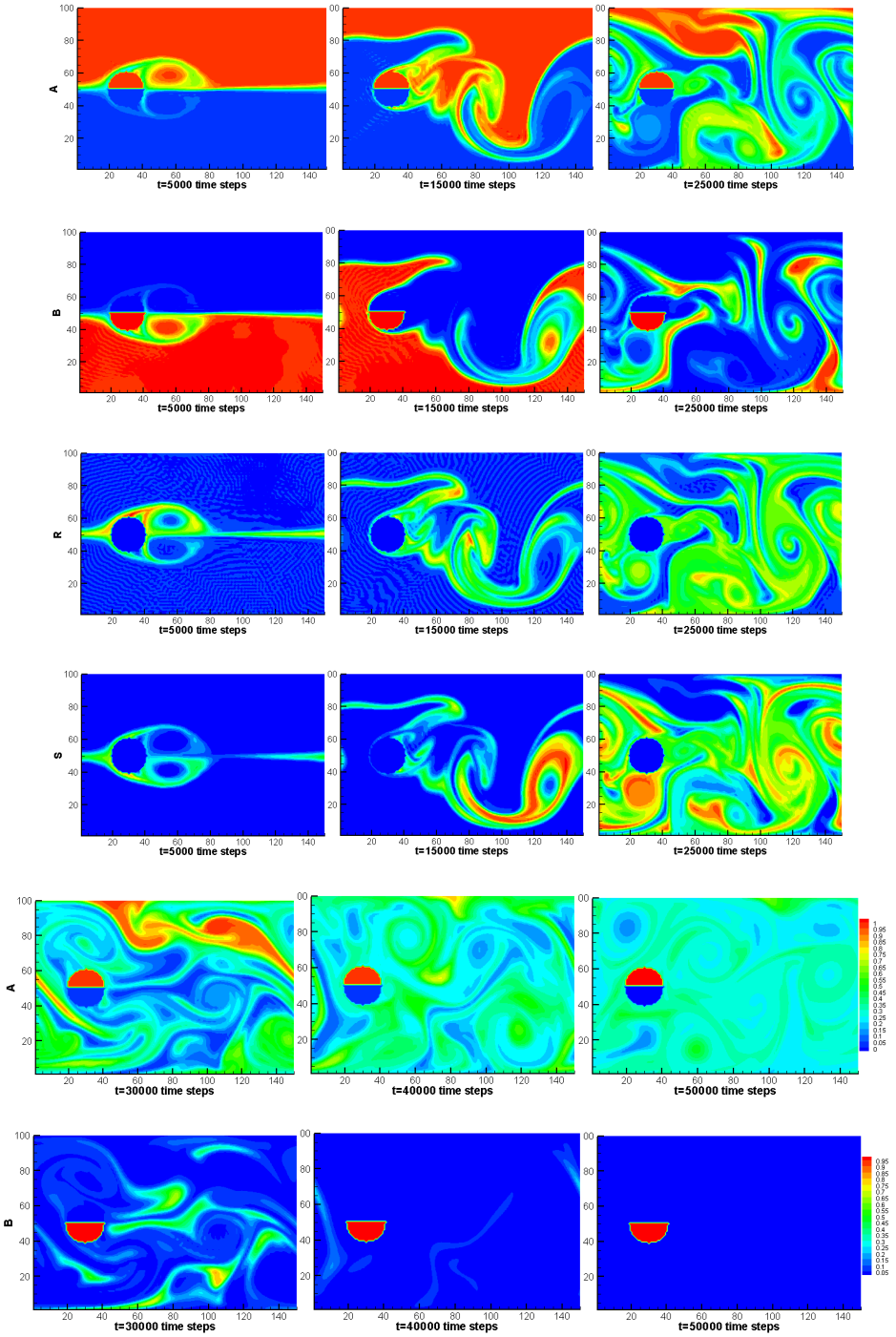
A
t=5000 time steps
t=15000 time steps
t=25000 time steps
B
t=5000 time steps
t=15000 time steps
t=25000 time steps
R
t=5000 time steps
t=15000 time steps
t=25000 time steps
S
t=5000 time steps
t=15000 time steps
t=25000 time steps
A
t=30000 time steps
t=40000 time steps
t=50000 time steps
B
t=30000 time steps
t=40000 time steps
t=50000 time steps

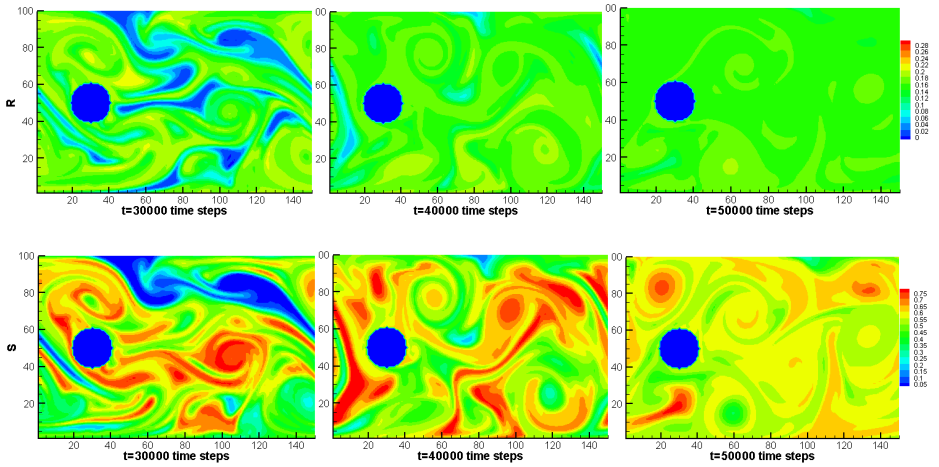

Fig. 5. Evolution of 2-D distribution of the reactant/product concentration

3. A hybrid lattice Boltzmann model

Nucleate boiling is a liquid-vapor phase-change process accompanying with the bubble formation, growth, departure and rising. Because the process plays a key role in the boiling heat transfer, it has been widely studied for half a century. Although the phenomenon of bubble motion with bubble growth can be explained qualitatively as demonstrated in the corresponding experimental investigations, main difficulty in quantitative prediction is that multiphase flows pose to be very complex, involving thermodynamics (co-existing phase), kinetics (nucleation, phase transitions) and hydrodynamics (inertial effects). "What role does a liquid-vapor interface play?" remains to be a core and open issue from the physical point of view. Fortunately, the development of numerical methods and computer technology has provided a powerful tool to predict vapor bubble behavior in nucleate pool boiling. For vapor bubble with phase-change, the vapor-liquid interface becomes extraordinary complicated because of its nonlinearity, variety, and time-dependence behavior induced by phase-change accompanying with heat and mass transfer. Therefore, treatment of the interface is a key problem in the simulation of multiphase flows including bubbly flows. Generally, numerical simulation of bubbly flows can be classified as: the singular interface model and the diffuse interface model. Earlier studies on vapor bubble dynamics were based on the Rayleigh equation and its modification, which were basically related to dealing with zero or one dimensional problems (Plesset & Zwick, 1953). Wittke & Chao (1967) studied the collapse of a spherical bubble with translatory motion. Cao & Christensen (2000) simulated the bubble collapse in a binary solution, in which the Navier-Stokes equation was transformed into the form of the stream function and vorticity in two-dimensional axisymmetric non-orthogonal body-fitted coordinates. Yan & Li (2006) simulated a vapor bubble growth as it rises in uniformly superheated liquid by using two numerical methods based on moving non-orthogonal body-fitted coordinates proposed by Li & Yan (2002a,2002b). Han et al. (2001) used a mesh-free method to simulate bubble deformation and growth in nucleate boiling. Fujita & Bai (1998) used the arbitrary Lagrange-

Eulerian (ALE) method to simulate the growth of a single bubble attached at a horizontal surface with a constant contact angle before its departure. These numerical simulations are the singular interface model, in which the grid is limited so as not to be fit to bubble large deformation in topology, such as coalescence and breakup of the bubble. In such a situation, the diffuse interface model, such as VOF (volume of fluid), the level set and phase field method etc., was proposed to recover the defects of the first kind of model. Tomiyama et al. (1993) simulated a single bubble by using the VOF. Hua & Lou (2007) developed the front tracking method to simulate the bubble rising in the quiescent viscous liquid due to buoyancy. Little progress had been made in the numerical simulation of bubbly flows with phase change based on the diffuse interface model. Son et al. (1998) simulated a growing and departing bubble on a horizontal surface and captured the vapor-liquid interface by the level set method which was modified to include the action of phase change. Ni et al. (2005) simulated the bubbly flows with phase change by the level set method as stated in Son et al. (1998)'s work. In their work, $\nabla \cdot u$ is applied to define the phase change and the interfacial velocity need to be separately obtained from the temperature condition at the interface. Nevertheless, little information in the literatures was reported about the vapor bubbles's behavior with phase change. In particular, few papers have been reported on the propagations of temperature field around a growing and deforming vapor bubble. Due to the complexity of environment about the realistic bubble flow like porous media, the treatment of boundary usually encounters a lot of embarrassment for the above-described methods. This point has limited and weakened the ability of these numerical methods to some extent.

Recently, the lattice Boltzmann method (LBM) became a popular tool to simulate the incompressible viscous flows due to its merits like the ease of boundary treatment and the parallel implementation. In the LB context, there were several models developed for multiphase and multi-component flows in the past two decades. The earlier works were the color method proposed by Rothman & Keller (1998), the potential method by Shan et al. (1993), the free energy method by Swift et al. (1996) and the method by He et al. (1999). These models have not been used in solving practical problems due to the limit of smaller density ratio between phases. Up to 2007, three models of large density ratio were proposed, the first one was an immiscible incompressible two-phase model with large density ratio proposed by Inamuro et al. (2004), the second one was that of Lee et al. (2005) and the third one was proposed by Zheng et al. (2006). Inamuro et al. (2004)'s model was used to track the two-phase interface by applying a diffuse equation which is analogy to the C-H equation. This kind of interface-tracking technique has the same principle as the level set method. In fact, the two-phase interface is also disposed as an index such as 0 and 1. Unlike Inamuro et al. (2004)'s and Lee et al. (2005)'s models, Zheng et al. (2006) approximated the C-H equation to track and define the two-phase interface without the artificial disposal adopted by other models in the physical background. Benefiting from the concept of the order parameter continuum in phase-change process following the regime of Landau mean-field theory, Zheng et al. (2006)'s model can be extended to non-isothermal systems with phase-change.

Therefore, we proposed a hybrid LBM model (Dong et al.,2009), which is a combination of the Zheng et al. (2006)'s multiphase model and a thermal LBM model (Inamuro et al. 2002) and is able to characterize the heat and mass transfer in multiphase flows. In this hybrid model, Zheng et al. (2006)'s model is added with a source term to the corresponding C-H equation to define the phase-change and the thermal LBM model is added by a source term to define the latent heat. The modified C-H equation has a much clearer physical

explanation to the treatment of phase change at the interface, thus enabling to track the interface automatically by following the change of the phase order parameter.

3.1 Zheng's lattice Boltzmann dynamic model

In the simulation of vapor bubbly flows, the binary model proposed by Zheng et al.(2006) is employed to track the dynamic evolution of the flow field. In Zheng et al. (2006)'s model, there are two independent macroscopic parameters, total number density, n=(ρ_A+ρ_B)/2 and number density difference, Φ=(ρ_A-ρ_B)/2, where ρ_A and ρ_B stand for the density of fluid A and fluid B, respectively. The parameter n is proportional to pressure and approximately constant in the whole flow field. The parameter Φ becomes positive in the region where $\rho_A > \rho_B$ and negative in the region with $\rho_A < \rho_B$, and thus it represents two-phase distribution, which is the same as the definition in the Swift et al. (1996)'s model.

Two sets of discretized distribution functions f_i and g_i are used to assign each site, which are related to the parameters n and Φ, respectively. The distribution function f_i can be used to model the transport of mass and momentum, while the distribution function g_i can be employed to track the interface. Thus, the corresponding LB BKG equation is written as follows,

$$f_i\left(x+e_i\Delta t,t+\Delta t\right)-f_i\left(x,t\right)=\Omega_i \tag{24}$$

with

$$\begin{aligned}\Omega_i &= \frac{1}{\tau_n}\left[f_i\left(x,t\right)-f_i^{eq}\left(x,t\right)\right]+\left(1-\frac{1}{2\tau_n}\right)\frac{\omega_i}{c_s^2}\left[\left(e_i-u\right)+\frac{\left(e_i\cdot u\right)}{c_s^2}e_i\right]\left(\mu\phi\nabla\phi+F_b\right)\delta t\\ g_i\left(x+e_i\Delta t,t+\Delta t\right)-g_i\left(x,t\right) &= \left(1-q\right)\left[g_i\left(x+e_i\Delta t,t\right)-g_i\left(x,t\right)\right]\\ &-\frac{1}{\tau_\phi}\left[g_i\left(x,t\right)-g_i^{eq}\left(x,t\right)\right]\end{aligned} \tag{25}$$

where, x is restricted to sites on the lattice and t is the discrete time, τ_n, τ_Φ is the dimensionless relaxation parameter. The equilibrium distribution functions to satisfy the conservation laws can be expressed as follows:

$$n=\sum_i f_i^{(eq)} \tag{26}$$

$$u=\frac{1}{n}\left[\sum_i f_i^{(eq)}e_i+\frac{1}{2}\left(\mu_\phi\nabla\phi+F_b\right)\right] \tag{27}$$

$$\sum_i f_i^{(eq)}e_{i\alpha}e_{i\beta}=\left(\phi\mu_\phi+c_s^2n\right)\delta_{\alpha\beta}+nu_\alpha u_\beta \tag{28}$$

$$\sum_i g_i=\sum_i g_i^{(eq)}=\phi \tag{29}$$

$$\sum_i g_i^{(eq)}e_{i\alpha}=\frac{\phi}{q}u_\alpha \quad \text{with} \quad q=\frac{1}{\tau_\phi+0.5} \tag{30}$$

$$\sum_i g_i^{(eq1)} e_{i\alpha} e_{i\beta} = \Xi_{\alpha\beta} \quad \text{with } \Xi_{\alpha\beta} = \Gamma \mu_\phi \delta_{\alpha\beta} \tag{31}$$

where, u is the macroscopic velocity of the fluid. The chemical potential is given by:

$$\mu_\phi = A\left(4\phi^3 - 4\bar{\phi}^2 \cdot \phi\right) - K\nabla^2\phi \tag{32}$$

By performing a Chapman-Enskog expansion to Eqs. (24) and (25), the macroscopic equations for n and ϕ in the second order precision can be derived as follows.

$$\frac{\partial n}{\partial t} + \nabla \cdot (nu) = 0 \tag{33}$$

$$\frac{\partial (nu)}{\partial t} + \nabla \cdot (nuu) = -\nabla\left(P + \phi\mu_\phi\right) + \phi\nabla\mu_\phi + \nu\nabla^2(nu) + F_b \tag{34}$$

$$\frac{\partial \phi}{\partial t} + \nabla \cdot (\phi u) = \theta_M \nabla^2 \mu_\phi \tag{35}$$

where, $\theta_M = q\left(\tau_\phi q - 0.5\right)\delta\Gamma$.

From Eqs. (33), (34) and (35), the corresponding equilibrium distribution functions can be constructed as follows:

$$f_i^{(eq)} = \omega_i A_i + \omega_i n\left(3e_{i\alpha}u_\alpha - \frac{3}{2}u^2 + \frac{9}{2}u_\alpha u_\beta e_{i\alpha}e_{i\beta}\right) \text{ (Based on D2Q9)} \tag{36}$$

where $A_1 = \frac{9}{4}n - \frac{15\left(\phi\mu_\phi + \frac{1}{3}n\right)}{4}$ $\qquad A_{i(i=2,\ldots,9)} = 3\left(\phi\mu_\phi + \frac{1}{3}n\right)$,

$$\omega_1 = \frac{4}{9},\ \omega_{i(i=2,\ldots,5)} = \frac{1}{9},\ \omega_{i(i=6,\ldots,9)} = \frac{1}{36}.$$

$$g_i^{(eq)} = A_i + B_i\phi + C_i\phi e_i \cdot u \text{ (Based on D2Q5)} \tag{37}$$

where $B_1 = 1$, $B_i = 0\left(i \neq 1\right)$, $C_i = \frac{1}{2q}$, $A_1 = -2\Gamma\mu_\phi$, Γ is the diffusion coefficient.

3.2 Inamuro's thermal LBM model

Inamuro et al. (2002) proposed a model for the diffusion system including heat transfer. In their model, there is the simplest distribution function h_i among other thermal models. The LBM equation can be written as:

$$h_i\left(x + e_i\Delta t, t + \Delta t\right) - h_i\left(x,t\right) = -\frac{1}{\tau_T}\left[h_i\left(x,t\right) - h_i^{eq}\left(x,t\right)\right], \tag{38}$$

where, τ_T is the dimensionless relaxation parameter.
The equilibrium distribution function (based on D2Q9) for the thermal model can be stated as follows:

$$h_i^{eq}(x,t) = \omega_i T\left(1 + 3e_i \cdot u\right) \tag{39}$$

where, T is the temperature.
The diffusion equation corresponding to the thermal model can be expressed as:

$$\frac{\partial T}{\partial t} + u_\alpha \frac{\partial T}{\partial x_\alpha} = \delta \frac{1}{3}\left(\tau_T - \frac{1}{2}\right)\frac{\partial^2 T}{\partial x_\alpha^2} \tag{40}$$

3.3 Phase change based on assumption of Stefan boundary

In the Landau mean-field theory, the phase change is considered as a continuous variable of order parameter. So, the corresponding C-H equation can also be extended to include a phase-change term in the non-isothermal system. The phase change can be identified by calculating the change of phase order parameter. Such a treatment can make the interface be automatically traced based on the change of the phase order parameter. At the same time, the corresponding phase-change latent heat is also considered in the LBM model.
In order to simulate the departure of the vapor bubble from a heated wall and its growth in superheated liquid, two assumptions have to be considered as follows:

1. The vapor inside the bubble is pure and approximately incompressible;
2. The heat transferred from the liquid to the interface is completely used to evaporate the liquid at the interface based on the Stefan boundary, which results in the net increase of bubble volume.

A vapor bubble of volume $V_b^{'}$ is introduced into the superheated liquid. In time interval from t' to $t' + \Delta t'$, the mass transferring into the bubble during the phase change process is expressed as:

$$\int_{V'} \frac{\Delta m}{\Delta t'} dV' = \int \rho_G \frac{dV_b'}{dt} dV' = -\frac{1}{h_{fg}} \int_{S'} \lambda_l \left(\frac{\partial T'}{\partial x'}\right)_b dS' = -\frac{1}{h_{fg}} \int_{V'} \lambda_l \left(\frac{\partial^2 T'}{\partial x'^2}\right)_{V'} dV' \tag{41}$$

where, ρ_G is vapor density, T' is temperature, h_{fg} and λ_l are the latent heat of evaporation and the thermal conductivity, respectively.
Based on phase order parameter, the phase-change is taken into account and expressed as:

$$\dot{\phi} = \frac{\Delta \phi}{\Delta t} = \frac{\left(\rho_L - \Delta m\right) - \left(\rho_G + \Delta m\right)}{2\Delta t'} - \frac{\rho_L - \rho_G}{2\Delta t'} = -\frac{\Delta m}{\Delta t'} \tag{42}$$

Equation (42) is normalized by the following equations:

$$V_b = \frac{V_b'}{V_{bo}'},\ t = \frac{t' U_T}{d_e},\ T = \frac{T' - T_\infty'}{T_b' - T_\infty'},\ x = \frac{x'}{d_e} \tag{43}$$

where V'_{bo} is the bubble volume at an initial stage, d_e is the equivalent diameter of the bubble, U_T is the terminal rising velocity of the bubble and T'_∞ is the temperature of liquid at the top boundary of the domain. So, the dimensionless form of equation (41) is written as:

$$\rho_G \frac{dV}{dt} = -\frac{\lambda_l \left(T_b' - T_\infty'\right)}{h_{fg} U_T d_e} \left(\frac{\partial^2 T}{\partial x^2}\right) \tag{44}$$

By introducing the *Jacob* number $Ja = \frac{1}{h_{fg}} C_{pl}\left(T_b' - T_\infty'\right)$ and the Peclet number $Pe = \frac{\rho_L U_T d_e C_{pl}}{\lambda_l}$, Eq. (41) can be expressed as:

$$\frac{dV}{dt} = -\frac{\rho_L}{\rho_G} \frac{Ja}{Pe} \left(\frac{\partial^2 T}{\partial x^2}\right) = \frac{\dot{\phi}}{\rho_L - \rho_G} \tag{45}$$

To include the phase change, the LBM equation (2) when $\phi < 0$ is rewritten as:

$$\begin{aligned} &g_i\left(x + \vec{e}_i \Delta t, t + \Delta t\right) - g_i\left(x,t\right) = \left(1-q\right)\left[g_i\left(x + \vec{e}_i \Delta t, t\right) - g_i\left(x,t\right)\right] \\ &-\frac{1}{\tau_\phi}\left[g_i\left(x,t\right) - g_i^{eq}\left(x,t\right)\right] + \omega_i \dot{\phi} \end{aligned} \tag{46}$$

In the LBM Eqs. (37), $\delta \frac{1}{3}\left(\tau_T - \frac{1}{2}\right) = \frac{1}{Pe}$. So when $\phi < 0$, the latent heat term $\frac{\rho_G}{\rho_L\left(\rho_L - \rho_G\right)} \cdot \frac{\dot{\phi}}{Ja}$ can be added into the LBM Eqs. (38).

$$h_i\left(x + \vec{e}_i \Delta t, t + \Delta t\right) - h_i\left(x,t\right) = -\frac{1}{\tau_T}\left[h_i\left(x,t\right) - h_i^{eq}\left(x,t\right)\right] + \omega_i \frac{\rho_G}{\rho_L\left(\rho_L - \rho_G\right)} \frac{\dot{\phi}}{Ja} \tag{47}$$

By using the Taylor series expansion and the Chapman-Enskog expansion with respect to Eqs. (46) and (47), the improved governing equations when Φ<0 can be approximately recovered In the second order form as

$$\frac{\partial \phi}{\partial t} + \nabla \cdot \left(\phi u\right) = \theta_M \nabla^2 \mu_\phi - \frac{\rho_L\left(\rho_L - \rho_G\right)}{\rho_G} \frac{Ja}{Pe} \left(\frac{\partial^2 T}{\partial x^2}\right) \tag{48}$$

$$\frac{\partial T}{\partial t} + u_\alpha \frac{\partial T}{\partial x_\alpha} = \delta \frac{1}{3}\left(\tau_T - \frac{1}{2}\right) \frac{\partial^2 T}{\partial x_\alpha^2} - \frac{\rho_G}{\rho_L\left(\rho_L - \rho_G\right)} \frac{\dot{\phi}}{Ja} \tag{49}$$

To validate the hybrid LBM model including phase change, a phase-change problem with available analytical solution is chosen as a test case, which is the bubble growth in a superheated liquid layer of infinite extent under the condition of no gravity. Initially, a small spherical bubble is rested in the superheated liquid layer. Numerical mesh system has 100*100 numerical cells. A comparison between numerical results and analytical solutions has been carried out and tabulated in Tab.1. It can be discovered that the numerically predicted bubble growth is in good agreement with the Mikic et al. (1970)'s analytical solution, which indicated that the treatment of phase change based on phase order parameter is feasible for the hybrid LBM model.

Jacob/Radius \ Time		10	20	30	40	50
Ja=0.0006	Mikic et al. (1970)	0.04375	0.06375	0.07937	0.09324	0.10552
	Present work	0.04339	0.06158	0.0744	0.08519	0.09811
Ja=0.0009	Mikic et al.(1970)	0.06551	0.09243	0.1136	0.1303	0.14406
	Present work	0.06013	0.08691	0.10819	0.12704	0.14412
Ja=0.0012	Mikic et al.(1970)	0.08736	0.12382	0.15126	0.17416	0.19613
	Present work	0.08197	0.11746	0.14672	0.17236	0.19579

Table 1. Comparison of the calculated radius of bubble growth with the Mikic's solution (*Pe*=3000)

Accounting for the buoyancy force as stated in the reference (Zheng et al., 2006), we define the Eo, M and Re as follows:

$$Eo = \frac{g(\rho_H - \rho_L)d^2}{\sigma},\ M = \frac{g(\rho_H - \rho_L)\mu_H^4}{\rho_H^2\sigma^3},\ \mathrm{Re} = \frac{\rho_H V_T d}{\mu_H}$$

The bubble volume is calculated by $V_b'(t) = \sum_{\phi<0}\phi(t) \Big/ \sum_{\phi<0}\phi(t_0)$ and the growth rate of bubble volume is calculated by $\dot{V}_b' = \left[V_b'(t+\Delta t) - V_b'(t)\right]/\Delta t$.

3.4 Numerical simulation of vapor bubble growth on and departure from a superheated wall

3.4.1 The Briant's treatment of partial wetting boundary

The Briant's treatment of the partial wetting boundary is introduced into the hybrid LBM model elaborated above. The details of this treatment is available in the literature (Biant et al., 2002). Adjustment aroused by the wetting boundary is considered as follows:

1. A little order parameter non-conservation induced by the distribution functions at inflow and outflow on the wetting boundary is counted and apportioned to every node occupied by the bubble.
2. The surface tension forces between the wall and fluids are adjusted to guarantee the vapor bubble to be able to expand and depart in integrality on the wetting boundary like action of an actual vapor bubble in practical processes. Therefore, according to the Young's law ($\cos\theta_w = \frac{\sigma_{SG} - \sigma_{SL}}{\sigma_{LG}}$), the order parameter Φ_G is set as -90 or smaller in this work. The contact angle is adjusted in relative to the corresponding Φ_L. The comparison of resulting effects is schematically shown in Fig.6.

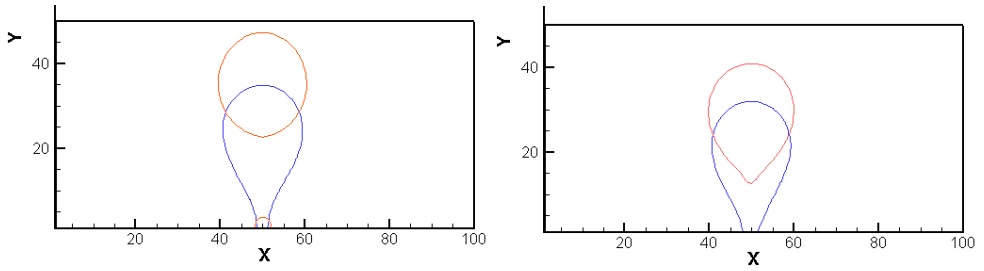

Fig. 6. Effect of different adsorb ability (left: Φ_G<-90; right: Φ_G>-90) on wetting boundary

The corresponding properties are taken as follows;

$$\rho_L = 1000\,,\ \rho_G = 1\,,\ \Gamma = 650\,,\ Peclet = 3000\,,\ Eo = 72\,,\ M = 3.44\,.$$

The mesh of the domain is generated as 100×50. A spherical bubble with radius of 3 is located in (50, 2). The flow field is surrounded with one partial wetting boundary (bottom boundary), one extrapolated-boundary (top boundary) and two stationary walls (left and right boundaries). The initial thermal boundary layer thickness is calculated from the correlation (Han et al., 1965):

$$\delta = 3/2 \frac{(T_w - T_\infty)R_c}{T_w - T_{sat}\left[1-(2\sigma / R_c\rho_v L)\right]}$$

where, R_c is the initial bubble radius.

As far as the bubble departure diameter is concerned, different physical parameters, such as body force, surface tension force, and partial wetting boundary and *Jacob* number are considered and investigated. The most widely used correlation for the bubble departure diameter on the heated surface was proposed by Fritz (1935), in which the bubble departure was determined by a balance between the buoyancy and surface tension force acting normal to the solid surface. Based on the experimental measurement of the departure diameter over a pressure range, and observation of the influence of the bubble growth rate on the departure diameter, Staniszewki (1959) modified the Fritz (1935) equation to obtain the departure diameter correlation as follows:

$$D_d = 0.0071\beta\left(\frac{2\sigma}{g\Delta\rho}\right)^{\frac{1}{2}}\left(1+34.3\frac{\partial D}{\partial t}\right)$$

where $\partial D/\partial t$ denotes the bubble growth rate.

Using the present method, the effect of physical parameters on the departure diameter is investigated. The calculated departure diameter for different gravity forces and surface tension forces are regressed to functions as $D \propto g^{-0.472}$ and $D \propto \sigma^{0.5}$. The result is in very good agreement with the Fritz (1935) relation. The calculated correlation of departure diameter and the *Jacob* number is a regressed function of $D \propto Jacob$. Because the *Jacob* number is a dominant factor of the bubble growth rate, the result shows indirectly the correlation between the departure diameter and the bubble growth as predicted by

Staniszewki (1959)'s correlation. The departure diameter changes with the adjustment of Φ_L. Because the contact angle is determined by Φ_L and Φ_G, the adjustment of Φ_L can change the contact angle and influence the bubble departure diameter. The precise quantitative relation between contact angle and departure diameter is still under investigation.

3.4.2 Propagation of flow field

Fig.7 presents the evolution of flow field accompanying with the corresponding stream traces. It can be seen from these figures how the bubble growth and departure affect the flow field. In the early stage, due to the bubble growth or expanding on the wetting boundary, two vortexes are formed on both sides of the bubble. The vortexes (including shape and intensity) are enforced to develop with the bubble further growing up. With the process continuing, the change of shape induces the vertex breaking up into twin-vortex. With the bubble starting with departure, the twin-vortexes on both sides incorporate into a single vortex and rise up with the bubble. In the late stage, the vortexes further strengthen their scopes and intensity and rise up accompanying with the bubble departure.

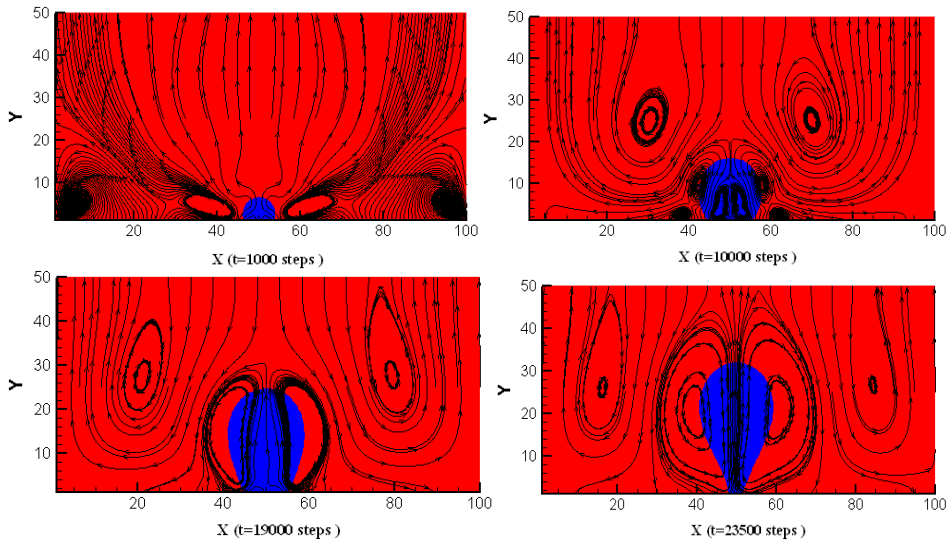

Fig. 7. Propagation of flow field

3.4.3 Propagation of temperature field

The evolution of temperature field is depicted in Fig.8. The effects of the bubble growth and departure on the temperature field around the bubble are clearly seen. In the early stage, due to its small volume, the bubble phase-change is dependent on the heat transfer in the micro layer and macro layer both. With growing up of the bubble, the contribution of heat transfer in the macro layer is gradually weakened. In the process of the bubble departure, the forced convection induced by the ascending bubble greatly affects the temperature field. The disturbance to the temperature field, in return, influences the bubble growth and departure to some extent.

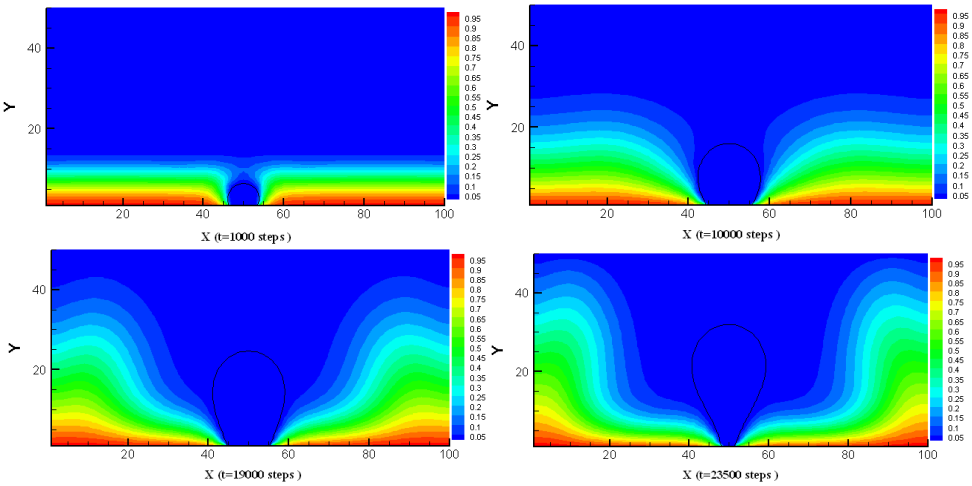

Fig. 8. Propagation of temperature field

3.4.4 Characteristics of two bubbles growth on and departure from the wall

Based on the LBM elaborated above, two bubbles coalescence dynamics on a horizontal surface are also investigated. The simulation focuses on the effect of twin-bubble distance (*dist*) on the bubble growth, coalescence and departure. The result is shown in Fig.9 and the bubble diameter is calculated from the summation of the two bubbles' volume. It is easily

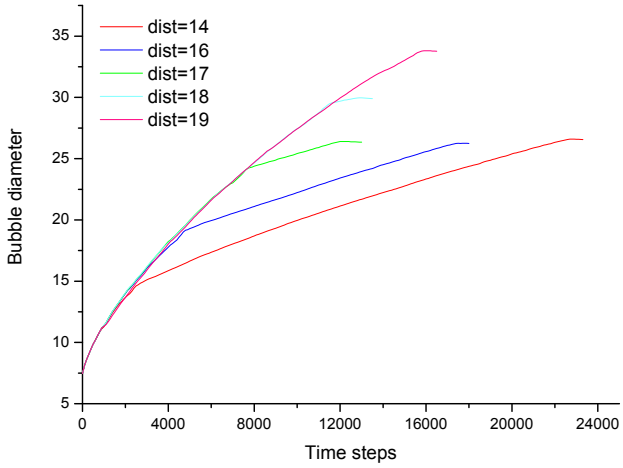

Fig. 9. Bubble growth and departure in different coalescence conditions

found that the final result is closely related to twin-bubble distance. With the distance increasing, the coalescence is delayed and the departure time is shortened to some extent. But the diameter of bubble departure does not change with the coalescence of bubbles of

different distance, like *dist*=14, 16, and 17. With the distance increasing further, the effect of coalescence on bubble growth rate disappears except the diameter of bubble departure is becoming larger, (see cases with *dist*=18 and 19). When the bubble departs from the surface in its integrality, the bubble growth rate tends to become zero, i.e.; the growth ceases.

Figs.10 and 11 show the evolving process of flow and temperature field, respectively. From Fig. 10, it is seen that before the bubble coalescence, two vortexes are forming on the outward side of the twin-bubbles, respectively. With growing up and coalescence of the bubbles, both vortexes are strengthened. They both are split into one clockwise vortex and one anti-clockwise vortex with the bubbles further growing up. After the two bubbles coalesce, we see firstly four bubbles with 2 of them locating on one side of bubble and the other 2 on the other side. Then the merged large bubble further grows up, until it departs from the wall. Vortexes on the same side of the merged bubble are developing further and converge into one. Afterwards, we see one bubble ascending in the liquid with 2 vortexes locating on right and left side respectively. Fig.11 shows the related temperature field. It is easily found that the forced convection directly influences the temperature field especially after bubble coalesces and departs.

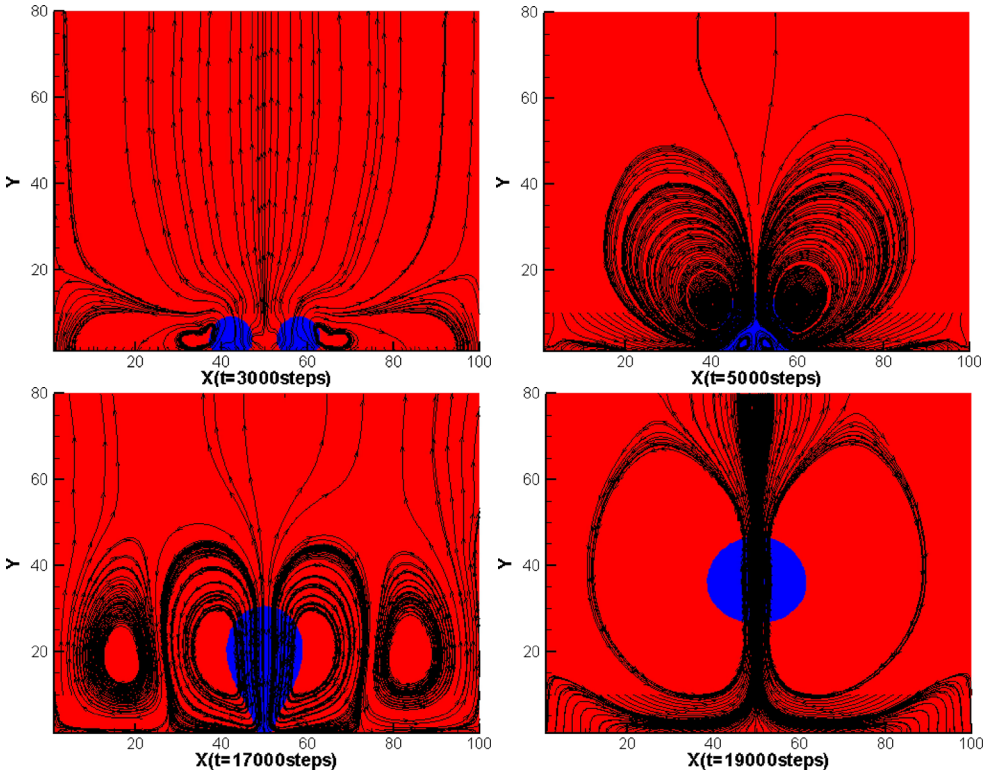

Fig. 10. Propagation of flow field

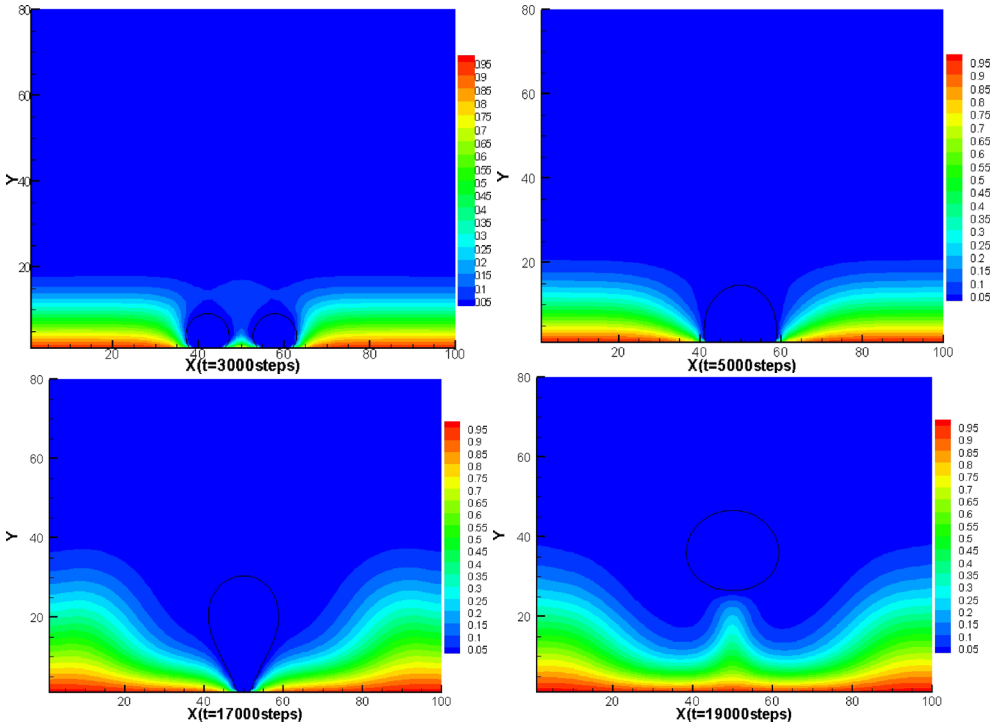

Fig. 11. Propagation of temperature field

4. Concluding remarks

In this chapter we reviewed the current state-of-the-art and recent advances of LBM through case studies. We presented firstly an improved LBM for modeling the mass transport in multi-component systems, which was used to simulate the mixing process in a rotating packed bed with a serial competitive reaction (A+B→R, B+R→S; A, B, R, and S denote different components.) occurring therein. The obtained results provide some guidance for further studying the forced mass-transfer in and for the design of the real rotating packed-bed in industries. Secondly, with a purpose to simulate phase change process, the LBM multiphase model being able to handle a large ratio of density between phases is combined with the LBM thermal model to form a hybrid LB model. By introducing the Briant's treatment to partial wetting boundary, this hybrid model was used to investigate growth and departure of a single bubble, and coalescence of twin-bubbles, on (or from) a heated horizontal surface. Numerical results exhibited correct parametric dependence of the departure diameter as compared to the experimental correlation available in the literatures. The capability and suitability of this hybrid LB model for modeling complex fluid and heat/mass transfer systems are thus demonstrated. Due to its terseness advantage in the treatment of complex boundary, our future work will further extend this hybrid model to simulate multiphase and/or multi-component flows in complex systems, such as in porous media of complex micro-pore structures encountered fuel cell (battery) realms.

5. Acknowledgement

Financial support received partially from the CAS "100 Talent" Program (FJ) is gratefully acknowledged.

6. References

Alexander, F, J., Chen , S., & Sterling J D. (1993). Lattice Boltzmann thermo hydrodynamics [J]. Phys. Rev E, , 47: 2249-2252

Bhaga, D. & Weber, M. E. (1981).Bubbles in viscous liquid: shapes, wakes and velocities, J. Fluid Mech.Vol.105.pp.61~85.

Bartoloni, A., Battisita, C., & Cabasino, S. (1993). Lbr Simulations of Rayleigh-Benard convection on the Ape100 parallel process [J]. Int.J.Mod.Phys, C4: 993-1006.

Briant, A,J., Papatzacos, P., & Yeomans, J,M. (2002). Lattice Boltzmann simulations of contact line motion in a liquid-gas system, Philos.Trans.Roy.Soc.London A 360: 485-495

Chen, H., Teixeira, C., & Molving K. (1997). Digital Physics Approach to computational fluid dynamics: some basic theoretical features [J]. Int. J. Mod. Phys, 8: 675-684.

Cao, J. & Christensen, R. N. (2000). Analysis of moving boundary problem for bubble collapse in binary solutions, Numerical Heat Transfer. Part A, Vol.38. pp.681~699.

Dong, Z., Li ,W., & Song, Y.(2009). Lattice Boltzmann simulation of growth and deformation for a rising vapor bubble through superheated liquid, *Numerical Heat Transfer*. Part A, 55:381-400.

Fritz, W. & Maximun. (1935). volume of vapor bubbles, Physik Zeitschr. 36 : 379-384

Fujita, Y. & Bai, Q. (1998). Numerical simulation of the growth for an isolated bubble in nucleate boiling, Proceedings of 11th IHTC. Kyongiu, Korea, August 23-28, Vol.2. pp. 437~442.

Frish, U., Hasslacher, B., & Pomeau, Y. (1986). Lattice-Gas Automata for the Navier-Stokes equation [J]. Phys.Rev. Lett, , 56 (14): 1505-1508.

He, X., Chen, S., & Zhang, R.(1999). A lattice Boltzmann scheme for incompressible multiphase flow and its application in simulation of Rayleigh-Taylor instability. J.Comput.Phys. 152 (2) 642-663.

Han, C. & Griffith, P. (1965). The mechanism of heat transfer in nucleate pool boling. Int.J.Heat MassTransfer 8, 887-914.

Han, Y. & Seiichi, K.Y.O. (2001). Direct calculation of bubble growth, departure, and rise in nucleate pool boiling, Int. J. of Multiphase Flow.Vol.27, pp.277~298.

Hua, J. & Lou, J. (2007). Numerical simulation of bubble rising in viscous liquid, J. Comp. Phys. Vol.222. pp.769~795.

Inamuro, T., Ogata, T., Tajima, S., & Konishi, N.(2004). A Lattice Boltzmann method for incompressible two-phase flows with large density differences. J. Comp. Phys. Vol.198. pp.628~644.

Inamuro, T., Yoshino, M., Inoue. H, Mizuno. R., & Ogino F. (2002). A lattice Boltzmann method for a binary miscible fluid mixture and its application to a heat-transfer problem [J].J. Comp. Phys, 179: 201-215.

Luo, X., Ni, M., Ying, A., & Abdou, M.(2005). Numerical modeling for multiphase incompressible flow with phase change, Numercial Heat Transfer. Part.B. Vol.48. pp.425~444

Liu, J. (2000). Study no micro-mixing and synthesis of nanometer particle of strontium carbonate by mixing two section of solutions in Rotating Packed Bed [D].Beijing: Beijing University of Chemical Technology.

Li, W. & Yan, Y. (2002). An alternating dependent variables(ADV) method for treating slip boundary conditions of free surface flows with heat and mass transfer, Numerical Heat Transfer (An International Journal of Computation and Methodology), Part B, Vol. 41, No.2, pp. 165~189.

Li, W. & Yan, Y.(2002). A direct-predictor method for solving terminal shape of a gas bubble rising through a quiescent liquid, Numerical Heat Transfer (An International Journal of Computation and Methodology), Part B, Vol. 42, No.1, pp. 55~71.

Lee, T. & Lin, C. (2005). A stable discretization of the lattice Boltzmann equation for simulation of in compressible two-phase flows at high density ratio, J.Comput.Phys.206:16-47.

Mukherjee, A. & Kandlikar, S.G.(2007). Numerical study of single bubbles with dynamic contact angle during nucleate pool boiling, Int, J. Heat and Mass Transfer, 50 : 127-138.

Mikic, B.B., Rohsenow, W.M., & Griffith, P.(1970). On bubble growth rate, Int. J. Heat Mass Transfer 13, 657-666 .

Plesset, M.S. & Zwick, S.A.(1953). The growth of vapor bubble in superheated liquids, J. Applied Physics.Vol.25.No.4.pp.293~500.

Rothman, D.H. & Keller, J.M.(1998). Immiscible cellular-automaton fluid, J. Statist. Phys. 52. pp.1119~1127.

Staniszewski, B.E. (1959). Nucleate boiling bubble growth and departure, MIT Tech..Rep.No.16, Cambridge, MA.

Soe, M., Vahala, G., Pavlo, P., Vahala, L., & Chen, H. (1998).Thermal lattice Boltzmann simulations of variable Prandtl number turbulent flows [J]. Phys. Rev E, 57(4): 4227-4237.

Shan, X. (1997). Simulation of Rayleigh-Benard convection using a lattice Boltzmann method [J]. Phys.Rev.E, 55: 2780-2788

Son, G. & Dhir, V.K. (1998). Numerical simulation of a single bubble during particle nucleate boiling on a horizontal surface, Proceedings of 11th IHTC. Kyongiu, Korea, August 23-28, Vol.2. pp.533~538.

Shan, X. & Chen, H. (1993). Lattice Boltzmann model for simulating flows with multiple phases and components, Phys. Rev. E47(3).pp.1815~1819.

Swift, M.R., Orlandini, E., Osborn,W.R., Yeomeans, J.M. (1996). Lattice Boltzmann simulations of liquid-gas and binary fluid systems, Phys.Rev. E54.pp.5041~5052.

Tomiyama, A., Sou, A.; Minagawa, H., & Sakaguchi, T. (1993). Numerical analysis of a single bubble by VOF method, JSME Int J. Series B. Vol.36.No.1.

Vahala, G., Pavlo, P., Vahala, L., & Martys, N. S. (1998). Thermal lattice-Boltzmann models (TLBM) for compressible flows[J]. Int. J. Mod. Phys C, 9: 1247-1261.

Vahala, L., Wah, D., Vahala, G., Carter, J., & Pavlo, P. (2000).Thermal lattice Boltzmann simulation for multispecies fluid equilibration[J]. Phys. Rev E, 62: 507-516.

Wittke, D.D. & Chao, T.B. (1967). Collapse of vapour bubbles with translatory motion, J. Heat Transfer. Vol.89. pp.17~24.

Yan, Y., & Li, W. (2006). Numerical modelling of a vapors bubble growth in uniformly superheated liquid, Int J. of Numerical Methods for Heat & Fluid Flow, Vol.16. No.7. pp.764~778.

Zheng, H.W., Shu, C., & Chew, Y.T.(2006). A Lattice Boltzmann for multiphase flows with large density ratio, J. Comput. Phys. Vol.218. pp.353~371.

9

Convergence Acceleration of Iterative Algorithms for Solving Navier–Stokes Equations on Structured Grids

Sergey Martynenko
Central Institute of Aviation Motors
Russia

1. Introduction

Basic tendency in computational fluid dynamics (CFD) consists in development of black box software for solving scientific and engineering problems. Numerical methods for solving nonlinear partial differential equations in black box manner should satisfy to the requirements:
a) the least number of the problem-dependent components
b) high computational efficiency
c) high parallelism
d) the least usage of the computer resources.
We continue with the 2D ($N = 2$) Navier–Stokes equations governing flow of a Newtonian, incompressible viscous fluid. Let $\Omega \in \mathbb{R}^N$ be a bounded, connected domain with a piecewise smooth boundary $\partial\Omega$. Given a boundary data, the problem is to find a nondimensional velocity field and nondimensional pressure such that:
a) continuity equation

$$\frac{\partial u}{\partial x} + \frac{\partial v}{\partial y} = 0\,, \tag{1}$$

b) X-momentum

$$\frac{\partial u}{\partial t} + \frac{\partial (u^2)}{\partial x} + \frac{\partial (vu)}{\partial y} = -\frac{\partial p}{\partial x} + \frac{1}{\mathsf{Re}}\left(\frac{\partial^2 u}{\partial x^2} + \frac{\partial^2 u}{\partial y^2}\right), \tag{2}$$

c) Y-momentum

$$\frac{\partial v}{\partial t} + \frac{\partial (uv)}{\partial x} + \frac{\partial (v^2)}{\partial y} = -\frac{\partial p}{\partial y} + \frac{1}{\mathsf{Re}}\left(\frac{\partial^2 v}{\partial x^2} + \frac{\partial^2 v}{\partial y^2}\right). \tag{3}$$

Reynold number Re is defined as

$$\mathsf{Re} = \frac{\rho u_s l_s}{\mu}\,,$$

where ρ and μ are density and viscosity, respectively. Choice of the velocity scale u_s and geometric scale l_s depends on the given problem.

Equations (1)–(3) can be rewritten in the operator form

$$\begin{cases} \mathcal{N}(\vec{V}) + \nabla P = F \\ \nabla \vec{V} = G \end{cases}, \tag{4}$$

where $\mathcal{N}$ is nonlinear convection-diffusion operator, F and G are source terms, $\vec{V}$ and P are velocity and pressure, respectively. It is assumed that the operator $\mathcal{N}$ accounts boundary conditions. Note that 2D and 3D Navier–Stokes equations can be written as equation (4), where first and second equations abbreviate momentum and continuity equations.
Linearized discrete Navier–Stokes equations can be written in the matrix form

$$\begin{pmatrix} A & B^T \\ B & 0 \end{pmatrix} \begin{pmatrix} \boldsymbol{\alpha} \\ \boldsymbol{\beta} \end{pmatrix} = \begin{pmatrix} \boldsymbol{f} \\ \boldsymbol{g} \end{pmatrix} \tag{5}$$

in which $\boldsymbol{\alpha}$ and $\boldsymbol{\beta}$ represent the discrete velocity and discrete pressure, respectively. Here nonsymmetric A is a block diagonal matrix corresponding to the linearized discrete convection-diffusion operator $\mathcal{N}$. The rectangular matrix B^T represents the discrete gradient operator while B represents its adjoint, the divergence operator.
Large linear system of saddle point type (5) cannot be solved efficiently by standard methods of computational algebra. Due to their indefiniteness and poor spectral properties, such systems represent a significant challenge for solver developers Benzi et al. (2005).
Preconditioned Uzawa algorithm enjoys considerable popularity in computational fluid dynamics. The iterations for solving the saddle point system (5) are given by

$$\begin{cases} A\boldsymbol{\alpha}^{(k+1)} = -B^T\boldsymbol{\beta}^{(k)} + \boldsymbol{f} \\ Q\boldsymbol{\beta}^{(k+1)} = Q\boldsymbol{\beta}^{(k)} + (B\boldsymbol{\alpha}^{(k+1)} - \boldsymbol{g}) \end{cases}, \tag{6}$$

where the matrix Q is some preconditioner.
Preconditioned Uzawa algorithm (6) defines the following way for improvement of the solvers for the Navier–Stokes equations:
1) *development of numerical methods for solving the boundary value problems.*
Uzawa iterations require fast numerical inversion of the matrices A and Q. Now algebraic and geometric multigrid methods are often used for the given purpose Wesseling (1991). Multigrid methods give algorithms that solve sparse linear system of N unknowns with $O(\mathrm{N})$ computational complexity for large classes of problems. Variant of geometric multigrid methods with the problem-independent transfer operators for black box or/and parallel implementation is proposed in Martynenko (2006; 2010).
2) *development of preconditioning.*
Error vector in Uzawa iterations satisfies to the condition

$$\left\|\boldsymbol{\beta} - \boldsymbol{\beta}^{(k+1)}\right\| \leqslant \left\|I - Q^{-1}BA^{-1}B^T\right\| \cdot \left\|\boldsymbol{\beta} - \boldsymbol{\beta}^{(k)}\right\|,$$

where $\boldsymbol{\beta}$ is an exact solution. Choice of the preconditioner Q so

$$\left\| I - Q^{-1} B A^{-1} B^T \right\| \leqslant q < 1$$

guarantees geometric convergence rate of the Uzawa iterations

$$\left\| \boldsymbol{\beta} - \boldsymbol{\beta}^{(k+1)} \right\| \leqslant q^{k+1} \left\| \boldsymbol{\beta} - \boldsymbol{\beta}^{(0)} \right\|.$$

Unfortunately the preconditioner Q is strongly problem-dependent component of the Uzawa algorithm. Additional problem arises at formulation of the boundary conditions for Q. As a rule, the preconditioner has some relaxation parameters and determination of their optimal values is sufficiently difficult problem. Now construction of the preconditioner is subject of intensive study Benzi et al. (2005).

3) *development of new approaches for convergence acceleration* of iterative algorithms for solving saddle point problems.

The main obstacles to be overcome are execution time requirements and the generation of computational grids in complex three-dimensional domains Benzi et al. (2005). Recently convergence acceleration technique based on original pressure decomposition has been proposed for structured grids Martynenko (2009). The technique can be used in black box software. The chapter represents detailed description of the approach and its application for benchmark and applied problems.

2. Remarks on solvers for simplified Navier–Stokes equations

Limited characteristics of the first computers and absence of efficient numerical methods put difficulties for simulation of fluid flows based on the full Navier–Stokes equations. As a result, computational fluid dynamics started from simulation of the simplest flows described by the simplified Navier–Stokes equations.

As an example, we consider 2D laminar flow between parallel plates. Figure 1 represents geometry of the problem. Assuming that the pressure is not changed across the flow ($p'_y = 0$ in case of $L \gg 1$), full Navier–Stokes equations can be reduced to the simplified form:

a) X-momentum and mass conservation equations

$$\begin{cases} \dfrac{\partial u}{\partial t} + \dfrac{\partial (u^2)}{\partial x} + \dfrac{\partial (vu)}{\partial y} = -\dfrac{\partial p}{\partial x} + \dfrac{1}{\mathrm{Re}} \left(\dfrac{\partial^2 u}{\partial x^2} + \dfrac{\partial^2 u}{\partial y^2} \right) \\ \displaystyle\int_0^1 u(t,x,y)\, dy = \int_0^1 u(t,0,y)\, dy \end{cases}, \tag{7}$$

b) continuity equation (1).

Since the mass conservation equation follows from the continuity equation (1), system (7) must be solved first. Solution of system (7) gives velocity components u and pressure p. After that the continuity equation (1) is used for determination of v. The computations are repeated until the convergent solution will be obtained.

Let us consider solution of system (7) in details. Assume that an uniform computational grid ($h = h_x = h_y$) is generated. Linearized finite-differenced equations with block unknowns

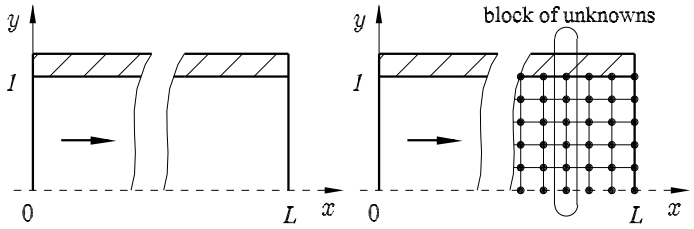

(a) Geometry of problem about the flow between parallel plates (b) Block ordering of unknowns

Fig. 1. Flow between parallel plates

ordering shown on Figure 1 are written as

$$\begin{cases} a_j u_{ij-1}^{(n+1)} + b_j u_{ij}^{(n+1)} + c_j u_{ij+1}^{(n+1)} = p_i^{(n+1)} + d_j \\ \sum_{j=1}^{N_y} u_{ij}^{(n+1)} = \frac{1}{h} G_0 \end{cases}, \tag{8}$$

where

$$G_0 = \int_0^1 u(t,0,y)\, dy$$

is the given inlet mass flow rate and superscript n denotes time layer. Missing the superscript $(n+1)$, the system (8) can be rewritten in the matrix form

$$\begin{pmatrix} b_1 & c_1 & & & \cdots & 1 \\ a_2 & b_2 & c_2 & & \cdots & 1 \\ & a_3 & b_3 & c_3 & \cdots & 1 \\ & & a_4 & b_4 & \cdots & 1 \\ \cdots & \cdots & \cdots & \cdots & \cdots & \cdots \\ 1 & 1 & 1 & 1 & \cdots & 0 \end{pmatrix} \begin{pmatrix} u_{i1} \\ u_{i2} \\ u_{i3} \\ u_{i4} \\ \cdots \\ p_i \end{pmatrix} = \begin{pmatrix} d_1 \\ d_2 \\ d_3 \\ d_4 \\ \cdots \\ h^{-1} G_0 \end{pmatrix}. \tag{9}$$

Comparison of systems (9) and (5) shows that solution of the simplified Navier–Stokes equations (7) also is reduced to solution of the saddle point system. The principal difference between systems (9) and (5) consists in size of zero block in the coefficient matrix. Since the zero block in system (9) has the least size 1×1 because of the pressure is independent on y, efficient iterative algorithms for solution of system (9) have been proposed and developed. The most promising of them is secant method Briley (1974), where error of the mass conservation equation

$$F(p_i^{(n+1)}) = \sum_{j=1}^{N_y} u_{ij}^{(n+1)}(p_i^{(n+1)}) - \frac{1}{h} G_0$$

is used for computation of pressure by the iterative method

$$p_i^{(k+1)} = p_i^{(k)} - \frac{p_i^{(k)} - p_i^{(k-1)}}{F_i^{(k)} - F_i^{(k-1)}} F_i^{(k)}, \qquad k = 1, 2, \dots,$$

where superscript k denotes the secant method iterations. Note that the approach requires two starting guesses $p_i^{(0)}$ and $p_i^{(1)}$. First starting guess can be obtained by extrapolation. For example, for uniform grid we obtain $p_i^{(0)} = 2p_{i-1} - p_{i-2}$ and compute $F^{(0)}$. Second starting guess can be given by perturbation of the first one, for example $p_i^{(1)} = 1.001 p_i^{(0)}$. It gives $F^{(1)}$. Function F depends almost linearly on $p_i^{(n+1)}$, but the secant method is direct solver for linear problems. Usually it is required several secant iterations to reduce error of the discrete mass conservation equation down to roundoff error.

Note that in 2D case the system (9) can be solved by direct methods, i.e. without the secant iterations. However in 3D case the direct methods require unpractical computational efforts due to five-diagonal structure of the coefficient matrix.

As contrasted to the Uzawa algorithm (6), the method does not require some preconditioner(s), relaxation parameter(s), extra computer memory and has high convergence rate. Unfortunately, basic assumption $p = p(t, x)$ does not allow apply the method directly for solving full Navier–Stokes equations (1)–(3). Accounting the attractive properties, the algorithm for solving the simplified Navier–Stokes equations can be used for convergence acceleration of the iterative methods intended for full Navier–Stokes equations.

Reduction of system (5) to the saddle point system with zero block of the least size is popular approach in CFD. For example, similar reduction based on special unknown ordering is used in Vanka smoother Vanka (1986).

3. Principle of formal decomposition of pressure

In order to apply the abovementioned approach for solving full Navier–Stokes equations, it is necessary artificially extract «one-dimensional parts of pressure» from the pressure field. For the given purpose, let add and subtract items $p^x(t, x)$, $p^y(t, y)$ and $p^z(t, z)$ depending only on one spatial variable, i.e.

$$\begin{aligned} p(t, x, y, z) = {} & p^x(t, x) + p^y(t, y) + p^z(t, z) \\ & + \Big(-p^x(t, x) - p^y(t, y) - p^z(t, z) + p(t, x, y, z) \Big), \end{aligned}$$

where superscripts x, y and z denote dependence of the functions on the spatial variables. Let us introduce a new function

$$p^{xyz}(t, x, y, z) = -p^x(t, x) - p^y(t, y) - p^z(t, z) + p(t, x, y, z).$$

Finally the pressure can be represented as

$$p(t, x, y, z) = p^x(t, x) + p^y(t, y) + p^z(t, z) + p^{xyz}(t, x, y, z). \tag{10}$$

Representation (10) will be called a principle of formal decomposition of pressure. *Basic idea of the method consists in application of the efficient numerical methods developed for the simplified Navier–Stokes equations for determination of part of pressure* (*i.e. for* $p^x(t,x) + p^y(t,y) + p^z(t,z)$). Fast computation of part of pressure results in reduction of total computational efforts needed for full Navier–Stokes equations.

In spite of simplicity of the representation (10), it is necessary to comment the principle of formal decomposition of pressure:

Remark 1. All items $p^x(t,x)$, $p^y(t,y)$, $p^z(t,z)$ and $p^{xyz}(t,x,y,z)$ have no physical meaning, but physical meaning has their sum. In follows, the items $p^x(t,x)$, $p^y(t,y)$ and $p^z(t,z)$ will be called as «one-dimensional components of the pressure», and $p^{xyz}(t,x,y,z)$ as «multidimensional component». The quotes «» will indicate absence of the physical meaning of the «pressure components».

Remark 2. In N-dimensional case ($N = 2,3$) pressure is represented as sum of $N+1$ «components», therefore the method requires N extra conditions for determination of the «one-dimensional components». The convergence acceleration technique uses N mass conservation equations as a priori information of physical nature.

Remark 3. In spite of representation of the pressure as sum of $N+1$ «components», all momentum equations have only two «pressure» gradients. For example, for X-momentum we obtain

$$\frac{\partial p}{\partial x} = \frac{\partial}{\partial x}\Big(p^x(t,x) + p^y(t,y) + p^z(t,z) + p^{xyz}(t,x,y,z)\Big) = \frac{\partial p^x}{\partial x} + \frac{\partial p^{xyz}}{\partial x}.$$

Remark 4. Efficiency of the acceleration technique depends strongly on the flow nature. For directed fluid flows (for example, flows in nozzles, pipes etc.) gradient of one of «one-dimensional component of pressure» $p^x(t,x)$, $p^y(t,y)$ or $p^z(t,z)$ is dominant. In this case impressive reduction of computational work is expected as compared with traditional algorithms (i.e. $p^x(t,x) = p^y(t,y) = p^z(t,z) = 0$). However for rotated flows (for example, flow in a driven cavity) the approach shows the least efficiency.

Remark 5. In 3D case the method will be more efficient than in 2D case.

Remark 6. Velocity components and corresponding «one-dimensional components» in equation (10) are computed only in coupled manner. Velocity components and «multidimensional component» $p^{xyz}(t,x,y,z)$ in equation (10) can be computed in decoupled (segregated) or coupled manner.

Remark 7. Gradients of the «one-dimensional components» can be obtained in analytical form for explicit schemes. Implicit schemes require formulation of an auxiliary problem for determination of gradients of the «one-dimensional components».

4. Development of explicit schemes

First, consider modification of the explicit schemes using well-known benchmark problem about rotated flow in a driven cavity (Figure 2). Let a staggered grid with grid spacing h_x and h_y has been generated. Classical three-stage splitting scheme is represented as

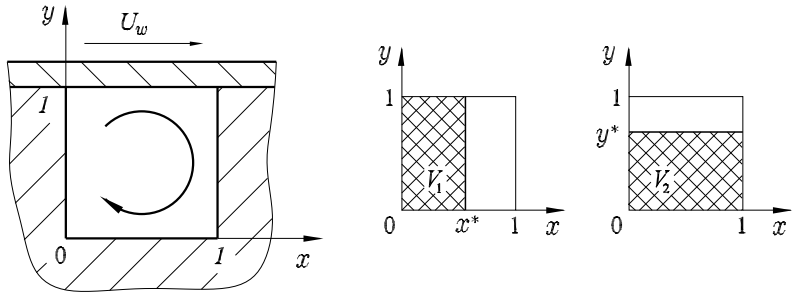

Fig. 2. Driven cavity and location of the control volumes V_1 and V_2

$$\text{Stage I:} \qquad \frac{V^{(n+1/2)} - V^{(n)}}{h_t} = -(V^{(n)}\nabla)V^{(n)} + \mathrm{Re}^{-1}\Delta V^{(n)},$$

$$\text{Stage II:} \qquad \Delta p = \frac{\nabla V^{(n+1/2)}}{h_t},$$

$$\text{Stage III:} \qquad \frac{V^{(n+1)} - V^{(n+1/2)}}{h_t} = -\nabla p,$$

where h_t is time semispacing, $V^{(n+1/2)}$ is intermediate velocity field and n is a time layer.
Stage I consists in solution of the momentum equations without pressure gradients. For simplicity X-momentum can be written as

$$\frac{u_{ij}^{(n+1/2)} - u_{ij}^{(n)}}{h_t} = \psi_{ij}, \tag{11}$$

where ψ_{ij} is the given function defined as

$$\psi_{ij} = \left(-\frac{\partial(u^2)}{\partial x} - \frac{\partial(vu)}{\partial y} + \frac{1}{\mathrm{Re}} \left(\frac{\partial^2 u}{\partial x^2} + \frac{\partial^2 u}{\partial y^2} \right) \right)_{ij}^{(n)}. \tag{12}$$

It is easy to see that intermediate velocity field $V^{(n+1/2)}$ is independent on pressure.
This disadvantage can be compensated partially by the pressure decomposition (10). Application of the decomposition requires two mass conservation equations for 2D problems. Integration of the continuity equation (1) over the control volumes V_1 and V_2 shown on Figure 2 gives

$$\int_0^1 u(t,x,y)\,dy = 0, \qquad \int_0^1 v(t,x,y)\,dx = 0. \tag{13}$$

Approximation of the mass conservation equations on the staggered grid is given by

$$h_y \sum_{j=1}^{N_y} u_{ij}^{(m)} = 0\,, \tag{14}$$

$$h_x \sum_{i=1}^{N_x} v_{ij}^{(m)} = 0\,, \tag{15}$$

where $m = n, n+1/2, n+1$ and $N_x = 1/h_x$, $N_y = 1/h_y$. As contrasted with equation (11) in the classical approach, the velocity component u and «one-dimensional component of pressure» p^x should satisfy to the system

$$\begin{cases} \dfrac{u_{ij}^{(n+1/2)} - u_{ij}^{(n)}}{h_t} = -\left(\dfrac{\partial p^x}{\partial x}\right)_i^{(n+1/2)} + \psi_{ij} \\ h_y \sum\limits_{j=1}^{N_y} u_{ij}^{(n+1/2)} = 0 \end{cases}, \tag{16}$$

i.e. u and p^x are computed in the coupled manner using the discrete mass conservation equation (14).

It is clear that the system (16) can be written in form of (5), where A is the diagonal matrix for explicit schemes. This fact allows obtain analytic solution of the saddle point system (16). Multiplication of the first equation in system (16) on h_y and summation give

$$\frac{1}{h_t}\left(h_y \sum_{j=1}^{N_y} u_{ij}^{(n+1/2)} - h_y \sum_{j=1}^{N_y} u_{ij}^{(n)}\right) = -\sum_{j=1}^{N_y} h_y \left(\frac{\partial p^x}{\partial x}\right)_i^{(n+1/2)} + h_y \sum_{j=1}^{N_y} \psi_{ij}\,. \tag{17}$$

Left-hand side of the equation equals zero due to equation (14). Furthermore

$$\sum_{j=1}^{N_y} h_y \left(\frac{\partial p^x}{\partial x}\right)_i^{(n+1/2)} = \left(\frac{\partial p^x}{\partial x}\right)_i^{(n+1/2)} \sum_{j=1}^{N_y} h_y = \left(\frac{\partial p^x}{\partial x}\right)_i^{(n+1/2)},$$

because $(p^x)_i'$ is independent on j and $\sum\limits_{j=1}^{N_y} h_y = 1$ is dimensionless height of the cavity. Equation (17) is reduced to

$$\left(\frac{\partial p^x}{\partial x}\right)_i^{(n+1/2)} = h_y \sum_{j=1}^{N_y} \psi_{ij}\,. \tag{18}$$

Substitution of the equation into system (16) gives a new form of the system

$$\begin{cases} \dfrac{u_{ij}^{(n+1/2)} - u_{ij}^{(n)}}{h_t} = -h_y \sum\limits_{j=1}^{N_y} \psi_{ij} + \psi_{ij} \\ \dfrac{(p^x)_i^{(n+1/2)} - (p^x)_{i-1}^{(n+1/2)}}{h_x} = h_y \sum\limits_{j=1}^{N_y} \psi_{ij} \end{cases}, \tag{19}$$

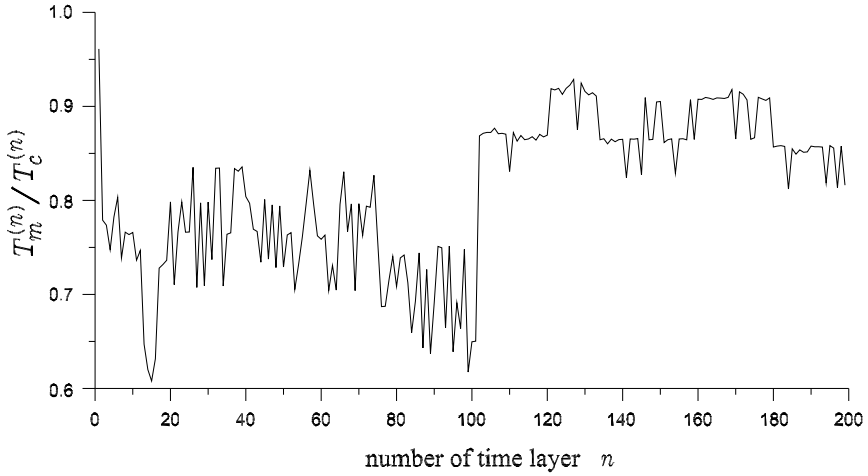

Fig. 3. Ratio of execution time at flow simulation in the driven cavity

where $(p^x)_0^{(n+1/2)}$ is some constant. It is clear that solution of system (19) is

$$u_{ij}^{(n+1/2)} = u_{ij}^{(n)} - h_t h_y \sum_{j=1}^{\mathrm{N}_y} \psi_{ij} + h_t \psi_{ij} \,,$$

$$(p^x)_i^{(n+1/2)} = (p^x)_{i-1}^{(n+1/2)} + h_x h_y \sum_{j=1}^{\mathrm{N}_y} \psi_{ij} \,.$$

Velocity component u and «one-dimensional component of pressure» p^x are computed in the coupled manner saving explicit nature of the computation. Other velocity components are computed in the similar way.
Accounting decomposition (10), other stages of the algorithm are written as

Stage II: $$\Delta p^{xy} = \frac{\nabla V^{(n+1/2)}}{h_t} \,,$$

Stage III: $$\frac{V^{(n+1)} - V^{(n+1/2)}}{h_t} = -\nabla p^{xy} \,.$$

In the stages only «multidimensional component» p^{xy} is used for computation of the velocity field.
For the numerical experiment law of the lid motion is taken as

$$U_w^{(n)} = \min\left(\frac{n}{100}; 1\right) .$$

Reynolds number $\mathrm{Re} = 1000$ is based on the cavity height and the lid velocity $\max U_w^{(n)} = 1$. Staggered uniform grid $h_x = h_y = h = 1/200$, $h_t = h/5$ is used for the flow simulation. Ratio

of the execution time $T_m^{(n)}/T_c^{(n)}$ is used as a criterion of the convergence acceleration, where $T_m^{(n)}$ and $T_c^{(n)}$ are execution time for abovementioned and classical approaches, respectively. Figure 3 shows result of the numerical test. Obtained result for $n = 200$

$$\frac{1}{200}\sum_{n=1}^{200} T_m^{(n)}/T_c^{(n)} = 0.81$$

illustrate the least acceleration efficiency arising at simulation of the rotated flows.

5. Development of implicit schemes

Application of the pressure decomposition (10) for improvement of the implicit schemes requires solution of an auxiliary problem because of the «pressure» gradients can not be determined in explicit form such as equation (18).

5.1 Auxiliary problem

Auxiliary problem is intended for fast computation of the «one-dimensional components» $p^x(t,x)$, $p^y(t,y)$ and $p^z(t,z)$ in decomposition (10). It is assumed that the solution of the auxiliary problem will be close to the solution of the Navier–Stokes equations.

Formulation of the auxiliary problem is based on replacement of the continuity equation (1) by the mass conservation equations. For example, for the driven cavity (Figure 2) the auxiliary problem with the mass conservation equations (13) instead of the continuity equation (1) takes the form:

a) X-momentum and mass conservation equations

$$\begin{cases} \dfrac{\partial u}{\partial t} + \dfrac{\partial (u^2)}{\partial x} + \dfrac{\partial (vu)}{\partial y} = -\dfrac{\partial p^x}{\partial x} - \left[\dfrac{\partial p^{xy}}{\partial x}\right] + \dfrac{1}{\mathrm{Re}}\left(\dfrac{\partial^2 u}{\partial x^2} + \dfrac{\partial^2 u}{\partial y^2}\right) \\ \int\limits_0^1 u(t,x,y)\,dy = 0 \end{cases}, \tag{20}$$

b) Y-momentum and mass conservation equations

$$\begin{cases} \dfrac{\partial v}{\partial t} + \dfrac{\partial (uv)}{\partial x} + \dfrac{\partial (v^2)}{\partial y} = -\dfrac{\partial p^y}{\partial y} - \left[\dfrac{\partial p^{xy}}{\partial y}\right] + \dfrac{1}{\mathrm{Re}}\left(\dfrac{\partial^2 v}{\partial x^2} + \dfrac{\partial^2 v}{\partial y^2}\right) \\ \int\limits_0^1 v(t,x,y)\,dx = 0 \end{cases}, \tag{21}$$

where square brackets mean that the «pressure» gradients $(p^{xy})'_x$ and $(p^{xy})'_y$ are fixed (i.e. its values are taken from previous iteration). Braces mean that the momentum and mass conservation equations are solved only in coupled manner.

Since the systems (20) and (21) are similar to the simplified Navier–Stokes equations (7), the systems can be solved by the same numerical methods. Main difference consists in stopping criterion: auxiliary problem can be solved approximately, i.e. it is necessary to perform several iterations of line Seidel method with the secant iterations. As a result, extra computational

work for approximated solution of the auxiliary problem is negligible small as compared with the total efforts. Note that the equations of the auxiliary problem are not pressure-linked.
To illustrate influence of the auxiliary problem on convergence rate, we use Uzawa algorithm (6) for simulation of stationary flow in the driven cavity starting the iterand zero: $u^{(0)} = 0$, $v^{(0)} = 0$ and $p^{(0)} = 0$. Accounting zero boundary conditions for v, first equation of system (6) is reduced to

$$\frac{\partial(u^2)}{\partial x} = \frac{1}{\mathrm{Re}}\left(\frac{\partial^2 u}{\partial x^2} + \frac{\partial^2 u}{\partial y^2}\right) \tag{22}$$

and $v = 0$. In the auxiliary problem the system (20) takes the form

$$\begin{cases} \dfrac{\partial(u^2)}{\partial x} = -\dfrac{dp^x}{dx} + \dfrac{1}{\mathrm{Re}}\left(\dfrac{\partial^2 u}{\partial x^2} + \dfrac{\partial^2 u}{\partial y^2}\right) \\ \displaystyle\int_0^1 u(x,y)\,dy = 0 \end{cases} \tag{23}$$

and $v = 0$. Finally both problem (22) and (23) are reduced to systems of linear algebraic equations $A\boldsymbol{x} = \boldsymbol{b}$. For clearness these equations are solved until

$$\frac{\|A\boldsymbol{x} - \boldsymbol{b}\|}{\|\boldsymbol{b}\|} < 10^{-7}.$$

The computations are performed with $\mathrm{Re} = 100$ on uniform staggered grid 101×101 ($h_x = h_y = 1/100$).
Figure 4 represents solution of the Navier–Stokes equations in "stream function–vorticity" (+) Ghia et al. (1982), primitive variables formulations (—) and solutions of equations (22) and (23) in the middle section of the cavity ($x = 0.5$) at $\mathrm{Re} = 100$. It is easy to see that use of the mass conservation equations in the auxiliary problem makes it possible to obtain more accurate approximation to solution of the full Navier–Stokes equations (1)–(3).

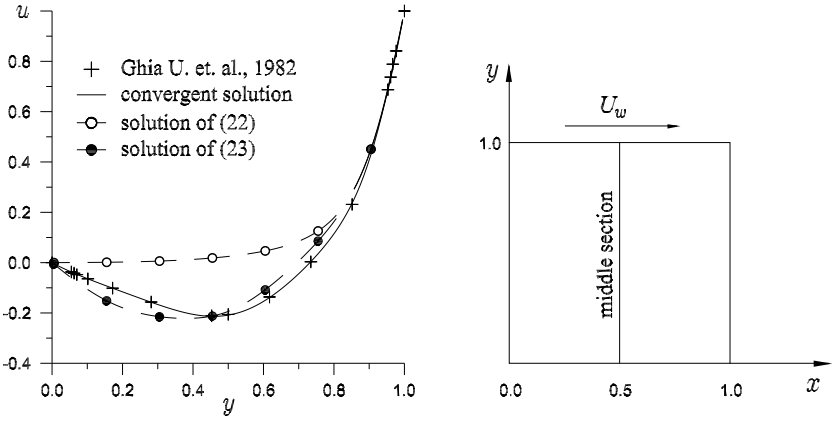

Fig. 4. Distribution of the velocity component u in the middle section of the cavity

5.2 Main problem

Accounting the pressure decomposition (10), the momentum equations in the main problem are written as

$$\frac{\partial u}{\partial t}+\frac{\partial (u^2)}{\partial x}+\frac{\partial (vu)}{\partial y}=-\left[\frac{dp^x}{dx}\right]-\frac{\partial p^{xy}}{\partial x}+\frac{1}{\mathsf{Re}}\left(\frac{\partial^2 u}{\partial x^2}+\frac{\partial^2 u}{\partial y^2}\right), \tag{24}$$

$$\frac{\partial v}{\partial t}+\frac{\partial (uv)}{\partial x}+\frac{\partial (v^2)}{\partial y}=-\left[\frac{dp^y}{dy}\right]-\frac{\partial p^{xy}}{\partial y}+\frac{1}{\mathsf{Re}}\left(\frac{\partial^2 v}{\partial x^2}+\frac{\partial^2 v}{\partial y^2}\right), \tag{25}$$

where square brackets mean that the «pressure» gradients $(p^x)'$ and $(p^y)'$ are fixed (i.e. the gradients have been computed in the auxiliary problem (such as equation (20) and (21) for the driven cavity)). Main problem consists of momentum (24), (25) and continuity equations (1). Algorithm for simulation of the flows with given mass flow rate can be represented as:

Stage I: *auxiliary problem*: several iterations of line (2D) or plane (3D) Seidel method with the secant iterations

Stage II: *main problem*: iterations of basic method (SIMPLE, Uzawa or Vanka iterations, etc.)

Stage III: check convergence, continue (go to 1) if necessary

5.3 Flow over a backward-facing step

The next benchmark problem about backward-facing step flow is used for illustration of the impressive convergence acceleration for the directed fluid flows.

Consider the stationary laminar flow over a backward-facing step, which is another well studied test case. Figure 5 shows the geometry of the flow. The fact that the solution of the incompressible Navier–Stokes equations over a backward-facing step at $\mathsf{Re} = 800$ is steady and stable has been confirmed in a number of recent works.

No-slip boundary conditions are imposed on the step and the upper and lower walls, a parabolic velocity u profile is specified at the channel inlet ($v = 0$), and zero natural boundary conditions ($v = 0$ and $u'_x = 0$) are imposed at the channel outlet. The Reynolds number Re is based on the channel height ($\mathrm{H} = 1$) and the average inlet velocity in the parabolic profile. The channel length is $\mathrm{L} = 14$.

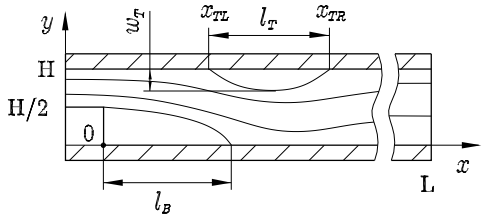

Fig. 5. Geometry of problem about the backward-facing step flow

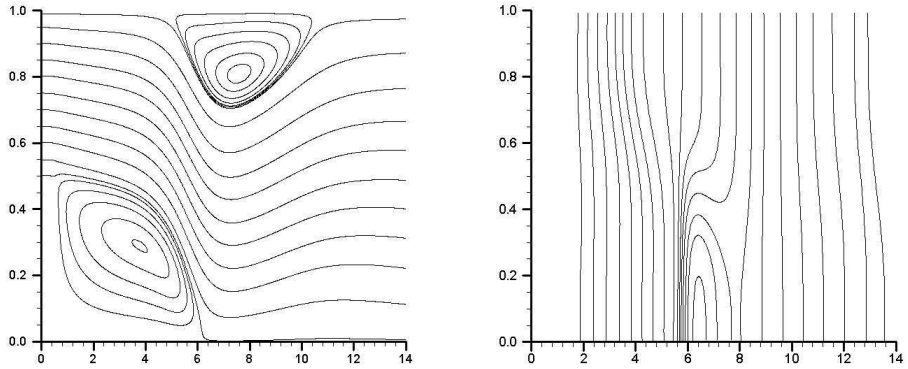

(a) Isolines of stream function (b) Isobars

Fig. 6. Stationary flow over a backward-facing step

Redefining velocity components to be zero inside the step, we obtain the following mass conservation equations for the given problem

$$\int_0^{\mathrm{H}} u(t,x,y)\,dy = \int_0^{\mathrm{H}} u(t,0,y)\,dy\,,$$

$$\int_0^{\mathrm{L}} v(t,x,y)\,dx = -\int_0^{y} \Big(u(t,L,\xi) - u(t,0,\xi)\Big)\,d\xi\,.$$

Numerical experiments show that execution time can be reduced in ~ 400 times for the given problem (staggered grid 101×1401, unpreconditioned Uzawa algorithm, $\mathrm{Re} = 800$). Figure 6 explains the impressive reduction of the computational efforts. It is easy to see that pressure is changed mainly in x direction except small subdomain near attachment point of bottom eddy (i.e. $p(x,y) \approx p^x(x)$). Since the «one-dimensional component of the pressure» $p^x(x)$ is computed in the auxiliary problem, the proposed algorithm is very efficient for solving the problem.
Table 1 represents comparison of obtained results.

Authors	l_B	l_T	w_T	x_{TL}	x_{TR}	Nodes
Barton (1997)	6.0150	5.6600	–	4.8200	10.4800	
Gartling (1990)	6.1000	5.6300	–	4.8500	10.4800	129681
Gresho et al. (1993)	6.0820	5.6260	–	4.8388	10.4648	245760
Gresho et al. (1993)	6.1000	5.6300	–	4.8600	10.4900	$\geqslant 8000$
Keskar & Lin (1999)	6.0964	5.6251	–	4.8534	10.4785	3737
present	6.1000	5.6300	0.28	4.8400	10.4700	141501

Table 1. Comparison of results of the flow simulation over backward-facing step ($\mathrm{Re} = 800$)

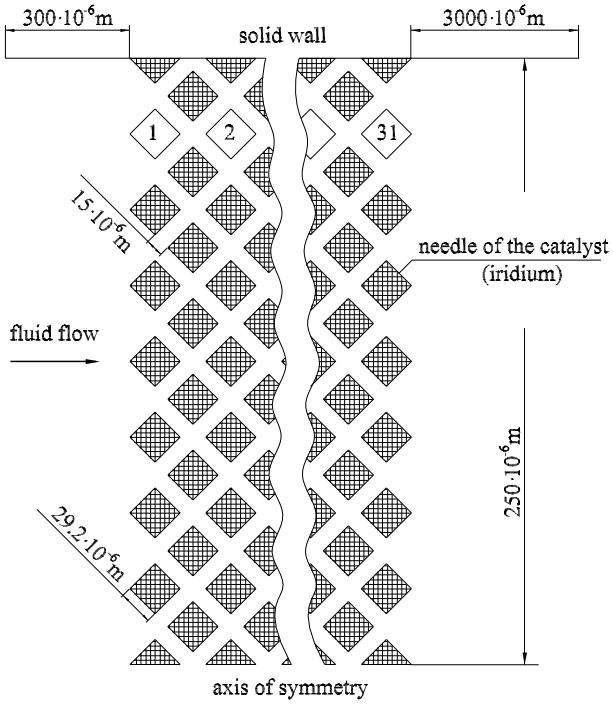

Fig. 7. Geometry of the microcatalyst

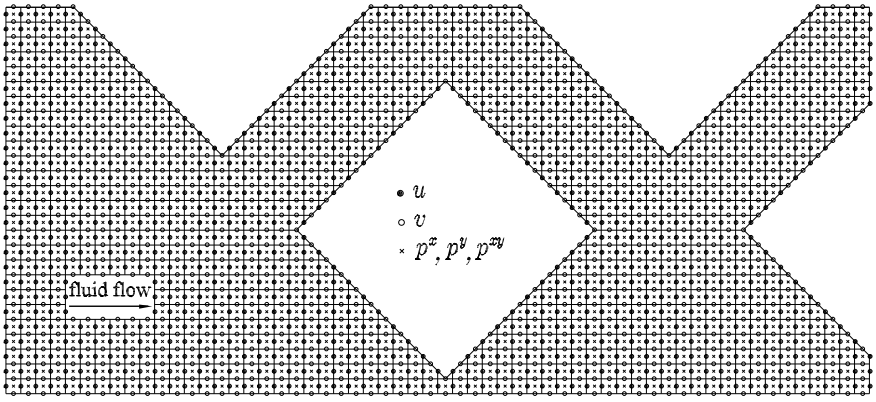

Fig. 8. Staggered grid in the microcatalyst

5.4 Flow in microcatalyst

Proposed approach has been used for simulation of incompressible fluid flows in microcatalyst. The microcatalyst represents 2D channel with iridium-covered needles located in chess order as shown on Figure 7.

Redefining velocity components to be zero inside the needles, there is no remarkable difference in formulation of the auxiliary problem for flow over backward-facing step and for

flow in the catalyst. Diffusion-dominant nature of fluid flow in the microcatalyst simplifies the grid generation. Example of the simplest computational grid for this problem is shown on Figure 8. No-slip conditions are approximated exactly on the needle surfaces.
Nonuniform staggered grid 385×3150 is used for the flow simulation ($\mathrm{Re} = 350$). Figure 9 represents distribution of the stream function and pressure near first column of the needles. Chess order of the needle location results in eddy-free flow inside the microcatalyst. However intensive eddy formation after last column of the needles is observed (Figure 10).

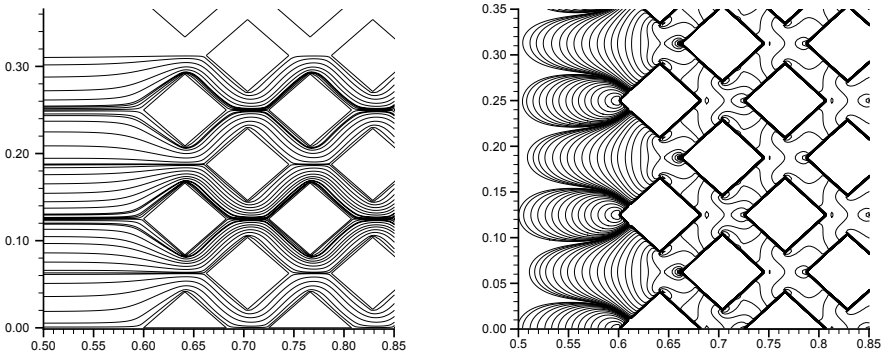

(a) Isolines of stream function (b) Isobars

Fig. 9. Flow near first column of the needles

5.5 Compressible flow in laval micronozzle

Recently the numerical methods for fluid flow prediction have been classified into two categories: density-based and pressure-based. For the pressure-based approach, methods are

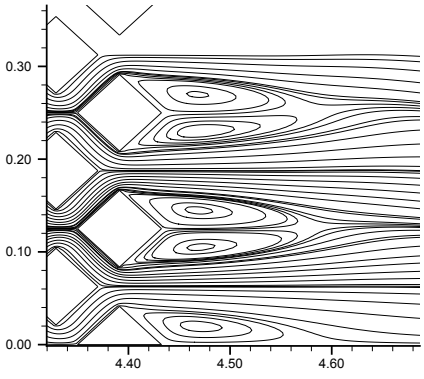

Fig. 10. Eddy formation after last column of the needles

classified into coupled and segregated (decoupled). Density-based algorithms traditionally are used to compute high speed compressible flows. Computational methods for low Mach number compressible flows are an active research field in recent years. The pressure-velocity coupling problem discussed earlier for incompressible flows are also encountered in the methods when used for low-speed applications.

Pressure decomposition (10) shows that there are not pure density-based and segregated solvers because of the velocity components and corresponding «one-dimensional components of pressure» (i.e. (u,p^x), (v,p^y) and (w,p^z)) always are computed in the coupled manner. «Multidimensional component» p^{xyz} in (10) can be computed by coupled or segregated method using density-based or pressure-based approach.

Consider application of the pressure decomposition for simulation of compressible flow in flat Laval micronozzle. Width of subsonic part of the micronozzle is 1 mm. Grid generation is based on mapping of the non-dimensional physical domain with nonuniform grid onto computational domain (unit square) with uniform grid. Direct (ABCD $\rightarrow$ $\bar{A}\bar{B}\bar{C}\bar{D}$) and reverse (ABCD $\leftarrow$ $\bar{A}\bar{B}\bar{C}\bar{D}$) mappings are shown on Figure 11, where the function $\varphi(x)$ describes the micronozzle profile. The mappings can be given by

$$\bar{x} = x\,, \qquad \bar{y} = -\frac{1}{\beta}\,\ln\Big(1-(1-e^{-\beta})\frac{y}{\varphi(x)}\Big)\,,$$

where (x,y) and $(\bar{x},\bar{y})$ are spatial variables in physical and computational domains, respectively. Parameter $\beta > 0$ is intended for the grid refinement near solid wall.

Jacobian (J) of the mapping

$$J = \begin{vmatrix} \bar{x}_x & \bar{x}_y \\ \bar{y}_x & \bar{y}_y \end{vmatrix} = \frac{1-e^{-\beta}}{\beta}\,\frac{e^{\beta\bar{y}}}{\varphi(\bar{x})}$$

is non-singular ($J \neq 0$). In addition, $J \rightarrow 1/\varphi(\bar{x})$ at $\beta \rightarrow 0$ for uniform grid in y direction.

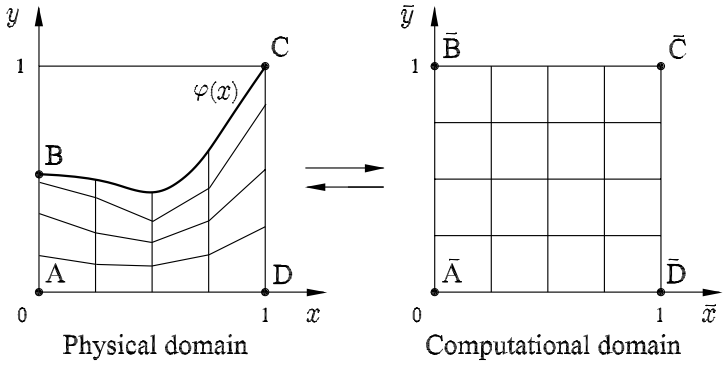

Fig. 11. Non-dimensional physical and computational domains

Finally, non-dimensional compressible Navier–Stokes equations in the computational domain are written as

$$\frac{\partial}{\partial t}\left(\frac{\boldsymbol{U}}{J}\right) + \epsilon\frac{\partial}{\partial\bar{x}}\left(\frac{\boldsymbol{E}}{J}\right) + \epsilon\frac{\partial}{\partial\bar{y}}\left(\frac{\bar{y}_x\boldsymbol{E}}{J}\right) + \frac{\partial\boldsymbol{F}}{\partial\bar{y}} = \frac{\boldsymbol{H}}{J}\,,$$

where

$$\boldsymbol{U} = \begin{pmatrix} \rho \\ \rho u \\ \rho v \\ \rho i \end{pmatrix}, \qquad \boldsymbol{H} = \begin{pmatrix} 0 \\ 0 \\ 0 \\ S \end{pmatrix},$$

$$\boldsymbol{E} = \begin{pmatrix} \rho u \\ \rho u^2 + p - \dfrac{4}{3}\dfrac{\epsilon}{\mathrm{Re}}\left(\dfrac{\partial u}{\partial \bar{x}} + \bar{y}_x \dfrac{\partial u}{\partial \bar{y}}\right) + \dfrac{2}{3}\dfrac{\bar{y}_y}{\mathrm{Re}}\dfrac{\partial v}{\partial \bar{y}} \\ \rho u v - \dfrac{\bar{y}_y}{\mathrm{Re}}\dfrac{\partial v}{\partial \bar{y}} - \dfrac{\epsilon}{\mathrm{Re}}\left(\dfrac{\partial v}{\partial \bar{x}} + \bar{y}_x \dfrac{\partial v}{\partial \bar{y}}\right) \\ \rho u i - \dfrac{\epsilon}{\mathrm{Pe}}\left(\dfrac{\partial T}{\partial \bar{x}} + \bar{y}_x \dfrac{\partial T}{\partial \bar{y}}\right) \end{pmatrix},$$

$$\boldsymbol{F} = \begin{pmatrix} \rho v \\ \rho v u - \dfrac{\bar{y}_y}{\mathrm{Re}}\dfrac{\partial u}{\partial \bar{y}} - \dfrac{\epsilon}{\mathrm{Re}}\left(\dfrac{\partial v}{\partial \bar{x}} + \bar{y}_x \dfrac{\partial v}{\partial \bar{y}}\right) \\ \rho v^2 + p - \dfrac{4}{3}\dfrac{\bar{y}_y}{\mathrm{Re}}\dfrac{\partial v}{\partial \bar{y}} + \dfrac{2}{3}\dfrac{\epsilon}{\mathrm{Re}}\left(\dfrac{\partial u}{\partial \bar{x}} + \bar{y}_x \dfrac{\partial u}{\partial \bar{y}}\right) \\ \rho v i - \dfrac{\bar{y}_y}{\mathrm{Pe}}\dfrac{\partial T}{\partial \bar{y}} \end{pmatrix}.$$

Parameter ϵ is the micronozzle width-to-length ratio.

First mass conservation equation is obtained by integration of the continuity equation as follows

$$\frac{\partial}{\partial t}\int_0^1\int_0^x \frac{\rho(t,\xi,y)}{J}\,d\xi\,dy + \epsilon\int_0^1 \left(\frac{\rho u}{J}\right)\Big|_x dy - \epsilon\int_0^1 \left(\frac{\rho u}{J}\right)\Big|_0 dy = 0\,.$$

In the auxiliary problem for incompressible flows, iterations of line (2D) or plane (3D) Seidel method are stopped then the velocity component satisfies to the mass conservation equation. Computation of compressible flows requires updating of thermophysical properties (density ρ, coefficient of viscosity in Re and heat conductivity coefficient in Pe) using updated pressure in the line or plane. In 3D case values of thermophysical properties of the fluid for X-momentum should be updated using pressure

$$p(t,x,y,z) = p^x(t,x) + [p^y(t,y) + p^z(t,z) + p^{xyz}(t,x,y,z)],$$

temperature T and equation of state. Here square brackets mean that the pressure components p^y, p^z and p^{xyz} are fixed.

Figure 12 represents isobars in the Laval micronozzles. It is easy to see that the isobars are almost vertical lines near throat and in supersonic part of the micronozzle. It means that the pressure is changed mainly along the micronozzle axis. In other words, «one-dimensional component of the pressure» p^x in decomposition (10) is dominant in this problem. For

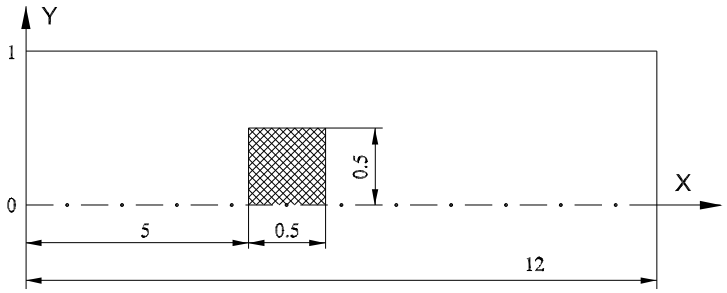

Fig. 13. Starting location of the plunger

the given problem, the auxiliary problem makes it possible to compute the most «part of pressure» (i.e. $p^x(t,x) + p^y(t,y)$) and corresponding change of thermophysical properties of the fluid based on simplified (pressure-unlinked) momentum equations in primitive variables formulation and mass conservation equations.

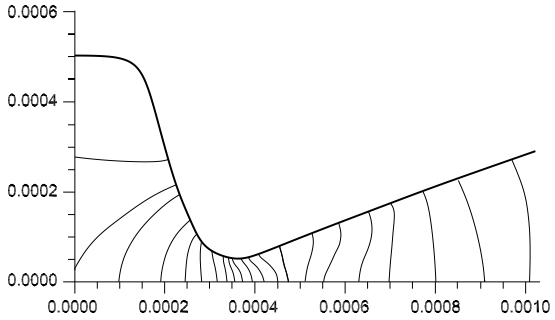

Fig. 12. Isobars in Laval micronozzle (sizes in meters)

5.6 Flows with unspecified mass rate

Previously fluid flows with the given mass rate have been simulated and analyzed. In some applications mass flow rate cannot be given in advance. The simplest example of such flows is problem about moving plunger. Immovable plunger is located between parallel plates filled by incompressible fluid. Figure 13 shows geometry of the problem and starting location of the plunger. Motion of the plunger causes the fluid flow. It is clear that mass flow rate depends on the plunger speed. Algorithm for simulation of the flows with unspecified mass rate should be modified as:

Stage I: *main problem*: iterations of basic method (SIMPLE, Uzawa or Vanka iterations, etc.)

Stage II: check convergence; continue if necessary

Stage III: *auxiliary problem*: several iterations of line (2D) or plane (3D) Seidel method with the secant iterations; continue (go to 1)

Assume that $\tilde{u}_{ij}$, $\tilde{v}_{ij}$ and $\tilde{p}_{ij}^{xy}$ are approximation to the solution of the Navier–Stokes equations obtained after iterations of the basic method. Then the mass conservation equation can be

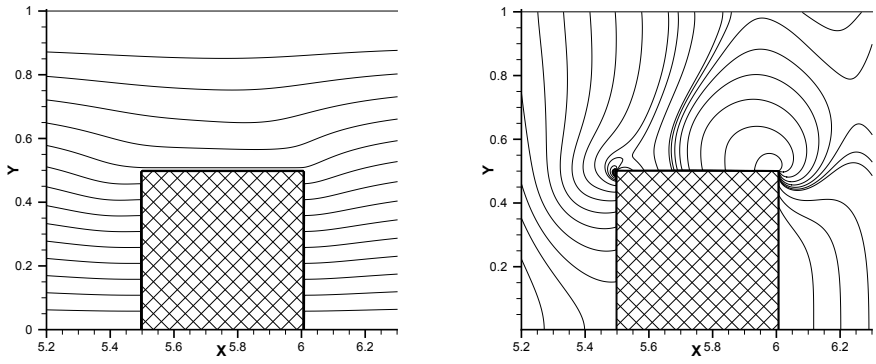

(a) Isolines of stream function (b) Isobars

Fig. 14. Flow near the moving plunger

formulated as

$$\int_0^1 u(t, x_i, y)\, dy = \max_i \int_0^1 \tilde{u}(t, x_i, y)\, dy$$

at accelerated or uniform plunger motion and in form

$$\int_0^1 u(t, x_i, y)\, dy = \min_i \int_0^1 \tilde{u}(t, x_i, y)\, dy$$

at decelerated plunger motion. As a result, the auxiliary problem ensures expansion of perturbations caused by the plunger on all domain in each iteration. Uniform staggered grid 201×2401 ($h_x = h_y = 1/200$) is used for simulation the fluid flow around the moving plunger. Reynolds number $\mathrm{Re} = 200$ is based on the plunger velocity and distance between the plates. Stream function isolines and isobars near the moving plunger are shown on Figure 14.

6. Pressure decomposition in geometric multigrid methods

Proposed convergence acceleration technique based on the pressure decomposition (10) should be incorporated with well-known algorithms for solving Navier–Stokes equations. Multigrid methods having (almost) optimal convergence rate for many applications seem to be the most promising solvers for many CFD problems. Our purpose is development of multigrid method with the least number of problem-dependent components for using in black box software.

6.1 Nonlinear multigrid iterations

To overcome problem of robustness, the Navier–Stokes equations (4) should be adapted for the multigrid algorithm Martynenko (2006). Adaptation of the Navier–Stokes equations (so called Σ-modification) consists in representation of the velocity $\vec{V}$ and pressure P as sum of

two functions

$$\vec{V} = C_{\vec{V}} + \hat{\vec{V}}, \qquad P = C_P + \hat{P},$$

where discrete analogues of the functions $C_{\vec{V}}$ and C_P will be coarse grid corrections and discrete analogues of the functions $\hat{\vec{V}}$ and $\hat{P}$ will be approximations to the solutions in the following multigrid iterations.

As a result, the Navier–Stokes equations (4) can be rewritten in the Σ-modified form

$$\begin{cases} \mathcal{N}(C_{\vec{V}} + \hat{\vec{V}}) + \nabla(C_P + \hat{P}) = F \\ \nabla(C_{\vec{V}} + \hat{\vec{V}}) = G \end{cases}.$$

Since $\mathcal{N}(C_{\vec{V}} + \hat{\vec{V}}) = \mathcal{N}^*(C_{\vec{V}}) + \mathcal{N}(\hat{\vec{V}})$, where $\mathcal{N}^* \neq \mathcal{N}$ for the nonlinear operator $\mathcal{N}$, we obtain

$$\begin{cases} \mathcal{N}^*(C_{\vec{V}}) + \nabla C_P = F^* \\ \nabla C_{\vec{V}} = G^* \end{cases}, \tag{26}$$

where $F^* = F - \mathcal{N}(\hat{\vec{V}}) - \nabla\hat{P}$ and $G^* = G - \nabla\hat{\vec{V}}$.

It is clear that main difference between Σ-modified and initial forms of the Navier–Stokes equations consists of the nonlinear convection-diffusion operator ($\mathcal{N}^*$ in equation (26) instead of $\mathcal{N}$ in equation (4)) and source terms (F^* and G^* in equation (26) instead of F and G in equation (4)). Note that Σ-modification does not require some linearization of the Navier–Stokes equations. Therefore modified Navier–Stokes equations with other transport equations can be solved in coupled manner on all coarse grids.

For example, 2D Σ-modified Navier–Stokes equations are written as:

a) Σ-modified continuity equation

$$\frac{\partial c^u}{\partial x} + \frac{\partial c^v}{\partial y} = R^{uv}(t,x,y),$$

b) Σ-modified X-momentum

$$\frac{\partial c^u}{\partial t} + \frac{\partial (c^u)^2}{\partial x} + 2\frac{\partial(\hat{u}c^u)}{\partial x} + \frac{\partial(\hat{u}c^v)}{\partial y} + \frac{\partial(\hat{v}c^u)}{\partial y} + \frac{\partial(c^u c^v)}{\partial y} = \\ = -\frac{\partial c^p}{\partial x} + \frac{1}{\mathrm{Re}}\left(\frac{\partial^2 c^u}{\partial x^2} + \frac{\partial^2 c^u}{\partial y^2}\right) + R^u(t,x,y),$$

c) Σ-modified Y-momentum

$$\frac{\partial c^v}{\partial t} + \frac{\partial(\hat{u}c^v)}{\partial x} + \frac{\partial(\hat{v}c^u)}{\partial x} + \frac{\partial(c^u c^v)}{\partial x} + \frac{\partial (c^v)^2}{\partial y} + 2\frac{\partial(\hat{v}c^v)}{\partial y} = \\ = -\frac{\partial c^p}{\partial y} + \frac{1}{\mathrm{Re}}\left(\frac{\partial^2 c^v}{\partial x^2} + \frac{\partial^2 c^v}{\partial y^2}\right) + R^v(t,x,y),$$

where discrete analogues of the functions c^u, c^v and c^p will be coarse grid corrections and discrete analogues of the functions $\hat{u}$, $\hat{v}$ and $\hat{p}$ will be approximations to the solutions in the following multigrid iterations. Source terms in the Σ-modified equations coincide with the

initial Navier–Stokes equations, i.e.

$$R^{uv}(t,x,y) = -\frac{\partial \hat{u}}{\partial x} - \frac{\partial \hat{v}}{\partial y},$$

$$R^{u}(t,x,y) = -\frac{\partial \hat{u}}{\partial t} - \frac{\partial (\hat{u}^2)}{\partial x} - \frac{\partial (\hat{v}\hat{u})}{\partial y} - \frac{\partial \hat{p}}{\partial x} + \frac{1}{\mathsf{Re}}\left(\frac{\partial^2 \hat{u}}{\partial x^2} + \frac{\partial^2 \hat{u}}{\partial y^2}\right),$$

$$R^{v}(t,x,y) = -\frac{\partial \hat{v}}{\partial t} - \frac{\partial (\hat{u}\hat{v})}{\partial x} - \frac{\partial (\hat{v}^2)}{\partial y} - \frac{\partial \hat{p}}{\partial y} + \frac{1}{\mathsf{Re}}\left(\frac{\partial^2 \hat{v}}{\partial x^2} + \frac{\partial^2 \hat{v}}{\partial y^2}\right),$$

Additional convection terms in Σ-modified momentum equations are result of nonlinear nature of the convection-diffusion operator $\mathcal{N}$, i.e. $\mathcal{N}^* \neq \mathcal{N}$. Approximation of the source terms R^{uv}, R^u and R^v defines the accuracy, monotonicity and conservatism of the numerical solutions. Approximation of other terms in the modified equations defines only multigrid convergence rate because $c^u \to 0$, $c^v \to 0$ and $c^p \to 0$ for convergent solution.

6.2 Multigrid structure

Recently variant of the geometric multigrid methods with the problem-independent transfer operators (so-called Robust Multigrid Technique) has been proposed and developed Martynenko (2006; 2010). The problem-independent restriction and prolongation operators are result of the multiple coarse grid corrections on subgrids of the finest grid.

Assume that a finest staggered grid G_1^0 has been generated in the domain. Coarsening in Robust Multigrid Technique is based on representation of the finest grid G_1^0 as union of 3^N ($N = 1, 2, 3$) coarse grids $G_1^1, G_2^1, \ldots, G_{3^N}^1$ with the following properties:

1. all coarse grids $G_1^1, G_2^1, \ldots, G_{3^N}^1$ have no common points, i.e. $G_n^1 \cap G_m^1 = \varnothing, \quad n \neq m$.
2. the finest grid G_1^0 is the union of all coarse grids $G_1^1, G_2^1, \ldots, G_{3^N}^1$, i.e. $G_1^0 = \bigcup_{k=1}^{3^N} G_k^1$.
3. all grids are similar to each other, but a mesh size on the coarse grids is three times as large as than the mesh size on the finest grid.
4. control volume on the coarse grids $G_1^1, G_2^1, \ldots, G_{3^N}^1$ is union of 3^N control volumes on the finest grid G_1^0.

The coarse grid generation is further recurrently repeated: each grid $G_1^1, G_2^1, \ldots, G_{3^N}^1$ gives 3^N coarser grids. The coarse grid generation is finished when no further coarsening can be performed. Finally we obtain G_k^l, $l = 0, 1, \ldots, L^+$, $k = 1, 3^{Nl}$ computational grids (so called a multigrid structure), where L^+ is number of the coarsest level and $N = 2, 3$. Details of the coarse grid generation is given in Martynenko (2006).

6.3 Multigrid cycle

Multigrid cycles for simulation of flows with given and unspecified mass flow rates are shown on Figure 15. There are two kinds of smoothing on the multigrid structure. One of them (marked as ○) is intended for solving Σ-modified Navier–Stokes equations with computation of correction of the «multidimensional component of pressure». Another smoothing (marked as ■) is intended for computation of correction of the «one-dimensional component of

pressure» on the finest grid. In other words solution of the modified auxiliary problem is additional smoothing on the finest grid.

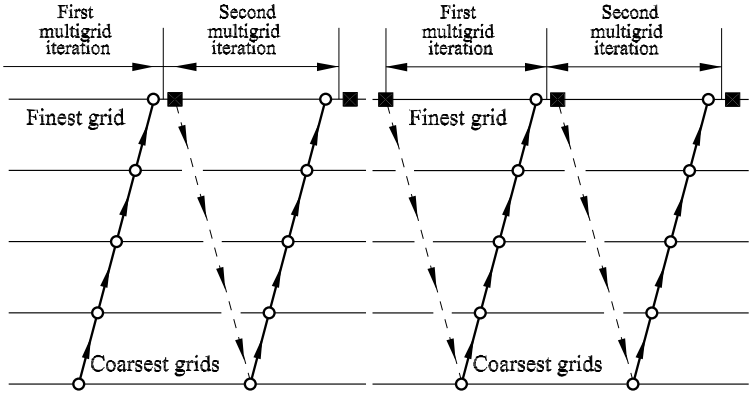

(a) Flows with unspecified mass flow (b) Flows with the given mass flow rate rate

Fig. 15. Multigrid cycles

6.4 Numerical test

The algorithm is tested by simulation of unsteady flow in a driven cavity at $\mathrm{Re} = 1000$. Law of the lid motion is taken as

$$U_w^{(n)} = \min\left(\frac{n}{50}; 1\right),$$

and stopping criterion is posed as

$$\max_{ij} \left| \frac{\partial u}{\partial x} + \frac{\partial v}{\partial y} \Big|_{ij}^{(n+1)} \right| < 10^{-10}.$$

Six-level multigrid structure with uniform finest staggered grid 501×501 ($h_t = h_x = h_y = 1/500$) is used for the test. Correction of the «multidimensional component of pressure» is computed using Uzawa algorithm with diagonal preconditioning.

Figures 16–18 show evolution of the flow in the cavity. The main vortex is located near the lid after finish of the lid acceleration. Then the vortex moves to upper right corner under influence of the lid motion. After that the vortex moves along diagonal of the cavity to the center (Figure 16). Motion of the main vortex generates two additional vortices (Figure 17). The first vortex is formed in the lower corner, but the second vortex is formed on right vertical wall of the cavity. Location of the corner vortex is stable because of its motion is limited by the cavity walls. However the wall vortex can moving under influence of the main vortex. Corner and wall vortices agglomerate in common vortex. Agglomerated vortex tends to stable corner position, but a new corner vortex is generated in the left lower corner of the cavity. Figure 18 represents close-to-steady flow picture in the cavity.

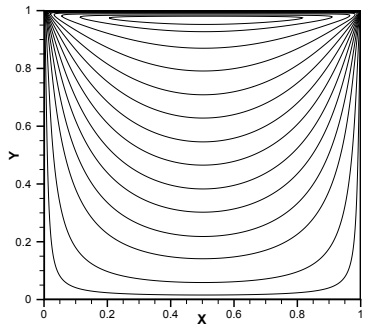

(a) Isolines of stream function ($n = 50$)

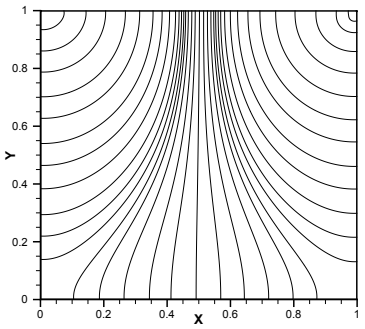

(b) Isobars ($n = 50$)

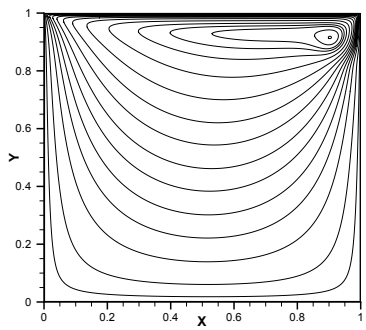

(c) Isolines of stream function ($n = 400$)

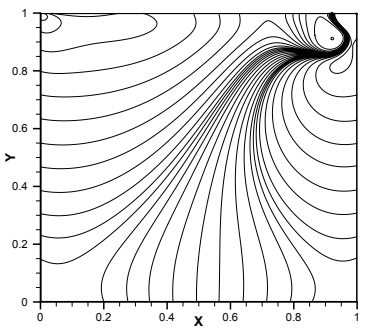

(d) Isobars ($n = 400$)

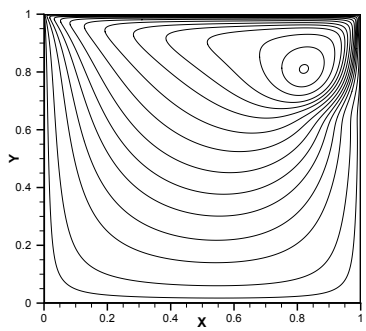

(e) Isolines of stream function ($n = 1000$)

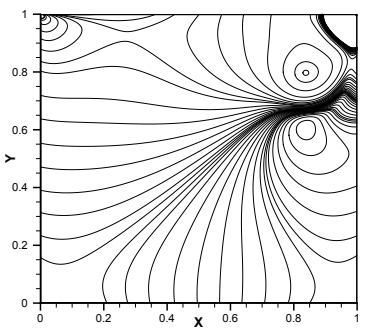

(f) Isobars ($n = 1000$)

Fig. 16. Flow picture in the driven cavity ($n = 50, 400, 1000$)

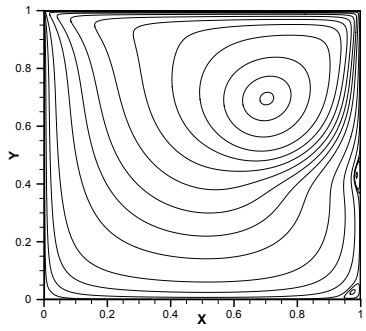

(a) Isolines of stream function ($n = 2250$)

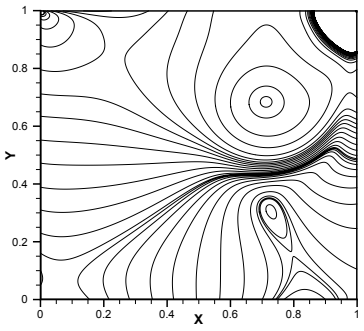

(b) Isobars ($n = 2250$)

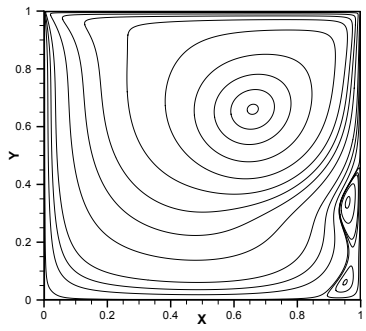

(c) Isolines of stream function ($n = 3000$)

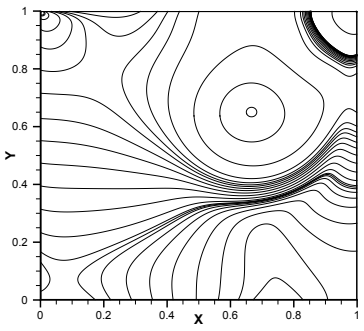

(d) Isobars ($n = 3000$)

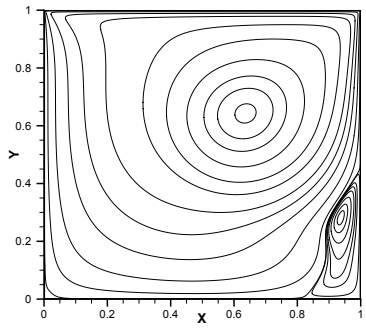

(e) Isolines of stream function ($n = 3500$)

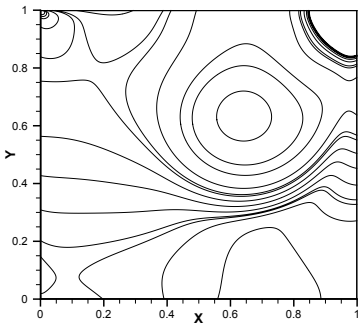

(f) Isobars ($n = 3500$)

Fig. 17. Flow picture in the driven cavity ($n = 2250, 3000, 3500$)

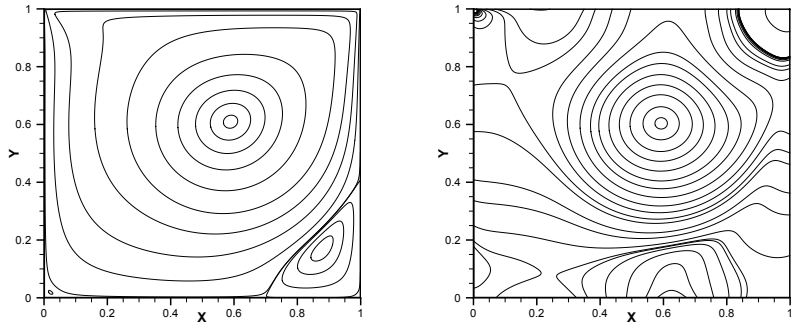

(a) Isolines of stream function ($n = 5000$) (b) Isobars ($n = 5000$)

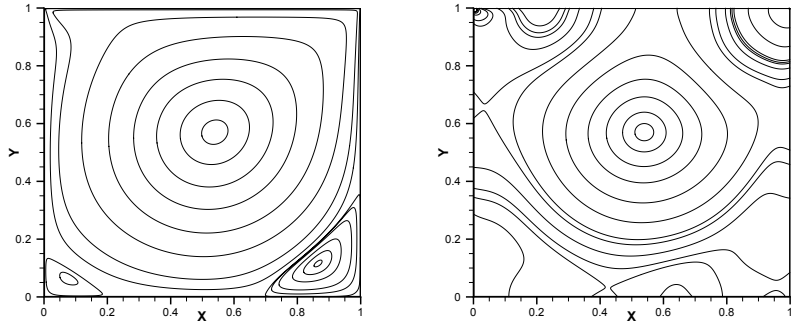

(c) Isolines of stream function ($n = 10000$) (d) Isobars ($n = 10000$)

Fig. 18. Flow picture in the driven cavity ($n = 5000, 10000$)

7. Acknowledgements

Work supported by Russian Foundation for the Basic Research (project no. 09-01-00151). I wish to express a great appreciation to professor M.P. Galanin (Keldysh Institute of Applied Mathematics of Russian Academy of Sciences), who have guided and supported the researches.

8. Conclusion

«Part of pressure» (i.e. sum of the «one-dimensional components» in decomposition (10)) can be computed using the simplified (pressure-unlinked) Navier–Stokes equations in primitive variables formulation and the mass conservation equations. «One-dimensional components of pressure» and corresponding velocity components are computed only in coupled manner. As a result, there are not pure segregated algorithms and pure density-based approach on structured grids. Proposed method does not require preconditioners and relaxation

parameters. Pressure decomposition is very efficient acceleration technique for simulation of directed fluid flows.

9. References

Barton I.E. (1997) The entrance effect of laminar flow over a backward-facing step geometry, *Int. J. for Num. Meth. in Fluids*, Vol. 25, pp. 633-644.

Benzi, M.; Golub, G.H.; Liesen, J. (2006) Numerical solution of saddle point problems, *Acta Numerica*, pp. 1-137.

Briley, W.R. (1974) Numerical method for predicting three-dimensional steady viscous flow in ducts, *J. Comp. Phys.*, Vol. 14, pp.8-28.

Gartling D. (1990) A test problem for outflow boundary conditions-flow over a backward-facing step, *Int. J. for Num. Meth. in Fluids*, Vol. 11, pp. 953-967.

Ghia, U.; Ghia, K.N.; Shin, C.T. (1982) High-Re solutions for incompressible flow using the Navier-Stokes equations and a multigrid method, *J. Comp. Phys.*, Vol. 48, pp.387-411.

Gresho, P.M.; Gartling, D.K.; Torczynski, J.R.; Cliffe, K.A.; Winters, K.H.; Garratt, T.G.; Spence, A.; Goodrich, J.W. (1993) Is a steady viscous incompressible two-dimensional flow over a backward-facing step at Re=800 stable? *Int. J. for Num. Meth. in Fluids*, Vol. 17, pp. 501-541.

Keskar, J.; Lin, D.A. (1999) Computation of laminar backward-facing step flow at Re=800 with a spectral domain decomposition method, *Int. J. for Num. Meth. in Fluids*, Vol. 29, pp. 411-427.

Martynenko, S.I. (2006) Robust Multigrid Technique for black box software, *Comp. Meth. in Appl. Math.*, Vol. 6, No. 4, pp.413-435.

Martynenko, S.I. (2009) A physical approach to development of numerical methods for solving Navier-Stokes equations in primitive variables formulation, *Int. J. of Comp. Science and Math.*, Vol. 2, No. 4, pp.291-307.

Martynenko, S.I. (2010) Potentialities of the Robust Multigrid Technique, *Comp. Meth. in Appl. Math.*, Vol. 10, No. 1, pp.87-94.

Vanka S.P. (1986) Block-implicit multigrid solution of Navier–Stokes equations in primitive variables, *J. Comp. Phys.*, Vol. 65, pp.138-158.

Wesseling, P. (1991) *An Introduction to Multigrid Methods*, Wiley, Chichester.

10

Neural Network Modeling of Hydrodynamics Processes

Sergey Valyuhov, Alexander Kretinin and Alexander Burakov
Voronezh State Technical University
Russia

1. Introduction

Many of the computational methods for equation solving can be considered as methods of weighted residuals (MWR), based on the assumption of analytical idea for basic equation solving. Test function type determines MWR specific variety including collocation methods, least squares (RMS) and Galerkin's method. MWR algorithm realization is basically reduced to nonlinear programming which is solved by minimizing the total equations residual by selecting the parameters of test solution. In this case, accuracy of solving using the MWR is defined by approximating test function properties, along with degree of its conformity with its initial partial differential equations, representing a continuum solution of mathematical physics equations.
On fig. 1, computing artificial neural network (ANN) is presented in graphic form, illustrating process of intra-network computations. The input signals or the values of input

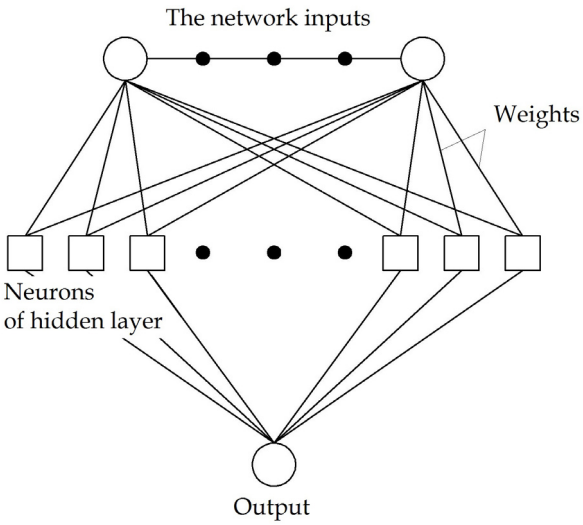

Fig. 1. Neural network computing structure

variables are distributed and "move" along the connections of the corresponding input together with all the neurons of hidden layer. The signals may be amplified or weakened by being multiplied by corresponding coefficient (weight or connection). Signals coming to a certain neuron within the hidden layer are summed up and subjected to nonlinear transformation using so-called activation function. The signals further proceed to network outputs that can be multiple. In this case the signal is also multiplied by a certain weight value, i.e. sum of neuron output weight values within the hidden layer as a result of neural network operation. Artificial neural networks of similar structure are capable for universal approximation, making possible to approximate arbitrary continuous function with any required accuracy.

To analyze ANN approximation capabilities, perceptron with single hidden layer (SLP) was chosen as a basic model performing a nonlinear transformation from input space to output space by using the formula (Bishop, 1995):

$$y(\mathbf{w},\mathbf{x}) = \sum_{i=1}^{q} v_i f_\sigma \left(b_i + \sum_{j=1}^{n} w_{ij} x_j \right) + b_0 , \tag{1}$$

where $\mathbf{x} \in \mathbf{R}^n$ is network input vector, comprised of x_j values; q – the neuron number of the single hidden layer; $\mathbf{w} \in \mathbf{R}^s$ – all weights and network thresholds vector; w_{ij} – weight entering the model nonlinearly between j-m input and i-m neuron of the hidden layer; v_i – output layer neuron weight corresponding to the i-neuron of the hidden layer; b_i, b_0 – thresholds of neurons of the hidden layer and output neuron; f_o – activation function (in our case the logistic sigmoid is used). ANN of this structure already has the universal approximation capability, in other words it gives the opportunity to approximate the arbitrary analog function with any given accuracy. The main stage of using ANN for resolving of practical issues is the neural network model training, which is the process of the network weight iterative adjustment on the basis of the learning set (sample) $\{\mathbf{x}_i, y_i\}, \mathbf{x}_i \in \mathbf{R}^n$, $i = 1,...,k$ in order to minimize the network error – quality functional

$$J(\mathbf{w}) = \sum_{i=1}^{k} Q\left(f_\varepsilon(\mathbf{w},i)\right), \tag{2}$$

where $\mathbf{w}$ – ANN weight vector; $Q\left(f_\varepsilon(\mathbf{w},i)\right) = f_\varepsilon\left(\mathbf{w},i\right)^2$ – ANN quality criterion as per the i-training example; $f_\varepsilon\left(\mathbf{w},i\right) = y\left(\mathbf{w},\mathbf{x}_i\right) - y_i$ – i-example error. For training purposes the statistically distributed approximation algorithms may be used based on the back error propagation or the numerical methods of the differentiable function optimization.

2. Neuronet's method of weighted residuals for computer simulation of hydrodynamics problems

Let us consider that a certain equation with exact solution $\overline{y}(x)$

$$L(\overline{y}) = 0 \tag{3}$$

for non-numeric value y^s equation (3) presents an arbitrary $\mathbf{x}^s$ within the learning sample. We have $L(y)=R$ with substitution of approximate solution (1) into equation (3), with R as equation residual. R is continuous function $R=f(\mathbf{w},\mathbf{x})$, being a function of SLP inner

parameters. Thus, ANN training under outlet functional is composed of inner parameters definition using trial solution (1) for meeting the equation (3) goal and its solution is realized through the corresponding modification of functional quality equation (2) training.
Usually total squared error at net outlets is presented as an objective function at neural net training and an argument is the difference between the resulted '*s*' net outlet and the real value that is known a priori. This approach to neural net utilization is generally applied to the problems of statistical set transformation along with definition of those function values unknown a priori (net outlet) from argument (net inlet). As for simulation issues, they refer to mathematical representation of the laws of physics, along with its modification to be applied practically. It is usually related to necessity for developing a digital description of the process to be modeled. Under such conditions we will have to exclude the a priori known computation result from the objective function and its functional task. Objective function during the known law simulation, therefore, shall only be defined by inlet data and law simulated:

$$E = \frac{1}{2}\sum_{S}\left(y^s - f\left(\mathbf{x}^s\right)\right)^2 . \tag{4}$$

Use of neuronet's method of weighted residuals (NMWR) requires having preliminary systematic study for each specific case, aimed at: 1) defining the number of calculation nodes (i.e. the calculation grid size); 2) defining number of neurons within the network, required for obtaining proper approximation power; 3) choosing initial approximations for training neural network test solution ; 4) selecting additional criteria in the goal function for training procedure regularization in order to avoid possible solution non-uniformity; 5) analyzing the possibilities for applying multi-criteria optimization algorithms to search neural network solution parameters (provided that several optimization criteria are available).
Artificial neural network used for hydrodynamic processes studying is presented by two fundamentally different approaches. The first is the NMWR used for direct differential hydrodynamics equations solution. The NMWR description and its example realization for Navier-Stokes equations solution is presented in papers (Kretinin, 2006; Kretinin et al., 2008). These equations describe the 2D laminar isothermal flow of viscous incompressible liquid. In the paper (Stogney & Kretinin, 2005), the NMWR is used for simulating flows within a channel with permeable wall. Neural network solution results of hydrodynamic equations for the computational zone consisting of two sub-domains are presented below. One is rotating, while another is immobile. In this case, for NMWR algorithm realization specifying the conjugate conditions at the two sub-domains border is not required.
In the second approach, neural network structures are applied to computational experiment results approximation obtained by using traditional methods of computational hydrodynamics and for obtaining of hydrodynamic processes multifactor approximation models. This approach is illustrated by hydrodynamics processes neural network modeling in pipeline in the event of medium leakage through the wall hole.

2.1 NMWR application: Preliminary studying

There are specific ANN training programs such as STATISTICA NEURAL NETWORKS or NEURAL TOOLBOX in the medium of MATLAB, adjusting the parameters of the network

to the known values of the objective function within the given points of its definitional domain. Using these packages in our case, therefore, does not seem possible. At the same time, many of optimization standard methods work well for ANN training, e.g. the conjugate gradients methods, or Newton, etc. To solve the issue of ANN training, we shall use the Russian program IOSO NS 1.0 (designed by prof. I.N. Egorov (Egorov et al., 1998), see www.IOSOTech.com) realizing the algorithm of indirect optimization method based on self-organizing. This program allows minimizing the mathematical model given algorithmically and presented as "black box", i.e. as external file module which scans its values from running variable file generated by optimization program, then calculates objective function value and records it in the output file, addressed in turn by optimization program. It is therefore sufficient for computer program forming, realizing calculations using the required neural network, where the input data will be network internal parameters (i.e. weights, thresholds); on the output, however, there'll be value of required equation sum residual based on accounting area free points. Let us suppose that the objective function $y = x^2$ is determined within the interval $[0;1]$. It is necessary to define parameters of ANN perceptron type with one hidden layer, consisting of 3 neurons to draw the near-objective function with given accuracy, computed in 100 accounting points x_i evenly portioned in determination field. Computer program for computing network sum residual depending on its parameters can be as follows (Fortran):

```
      dimension x(100),y(100)
      dimension vs(10)
      common vs
c     vs- values of ANN internal parameters
      open(1,file='inp')
      read(1,*)vs
      close(1)
c     'inp'- file of input data,
c     generated by optimization program
      do i=1,100
      x(i)=(i-1)/99.
      end do
c     calculation by subprogram ANN ynet
c     and finding of sum residual del
      del=0.
      do i=1,100
      y(i)=ynet(x(i))
      del=del+(y(i)-x(i)**2)**2
      end do
c     'out'-file of value of the minimization function ,
c     sent to optimization program
      open(2,file='out')
      write(2,*)del
      close(2)
      end
      function ynet(t)
      dimension vs(10),w(3),b(3),v(3),t1(3),q(3)
```

```
      common vs
c     w-weights between neuron and input
c     b-thresholds of neurons
c     v-weights between neuron and output neuron
c     bv-threshold of output neuron
      do i=1,3
      w(i)=vs(i)
      b(i)=vs(i+3)
      v(i)=vs(i+6)
      end do
      bv=vs(10)
      vyh=0.
      do i=1,3
      t1(i)=w(i)*t-b(i)
      q(i)=1./(1.+exp(-t1(i)))
      vyh=vyh+v(i)*q(i)
      end do
      ynet=vyh-bv
      end
```

With IOSO NS 1.0, ANN internal parameter values were obtained with sum residual there were received the values of the internal parameters of the ANN, giving the sum $E = 0.000023$ (fig. 2).

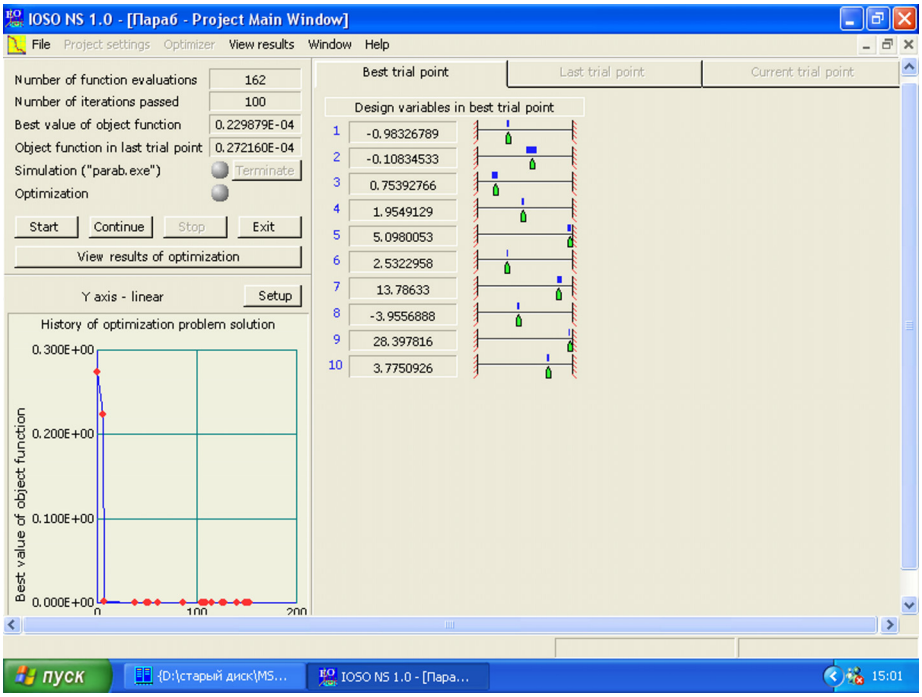

Fig. 2. Results of using IOSO NS 1.0 for the ANN training

Hence we have neural network approximation for given equation, which can be presented by the formula

$$y = 13.786\frac{1}{1+e^{1.954913+0.983267\cdot x}} - 3.95569\frac{1}{1+e^{5.098+0.108345\cdot x}} + 28.3978\frac{1}{1+e^{2.532-0.75393\cdot x}} - 3.7751 \quad (5)$$

Using nonlinear optimization universal program products for ANN training is limited to neural networks of the simplest structure, for dimension of optimization tasks solved by data packages does not normally exceed 100; however, it frequently forms 10-20 independent variables due to the fact that efficiency of neural network optimization methods generally falls under the greater dimensions of the nonlinear programming free task. On the other hand, the same neural network training optimization methods prove efficient under much greater dimensions of vector independent variables. Within the framework of given functioning, the standard program codes of neural network models are applied, using the well-known optimization procedures, e.g. Levenberg-Markardt or conjugate gradients - and the computing block of trained neural network with those obtained by the analytical expressions for objective function of the training anti-gradient components, which in composition of the equation under investigation acts as a "teacher" is designed.

2.2 Computing algorithm of minimization of neural network decision

Let us consider perceptron operation with one hidden layer from N neuron and one output (1). As training objective function, total RMS error (4) will be considered. The objective function shall be presented as a complex function from neural network parameters; components of its gradient shall be calculated using complex function formula. Network output, therefore, is calculated by the following formula:

$$y\left(\mathbf{x}^s\right) = \sum_j w_j \sigma_j\left(\mathbf{x}^s\right), \quad (6)$$

where **x** - vector of inputs, *s* - number of point in training sample, $\sigma(x)$ - activation function, w_j - weights of output neuron, *j* - number of neuron in hidden layer. For activation functions, logistic sigmoid will be considered

$$\sigma_j\left(\mathbf{x}\right) = \frac{1}{1+e^{-t_j\left(\mathbf{x},b_j\right)}}. \quad (7)$$

Here b_j - threshold of *j*-number neuron of hidden layer; the function $t_j(\mathbf{x},b_j)$, however, has form of $t_j\left(\mathbf{x},b_j\right) = \sum_i v_{ij}\cdot x_i - b_j$, where v_i - neuron weight of hidden layer.

While training on each iterations (the epoch) we shall correct the parameters of ANN toward the anti-gradient of objective function - $\nabla E(\mathbf{v},\mathbf{w},\mathbf{b})$, which components are presented in the following form:

$$\frac{\partial E^s}{\partial w_{ij}} = \sigma_j\left(\mathbf{x}^s,b_j\right)\cdot\left(y^s - f\left(\mathbf{x}^s\right)\right); \quad (8)$$

$$\frac{\partial E^s}{\partial v_{ij}} = \left(y^s - f\left(\mathbf{x}^s\right)\right) \cdot w_j \cdot \sigma_j\left(\mathbf{x}^s, b_j\right) \cdot \left(1 - \sigma_j\left(\mathbf{x}^s, b_j\right)\right) \cdot x_i^s ; \tag{9}$$

$$\frac{\partial E^s}{\partial b_j} = -\left(y^s - f\left(\mathbf{x}^s\right)\right) \cdot w_j \cdot \sigma_j\left(\mathbf{x}^s, b_j\right) \cdot \left(1 - \sigma_j\left(\mathbf{x}^s, b_j\right)\right). \tag{10}$$

Thereby, we have got all the components of the gradient of the objective function of minimization, comparatively which iterations will be consecutively realized in accordance with the general formula

$$\Delta \mathbf{w} = -\varepsilon \nabla E\left(\mathbf{w}\right). \tag{11}$$

Here **w** is vector of current values of network weights and thresholds.

3. Using NMWR for hydrodynamics equations solving

Parameter optimization of neural network trial solutions is achieved by applying several optimization strategies and by subsequently choosing the maximum effective one (see Cloete & Zurada, 2000). First strategy is to apply totality of effective gradient methods "starting" from various initial points. The other strategy is to apply structural-parametrical optimization to ANN training; this method is based on indirect statistic optimization method on self-organizing basis or parameter space research (see: Egorov et al., 1998; Statnikov & Matusov, 1995).

Any versions for multi-criterion search of several equations system solution are based on different methods of generating multiple solutions, satisfying Pareto conditions. Choosing candidate solution out of Pareto-optimal population must be based on analysis of hydrodynamic process and is similar to identification procedure of mathematical model. In any case, procedure of multi-criterion optimization comes to solving single-criterion problems, forming multiple possible solutions. At the same time particularities of some computational approaches of fluid dynamics allows using iteration algorithms, where on each step solution at only one physical magnitude is generated.

3.1 Modeling flows – the first step

The computational procedure described below is analogous to MAC method (Fletcher, 1991), investigating possibility of NMWR application based on neural net trial functions.

Laplace equation solution

Computational capabilities of the developed algorithm can be illustrated by the example of the solution of Navier-Stokes momentum equations, describing two-dimensional isothermal flows of viscous incompressible fluid. On the first stage we will be using this algorithm for Laplace equation solution

$$\frac{\partial^2 \varphi}{\partial x^2} + \frac{\partial^2 \varphi}{\partial y^2} = 0 . \tag{12}$$

Let us consider the flow of incompressible fluid in the channel (fig. 3).

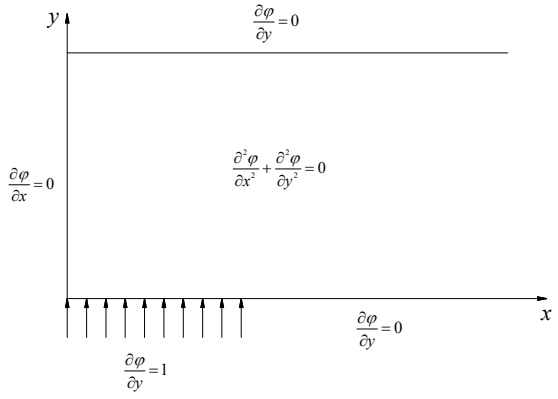

Fig. 3. Computational area

Here's how the boundary conditions are defined: on solid walls u=v=0, on inflow boundary u=0, v=1, on outflow boundary $\frac{\partial u}{\partial x}=\frac{\partial v}{\partial x}=0$. There are no boundary conditions for pressure except for one reference point, where p=0 is specified (in the absolute values p=p_0), considering which indication of incoming into the momentum equation $\frac{\partial p}{\partial x}$ and $\frac{\partial p}{\partial y}$ is realized.

For solving flow equations by predictor method it is necessary to specify initial velocity distribution within the computational area, satisfying the equation of continuity. For this purpose, velocity potential $\varphi(x,y)$ is introduced and $u=\frac{\partial\varphi}{\partial x}$ and $v=\frac{\partial\varphi}{\partial y}$. As a result of Laplace equation solution, velocity distribution is generated, which can be indicated as free-vortex component of the sought quantity.

If the result of learning sample neuronet calculations is defined by the following formula $\varphi(\mathbf{x}^s)=\sum_j v_j f_j(\mathbf{x}^s)$, where $\mathbf{x}=\{x,y\}^T$ -input variables vector, s - point number in the learning sample, $f(\mathbf{x})$ - activation function, v_j - output neuron weights, j - neuron number in the hidden layer as activation function the logistical sigmoid is used $f_j(\mathbf{x})=\frac{1}{1+e^{-t_j(\mathbf{x},b_j)}}$, where b_j - threshold of the j-number neuron hidden layer, and the function $t_j(\mathbf{x},b_j)$ looks like $t_j(\mathbf{x},b_j)=\sum_i w_{ij}\cdot x_i-b_j$ where w_{ij} - hidden layer neurons weights, then analytical expressions for the second speed potential derivatives can be calculated using the following formula

$$\frac{\partial^2\varphi}{\partial\left(x_i^s\right)^2}=\sum_j\left(v_j w_{ij}^2\left(f_j(\mathbf{x}^s,b_j)-3f_j^2(\mathbf{x}^s,b_j)+2f_j^3(\mathbf{x}^s,b_j)\right)\right). \quad (13)$$

Equation summary residual with substituted trial solutions (1) on arbitrary calculation area points with coordinates $\mathbf{x}^s$ with expressions application (13) can also be calculated analytically

$$E = \frac{1}{2}\sum_s \sum_i \left(\frac{\partial^2 \varphi}{\partial \left(x_i^s \right)^2} \right)^2 = \frac{1}{2}\sum_s \left(\frac{\partial^2 \varphi}{\partial \left(x^s \right)^2} + \frac{\partial^2 \varphi}{\partial \left(y^s \right)^2} \right)^2 . \quad (14)$$

Therefore, trial solution (1) training problem of neural network equation consists in SLP hidden layer parameter selection (weights and thresholds) at which the summary residual (14) has the minimal value limited to zero. The computer program described above, with training procedure target function being set functionally by applying analytical expressions for second derivatives $\frac{\partial^2 \varphi}{\partial x^2}$ and $\frac{\partial^2 \varphi}{\partial y^2}$, is used for parameter adjustment of learning model.

Efficiency of searching of neuronet learning solution parameters depends on problem dimension, i.e. weights and perceptron thresholds variable adjusted quantity. The more significant is neurons quantity in trial solution, the higher is ANN approximate capacity; however, achieving high approximation accuracy is more complicated. At the same time, neuron quantity depends not only on simulated function complexity, but also on calculation nodes quantity in which the residual equation is calculated. It is known that generally points' quantity increase in statistical set used for neural network construction is followed by increase in necessary neurons network (Galushkin, 2002; Galushkin, 2007) quantity. Consequently, the dense calculation grids application results in nonlinear programming problems; while applying rare calculation grids, it is necessary to check the solution realization between calculation nodes, i.e. there is a problem of learning solution procedure standardization. In the neuronet solution reception context on known equation, it is convenient using traditional additive parameter of training neural model quality - a control error which is calculated on the set of additional calculation nodes between calculation grid nodes. Number of these additional calculation grid nodes can be much more significant, and they should cover the whole calculation area, because the nodes number increase with control error on known network parameters does not result in essential computing expenses growth. Hence, referring to learning solution neuronet parameters reception, there exists an issue of solving twice-criterion problem of nonlinear optimization along with minimizing simultaneously both summary residual in control points, or the control error can appear as a restriction parameter, in the limited set of calculation nodes and in this case the neural network solution parameters reception is reduced to the conditional nonlinear optimization problem.

At the first stage, residual distribution of the current equation (5) on various calculation nodes and the corresponding speed vector distribution $\mathbf{v} = \{u, v\}^T$, where speed nodes $u = \frac{\partial \varphi}{\partial x}$ and $v = \frac{\partial \varphi}{\partial y}$. As a whole, the received neural network solution satisfies the equation (5) except for calculation nodes group, for example, in the input border right point vicinity, due to a sudden change of the boundary conditions in this point. In areas with the solution insufficient exactness we will place the calculation nodes additional quantity using the

following algorithm. Let us formulate the Cohonen neural network with three inlet variables presented by the coordinates of available computation nodes x and y, and also the equations (5) residual value in these nodes, along with the required cluster centers quantity equal to the additional nodes quantity. The cluster center coordinates which will generally be placed in areas with the learning solution low precision (Prokhorov et al., 2001) we will consider additional computation nodes coordinates. The number of these additional nodes in each case is different and defined by iterations, until the decision error does not accept comprehensible value. As a result of the additional formation of received neural network learning solution using additional computation nodes, it turned out to be possible to increase the solution local accuracy in the point B vicinity while maintaining the accuracy high in all other points.

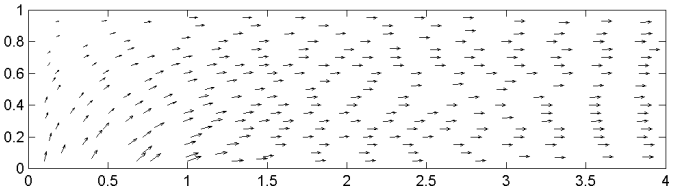

Fig. 4. Formation of additional computation nodes for Laplace equation solution

Therefore, not only has the computing experiment proven reception opportunity of the general neural network solution in the calculation area, but also defined coordinate calculation logic of computational nodes for increasing the accuracy of neural network initial equation solution. Let us study a reception opportunity of the Poisson equation solution using an irregular computational grid, i.e. equation total residual with solutions (1) will be calculated in nodes located in the casual image or certain algorithm, which use has not been connected with the necessity of computational grid coordination and computational area borders.

Poisson equation

Let us study a neural network solution precision on irregular calculation scales for Poisson equation

$$\frac{\partial^2 p}{\partial x^2} + \frac{\partial^2 p}{\partial y^2} = \Delta \neq 0 \,. \tag{15}$$

This equation is particularly used for calculating the pressure distribution as well as for time iterations organization at the Navier-Stokes equations solution by pseudo-non-stationary algorithms (Fletcher, 1991). For the solution we shall use an irregular calculation grid, because, in contrast to fluid dynamics classical numerical methods, it does not result in the neutral network learning functions algorithm complication. Meanwhile, advantages using calculation nodes located in calculation area for the complex geometry study current are obvious. The decision is defined by the equations (15) with the right side as follows

$$\frac{\partial^2 p}{\partial x^2} + \frac{\partial^2 p}{\partial y^2} = \Delta = 2\left(\frac{\partial u}{\partial x}\frac{\partial v}{\partial y} - \frac{\partial v}{\partial x}\frac{\partial u}{\partial y}\right), \tag{16}$$

where speed nodes $u=\frac{\partial\varphi}{\partial x}$ also $v=\frac{\partial\varphi}{\partial y}$ are received as a result of the Laplace equation solution (12). Calculation grid points are formed as centers of Cohonen network clusters constructed on units coordinates of the uniform rectangular scale and on the right part of the equation (16) corresponding to these units values Δ. Fig. 6 (a) presents formation re sults of the calculation grid and the speed distribution on the pseudo-non-stationary algorithm first iterative step of the Navier-Stokes equation solution. Here it was possible to receive an exact neural network solution for the whole calculation area without using additional set of calculation nodes.

Let us now study am incompressible fluid internal flow within a channel with a stream turning (fig. 3). Navier-Stokes equation system describing two-dimensional isothermal flows of the viscous incompressible fluid (Fletcher, 1991):

$$\frac{\partial u}{\partial x}+\frac{\partial v}{\partial y}=0; \tag{17}$$

$$\frac{\partial p}{\partial x}+u\frac{\partial u}{\partial x}+v\frac{\partial u}{\partial y}-\frac{1}{\mathrm{Re}}\left\{\frac{\partial^2 u}{\partial x^2}+\frac{\partial^2 u}{\partial y^2}\right\}=0; \tag{18}$$

$$\frac{\partial p}{\partial y}+u\frac{\partial v}{\partial x}+v\frac{\partial v}{\partial y}-\frac{1}{\mathrm{Re}}\left\{\frac{\partial^2 v}{\partial x^2}+\frac{\partial^2 v}{\partial y^2}\right\}=0. \tag{19}$$

Here *u, v* – nodes speed, Re - Reynolds number. Hydrodynamics equations system is written in the non-dimensional view; i.e. it includes non-dimensional values $u^*=\frac{u}{u_\infty}$, $v^*=\frac{v}{u_\infty}$, $r^*=\frac{r}{D}$, $p^*=\frac{p}{\rho\cdot u_\infty^2}$, $\mathrm{Re}=\frac{\rho\cdot u_\infty\cdot D}{\mu}$. Quality of u_∞ and any speed and linear size values can be chosen in the current field, for example an input fluid speed value in the channel and the channel width h.

Boundary conditions are stated as follows: on solid walls *u=v=0*, on the input border *u=0*, *v=1*, on the output border $\frac{\partial u}{\partial x}=\frac{\partial v}{\partial x}=0$. Let us consider that there is rectangular region [a,b]×[c,d] within the plane *XY*, and there is a rectangular analytical grid, specified by Cartesian product of two one-dimensional grids $\{x_k\}$, *k=l,…,n* and $\{y_l\}$, *l*=l,…,*m*.

We will understand neural net functions $u,v,p=f_{NET}(\mathbf{w},x,y)$ as the (17)-(19) system solution giving minimum of the total squared residual in the knot set of computational grid. The trial solution (fig. 5) of the system (17)-(19) *u, v, p* can be presented in the form equation (1):

$$u(\mathbf{w},x,y)=\sum_{i=1}^{q}v_i f_\sigma(b_i+w_{i1}x+w_{i2}y)+b_u; \tag{20}$$

$$v(\mathbf{w},x,y)=\sum_{i=q+1}^{2q}v_i f_\sigma(b_i+w_{i1}x+w_{i2}y)+b_v; \tag{21}$$

$$p(\mathbf{w},x,y)=\sum_{i=2q+1}^{3q} v_i f_\sigma(b_i+w_{i1}x+w_{i2}y)+b_p\,. \tag{22}$$

Here again, **w** is the vector of all the weights and thresholds of the net. In this case the amount of q neurons in the trial solutions remains the same for each decision variable set. This is the parameter on which depend approximated capabilities of neural net trial solution. Result of computational algorithm functioning should be achievement of necessary accuracy level of solution at q minimum value.

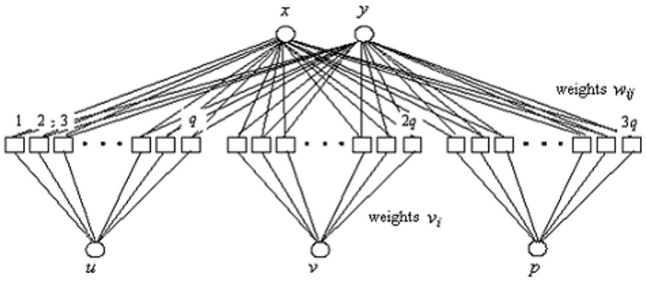

Fig. 5. Neural net trial solution

Let us name the residuals of equations (17)-(19) R_1, R_2 and R_3 correspondingly, then for the vase of NMWR realization for parameters setup of the trial solution it is necessary to minimize three objective functions $R_1^2;R_2^2;R_3^2\to\min$. In the simplest case, the only solution of the multi-criterion problem of minimization can be generated substituting of three criterions by one, presented in compression form; for example, $R^2=R_1^2+R_2^2+R_3^2\to\min$. Presenting the trial solution in the form of continuous functions (20)-(22) allows to define analytically the first and the second differential coefficient in the equations (17)-(19), knowing which one can generate analytic expressions of the function of residuals R^s(**w**,*x,y)* and further for antigradient component of the total residual in the *s*-reference point at ANN inner parameters $\frac{\partial R}{\partial v_j}$, $\frac{\partial R}{\partial w_{ij}}$ and $\frac{\partial R}{\partial b_j}$, being later used in the minimization algorithm in accordance with anti-gradient direction.

For the momentum equations solution by MAC method, it is necessary to specify an initial speeds distribution in the calculation area satisfying to the continuity equation. For this purpose, the speed potential $\varphi(x,y)$ is introduced, $u=\frac{\partial\varphi}{\partial x}$ and $v=\frac{\partial\varphi}{\partial y}$. As a Laplace equation solution result, we obtain speed distribution which can be called non-vortex required value.Final speeds and pressure distribution are results of the momentum equations solution according to the following algorithm.

The speed distribution on the following time layer is calculated according to the formula

$$\mathbf{u}^{n+1}=\mathbf{F}^n-\Delta t\cdot\nabla p^{n+1}\,, \tag{23}$$

where pressure distribution to each iterative step is defined upon the Poisson equation solution

$$\nabla^2 p^{n+1} = \frac{1}{\Delta t}\nabla \mathbf{F}^n = f_{NET}(x,y) \quad . \tag{24}$$

Vector $\mathbf{F} \equiv (F,G)^T$ introduced to this algorithm can be calculated by the momentum equations (18-19); or Poisson equation (16) can be used for pressure calculation. Thus, the solution for pressure received from the equation (16) results in the continuity equation realization at the moment of time $n+1$. Once p^{n+1} is calculated, substitution of these values in the formula $\mathbf{u}^{n+1} = \mathbf{F}^n - \Delta t \cdot \nabla p^{n+1}$ allows to determine v^{n+1}. The iterative process goes on until speed distribution stops varying.

Let us briefly generalize the above mentioned results of calculation experiment in methodic form to set dynamic calculation scale at the Navier-Stokes equations (17)-(19) solution by the establishment method. First, Laplace equation (12) solution is calculated with the received scale or with rectangular scale, or by means of random numbers generator, or by using the Sobol - Statnikov generator of LP_τ (Statnikov & Matusov, 2002); then, distribution solving equation residual in the grid nodes; third, the additional multitude of calculation nodes is generated with using the Cohonen network; then, if the precision is not achieved, points 2 and 3 are realized and the additional calculation components quantity grows until exact neural network solution for the whole calculation area is found; further, pseudo-non-stationary algorithm iterations are organized by using the equations (23)-(24) where equation (16) solution is found on each time step on the multitude of calculation components, the coordinates of which vary depending on the Poisson equation right part distribution for each iterative step; finally, at steps 3 and 5 realization of structural optimization algorithms and learning neural network solutions standardization formation

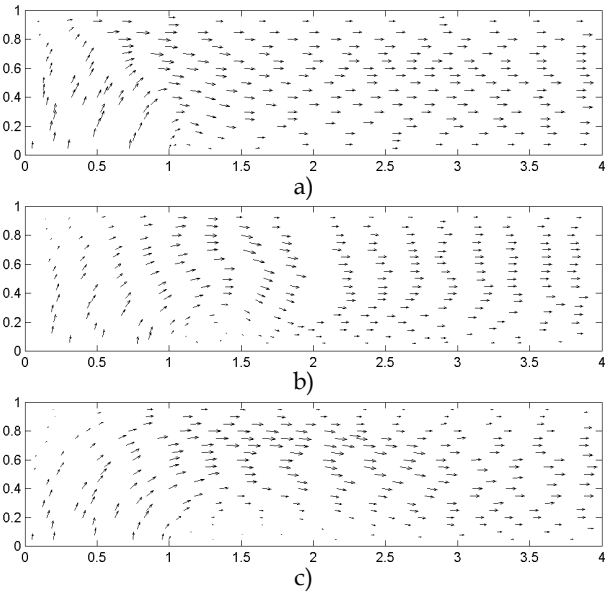

Fig. 6. Net velocity distribution

stated in (Kretinin et al., 2010). On fig. 6 (a-c), changing dynamics of calculation components during realizing various moments of time of equations (23)-(24) algorithm is shown, the speed vector distribution reorganization during the transition from the equation (12) solution to the equations (17)-(19) solution is also illustrated.
Finally, analytical solution (as neural network function) for Navier-Stokes equations (17)-(19) systems within the channel with stream turning at Re = 100 which is expressed by the formula (23) on last iterative layer and neural network dependence of the pressure distribution on this layer

$$p(\mathbf{w},x,y)=\sum_{i=2q+1}^{3q} v_i f_\sigma(b_i+w_{i1}x+w_{i2}y)+b_p$$

with weights calculated array and the boundary network $\mathbf{w}=\{w,v,b\}$.

3.2 Modeling flows in rotating ring zone - the equations that are applicable to rotating reference frame

For this flow, NMWR solves conservation equations for mass and momentum describing incompressible flows of viscous Newtonian fluid.
Continuity equation

$$\frac{\partial \overline{u}_j}{\partial x_j}=0\,. \tag{25}$$

Momentum equations

$$\frac{\partial}{\partial x_j}\left(\overline{u_i u_j}\right)+\frac{\partial}{\partial x_j}\left(\overline{u_i' u_j'}\right)=-\frac{\partial p}{\partial x_i}+\frac{\partial}{\partial x_j}\left[\mu\left(\frac{\partial \overline{u_i}}{\partial x_j}+\frac{\partial \overline{u_j}}{\partial x_i}\right)\right]+f_i\,. \tag{26}$$

For flows in rotating domain (fig. 7), the equations for conservation of mass and momentum are written for the relative velocity formulation, where f_i in right hand side is given by

$$\vec{f}_i=-\rho\left(2\vec{\omega}\times\vec{u}+\vec{\omega}\times\left(\vec{\omega}\times\vec{r}\right)\right). \tag{27}$$

The absolute velocity formulation is used in the non-rotating domain, and f_i=0. Thus, the standard $k-\varepsilon$ turbulence model is used.
Let us consider the neural network functions $\overline{u}_i,p,k,\varepsilon=f_{NN}(\mathbf{w},x,y)$ as equations solution, where **w–** all weights and network thresholds vector that assure summary quadratic residuals minimums for each equation in optional totality of computation nodes coordinating each neural network solution learning iteration, are generated using the random number generator.
Neuronet learning solution parameter search process efficiency depends on problem dimension, i.e. weights and perceptron thresholds varying adjusted quantity. The more significant is neurons quantity in trial solution, the higher is ANN approximate capacity; however, achieving high approximation accuracy is more complicated.

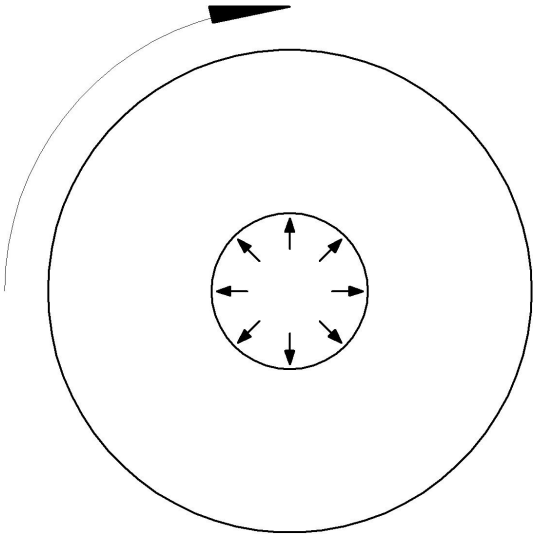

Fig. 7. Rotating Domain

At the same time, neuron quantity depends not only on simulated function complexity, but also on calculation nodes quantity in which the residual equation is calculated. It is known that generally points' quantity increase in statistical set used for neural network construction is followed by increase in necessary neurons network (Galushkin, 2002; Galushkin, 2007) quantity. Consequently, the dense calculation grids application results in nonlinear programming problems; while applying rare calculation grids, it is necessary to check the solution realization between calculation nodes, i.e. there is a problem of learning solution procedure standardization. In the neuronet solution reception context on known equation, it is convenient using traditional additive parameter of training neural model quality - a control error which is calculated on the set of additional calculation nodes between calculation grid nodes. The number of these additional calculation grid nodes can be much more important and they should cover all calculation area because the nodes number increase in which the control error on known network parameters does not result in essential computing expenses growth. Hence, at the learning solution neuronet parameters reception there is a problem of solving the multi-criterion problem of the nonlinear optimization and to minimize simultaneously both the summary residual in control points, or the control error can appear as a restriction parameter, in the limited set of calculation nodes and in this case the neural network solution parameters reception is reduced to the conditional nonlinear optimization problem.

On figure 8, velocity distribution vector within the current random computation nodes of revolving ring on one of neural network training iteration of equation (25)-(26) decisions is presented. Contours of stream function within the computational zone obtained by using NMWR are presented on fig. 9.

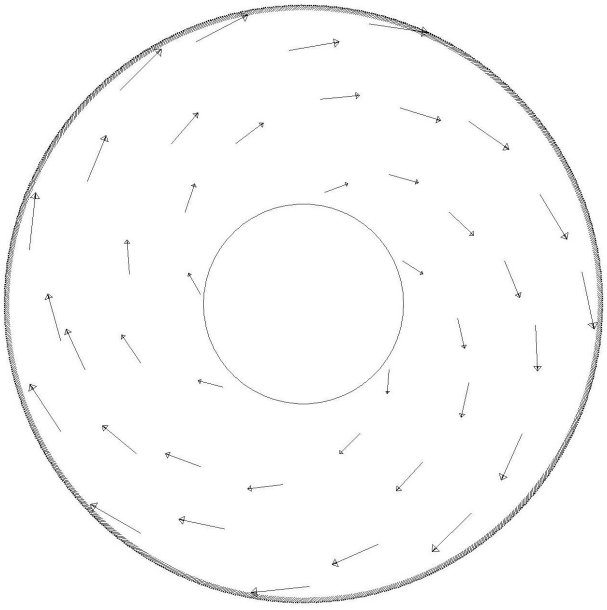

Fig. 8. Velocity distribution on one of neural network training iteration

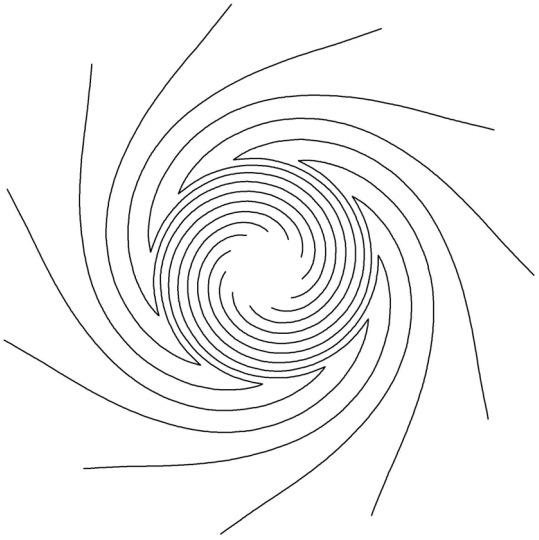

Fig. 9. The contours of stream function

4. Modeling leakage in a fuel transfer pipeline

Method of leakage zonal location (Zverev & Lurie, 2009), which generalizes the known method of leakage detection by hydraulic gradient line salient point, can be used to define of pipeline leakage position. When using the "base" zone location method variant, it is supposed that in case of stationary process, hydraulic gradients i_1 and i_2 before and after the leakage are constant and can be designed by the known values of liquid charge at the ends of controllable site. I.e., the distribution indignation of hydrodynamic parameters is not taken into account in comparison with the established flow which arises because of the environment outflow influence through the leakage aperture. It results in speed profile deformation within the cross sections of the pipeline near the leakage and the nonlinear dependence of hydraulic gradient in the function of distance from position of leakage downwards the stream. In order for pipe cross section speed distribution of the pipe to become appropriate for the established flow, the distance up to 40-60 calibres from leakage coordinate x_y can be required. Defining nonlinear dependence of hydraulic gradient function near the leakage is possible either based on special experimental researches, or based on the numerical decision of hydrodynamics equations in three-dimensional statement. The given function can be added to the algorithm of zone location methode to reduce the leakage position coordinate definition error.

One pipeline section of 300 m length and diameter $D = 1\,\text{m}$ is used for the nonlinear dependence of the total pressure drop determination along the pipeline length in the leakage neighborhood through the wall hole. The leakage position coordinate is fixed $x_y = 155.5\,\text{m}$. On the segment $x \in [140, 200]\,\text{m}$ computational faces are formed with an interval $h = 1\,m$. In segments $x \in [100, 140]\,\text{m}$ and $x \in [200, 250]\,\text{m}$ computational faces are disposed with an interval $h = 10\,\text{m}$. Such a leakage location (approximately in the middle of the pipeline sector into a question) and computational faces disposition have been chosen for the influence elimination of the boundary conditions setting in the computational zone inlet and outlet on the flow distribution near leakage position. The leakage hole D_l/D relative diameter during the computational planed experiment is constant. The mathematical model includes conservation equations for mass and momentum enclosed by the standard $k-\varepsilon$ turbulence model. The local hydraulic friction coefficient in any section of the pipeline is defined by the ratio

$$\lambda = -\left[8\mu \left.\frac{\partial u}{\partial r}\right|_{r=R}\right] \Big/ \left(\rho \bar{u}^2\right), \tag{27}$$

where $|\bar{u}| = \frac{1}{R^2}\int_0^R 2urdr$ - design section average speed, μ - dynamic factor of liquid viscosity.

Turbulent flow speed distribution within the pipe cross section is described by the universal logarithmic dependence

$$\frac{u}{u_*} = A \log \frac{u_* y}{\nu} + B, \tag{28}$$

where $u_* = \bar{u}\sqrt{\frac{\lambda}{8}}$ - the dynamic speed, y - the distance from the wall, ν - the kinematic viscosity.

At the statement of boundary conditions on the input, mass charge $\dot{m}_1$ or the speed $\bar{u}_1$ appropriate to this charge is set. In the grid units belonging to the leakage aperture, liquid outflow speed u_y is appointed. The given parameter at numerical researches varies for the modeling leakages of various intensity. For any point of the calculating area, any operational value of pressure $\partial/\partial x$ of all the hydrodynamical parameters are equaled to zero, for the concerning of which differences of pressure will be calculated, is set. On the output from the calculating area the conditions of the established current are set, i.e. the derivatives modeling of the boundary layer the standard wall functions for parameters of turbulence *k* and ε (Fletcher, 1991) are used.

The equations discretization is effectuated on the base of finite volumes method in the combination with hexagonal grid. On fig. 10 the formation of the grid in the calculating sections of the pipeline is represented.

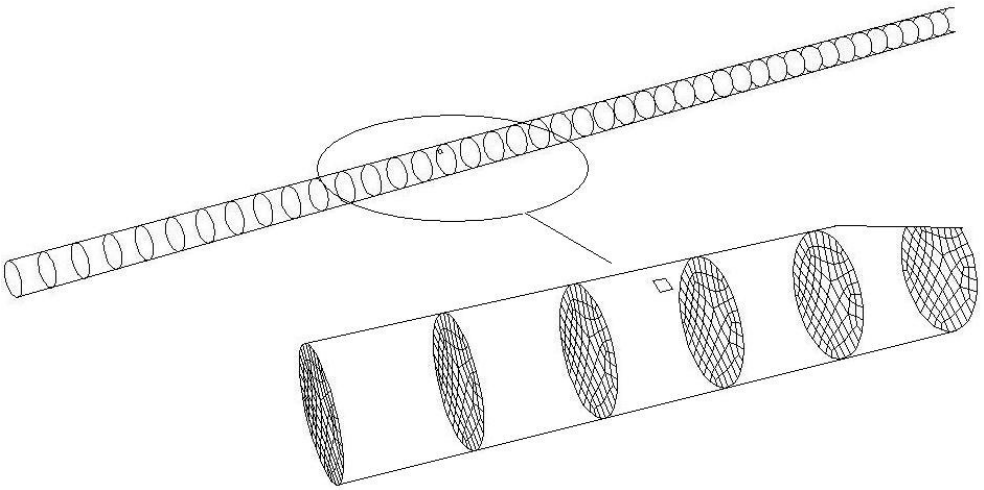

Fig. 10. Calculation grid in the pipeline sections

4.1 The plan of computing experiment

If x_1, x_2 are the coordinates of the beginning and the end of the controllable pipeline sector, then i_1, i_2 are hydraulic gradients before and after the leakage respectively, Δp_0 is total pressure drop of the sector, so in case of $i_1 = const$ from the beginning of the sector to the leakage and $i_2 = const$ from the leakage up to the end of the sector, in the stationary hydrodynamic mode, leakage coordinate shall be defined by the formula

$$x_y = \frac{\Delta p_0 + \rho g\left(i_1 x_1 - i_2 x_2\right)}{\rho g\left(i_1 - i_2\right)}. \tag{29}$$

Let us present the total pressure drop nonlinear dependence for its calculation in leakage neighbourhood in nonlinear function form $i = f_{NN}^{i}\left(i_1, i_2, x - x_{NN}\right)$ on the pipeline sector $x \in \left[x_{NN}, x_{NN} + l_{NN}\right]$, where for our computational model the left area limit coordinate of the nonlinear leakage function determination $x_{NN} = 150$ m and the determination length fragment area $l_{NN} = 60$ m (leakage is situated in the point with coordinate $x_y = 155{,}5$ m). In this case, total pressure drop in the controlled sector $\left[x_1, x_2\right]$ is calculated by the following formula

$$\frac{\Delta p_0}{\rho g} = i_1\left(x_{NN} - x_1\right) + i_2\left(x_2 - \left(x_{NN} + l_{NN}\right)\right) + \int_0^{l_{NN}} f_{NN}^{i}\left(i_1, i_2, x - x_{NN}\right) dx. \tag{30}$$

In the known function $f_{NN}^{i}\left(i_1, i_2, x - x_{NN}\right)$, the present equation is nonlinear with one unknown value x_{NN}. After solving this equation, we can define the pipeline leakage coordinate x_l.

Starting from above-mentioned, computational experiment is effectuated with the purpose of function determination $f_{NN}^{i}\left(i_1, i_2, x - x_{NN}\right)$, i.e. the total pressure drop dependence in the leakage neighbourhood i (criterion) of three variables $i_1^{NN} = \rho g i_1$, $i_2^{NN} = i_2 / i_1$ and $\Delta x_{NN} = x - x_{NN}$ (factors). Earlier, the interval forfactor variation $\Delta x_{NN} \in \left[0, 60\right]$ was determined. Let us determine the intervals $i_1^{NN} \in \left[10, 20\right]$, $i_2^{NN} \in \left[0{,}5; 0{,}95\right]$. The plan of computing experiment is made with the points received with the help of Sobol-Statnikov generator of quasiuniform number sequences (Statnikov & Matusov, 2002). The working hypercube of space $\mathbf{R}^3$ is filled with the points $\left(i_1^{NN}, i_2^{NN}, \Delta x_{NN}\right)$ according to LP_τ algorithm (Statnikov & Matusov, 2002). Choice of this algorithm for the experiment plan formation is made by high efficiency of the research method of parameter space based on the sounding of computational area by points of the uniform distributed sequence.For each variable, parameter combinations i_1^{NN}, i_2^{NN} from the experiment plan limitation boundary conditions in the computational model are selected by determining values corresponding tothe inlet mass flow $\dot{m}_{in}$ and leakage intensity $\dot{m}_l$, where the hydraulic friction coefficient is calculated by the implicit formula of Altschul for "smooth" pipes

$$\frac{1}{\sqrt{\lambda}} = -2{,}04 \log\left(\frac{2{,}82}{\mathrm{Re}\sqrt{\lambda}}\right).$$

As a result of computational hydrodynamics equations decision, we obtain the value distribution of total pressure drop on the length of the controlled pipeline sector, from which we are exterminating the criteria value i for the corresponding value Δx_{NN} from the experiment plan. Let us now register the obtained vector $\left(i_1^{NN}, i_2^{NN}, \Delta x_{NN}, i\right)$ in database for the posterior generation of neural network dependence $i = f_{NN}^{i}\left(i_1^{NN}, i_2^{NN}, \Delta x_{NN}\right)$.

For the illustration of numerical calculations, the distribution of speed in the leakage neighbourhood is presented on Fig. 11, and on fig. 12 the distribution of the hydraulic gradient on the pipeline sector $x \in \left[100, 250\right]$ m for factor values $i_1^{NN} \approx 14 \frac{\mathrm{Pa}}{\mathrm{m}}$, $i_2^{NN} = i_2 / i_1 = 0{,}5; 0{,}57; 0{,}64; 0{,}71; 0{,}8; 0{,}9$ is presented.

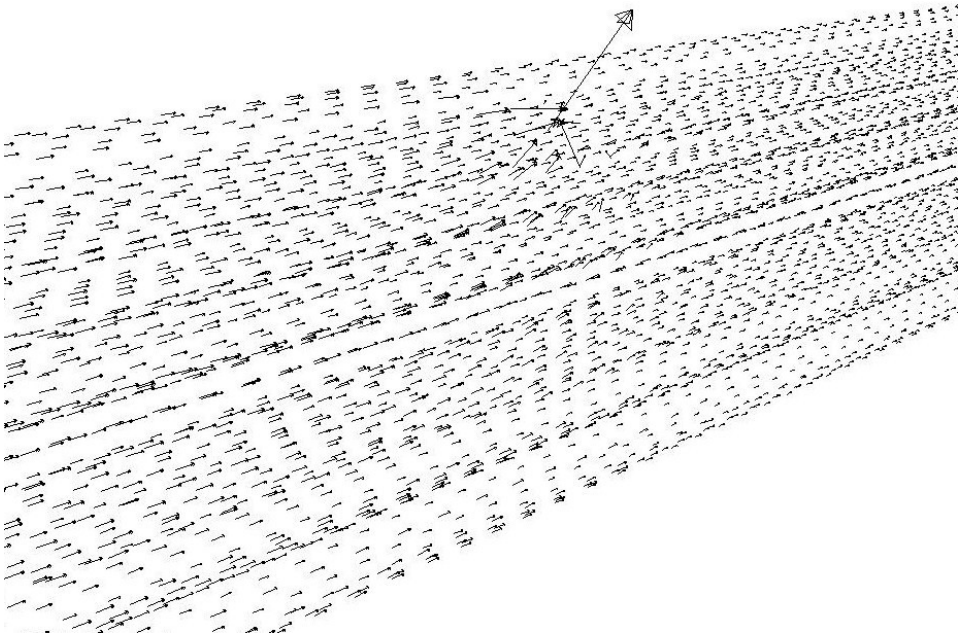

Fig. 11. Speed distribution in the leakage neighbourhood

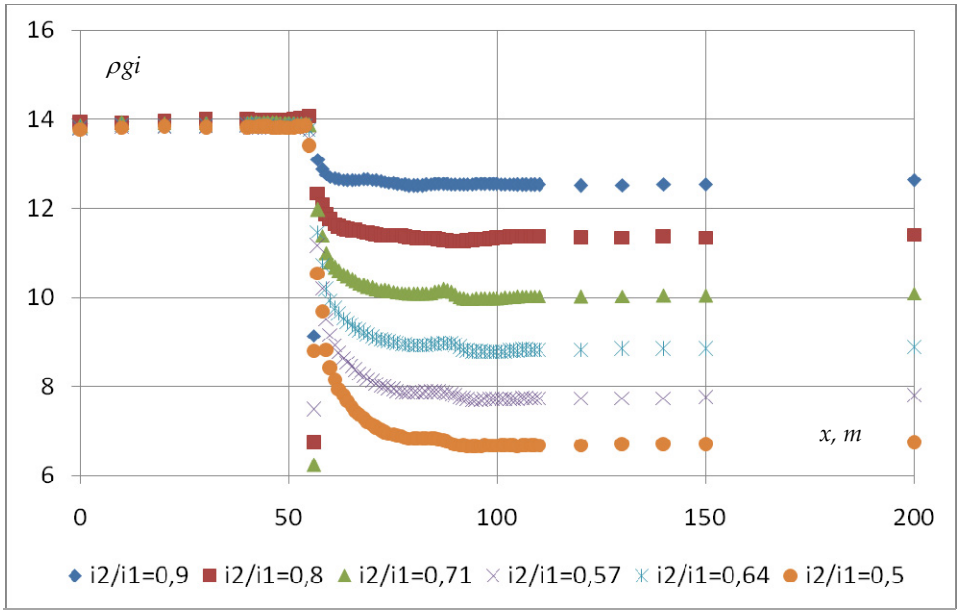

Fig. 12. Total pressure drop distribution for 1 meter of pipeline length

4.2 The neural network regressive model

For the regressive dependence construction, $i = f_{NN}^{i}\left(i_1^{NN}, i_2^{NN}, \Delta x_{NN}\right)$ artificial neural networks device is used. For the formation of display $i = f_{NN}^{i}\left(i_1^{NN}, i_2^{NN}, \Delta x_{NN}\right)$, the standard structure of the multilayer perceptron (MLP) with 3 inputs, one output and two latent layers with 7 and 5 neurons accordingly was used. At training, MLP algorithm of Levenberg-Markardt was used. The total RMS error on 512 points of statistical sample was *E=0.001*.
The comparative analysis of dependences calculation results obtained for inlet parameters values $\rho g i_1 = 16\,\frac{\text{Pa}}{\text{m}}$, $i_2 / i_1 = 0.9$ is presented on Fig. 13 and $\rho g i_1 = 10\,\frac{\text{Pa}}{\text{m}}$, $i_2 / i_1 = 0.8$ for $\Delta x_{NN} \in [0,60]\,\text{m}$ from the differential equation computational solution– continuous lines and determined with neural network dependence – markers. It is also necessary to note the high approximation precision.

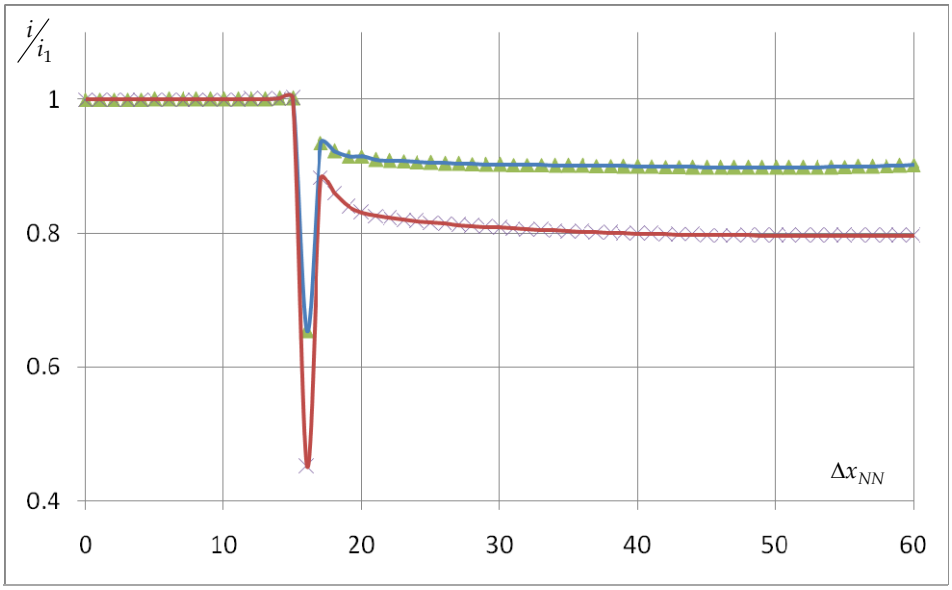

Fig. 13. Comparative analysis of neural network data and numerical solution results

5. Conclusion

Results presented in this chapter concern one of many applications of neural network learning functions to the mathematical physics problems solution, which is solution of hydrodynamics equations. Using learning functions of neural network allows to exclude the errors in solving differential equations caused by derivatives discretization and the borders low precision representation. Numerical algorithm of Navier-Stokes equations system solution differing from known fluid dynamics methods by the possibility of computational grid arbitrary formationis developed. The formation technique of the additional nodes file depending on learning solution local accuracy is offered.

The formation of the finite-elemental models for all extended pipelines and the numerical decision of equations of liquid movement for modeling the hydrodynamics processes now is limited to computer resources as by the quantity of the final elements of model calculated grid, so as by the time of finding of the decision. Even with such model, its use for system functioning operative analysis is quite doubtful. However, the numerical models of hydrodynamics processes can be used for the formation of information databases based on the neural network computing architecture which, after "training", have high speed of calculation. Neural networks are the universal approximation tool of multivariate nonlinear dependences, capable "to be arranged" under appearing of the new information of the researched process, i.e. they can serve as an intellectual tool for monitoring, which is constantly filled up and clarified. Thus, the introduction of neural algorithms in the approved and well-recommending methods of pipeline leakage detection is expedient for increased accuracy and the efficiency of accepted decisions.

6. References

Bishop, C.M. (1995) *Neural networks for pattern recognition*, Oxford University Press

Cloete, L. & Zurada, J.M. (2000) *Knowledge-Based Neurocomputing,* MIT Press

Egorov, I. N.; Kretinin, G.V.; Matusov I.B. & Statnikov, R.B. Problems of design and multicriteria control of controlled engineering systems. *J. Reports of RF Academy of Sciences,* Vol. 359, No. 3, 1998, pp. 330-333. ISSN 0869-5652

Fletcher, K. (1991). *Computational techniques for fluid dynamics,* Mir, Moscow, ISBN 5-03-001881-6

Galushkin, A.I. (2002). *Neuromathematics,* IPRJR, Moscow

Galushkin, A.I. (2007). *Neural networks theory,* Springer

Kretinin, A.V. The weighted residuals method based on neuronet approximations for simulation of hydrodynamics problems, *Siberian J. Num. Math*, 2006, Vol. 9, No.1, pp. 23-35.

Kretinin, A.V.; Bulygin, Yu. A. & Kirpichev, M.I. Method of Weighted Residuals on the Base of Neuronet's Approximations for Computer Simulation of Hydrodynamics Problems, *Proceedings of IEEE 6th International Conference on Computational Cybernetics ICCC 2008*. pp. 237-240, Stara Lesná, Slovakia, 2008.

Kretinin, A.V.; Bulygin, Yu. A.; Kirpichev, M.I. & Darneva, T.I. Neuronet's method of weighted residuals for computer simulation of hydrodynamics problems, Proceedings of 2010 International Joint Conference on Neural Networks. ISBN 978-1-4244-6916-1, Barcelona, Spain, 2010.

Prokhorov, D.; Feldkamp, L. & Feldkamp, T. A new approach to cluster weighted modeling. *Proceedings of International Joint Conference on Neural Networks (IJCNN),* Washington DC, July 2001

Statnikov, R.B. & Matusov, J.B. (1995). *Multicriteria Optimization and Engineering,* Chapman & Hall, N.Y.

Statnikov, R.B. & Matusov, J.B. (2002). *Multicriteria Analysis in Engineering,* Kluwer Academic Publishers, Dordrecht/ Boston / London

Stogney, V.G. & Kretinin, *A.V.* Simulation of Flows in a Channel with Permeable Wall Using Artificial Neural Networks. *Izv.Vuz. Av. Tekhnika*, Vol. 48, No. 1, 2005, pp. 34–38 [*Russian Aeronautics* (Engl.Transl.)]

Zverev, F.C. & Lurie, M.V. Generalized zonal location method of pipeline leakage detection, *Oil industry*, No 8, 2009, pp. 85-87

Part 3

Complex Hydraulic Engineering Applications

11

Interaction Between Hydraulic and Numerical Models for the Design of Hydraulic Structures

Angel N. Menéndez and Nicolás D. Badano
INA (National Institute for Water), Hydraulics Laboratory
Argentina

1. Introduction

The design of complex hydraulic structures requires its testing through hydraulic models (i.e., reduced scale physical representations). The main practical limitation of hydraulic models are the so called 'scale effects', i.e., the fact that only the primary physical mechanisms can be correctly represented, while the secondary ones are distorted. In particular, for free surface flows the gravitational driving forces – primary mechanism – must be correctly scaled in relation to inertia (Froude scaling), leading to an incorrect representation of viscous forces (no Reynolds scaling) – usually the leading secondary mechanism – as the fluid in the hydraulic model is the same as in the prototype (water). Though for most applications Reynolds number effects introduce only small quantitative deviations, which can be readily absorbed within the margin of safety assumed for design, this is not always the case. In fact, they can for example accumulate, in such a way that the effects compete with those arising from the primary mechanism. In those cases, being the Reynolds effects distorted in the hydraulic model, the observed response deviates from the one corresponding to the prototype, thus needing some empirical correction.
Numerical modeling is the appropriate tool to help solving in a rigorous way this type of difficulty. A sound numerical model should be able to correctly represent both the primary and secondary mechanisms, i.e., it is not subject to 'scale effects'. Its main limitations might arise from insufficient resolution, or from inaccurate representation of turbulence effects. The first limitation could be overcome by reducing the spatial step of the numerical grid; the second one, by resorting to more elaborated theoretical approaches.
Based on these observations, the following strategy is proposed: (i) the flow in the hydraulic model is numerically simulated, i.e., the dimensions of the hydraulic model are used (thus accounting for the 'spurious' scale effects); this constitutes a way of validating the theoretical model; eventually, adjustments in the representation (higher resolution, more elaborated theoretical approaches) are introduced in order to improve the comparison; (ii) the flow in the prototype is numerically simulated, by introducing the dimensions of the prototype in the validated numerical model (i.e., distortion of secondary mechanisms is now avoided); this constitutes the adequate way of extrapolating the results to the prototype dimensions.
Two problems (with quite different levels of complexity) are presented as case studies in order to illustrate the proposed approach, both of them associated to the design of the Third Set of Locks of the Panama Canal (communicating the Atlantic and Pacific Oceans), for which the present authors were responsible: (a) the determination of the time for water level

equalization between chambers, for which a one-dimensional numerical model was used; (b) the calculation of the amplitude of free surface oscillations in the lock chambers (which leads to increments in the hawser forces) due to close-to-resonance conditions under interaction with an oscillation in a flow partition component of the filling/emptying system (triggered by large turbulent eddies), for which a full three-dimensional numerical model – i.e., a CFD approach – was applied.

2. Equalization times

The equalization time, named as Filling/Emptying (F/E) time during the study, is a key parameter in establishing the system performance of a Lock Complex, as it has a direct impact on the vessel throughput, measured as the number of vessels passing through the system per day. Contractual requirements existed for the design of the Third Set of Locks of the Panama Canal, imposing maximum allowable F/E times for different scenarios. Minimization of these F/E times, through the reduction of local head losses, was the main strategy used during the design optimization process. Consequently, scale effects affecting these F/E times were carefully studied.

2.1 Description of the physical system

The Third Set of Locks of the Panama Canal, presently under construction, comprises twin lock complexes located near each ocean. Each complex has three lock chambers in series (Fig. 2.1). These lock complexes allow vessels to be transported up or down between Gatun Lake and the oceans, spanning a 27 m water level difference. Each lock chamber has three side pools, called Water Saving Basins (WSB). This WSBs store part of the water used during the equalization operations, that otherwise would be flushed downstream towards the ocean. This stored water is then utilized to refill part of the lock, allowing a reduction of freshwater consumption during dry hydrological seasons.

The lock chambers are connected through two longitudinal main culverts located within the lateral walls, running from the lake to the ocean. Four sets of valves are located along these culverts, which can isolate each chamber (Fig. 2.1). The operation of these valves allows the successive equalization of the water level between chambers by gravity flow.

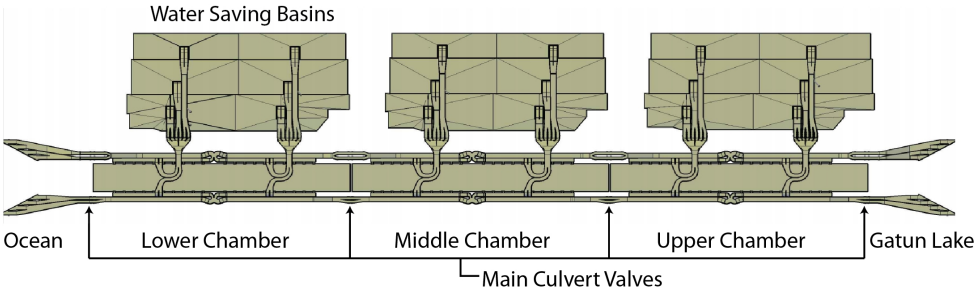

Fig. 2.1. Panama Canal Third Set of Locks F/E System – Bottom up view

In order to allow an even filling or emptying of the chambers, thus minimizing longitudinal water surface slopes and consequently hawser forces, water enters or exits each lock chamber through 20 ports located on each lateral wall. They are connected to secondary culverts which, in turn, connect to the main culvert at the midpoint of each chamber, through a carefully designed hydraulic component called Central Connection (CC) (Fig. 2.2). The CC was designed so as the flow coming from the main culvert is evenly split between both secondary culverts, before filling the chamber through the ports. Additionally, during the opposite operation, i.e., chamber emptying, equal discharges should flow through both secondary culverts, before its confluence towards the main culvert. The symmetry of the flow with respect to the chamber midpoint, for both the filling and emptying operations, is what ultimately guarantees low longitudinal water slopes and, consequently, low longitudinal hawser forces.

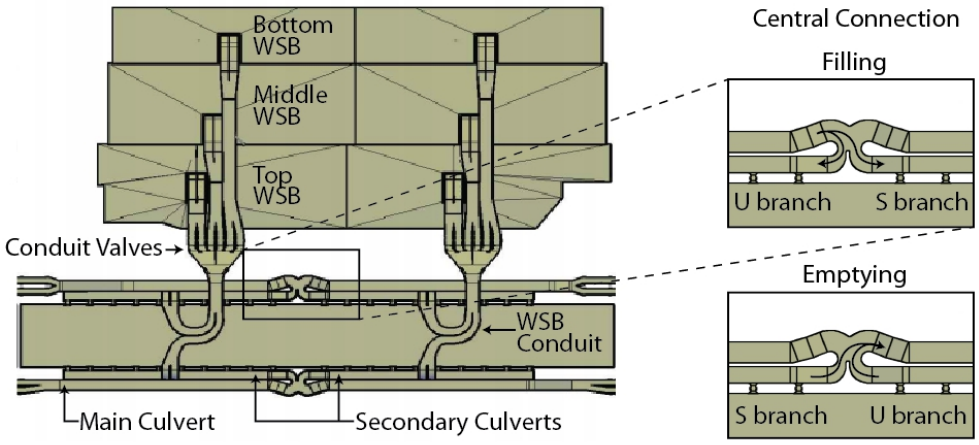

Fig. 2.2. Detail of the F/E system and Central Connection

The two branches of the CC are called 'U' and 'S' branches, in reference to the trajectory followed by the incoming flow (Fig. 2.2). Note that the role as a U or a S branch depends on the hydraulic operation (filling or emptying).
A conduit arising from the midpoint of each secondary culvert, and running below the chambers, connects them with the WSBs, after traversing a 'trifurcation' and a set of valves (Fig. 2.2).

2.2 Description of numerical model

The hydrodynamic model of the F/E system was built using Flowmaster V7 (http://www.flowmaster.com/), a commercial code which solves one-dimensional transient flow over a network of conduits. Incompressible fluid and rigid pipe hypothesis were made, without compromising accuracy. For convenience, the whole F/E system was divided into sub models, one for each type of operation, such as equalization of the Upper Chamber with the Lake, equalization of two contiguous chambers, equalization of chamber with its Water Saving Basins, and so on.

The F/E system was represented as a network of interconnected component elements, namely:

- Reservoirs, representing the lock chambers, WSBs, the lake, and the oceans. Level-Area relations were specified for each one of them. The lake and oceans were considered as infinite area constant level reservoirs.
- Rigid rectangular pipes, representing primary and secondary culverts, WSB conduits, etc. The calculation of friction losses was made using Darcy-Weisbach and Colebrook-White equations, as a function of the flow Reynolds number and the effective roughness height of the conduit walls.
- Local energy losses parameterized with a cross-section area and a head loss coefficient, representing most of the special hydraulic components, such as bends, bifurcations, transitions, etc.
- Local energy losses expressed as laws for cross-section area and head loss coefficient in terms of a control parameter, representing valves for which the control parameter is the aperture.

2.3 Numerical modeling of physical model

The Third Set of Locks has been subject to physical modeling, both during the development of the conceptual design, and later during the design for the final project. Both physical models where commissioned to the Compagnie Nationale du Rhône (CNR), Lyon, France.

The physical models were built at a 1/30 scale, comprising 2 chambers and one set of three WSBs. Extensive tests were made for various normal and special operations, measuring water levels, discharges, pressures and water slopes in the chambers. Some tests included the presence of a design vessel model, measuring hydraulic longitudinal and transversal forces over its hull. Based on these tests, a correlation between forces on the ship, and water surface slopes in the chamber in the absence of the ship (easier to measure and allegedly more repeatable), was established. This correlation was used to impose maximum values to the longitudinal and lateral water surface slopes, as contractual requirements.

The flow in the hydraulic model was numerically simulated. Real physical dimensions of the physical model components (culverts, conduits, chambers) were used.

Local head loss coefficients for the special hydraulic components were obtained through steady CFD modeling (see Section 3 for more details on CFD modeling), by calculating the difference between upstream and downstream mechanical energy, and subtracting energy losses due to wall friction. Most parts of the physical model were made out of acrylic (with a 0.025 mm roughness height), which behaves as a hydraulically smooth surface, for which the roughness height is completely submerged within the viscous sublayer (White, 1974). Some of the special hydraulic components, though, were built with Styrofoam (enclosed inside of acrylic boxes), as the initial expectations were that many alternative geometries would have to be tested, so this system would allow swapping with relative ease (very few alternatives were finally tested, due the great success of the optimization process carried out with CFD models). As it was later demonstrated that Styrofoam behaves as hydraulically rough at the physical model scale, most of it had to be coated with a low roughness layer of paint in order to avoid a spurious response (a scale effect in itself).

The results obtained with the numerical model (water levels, discharges, pressures) showed a very good agreement with physical model measurements, for different operations and conditions. As an illustration, Figs 2.3 and 2.4 show comparisons for a typical Lock to Lock operation, with maximum initial head difference. All comparisons are presented with results scaled up to prototype dimensions.

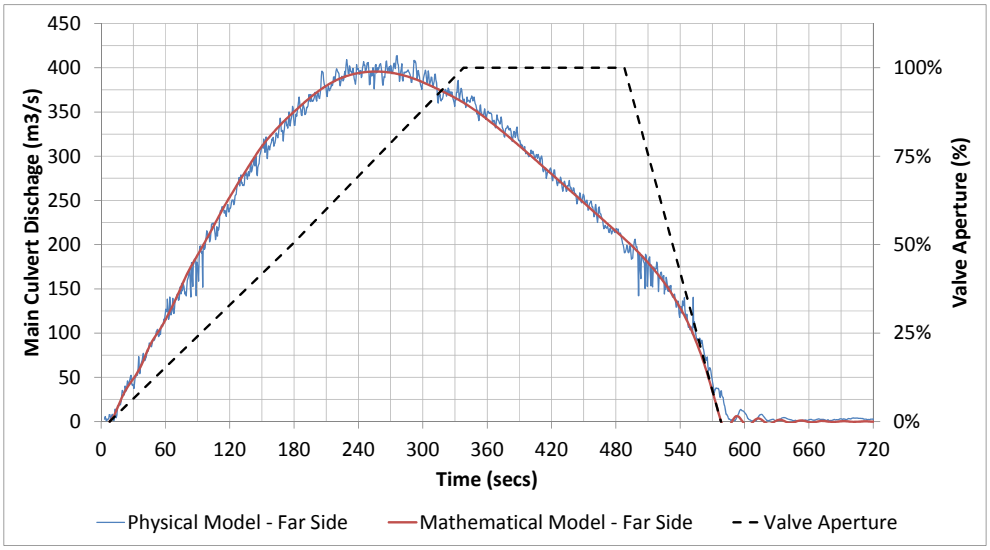

Fig. 2.3. Comparison of physical and numerical models: Discharge in the Main Culvert, for a Lock to Lock operation with 21 m of initial head difference.

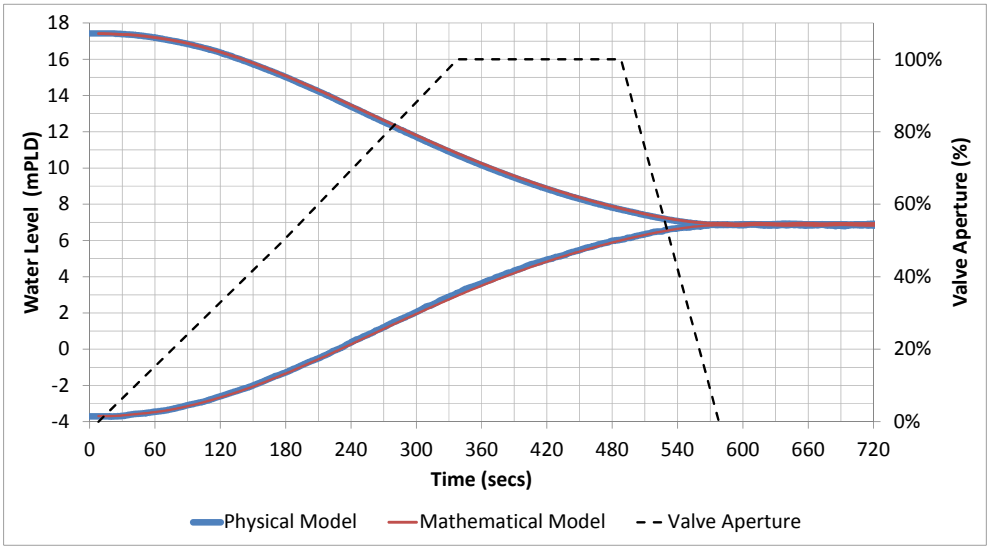

Fig. 2.4. Comparison of physical and numerical models: Water levels in the chambers, for a Lock to Lock operation with 21 m of initial head difference.

2.4 Numerical modeling of the prototype

Practical knowledge exists about the discrepancies between F/E times as measured in a physical model and those effectively occurring at the prototype. For instance, USACE manual on hydraulic design of navigation locks (2006) states:

> ..."A prototype lock filling-and-emptying system is normally more efficient than predicted by its model"..."The difference in efficiency is acceptable as far as most of the modeled quantities are concerned (hawser forces, for example) and can be accommodated empirically for others (filling time and over travel, specifically)."...

In the specific commentaries about F/E times, it suggests quantitative corrections:

> ..."General guidance is that the operation time with rapid valving should be reduced from the model values by about 10 percent for small locks (600 ft or less) with short culverts; about 15 percent for small locks with longer, more complex culvert systems; and about 20 percent for small locks (Lower Granite, for example) or large locks having extremely long culvert systems."...

The alternative, rigorous strategy proposed in the present paper is to numerically simulate the flow in the prototype. This means using the physical dimensions of the prototype, the corresponding local head loss coefficients for the special hydraulic components, and the roughness height for concrete. Though the concrete wall also behaves as hydraulically smooth, the friction coefficient for smooth pipes is a function of the flow Reynolds number, as indicated by the "smooth pipe" curve in the Moody chart (Fig. 2.5).

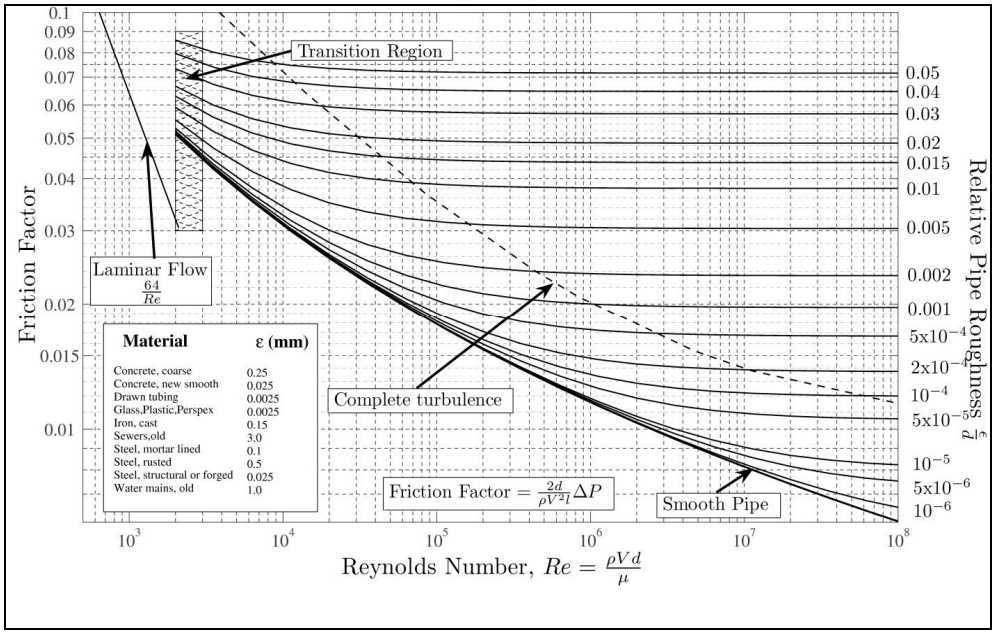

Fig. 2.5. Friction coefficient as a function of Reynolds number (Moody chart)

For example, the Reynolds number in the primary culvert (in which most of the friction losses are produced) changes in time following the flow hydrograph, from zero to the peak discharge, and back to zero again. The peak discharge for 21 m initial head difference in a Lock to Lock operation is around 425 m^3/s (the corresponding flow velocity is 7.87 m/s). This leads to a Reynolds number of around 6.5 10^7 for the prototype. When scaled to the physical model, the Reynolds number is only 3.9 10^5, i.e., a drop of more than two orders of magnitude. The associated friction coefficients are then below 0.008 for the prototype, and about 0.014 for the physical model. The consequently higher friction losses produced in the physical model, exclusively due to scale effects, reduce the flow velocities, then increasing the F/E times.

The numerical model contemplates the variation of frictional losses with the Reynolds number. Hence, it allows to be used in order to extrapolate the physical model results to those expected for the prototype, overcoming the distortion introduced by scale effects in the physical model results.

For the Panama Canal Third Set of Lock, the validated 1D model was scaled up to prototype dimensions. Variations in local head loss coefficients, indicated by 3D models, were also introduced. Relatively little effects were observed in the simulations because of the change in local head loss coefficients. On the contrary, friction losses decreased significantly, as already explained. Consequently, for a typical Lock to Lock operation with maximum initial head difference, F/E times showed a 10% decrease (61 seconds) (Fig. 2.6).

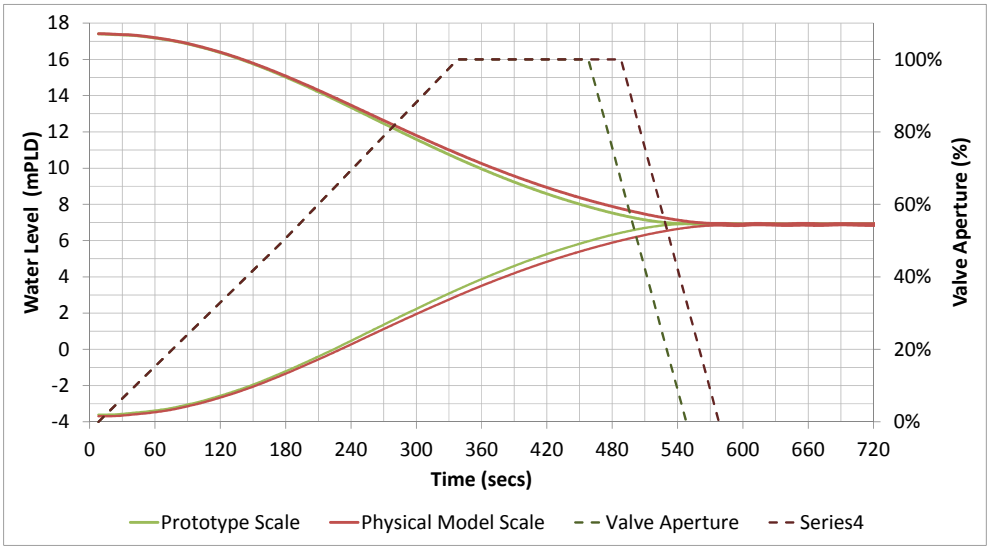

Fig. 2.6. Comparison of physical model scale and prototype scale numerical models: Water levels in the chambers, for a Lock to Lock operation with 21 m of initial head difference.

Additionally, a 5% increase in the peak discharge of the main culverts was also observed (Fig. 2.7). This has an effect over the pressures on the vena contracta, downstream of the main culvert valves (Fig. 2.8), which had to be contemplated during the design stage, as air intrusion had to be avoided (for contractual reasons), and because piezometric levels downstream of the valves were close to the roof level of the culvert for various special operating conditions. So avoiding scale effects was also significant to correctly deal with these two limitations.

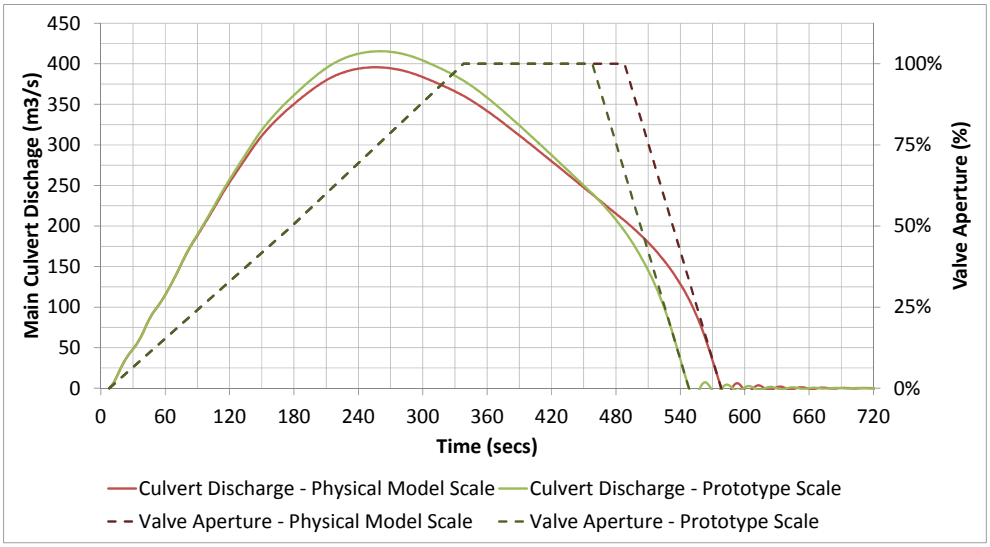

Fig. 2.7. Comparison of physical model scale and prototype scale numerical models: Discharge in the Far Main Culvert, for a Lock to Lock operation with 21 m of initial head difference.

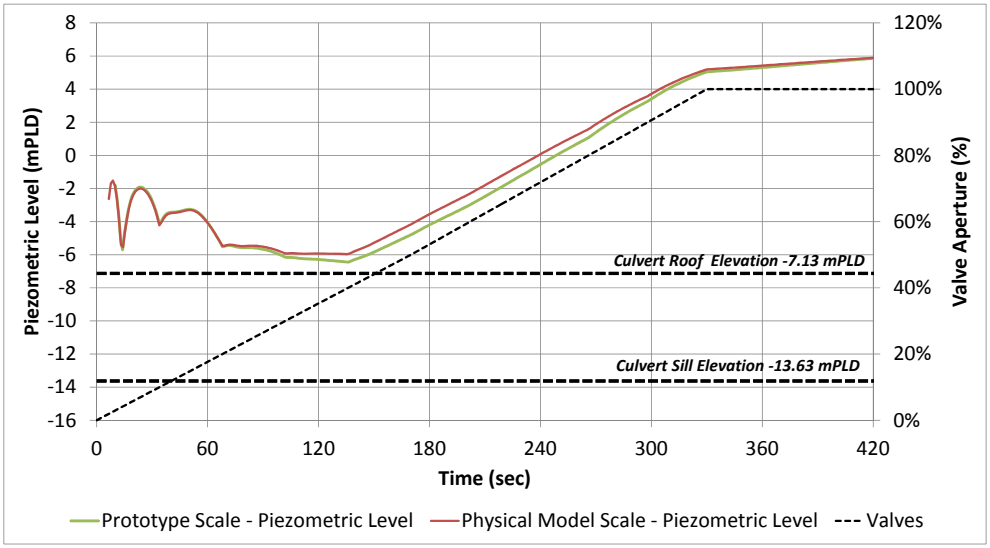

Fig. 2.8. Comparison of physical model scale and prototype scale numerical models: Piezometric level at the vena contracta, for a Lock to Lock operation with 21 m of initial head difference.

3. Free surface oscillations

Free surface oscillations in the lock chambers leads to forces in the hawsers. Based on results from the physical model constructed during the development of the conceptual design, a correlation was found between these forces and the free surface slope in the absence of the vessel, as already mentioned in Section 2. Hence, the free surface slope was used as an indicator for the hawser forces. As a design restriction, a maximum value of 0.14 ‰ was contractually established for the longitudinal water surface slope.

3.1 Description and modeling of phenomenon

Free surface oscillations in the lock chambers are triggered by asymmetries both in the flow distribution among ports, and in the geometry of the chambers (Figure 3.1).

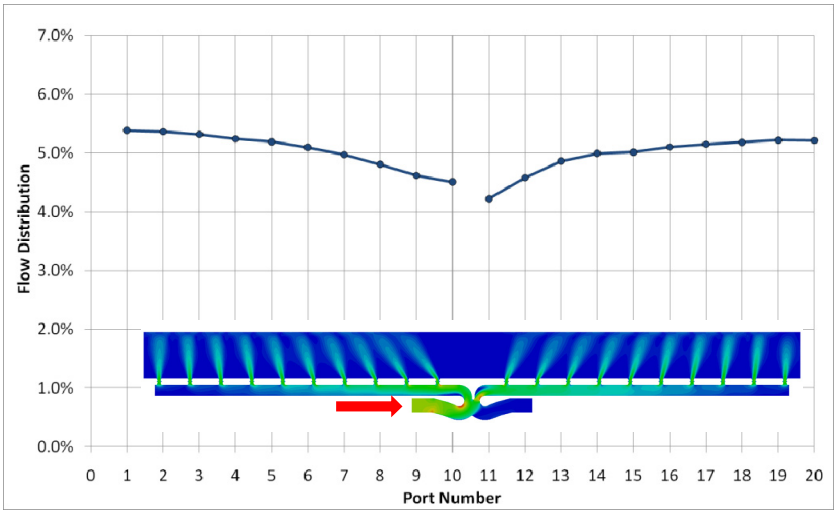

a) Flow distribution according to 1D model

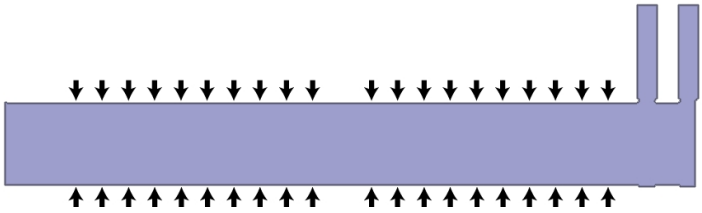

b) Plan view of chamber

Fig. 3.1. Asymmetries which trigger free surface oscillations.

A 2D (vertically averaged) hydrodynamic model, based on code HIDROBID II developed at INA (Menéndez, 1990), was used to simulate the surface waves. It was driven by the inflow from the ports, specified as boundary conditions through time series for each one of them, that were obtained with the 1D model described in the Section 2.

Fig. 3.2 shows the comparison between the calculated longitudinal free surface slope (using the dimensions of the physical model) and the recorded one at the physical model, for a case

with a relatively low initial head difference (9 m in prototype units) between the Lower Chamber and the Ocean. The agreement is considered as very good, taking into account that the numerical model does not include the resolution of turbulent scales (which introduce a smaller-amplitude, higher-frequency oscillation riding on the basic oscillation).

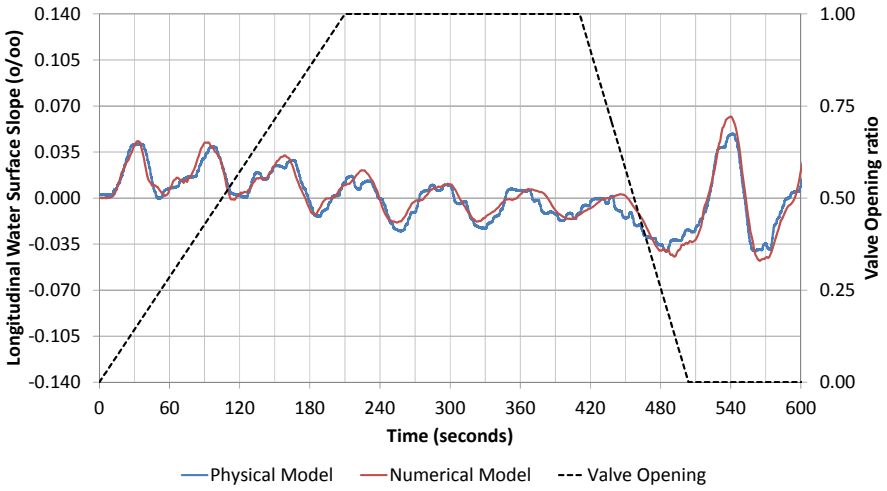

Fig. 3.2. Longitudinal water surface slope using 1D model input. Low initial head difference.

However, the 2D model completely fails to correctly predict the longitudinal free surface slope for higher initial head differences, as observed in Fig. 3.3 for a Lock to Lock operation with an initial head difference of 21 m. More specifically, the recorded oscillation indicates a quite more irregular response, with a much higher amplitude than the one calculated with the

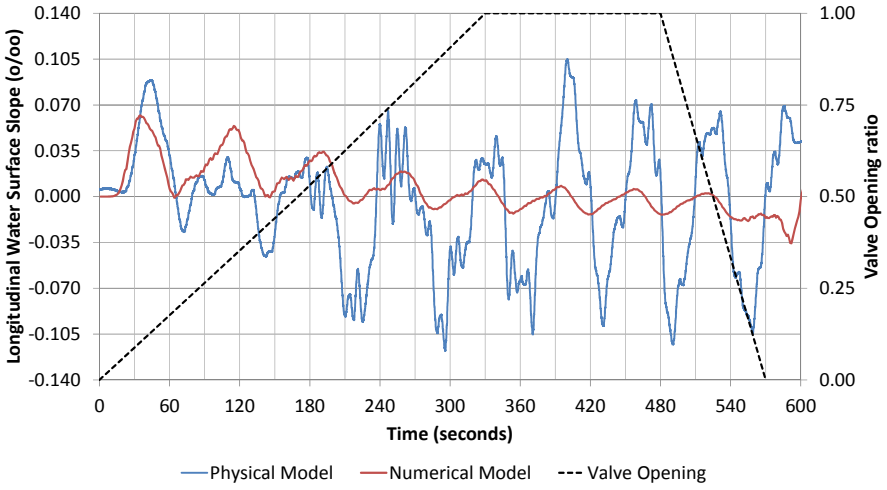

Fig. 3.3. Longitudinal water surface slope using 1D model input. High initial head difference.

numerical model. This indicates that turbulence scales are exerting a significant influence, so a more elaborated theoretical approach is needed. Hence, 3D modeling of the combination Central Connection + Secondary Culvert + Ports + Lock Chamber (actually, only half of the chamber, assuming that the flow is symmetrical with respect to the longitudinal axis) was undertaken using a Large-Eddy Simulation (LES) approach (Sagaut, 2001).

3.2 Improved theoretical approach

As sub-grid scale (SGS) model for the LES approach, a sub-grid kinetic energy equation eddy viscosity model was used (Sagaut, 2001). Deardorff's method was selected to define the filter cutoff length (Sagaut, 2001). A wall model was considered to treat the boundary conditions at solid borders; Spalding law-of-the-wall – which encompasses the logarithmic law (overlap region), but it holds deeper into the inner layer – was selected for the velocity (White, 1974), while a zero normal gradient condition was taken for the remaining variables. At the inflow boundary, in addition to the ensemble-averaged velocity (which arises from the 1D model), the amplitude of the stochastic components were provided (Sagaut, 2001): 4% for the longitudinal component, and 1.3% for the transversal one, values associated to a fully developed flow, very appropriate for the present problem; additionally, a weighted average of the previous and present generated stochastic components was imposed in order to add some temporal correlation; for the turbulent kinetic energy, a zero normal gradient was taken. For the free surface at the Chamber, the rigid-lid approximation was used, where uniform pressure was imposed, together with zero normal gradient conditions for the remaining quantities. The model was implemented using OpenFOAM (Open Field Operation And Manipulation), an open source toolbox for the development of customizable numerical solvers and utilities for the solution of continuum mechanics problems (Weller et al., 1998). The model solves the integral form of the conservation equations using a finite volume, cell centered approach in the spirit of Rhie and Chow (1983). PISO (Pressure Implicit with Splitting of Operators) algorithm is used for time marching (Ferziger & Peric, 2001).

Fig. 3.4 presents a view of the model domain. The computational mesh was composed by 1.5 million elements. Special considerations were made for the mesh near the wall, as the center of the first cell has to lie within a distance range to the wall – $30 \leq y+ \leq 300$ – to rigurously apply the logaritmic velocity profile as boundary condition (Sagaut, 2001). Typical computing times for stabilization with a steady discharge, in a Core i7 PC running 8 parallel processes, were 3 to 8 days. When complete hydroghaphs were simulated (of approximately 550 secs), 15 to 30 days of computing time were required. By parallelizing the simulation using more than one PC, computing times were reduced, though non-linearly.

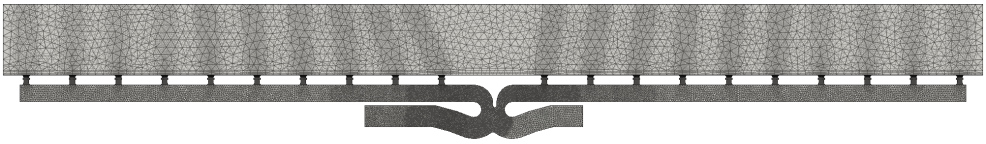

Fig. 3.4. Model domain for 3D model.

Note that the rigid-lid approximation implies that the free surface oscillations are not solved by the 3D model; this was done in order to avoid extremely high computing times. Instead, the 3D model provided the time series of the flow discharge for each port, which were used to drive the 2D model of the chamber. Alternatively (and less costly in post-processing), the time series of the discharges at the U and S branches of the Central Connection, provided by the 3D model, were used to feed the 1D model, from which the discharge distribution among ports was obtained, and used to feed the 2D model.
Fig. 3.5 shows the longitudinal water surface slope obtained with the two approaches (using the dimensions of the physical model), and their comparison with the results from the physical model, for the high initial head difference case. It is observed that both numerical simulations are now able to capture the high amplitude oscillations, indicating that large eddies must be responsible for this amplification phenomenon. Note that the numerical results with input straight from the 3D model show oscillations, associated to large eddies, which are not present in the ones with input through the 1D model (which filters out those oscillations), but they are quite compatible between them.

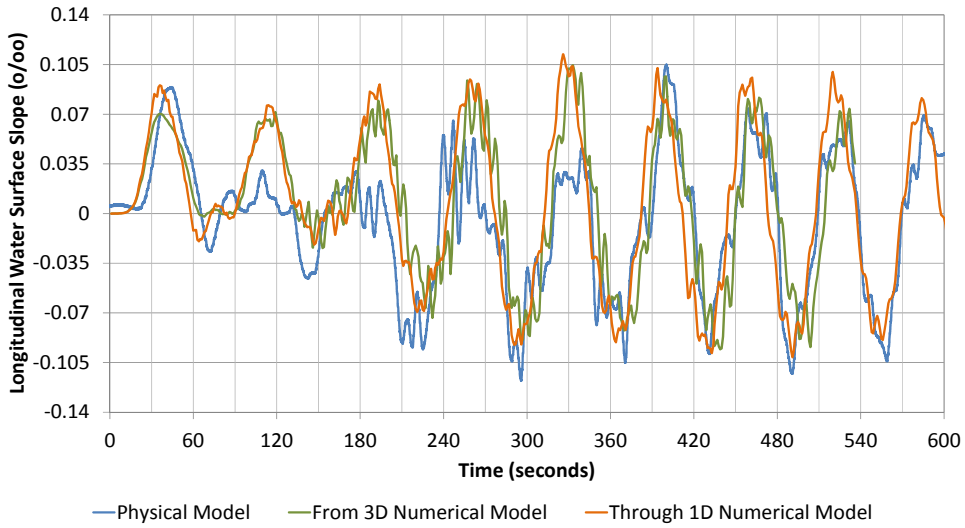

Fig. 3.5. Longitudinal water surface slope using 3D-LES model input. High initial head difference.

The differences between the numerical results and the measurements at the physical model are due essentially to the variability of the system reponse (variations in amplitude and phase of the oscillations), under the same driving conditions, due to the stochastic nature of turbulence. This was verified both experimentally (Fig. 3.6a) and numerically (Fig. 3.6b) by repeating the same test (in the case of the numerical model, using the 'through 1D model' approach, and different initializations for the stochastic number generator). This behavior puts a limit to the degree of agreement that can be attained between the results from the numerical and physical models. In any case, the maximum amplitudes for any of the experimental or numerical realizations are relatively consistent among them.

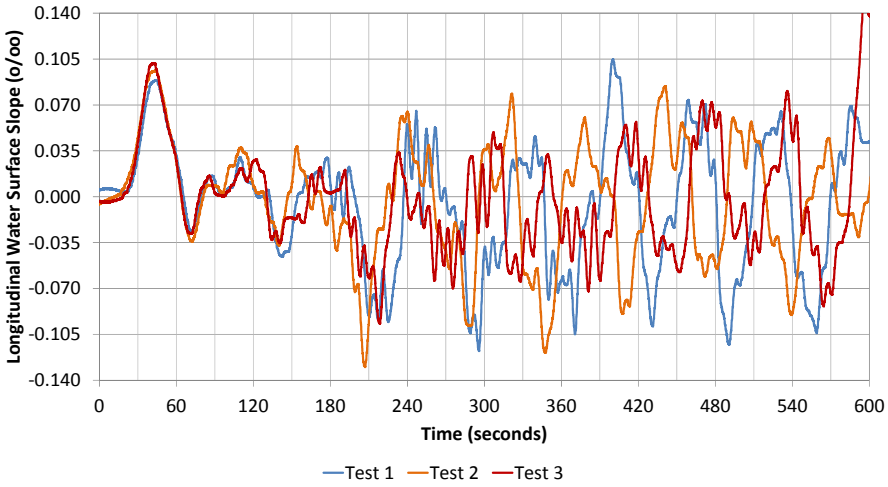

a) Experimental realizations

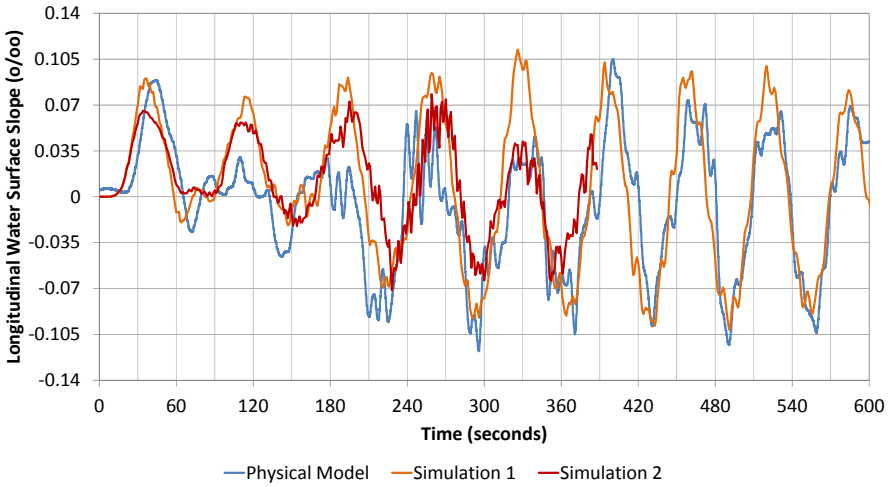

b) Numerical realizations

Fig. 3.6. Variability of longitudinal water surface slope. High initial head difference.

Before proceeding to simulate prototype conditions, it is relevant to analyze the response provided by the numerical model, in order to be confident about using this tool to make such a prediction. Specifically, the physical mechanisms involved in the present problem should be fully understood. This is performed in the following.

Fig. 3.7a shows the time series of the discharges through the U and S branches of the Central Connection (in prototype units), according to the 3D numerical model. It is observed that, for the higher discharges, they present oscillations, which seem coherently out-of-phase. The difference between those discharges is shown in Fig. 3.7b (together with the total discharge, i.e., the one through the Main Culvert). It is effectively observed that this difference oscillates, and that during the time window of higher discharges (above about 250 m^3/s) there is a dominant period of oscillation which spans from 40 to 80 seconds, approximately.

Now, these periods are close to, and include, the period of free surface oscillations in the Chamber (around 70 seconds), indicating that conditions close to resonance are achieved, thus resulting in an amplification of the free surface oscillation, which is the observed effect on the water surface slope. As in the numerical simulation the free surface was represented like a rigid lid, the oscillation in the discharge difference between the two branches of the Central Connection is not influenced at all by free surface oscillations themselves, i.e., the dominant period arises from the flow properties in the Central Connection. This dominant period must then be associated to the largest, energy-containing eddies (the ones resolved with the LES approach).

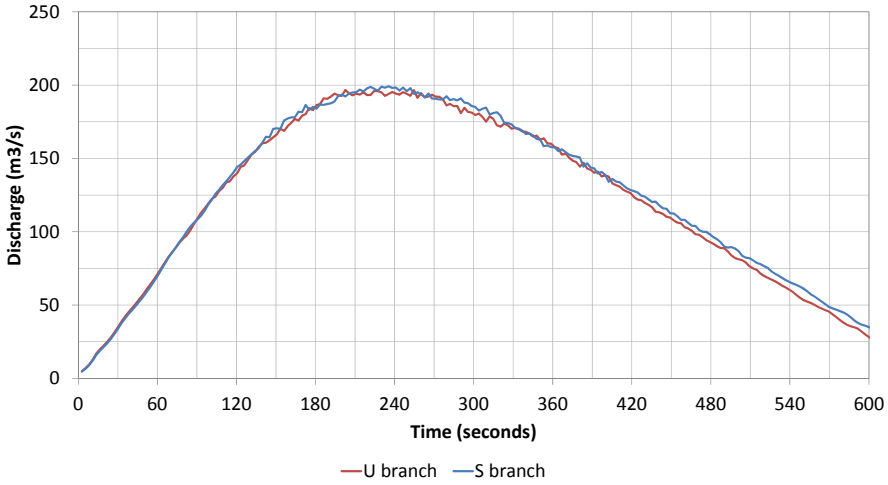

a) Discharge through U and S branches

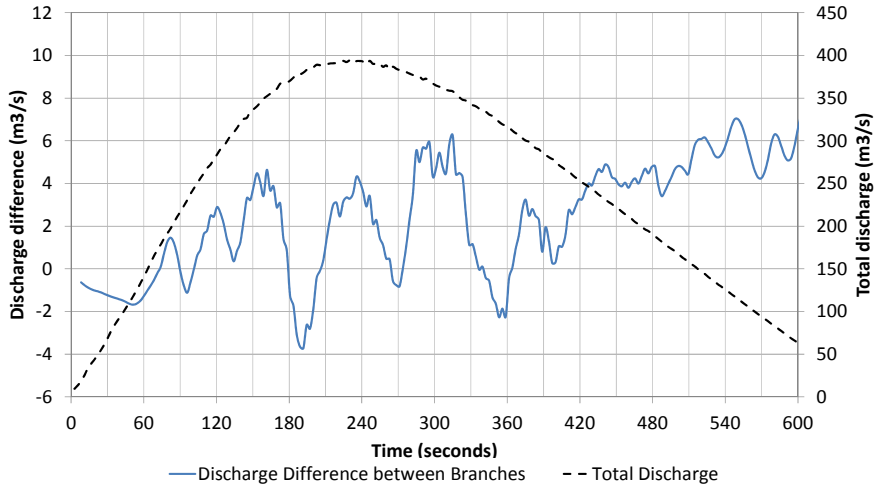

b) Discharge difference between branches

Fig. 3.7. Time series of discharge according to numerical model. High initial head difference.

Before pursuing with the analysis, it is worth to confirm that the close-to-resonance conditions are responsible for the amplification of the free surface oscillations. Hence synthetic hydrographs for the U and S branches of the Central Connection were built, introducing a purely sinusoidal oscillation to their difference during the higher-discharges time window, as indicated in Fig. 3.8a for 2 m^3/s amplitude of oscillation, and two different

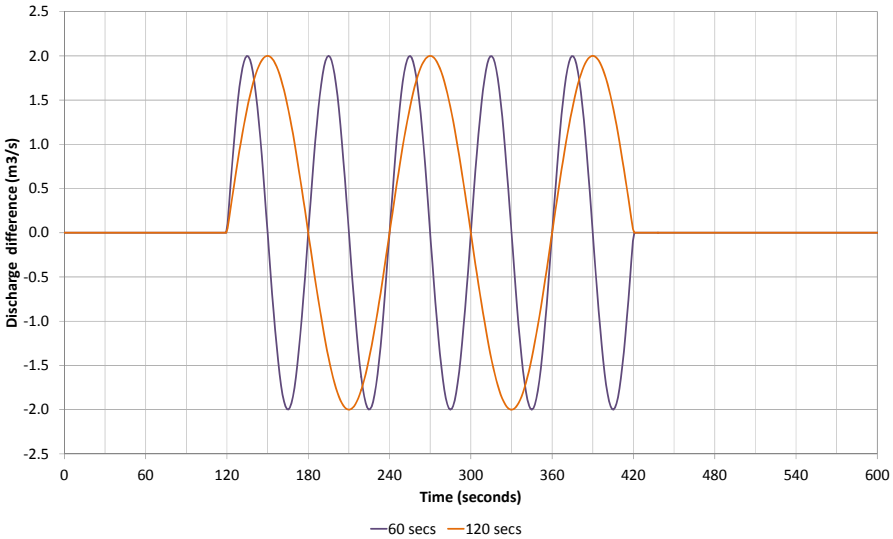

a) Discharge difference (driving force)

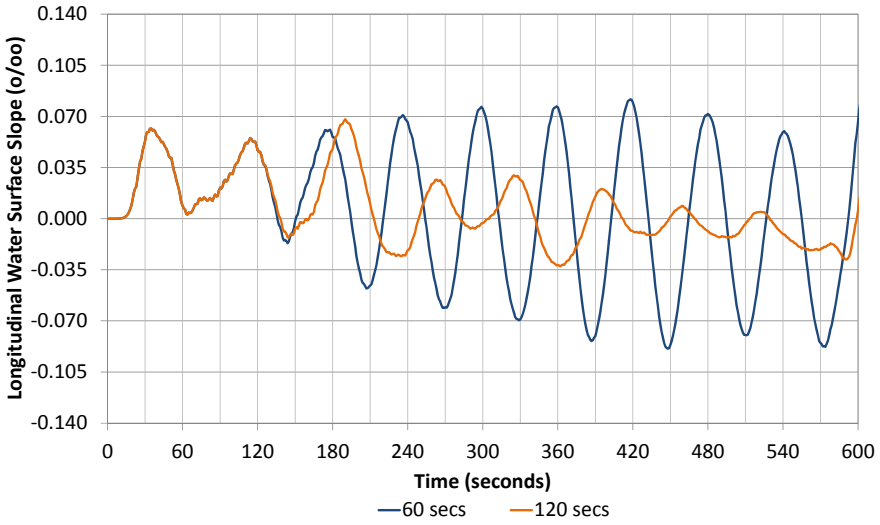

b) Longitudinal water surface slope (system response)

Fig. 3.8. Synthetic discharge difference and system response for different periods of oscillation.

periods: 60 and 120 seconds. Fig. 3.8b presents the results from the 2D model for the two different periods. It is clearly observed that amplitude amplification occurs for the 60 seconds period (during the time window of forced discharge oscillation), which is under close-to-resonance conditions. On the contrary, the amplitude attenuates for the 120 seconds period, which is far from the resonant period.
In Fig. 3.9 the results of the 2D model with the synthetic hydrographs, for the 60 seconds case, are compared with the physical model measurements, indicating a quite reasonable agreement, providing an extra validation to the physical explanation of the observed phenomenon. The 2D model results are much 'cleaner' than the measurements because the triggering signal (discharge difference) has a single frequency, in lieu of the set of frequencies associated to the turbulent eddies.

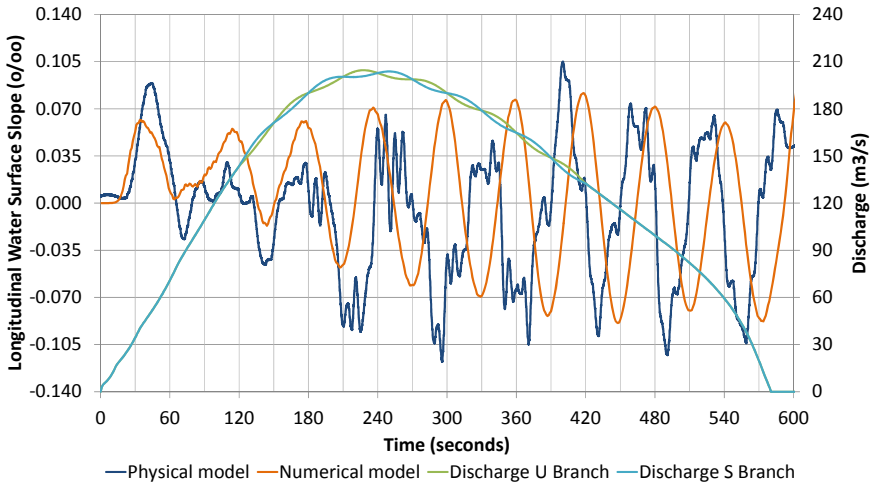

Fig. 3.9. Comparison of longitudinal water surface slope from numerical model with synthetic, 60 seconds period hydrograph, and from measurements.

Now, the relation between the discharge oscillation and the larger, energy-containing eddies generated at the wake zones, in the U and S branches (Fig. 3.10), is analyzed. The characteristics of those large eddies are quantified based on an analysis of scales (Tennekes & Lumley, 1980). The size of these eddies, the so called 'integral scale' of turbulence in the wake region, is limited by the physical dimensions of the Secondary Culvert. Hence, it is of the order of the conduits widths (4.5 m for the U branch, and 3.1 m for the S branch). On the other hand, the relation between the velocity-scale of the largest eddies and the ensemble-mean of the incoming velocity is of the order 10^{-2}. It is assumed that this relation is 1% if the section-averaged velocity at the Secondary Culvert (which changes with the total discharge) is taken as a reference. The relation between the integral scale and the velocity scale provides a scale for the period of the largest eddies. Fig. 3.11 shows the variation of the period-scale of the largest eddies, for the two branches of the Central Connection (which differ between them due to the different incoming velocities), with the total discharge (i.e., the one through the Main Culvert). It is claimed that the interaction of the largest eddies of the U branch with those of the S branch is responsible for the generation of the coherent out-

of-phase oscillations in the discharges through each branch (as explained below). When this oscillation has a period close to the Chamber free surface oscillation period, also represented in Fig. 3.11, amplification occurs, as already explained. From Fig. 3.11, it is observed that close-to-resonance conditions should be expected for total discharges higher than about 200 m^3/s, and up to at least 500 m^3/s. This is completely consistent with the numerical and physical model results obtained for high initial head difference.

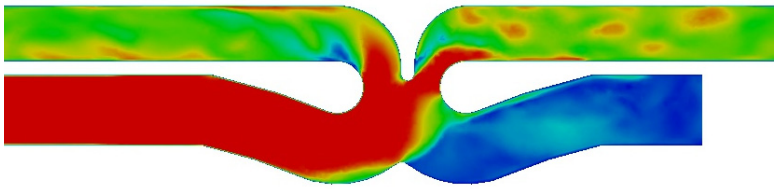

Fig. 3.10. Large eddies generated after separation in the U and S branches.

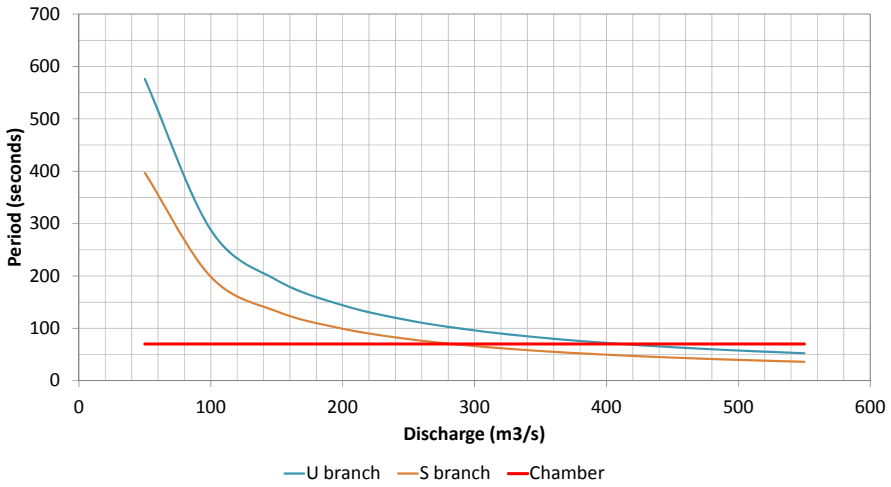

Fig. 3.11. Period-scale of largest eddies as a function of total discharge.

In order to complete the analysis, an explanation for the mechanism of interaction between the largest eddies of the U and S branches, leading to the coherent out-of-phase oscillations in the discharges through each branch, is undertaken, inspired in the one for a von Karman vortex street (Sumer & Fredsoe, 1999). Vortices (largest eddies) are shed from the separation points. Subject to small disturbances, one of those vortices, for example the one on the U branch, grows larger, increasing the blockage effect in that branch; as a result, the discharge through the U branch decreases, leading to an increase of the discharge through the S branch (in order to maintain the total discharge). Now, the next vortex shed in the S branch is of higher intensity, due to the increased incoming flow velocity in this branch; but this has the effect of increasing the blockage of the S branch, then producing a decrease in the discharge through that branch, and a consequent increase of the discharge through the U

branch. Then, the phenomenon described for the S branch now occurs in the U branch, leading to a cyclic behavior, as observed.

3.3 Numerical modeling of the prototype

Having understood and numerically modeled, with a reasonable degree of satisfaction, the oscillatory phenomenon which develops in the Central Connection for the physical model, the flow in the prototype was simulated in order to determine the behaviour at that scale.

The calculation with the 3D model was undertaken using the same (rescaled) mesh as for the physical model. Though the condition on the location of the first node, in order to correctly represent the wall shear stress, is not fulfilled, it is considered that this should not significantly affect the results, based on the fact that tests performed in the physical model including triggering devices indicated that the appearance of the oscillatory phenomenon is not conditioned by the location of the separation point.

Fig. 3.12a shows the evolution of the longitudinal water surface slope arising from the results of the 3D model. It is compared with the numerical results for the physical model; the ones arising from the 1D modeling approach (no 3D LES model) are also represented, as a reference. Note that the prototype response is significantly more noisy than the physical model response, as it includes a higher range of turbulent frequencies. It is observed that, though the amplification effect manifest in the prototype (the amplitude of oscillation is higher than the one predicted by the 1D model), its amplitude is definitely smaller than the one for the physical model. In fact, the oscillation in the discharge difference, presented in Fig. 3.12b, is sensitively less significant for the prototype than for the physical model (compare with Fig. 3.6b). It is especulated that this should be due to differences in the energy spectrum: the larger eddies of the prototype would contain less energy than the corresponding ones in the physical model. It is concluded that, for this problem, scale effects tend to increase the amplification effects.

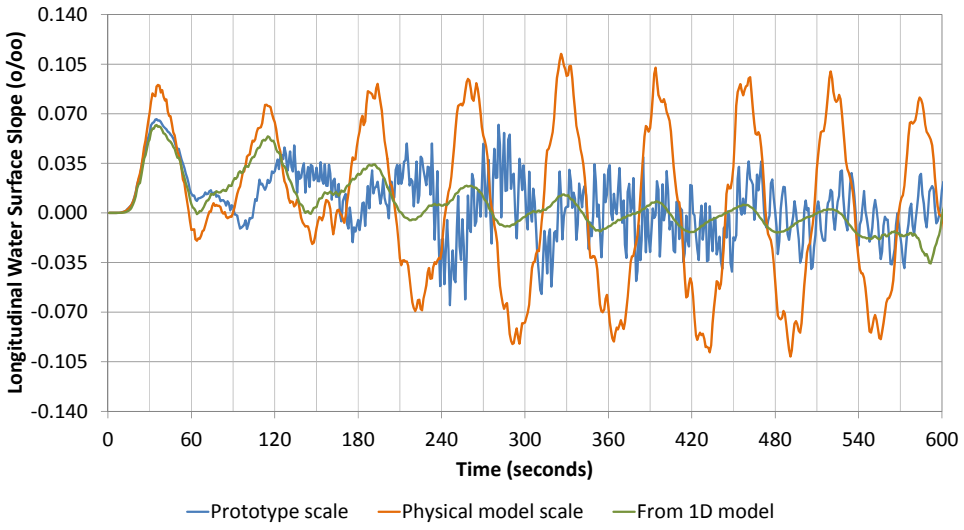

a) Longitudinal water surface slope

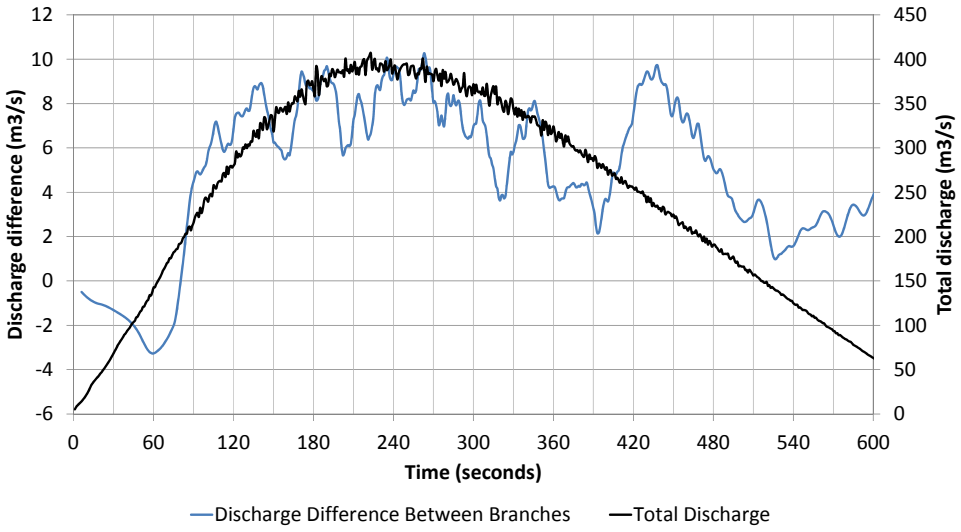

b) Discharge difference between the U and S branches

Fig. 3.12. Prototype response.

4. Conclusions

The proposed strategy for the design of hydraulic structures, consisting in a first stage where the flow in the physical model is numerically simulated, in order to validate the numerical model, and in a second stage where the flow in the prototype is numerically simulated, in order to extrapolate the results to this scale, has been shown to be effective in correcting for the scale effects present in the physical model.

This has been illustrated for the particular case of the design of the Third Set of Locks of the Panama Canal, for two problems with quite different levels of complexity.

The first problem was the determination of the time for water level equalization between chambers, using a one-dimensional numerical model. Friction losses are shown to be over-represented in the physical model, leading to larger equalization times. Differences of the order of 10% are calculated for a case with maximum initial head difference.

The second problem was the calculation of the amplitude of free surface oscillations in the lock chambers, due to close-to-resonance conditions, under interaction with an oscillation in a flow partition component of the filling/emptying system, using a full three-dimensional numerical model with a LES approach. Differences in the energy spectrum lead to a significant amplification of the amplitude of oscillation in the physical model.

The paper indirectly stresses, through an in-depth analysis of the involved physical mechanisms for the case studies, the necessity of thoroughly understanding the responses provided by the numerical model, in order to be confident in using the tool to make predictions at the prototype scale.

5. Acknowledgments

In addition to the present authors, Emilio Lecertúa, Martín Sabarots Gerbec, Fernando Re and Mariano Re were part of the numerical modeling team for the Panamá Canal Project. The team worked under the coherent supervision of Nicolás Badano (MWH), responsible for the hydraulic studies, with the help of Mercedes Buzzela. The smooth interaction with the responsible for the physical model, Sébastien Roux, from CNR, was fundamental in order to achieve the goals of the study.

6. References

Ferziger, J. H.; Peric, M. (2001). *Computational Methods for Fluid Dynamics*. Springer-Verlag, 3rd Ed., 2001. ISBN 3-540-42074-6, New York, USA

Menéndez, A. N. (1990). *Sistema HIDROBID II para simular corrientes en cuencos*. Revista internacional de métodos numéricos para cálculo y diseño en ingeniería, Vol. 6, 1, pp 25-36, ISSN 0213-1315

Rhie, C.M.; Chow, W.L. (1983). *A numerical study of the turbulent flow past an isolated airfoil with trailing edge separation*. AIAA Journal, 21, 1525-1532.

Sagaut, P. (2001). *Large Eddy Simulation for Incompressible Flows,* Springer-Verlag, ISBN 3-540-67890-5, New York, USA

Sumer, B.M.; Fredsoe, J. (1999). *Hydrodynamics around cylindrical structures*. Advances Series on Coastal Engineering, Vol. 12, ISBN 981-02-3056-7, World Scientific, Singapore

Tennekes, H.; Lumley, J.L. (1980). *A First Course in Turbulence*. MIT Press, ISBN 0-262-20019-8, USA

USACE, (2006). "Engineering and Design - Hydraulic Design of Navigation Locks". United States Army Corps of Engineers EM 1110-2-1604, 2006.

Weller, H.G. ; Tabor, G. ; Jasak, H. & Fureby, C. (1998). *A tensorial approach to computational continuum mechanics using object orientated techniques*. Computers in Physics, 12(6):620 - 631, 1998.

White, F.M. (1974). *Viscous Fluid Flow,* McGraw-Hill, ISBN 0-07-069710-8, USA

12

Turbulent Flow Around Submerged Bendway Weirs and Its Influence on Channel Navigation

Yafei Jia[1], Tingting Zhu[1] and Steve Scott[2]
[1]*The University of Mississippi*
[2]*US Army ERDC Waterways Experiment Station*
United States

1. Introduction

Flow in curved channel bends is typically characterized by helical secondary currents (HSC) which play an important role in redistributing the momentum of river flow in a cross-section, resulting in lateral sediment transport, bank erosion and channel migration. Secondary current introduces difficulties for channel navigation because it tends to force barges toward the outer bank. Submerged weirs (SWs) are engineering structures designed to improve navigability of bendways. They have been constructed along many bends of the Mississippi River for improving barge navigation through these bends (Davinroy & Redington, 1996). Because of the complexity of channel morphology and flow conditions, not all the installed SWs were effective as expected (Waterway Simulation Technology, Inc., 1999). It is necessary, therefore, to study the turbulent flow field around submerged weirs and the mechanisms affect navigation.

The HSCs can be computed analytically if the channel form and cross-section can be approximated as circular and rectangular (Rozovskii, 1961). Curved channel flows can be simulated by depth averaged models. Although the main flow distribution can be predicted quite satisfactorily using two-dimensional (2D) models (Jia et al., 2002a; Jin & Steffler, 1993), the secondary flow resulting from hydraulic structures is difficult to simulate with these models. The approach of embedding an analytical solution (Hsieh and Yang, 2003) or three-dimensional (3D) simulation results (Duan et al., 2001) into a 2D model may not be appropriate when submerged weir(s) are present. Compared with two-dimensional models, three-dimensional models are more suitable and have been widely used for open channel flow simulations particularly for flows in curved channels. From early research by Leschziner & Rodi (1979) to the growing popularity of applications by Jia & Wang (1992), Wu et al. (2000), Morvan et al. (2002), Wilson et al. (2003), Olson (2003) etc., three-dimensional numerical models have been proven to be capable of predicting general helical currents in curved channels. Wilson et al. (2003) solved a multiple-bend curved-channel flow problem using the k-ε closure and rigid lid assumption with a finite volume code of non-orthogonal structured grid. Morvan et al. (2002) simulated flow in a meander channel with flood plains. Both the k-ε closure and Reynolds stresses model were applied with a rigid lid. Olsen (2003) applied a 3D model with the $k-\varepsilon$ closure to simulate the channel meandering process. Natural river flow, sedimentation and bed change were computed by Wu et al. (2000) using a 3D model, with k-ε closure used for the hydrodynamics

computation. Lai et al. (2003) simulated a curved channel in laboratory scale using a finite volume model of non-structured grid with a rigid lid and free slip boundary condition specified at the free surface. Although the general helical current can be simulated by using different turbulence closure schemes, the outer bank vortex cell, with its size being the order of the water depth (Blanckaert & Graf, 2001; De Vriend, 1979), could not be captured without considering the non-linearity of turbulence stresses. Jia et al. (2001a) and Wang et al. (2008) reported the simulation of curved channel flows using a nonlinear $k-\varepsilon$ closure. The non-linear model can predict secondary circulation near the water surface and outer bank in addition to the general helical current driven by channel curvature and gravity. A large eddy simulation (LES) model which could also simulate this vortex adequately was reported by Booij (2003).

The US Corps of Engineers (Davinroy & Redington, 1996) determined that one practical option for improving navigation through bendways is to install submerged weirs (dikes) that project from the outer bank into the channel and are oriented upstream. Pilots operating barge vessels on the river reported that the submerged weirs, placed across the channel thalweg and angled upstream, realigned the flow away from the outer bank to the middle of the channel, thus allowing more room for maneuvering through the bend. From 1989 to 1995, there were 114 submerged weirs constructed in 13 bends of the Mississippi River (Davinroy & Redington, 1996). However, not all the submerged weirs yielded satisfactory results (Waterway Simulation Technology, 2002). Apparently, the impact of these submerged weirs on bendway hydrodynamics and their effectiveness on channel navigation are not well understood.

Submerged weirs (SW) can realign general channel flow distribution because of their obstruction to approaching flow. Kinzli and Thornton (2010) developed empirical equations for eddy velocities in bendway weir fields using a rigid bed physical model. Three design parameters were tested: weir spacing, length and orientation angle. Jarrahzade and Bejestan (2011) conducted experiments to study the local scour depths around the submerged weirs installed at the outer bank of a bendway in the laboratory flume. Hydraulic structures similar to submerged weirs (such as spur dikes) have been studied using numerical simulations (Jia & Wang, 1993; Ouillon & Dartus, 1997) for various purposes. Jia & Wang (1993) applied 3D free surface models to simulate flows around hydraulic structures such as spur dikes; numerical solutions of velocity field and shear stress on the bed agreed with those observed (Rajaratnam & Nwachukwu, 1983). Submerged vanes (Odgaard & Kennedy, 1983) were introduced in bendways to reduce the strength of helical current. For preventing bank erosion of a curved channel reach, Bhuiyan & Hey (2001) studied a J-vane installed near the outer bank with a sharp angle to the bank line. Olsen & Stokseth (1995) computed a 3D flow in a short channel with large rocks. A porosity model was used to handle the rock elements which were comparable to mesh sizes. Bhuiyan & Olsen (2002) studied local scouring process around a dike with a 3D model; reattachment length and shear stress distribution on the bed prior to scouring were used to test mesh sensitivity and validate the model qualitatively. Jia et al. (2005) studied the turbulent flow around a submerged weir in a curved channel using a 3D model. The computational model was also applied to study the flow in a reach of the Mississippi River with a weir field (Jia et al., 2009). Martin & Luong (2010) applied a 3D curvilinear hydrodynamics and sediment (CH3D-SED) model to a river reach of Atchafalaya River at Morgan City, LA. Several design alternatives of multiple submerged weirs were simulated and the favorable options were identified to reduce shoaling and dredging.

In this chapter, computational studies of the channel flow affected by SWs are introduced. A finite element based three-dimensional numerical, CCHE3D, was used to study HSC and the

flow distribution around submerged weirs. The computational model has been validated using physical experiment data collected by the US Army Corps of Engineers. The numerical simulations indicated that the submerged weirs significantly altered the general HSC. Its presence induced a skewed pressure difference across its top and a triangular-shaped recirculation to the downstream side. The overtopping flow tends to realign toward the inner bank and therefore improves conditions for navigation. Validated by physical experiment data, this numerical model was applied to a field scale study of hydrodynamics in the Victoria Bendway in the Mississippi River. 3D flow field data were also used to validate this model with good agreement. The simulated flow realignment near the free surface indicates that the flow conditions in the bendway were improved by the submerged weirs; however, the effectiveness of each weir depends on its alignment, local channel morphology, flow and sediment transport conditions.

2. Numerical model – CCHE3D

The CCHE3D model developed at the National Center for Computational Hydroscience and Engineering is a three-dimensional finite element based, numerical simulation model for unsteady free surface turbulent flows, and it is capable of handling flows and sediment transport in complex channel domains and irregular bed topography. The model solves unsteady three-dimensional Reynolds equations using the Efficient Element Method based on the collocation approach (Mayerle et al., 1995; Wang & Hu, 1992). The CCHE3D model has been verified by analytical methods and validated using many sets of data from physical experiments, including simulation of near field flows around hydraulic structures like bridge piers, abutments, spur dikes, submerged dikes and submerged weirs (Jia & Wang, 2000a, 2000b; Jia et al., 2005; Kuhnle et al.; 2002).

2.1 Governing equations

The unsteady, three-dimensional Reynolds-averaged momentum equations and continuity equation are solved in the CCHE3D model

$$\frac{\partial u_i}{\partial t} + u_j \frac{\partial u_i}{\partial x_j} = -\frac{1}{\rho}\frac{\partial p}{\partial x_i} + \frac{\partial}{\partial x_j}\left(\nu \frac{\partial u_i}{\partial x_j} - \overline{u_i' u_j'}\right) + f_i \tag{1}$$

$$\frac{\partial u_i}{\partial x_i} = 0 \tag{2}$$

where u_i (i=1,2,3) represent the Reynolds-averaged flow velocities (u, v, w) in Cartesian coordinate system (x, y, z), u_i' is velocity fluctuation, $-\overline{u_i' u_j'}$ are the Reynolds stresses, u_i represent the mean behavior of the flow over a time scale much larger than that for u_i', p(=p_h+ p_d) is pressure with p_h being hydrostatic and p_d non-hydrostatic pressure, ρ is the fluid density, ν is the fluid kinematic viscosity and f_i are body force terms. The motion of free surface is computed using the free surface kinematics equation:

$$\frac{\partial S}{\partial t} + u_s \frac{\partial S}{\partial x} + v_s \frac{\partial S}{\partial y} - w_s = 0 \tag{3}$$

where S and the subscript, s, denote the free surface elevation and velocity components at the surface, respectively. Because free surface elevation determines the hydrostatic pressure distribution, $p_h = g(S - z)$, the main driving force of open channel flows, it is one of the key variables in this study. The non-hydrostatic pressure was solved by using velocity correction method on a staggered grid and applied to enforcing the computed flow to satisfy the divergence free condition (Jia et al., 2001b). In the application to the turbulence flow around submerged weirs, due to the strong three-dimensionality of the flow near the weirs, the non-hydrostatic pressure was computed and applied.

2.2 Turbulence closure model

There are six turbulence closure models included: constant, parabolic and mixing length eddy viscosity models, and standard, RNG and non-linear κ–ε two equation models (Speziale, 1987). Considering that the transport of turbulence is significant with the presence of submerged weirs, two-equation models are applicable. As the non-linear k–ε model requires high grid density to resolve the secondary flow structures driven by turbulence normal stresses (Jia et al., 2001a), and the problem concerned in this study is shear dominated, the non-linear closure was not selected. For this particular application the standard κ–ε turbulence closure was used:

$$\frac{\partial k}{\partial t} + u_j \frac{\partial k}{\partial x_j} - \frac{\partial}{\partial x_j}\left(\frac{\nu_t}{\sigma_k}\frac{\partial k}{\partial x_j}\right) = P - \varepsilon \tag{4}$$

$$\frac{\partial \varepsilon}{\partial t} + u_j \frac{\partial \varepsilon}{\partial x_j} - \frac{\partial}{\partial x_j}\left(\frac{\nu_t}{\sigma_\varepsilon}\frac{\partial \varepsilon}{\partial x_j}\right) = c_{\varepsilon 1} P \frac{\varepsilon}{k} - c_{\varepsilon 2}\frac{\varepsilon^2}{k} \tag{5}$$

where k represents the turbulent kinetic energy $\overline{u_i' u_i'}/2$, ε represents the rate of dissipation of turbulent kinetic energy, ν_t denotes the turbulent viscosity given by:

$$\nu_t = c_\mu \frac{k^2}{\varepsilon} \tag{6}$$

and P is the production of turbulent kinetic energy computed from:

$$P = \nu_t\left(\frac{\partial u_i}{\partial x_j} + \frac{\partial u_j}{\partial x_i}\right)\frac{\partial u_i}{\partial x_j} \tag{7}$$

Standard values of coefficients appearing in the preceding equations were assigned: c_μ=0.09, σ_κ=1.0, σ_ε=1.3, $c_{\varepsilon 1}$=1.44, $c_{\varepsilon 2}$=1.92. It is well known that by using this closure scheme, the prediction of recirculation length behind an obstacle or a step in straight channels may be somewhat shorter than those measured. This closure scheme is acceptable in the investigation of flows around submerged weirs as the overall flow pattern and structure around the weir were more of a concern to the study than the exact length of the recirculation. A structured 3D grid was used with each finite element formed by a hexahedron (Fig. 1). The local space coordinates, (ξ, η, ζ), are transformed to the global Cartesian coordinate in a way analogous to the 2D case (Jia & Wang, 1999). All of the 3D first-order non-convective and second order operators are constructed using this 1D quadratic interpolation function.

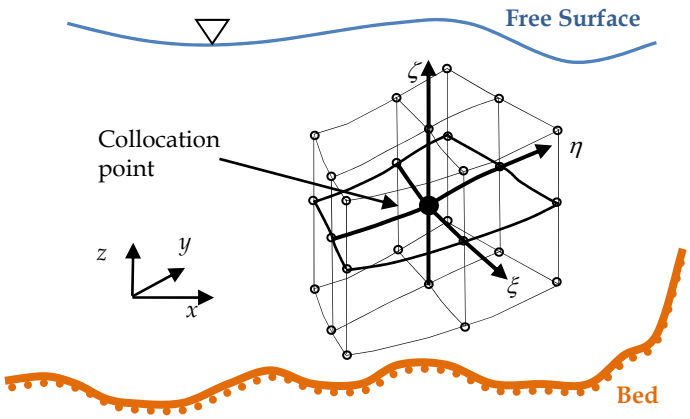

Fig. 1. Sketch of 3D element configuration in physical space

2.3 Boundary conditions

Measured steady water stage and flow discharge were used as the downstream and upstream boundary conditions. The turbulence energy, k, at the inlet was approximated by using the formula proposed by Nezu & Nakagawa (1993) and the rate of energy dissipation, ε, was computed by k and the assumption of parabolic turbulent eddy viscosity distribution for uniform flows. The wall function was specified for the wall boundaries such as the channel bed and the submerged weirs with different roughness, and the turbulence energy and dissipation were assumed to be in local equilibrium. Due to the near parabolic shape of the channel cross-section, the water depth along the water edge near the bank line was zero. A very small flow depth was set for the boundary mesh lines and the k and ε values for uniform flow were specified for the k-ε model.

2.4 Upwinding scheme

To eliminate oscillations due to advection, upwinding was introduced via a unique convective interpolation function, which takes into account the local flow direction and emphasizes the upstream influence. It is applied to compute advection terms in the momentum equations (1), the convection terms in the free surface kinematics equation (3) and those in the turbulence transport equations (4, 5). This convective interpolation function was obtained by solving a linear and steady convection-diffusion equation analytically over a one-dimensional local element:

$$c_1 = \frac{1}{2T}\left[\left(2e^{p_e\xi} - e^{-p_e} - e^{p_e}\right)\left(1 - \frac{\xi_0(R+1)}{\xi_0 R+1}\right) + T - \frac{\xi T(R+1)}{\xi_0 R+1}\right] \tag{8a}$$

$$c_2 = 1 - c_1 - c_3 \tag{8b}$$

$$c_3 = \frac{1}{2T}\left[\left(2e^{p_e\xi} - e^{-p_e} - e^{p_e}\right)\left(1 - \frac{\xi_0(R-1)}{\xi_0 R+1}\right) + T - \frac{\xi T(R-1)}{\xi_0 R+1}\right] \tag{8c}$$

$$T = e^{p_e} + e^{-p_e} - 2e^{p_e \xi_o} \tag{9a}$$

$$R = (e^{p_e} - e^{-p_e}) / T \tag{9b}$$

$$p_e = u_c / v_t \tag{9c}$$

where u_c is the flow velocity at the collocation node in the direction of the local coordinate ξ. Upwinding is adjusted by the local *Peclet* number $p_e = u_c / v_t$ (the length scale of the local element is $\xi \pm = 1.0$). The limiting scheme to p_e (Jia & Wang, 1999) was applied to minimize the numerical diffusion. This convective interpolation function is applied to all three directions locally. Gradients of velocities and other transport variables in the local directions are computed analytically. The convective operators thus obtained are then transformed to the Cartesian coordinate system via

$$\begin{pmatrix} \frac{\partial}{\partial x} \\ \frac{\partial}{\partial y} \\ \frac{\partial}{\partial z} \end{pmatrix} = \begin{vmatrix} \frac{\partial y}{\partial \eta}/D, & -\frac{\partial y}{\partial \xi}/D, & -\frac{\left(\frac{\partial y}{\partial \eta}\frac{\partial z}{\partial \xi} - \frac{\partial y}{\partial \xi}\frac{\partial z}{\partial \eta}\right)}{D\frac{\partial z}{\partial \zeta}} \\ -\frac{\partial x}{\partial \eta}/D, & \frac{\partial x}{\partial \xi}/D, & -\frac{\left(-\frac{\partial x}{\partial \eta}\frac{\partial z}{\partial \xi} + \frac{\partial x}{\partial \xi}\frac{\partial z}{\partial \eta}\right)}{D\frac{\partial z}{\partial \zeta}} \\ 0, & 0, & \frac{1}{\frac{\partial z}{\partial \zeta}} \end{vmatrix} \cdot \begin{pmatrix} \frac{\partial}{\partial \xi} \\ \frac{\partial}{\partial \eta} \\ \frac{\partial}{\partial \zeta} \end{pmatrix} \tag{10a}$$

$$D = -\frac{\partial x}{\partial \eta}\frac{\partial y}{\partial \xi} + \frac{\partial x}{\partial \xi}\frac{\partial y}{\partial \eta} \tag{10b}$$

Eq. 10 transforms operators for the element (Fig. 1) with the local coordinate ζ in the vertical (z) direction.

Eq. 10a & 10b indicate that vertical distributions of horizontal velocities are used to compute terms as part of $\partial / \partial x$ and $\partial / \partial y$ when mesh surface of ξ–η plan is inclined, creating a vertical convective term. Although there are other options of upwinding schemes in the CCHE3D model such as a second order upwinding and the QUICK scheme, the convective interpolation function was selected in this study due to its simplicity for the implicit time marching scheme: it requires only three nodes in each direction of the mesh lines; and some level of numerical diffusion is not so critical as in the case of jet impinging flow simulation (Jia et al., 2001b). A verification test of this scheme using a 3D manufactured analytical solution indicated that this scheme is about 1.6 order of accuracy (Wang et al., 2008). Wilson et al. (2003) tested that a second order upwinding scheme improved the helical flow computation by less than five percent. The system of equations is solved implicitly by using the Strongly Implicit Procedure (Stone, 1968) with the Euler's time marching scheme.

The CCHE3D model has been validated using physical model and field data. For this particular study, a physical experiment and a field case, Victorial Bendway of the Mississippi River, were also used for validation. The comparison between the simulated and measured flow field, the secondary flow field around the structures, and the impacts of weirs on the flow field will be presented.

3. Model validation using physical experiment

3.1 Physical model

Computational model validation was performed based on flow data measured in the physical model study conducted at Coastal and Hydraulic Laboratory of Engineer Research and Development Center (ERDC), US Army Corps of Engineers, Waterways Experimental Station, Vicksburg, Mississippi. Velocity data measured with an ADVP device were used to validate the computed flow field. To speed up the computations, CCHE2D (Jia et al., 2002a) was used to simulate the flow in the entire experimental channel. Using the boundary conditions provided by the 2D model, a shorter reach in the bendway that contained the submerged weir was then simulated with the 3D model. The effective roughness heights of the channel were obtained by calibration using the measured water surface elevation along the channel. This roughness was used for the 3D simulation with the exception of the surface roughness of the SW. The channel plan form, cross sectional form, the location of the submerged weir and the 2D and 3D simulation domains are shown in Fig. 2.

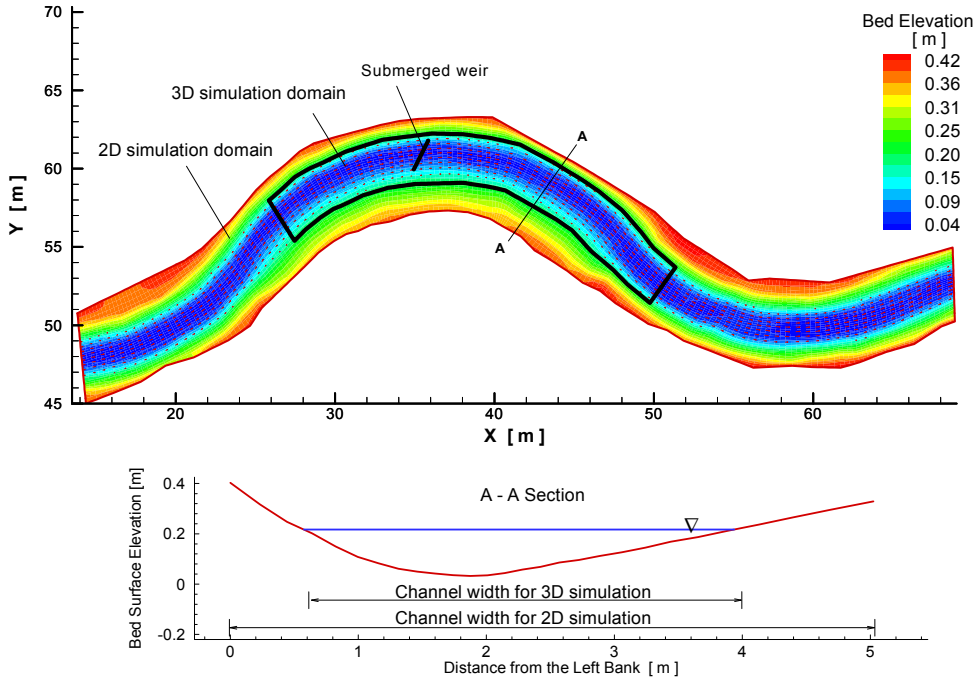

Fig. 2. Physical model set up and numerical simulation domain

Table 1 presents two flow conditions for the single submerged weir design tests; both were used for experiments with and without this submerged weir. The weir was made of approximately 2 cm size gravel and installed in the channel bend apex, attaching to the outer bank angled 20˚ upstream with a flow depth (clearance) of 9.5 cm. The shape of the weir was a trapezoid with a top width of 4 cm and a base width of 32 cm. The channel bed surface was of fine sand (median size: 0.43 mm). The effective channel bed roughness was a model parameter obtained by calibration. The flow velocity was mild (Re<2.8x10^4, Fr<0.25) to avoid erosion and entrainment of the loose bed material. Since the governing equations are time-dependent and the cases of this study are of steady state, simulations were terminated when the maximum incremental variation of solutions of each variable (u_i , S, k and ε) in the entire computational domain became small (10^{-4}~10^{-5}). When a steady state is reached, the flow discharge along the channel approaches to a constant: MAX [|Q_{cs}-Q|/Q] <0.01 (Q_{cs} is the discharge through a cross-section).

	Discharge Q (m^3/s)	Mean Velocity, U (m/s)	Effective bed roughness height, k_s (m)	Roughness of submerged weir (m)	Width W (m)	Reynolds number, R_e	Froude number , F_r
Run1	0.0413	0.125	0.005	0.02	3.1	13,250	0.123
Run2	0.0851	0.252	0.008	0.02	3.17	27,700	0.248

Table 1. Flow conditions for the physical models Radius of curvature R=15.24m, Weir length L=1.8m, Weir angle α=20^o, maximum depth H_m=0.182m, clarence H_c=0.095m, average depth H_a=0.106m. Mean water depth was used to calculate Reynolds number and Froude number.

A mesh sensitivity test was conducted to determine if the computational mesh had sufficient density for the problem. Simulation results of three mesh resolutions ($I_{\max} \times J_{\max} \times K_{\max}$ = 45x142x11, 79x142x11 and 45x142x31, in transversal, longitudinal and vertical directions, respectively) were compared. These meshes were designed to have much higher nodal density near the weir than that in the up and downstream part of the channel with smooth transitions. The second and the third mesh had a much higher number of nodes in the cross section and vertical direction. These extra mesh lines result in a higher element concentration around the weir and near the tip of the weir in particular. Simulations of the same flow scenario were conducted and the computational results compared to see if significant improvements were gained from the finer meshes. No significant difference was found in the near and far field of computed flows with the first two meshes. The third mesh results in more details in the recirculation zone, but no significant change in the flow in general. The validity of the first mesh for production runs was therefore confirmed.

3.2 Comparison of the simulation results and the measurements

Fig. 3 shows the bed bathymetry of the channel near the bend apex. The channel thalweg is closer to the outer bank to which the weir shoulder is attached. The submerged weir of α = 20^o and L= 1.8 m is clearly seen. The dot lines aligned parallel to the weir are measurement ranges. The ranges are numbered from upstream to downstream, with three ranges on the front side (upstream) and the remaining on the back or downstream side. The longitudinal spacing between the first and the second range, the third and fourth, and between the

seventh and those that follow were 0.3048 m. The spacing between the other ranges is 0.1524 m. The transversal spacing of points along range 1, 8, 9, and 10 is 0.3048 m, with a spacing of 0.1524 m for the rest of ranges. Velocity data were taken at three levels (0.2 *h*, 0.6 *h* from surface and close to bed) at each measuring location. The data were sufficient to study the general flow distributions.

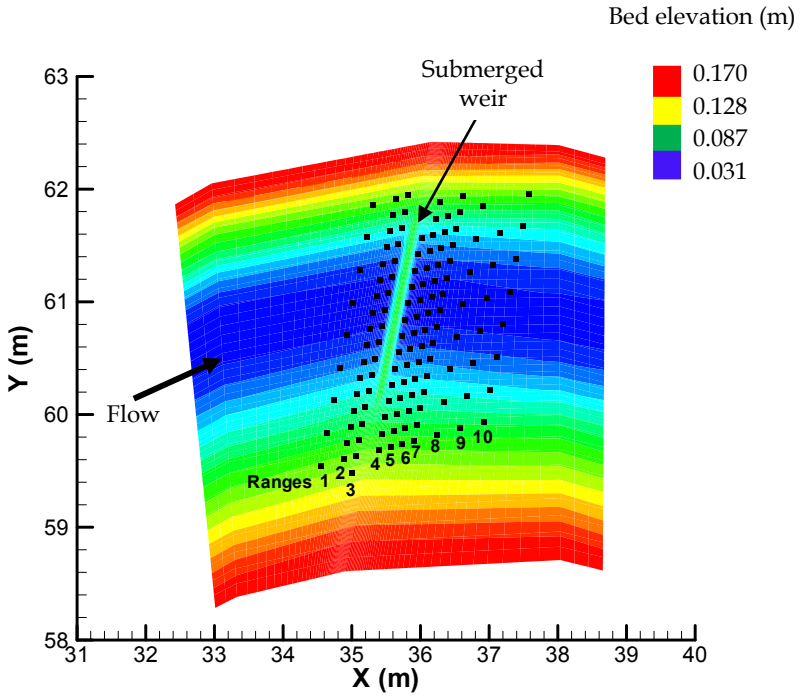

Fig. 3. Configuration of velocity measurement points around the submerged weir

Fig. 4a shows computed and measured velocity magnitude (Run2) along the 10 measurement ranges (transects) shown in Fig. 3. The velocities shown were measured at 20% of local flow depth (0.2 *h*) from the water surface. The horizontal axes are the distance from the left (outer) bank of the channel. The comparison of simulation and measurements for Run1 showed similar agreement in trend.

At Ranges 1, 2, and 3 located in front of the weir, the flow velocities were suppressed near the center part of the channel while the near bank velocities increase toward the weir. This was due to the high pressure resulting from the blockage of flow by the weir. This phenomenon was also evident for the velocity at the other levels (0.6 *h* and near bottom level). The increase of velocity near the tip of the weir in the physical model had resulted in some visible erosion or scouring of the bed. Ranges 4 through 10 were aligned behind the weir. Immediately downstream of the weir, the surface velocities were very high due to the pressure difference across the weir top (Section 4, 5, and 6). Because of the low pressure behind the weir, the velocities in further downstream sections were reduced, particularly in the center area. The

velocities near the bank were higher than those in the center part of the channel. The trend of decreasing velocity near the channel center line extends downstream beyond the last measuring section. Further downstream, the influence of the weir decreased and flow gradually recovered so that the maximum velocity re-appeared at the center of the channel.

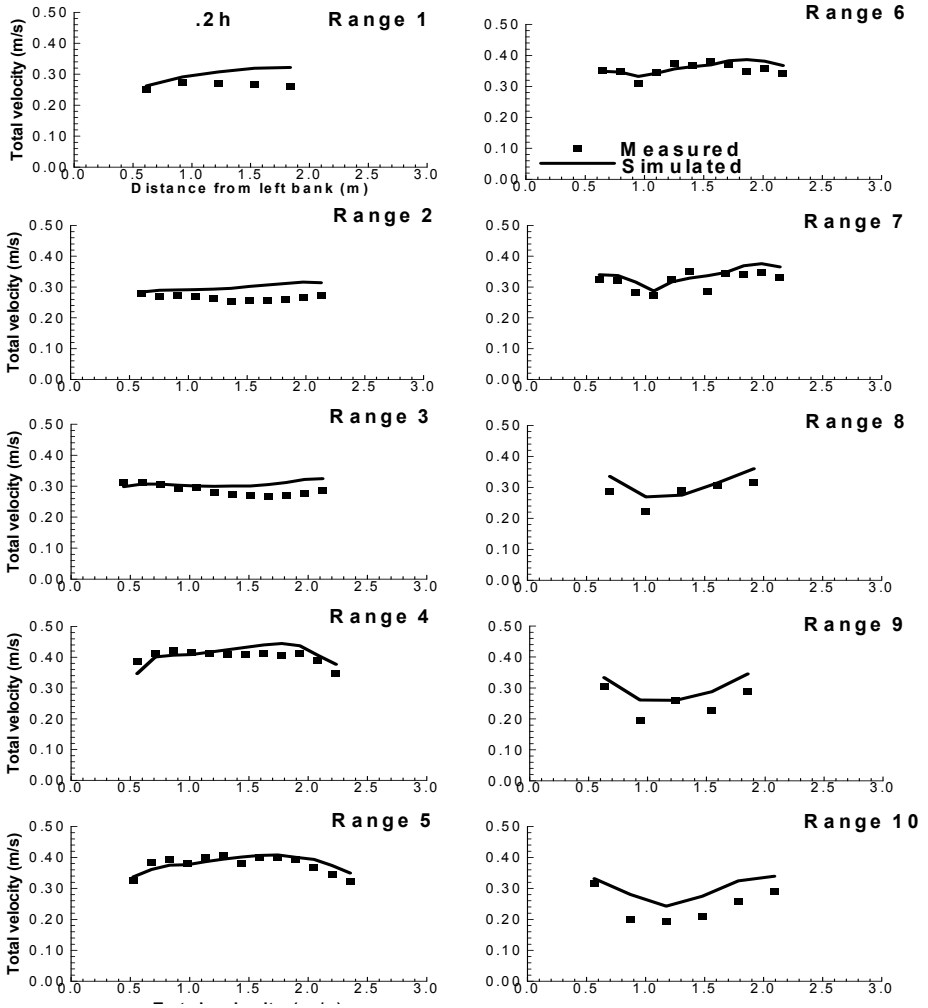

Fig. 4a. Comparison of simulated and measured total flow velocities at 0.2 *h* from the water surface around the submerged weir. Horizontal axis is the distance from the outer bank.

Fig. 4b shows the comparison of measured and computed velocities in these ten sections at the level 0.6 *h* from the water surface. The deceleration and separation of flow on the upstream side of the weir are more significant than those near surface. The trend that the flow accelerates along the streamlines near the banks is more pronounced. Downstream of the weir, the velocity decrease near the channel centerline is also more significant than the velocity decrease near the surface due to the existence of the recirculation flow. Since this

level is close to or cuts across the shear layer with a sharp angle where velocity varies rapidly in the vertical direction, the comparisons at this level on the downstream side have larger discrepancy than at other locations.

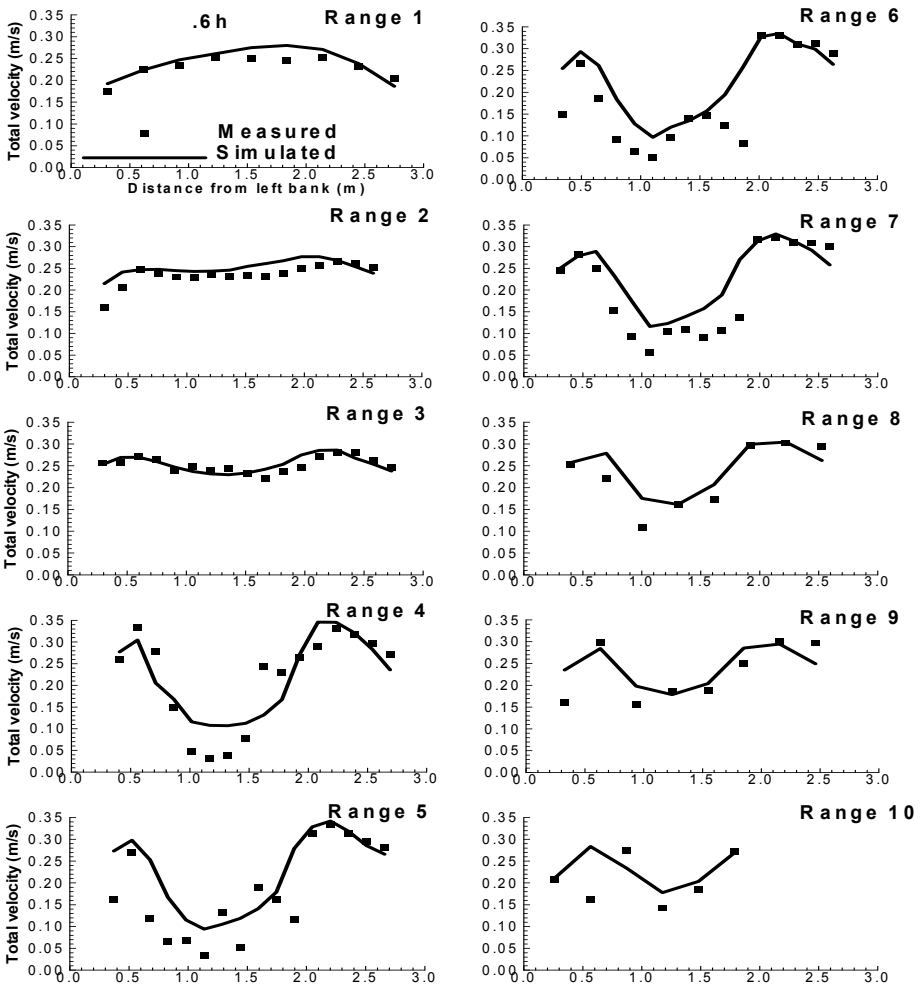

Fig. 4b. Comparison of simulated and measured total flow velocities at 0.6 *h* from the water surface around the submerged weir. Horizontal axis is the distance from the outer bank.

Fig. 4c shows the comparison of measured and computed velocities near the bed. The trend of approaching flow deceleration and separation just upstream of the weir are similar to those at the 0.6 *h* level. Because the front surface of the weir was not vertical, the flow tends to adhere to the sloping surface. No recirculation of horseshoe type was observed. Directly downstream of the weir, the near bed measurement level is in the recirculation zone. Both measured and computed velocities at Range 4 and 5 are negative (downstream direction is defined positive) close to the weir. Further downstream, negative velocities become positive

and increase gradually over the zone of reattachment. The near bed velocity in the thalweg changed direction near the Range 6 and the computed velocities agreed well with those measured. The overall agreement of measured and computed velocities at this level is better than those at the 0.6 *h* level. Since the reattachment occurred along the triangle-shaped edge of the recirculation zone and the measurements were taken along straight lines with relatively large spacing, it is difficult to compare reattachment directly.

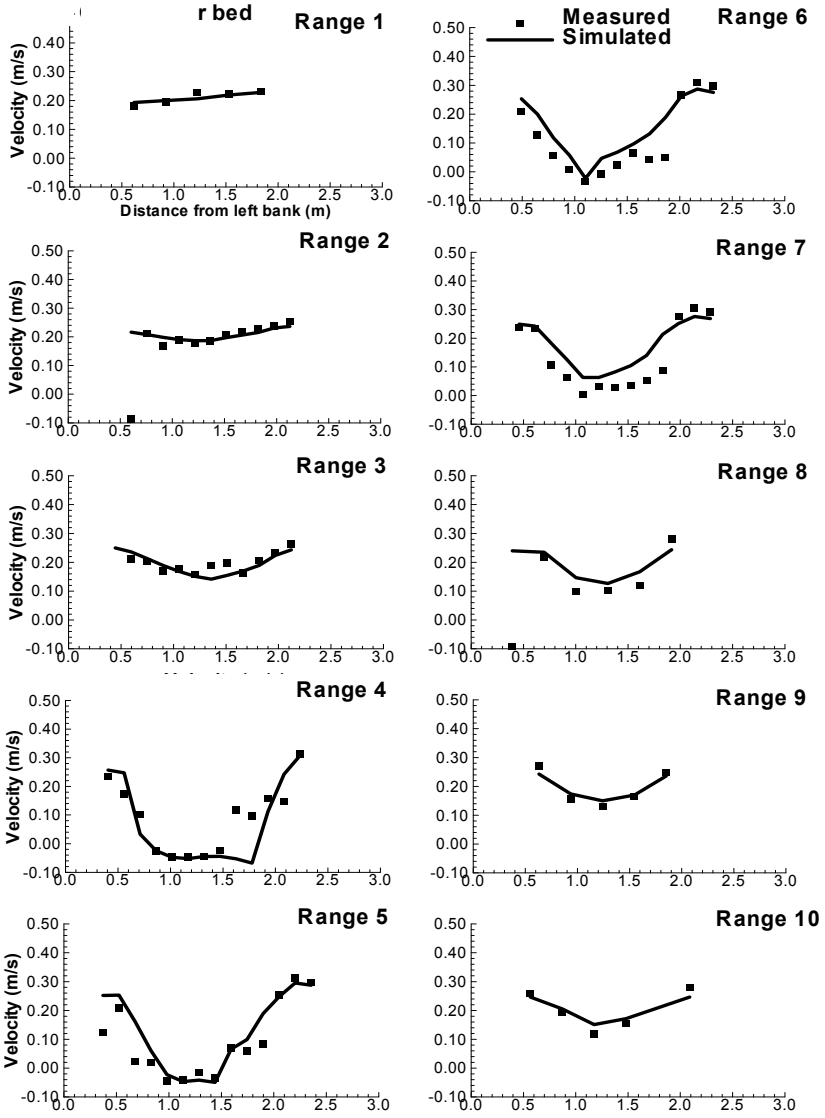

Fig. 4c. Comparison of simulated and measured horizontal flow velocities near the bed around the submerged weir. Horizontal axis is the distance from the outer bank.

3.3 Flow structure around a submerged weir

The flow near a submerged weir in a channel bendway is highly three-dimensional and complex. Because the weir is the largest obstacle in the flow path, the flow pattern in the vicinity of the weir is dominated by parameters such as weir length, height, angle, shape and roughness. Fig. 5 shows computed flow (vector) field in the recirculation zone directly behind the weir with the vertical scale enlarged (4x) to enhance clarity. Fig. 5a is the vector pattern near the bed. Fig 5b is a vertical section cut through middle of the circulation. The

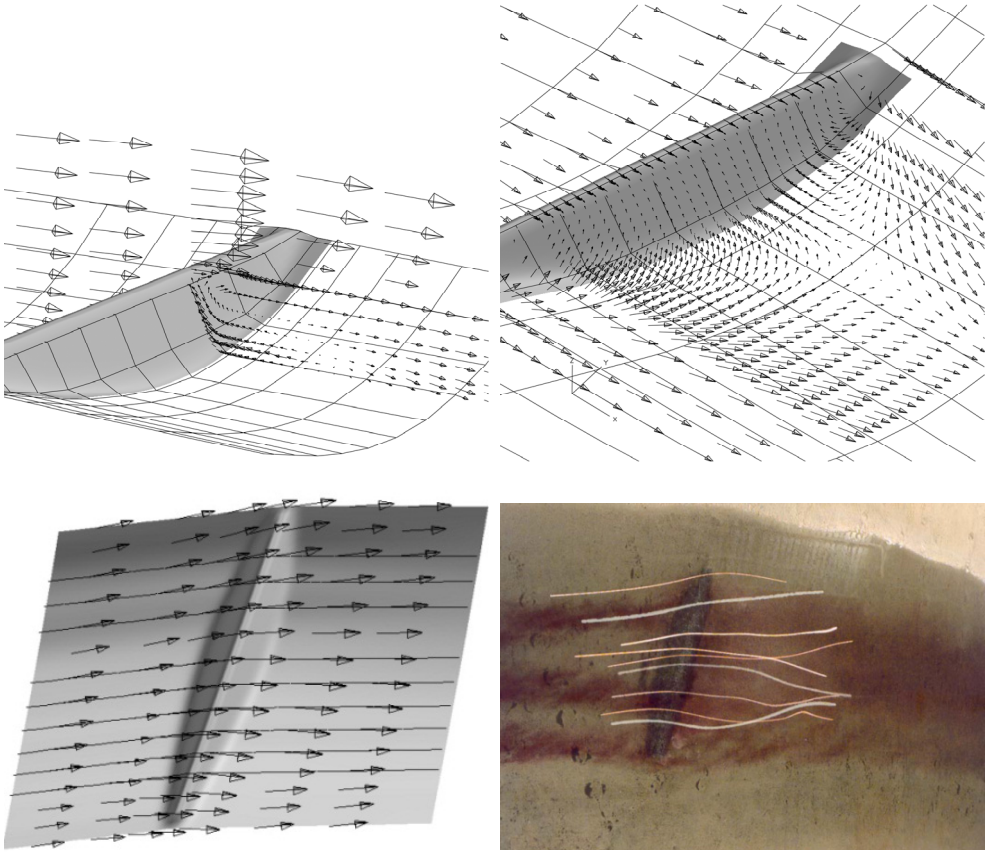

Fig. 5. Vector field of the flow behind the submerged weir (velocity near water surface is about 0.3 m/s). a: computed vectors near the bed; b: computed vectors in a vertical section across the weir; c: computed vectors on the water surface; d: observed confetti trace lines.

flow in the recirculation zone behind the weir is directed backward against the weir and entrained by the shear layer. Fig. 5c shows the flow vectors on the water surface, with some longitudinal mesh lines shown as references. The vectors near the tip of the weir turn to the inner bank while those near the shoulder are toward the outer bank. Apparently, the pattern of a typical helical secondary current in a channel bendway has been altered due to the

presence of the submerged weir. Significant flow velocity change occurs over the top of the weir. Because the water depth over the weir was small, comparable to the size of the ADVP device, velocity measurement over the weir top was difficult. Similarly, the velocities at the flow surface could not be measured. Due to these shortages one was unable to validate the computed secondary flow direction at the surface. Confetti trace lines of the physical model (Fig. 5d) and the particle trace lines released on the water surface level of the computed flow field were compared. The distributions of these trace lines are very similar which indicate the predicted surface velocity directions are consistent with the physical model.

Fig. 6 shows the surface elevation contour lines. A high pressure zone forms at upstream of the weir with a low pressure zone forming just downstream. The well known pattern of water surface superelevation in a bendway is altered significantly due to the presence of the weir. Because the alignment is 20˚ toward upstream, the high pressure zone is located closer to the outer bank and low pressure zone is closer to the tip of the weir and the inner bank. The flow passing the top of the weir inevitably turns toward the inner bank under such a pressure distribution. The pressure skew seems to be the key to understanding why the secondary current near the weir changes direction and become favorable to navigation.

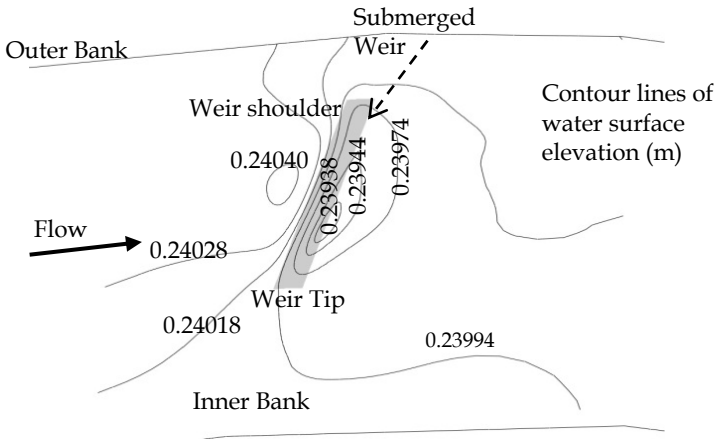

Fig. 6. Pattern of water surface elevation contour (m) near the submerged weir

Summarizing the observations in the physical model and numerical simulation, the flow pattern sketch around a submerged weir is shown in Fig. 7. Upstream of the weir, the high pressure zone slows down the approach flow and tends to force the flow to separate. The general helical secondary flow pattern in the approach channel is thus being changed. The high pressure difference across the weir (shown in Fig. 6) accelerates the flow which tends to pass over the top of the weir perpendicularly and creates a recirculation zone behind the weir near the bottom. This recirculation zone and the overtop flow are separated by a shear layer. Due to the shape of the channel bed, the recirculation zone is approximately triangular. In the deeper portion of the channel, the recirculation enhanced by the shear flow is stronger and requires a longer distance to dissipate. This triangular recirculation zone can be clearly seen in the physical experiments. After the flow has passed the weir, the flow pattern caused by the weir dissipates gradually downstream. The distance to fully recover the flow pattern depends on the flow condition and the weir configuration. This distance is important for determining optimal weir spacing when a multiple weir design is considered.

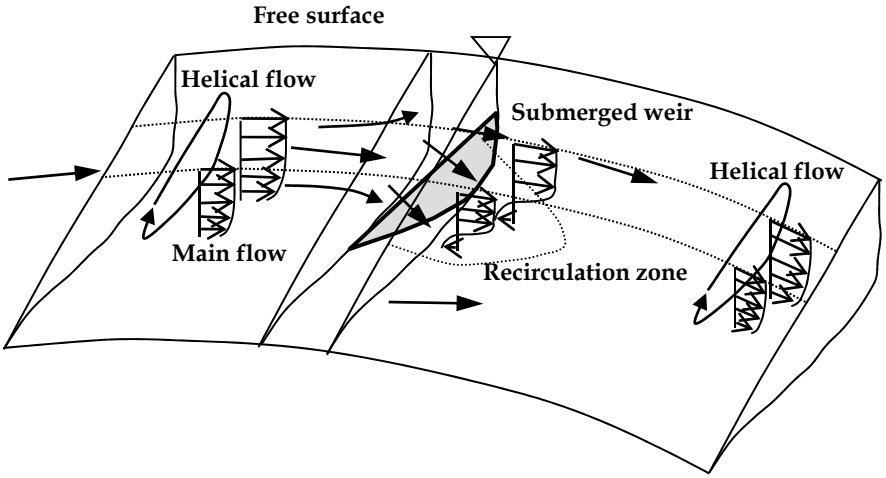

Fig. 7. Flow structure around a submerged weir

3.4 Flow field of the helical secondary currents

In order to illustrate secondary flow patterns, the computed flow fields are presented in a series of cross-sections. These cross-sections are aligned in the direction of the radius of curvature; the secondary current was defined as the velocity normal to the main flow direction. The main flow direction was defined as the mean flow direction in the channel without the submerged weir. Additional simulations were conducted to compute the main flow directions for each submerged weir case.

Fig. 8 shows the weir alignment near the bendway apex and the display cross-sections (J). All the cross-sections are equally spaced (Δl) along the centerline. For clarity, the spacing between these sections in the figure was exaggerated. The secondary currents presented in Fig. 9 are from some of these sections.

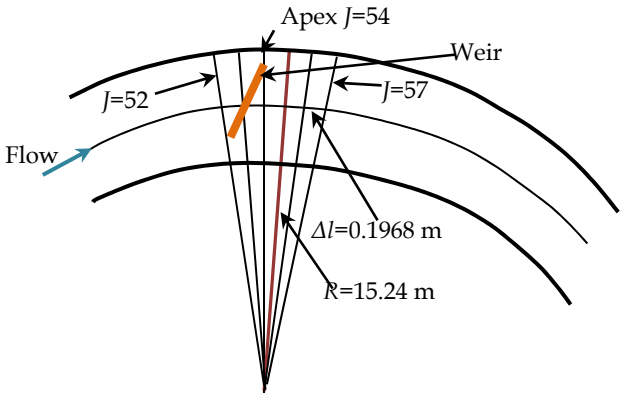

Fig. 8. Sketch of the simulation channel and the display cross-sections

The cross-sections in Fig. 9 are from upstream (Fig. 9a) to downstream (Fig. 9k), with the outer bank on the left and inner bank on the right side. The counter clockwise secondary current shown in section 40 (Fig.9a), far upstream of the SW, is a typical helical flow pattern. Closer to the SW in section 47 (Fig. 9b), the helical structure is altered because the main flow decelerates and separates. Since the weir has an angle of 20° from the radius line, it intercepts with several display sections (Fig. 8). The presence of the SW is reflected by highly complex secondary current and strong vertical motion shown in section 49, 50, 51, 52, (Fig. 9c, 9d, 9e, 9f) which cut across the SW.

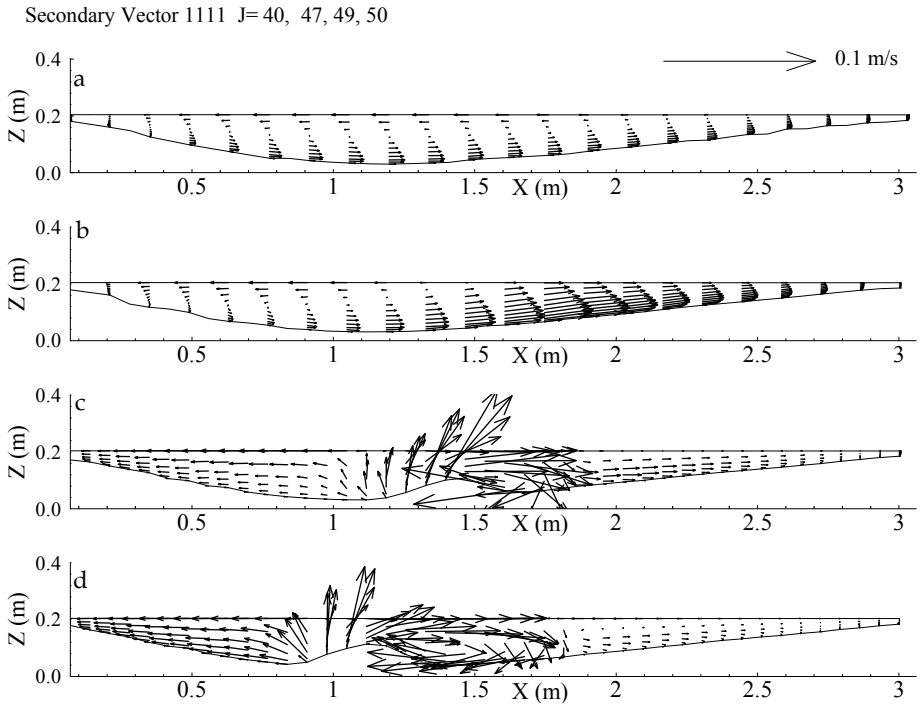

Fig. 9. (a) (b) (c) (d). Secondary current in the approach flow

The single celled, counter-clockwise helical current in the approaching flow becomes three cells behind the weir: the one in the center is strong and has inverse, clockwise direction; the other two near the banks are weaker (Fig. 9g and 9h). The inverse cell appearing on the right side of the weir is actually on the downstream side if one observes a top view of the flow pattern. The inverse cell is strong near the weir and dissipates gradually downstream, indicating that the influence of the weir is in a limited distance. The two cells near the banks are much weaker than the inverse center cell, however, they are of the same direction as that of the helical current in the approach flow. These two concomitant circulations are partly driven by the inverse cell and partly influenced by the flow around the tips of the weir. They gain strength gradually as the inverse cell is dissipated (Sec. 54, 58, 60, 66, Fig 9g, 9h, 9i, 9j). They finally reconnect and form a single helical current cell

across the channel (Sec. 78, Fig. 9k). The helical current will strengthen further downstream until complete recovery.

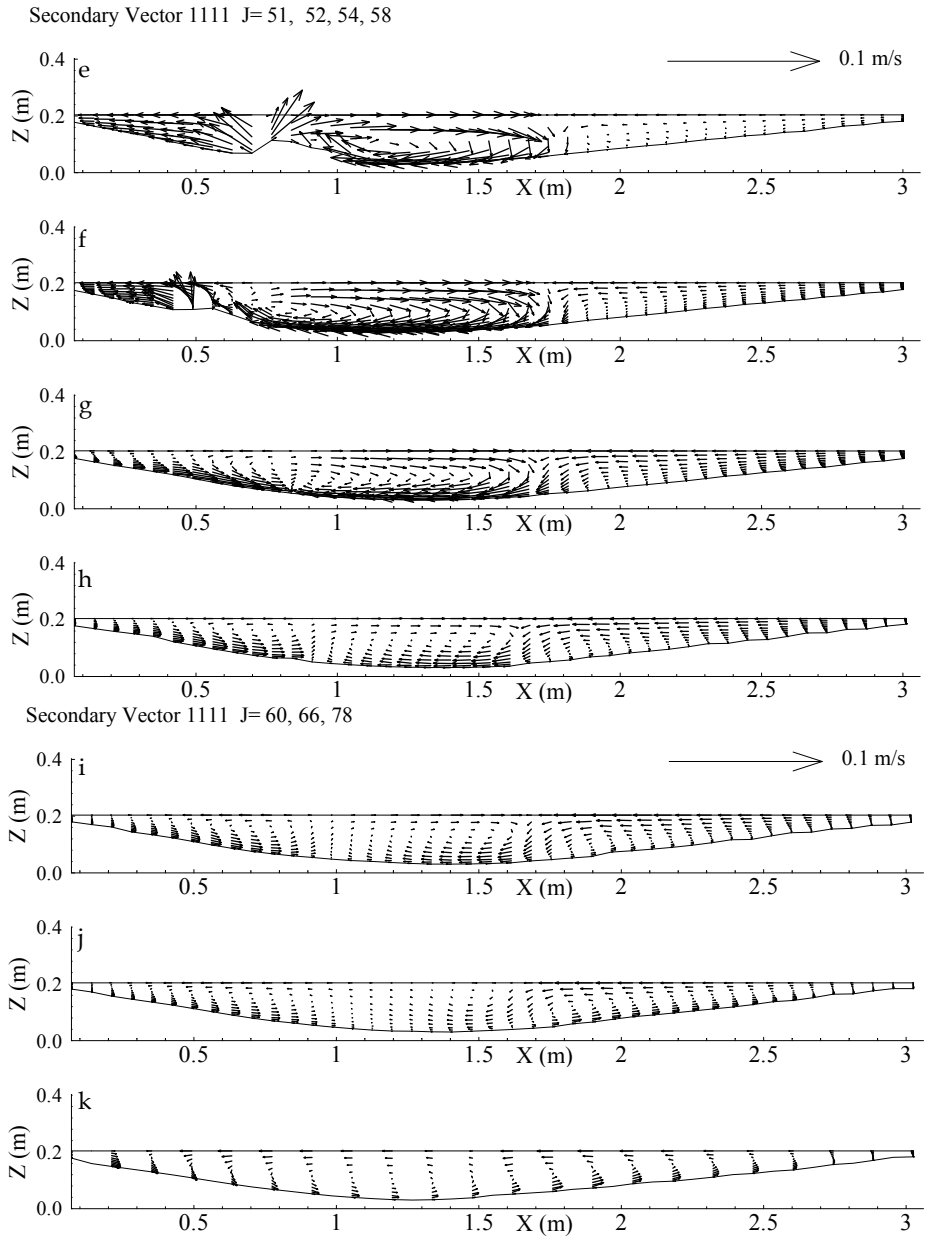

Fig. 9. (e) (f) (g) (h) (i) (j) (k) Secondary flow passing the submerged weir

Because of the inverse flow cell, the flow velocity near the centerline on the water surface is toward the inner bank instead of the outer bank. This cell of secondary flow inverse to the normal helical cell is beneficial to navigation because it cancels the effect of the general helical current and realigns flow toward the inner bank. The foot print of the inverse secondary current on the free surface is an area extending downstream from the SW. The length, width, and location of this realigned area are important to the safety of channel navigation. Since the flow velocity could not be measured close to water surface and the measuring ranges were set near the SW, one could not directly validate the predicted surface flow realignment. More detailed measurements covering the entire zone would be necessary to confirm the numerical results.

4. Study of Victoria Bendway

4.1 River geomorphology, hydraulic structures and measured velocity data

In 1995, six submerged weirs were constructed on the outer bank of Victoria Bend in the Mississippi River in an attempt to improve navigation conditions (Fig. 10). The effectiveness of submerged weirs on surface flow realignment in Victoria Bendway (VBW) of the Mississippi River was studied.

VBW is located at the confluence of the White River, between the State of Arkansas and Mississippi. The discharge in the Mississippi River upstream of the VBW is influenced by the White River. VBW is a highly curved bend, with a ratio of the radius of curvature to the channel width varying from 1 to 3 approximately, depending on the river stage. It has a 108^{o} heading change and a radius of 1280 m. It is expected that the secondary current would be very strong in such a channel, which creates a navigation hazard to navigating barges.

The submerged weirs were oriented upstream with angle from 69 to 76 degrees between the weirs and the bend longitudinal line. Post-construction surveys indicated deposition at the upstream reach of the weir field and scouring throughout the rest of the weir system. Three long spur dikes were constructed on the flood plain or point bar of the VBW. The effect of these dikes is to converge the flow to the main channel, therefore the point bar is protected from erosion, and the channel is re-aligned to enhance navigation.

A comprehensive survey of this reach was conducted by the US Army Corps of Engineers in 1998. The data were measured by acoustic devices with bed elevation referenced to a Cartesian coordinate system. In addition to the bed elevations, velocity data were taken in VBW using Acoustic Doppler Current Profiler instrumentation on June 11 and June 12, 1998. Three velocity transects were taken adjacent to each of the six submerged weirs: one upstream, one downstream, and one over the top of the weirs (Fig. 11). A few transects were taken between weirs with others downstream of the weir field where strong scouring occurred. Because of the highly turbulent flow in the bendway, the surveyed velocity transects were not straight across the channel.

The flow discharge in these two days was about that of a one year return flow and almost constant. The flow depth and width of the channel were large at this discharge with the flow depth in the main channel at about 15-35 m. The depth clearance above the weirs for navigation is about 6 m. The point bar was fully submerged with two of the three dikes partially submerged and the third one (downstream) completely submerged at this flow condition. The discharge was determined by integrating the measured flow flux in transects. Integrations of the flow flux using the measured velocities in each survey path indicate these surveys were quite consistent, resulting in a near constant discharge (~12,600 m^3/s) with only a few exceptions.

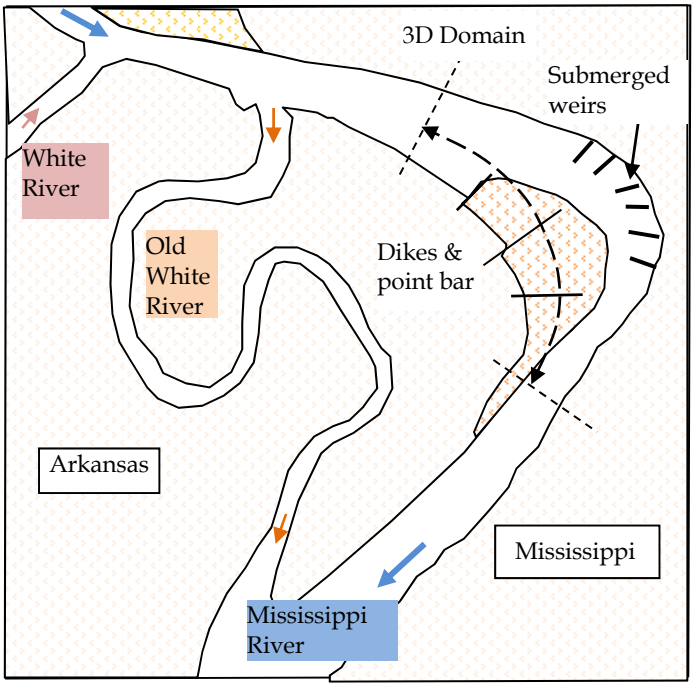

Fig. 10. Victoria Bendway of the Mississippi River, the White River and submerged weirs

Fig. 11 shows the bathymetry of the VBW and the 34 survey transects for measuring the velocity field. The weirs constructed in the main channel are depicted using contours of bed elevation. At each survey point, three-dimensional velocities were obtained along a vertical line at a number of points ranging from 5 to more than 100, depending on the flow depth. The velocity data measured on June 11, have 17 sections with a total of 2210 survey points while the data taken on June 12, include 17 transects with a total of 2494 survey points. Due to turbulent flow and complex bed bathymetry, the transects could not be held straight, particularly at where the point bar and thalweg meet. Actual transects are longer than those shown in Fig. 11, extending from the outer bank onto the point bar. The survey paths shown are the portion in the main channel consisting of about 35% of the total length of transects. Because the beam angle of the ADCP was 20˚, the sampling diameter near the bottom of the main channel (~30 meter deep) would be around 22 meters. This implies that scattering of the data would be large, particularly close to the irregular part of the bed and weirs, and the data may not be able to resolve flow structures in the weir field. Muste et al. (2004) discussed factors influencing the accuracy of ADCP measurement in general and evaluated a particular velocity profile measured in the middle of a straight reach of the Upper Mississippi River (Pool 8 near Brownsville, MN). For a steady flow of 4.5 m deep at the measuring point, sampling duration of 11 minutes were necessary at a fixed point to obtain a stable mean velocity profile. The measured mean velocity could differ as much as 45% if the sampling duration was less than 7 minutes. Since the flow velocity in the VBW was stronger and the flow depth larger, the measured mean velocity therefore could have a larger error because the survey vessel was moving continuously and the data was obtained

by averaging signals sampled in a short distance. The average time for measuring one transect of the VBW was about 10 minutes and that for a point was a few seconds. The velocities measured at the surface level often have large differences from those measured at lower levels, due to perhaps the influence from navigation traffic in the river, the survey vessel, or limitations of the measuring instrumentation.

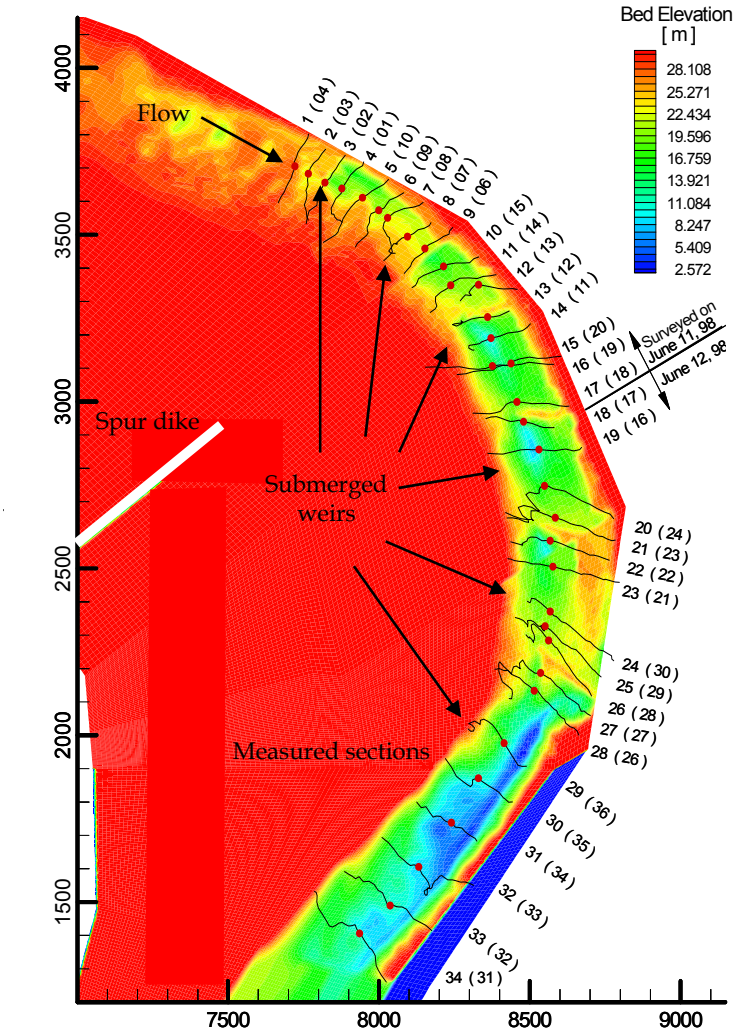

Fig. 11. Bed bathymetry, submerged weirs and the survey paths in the main channel. Section numbers are marked along the outer bank.

There was a large elevation difference between the main channel bed and the point bar, particularly near the downstream of the bendway. The weir field has caused additional

deposition and erosion at the upstream and downstream channel of the bendway, respectively. The bed between the weirs was also severely scoured. The resistance of the weir field would slow down the approach flow, stimulate deposition and cause additional flow toward point bar. The scouring in and downstream the weir field may result from additional turbulence due to the weirs and the reduced sediment load in the flow.
The approach of this study is to apply the 3D numerical model validated using experiment data to simulate the flow and evaluate the effectiveness of weirs. The numerical solutions provide a much higher resolution of the flow field and make it possible to resolve more detailed flow around the submerged weirs. The field velocity measurements were used to validate again the three-dimensional flow model. Comparison of the simulations for the pre- and post-weir channel revealed the effect of the weirs on the flow pattern.

4.2 Numerical simulation and model validation

Although the three-dimensional velocity data obtained were very detailed, the resolution of the three survey transects adjacent to a weir were not sufficient for analyzing the near field flow and its effect on navigation. Because the river channel near the Victoria Bendway was at the confluence with the White River, the channel pattern was complicated (Fig. 10). In order to use available computational resources efficiently, the 3D simulation was limited to a short bendway reach with a curved computational domain of 4.6 km along the main channel and 1.8 km wide in the apex section. A two-dimensional model (CCHE2D, Jia & Wang 1999; Jia et al., 2002a) was used to simulate a much longer reach (a 33.866 km stretch) to calibrate the resistance parameter and to establish initial flow, upstream and downstream boundary conditions for the 3D simulation. The effective roughness heights of the channel were obtained by calibration using measured water surface elevation along the channel. This roughness was used for the 3D simulation with the exception of the surface roughness of the SW. It was approximated to be one half of the gravel of which it was constructed. The upstream flow boundary conditions for the 3D model (flow rate and direction distributions) were specified with the 2D model results. The depth-averaged velocity at each point of the boundary of the 3D domain was converted to a logarithmic profile and no secondary flow was imposed since the inlet boundary was located in a relatively straight portion of the channel (Fig. 10).
The extended 2D channel stretches upstream and downstream of the VBW with a mesh size of 123 (transversal) x 622 (longitudinal); more than 50% of the horizontal mesh nodes were in the range of the bendway where 3D computations were carried out. The 3D computation is for the flow in the bend with a mesh of 123 (transversal) x 322 (longitudinal) x 11 (vertical); more vertical mesh points were located near the bed. Three 3D grids (G_1:58x189x8, G_2:123x322x11, and G_3:123x324x14) were tested. Using the three meshes, the RMS error of the simulation results and the measured data were computed and indicated in Table 2. Non-dimensional σ_u and σ_v are for the u and v velocity component, respectively. Computational points in the domain are much more than those measured. RMS errors were computed using measured data and computational results interpolated to the measuring point. The error of simulations is considerably less in the upper part of the flow (less than 8 m from the surface) than that in the lower part (deeper than 8 m from surface). The accuracy of the simulations did not significantly improve when mesh resolution was increased. As was mentioned earlier the scatter of the ADCP data was quite large particularly near the bed. This is attributed to larger data scatter near the bed such that the numerical accuracy improvement due to mesh refinement was much smaller than the data scattering.

Mesh	No. of vertical points	Zone of calculation	σ_u / U_{mean}	σ_v / U_{mean}
G_1	8	Upper profile	0.219	0.269
		Lower profile	0.363	0.34
G_2	11	Upper profile	0.218	0.262
		Lower profile	0.36	0.336
G_3	14	Upper profile	0.220	0.269
		Lower profile	0.36	0.337

U_{mean}~1.4 m/s is the mean velocity for the entire reach. Upper profile is the water surface to the 8 meters deep point, Lower profile is from the point to the bed.

Table 2. RMS error of the data and simulation results using three meshes

The mesh size of G_2 in the main channel ranges from 12 to 30 m, approximately. A submerged weir was resolved by 15 to 20 grid points. The submerged weirs are the largest resistance elements in the main channel. The back side slope of the weirs observed from the bed topography is less than 15°. The largest weir in the bendway was about 230 m long and 10 m high. The first weir upstream was hardly visible due to significant deposition in front of the weir.

2D simulation was used as a tool to calibrate roughness of the channel. The calibrated Manning's coefficient n=0.037 is reasonable considering large scale of bed forms, the number of structures (dikes, submerged weirs) built in this channel reach. Water stage data on June 11, 1998, from five gauge stations along the reach of 2D simulation, were used for the calibration. The calibrated Manning's coefficient was then transformed to equivalent roughness height for the three-dimensional model by using Strickler's function

$$n = \frac{d^{1/6}}{A} \tag{11}$$

where A is an empirical constant which may represent both grain and form resistance (A=19 according to Chien and Wan, 1999), and d (~0.121 m) is the effective roughness height which is consistent with a large data set for the Mississippi River (van Rijn, 1989). Graf (1998) showed that A could vary from 20 to 45 in rivers with cobble or gravel bed. The effective roughness is used in the wall function for specifying hydraulic rough boundary condition:

$$\frac{u_0}{u_*} = \frac{1}{\kappa}\ln(\frac{z}{z_0}) \qquad \text{for} \quad \frac{u_* k_s}{\nu} > 70 \tag{12}$$

$$z_0 = 0.03 k_s$$

where u_o is the near bed flow velocity, u_* is shear velocity, κ (=0.41) is the Karman's Constant, z is the distance from a wall, ν is the fluid viscosity and k_s (~d) is the roughness height. Although roughness height can be converted from the Darcy-Weisbach factor, Chezy's coefficient or Manning's coefficient more rigorously (van Rijn, 1989), Eq. 11 was used for its simplicity. Since d was a calibrated parameter, it lumps many factors related to the resistance such as bed forms and grain roughness. The three point-bar dikes are large

and resolved by the 2D model. The area of the submerged weir field was less than two percent of the 2D simulation domain; the effective roughness height thus evaluated was affected by the weir field only slightly. Measurement of bed form in the Mississippi River (Leclair, 2004) revealed that the size of dunes ranges from 120 to 11 m with height ranges from 3 to 1 m; dune length near a bendway is about 69 m. Considering the mesh size of the main channel (12-30 m), the bedforms were not resolved by the model. Therefore, it is reasonable to model their resistance using a lumped effective roughness height, and the computational grid was considered being over the roughness elements (Wu et al., 2000). The mixing length and k-ε turbulence closure schemes were applied in this study. Results indicate that the solutions from these two schemes had no significant differences in terms of defining the main and helical flow. Bed roughness varies spatially in the channel and the effective roughness used was a constant calibrated according to water surface profile.

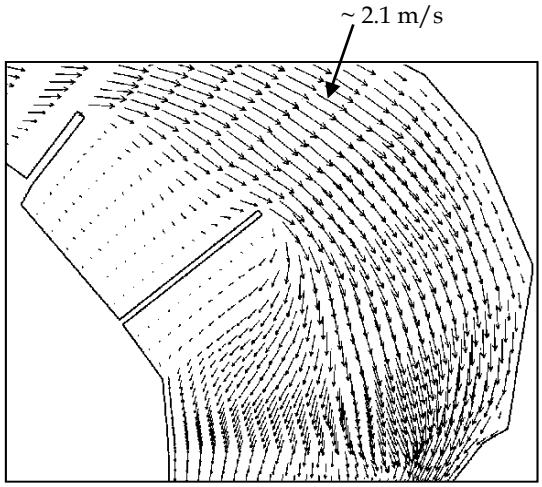

Fig. 12. Simulated flow pattern (velocity m/s) near water surface in Victoria Bendway

Fig. 12 demonstrates the simulated flow field near the free surface of the channel. For clarity, the resolution (velocity points) shown is only a few percent of the original. The first and second dikes on the point bar were submerged only slightly. They were treated as un-submerged in the simulation. A large area of recirculation was present between the first and second long spur dikes, with the recirculation lengths limited by the dike spacing. The recirculation behind the second dike was limited closely behind it and small in size, due to channel curvature. One can also observe the flow pattern from the point bar returning to the main channel near the end of the bendway.

Contour lines of surface velocity magnitude on the background of bed elevation shading are shown in Fig. 13. The river stage was high with the point bar and the third dike on the right bank submerged. One can see the flow velocity variation along the channel due to the existence of the second dike and weir structures. Because the water depth was less over the submerged weirs, the flow accelerates over the weirs.

Fig. 14 shows the computed water surface elevation contour overlaying the image of bed elevation. More contour lines are concentrated near the weir and show a similar pattern: the contour lines align parallel to the weirs and widen near the tips of the weirs. This distribution

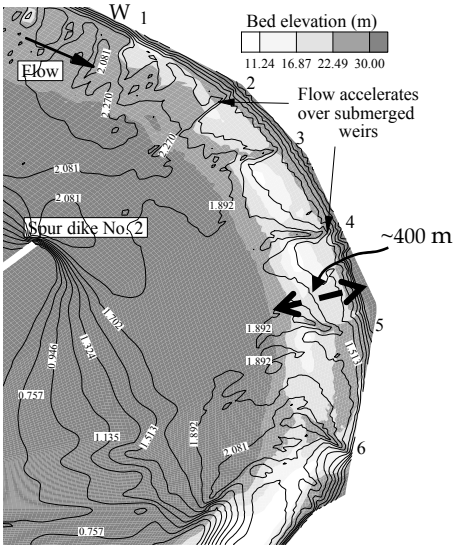

Fig. 13. Simulated distribution of velocity magnitude (m/s) near the water surface level

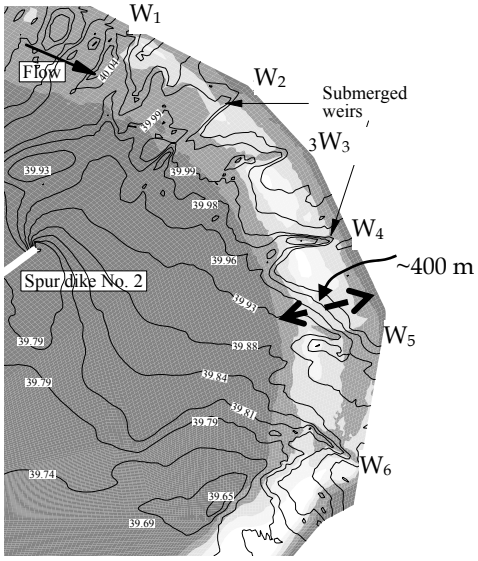

Fig. 14. Water surface elevation contours (m) in the main channel with submerged weirs

would accelerate the flow over the weir top normally and tends to turn the flow toward the inside of the bend. The helical current due to channel curvature is toward the outer bank; therefore, such a surface elevation pattern resulting from the submerged weirs reduces the strength of the helical current. In Fig. 6, the simulated surface elevation contours for the experiment case was also aligned parallel to the weir, similar to this field case; although due

to the difference in channel bathymetry, flow depth, and weir size relative to channel, etc., the patterns of the simulated water surface in these two cases are not exactly the same. However, the paralleled contours produce pressure gradients perpendicular to the weirs and thus help improving navigation.

To evaluate the quality of numerical simulations, model validation was performed by comparing the simulation and the measured 3D velocity data. Because the computational mesh points were different from those of the velocity survey, one has to interpolate the numerical solution to the 3D survey points. Inverse distance interpolation was used to compute the velocity from the eight vortices of a hexahedral mesh cell containing a measuring point.

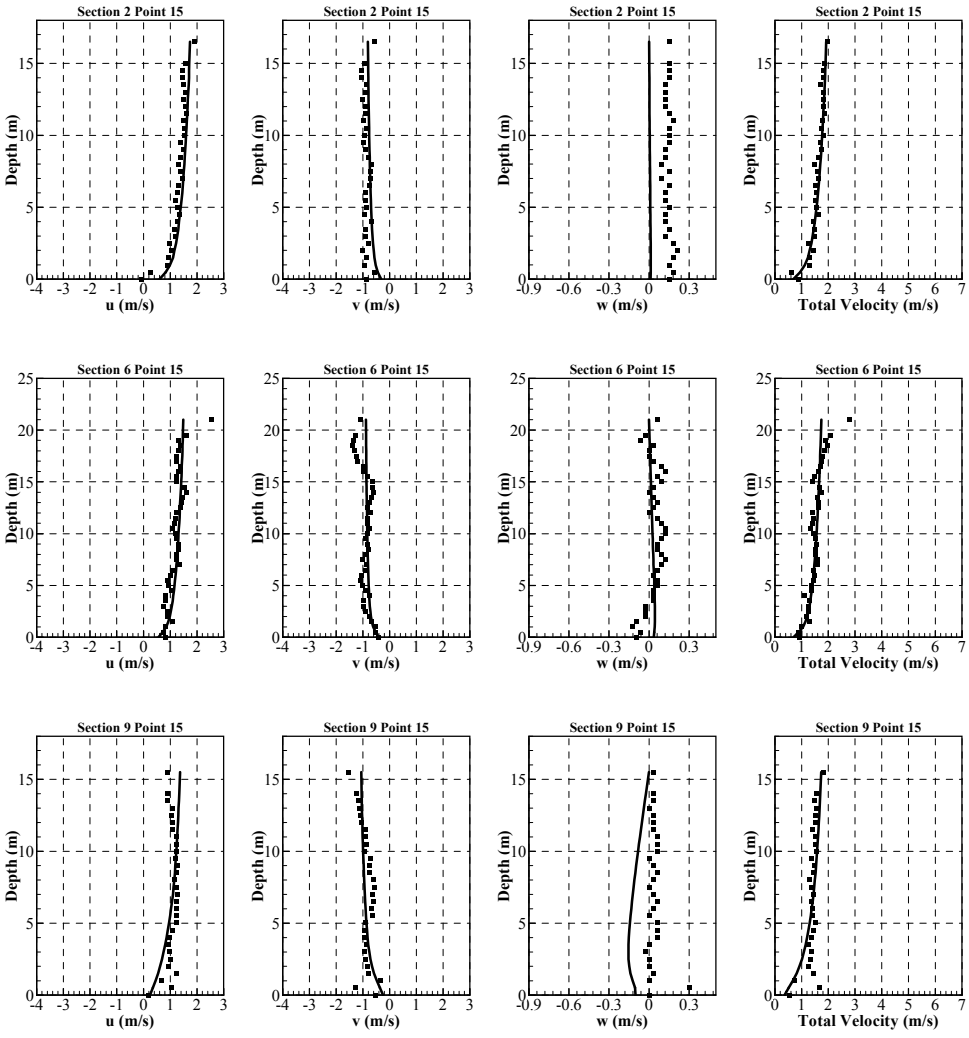

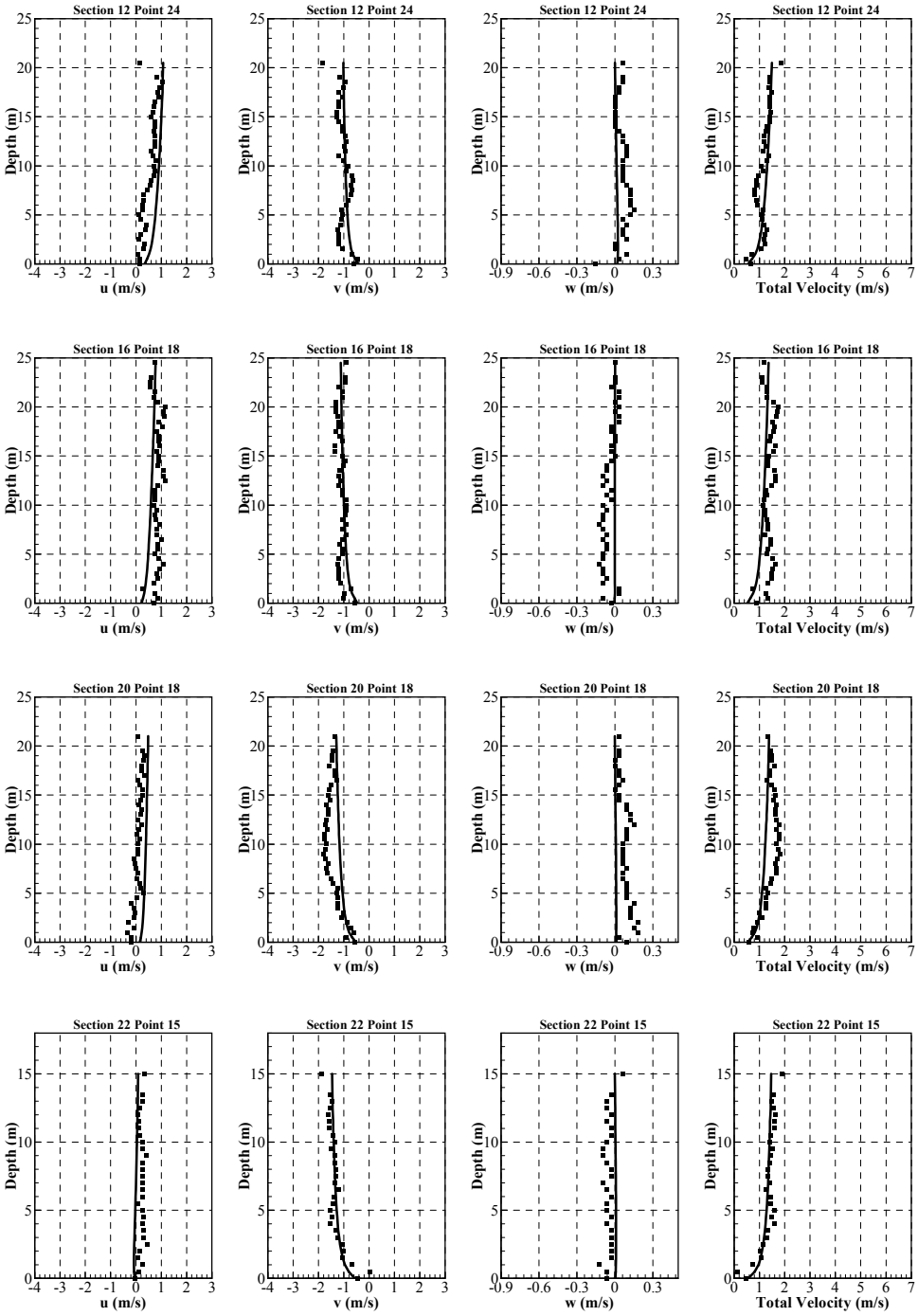
Section 12 Point 24
Depth (m)
u (m/s)
Section 12 Point 24
Depth (m)
v (m/s)
Section 12 Point 24
Depth (m)
w (m/s)
Section 12 Point 24
Depth (m)
Total Velocity (m/s)
Section 16 Point 18
Depth (m)
u (m/s)
Section 16 Point 18
Depth (m)
v (m/s)
Section 16 Point 18
Depth (m)
w (m/s)
Section 16 Point 18
Depth (m)
Total Velocity (m/s)
Section 20 Point 18
Depth (m)
u (m/s)
Section 20 Point 18
Depth (m)
v (m/s)
Section 20 Point 18
Depth (m)
w (m/s)
Section 20 Point 18
Depth (m)
Total Velocity (m/s)
Section 22 Point 15
Depth (m)
u (m/s)
Section 22 Point 15
Depth (m)
v (m/s)
Section 22 Point 15
Depth (m)
w (m/s)
Section 22 Point 15
Depth (m)
Total Velocity (m/s)

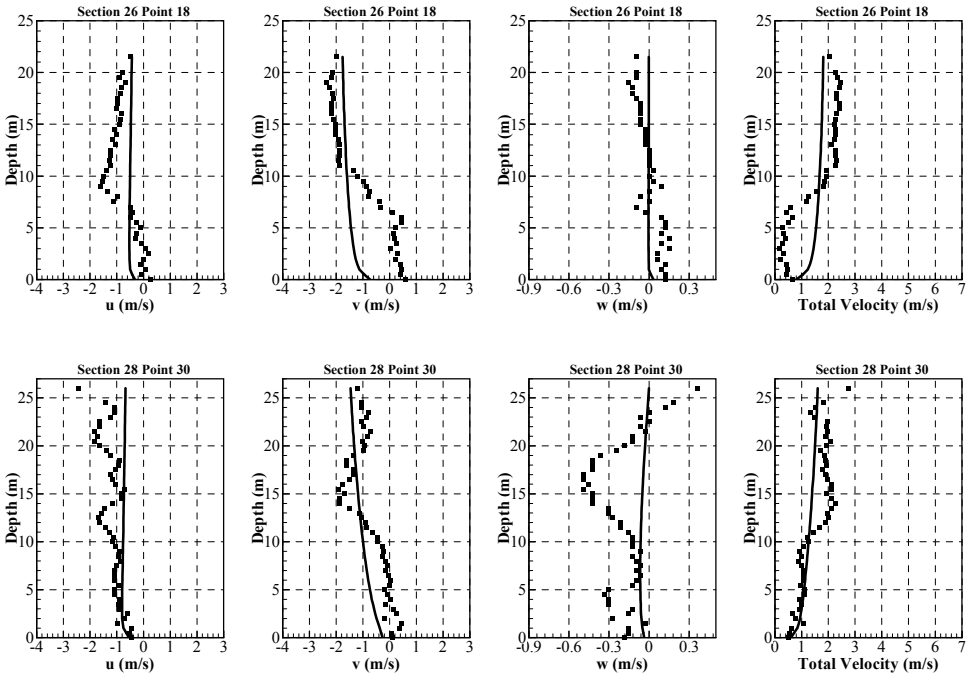

Fig. 15. Comparisons of computed and measured velocity profiles, along the main channel, Victoria Bendway

Because there were more than 4500 survey points, it is impossible and unnecessary to show all the comparisons. Instead, only a limited number of points are presented. Several vertical profiles are selected along the main channel (Fig. 11). Some points are located in scour holes between weirs, and others are very close to the weirs. Fig. 15 shows comparisons of these velocity profiles. Along each profile, computed and measured velocity components u, v, w and total velocity are compared. The depth of the flow at these survey points ranges from less than 20 m to about 35 m. Results indicate that the computed velocity profiles are smooth curves in most areas of the channel, with the velocity magnitude increasing toward water surface. Most of the comparisons show adequate agreement between data and simulation, particularly in trend. The agreement is generally better for points away from the weirs. No recirculation zone was found behind the weirs in the field data. In general, measured data show scatter and variation along vertical lines and transects, and the scatters appear to be random. For example, at measuring point 30 of Section 28, the measured velocities indicate stronger variations along the vertical. Distributions like this are often located either near abrupt bed change or close to a weir. At these locations, turbulence would be very strong and the upper and lower portion of the flow may have different directions. Simulating a mean turbulent flow, the numerical model resulted in a much smoother flow field than the measured velocities taken in highly turbulent and unsteady natural conditions.

Fig. 16 shows the computed and measured velocity magnitude at ten selected transects. Comparisons at three levels $0.05h$, $0.4h$ and $0.8h$ (from the bed to water surface) are

presented. One finds general agreements along each level and section. The data scatter near the channel bed is, in general, greater than in the upper portion of the water column, consistent with the RMS errors indicated in Table 2, which could be resulted from the large near-bed sampling volume of the ADCP and complex channel topography. The comparisons were performed for the main channel rather than the point bar, because the main interest of this study was the flow characteristics in the main channel. Although the differences between the computed and measured data are large for many points, the trend of the numerical results generally agrees with the data, particularly near the free surface (0.8*h*). These comparisons (Fig. 15 and Fig. 16) have confirmed the consistency of the numerical model with the field data and its applicability to this particular problem.

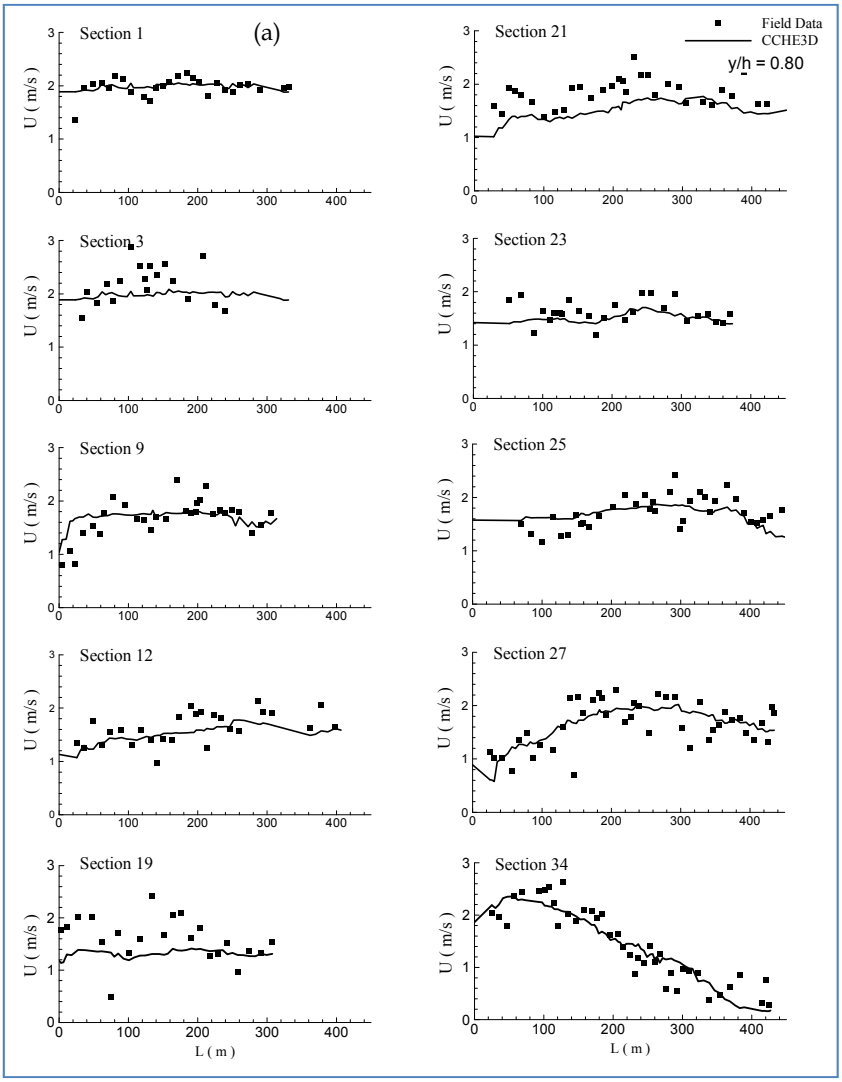

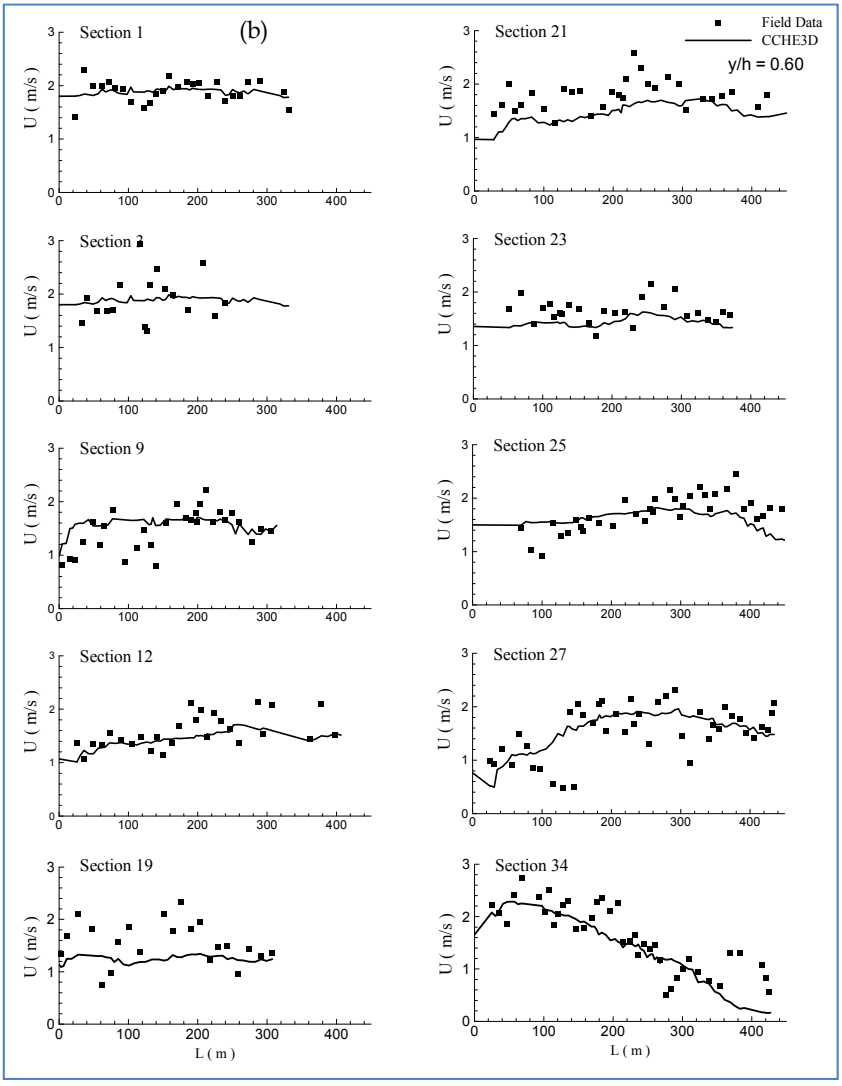
(b)
Field Data
CCHE3D
y/h = 0.60
Section 1
Section 21
Section 3
Section 23
Section 9
Section 25
Section 12
Section 27
Section 19
Section 34
U (m/s)
L (m)

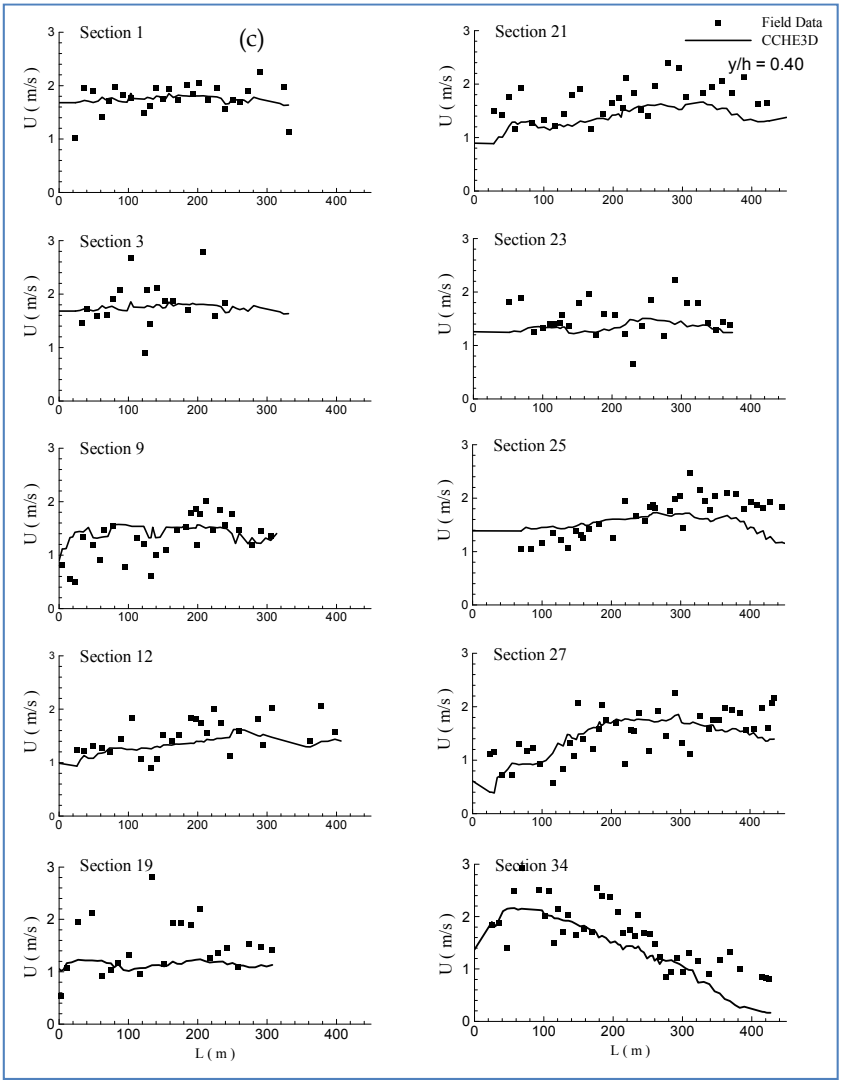
(c)
Field Data
CCHE3D
y/h = 0.40
Section 1
Section 21
Section 3
Section 23
Section 9
Section 25
Section 12
Section 27
Section 19
Section 34
U (m/s)
L (m)

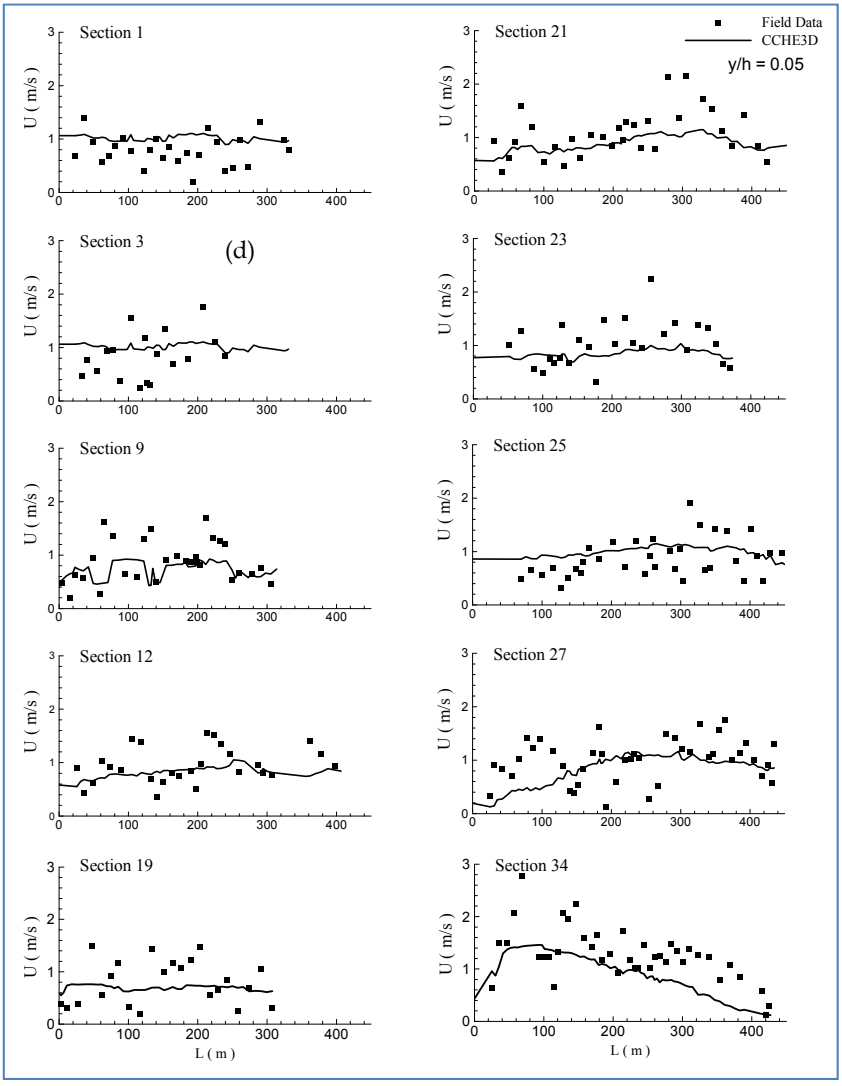

Fig. 16. Comparison of computed and measured flow velocity at selected sections (a) near water surface (z/h=0.8); (b) near middle depth (z/h=0.6); (c) near middle depth (z/h=0.4); and (d) near bed (z/h=0.05).

4.3 Helical secondary current and submerged weirs

Fig. 17 shows a plan view of the simulated 3D flow and comparison of computed and measured secondary flows in a transect. Vectors (in red) at surface level (Fig. 17a) are plotted with those near the bed (in black). The difference in their directions at each point represents the helical current. For clarity, only a limited number of vectors are shown.
Looking upstream, the main helical current in the main channel is clockwise. The secondary flow near the tip of the spur dike is also clockwise, but has been weakened or even reversed at some locations. Since it does not follow the channel curvature, the flow over the point bar goes directly into the main channel and alters the main flow there.

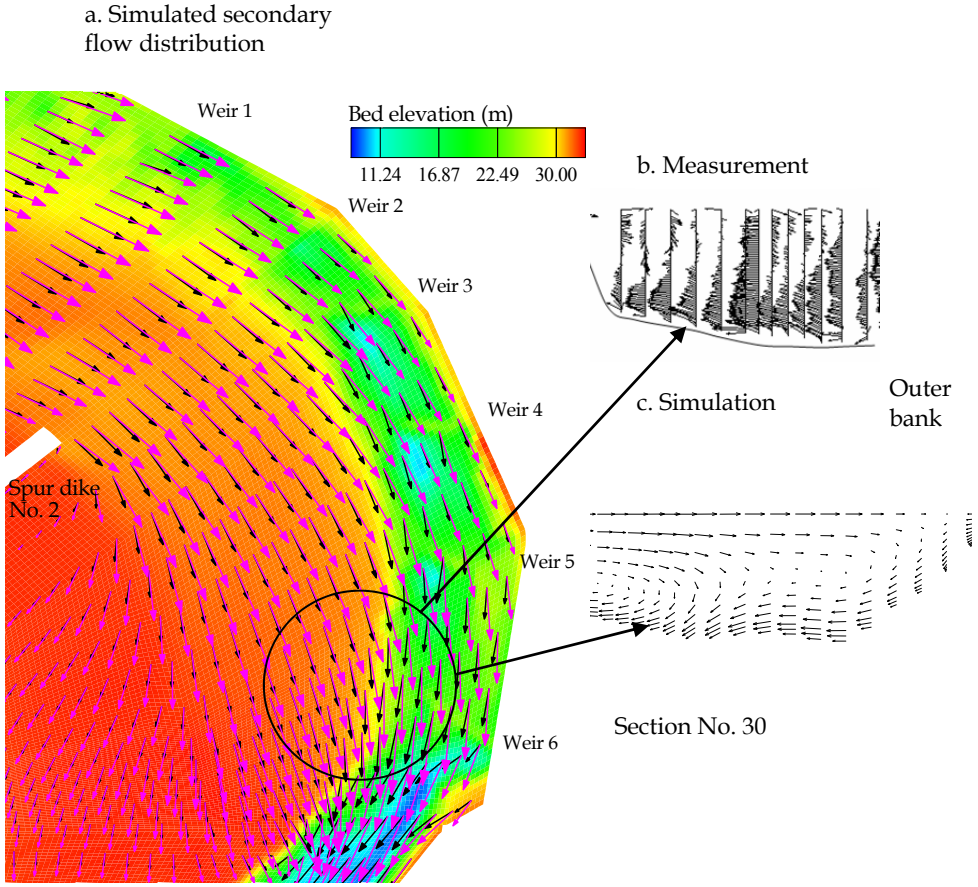

Fig. 17. Simulated secondary helical current in the bendway. a) General flow pattern; b) Measured secondary velocity in the main channel near the point bar; and c) Computed secondary velocity in the main channel near the point bar.

The flow over the point bar starts to converge back to the main channel at the downstream port of the bend. The returning flow near the edge of the point bar is not parallel to the edge; the component normal to the main flow affects secondary current in the main channel. With this particular bendway morphology configuration, the flow from the point bar back to the main channel tends to enhance the helical current. Since the main channel deepens near the 6th SW, a large bed elevation step appears between the point bar and the main channel. Affected by the flow from the point bar, the secondary current in the main channel appears to be intensified (around survey section 30, Fig. 11), as indicated by measurement (Fig. 17b) and simulation (Fig. 17c). The influence on the channel flow is similar to those observed by Sellin (1995) and by Shiono & Muko (1998) in their experiments in which the flow from a flood plain affects the secondary flow in the main channel. This indicates that the helical flow in the main channel is strengthened, consistent with the observation that severe channel erosion occurs on the downstream portion of the bend.

5. Influence of submerged weirs on navigation in VBW

Navigation problems in bendways are mainly attributed to the helical secondary current which tends to push vessels toward the outer bank (the inertial and centrifugal forcing due to the vessel's own motion are not considered). The simulated secondary flows with and without the submerged weirs were compared to assess the effectiveness of these weirs in reducing the strength of the secondary flow. The submerged weirs were removed from the computational domain; the deposition and erosion patterns, due to the presence of the weirs, were corrected using the channel bathymetry (cross-sections) surveyed in 1994 before the weir field installation as a reference. A 2D simulation was also conducted for producing boundary conditions.

The influence of the submerged weirs on the helical current was evaluated by the difference in the secondary current with and without weirs. Fig. 18a shows the computed secondary current in sections upstream, over, and downstream submerged weir No. 4. The orientation of these sections was approximately normal to the main flow direction. The secondary flow is strongly changed by this submerged weir. In the section over the weir, the changes in the secondary flows are dramatic. Near the water surface, the transversal flow toward the outer bank is reduced or reversed. Because vessels in bendways are pushed laterally by the transverse flow, this submerged weir effect would be beneficial to the channel navigation. In sections between weirs, the secondary current tends to recover the normal pattern of curved channel flows. Fig. 18b shows the computed helical current in the corresponding sections without the submerged weir.

The direction of the near surface flow defined by the angle

$$\theta = \arctan \frac{u_{transversal}}{u_{longitudinal}} \tag{14}$$

was used as an indicator of the flow alignment or navigation condition in bendways. If the angle (θ) is very small, the navigation condition is considered good because the flow would be aligned more along the main channel. To evaluate how the weir system influenced the flow angle, the difference of the flow angle at the free surface in the main channel with and without weirs, $\Delta\theta$ (= $\theta_{\text{with weirs}}$ - $\theta_{\text{without weirs}}$) was computed and presented in Fig. 19. Considering the secondary flow is normally in the order of $0.1u_{longitudinal}$, or less, the change of flow angle in the order of 5.7 degree would be sufficient to cancel the near surface secondary velocity.

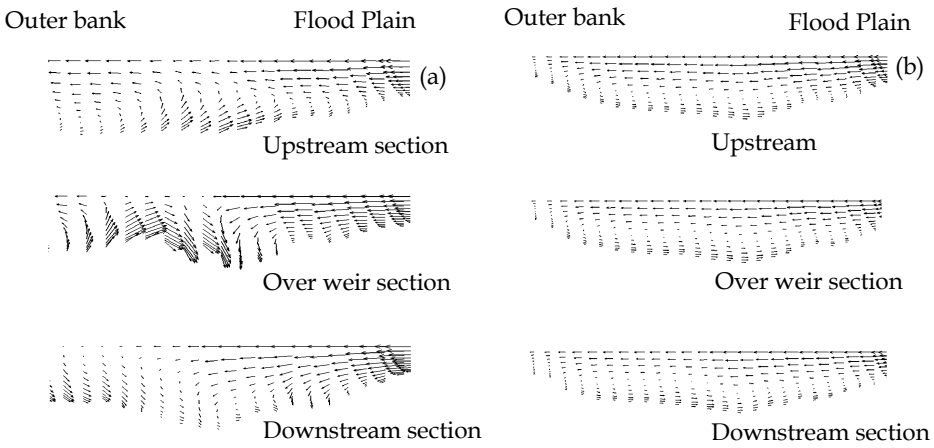

Fig. 18. Secondary currents around submerged weir No. 4; a) with weirs, b) without weirs

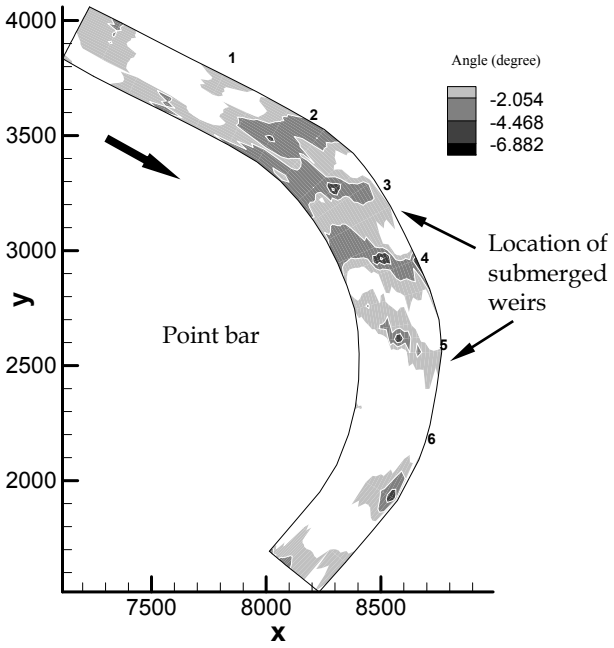

Fig. 19. The difference of the flow angles between the flows with and without submerged weirs. Only the main channel is shown. The portion with improved condition (with negative $\Delta\theta$) is shaded.

The areas with a negative angle represent where the flow condition is improved, whereas the areas with a positive value indicate where the condition became worse. To distinguish the areas with an improved condition, the contours of the area with a worsened condition is replaced with white. It is seen that the total improved area is larger than 50% and that conditions are better near the weirs. The flow angle change is high over the weir tops and low between them. The maximum angle change reaches about 6.8˚ with less change between weirs. The flow condition near weir No. 6 is worsened, because the strong flow from the point bar returns to the main channel and the secondary current intensifies. After the construction of the weirs, the resistance of the main channel increased resulting in more water flowing over the point bar at the entrance of the bend and then returning to the main channel. The strength of the secondary current near weir No. 6 is thus increased (Fig. 17). The excessive deposition upstream of the weir field in the main channel has disabled the first weir; thus, the first weir is not functional (Fig. 19). In addition, the first and last weir were angled less than others, so they should be less effective even without the influence of the flow from the point bar and sedimentation. To a certain extent, a weir would be more effective if it is angled more toward upstream; its effect on realigning the flow is also influenced by relative length, relative depth, and channel curvature, etc. (Jia et al., 2002b). Future submerged weir designs should consider the influence of local morphology (flood plain). Since the influence of the weirs varies in terms of water depth and relative weir height, additional studies with several more flow conditions are necessary to enhance submerged weir designs.

6. Conclusions

A three-dimensional computational model for free surface turbulent flows, CCHE3D, has been applied to study flows in bendways affected by submerged weirs. Both experimental data and field data were used for model validation. The flow distribution due to a weir in a bendway was discussed and the effect of multiple weirs in the Victoria Bendway in the Mississippi River on channel navigation was studied. The comparisons showed good agreement in both the experiment and field cases between measured and simulated data which confirmed the consistency of the numerical model, the physical model and the large scale field case.

The general helical secondary current pattern in the experimental channel was disturbed by the single weir, particularly in its vicinity. In the experiments with a submerged single weir, it was found that the weir resulted in a high pressure zone forming on its upstream side and a low pressure zone on the downstream side. The high pressure zone slows the approaching flow and tends to separate it, forcing more flow toward the ends of the weir with the velocities near the tips increasing and higher than in the center region of the weir and the channel. The low pressure behind the weir creates a triangle-shaped recirculation zone. Due to the alignment of the weir (angled toward upstream), the high pressure and the low pressure zones are not located along the general stream direction. The high pressure zone is located closer to the outer bank and the low pressure zone is closer to the inner bank (tip of the weir). The skewed distribution tends to realign the overtopping flow toward the inner bank, which is opposite to the general helical current direction. The realigned surface current and the recirculation behind the weir form an inverse secondary cell. Two weaker secondary cells along the banks were also observed parallel to the inverse cell.

Due to the submerged weir, the flow velocity near the center of the experimental channel decreases and that near the tips of the weir increases. These high velocity zones may result in bed erosion and channel widening. The contours of the water surface are parallel to the weir direction and surface flow direction was realigned to the inner bank, thus being favorable to navigation. The effect of the weir is limited, and normal curved channel flow pattern may recover downstream. Further research is necessary to quantify sediment transport characteristics of bendways containing submerged weir fields.

In Victoria Bendway with multiple weirs, the simulation indicated that the helical current was only significant in the main channel. The flow over the point bar has little curvature and secondary current structure under the flow conditions studied is very weak. The helical current in the main channel was enhanced by the flow returning back to the main channel from the point bar.

For the case of Victoria Bendway, the computed velocities were smooth curves varying in the vertical direction, while the measured velocities show scatters much larger than the experiment case. Because of the nature of the ADCP instrument, the scatters are particularly strong near the bed, in close vicinity of weirs, and where the main channel and point bar join. A larger discrepancy of velocity comparisons would appear in these areas. The comparisons along measured transects at several vertical levels show reasonable agreement with the best agreement appearing near the water surface ($0.8h$).

In the main channel of Victoria Bendway, the direction and magnitude of the secondary current were affected by the submerged weirs. Not only was the secondary current structure changed, the secondary flow near the free surface around the weirs was weakened. This is consistent with the simulated water surface elevation pattern which tends to realign the flow over the top of the weirs. The way the flow is affected by these weirs is similar to that observed in the experimental channel of the physical model.

To study the overall effectiveness of the weir field, numerical simulations without weirs were also carried out and the solutions were compared to that with weirs in Victoria Bendway. Flow direction change in the main channel was compared and the weir effectiveness was evaluated. Most of the weirs (four out of six) were found effective, but the first and last weir were not. The ineffectiveness was caused by the channel deposition and the flow returning from the point bar enhanced the helical current. In addition, a smaller alignment angle made them less effective.

7. Acknowledgement

This investigation was conducted under contract agreement No. DACW42-01-P-0243 and No. DACW42-00-P-0456 with the US Army Corps of Engineers, Waterways Experimental Station, and the National Center for Computational Hydroscience and Engineering, The University of Mississippi. Professor Pierre Julien of Colorado State University provided valuable suggestions in reviewing a part of this study. Mr. Michael F. Winkler of USACE provided the physical model data. The authors appreciate the help of Dr. Yaoxin Zhang at NCCHE for his technical assistance.

8. References

Bhuiyan, A.B.M.F. & Hey, R.D. (2001). Instream J-vane for bank protection and river restoration, *XXIX IAHR Congress Proceedings*, Beijing, China. Theme D, Vol. II, pp 161-166.

Bhuiyan, F & Olsen, N.R.B., (2002). Three-dimensional numerical modeling of flow and scour around spur-dikes, *Proceedings of the Fifth International Conference on Hydroinformatics,* Cardiff, UK, 2002, 70-75

Blanckaert, K. & Graf, W.H. (2001). Mean flow and turbulence in open-channel bend, *J. Hydraulic Eng*., 127(10), 835-847.

Booij, R. (2003). Modeling the flow in curved tidal channels and rivers, *Proceedings, International Conference on Estuaries and Coasts,* Nov. 11, 2003, Hangzhou, China, pp786-794.

Chien, N. & Wan, Z. (1999). *Mechanics of Sediment Transport*, ASCE press, ASCE, 1801 Alexander Bell Drive, Reston, Virginia 20191-4400.

Davinroy, R. D. & Redington, S.L. (1996). Bendway weirs on the Mississippi River, a status report, *Proceedings of the 6th Federal Interagency Sedimentation Conference*, March 10-14, 1996, Las Vegas, NV, pp III32-37.

De Vriend, D.J. (1979). *Flow measurements in a Curved Rectangular Channel*, Laboratory of Fluid Mechanics, Department of Civil Engineering, Delft University of Technology, Internal Report No. 9-79.

Duan J.G., Wang, S.S.Y., & Jia, Y. (2001). The application of the enhanced CCHE2D model to study the alluvial channel migration processes, *J. Hydraul. Res*., 39(5) 2001, 469-480.

Graf, W.H. (1998). *Fluvial Hydraulics*, John Willey & Sons Ltd, Baffins Lane, Chichester, West Sussex PO19 1UD, England.

Hsieh, T.Y. & Yang, J.C. (2003). Investigation of the suitability of two-dimensional depth-averaged models for bend flow simulation, *J. Hydraul. Eng.,* 129(8), 597-612.

Jarrahzade, F. & Bejestan, M.S. (2011). Comparison of maximum scour depth in Bank line and nose of submerged weirs in a sharp bend, *Scientific Research and Essays,* Vol. 6(5), pp. 1071-1076, 4 March, 2011, available online at http://www.academicjournals.org/SRE

Jia, Y., & Wang, S.S.Y. (1992). Computational model verification test case using flume data, *Proceedings: Hydraulic Eng.,* 436-441, ASCE.

Jia, Y., & Wang, S.S.Y. (1993). 3D Numerical Simulation of Flow Near a Spur Dike, *Advances in HydroScience and Engineering*, *Proceedings of International Conference for Hydroscience and Engineering,* Vol. I Part B, pp2150-2156. University of Mississippi, June, 1993.

Jia, Y & Wang, S.S.Y. (1999). Numerical model for channel flow and morphological change studies, *J. Hydraul. Eng.*, ASCE, 125(9), 924-933.

Jia, Y., & Wang, S.S.Y. (2000a). Numerical Study of Turbulent Flow around Submerged Spur Dikes, *2000 International Conference of Hydroscience and Engineering*, Korea.

Jia, Y., & Wang, S.S.Y. (2000b). Numerical simulations of the channel flow with submerged weirs in Victoria Bendway, Mississippi River, *Technical Report No. NCCHE-TR-2000-3*, National Center for Computational Hydroscience and Engineering, The University of Mississippi.

Jia, Y., Blanckaert, K., & Wang, S.S.Y. (2001a). Simulation of secondary flow in curved channels, *Proceedings of the FMTM2001 International Conference*, Tokyo, Japan.

Jia, Y., Kitamura, T., & Wang, S.S.Y. (2001b). Simulation of scour process in plunging pool of loose bed-material, ASCE, *J. Hydraul. Eng.*, 127(3), 219-229.

Jia, Y., Wang, S.Y.Y., & Xu, Y. (2002a). Validation and application of a 2D model to channels with complex geometry, *International Journal of Computational Engineering Science*, 3(1) (March 2002), 57-71.

Jia, Y., Wang, S.S.Y., Xu, Y., & Huang, S.L. (2002b). Research on Optimal Parameters of Submerged Weirs Using Numerical Simulation and Physical Model Data, *Technical Report TR-2003-2,* National Center for Computational Hydroscience and Engineering, The University of Mississippi.

Jia, Y., Scott, S., Xu, Y.C., Huang, S.L., & Wang, S.S.Y. (2005). Three-Dimensional Numerical Simulation and Analysis of Flows around a Submerged Weir in a Channel Bendway, *J. Hydraulic Eng.*, 131(8), 682-693, August 1, 2005.

Jia, Y., Scott, S., Xu, Y.C., & Wang, S.S.Y. (2009). Numerical Study of Flow Affected by Bendway Weirs in Victoria Bendway, the Mississippi River, *Journal of Hydraulic Engineering*, 135(11), ASCE, p902–916.

Kuhnle, R., Jia, Y., & Alonso, C. (2002). 3-Dimensional Measured and Simulated Flow for Scour Near Spur Dikes, *First International Conference on Scour of Foundations, ICSF-1*, Texas A&M University, College Station, Texas, USA, November 17-20, 2002, Vol.1 349-363.

Jin, Y.C. & Steffler, P.M. (1993). Predicting flow in curved open channels by depth-averaged model, *J. Hydraul. Eng.*, ASCE, 119(1), 109-124.

Kinzli, K.D. & Thornton, C.I. (2010). Predicting velocity in bendway eddy fields, *River Res. Applic.* 26: 823–834 (2010), DOI: 10.1002/rra.1289

Lai, Y.G., Weber, L.J., & Patel, V.C. (2003). Nonhydrostatic three-dimensional model for hydraulic flow simulation, I: formulation and verification, *J. Hydraul. Eng*. 129(3), 196-205.

Leclair, S.F. (2004). Multi-scale dunes of the Mississippi River: the analysis of time variation of probability distributions of bed elevation as s step toward the understanding of bed load sediment transport, *Denver Annual Meeting (November 7-10, 2004), Paper No. 198-8*, Geological Society of America, Abstract with Programs, Vol. 36, No. 5, p. 461

Leschziner, M.A. & Rodi, W. (1979). Calculation of strongly Curved Open Channel Flow, *J. Hydraulics Division*, ASCE, 105(10), 1297-1313.

Martin, S. K & Luong, P.V. (2010). Analyzing shoaling reduction techniques on the Atchafalaya River at Morgan City, LA, *2nd Joint Federal Interagency Conference*, Las Vegas, NV, June 27 - July 1, 2010.

Mayerle, R., Toro, F.M., & Wang, S.S.Y. (1995). Verification of a three dimensional numerical model simulation of the flow in vicinity of spur dikes, *J. Hydraul. Res.*, 33(2), 243-256.

Morvan, H., Pender, G., Wright, N.G., & Ervine, D.A. (2002). Three-dimensional hydrodynamics of meandering compound channels, *J. Hydraul. Eng.*, 128(7), 674-682.

Muste, M., Yu, K., Pratt, T., & Abraham, D. (2004). Practical aspects of ADCP data use for quantification of mean river flow characteristics; Part II: fixed vessel measurements, *Flow Measurement and Instrumentation*, 15 (2004) 17-28.

Nezu, I., & Nakagawa, H. (1993). *Turbulence in Open Channel Flows*, A.A. Balkema, Rotterdam, Netherlands.

Odgaard, A.J. & Kennedy, J.F. (1983). River-bend bank protection by submerged vanes, *J. Hydraulic Eng.*, ASCE, 109(8), 1161-1173.

Olsen, N.R.B. (2003). Three-dimensional CFD modeling of self-forming meandering channel, *J. Hydraul. Eng.*, 129(5), 366-372.

Olsen N.R.B. & Stokseth S. (1995). Three-dimensional numerical modelling of water flow in a river with large bed roughness, *Journal of Hydraulic Research* 33: 571–581.

Ouillon, S. & Dartus, D. (1997). Three-dimensional computation of flow around groyne, *J. Hydraulic Eng.*, ASCE, 123(11), 962-970.

Rajaratnam, N. & Nwachukwu, B.A. (1983). Flow Near Groin-Like Structure, *J. Hydraul. Eng.*, ASCE, 109(3), 463-480.

Rozovskii, I.L. (1961). *Flow of Water In Bends Of Open Channels*, Academy of Science of the Ukrainian SSR, Institute of Hydrology and Hydraulic Engineering, The Israel program for Scientific Translations.

Sellin, R.H.J., (1995). Hydraulic performance of a skewed two-stage flood channel, *J. Hydraulic Res.*, 30 (1), 43-64.

Shiono, K. & Muto Y. (1998). Complex flow mechanisms in compound meandering channels with over bank flow, *Journal of Fluid Mechanics*, 376, 221-261.

Speziale, C. G. (1987). On nonlinear *k-l* and *k-ε* models of turbulence, *J. Fluid Mech.*, 178, 459-475.

Stone, H. L. (1968). Iterative solution of implicit approximation of multidimensional partial differential equations, *SIAM Journal on Numerical Analysis*, 5, 530-558.

van Rijn, L.C., (1989). *Handbook: Sediment Transport by Currents and Waves*, Delft Hydraulics, Report H 461.

Wang Sam S.Y. & Hu, K.K. (1992). Improved methodology for formulating finite-element hydrodynamic models, In T.J. Chung, (ed) *Finite Elements in Fluids*, Volume 8, Hemisphere Publication Cooperation, pp457-478.

Wang, S.S.Y., Roche, P.J., Schmalz, R.A., Jia, Y. & Smith, P.E. (ed.) (2008). *Verification and Validation of 3D Free-Surface Flow Models*, American Society of Civil Engineering.

Waterway Simulation Technology, Inc. (1999). A physical model test plan for bend way weir design criteria, *Project summary report to the Navigation Branch of the Coastal and Hydraulics Laboratory*, Waterway Experiment Station.

Waterway Simulation Technology, Inc. (2002). Physical model test for bendway weir design criteria, US Army Corps of Engineers, Engineer Research and Development Center, *ERDC/CHL TR-02-28*, October 2002.

Wilson, C.A.M.E., Boxall, J.B., Guymer, I. & Olsen, N.R.B. (2003). Validation of a three-dimensional numerical code in the simulation of pseudo-meandering flows, *J. Hydraul. Eng.* 129(10), 758-768.

Wu W.M., Rodi W. & Wenka T. (2000). 3D Numerical Modeling of Flow and Sediment Transport in Open Channels, *J. Hydraulic Eng.*, ASCE 126 (1) 4-15.

13

Analysis of Two Phase Flows on Stepped Spillways

R. J. Lobosco[2], H.E. Schulz[1,2] and A. L. A. Simões[2]
[1]*Nucleus of Thermal Engineering and Fluids*
[2]*Department of Hydraulics and Sanitary Engineering*
School of Engineering of São Carlos, University of São Paulo
Brazil

1. Introduction

Self-areation is a very relevant phenomenon that occurs in flows on stepped chutes, and is one of the reasons of building such structures. In this sense, the main purposes of stepped chute structures is to increase the energy dissipation of the flows by internal friction and to protect the bed of spillways through the presence of the air absorbed from the atmosphere. It is a "lucky coincidence" that, while the steps significantly increase the energy dissipation rate, they also increase the air uptake, reducing the risks of cavitation along the bed of the channel (Peterka, 1953; Frizell & Melford, 1991).

An additional consequence of the use of stepped chutes is the reduction of the size of the energy dissipation basins at the toe of the spillways, implying in reduction of the total costs of the spillway structures. Physically, it is observed that the superficial air uptake begins at the cross section where the turbulent boundary layer attains the water surface, as described for example by Chanson (1997), and predictions of the location where water depth and boundary layer thickness coincide, and of the amount of air absorbed by the water, are important for the design of spillways.

As a consequence of the abovementioned characteristics, stepped chutes are extensively used in hydraulics and environmental engineering. The air-water two-phase flow along the stepped channels is generally classified accordingly to its regime, as Skimming flow, Nappe flow and Transition flow, and the change from one regime to the other is still matter of discussion in the literature.

In this chapter, a procedure is followed, aiming to adjust numerical tools in order to adequately represent the air-water interface along stepped chutes. In this case, it implies in finding conditions that allow the "breaking" of the surface, so that air can be incorporated by the water. Such a tool is interesting for the prediction of gas transfer in stepped spillways, and it is expected to be used by designers that need to quantify the so called self-aerated flows. As mentioned, the air is incorporated into the water through the surface, and knowing the distribution of the entrained air and the flow conditions, the gas transfer along the different positions in the cross section of the flow can be estimated, until it attains the bottom of the chute. In addition, having a good numerical code, it may be possible to obtain the pressure distribution along the structure and to localize the potential cavitation regions, allowing to "test numerically" possible solutions to enhance the air content and to reduce

cavitation damages (Gomes, 2006; Olinger, 2001). The obtained results presented in this chapter are still approximate, but already show that the problem is treatable using numerical tools. The main problems, as shown in this chapter, are related to the behavior of the free surface.

This study considers the skimmimg flow regime, which generally occurs for large specific water discharges (Chanson, 2000). It is expected that the bed profile of the inlet structure affects the position of the inception point of the aeration (Boes & Hager, 2003a; Chanson, 2001). This study presents results of computational analyses for two inlet conditions of a stepped chute with an ogee crest. The aeration of the flows was investigated for an entry profile containing 1) steps with the same size, and 2)"transition steps" (steps with sizes increasing between the smooth bed and the stepped bed).

In the last few decades, the computational fluid dynamics, CFD, has imposed itself as one of the best tools for the prediction of flow fields with accuracy and detail (Versteeg & Malalasekera, 1995). But even considering its success, complex flows still need many efforts to be completely understood. The description of the physical processes of a two phase flow involves a broad variety of computational methodologies to predict the quantities of the constituent components and the behavior of the interface. In the present study, the numerical procedures for the stepped channel flow simulations were conducted using the open softwares Salome and OpenFoam® (Open Source Field Operation and Manipulation), for mesh generation and CFD, respectively. In a general way, it may be commented that the implementation of CFD modeling is still limited, due, in part, to the relatively high costs of the commercial softwares. OpenFoam® is an open CFD software that helps to fill this gap. For the purposes of this chapter, the particularly relevant characteristic of the mentioned software is its ability to simulate flows interacting with hydraulic structures.

The skimming flows along stepped chutes are inherently turbulent (Lima, 2003, Chamani, 2000), and their "turbulent characteristics" were investigated here using the "k-ε" model of turbulence, and adequate wall functions for the wall boundaries. The VOF method (Volume Of Fluid), was used for the interface-capturing procedures in the two-fluid model. Further, the PISO method (Pressure-Implicit with Splitting of Operators) was used as the pressure-velocity coupling scheme. In the calculations performed for this chapter, the rasInterFoam solver was chosen because, traditionally, the flow along spillways is considered incompressible (its velocity is much lower than the speed of the sound in water). The main purposes of this chapter were to show the implementation of the mentioned open softwares for the problem of aerated flows over stepped chutes, and to compare some calculated hydrodynamics characteristics with the literature, like the pressure distribution on the steps.

The literature addresses the position of the inception point by empirical correlations (see, for example, Chanson (2006)). In the present study, numerical models are applied to evaluate the interface behavior, air concentrations along the flow, and to investigate the dependence between the inception point position and the bed profile characteristics. First results are shown, which show that these calculations are possible, and that more studies are necessary to improve the results.

2. Physical model description

2.1 Structure design

The parameters to be adjusted for stepped spillways during the design phase, such as step height, flow regime, and the desired air flow rate will of course depend on the application

proposed for the steps. In general the stepped design takes into account the higher energy dissipation efficiency of the stepped chutes, when compared with smooth chutes, because it implies in reduction of costs of the dissipation basin (Arantes, 2007). Fig. 1 shows structures of spillways with different geometries, which illustrate that the purposes of the structure define the kind of spillway to be used.

Fig. 1. Illustration of dam structures: *a*) Traditional smooth chute, *b*) Flow over a stepped chute, c) Labyrinth (Picture acknowledgements: Fig.1a: Stuart Longley; Fig.1b and Fig.1c: Engevix Company).

The spillway profiles used in this chapter are based on the WES profile (Waterways Experiment Station). The WES standard spillway profile is shown in Fig. 2. It has a basic slope of 0.78H: 1V, and the curved shape upstream from the crest is a composition of two circumferences. For the sizes considered in this study, Fig. 2 shows that the tangency point between the two circumferences occurs at (x= 0.61m, y=0.48m). Transition steps were proposed by García & Mateos (1995) after the crest. The steps grow continuously from a relatively small height to the constant step height.

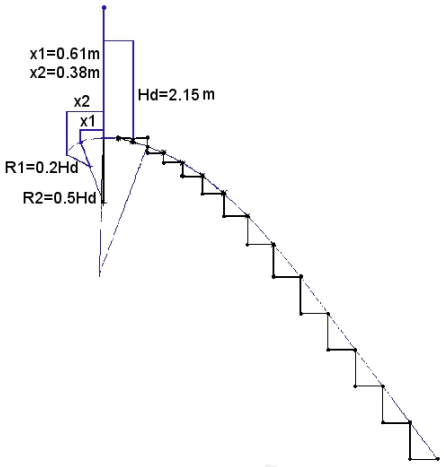

Fig. 2. WES standard spillway profile with the transition steps proposed by García & Mateos (1995).

The crest inlet profile strongly depends on the structure discharge operation capacities. And the flow over the structure is analyzed based in the structure inlet design to achieve a minor impact on the structure, to reduce cavitation risks and to optimize stilling basin. With the pressure diagrams, it is possible to compute an operation curve to optimize the flow over the structure. In this matter, all parameters as inflow conditions, reservoir volume, outflow discharge and the maximum discharge capacity are enrolled in the optimization process.

As already mentioned, basically two distinct flow regimes occur on stepped spillways, as a function of the discharge and the step geometry (Povh, 2000). In the nappe flow, the steps act as a series of falls and the water plunges from one step to the other. Nappe flows are representative of low discharges capacities and large steps. On the other hand, small steps and large discharges are addressed by the skimming flow regime. This flow regime is characterized by a main stream that skims over the steps, which are usually assumed as forming the so called "pseudo-bottom". In the cavities formed by the steps and the pseudo-bottom, recirculation vortices are generated by the movement of the main flow. Perhaps the simplest form to quantify the transition from nappe to skimming flow is to express it through the ratio between the critical flow depth Yc and the step height Sh. Rajaratnam (1990) suggested the occurrence of the skimming flows for $Yc/Sh > 0.8$. This theme was also a matter of study of Stephenson (1991), who introduced a Drop term, $D= q^2/gSh^3$ to distinguish between both regimes: for nappe flow, $D< 0.6$, and for skimming flow, $D > 0.6$. Chanson (2006) proposed limits for both flow regimes. He suggested, as a limit for the nappe flow, the approximated equation $\frac{Y_c}{S_h} = 0.89 - 0.4\frac{S_h}{l_s}$, while the limit for the skimming flow was given by the following approximation: $\frac{Y_c}{S_h} = 1.2 - 0.325\frac{S_h}{l_s}$. This short presentation shows that this transition is still a matter of studies, and that a more general numerical tool is desirable to overcome the difficulties of defining a priori the flow regime along a stepped chute, (Chinnarasri & Wongwises, 2004; Chanson, 2002). Fig. 3 shows the main characteristics of the two flow regimes mentioned here.

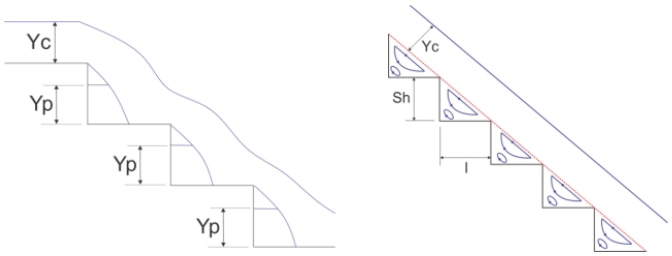

Fig. 3. Flow regimes along stepped chutes: *a*) Nappe flow (low discharges capacities), *b*) Skimming flow (large discharges capacities).

3. Mathematical aspects

3.1 Free surface flow

The most difficult part of the interface simulation procedures is perhaps to obtain a realistic free surface flow solution. In a free surface flow, special numerical techniques are required to keep the position of the interface between the two phases. There are many free surface techniques available in the literature, which involve different levels of difficulties and several procedures to obtain a solution.

In general, the numerical methods are under constant modifications, in order to improve their results and to avoid, as best as they can, nonphysical representations. Because the computational tool itself is under constant improvement, increasing both, the storage and the calculation speed capacities, this situation of constant improvement of the numerical methods is understood as a "characteristic" of this methodology of study. In this sense, the prediction of the behavior of interfaces is one of the problems that is being "constantly improved", so that different "solutions" can be found in the literature.

Some of the procedures devoted "to the capture of the interface" introduce an extra term that accounts for the "interface compression", which acts just in the thin interface region between the phases. Some improvements related to the stability and efficiency calculations are described, for example, in Rusche (2002). In the present study a time step was adjusted to impose a maximum Courant number, and the prediction of the movement of the interface was viewed as a consequence of drag forces and mass forces acting between the phases. More details of the numerical procedures followed in this chapter are presented in the Section 4.

3.2 Self-aerated flow

The phenomenon of air entrainment and bubble formation is initiated by the entrapment of air volumes at the water surface, which are then "closed into bubbles", or really entrained into the flow. At the upstream end of usual spillways, the flow is smooth and no air entrainment occurs, so that it is called briefly as "black water". The flow turns into the so called "white water", or two-phase flow, only after a distance has been traversed, which may involve several steps, (see Fig. 4). The inception point of aeration is generally defined as the position where the boundary layer formed at the bed of the chute attains the water surface, (Carvalho, 1997; Boes & Hager, 2003b).

The distance travelled by the water until attaining the inception point is commonly named as "black water length". Downstream, after a distance in which the air is transported from

the surface of the flow to the bottom of the chute (named "transition length" by Schulz & Simões, 2011, and Simões et al., 2011), the flow attains a "uniform regime". Fig. 1b illustrates this uniform flow far from the inception point (in this example, it is impossible to attest for the uniformity of the velocity profiles, but it is possible to verify that the white-water global characteristics are maintained). The air uptake is generally described as a consequence of the turbulent movement at the water surface.

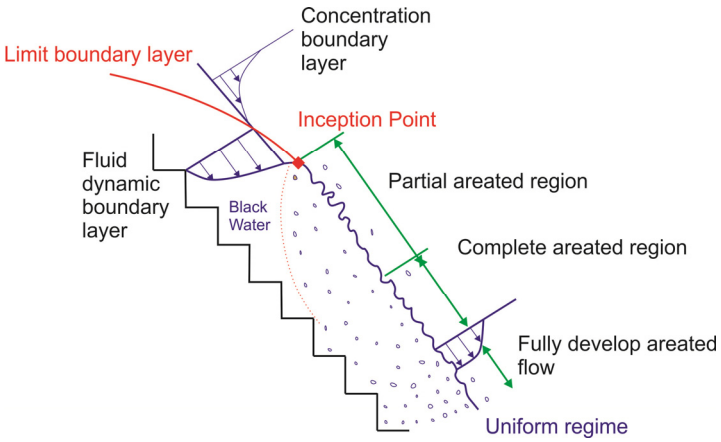

Fig. 4. Self-aeration: inception point and the distinct boundary layers.

Fig. 5 shows two sketches of the position of the inception point, for the two geometries considered here (only large steps in figure 5a, and transition steps in figure 5b). As can be seen, air is captured by the water only after the boundary layer has attained the surface.

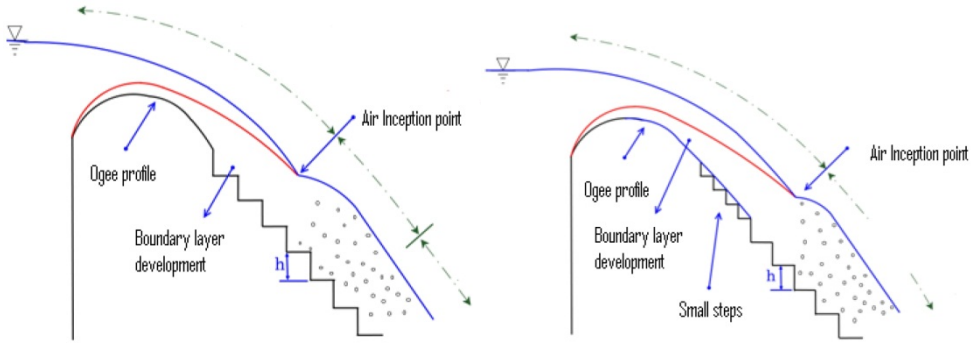

Fig. 5. Boundary layer growth and the differences of the inlet profiles used in this study. *a*) With same size for all steps, *b*) Initial steps with smaller size.

The black water length (position of the aeration inception point) is a matter of continuing studies. Tombes & Chanson (2005), for example, furnished the predictive Eq. 1.

$$\frac{L_I}{K_s} = 9.719(sin\theta)^{0.0796}(F_*)^{0.713} \quad (1)$$

$$\frac{Y_I}{K_s} = \frac{0.4034}{(sin\theta)^{0.04}}(F_*)^{0.592} \quad (2)$$

$$F_* = \frac{q_w}{\sqrt{g\ sin\theta(K_s)^3}} \quad (3)$$

It is based on the distance L_i with origin at the crest of the spillway, the flow depth Y_i, $K_s = S_h cos\theta$ (which represents the step depth per unit width), where q_w is the discharge per unit width, g is the gravity acceleration, θ is the angle between the bed of the chute and the horizontal, S_h is the step height and F_* is the dimensionless discharge. Other expressions for the location of the inception point have been proposed by several authors. See, for example, Chanson (1994).

The air concentration distribution, downstream of the inception point, may be obtained, for example, using a diffusion model (Arantes et al., 2010), as proposed by Chanson (2000), which leads to Eq. 4.

$$C = 1 - tanh^2\left(k' \frac{y}{2D' Y_{90}}\right) \quad (4)$$

C is the void fraction, tanh is the notation for hyperbolic tangent, y it is a transverse coordinate with origin at the pseudo bottom, D´ is a dimensionless turbulent diffusivity, K´ is an integration constant, Y_{90} is the normal distance to the pseudo-bottom where C is equal to 90%. D´ e K´ are functions of the depth-averaged air concentration, C. As can be seen, such equations involve constants which must be obtained from measurements.

In this study, the transition between the black water and the white water is of the major interest. That is, the simulation of the transition of the smooth surface to the turbulent multiphase surface flow, and the calculation of the void fraction distribution along the flow are important for the present purposes. A sketch of the mentioned region is seen in Fig. 6.

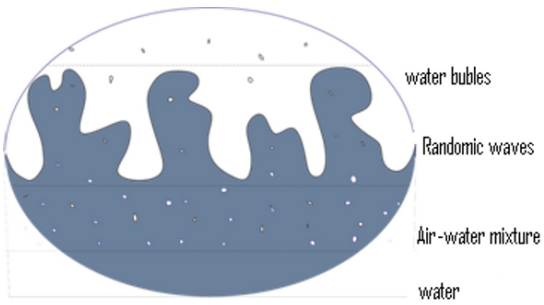

Fig. 6. Sketch of superficial disturbances and formation of drops and bubbles around the interface.

3.3 Two phase flow

A two phase flow is essentially composed by two continuing fluids at different phases, which form a dispersed phase in some "superposition region". According to the volume fraction of the dispersed phase, the prediction of multi-phase physical processes may differ substantially. According to Rusche (2002), the CFD methodologies for dispersed flows have been focused on low volume fraction so far. Processes which operate with large volumes of the dispersed fraction present additional complexities to predict momentum transfer between the phases and turbulence.

In the self-aerated flow along a stepped spillway, the flow behaves like an air-water jet that becomes highly turbulent after the air entrainment took place, where the flow can be topologically classified as dispersed. To computationally represent the localization of the interface with the dispersed phase (composed by drops and bubbles) is an extremely difficult task. Considering the traditional procedures, the optimization of the design of stepped structures crucially depends on the measurement of the inception point and the void fraction distribution (Tozzi, 1992). Both are mean values (mean position and mean distribution), obtained from long term observations. Energy aspects are obtained from mean depths and mean velocities (Christodoulou, 1999; Peterka, 1984). But, as such measurements are generally made in reduced models, the scaling to prototype dimensions may introduce deviations. When considering the cavitation risks, the scaling up questions may be more critical (Olinger & Brighetti, 2004). The main numerical simulation advantages rely, in principle, on the lower time consumption and lower costs, in comparison to those of the experimental measurements (Chatila & Tabbara, 2004). However, when simulating the flow, it is necessary to generate first a stable surface, continuous and unbroken, and then allow its disruption, generating drops, bubbles, and a highly distorting interface. Further, this disruption must happen in a "mean position" that coincides with the observation, and it must be possible to obtain void fraction profiles that allow concluding about cavitation risks. As can be seen, many numerical problems are involved in this objective.

4. Numerical aspects

4.1 Equation for the movement of fluids

The two phase flow along a stepped spillway is modeled by the averaged Navier Stokes equations and the averaged mass conservation equation, complemented by an equation to address fluid deformations and stresses. In this chapter the heat and mass transfers, as well as the phase changes, were not considered.

The flows are inherently turbulent and their characteristics were investigated here using the k-ε turbulence model and adequate wall functions for the wall boundaries.

The averaged Navier Stokes equations neglect small scale fluctuations from the two phase model. However, if the two phase flow has small particles in the dispersed phase, it has to be taken into account in the analysis, in order to achieve an accurate prediction of the void fraction.

Eq. 5 represents the Navier-Stokes equations for incompressible, viscous fluids (it is represented here in vectorial form, thus for the usual three components). It is not discretized in this chapter, because the rules for discretization may be found in many basic texts. But it is understood that it is important to show that the analysis considers the classic concepts in fluid motion.

$$\frac{\partial \rho}{\partial t}\rho\vec{v} + \nabla(\rho\vec{v}\vec{v}) = -\Delta P + \nabla\tau + \rho\vec{f} \quad (5)$$

v is the velocity, ρ is the density, P is pressure, t is time, τ represent the shear forces and f represent the body forces. An outline of the boundary conditions applied to solve the equations is presented in Section 3.4.

4.2 Closure problem

As known, the averaging procedures applied to the Navier Stokes equations introduce additional terms in the transport equations, that involve correlations of the fluctuating components. These terms require new equations, which is known as the problem of "turbulence closure". Based on the Boussinesq hypothesis, it is possible to express the turbulent stresses and the turbulent fluxes as proportional to the gradient of the mean velocities and mean concentrations or temperatures, respectively. For the two phase flow it is still required to examine the effects of the dispersed phase on the turbulent quantities. There is a very wide spectrum of important length and time scales in such situations. These scales are associated with the microscopic physics of the dispersed phase in addition to the large structures of turbulence. The complexity of such flows may still be hardly increased if considering high compressibility and the simultaneous resolution of the large scale motion and the flow around all the individual dispersed particles.

4.3 Two phase methods

The physical representation of the air inception point is an application which considers the primary complex phenomena of the breakup of a liquid jet. When considering the simulation of the jet surface, it is necessary to track it. In general, the tracking methodologies are classified into different categories. We have, for example the Volume Tracking Methodology where the method maintains the interface position, the fluids are marked by the volume fraction and conserves the volume. The volume is also conserved in the moving mesh method, but the mesh is fitted to follow the fluid interface (Rusche, 2002).

In this study an Euler-Euler methodology is applied, in which each phase is addressed as a continuum and both phases are represented by the introduction of the phase fractions in the conservation equations. An "interface probability" is considered, and closure methods are adopted to account for the terms that involve transfer of momentum between the continuous and the dispersed phases.

In general, the numerical models are able to predict the mean movement of the free surface, but they fail to predict the details of the interface (which are important, for example, to incorporate air). In this study the disruption of the interface was imposed, in order to verify if it is possible to generate realistic interface behaviors and to obtain mean values of the relevant parameters. To attain these objectives, the conservation equations were discretized using the finite volume method, and the PISO (Pressure-Implicit with Splitting of Operators) algorithm was adopted as the pressure-velocity coupling scheme.

Considering the Volume of Fluid Method, VOF, the fluids are marked by the volume fraction to represent the interface and it is based on convective schemes. The volume fraction are bounded between the values 0 and 1 (values that correspond to the two limiting phases).

As mentioned, in this study the VOF method was used. The volume of the fluid 1 in each element is denoted by V_1, while the volume of fluid 2 in the same element is denoted by V_2. Defining $\alpha = V_1/V$, where V is the volume of the cell or element, it implies that V_2=1-α. In this chapter, if the cell is completely filled with water, α =1, and if the cell is completely filled with the void phase, α =0. As usual, mass conservation equation (relevant for the mentioned volume considerations) is given by:

$$\frac{D\rho}{Dt} + \rho\nabla\vec{v} = 0 \tag{6}$$

Where, ρ is the density, t is time, v is velocity.
A sharp interface can be achieved in the solver activating the term to interface compression. Eq. 7 illustrates the mass conservation equation with the additional compression term.

$$\frac{\partial\rho}{\partial t} + \nabla(\rho\vec{v}) + \nabla(\rho(1-\rho)\overrightarrow{v_r}) = 0 \tag{7}$$

Where v_r is a velocity field suitable to compress the interface.
Literature examples show that the mathematical model for two phase flows used by interFoam (OpenFoam® two phase flow solver), allowed to obtain appropriated solutions when using the mentioned interface capturing methodology. For example, when simulating the movement of bubbles in bubble columns, two types of bubble trajectories were obtained: a helical trajectory, for bubbles larger than 2mm, and a zigzag trajectory, for smaller bubbles. Rusche (2002) mentions the agreement of the terminal velocity of the air bubbles with literature empirical correlations, which are also based on the bubbles diameters, with diameters between 1 and 5 mm. Although in the present analysis the problem of isolated bubbles is not considered, the mentioned agreement is a positive conclusion that points to the use of this method.

4.4 Boundary conditions

In the traditional CFD methodologies, the wall boundary condition is highly depending on the mesh size. The no-slip condition can be applied when the size near the wall is very fine. On the other hand the slip condition is used when the near wall mesh is very coarse. Most of the times, the use of wall functions are appropriate and it imposes a source term at the boundary faces (Versteeg & Malalasekera, 1995).
For the inlet boundary, two conditions were adopted here. 1) An initial condition similar to a dambreak problem, with a column of water having a predefined finite height above the weir crest. 2) A constant water discharge having a uniform velocity profile. The water surface elevation upstream of the spillway crest was not specified as a boundary condition because this height is part of the numerical solution. The constant discharge (or constant flow rate) was imposed by a "down entrance" of water into the domain.
The dam break problem has been studied by theoretical, experimental, and numerical analysis in hydraulic engineering due to flow propagation along rivers and channels (Chanson & Aoki, 2001). However, in this study we were interested in the shape of the flow generated by an abrupt break of a dam gate, which then flows over the stepped spillway. Note that, if a constant water height would be defined upstream and far from the weir crest, only the transient related to the growing of the depth would be observed. So, a "water column" was imposed, and the growing and decreasing of the water depth

along the spillway was observed. The initial boundary conditions and a subsequent moment of the flow can be visualized in Fig.7a and Fig 7b. The second moment was taken close to the end of the flow of the phenomenon. (Physically, it corresponds to the time of 16s).

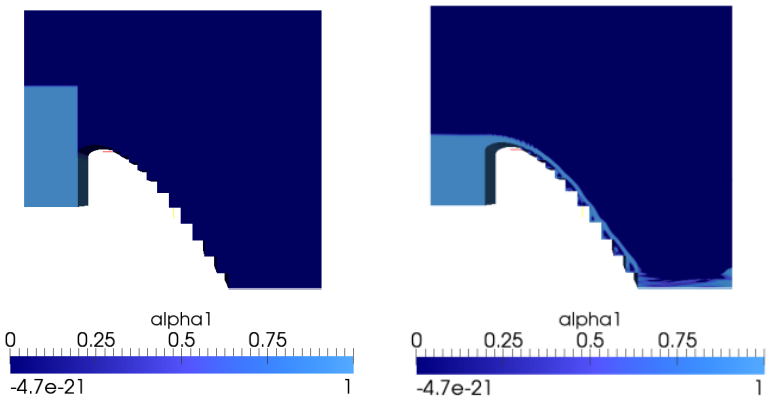

Fig. 7. Phase fraction diagram. *a*) Initial water column (As an initial condition for phase fraction, InterFoam solver requires that both phases exist into the domain, at least into some volume cells), *b*) Water discharge following the structure slope.

At the outlet boundary, an extrapolation of the velocities was applied. It was applied locating the outlet of the flow far from the flow region of main interest. The local phase fraction varies accordingly to the diagram of Fig. 7, and it was observed that it tends to reach a more uniform characteristic at the structure toe (this was better observed for the constant inflow condition).

When using the k- ε model, the turbulent kinetic energy and the energy dissipation rate must be imposed at the inlet boundaries. The actual value of these two variables is not easy to estimate. A too high turbulence level is not desirable since it would take too much time to dissipate. In this study, as the flow has a "visual laminar" behavior at the inlet, this condition allowed some simplifications. The closing equations originated from k-ε model are described by Eqs. 8,9,10,11 and 12.

$$\frac{\partial u}{\partial t}+\nabla\cdot(uu)=-\nabla p_e+\frac{1}{\mathrm{Re}}\nabla^2 u+\frac{1}{Fr^2}g+\frac{1}{\mathrm{Re}}\nabla\cdot(\upsilon_t D) \tag{8}$$

$$\frac{\partial \kappa}{\partial t}+\nabla\cdot(ku)=\frac{1}{\mathrm{Re}}\nabla\cdot\left(\left(1+\frac{\upsilon_t}{\sigma_\kappa}\right)\nabla\kappa\right)+P-\varepsilon \tag{9}$$

$$\frac{\partial \varepsilon}{\partial t}+\nabla\cdot(\varepsilon u)=\frac{1}{\mathrm{Re}}\nabla\cdot\left(\left(1+\frac{\upsilon_t}{\sigma_\varepsilon}\right)\nabla\varepsilon\right)+\frac{(C_{1\varepsilon}P-C_{2\varepsilon}\varepsilon)}{T_t} \tag{10}$$

$$T_t = \frac{\kappa}{\varepsilon} \tag{11}$$

$$\upsilon_t = C_\mu \kappa T_t \tag{12}$$

Although known, the above equations are presented here to stress that the present chapter considers the classical *ad hoc* approximations for turbulent flows. The k- ε constant models are described at Table 1 in Section 6.1.2.

5. Simulation tools

As mentioned the open softwares Salome and OpenFoam® were used here for mesh generation and CFD, respectively. A Table with the software versions applied for simulations in this study is described at the Appendix II, as well as those respective websites for download.

5.1 Mesh generation

To simulate the flow over the domain, a structured mesh was generated at Salome software that is produced by OpenCascade. Some difficulties arise for the mesh generation in classical spillways, which are associated with the shape of the crest of the inlet structure (used to provide a sub-critical inflow condition). The structured mesh generation was a choice to have a mesh with hexahedral elements, which are highly recommended in the literature for treatment of free surface problems.

There are many free softwares for mesh generation available for download, therefore many of them don´t have the ability to generate a hexahedral mesh. In this way, it must also be mentioned that some of the aroused difficulties may be related to the limitations of the specific software. In this case, a structured mesh was generated, based on the software characteristics for hexahedral algorithms.

Limiting the y+ value (One of the parameters that indicate mesh refinement), it is possible to reach more accurate results. However, the computational costs may significantly increase.

Some general characteristics are mentioned here, as the case of adopting a too coarse grid, which leads to the situation that the results obtained are rather independent of the turbulence model, because the numerical diffusion dominates over the turbulent diffusion.

As an auxiliary tool to the mesh algorithm the domain were partitioned with many horizontals and vertical plans to direct the algorithm in the specific regions as small steps and crest. In this way the mesh is extremely refined in these regions, as shown in Fig. 8.

The mesh used to represent the domain in this study has approximately 3,5 million of hexahedral elements. It is a tri-dimension mesh. However the domain in the z-direction is simulated for 1m of length and the mesh for this direction has a reduced number of eight columns.

After generating the mesh, and creating the faces to apply the boundary conditions at Salome software, it can be easily exported to OpenFoam® through the ".*UNV" file format. At OpenFoam® all mesh properties can be checked and at the boundary file at the "\case\constant\polymesh\" path the boundary condition properties for any face can be visualized and edited.

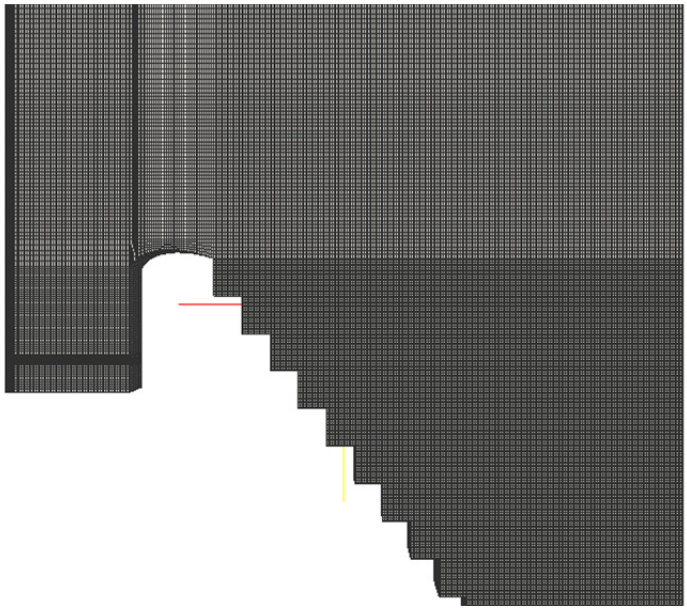

Fig. 8. Ilustration of structured hexahedral mesh.

6. Simulation and flow details

6.1 Setup

In this study, OpenFoam-1.7.1 were used to conduct the numerical results (as described in Appendix II). All the numerical analyses were processed considering that the chute is composed by a prismatic channel with rectangular cross section and having a stepped bed.

The flow calculations involved discharges varying from $0.5m^3/s$ to $20m^3/s$. The discharge condition directly influences the flow regime over the structure. This range was used to test the performance of the program and the adopted procedures.

The inlet conditions for the gas phase fraction and the liquid velocity were taken directly from inlet water discharge measurements found in the literature. By The maximum specific discharge applied for a good hydraulic performance is 25-30 m^3/s m (Boes & Minor, 2000). The interface momentum transfer (Rusche, 2002) is used to account for the lift force and predict the phase fraction.

The surface tension coefficient between the two phases is set with the value of 0.07N/m. The gravitational acceleration had the value of 9.81 m/s^2. The outlet velocity was fixed with a zero gradient far from the interesting flow region and all walls were treated with wall boundaries lawyers. The water properties were considered at the temperature of 298K.

The time precision was automatically adjusted by the solver. Initially it was set to have the value of 0.0001s. Therefore with the solver feature to automatically adjust the time step, it suffered changes trough the time to attempt the maximum Courant Number specified as a precision acceptable to the numerical simulation.

In the phase fraction field the solver allow to set a number of sub-cycles in which the phase fraction equation is solved without doing an extremely reduction in the time step and hardly increasing the cost with time precision.

In the PISO algorithm, the number of correction for the pressure was set to three. To the initial conditions group of sets, all patches defined as faces in the process of mess generation to represent the described domain in the Salome software had a value assigned for volume fraction, pressure and velocity respecting the interaction between them to represent the initial physical properties of the domain described in the Section 4.4.
The divergence terms in the velocity equations and in phase fraction equations were discretized using a central difference scheme. While for the Laplacian terms a Gauss upwind scheme was defined. For temporal discretization a Crank-Nicolson method was used.

6.1.1 Discretization schemes

An accurate numerical scheme is very important to obtain a solution. In order to check the influence of the numerical scheme on the solution, two different configurations for the numerical discretization have been used. With the present model, the two phase flows are better predicted with a higher order scheme. The first order scheme is not able to correctly predict the flow around the spillway crest without producing very large oscillations, as shown in Fig. 9. On the other hand, the second order schemes produce a large and stable recirculation bubble zone between the steps (while the first order did not generate such recirculation zone). Both schemes were used, because the main characteristics of the flow were still being adjusted, but it is necessary to use a more adequate scheme to reproduce the interfaces between air and water (free flow and between the steps). Due to the large size of the domain, and the related computational costs, only some more critical regions were refined. The numerical mesh was refined, for example, around the ogee profile, where the oscillations were observed. The different discretization schemes and mesh refinements were also used to check the sensibility of the model. It was observed, as expected, that not refined discretization lead to unreal interface waves, which increase significantly. As pressure condition in the flow, the hydrostatic pressure gradient was used. Further, most of the tests in this study were run using an upwind scheme.
Depending on the boundary conditions applied, the flow can be always supercritical, or it can achieve a supercritical condition inside the domain. In this case, the relevant boundary condition is the discharge applied at the inlet, which directly influences the flow regime.

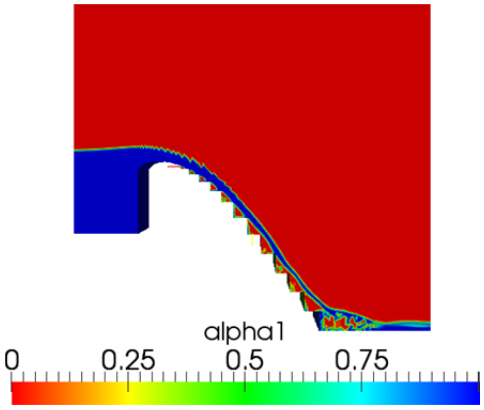

Fig. 9. The influence of the first order discretization scheme along the first part of the surface for the flow over the spillway with varying step sizes.

The distance covered by the subcritical flow, for the adopted inlet conditions, allowed investigating the surface characteristics of the flow along the hydraulic structures for both the proposed inlet profiles, as shown in Fig. 5a and Fig. 5b, and Fig. 10a and Fig. 10b, respectively. Although in all situations a region with "unbroken liquid" is observed, followed by the broken liquid, the calculated surface did not maintain a smooth characteristic, although with smaller instabilities in relation to Fig. 9. As the breaking of the interface was an objective of this study, the numerical schemes were not chosen to guarantee the unconditional stability of the surface. However, as mentioned, they produced instabilities from the very beginning of the accelerated region (spillway entrance), and not only after attaining the position where the boundary layer coincides with the surface of the liquid.

The algorithm PISO used in this study is based on the assumption that the momentum discretization may be safely kept through a series of pressure correctors. It needs small time-steps. As a consequence, the PISO algorithm is also sensitive to the mesh quality. Aiming to guarantee the convergence, the Courant number, Co, must keep a low value (it is function of the time step, the magnitude of the velocity through the element, and the element size) (Versteeg & Malalasekera, 1995). In order to check the influence of the mesh size in the solution, a more refined mesh can be tested.

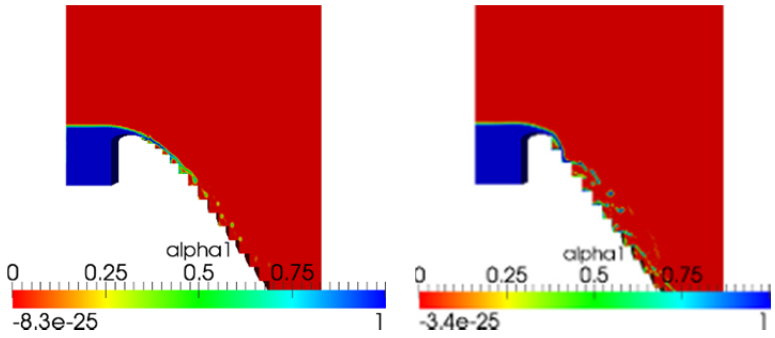

Fig. 10. Inlet profile: *a*) Initial structure steps with smaller size. *b*) With same size for all structure steps.

6.1.2 Turbulence properties

As mentioned, the k-ε averaged turbulence model was used. As expected in the RANS computations, the simulations converged to steady solutions. Table 1 shows the values of the constants usually adopted for the k-ε model (see Eq. 7 through 11).

C_μ	$C_{\varepsilon 1}$	$C_{\varepsilon 2}$	σ_k	σ_ϵ
0.09	1.44	1.92	1.0	1.3

Table 1. Empirical constants of k-ε model.

7. Preliminary Results

7.1 Pressure diagram distribution

The pressure distributions along the steps are important to study the risk of cavitation in stepped chutes (Franc & Michel, 2004). It is not only the position of the lower pressure that is important, but also its value and frequency. In particular, the results calculated in the present study show no qualitative differences between the measured literature data, when considering the position and the mean pressure distribution analysis (Amador, 2005). As mentioned, the frequency of the low values is important, which points to the need of instantaneous values, and not only the mean profiles.

The negative pressure plotted in Fig. 11 were also predicted by Chen et al. (2002) for a WES structure with the transition steps.

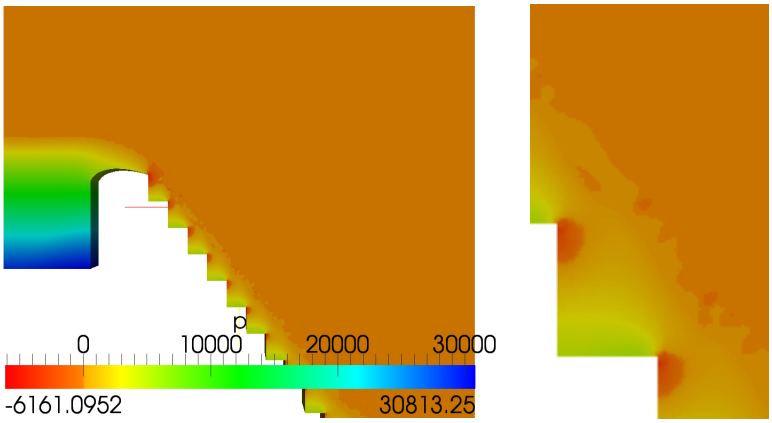

Fig. 11. Negative Pressure. *a*) Along stepped chute, *b*) In a step along the structure.

The pressure distributions over the steps in a stepped chute depend on the position of the faces of the steps. In the vertical face a separation flow region occurs and the pressure achieve negative values. Over the horizontal face the pressure distribution is influenced by the recirculation in the cavity, which results in a positive value for the mean pressure. The last step of Fig. 11a, amplified in Fig. 11b, shows this difference between the behavior of the pressure along the horizontal and vertical surfaces.

7.2 Velocity distribution

The velocity of an aerated flow is expected to be higher than the velocity of an unaerated flow, because the entrained air reduces the wall friction (Steven & Gulliver, 2007). Fig. 12 shows a velocity diagram obtained in the present simulations. The values obtained, though not directly compared to the results of other sources Cain & Wood (1981), are of the same order.

Amador (2005) described results of experiments of velocity fields over steps located in the developing flow region, were the growth of the boundary layer was analyzed (upstream of the inception point). The study shows the presence of large size eddies at the corner of the step faces, and recirculation areas. Recirculation and air concentration distributions were also investigated by Matos et al. (2001). The authors mentioned differences for the flows between the step edges and in the steps cavities, describing it and mentioning the effects of turbulence intensity.

In this study, a calculated velocity field is shown in Fig. 12, where the region of maximum velocity, for example, is easy to be observed. As can be seen, the mentioned recirculation is adequately reproduced, which corresponds to the negative horizontal velocity that can happen between the steps.

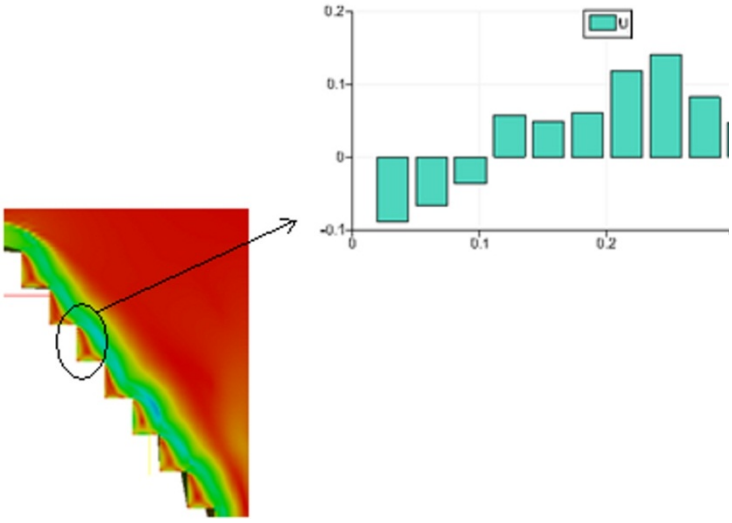

Fig. 12. Velocity distribution along the structure.

7.3 Void fraction distribution

As described before, the attention of this chapter is more concentrated in the phenomena related with the air transfer between the two phases interface. Fig. 13 shows an instantaneous of the position of the interface and of the void distribution, obtained following the present procedures. In this case, the example is for constant steps. The imposed flow rate was 15 m^3/s m.

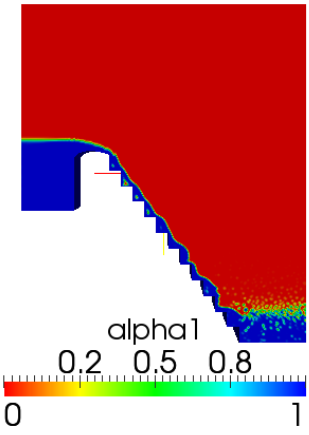

Fig. 13. Skimming flow regime. Result for constant steps at the entrance.

As can be seen, the surface is highly distorted, reproducing the conditions found in real flows. The deformations characterize entrapped air, as defined by Wilhelm & Gulliver (2005), and not entrained air, but they also allow to calculate a mean "void concentration", a procedure followed to check the methodology which is being tested here. As showed by Lima et al. (2008), measured concentration profiles may involve a relative high percentage of entrapped air, which may induce to mistakes in the calculations of the air flow rate introduced by the water flow. In this sense, the present methodology shows that this "entrapped air concentration profile" may be calculated to correct the evaluation of the entrained air. In Fig. 14 the results of the present calculation of the void fraction obtained for different depths is shown. The flow conditions are those imposed to obtain Fig. 13. As mentioned, these simulation results show that the method allows to obtain void fraction profiles.

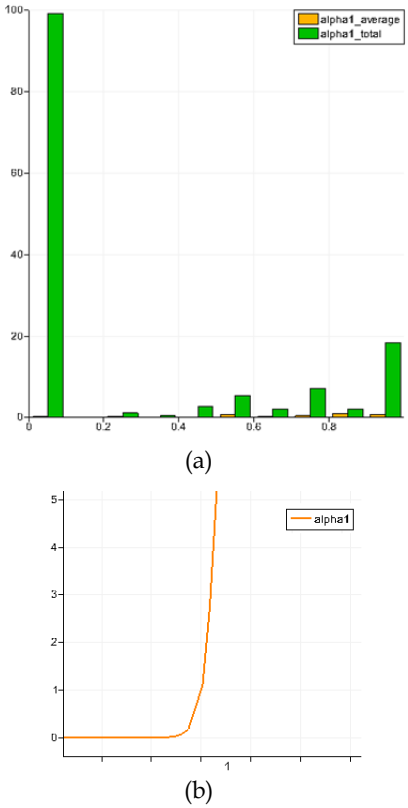

Fig. 14. Volumetric fraction along the flow. The position 0.0 corresponds to the bottom, and the position 1.0 corresponds to the surface. a) Histogram of void fraction where alpha1_average represents a statistic temporal alpha average, b) presents first results of air entrainment at any location of the spillway, allowing the prediction of the air concentration profiles (void fraction profiles) for all calculation domains.

Fig. 15 is an example of shown in Fig. 14b, obtained for the position indicated in Fig. 15b. With the distribution of entrained air, the gas transfer along the flow can be estimated, or, in

other words, the air flow discharge is obtained. This quantification is relevant, allowing to check experimental results and predictive equations obtained from simplified models, conducting (in a more complete stage of these studies) to a better understanding of the air entrainment phenomena on stepped chutes. In addition, concentration fields like that shown in Fig. 15a will allow to correlate pressure and void fraction distributions, and to recognize regions where the air content is not enough to reduce cavitation damage (that is, the the regions under risk of cavitation). From Peterka (1953), the air concentration that is sufficient to avoid cavitation damage is about 5 to 8%. The inlet of air increases the mixture compressibility and the flow becomes able to absorb the impact of collapsing vaporized bubbles.
Fig. 15a also shows the concentration regions defined by Chanson (1997), considered here to verify the possibility of obtaining practical information of such simulations. Accordingly to Chanson (1997), three concentration ranges can be considered in the concentration analyses, as shown in Table 2.

Rate Classification	
C < 0.3 to 0.4	Clear water comprising air bubbles
C > 0.6 to 0.7	Air flow comprising water droplets
C > 0.7	Two-phase flow with equal air and water contents

Table 2. Main regions of concentration profiles. (Chanson, 1997)

As already mentioned, two examples are considered: The opening of a dam gate, a transient situation, and a steady-state simulation that allows evaluating changes of the void ratio along the self-aerated spillway flow. Air concentration profiles C(y) are taken in several cross sections at steps downstream from the inception point.

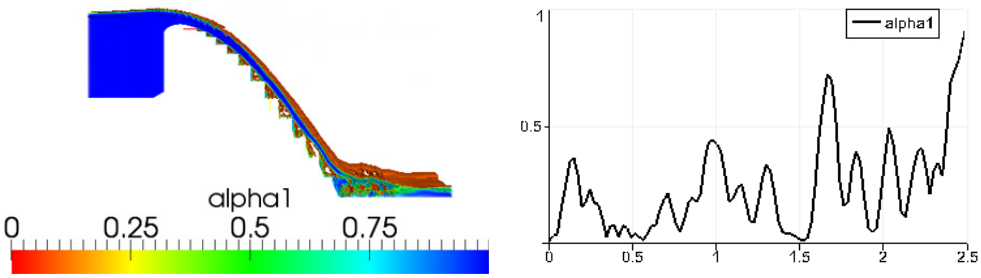

Fig. 15. Phase fraction *a*) Contours of isosurfaces, *b*) Distribution of void fraction for the 4th step.

8. Continuing studies

The results presented in this chapter show that the proposal of studying the breaking of the air-water interface and the formation of a dispersed phase is a challenging issue, and is still not definitively quantified. It was possible to show that instabilities can be produced at the interface in a way to maintain the main flow stable, but these instabilities did not follow a realistic behavior. The aim is to break the surface in the position of the inception point of aeration, but the instabilities were formed in the very beginning of the accelerated region of the flow, at the spillway entrance.

Bubbles and drops were "formed" in the numerical simulations, as shown in Fig. 16. However, the sizes of both depend of the numerical mesh used, and, in this sense, the reproduction of these geometrical characteristics is still limited by the mesh. In practice, smaller drops and bubbles are formed. The numerical solution were processed with the discharge of 20 m^3/s m.

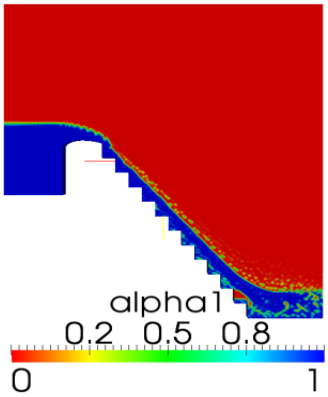

Fig. 16. General characteristics observed in a simulated flow: 1) Unrealistic superficial instabilities in the accelerated region of the flow; 2) Formation of drops and bubbles, as expected; 3) Cavities between the steps.

Depending on the conditions of the flow, the abovementioned characteristics are damped, or not observed. This is the case shown in Fig. 17, where the instabilities were minimized and no drops or bubbles were formed along the spillway. As a conclusion, the hydrodynamic characteristics still need to be better reproduced in the simulations, in order to guarantee the formation of the dispersed phase. The numerical solution were processed with the discharge of 15 m^3/s m.

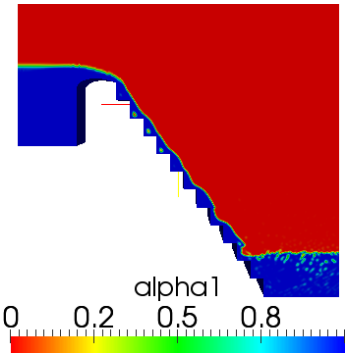

Fig. 17. Velocity distribution along the structure. In this case, no drops and bubbles are formed.

Numerical simulations over stepped spillways which take into account the stable and unstable regions of the interface, disrupting it and forming the dispersed phase, have not been yet presented in the literature. However high quality measurements of different

characteristics of such flows, including cavitation predictions, are found in the literature, and can serve as guide for the mentioned simulations.

9. Conclusions

Skimming flow over stepped chutes were simulated to verify the possibility of obtaining results of air entrainment in stepped spillways. The stable/unstable behavior of the air-water interface was discussed, and the difficulties to obtain a realistic breaking of the interface and the formation of the dispersed phase were exposed.

Two situations related to the geometry of the spillways were considered: constant step sizes and varying step sizes. Also two situations related to the flow conditions were considered: constant inlet water discharge, and a "sluice-gate-brake", that is, a kind of "dam-break" situation flowing over the stepped spillway.

Results of pressure fields, velocity fields, void fraction profiles, along the simulated spillways were furnished, showing behaviors similar to those observed and simulated in the literature. For the void fraction profiles, also a "entrapped air" profile was furnished, showing that the methodology allows to confirm experimental studies about entrapped air found in the literature.

Unrealistic behavior of the surface instabilities were observed. They were formed in the accelerated region of the flow over the spillway, and for some flow conditions they produced large disturbances, a negative characteristic that still need to be solved.

Drops and bubbles could be formed in the flow over the spillway, but their size was shown to be limited by the mesh characteristics. The two fluid model adopted neglects the effects of large scales and uses an average momentum transfer between the phases. Although the surface deformation could be reproduced, the interface tracking calculation showed to be difficult to apply when considering the formation of a dispersed phase.

The open codes "OpenFoam®" and "Salome" were used, showing that such codes are capable to furnish useful results for engineers and researchers in hydraulics and fluid mechanics.

10. APPENDIX I: Software information

The OpenFoam® software is a continuum mechanics simulation tool, but it is also an object-oriented numerical code, and a toolkit for programming. It is written in C++ programming language and can be freely download at the website https://www.opencfd.co.uk. The CFD library is extensive and incorporates several types of solvers. The software also contains tools for mesh conversion from many mesh generation softwares, including commercial and free codes. The open source code has the advantage of the "transparency", that is, it allows following the methodology adopted for the calculus, and the assumptions made to obtain a solution (ever present in any code). The results also can be converted to be visualized and post processed in a number of different softwares. A version of the Paraview software is integrated in OpenFoam® as its standard post processing tool.

11. APPENDIX II: Useful information about the open software

Some useful links with open software information are addressed in Table 3 with the respective version of software applied in this study.

Tools applied for numerical simulations	
OpenSuSe 11.2	http://www.opensuse.org
OpenFoam 1.7.1	http://www.OpenFoam.com
ParaFoam 1.7.1	http://www.OpenFoam.com
Salome 5.4	http://www.salome-platform.org

Table 3. Open software.

12. APPENDIX III: Numerical procedures in CFD software

The numerical simulations using the OpenFoam® software are basically performed by file editing. The software is structured using three basic directories. The constant sub-directory contains all properties folders for the fluids settings and mesh characteristics. Some physical constants.
For InterFoam solver this directory contains three files designed as: transportProperties, enviromentalProperties and dynamicMeshDict and a specific folder for mesh properties named as polyMesh. Into the transportProperties all information about the properties of the two phases can be edited. The dynamicMeshDict file allows to enable the mesh movements. The polyMesh constant sub directory keeps all information about the mesh.
In the OpenFoam® the system sub-directory contains exactly five files: ControlDict, DecomposeParDict, fvSchemes and setFieldsDict. The contolDict file allows users set the simulation process information like starting, end and time step. User also can choose the methods to save the simulation data.
In the fvSchemes system file, the descritization schemes can be setted. The fvSolution file is responsible for all solver settings like the number of iterations.
In the free surface problems, the initial condition for the volume fraction of the two fluids also needs to be defined. The setFieldsDict allows setting different density values for each part of the domain. The decomposeParDict file describes the decomposition for multiprocessing simulation.

13. Acknowledgements

The authors are indebted to the Conselho Nacional de Desenvolvimento Científico (CNPq) and FAPESP-Fundacão de Amparo Pesquisa do Estado de São Paulo (proc. 2010/52071-0*) for the financial support to this study.

14. References

Amador, A. (2005). Comportamiento hidráulico de los aliaderos escalonados em presas de hormigòn compactado. Master's thesis, Universitat Politécnica de Cataluya, Barcelona.

Arantes, E., Porto, R., Gulliver, J., Lima, A., & Schulz, H. (2010). Lower nappe aeration in smooth channels: experimental data and numerical simulation. Anais da, 82(2):521{537}.

Arantes E.J. (2007). Caracterização do Escoamento sobre Vertedores em Degraus via CFD. Tese de Doutorado, Escola de Engenharia, Universidade de São Paulo, São Carlos, Brasil, 204 p.

Boes, R.M. & Hager, W.H. (2003a). “Hydraulic design of stepped spillways”. ASCE, Journal of Hydraulic Engineering. v.129, n.9, p.671-679, Sep.

Boes, R.M. & Hager, W.H. (2003b). "Two-Phase flow characteristics of stepped spillways. ASCE, Journal of Hydraulic Engineering". v.129, n.9, p.661-670.

Boes, R. M.; Minor, H. E. Guidelines for the hydraulic design of stepped spillways. Proc. Int. Workshop on Hydraulics of Stepped Spillways, VAW, ETH, Zurich. Balkema Rotterdam, 2000. p. 163-170.

Cain P. & I.R. Wood (1981). Measurements of self-aerated flow on a spillway. Journal of Hydraulic Engineering, ASCE, vol. 107(11), pp. 1425-1444.

Carvalho, P.D. (1997) Aeração de Escoamentos de Alta Velocidade em Canais de Forte Declividade; Tese de doutorado apresentada à Escola de Engenharia de São Carlos da Universidade de São Paulo, São Carlos, S.P, 1997.

Chamani, M. R. (2000). "Air inception in skimming flow regime over stepped spillways". In. H. E. Minor e W. H. Hager (Ed.) International Workshop on Hydraulics of Stepped Spillways, Zürich, Switzerland: 61-67. Balkema.

Chanson, H. (1994). Aeration and de-aeration at bottom aeration devices on spillways. Canadian Journal of Civil Engineering, 21(3):404{409}.

Chanson, H. (1997). Air bubble entrainment in free surface turbulent shear flows. Academic Press, page 401.

Chanson, H. (2000). Discussion of characteristics of skimming flow over stepped spillways. Journal of hydraulic Engineering.

Chanson, H. (2001). "Hydraulic design of stepped spillways and downstream energy dissipation". Dam Engineering, v.11, n.4, p.205-242.

Chanson, H. (2002). The hydraulics of stepped chutes and spillways. The Netherlands: A. A. Balkema Publishers. 384 p.

Chanson, H. (2006). Hydraulics of skimming fows on stepped chutes: The effects of infow conditions? Journal of Hydraulic Research, 44:51{60}.

Chanson, H. & Aoki, S. (2001). "Dam Break Wave with Significant Energy Dissipation : Two Case Studies." Proc. 29th IAHR Congress, Beijing, China, Theme C, Tsinghua University Press, Beijing, G. LI Ed., pp. 311-318.

Chatila, J. & Tabbara, M. (2004). Computational modeling of fow over an ogee spillway. Computers & Structures, 82:1805{1812}.

Chen, X., Dai, G. & Liu, H. (2002). Volume of fuid model for turbulence numerical simulation of stepped flow. Journal of Hydraulic Engineering, 128(7):683{688}.

Chinnarasri, C. & Wongwises, S. (2004). "Flow regime and energy loss on chutes with upward inclined steps". Canadian Journal of Civil Engineering. v.31, p.870-879, Oct..

Christodoulou, G. (1999). "Design of stepped spillways for optimal energy dissipation". Hydropower & Dams. 6(5): 90-93. X Simpósio de Recursos Hídricos do Nordeste 14.

Essery, I. & Horner, M. (1978). The hydraulic design of stepped spillways. Technical report, CIRIA.

Franc, J. & Michel, J. (2004). Fundamentals of Cavitation (Fluid Mechanics and Its Applications). Springer.

Frizell, K. & Melford, B. (1991). Designing spillways to prevent cavitation damage. Concrete International, 13:58{64}.

Hager, W.H. (1991). "Uniform aerated chute flow". Journal of Hydraulic Engineering, v.117, n.4, p.528-533, April.

García, E. & Mateos, I. (1995). Aliviaderos escalonados. diseno de la transicion entre el umbral y la rápida escalonada. Ingenieria Civil, 99:3323 {3341}.

Gomes, J.F. (2006). Campo de pressões: condições de incipiência à cavitação em vertedouros em degraus com declividade 1V:0,75H. 2006. 161 f. Tese (Doutorado) – Instituto de Pesquisas Hidráulicas, Universidade Federal do Rio Grande do Sul, Porto Alegre.

Jacobsen, F. (2009). Application of OpenFoam for designing hydraulic water structures. Open source CFD Iternational conference.

Lima, A.C.M. (2003) Caracterização de Estrutura Turbulenta em Escoamentos Aerados em Canal de Forte Declividade com auxílio de Velocimetria a Laser, 2003. Tese de doutorado apresentada à Escola de Engenharia de São Carlos da Universidade de São Paulo, São Carlos, S.P., Brasil.

Lima, A.C.M.; Schulz, H.E. & Guliver, J.S. (2008) "Air Uptake along the Lower Nappe of a Spillway Aerator", Journal of Hydraulic Research, v. 46, n. 6, p. 839-843.

Matos, J., Pinheiro, A. N., de Carvalho Quintela, A., and Frizell, K. H. (2001). "On the role of stepped overlays to increase spillway capacity of embankment dams." ICOLD European Symposium (NNCOLD), Geiranger, Norway, 473-483.

Ohtsu I., Yasuda Y. & Takahashi, M. (2004). "Flows characteristics of skimming flows in stepped channels". ASCE, Journal of Hydraulic Engineering. v.130, n.9, p.860-869, Sept.

Olinger, J. C. (2001). Contribuição ao estudo da distribuição de pressões nos vertedouros em degraus. 2001. 230 f. Tese (Doutorado) - Escola Politécnica, Universidade de São Paulo.

Olinger, J. C. & Brighetti, G. (2004). "Distribuição de Pressões em Vertedouros em Degraus". RBRH: Revista Brasileira de Recursos Hídricos, v.9, n.1, p.67-83, Jan/Mar..

Peterka, A. J. (1953). "The effect of entrained air on cavitation pitting". Joint Meeting Paper, IAHR/ASCE, Minneapolis, Minnesota, Aug..

Peterka, A. J. (1984). Hydraulic design of spillways and energy dissipators. A Water Resources Technical Publication, Engineering Monograph Nº 25, United States Department of the Interior, Bureau of Reclamation. Denver, Colorado: eight printing, May.

Posvh, P.H. (2000). Avaliação da energia residual a jusante de vertedouros em degraus com fluxos em regime skimming flow. 2000. 142 f. Dissertação (Mestrado em Engenharia Hidráulica) - Departamento de Tecnologia, Universidade Federal do Paraná, Curitiba.

Rajaratnam, N. 1990. Skimming flow in stepped spillways. Journal of Hydraulic Engineering, ASCE, 116 (4): 587-591. Discussion: 118 (1): 111-114.

Rusche, H. (2002). Computational fluid dynamics of dispersed two-phase flows at high phase fractions. PHD Thesis, Imperial College of Science, Technology and Medicine, UK.

Simões, A.L.A.; Schulz, H.E. & Porto, R.M. (2011) Transition length between water and air-water flows on stepped chutes. WIT Transactions on Engineering Sciences (Computational Methods in Multiphase Flow VI, Kos, Greece), Vol 70, pp.95-105.

Schulz, H.E. & Simões, A.L.A (2011). Desenvolvimento da superfície livre em escoamentos aerados: analogia com leis básicas de transferência. Laboratório de Turbulência e Reologia - LTR, Relatório I/II/11.

Stephenson, D. Energy dissipation down stepped spillways. Water Power & Dam Construction, Sutton, v.43, n.9, p.27-30, Sept. 1991.

Tozzi, M.J. (1992). Caracterização/comportamento de escoamentos em vertedouros com paramento em degraus. 1992. Tese (Doutorado) – Universidade de São Paulo 1992.

Toombes, L. & Chanson, H. (2005). Air entrainment and velocity redistribution in a bottom outlet jet flow. XXXI IAHR Congress, pages 2716{ 2726}.54

Versteeg, H.K. & Malalasekera, W. (1995). An introduction to computational fuid dynamics. The finite volume method. Longman Scientific & Technical.

Wilhelms, S.C. & Gulliver, J.S. (2005). Bubbles and Waves Description of Self-aerated Spillway. Journal of Hydraulic Research, 43(5): 522–531.

Part 4

Hydrodynamics and Heat/Mass Transfer

14

The Influence of the Hydrodynamic Conditions on the Performance of Membrane Distillation

Marek Gryta
West Pomeranian University of Technology, Szczecin
Poland

1. Introduction

Membrane distillation (MD) is an evaporation/condensation process of volatile components through a hydrophobic porous membrane. The maintenance of gas phase inside the membrane pores is a fundamental condition required to carry out the MD process. A hydrophobic nature of the membrane prevents liquid penetration into the pores. Membranes having these properties are prepared from polymers with a low value of the surface energy, such as polypropylene (PP), polytetrafluoroethylene (PTFE) or polyvinilidene fluoride (PVDF) (Alklaibi & Lior, 2005; Bonyadi & Chung, 2009, Gryta & Barancewicz, 2010). Similar to other distillation processes also MD requires energy for water evaporation. The hydrodynamic conditions occurring in the membrane modules influence on the heat and mass transfers, and have a significant effect on the MD process efficiency.

The MD separation mechanism is based on vapour/liquid equilibrium of a liquid mixture. For solutions containing non-volatile solutes only the water vapour is transferred through the membrane; hence, the obtained distillate comprises demineralized water (Alklaibi & Lior, 2004; Gryta, 2005a; Schneider et al., 1988). However, when the feed contains various volatile components, they are also transferred through the membranes to the distillate (El-Bourawi et al., 2006; Gryta, 2010a; Gryta et al., 2006a). Based on this separation mechanism, the major application areas of MD include water treatment technology, seawater desalination, production of high purity water and the concentration of aqueous solutions (El-Bourawi et al., 2006; Drioli et al., 2004, Gryta, 2006a, 2010b; Karakulski et al., 2006; Martínez-Díez & Vázquez-González, 1999; Srisurichan et al., 2005; Teoh et al., 2008).

A few modes of MD process are known: direct contact membrane distillation (DCMD), air gap membrane distillation (AGMD), sweeping gas membrane distillation (SGMD), vacuum membrane distillation (VMD) and osmotic membrane distillation (OMD). These variants differ in the manner of permeate collection, the mass transfer mechanism through the membrane, and the reason for driving force formation (Alklaibi & Lior, 2005; Gryta, 2005a).

The most frequently studied and described mode of MD process is a DCMD variant. In this case the surfaces of the membrane are in a direct contact with the two liquid phases, hot feed and cold distillate (Fig. 1). The DCMD process proceeds at atmospheric pressure and at temperatures that are much lower than the normal boiling point of the feed solutions. This allows the utilization of solar heat or so-called waste heat, e.g. the condensate from turbines or heat exchangers (Banat & Jwaied, 2008; Bui et al., 2010; Li & Sirkar, 2004).

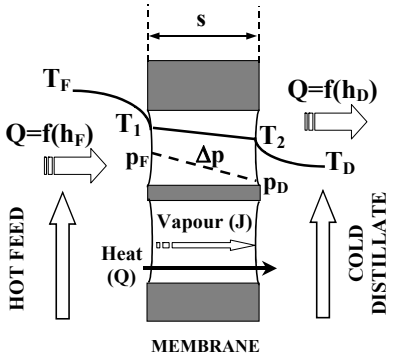

Fig. 1. Principles of DCMD: T_1, T_2, T_F, T_D — temperatures at both sides of the membrane, and temperatures of feed and distillate, respectively; p_F, p_D and h_F, h_D — water vapor partial pressure and heat transfer coefficients at the feed and distillate sides, respectively

The driving force for the mass transport in DCMD is a difference of the vapour pressure (Δp), resulting from different temperatures and compositions of solutions in the layers adjacent to the membrane (Fig. 1). The stream parameters (temperature, concentration) at the solution/membrane interface differ significantly from those in the bulk, as a result of the polarization phenomena associated with both the temperature and concentration. These phenomena cause a decrease in the vapour pressure difference across the membrane which in turn leads to the reduction of the permeate flux in the MD process. Therefore, the hydrodynamic conditions have a pronoun influence on the efficiency of the MD process (Alklaibi & Lior, 2005; Gryta, 2002a, 2005a, 2005b; Gryta et al., 2000; Martínez-Díez & Vázquez-González, 1999; Li & Sirkar, 2004).

The feed temperature in the MD module decreases due to evaporation, which also causes a reduction of MD driving force, in addition to the temperature polarisation. Therefore, the permeate flux can be increased several times when the flow rate and temperature of the feed is enhanced in an appropriate way. Moreover, the shape and dimensions of the channels through which liquid flows in the module has an important effect on the permeate flux (Gryta et al., 2000; Schneider et al., 1988; Teoh et al., 2008).

The efficiency of MD process depends, in a significant degree, on the morphology of used membranes. The permeate flux increases along with an increase in membrane porosity and pore diameter (El-Bourawi et al., 2006). The higher the wall thickness of membrane, the larger the diffusion resistance. Therefore, a larger efficiency can be achieved for thinner membranes. However, the thick membranes undergo mechanical damage more easily, and, the manner of their assembly in the MD module plays an essential role (Gryta et al., 1997).

2. Heat and mass transfer in MD process

In the MD process both heat and mass transfer occur simultaneously, therefore, both temperature and concentration polarization effects should be taken into consideration. A number of theoretical models have been developed for the description of the membrane distillation (Alklaibi & Lior, 2005; El-Bourawi et al., 2006; Gryta, 2002b, 2008; Gryta et al., 1997, 1998; Lawson & Lloyd, 1997; Li & Sirkar, 2004; Martínez-Díez & Vázquez-González, 1999). The models of direct contact MD were based on the assumption that vapour

permeates through the porous membrane, as a result of the molecular diffusion, Knudsen flow and/or the transition between them. The permeate flux can be described by:

$$J = \frac{\varepsilon}{\chi} \frac{M}{s RT_m} D_{WA} P ln \frac{P - p_D}{P - p_F} \tag{1}$$

where p_F and p_D are the partial pressures of saturated water vapour at temperatures T_1 and T_2 (Fig. 1), and ε, χ, s, T_m are the porosity, tortousity, thickness, and mean temperature of the membrane, respectively, and M is the molecular weight of water, R is the gas constant, P is the total pressure, and D_{WA} is the effective diffusion coefficient of water vapour through the membrane pores. The vapour pressure of water for the diluted solutions can be determined e.g. from the Antoine equation (Gryta et al., 1998). However, for concentrated solutions the effect of solute concentration on the partial vapour pressure it should be taken into account. The literature offers a considerable number of equations and the experimental data, which can be used to solve this problem.

The temperatures in the layers adjacent to the membrane (T_1, T_2) are dependent on the values of the heat transfer coefficients in the MD module (Gryta et al., 1997, 1998). The values of these coefficients increase along an increase of the flow rates, thus, the temperature polarization can be considerably reduced by the application of high flow rates. Moreover, a higher flow rate decreases the temperature difference of streams at the inlet and outlet of the module, resulting in the increase of the temperature difference across the membrane.

The temperatures T_1 and T_2 cannot be measured directly. A series of equations for their calculations have been presented in the MD literature (Alklaibi & Lior, 2005; Gryta et al., 1997, 1998; Khayet et al., 2004; Lawson & Lloyd, 1997; Schofield et al., 1990). These equations were derived for the steady state conditions, under which the amount of heat transferred to and from the surfaces adjacent to the membrane is equal to the amount of heat transferred inside the membrane. For the case presented in Fig. 1 we can write:

$$Q = h_F(T_F - T_1) = J\Delta H + \frac{\lambda_m}{s}(T_1 - T_2) = h_D(T_2 - T_D) = H(T_F - T_D) \tag{2}$$

A solution of the above equations allows to determine the temperatures T_1 and T_2 – Eqs. 2 and 3. These equations were derived with the assumption of the linear temperature change in the membrane and isoenthalpic flow of vapour (Gryta et al., 1998).

$$T_1 = \frac{\frac{\lambda_m}{s}\left(T_D + \frac{h_F}{h_D}T_F\right) + h_F T_F - J\Delta H}{\frac{\lambda_m}{s} + h_F\left(1 + \frac{\lambda_m}{h_D s}\right)} \tag{3}$$

$$T_2 = \frac{\frac{\lambda_m}{s}\left(T_F + \frac{h_D}{h_F}T_D\right) + h_D T_D + J\Delta H}{\frac{\lambda_m}{s} + h_D\left(1 + \frac{\lambda_m}{h_F s}\right)} \tag{4}$$

where ΔH is the vapour enthalpy, H and h_i are the overall and convective heat transfer coefficients, and λ_m is the membrane thermal conductivity. The h_i coefficients can be estimated from the Nusselt number: $Nu=h_i d_h/\lambda$, where d_h is the hydraulic diameter and λ is the thermal conductivity of liquid.
The thermal conductivity coefficient for membranes utilized in MD changes in a small range of 0.04–0.06 W/mK, and it can be determined on the basis of the membrane material data (Phattaranawik et al., 2003):

$$\lambda_m = \lambda_g \varepsilon + (1-\varepsilon)\lambda_s \tag{5}$$

The convective heat-transfer coefficient (h_i) can vary in a wide range, depending on the design and working conditions of the MD module. Thus, the accurate determination of its value has an essential meaning. The coefficients h_D and h_F can be calculated from equation:

$$h_i = \frac{\mathrm{Nu}\ \lambda_i}{d_h} \tag{6}$$

The Nusselt number occurring in this equation is most often determined from the following correlation:

$$\mathrm{Nu} = C\,\mathrm{Re}^a\,\mathrm{Pr}^b\left(\frac{d_h}{L}\right)^c \tag{7}$$

where C, a, b, c are the coefficients depending on a channel configuration of the heat exchanger and a flowing character of the streams. Nusselt number correlations developed for the heat exchangers can be used for heat transfer calculations in MD modules. However, care must be taken in the selection of the appropriate correlation. The Nu correlations selected for the tubular exchanger were also applied successfully for the model calculation of MD process in the capillary module. For a MD module with the membranes arranged in a form of braided capillaries the following form of the Nusselt number was successfully used for laminar flow (Gryta et al., 1998):

$$\mathrm{Nu} = 4.36 + \frac{0.036 \times \mathrm{Pe} \times \frac{d_h}{L}}{1 + 0.0011 \times \left(\mathrm{Pe} \times \frac{d_h}{L}\right)^{0.8}} \tag{8}$$

where L is the module length, the Peclet number (Pe) is given by the equation $Pe=PrRe$, the Prandtl number (Pr) is $Pr=c_{PS}\mu/\lambda$, the Reynolds number (Re) is $Re=v\,d_h\rho/\mu$ and μ, ρ, c_{PS}, are the viscosity, density and the specific heat of solution, respectively.

2.1 MD process parameters

The feed stream temperature has a significant effect on the level of permeate flux in the MD process (Fig. 2). At constant distillate temperature (293 K) the elevation of T_F from 333 K to 358 K caused an increase in the permeate flux by about 100-200% (Wang et al, 2008). The presented results confirmed that a high efficiency in the MD process could be achieved when the feed temperature is close to the boiling point. Such a high increase of the flux can

be explained by an exponential dependence of the vapour pressure on temperature (Fig. 2 – broken line). Thus, the driving force for the mass transfer also increases with increasing the feed temperature. Increasing the distillate temperature causes the reverse effect, i.e. declines of permeate flux. However, the changes of permeate flux are not so pronounced as in the case of feed temperature variation. As a results of the exponential function $\Delta p=f(T)$ considerably large changes of Δp were achieved for the feed (e.g. from 333 to 358 K) than for distillate (e.g. from 293 to 318 K) (Gryta, 2002b; Gryta et al., 2000).

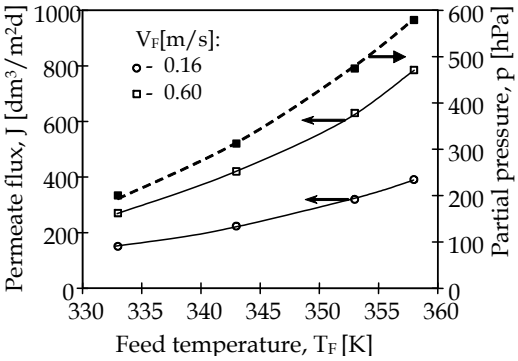

Fig. 2. The influence of feed temperature on the permeate flux and water vapour pressure. Capillary Accurel PP S6/2 membrane, module length 0.6 m, counter-current flow, T_D=293 K

The results presented in Figs. 2 and 3 demonstrate that the flow rate of streams also considerably affects the efficiency of the MD process. Generally, the efficiency of MD module increases with an increase of the flow rate. This effect is particularly significant for the feed flow rate and is slightly smaller for the distillate flow rate (Gryta et al, 1998, 2000). The effect of the feed flow rate was particularly noticeable in a region of low flow rates. Moreover, the improvement of module efficiency obtained by a variation of the flow rate is limited, since the optimum flow rate of streams exists for each MD module. The experimental results demonstrate that the efficiency of MD module used in the studies (Fig. 3) approaches to a plateau for the feed flow rates above 0.6 m/s.

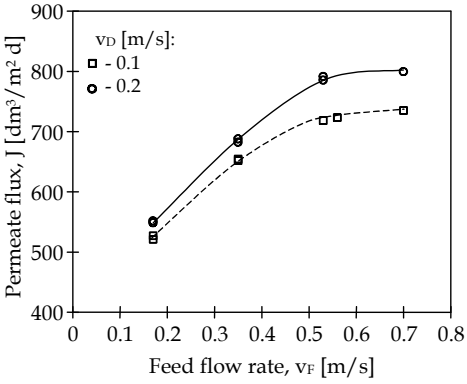

Fig. 3. Influence flow rate of the streams on the MD module efficiency. Module length 1 m, T_F= 358 K, T_D=293 K

The observed dependence of permeate flux on the flow rate is essential due to two effects. Firstly, the values of the heat transfer coefficients rise along with an increase of the flow rate, thus a negative influence of temperature polarization decreases. The value of coefficient h equal to 5000 W/m²K is considered a threshold value; above this value the effect of temperature polarization may be neglected (Gryta et al, 1998, 2000). This value was achieved at v_F of about 0.6 m/s. Secondly, an enhancement of the flow rate caused that the outlet temperatures of streams were closer to their temperatures at the module entrance (Fig. 4), which also increases the driving force for mass transfer (Gryta, 2002b; Gryta et al., 2000).

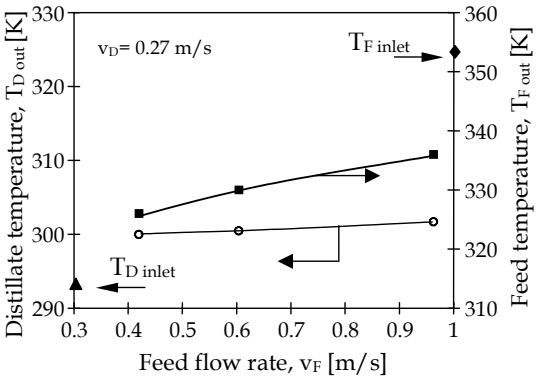

Fig. 4. Influence the feed flow rate on the stream temperature inside the MD module. Module length 1 m, 3 capillary membranes Accurel PP S6/2 arranged inside the ½ " shell

2.2 Heat exchanging between feed and distillate stream

The heat transfer inside the membrane takes place by two possible mechanisms, as conduction across the membrane material (Q_C) and as the latent heat associated with vapour diffusing through the membrane (Q_V). The amount of heat exchanged in the MD module increases along with an increase of the feed temperature (Fig. 5). However, under these

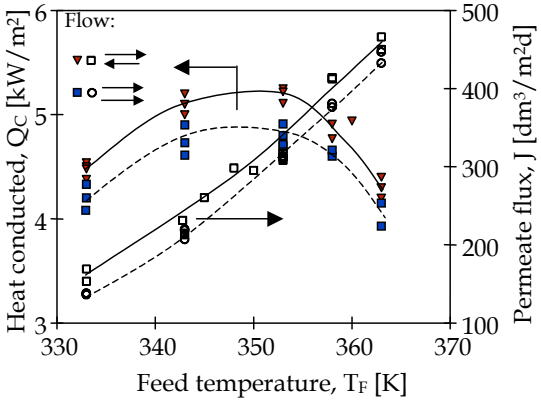

Fig. 5. Influence feed temperature on the MD process efficiency

conditions the permeate flux also increases, which causes the limitation of heat losses (heat conducted through the membrane material). As a result, an increase in the module yield influences on the enhancement of heat efficiency of the MD process and the amount of heat conducted across the membrane (Q_C) decreases (Criscuoli et al. 2008; Gryta, 2006b). The streams in MD modules may flow either co-currently, or counter-currently similarly as in the heat exchangers. The larger driving temperature differences can be achieved using the counter-current flow. As a result, an adverse increase in the amount of heat conducted (Q_C) take place in the MD process, whereas the permeate flux is only slightly enhanced (Fig.5).

A serious drawback of the counter-current flow is that the flow enables the accumulation of inert gases inside a MD module (Fig.6). The gas bubbles fill the channels hindering the liquid flow and they adhere to the membrane surface, which hinders the mass transfer and

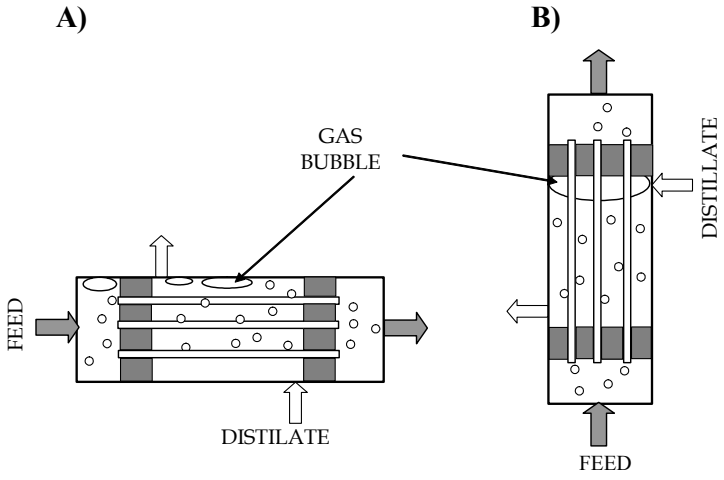

Fig. 6. Accumulation gas bubbles inside the MD modules

as a consequence the MD module efficiency is reduced (Gryta, 2006c). The amount of gases evolved from liquid increases with increasing feed temperature. During the desalination of natural water by MD the desorption of gas form the separated feed is particularly intensive above 343 K. The horizontal arrangement of MD module allows, in a certain degree, to remove a portion of gas bubbles accumulated in the module channels. In the case of module working in a vertical position, the gas will be removed only from the space in which the liquid flows upwards, whereas on the other side of the membrane (e.g. on the shell side – Fig. 6) a volume of entrapped gas phase will be systematically increasing. As a result, the efficiency of module positioned vertically is definitely smaller than that obtained for modules working in a horizontal position (Fig. 7). The inert gases can be removed from the MD installation using degassing of water feeding the membrane module. However, this requires an additional operation that increases the process costs.

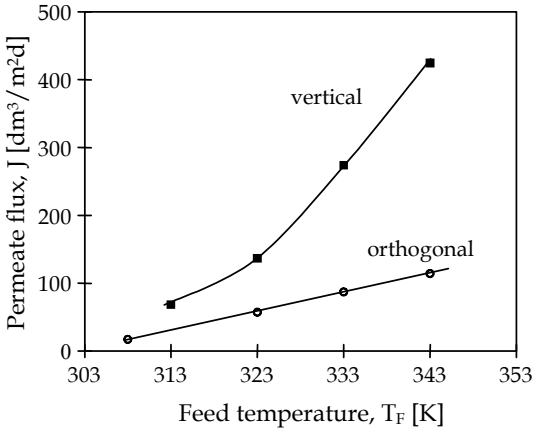

Fig. 7. Influence the position of MD module (vertical or orthogonal) on the permeate flux in the case, when inert gas is accumulated inside the module shell

The problem of inert gases can be solved in a simple way when an additional port-valve is added to the upper part of housing of vertically positioned module (Fig, 8). It enables the removal of inert gases accumulated in the shell of the module. This prevents a decline of the permeate flux and the module efficiency was progressively increased along with increase of feed temperature (Fig. 9). Similarly as before (Fig. 5), the permeate flux for the counter-current flow was only slightly larger than that obtained for the co-current flow. For this reason, it is advantageous to eliminate gas accumulation in the module channels using co-current flow (Gryta, 2005b). In this case the MD module is vertically positioned, and the streams of feed and distillate flows upwards in the module. This allows to remove the bubbles of inert gases formed from MD module in a natural way.

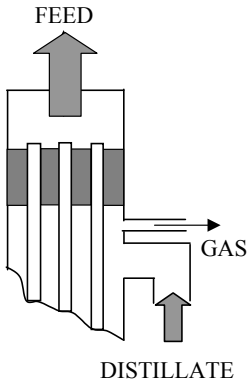

Fig. 8. The design of module head enables to remove inert gas from module shell

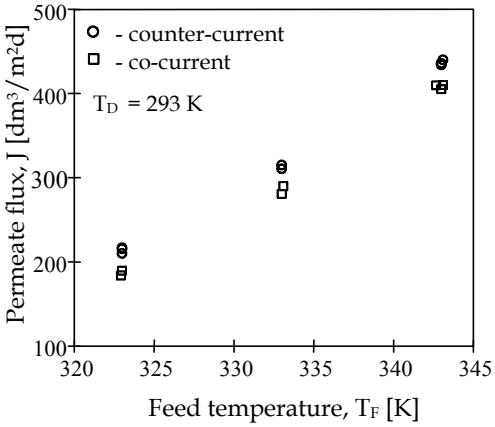

Fig. 9. Influence the feed temperature and direction of streams flow inside the MD module on the permeate flux

2.3 Hydrodynamic entrance length

The distance from the channel inlet to the point of the stabilization of laminar velocity profile is defined as the hydrodynamic entrance length (marked as "L_H") (Andersson & Irgens, 1990; Chu-Lien et al., 2010; Doughty & Perkins, 1970; Zhang et al., 2010). Different correlations for the calculation of the Nusselt number are presented in literature for entrance and fully developed flow regions (Gryta et al., 1997, 1998). In the membrane systems often the laminar flow is applied. The membrane modules are relatively short; therefore, the flow development in the entrance region cannot be sometimes omitted. It will be suitable only in the case, when the ratio of the entrance region to the total membrane area is low.

Heat and mass transfer in membrane-formed parallel-plates channels play a key role for performance analysis and system design. The streams flow in the plate-and-frame module is similar to laminar flow inside the rectangular channel. Therefore, the calculation of L_H entrance length can be made based on the Navier-Stokes equations (Bennett & Myers, 1962; Zhang et al., 2010). For the symmetric channels the growing of hydrodynamic boundary layer is completed when the axial line of duct is reached. The solution of Navier-Stokes equations for the flow between the parallel walls is given by Howarth, and for this case we have (Bennett & Myers, 1962):

$$L_H = 0.015 \, Re \, h \tag{9}$$

where h is a high of channel.

A similar relation for analysis of flow inside the broad rectangular channel was obtained, but the coefficient value was 0.04 (Prandtl, 1949). The correlation allowing to calculate the L_H value for the flow in tubes have a similar form to that presented by equation (9). Most frequently the value of this coefficient is given as equal to 0.03 or 0.0575, whereas the Re number is determined for an average flow rate in the tube. The permeate flow through the porous wall influenced on the velocity profile, however, for most membrane processes (wall Re <1) the analytical solution is sufficient because the symmetric radical of velocity profiles exists.

Parallel-plates channels are the most common structure for plate-and-frame modules. They are simple, and easy to assemble. In plate-and-frame modules usually occur a number of smaller parallel channels instead of one wide channel (Gryta et al., 1997). This caused, that the interaction of side walls also have the influence on the formation of velocity profile. The studies carried out to determine the L_H value for a channel with width 45 mm and height respectively: 5, 10 and 15 mm gave different results in a comparison with those calculated from Eq.(9). The velocity parabolic profile in XY plane (flow only between parallel plates) was formed earlier, and the observed side–walls effect increases with increasing L_H values. Due to the side-walls interactions, the hydrodynamic entrance length was established faster, and indicated nonlinear function (Fig. 10). In the rectangular channel the created temporary parabolic profile (plane XY) was transformed into the deformed parabolic profile (plane XYZ).

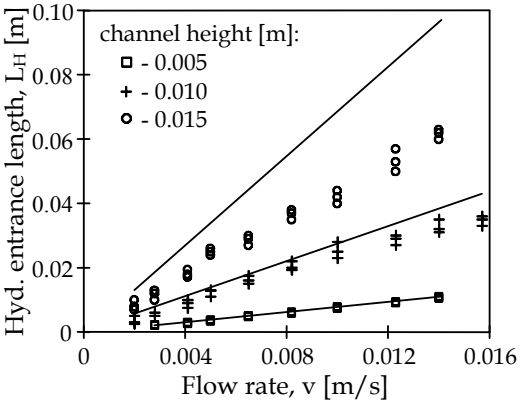

Fig. 10. Variation of hydrodynamic entrance length with flow rate (profile formed in XY plane). Lines – calculated from Eq. (9) described the flow between parallel plates.

According to the theory of boundary layer, the entrance length L_H is dependent as follows:

$$L_H = f(v_A, \nu, a, h) \tag{10}$$

where a is the channel width, v_A and ν are average flow rate and kinematic viscosity, respectively. Taking into consideration a non-linear form of function and the dimensional analysis, the expected function can be expressed as:

$$L_H = b1\, Re^{b2}\, d_h \frac{a}{h} \tag{11}$$

where d_h is hydraulic diameter.

The b1 and b2 coefficients were estimated from the Levenberg-Marquardt Method with minimization of sum of the square deviation. Two hundred of measuring points were used for this analysis. The Snedecors test (F) for significations correlation study has been applied (Volle, 1969). The significance of coefficients study was carried out using Student test (t). In the both tests the signification level has been taken as α=0.05. The obtained function was as:

$$L_H = 0.069\, Re^{0.5}\, d_h \frac{a}{h} \tag{12}$$

The calculated values of squared coefficient of variation for this equation was 0.95.
The results presented in Fig.11 indicated, that the correlation between experimental and calculated data is very good. This confirmed the usefulness of proposed Eq. (12) to calculate the hydrodynamic entrance length under a laminar flow inside the rectangular channel. An estimation of L_H values gives possibility to calculate the area of entrance region for the plate and frame modules (Zhang et al., 2010).

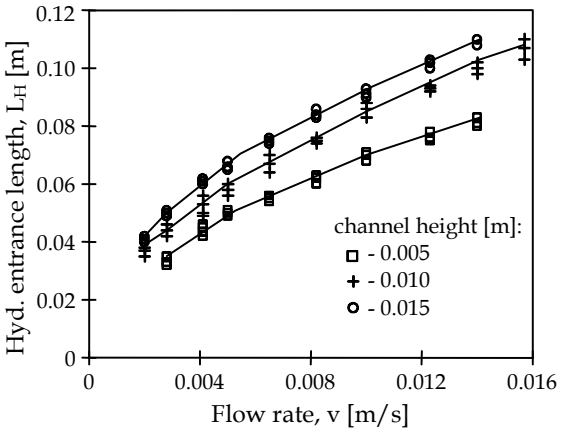

Fig. 11. Variation of hydrodynamic entrance length with velocity for water flow inside rectangular channel (velocity profile formed in XYZ plane). Lines – calculated from Eq. (12)

3. Membrane modules for MD process

The availability of the industrial MD modules is currently one of the limitations for MD process implementation. Flat-sheet membranes in plate-and-frame modules or spiral wound modules and capillary membranes in tubular modules have been used in various MD studies (Gryta et al, 2000; Schneider et al., 1988). The design of the MD modules should provide not only good flow conditions, but also has to improve the heat transfer and thermal stability (Teoh et al., 2008; Srisurichan et al., 2006; Phattaranawik et al., 2003).

3.1 Capillary MD modules

The capillary membrane module is a bundle of porous capillaries packed into a shell similar in configuration to a tube-and-shell heat exchanger (Ju-Meng et al., 2004; Schneider et al., 1988). Because of their very high rate of mass transfer, the capillary modules have been used in many practical applications, such as liquid/liquid extraction, artificial kidney, and desalination studies (Singh, 2006). As a thermally driven process, MD can be significantly affected by temperature polarization (Alklaibi & Lior, 2005; El-Bourawi et al., 2006, Su et al., 2010). Among various types of membrane modules, the capillary module shows the least temperature polarization, so it must have a great future in this field (Zhongwei et al., 2003).
In a capillary module used in MD process, the fluid temperatures and transmembrane flux may vary axially alongside the module (Gryta, 2002b). Usually, the feed flows inside the capillary lumen, and distillate flows on the shell side. Theoretically, the capillaries in a bundle can be packed regularly across the shell of a module as in tube-and-shell heat

exchanger. In most industrial modules, however, the distribution of capillary is far more arbitrary; the capillaries are randomly packed in the shell. This leads to a range of duct sizes and shapes in the shell, or the module shows a certain extent variation of the local packing fraction (Gryta et al., 2000, Ju-Meng et al., 2004; Zhongwei et al., 2003). The vast majority of the MD processes occur in the regions with the local packing fraction, φ between 0.3 and 0.6. Production rate (93%) of the module is from these regions, and they occupy only 75% of the overall membrane area of the module. In the regions with φ larger than 0.6, the distillate flow rates are too much smaller than that of the feed, so their temperatures are very close to that of the feed. This means that more than 20% of the feed stream goes through the module almost without any driving force for MD process, so the associated membrane area, more than 20% of the total, is ineffective (Ju-Meng et al., 2004).
A dislocation of the membranes can be limited using a high value of packing fraction φ. However, this caused a reduction of the channel dimensions on the shell side and the increase in the flow resistance, which hinders the application of appropriate high flow rate of distillate. This is an important aspect, because when the distillate flow rate increases, its temperature will become less affected by heat transfer and vapor condensation from the feed side of the membrane, and so does the feed stream. This means that the increment of flow rates can enlarge the temperature difference between these two streams in the module, and in this way the MD process is improved (Zhongwei et al., 2003).
With regards to this, a value of the φ coefficient in MD modules should amount to 0.4-0.6 (Gryta et al., 2000; Ju-Meng et al., 2004; Schneider et al., 1988). In order to limit the changes of capillaries arrangement inside the shell, one should use such assembly of capillaries, which prevents their free displacements. Good results have been obtained by assembling the membrane capillaries inside the sieve baffles or by a tight packing of membranes in a form of braided capillaries (Gryta et al., 2000; Schneider et al., 1988). A comparison of results obtained for the module having the same value of φ coefficient equal to 0.33, but differing in the manner of membranes assembling is presented in Fig. 12. A traditional construction (module M1) based upon the fixation of a bundle of parallel membranes solely at their ends

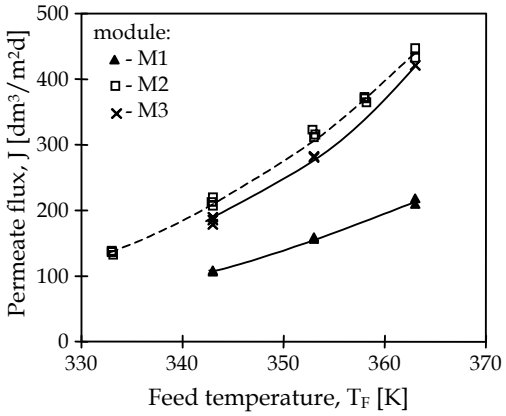

Fig. 12. The influence of feed temperature and the mode of membrane arrangement in a capillary module on the permeate flux. M1 - bundle of parallel membranes; M2 - braided capillaries; and M3 – capillaries mounted inside mesh of sieve baffles

results in that the membranes arrange themselves in a random way. This creates the unfavorable conditions of cooling of the membrane surface by the distillate, which resulted in a decrease of the module efficiency (Gryta et al., 2000; Schneider et al., 1988; Zhongwei et al., 2003). In module M3 the membranes were positioned in every second mesh of six sieve baffles, arranged across the housing with in 0.1–0.15 m. The most advantageous operating conditions of MD module were obtained with the membranes arranged in a form of braided capillaries (module M2). This membrane arrangement improves the hydrodynamic conditions (shape of braided membranes acted as a static mixer), and as a consequence, the module yield was enhanced (Gryta et al., 2000)

A good indicator of the hydrodynamic conditions in a module is the analysis of residence time distribution (RTD). The value of liquid flowing time through the module with good design solution should be closed to the RTD value. The effect of shell-side residence time distribution on mass transfer performance was studied (Lemanski & Lipscomb, 1995). It was pointed out that plug flow would be obtained in an ideal hollow fiber module, but in real shell-side flow the distribution of fluid across the capillary bundle tended to broaden the RTD.

The studies of residence time distribution for a colored impulse in the modules M1-M3 were shown in Figs. 13-14. The RTD value was calculated for assumed plug flow, taking into account a value of φ=0.34. A dye injected into the module appeared the fastest at the outlet of module in the case of module M1 (bundle of parallel capillaries), moreover, the residence time of dye in this module was also the longest. Such result indicates that the non-uniform distribution of capillaries inside the shell caused the formation of channels with different diameters. The distillate was flowing faster in wider channels than the calculated average velocity. As a result, colored water was out flowing faster from the module exit than the calculated RTD value.

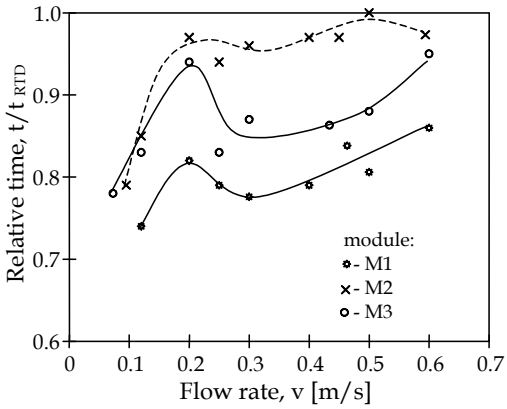

Fig. 13. The influence of flow rate on the relative initial time of colour water residence inside the module. M1 - bundle of parallel membranes; M2 - braided capillaries; and M3 – capillaries mounted inside mesh of sieve baffles

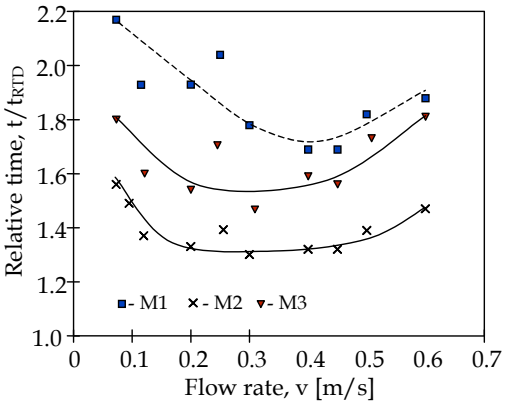

Fig. 14. The influence of flow rate on the total time of dye residence inside the module. M1 - bundle of parallel membranes; M2 - braided capillaries; and M3 – capillaries mounted inside mesh of sieve baffles

As a result of larger values of local capillary packing, the water flows slower in the narrow channels (larger resistance of flow), what prolonged the residence time of dye in the module. An increase in the flow rate increases the turbulence of water flow in the module and dye was washing out faster also from the narrow channels. Due to, the residence time of liquid in the module for larger velocities was closer to the average value. The housings of modules M1-M3 were made of glass tube. This enables the observation of dye spreading out inside their interior. The visual observations of colored streams confirmed these conclusions. The time of water flow in the two remaining modules (M2 and M3) was definitely closer to the RDT value. This indicates, that the dimensions of channels between the capillary membranes had the similar dimension and liquid flows uniformly through the module cross-section. The visual observations also confirmed this fact; dye was uniformly filling up the housing space. The situation was different in the case of module M1, where due to differences in the flow rates, preceded diversity in the intensity of water coloration.
A prolongation of residence time of dye in the module was observed at the flow rates higher than 0.5 m/s. This was associated with growing intensity of liquid mixing in their internal. It was observed, that the vortexes appeared along with the increase in the flow rates. As a result, the portion of colored water were backward transferred, what caused the coloration of new portion of water and due to growing volume of colored water, an apparent longer time of residence in the module was noticed.

3.2 Module with flat sheets membranes

The flat sheet membranes are used in the plate-and-frame modules and spiral-wound module design. In the first case, the flat sheet membranes are assembled between the plates having several channels. The membranes are stacked in flow channels connected in series or in parallel. Usually, the plates are rectangular with the flow from one end to the other. The spiral-wound module uses the flat sheet membranes wound around a central tube. The membranes are glued along three sides to form “leaves” A feed channel spacer (a net-like sheet) is placed between the leaves to define the channel height. A three-channel design can be used in the spiral wound module, which allows the recovery of heat transferred from the feed to distillate (Fig.15).

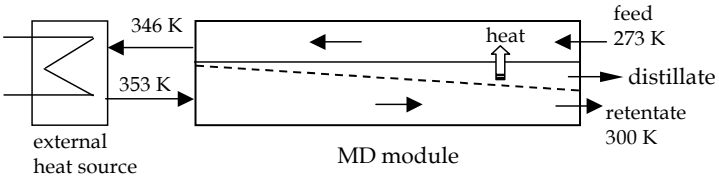

Fig. 15. Module channel arrangement for permeate gap membrane distillation (Winter et al., 2011)

Based on this solution, spiral wound MD modules with a 5-14 m^2 effective membrane area have been developed by Fraunhofer Institute for Solar Energy System (Winter et al., 2011). The cold feed water enters the condenser channel and is heated to approximately 346 K due to internal heat recovery. An external heat source (e.g. solar collector) heats the feed water up to 353 K. The hot feed flows through the evaporator channel in a counter-current direction and exits the module at 300 K. Water vapour passes through the membrane and condenses in the distillate channel. The latent and sensible heat is transferred through the condenser foil to preheat the feed water in the condenser channel. Due to increasing flow resistance, a fast feed flow cannot be used in such a module. As a result, decreasing the vapour pressure with salinity reduces the process driving force. The feed water salinity is considered one of the most important parameters affecting the spiral wound module concept. Larger flow velocities can be used in the plate-and-frame module than in the spiral wound modules. Therefore, the plate-and-frame modules can be utilized for the separation of concentrated salt solutions. The channels in the plate-and-frame modules are shorter; and as a result, an excessive increase of hydraulic pressure is limited. For this reason, several authors suggest the use of spacers as the turbulence promoters (Chu-Lien et al., 2010, Martínez & Rodríguez-Maroto, 2006), because turbulent flow is an appropriate method to decrease the negative effect of polarization phenomena. The turbulent or upper transition flow regime was found in the spacer-filled channels for UF although the Reynolds numbers were still in the laminar regime (Phattaranawik et al., 2003). Net-type spacers are often put into the flow channels in the membrane processes to improve the mass transfer and to reduce the effect of concentration polarization and fouling. The spacers can also be utilized in MD since they destabilize the flow and create eddy currents in the laminar regime so that heat, and mass transfer are enhanced (Teoh et al., 2008; Phattaranawik et al., 2003).

The permeate fluxes obtained from the experiments with spacer-filled channels were compared with those obtained in the experiments performed under laminar and turbulent flow conditions, but for modules with non-filled channels. In the case of experiments with the spacers, a 26–56% increase in the permeate fluxes was achieved, compared with the fluxes performed under laminar flow (Martínez & Rodríguez-Maroto, 2006). However, these fluxes were much lower than those obtained from turbulent flow conditions in the empty channels. This results from the fact, that the feed evaporates during the flow through a module, causing a relatively fast decrease of the feed temperature, which reduces a value of driving force for mass transfer. Thus, in the MD process both the value of the flow rate (m/s) and the volumetric flow (m^3/s of feed per unit of the membrane area) have a considerable importance. A sufficiently large value of heat transfer coefficient (e.g. 5000 W/m^2K) allowing to eliminate the temperature polarization, can be generated for laminar

flow (Gryta, 2002b). Although a further increase in the flow rate will not have a substantial influence on the reduction of the temperature polarization, the value of volumetric flow ($m^3/s\ m^2$) will increase significantly, and beneficial results, such as enhancement of the permeate flux, will be obtained.
The nets exhibit the filtration properties, which hinder the use of modules with the channels filled with the nets in certain applications (Fig.16).

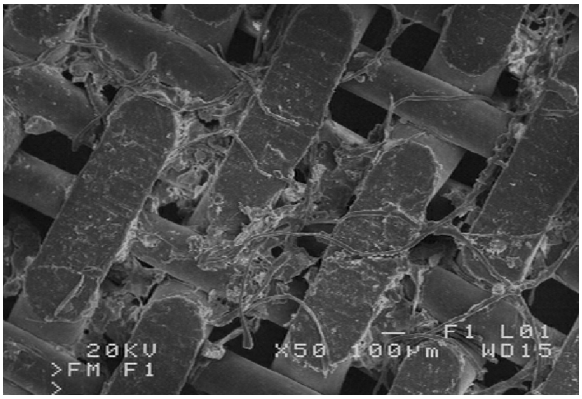

Fig. 16. SEM image of deposit formed inside the net supporting the membrane in the MD module

The concentration of non-clarified juices cannot be carried out with the utilization of such modules (Jiao et al., 2004). The desalination process of hard water, in which significant amounts of $CaCO_3$ precipitates are formed (Gryta, 2005a, 2006b), can be another negative exemplary. As demonstrated the nets, favors the hydrogenous crystallization (Gryta, 2009), which would increases the intensity of scaling in the module.
The flat sheet membranes exhibit a low resistance to mechanical damage; therefore, they are reinforced by the application of supporting nets. However, the presence of nets decreases the heat and mass transfer to membrane surfaces, while significantly enhancing the polarization phenomena. These phenomena reduce the difference between T_1 and T_2 interfacial temperatures (Fig. 1), compared to the design when no net was used. Consequently, the driving force for mass transfer is also reduced in the case of net supported membranes. Therefore, a module design in which a part of channel is empty, while a part is filled by net supporting the membrane, significantly influenced reduction of MD efficiency (Gryta et al., 1997).
The module performance can be improved by elimination of nets and by an increase of the number of channels on a module plate so that their walls fill the role of edges supporting the membrane (Fig. 17). It was found that an arrangement of edges every 15-20 mm was appropriate for the membranes made of PVDF and PTFE with the thickness of 100-150 μm (Gryta et al., 1997; Tomaszewska et al., 2000).

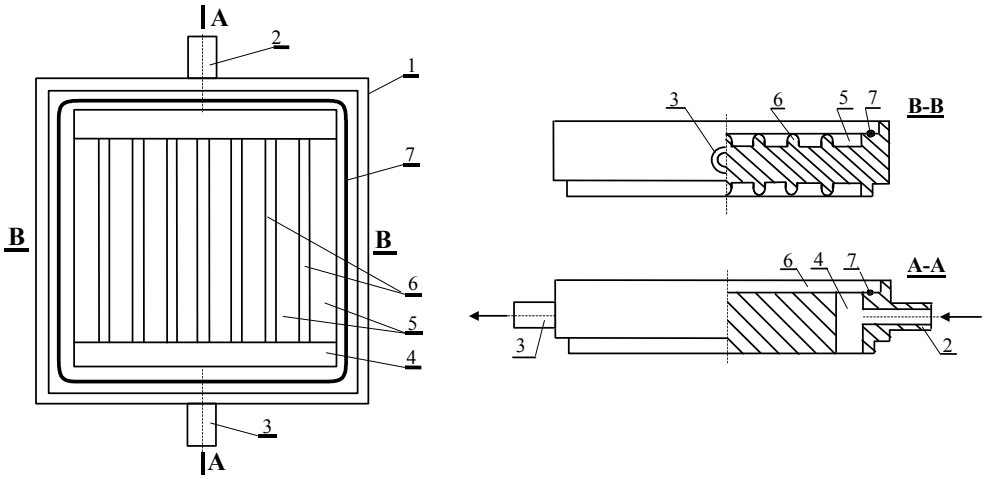

Fig. 17. Plate-and –frame MD module design. 1 – module plate, 2 – inlet channel, 3 – outlet channel, 4 – lateral feeding channel, 5 – distribution channels, 6 – edges supporting the membrane, 7 – o-ring

The individual plates of the module possess a series of channels connected most frequently with one feeding channel. As the pressure in this channel increases along with the increase in the flow rate, it may lead to membrane damage in this region. This problem was solved by placing an inlet opening of feeding channel below a plane of the distribution channels, which were connected by an additional lateral channel (Fig.17). As a result, liquid with large velocity flew out from the inlet channel and spreads on sides in the lateral channel. As its cross-section is several times larger, liquid flow rate slows down and flows into the distribution channels with a lower energy (Fig. 18).
A visualization of feed flow in the distribution channel of the plate-and–frame module with a central one-point feeding of the plate was shown in Fig. 19.

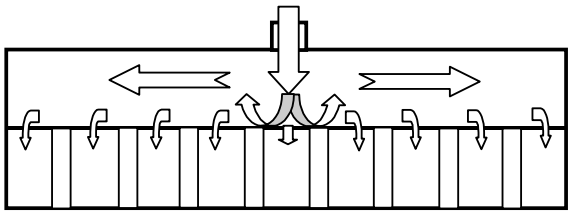

Fig. 18. The schema of water flow inside the distribution channel of the plate-and-frame module presented in Fig. 17

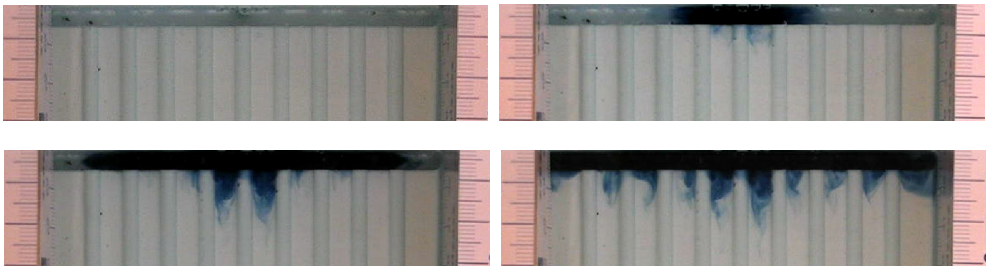

Fig. 19. A visualization of feed flow in the distribution channel

3.2.1 Uniformity of flow

In the capillary modules good conditions of mixing and a flow close to plug flow can be achieved by using an appropriate design, e.g. by assembling the braided capillaries. However, the achievement of uniform flow of liquid throughout the entire cross-section of plate-and-frame modules is definitely more difficult. As a rule, one can expect different flow rates in the particular channels. The studies have demonstrated that this variability is dependent not only on the location of channels, but also on the rate of module feeding. A visualization of variations in the flow rates of liquid in the particular channels of the module with a central one-point feeding of plate was shown in Figs. 19 and 20. The larger is the fraction of a given channel filled with colored water, the larger is the flow rate of liquid in this channel (relative for each case). In these studies, a module was feed with a flow rate of 0.1-0.86 dm^3/min, which corresponds to the average flow rate of 0.007-0.06 m/s. The obtained results indicate that the highest flow rate was achieved in the terminal channels, whereas the lowest rate was obtained in the module axis. This tendency was growing along with an increase in the supply flow. Most likely, a slight increase in the middle channel width would reduce the flow rate resistance, and as a result, cause a larger uniformity of flow rate distribution across the entire plate of the module.

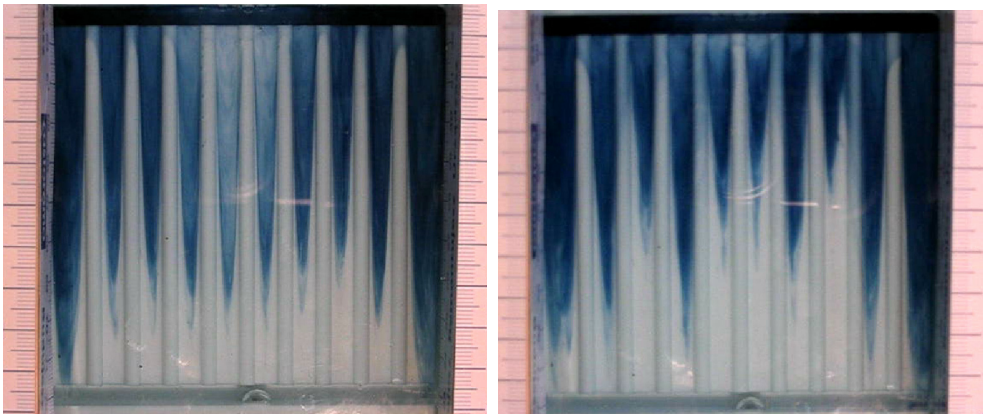

A) feeding 0.1 dm^3/min B) feeding 0.21 dm^3/min

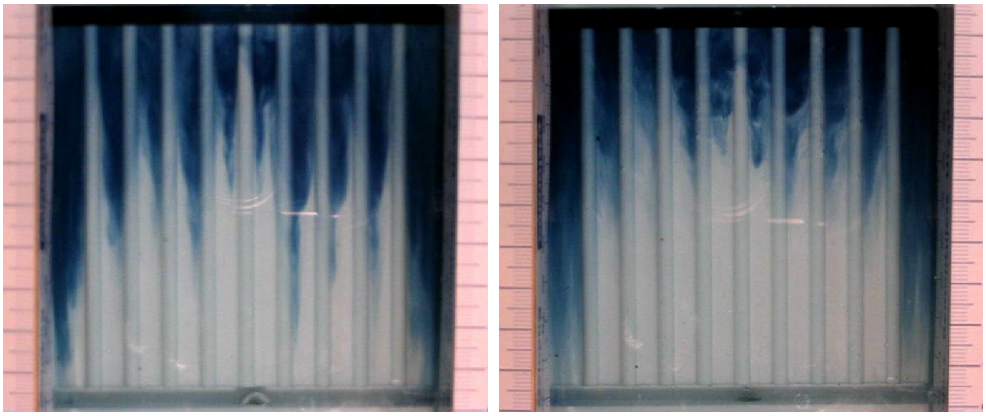

C) feeding 0.44 dm^3/min D) feeding 0.86 dm^3/min

Fig. 20. Visualization of variations in the flow rates of water (302 K) in the particular channels of the module (channel dimension 6x3.9 mm) with a central one-point feeding of plate

A substantial improvement in the flow uniformity was achieved when the water was feed into the feeding channel in two places (Fig. 21). In this case, the connections were assembled in a distance of ¼ plate width from each end of the channel. The module was

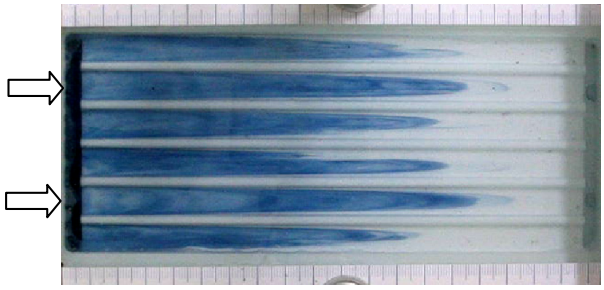

A) feeding 0.1 dm^3/min

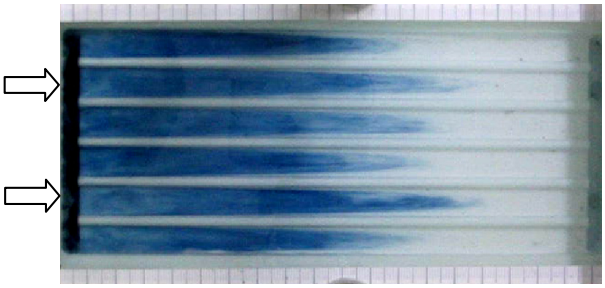

B) feeding 0.21 dm^3/min

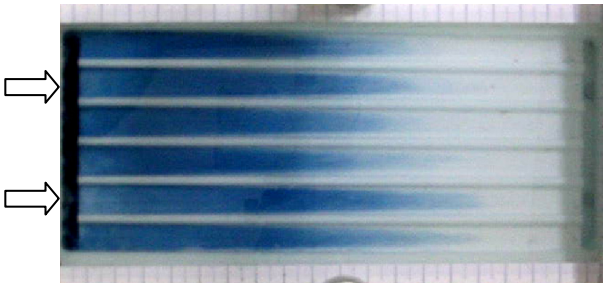

C) feeding 0.44 dm^3/min

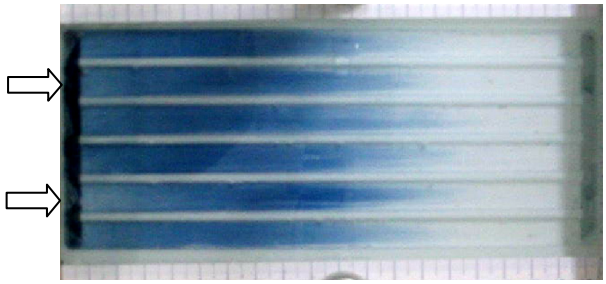

D) feeding 0.86 dm^3/min

Fig. 21. Visualization of variations in the flow rates of water (302 K) in the particular channels of the module (channel dimension 10x3.5 mm) with a two-point feeding of module plate

feeding with the flow rate of 0.1-0.86 dm^3/min, which corresponds to the average flow rate 0.008-0.07 m/s. The presented pictures indicate that a velocity profile characteristic for the laminar flow can be observed only for a very slow flow (0.008 m/s). An increase in the uniformity of liquid coloration in the channels was observed at larger supply flows what indicates for a flow close to the plug flow. Most probably this effect was obtained due to an increase in the turbulent flow of liquid in the feeding channel. This may equalize the hydraulic pressure along this channel, and cause liquid to flow more uniformly into the distribution channels.

4. Conclusions

The driving force of MD depends, in a significant degree, on turbulence of stream flow in the membrane module. Therefore, the hydrodynamic conditions existing in the module have a large influence on the MD process efficiency. Just as in the modules used for pressure-driven processes, it is important to minimize the flow resistance through the MD module channels. However, the reason for this was different, because the pressure drop is not limited, rather, the hydraulic pressure should be as low as possible, so as to restrict the membrane wettability.

The maintenance of adequately high flow rates limits the concentration polarization and fouling, but in the case of MD modules the magnitude of temperature polarization also has a

substantial influence. The latter polarization can be significantly reduced when the flow turbulence yield a heat transfer coefficient above 5000 W/m²K. This coefficient is affected by the value of the flow rate as well as by the design of flow channels. The filling of channels with nets or an arrangement of braided capillary membranes ensures an increase in the flow turbulence and good conditions for heat transfer can be achieved at lower values of flow rates. Therefore, in the case of MD modules construction, one should consider design requirements typical for pressure driven membrane processes as well as a necessity to ensure the appropriate conditions for heat transfer.

The efficiency of MD capillary modules is significantly affected by the manner in which the membranes are arranged within a housing. A traditional construction based upon the fixation of a bundle of parallel membranes solely at their ends causes that the membranes arranged themselves in a random way. This creates unfavorable conditions of cooling of the membrane surface by the distillate; hence, the module efficiency is reduced due to the enhancement of temperature polarization. On the other hand, arranging the membranes in a way to ensure a uniform distribution over the module cross-section (braided membranes or supported by sieve baffles alongside module) increases the efficiency over 100%.

The feed temperature in MD module decreases due to the evaporation, which also causes a reduction of MD driving force, besides the temperature polarization. Therefore, the permeate flux can be increased several times when the feed outlet temperature is closed to its inlet temperature, which is obtained by increasing the flow rate. The optimal value of the flow rate for several studied modules amounts to 0.6–1 m/s and 0.4–0.7 m/s for feed and distillate, respectively.

5. References

Alklaibi, A.M. & Lior, N. (2005). Membrane-distillation desalination: status and potential, *Desalination*, Vol.171, No.2, (January 2005), pp. 111–131, ISSN 0011-9164

Andersson, H.I. & Irgens, F. (1990) Hydrodynamic entrance length of non-newtonian liquid films. *Chemical Engineering Science*, Vol.45, No.2, (January 1990), pp. 537–541, ISSN 0009-2509

Banat, F. & Jwaied, N. (2008). Economic evaluation of desalination by small-scale autonomous solar-powered membrane distillation units. *Desalination,* Vol.220, No.1-3, (March 2008), pp. 566–573, ISSN 0011-9164

Bennett, C.O. & Myers, J.E. (1982). *Momentum, heat and mass transport* (3 rd ed.), Mc Grow-Hill Book Company, ISBN 0070046719, New York, USA

Bonyadi, S. & Chung, T.S. (2009). Highly porous and macrovoid-free PVDF hollow fiber membranes for membrane distillation by a solvent-dope solution co-extrusion approach, *Journal of Membrane Science,* Vol.331, No.1-2, (April 2009), pp. 66–74, ISSN 0376-7388

Bui, V.A.; Vu, L.T.T. & Nguyen, M.H. (2010). Simulation and optimization of direct contact membrane distillation for energy efficiency. *Desalination*, Vol.259, No.1-3, (September 2010), pp. 29–37, ISSN 0011-9164

Chu-Lien, L.; Yu-Feng, Ch.; Wen-Junn, S. & Chi-Chuan, W. (2010). Effect of flow deflector on the flux improvement in direct contact membrane distillation. *Desalination*, Vol.253, (April 2010), pp. 16–21, ISSN 0011-9164

Criscuoli, A.; Carnevale, M.C. & Drioli, E. (2008). Evaluation of energy requirements in membrane distillation, *Chemical Engineering and Processing*, Vol.47, No.7, (July 2008), pp. 1098-1105, ISSN 0009-2509

Drioli, E.; Curcio, E.; Criscuoli, A. & Di Profio, G. (2004). Integrated system for recovery of $CaCO_3$, NaCl, $MgSO_4 \cdot 7H_2O$ from nanofiltration retentate, *Journal of Membrane Science,* Vol.239, No.1, (August 2004), pp. 27–38, ISSN 0376-7388

Doughty, J.R. & Perkins JR, H.C. (1970). Hydrodynamic entry length for laminar flow between parallel porous plates. *Journal of Applied Mechanics*. Vol.37, (May 1970), pp. 548, ISSN 0021-8936

El-Bourawi, M.S.; Ding, Z.; Ma, R & Khayet, M. (2006). A framework for better understanding membrane distillation separation process. *Journal of Membrane Science,* Vol.285, No.1-2, (November 2006), pp. 4–29, ISSN 0376-7388

Gryta, M.; Tomaszewska, M. & Morawski, A.W. (1997). Membrane distillation with laminar flow. *Separation and Purification Technology*, Vol.11, No.2, (June 1997), pp. 93–101, ISSN 1383-5866

Gryta, M.; Tomaszewska, M. &. Morawski, W. (1998). Heat transport in the membrane distillation process, *Journal of Membrane Science,* Vol.144, No.1-2, (June 1998), pp. 211–222, ISSN 0376-7388

Gryta, M.; Tomaszewska, M. & Morawski, A.W. (2000). A capillary module for membrane distillation process, *Chemical Papers*, Vol.54, No.6a, (July 2000), pp. 370–374, ISSN 0366-6352

Gryta, M. (2002a). Direct contact membrane distillation with crystallization applied to NaCl solutions, *Chemical Papers*, Vol.56, No.1, (January 2002), pp. 14–19, ISSN 0366-6352

Gryta, M. (2002b). Concentration of NaCl solution by membrane distillation integrated with crystallization. *Separation Science and Technology.* Vol.37, No.15, (November 2002), pp. 3535–3558, ISSN 0149-6395

Gryta, M. (2005a). Osmotic MD and other membrane distillation variants. *Journal of Membrane Science,* Vol.246, No.2, (January 2005), pp.45–56, ISSN 0376-7388

Gryta, M. (2005b). Long-term performance of membrane distillation process, *Journal of Membrane Science.*, Vol.265, No.1-2, (November 2005), pp. 153–159, ISSN 0376-7388

Gryta, M. (2006a). Water purification by membrane distillation process, *Separation Science and Technology*. Vol.41, No.9, (September 2006), pp. 1789–1798, ISSN 0149-6395

Gryta, M. (2006b). Heat efficiency of the capillary modules for membrane distillation process, *Inżynieria Chemiczna i Procesowa*, Vol.27, No.1, (January 2006), pp. 305-314, ISSN 0208-6425

Gryta M. (2006c). Deareation capillary modules during membrane distillation (in Polish). *Inżynieria i Aparatura Chemiczna*, Vol.45, No.3, (June 2006), pp. 20–23, ISSN 0368-0827

Gryta, M. (2008). Fouling in direct contact membrane distillation process, *Journal of Membrane Science,* Vol.325, No.1, (November 2008), pp. 383–394, ISSN 0376-7388

Gryta, M, (2009). Scaling diminution by heterogeneous crystallization in a filtration element integrated with membrane distillation module, *Polish Journal of Chemical Technology*, Vol.11, No.1, (February 2009), pp. 59–64, ISSN 1509-8117

Gryta, M. & Barancewicz, M. (2010). Influence of morphology of PVDF capillary membranes on the performance of direct contact membrane distillation, *Journal of Membrane Science,* Vol.358, No.1-2, (August 2010), pp. 158–167, ISSN 0376-7388

Gryta, M. (2010a). Application of membrane distillation process for tap water purification. *Membrane Water Treatment*, Vol.1, No.1 (January 2010), pp. 1-12, ISSN 2005-8624

Gryta, M. (2010b). Desalination of thermally softened water by membrane distillation process. *Desalination*, Vol.257, No.1-3 (July 2010), pp. 30–35, ISSN 0011-9164

Jiao, B.; Cassano, A. & Drioli, E. (2004). Recent advanced on membrane processes for the concentration of fruit juices: a review, *Journal of Food Engineering,* Vol.63, No.3 (August 2004), pp. 303–324, ISSN 0260-8774

Ju-Meng, Z.; Zhi-Kang, X.; Jian-Mei, L.; Shu-Yuan, W. & You-Yi, X. (2004). Influence of random arrangement of hollow fiber membranes on shell side mass transfer performance: a novel model prediction. *Journal of Membrane Science*, Vol.236, No.1-2, (June 2004), pp. 145–151, ISSN 0376-7388

Karakulski, K.; Gryta, M. & Sasim,M. (2006). Production of process water using integrated membrane processes, *Chemical Papers*, Vol.60, No.6, (November 2006), pp. 416–421, ISSN 0366-6352

Khayet, M.; Godino, M.P. & Mengual, J.I. (2004). Study of asymmetric polarization in direct contact membrane distillation, *Separation Science and Technology*, Vol.39, No.1 (January 2004), pp. 125–147, ISSN 0149-6395

Lawson, K.W. & Lloyd, D.R. (1997). Membrane distillation. *Journal of Membrane Science*, Vol.124, No.1, (February 1997), pp. 1–25, ISNN 0376-7388

Lemanski, J. & Lipscomb, G.G.(1995). Effect of shell-side flows on hollow fiber membrane device performance, *American Institute of Chemical Engineering Journal*. Vol.41, No.10, (October 1995), pp. 2322–2326, ISSN 1547-5905

Li, B. & Sirkar, K.K. (2004). Novel membrane and device for direct contact membrane distillation-based desalination process, *Industrial Engineering Chemical Research*, Vol.43, No.17, (August 2004), pp. 5300–5309, ISSN 0888-5885

Martínez-Díez, L. & Vázquez-González, M.I. (1999). Temperature and concentration polarization in membrane distillation of aqueous salt solutions, *Journal of Membrane Science,* Vol.156, No.2, (April 1999), pp. 265–273, ISSN 0376-7388

Martínez, L. & Rodríguez-Maroto, J.M. (2006). Characterization of membrane distillation modules and analysis of mass flux enhancement by channel spacers. *Journal of Membrane Science*, Vol.274, No.1-2, (April 2006), pp. 123–137, ISSN 0376-7388

Phattaranawik, J.; Jiraratananon, R. & Fane, A.G. (2003). Heat transport and membrane distillation coefficients in direct contact membrane distillation, *Journal of Membrane Scienc*e, Vol.212, No.1-2 (February 2003), pp. 177–193, ISSN 0376-7388

Prandtl, L. (1949). *Fuhrer durch die Stromungslehre*. Friedrich Vieweg u. Sohn, Braunschweig, Germany

Schneider, K.; Hölz, W. & Wollbeck, R. (1988). Membranes and modules for transmembrane distillation, *Journal of Membrane Science*, Vol.39, No.1, (October 1988), pp. 25–42, ISSN 0376-7388

Singh, R (2006). *Hybrid Membrane Systems for Water Purification,* Elsevier, ISBN 1-856-17442-5, Kidlington, UK

Schofield, R.W.; Fane, A.G.; Fell, C.J.D. & Macoun, R. (1990). Factors affecting flux in membrane distillation. *Desalination*, Vol.77, (March 1990), pp. 279–294, ISSN 0011-9164

Srisurichan, S.; Jiraratananon, R. & Fane, A.G. (2005). Humic acid fouling in the membrane distillation, *Desalination*, Vol.174, No.1, (April 2005), pp. 63–72, ISSN 0011-9164

Srisurichan, S.; Jiraratananon, R. & Fane, A.G. (2006). Mass transfer mechanisms and transport resistances in direct contact membrane distillation process, *Journal of Membrane Science,* Vol.277, No.1-2, (June 2006), pp. 186–194, ISSN 0376-7388

Su, M.; Teoh, M.M.; Wang, K.Y.; Su, J. & Chung, T.S. (2010), Effect of inner-layer thermal conductivity on .ux enhancement of dual-layer hollow .ber membranes in direct contact membrane distillation. *Journal of Membrane Science*, Vol.364, No.1-2, (November 2010), pp. 278–289, ISSN 0376-7388

Teoh, M.M.; Bonyadi, S. & Chung, T.S. (2008). Investigation of different hollow fiber module designs or flux enhancement in the membrane distillation process, *Journal of Membrane Science,* Vol.311, No.1-2, (March 2008), pp. 371–379, ISSN 0376-7388

Tomaszewska M.; Gryta, M. & Morawski, A.W. (2000). Mass transfer of HCl and H_2O across the hydrophobic membrane during membrane distillation. *Journal of Membrane Science,* Vol.166, No.2, (February 2000), pp. 149–157, ISSN 0376-7388

Wang, K.Y.; Chung, T.S. & Gryta, M. (2008). Hydrophobic PVDF hollow fiber membranes with narrow pore size distribution and ultra-thin skin for the freshwater production through membrane distillation, *Chemical Engineering Science*, Vol.63, No.9, (May 2008), pp. 2587–2594, ISSN 0009-2509

Winter, D.; Koschikowski, J. & Wieghaus, M. (2011). Desalination using membrane distillation: Experimental studies on full scale spiral wound modules. *Journal of Membrane Science*, Vol.375, No.1-2 (June 2011), pp. 104–112, ISSN 0376-7388

Volk, W. *Applied statistics for engineers* (1969), McGraw-Hill, ISBN 0070675511, New York, USA

Zhang, L.Z.; Liang, C.H. & Pei, L.X. (2010). Conjugate heat and mass transfer in membrane-formed channels in all entry regions. *International Journal of Heat and Mass Transfer*, Vol.53, No.5, (February 2010), pp. 815–824. ISSN 0017-9310

Zhongwei, D.; Liying, L. & Runyu, M. (2003). Study on the effect of flow maldistribution on the performance of the hollow fiber modules used in membrane distillation. *Journal of Membrane Science,* Vol.215, No.1-2, (April 2003), pp. 11–23, ISSN 0376-7388

15

Gas Hydrate Formation Kinetics in Semi-Batch Flow Reactor Equipped with Static Mixer

Hideo Tajima
Niigata University
Japan

1. Introduction

Gas hydrate is an ice-like solid and a kind of inclusion compounds of which the cage-like structure formed by hydrogen-bonded water molecules can include various kinds of guest gas molecules. In general, gas hydrates are formed with "host" water and "guest" gas molecules under lower temperature and higher pressure conditions, but sometimes large differences in the hydrate formation conditions are observed among guest gases. In such cases, if gas hydrate is formed with such a gaseous mixture, it can be anticipated that the component of which the hydrate formation condition is milder (that is, higher temperature and lower pressure conditions relatively) could be enriched in the hydrate phase. Effective gas separation, or higher selectivity, can be achieved for gas mixtures with larger differences in the hydrate formation conditions. On the other hand, multi-component gas hydrates are formed under higher pressure and lower temperature conditions in which any component of gaseous mixture can change to hydrate.

Several applications have been proposed in environmental and energy fields by using the inclusion abilities in the framework of gas hydrates; natural gas transport (Gudmundsson & Børrehaug, 1996), gas storage (Lee et al., 2005), and gas separation (Kang & Lee, 2000) and so on, and thus many investigations for gas hydrate formation, especially thermodynamics and gas hydrate formation kinetics, have been carried out in batch systems. The solid hydrate can be dissociated to recover a product gas. The selectivity and production rate are key factors in determining the performance of hydrate-based applications. Although the selectivity is limited by the thermodynamic equilibrium of the hydrate phase and the feed vapour phase (Nagata et al., 2009), the production rate is dependant on the hydrate formation rate and the system design.

Gas hydrate-based applications would require an efficient formation or production process of gas hydrates, and the elucidation of the formation mechanism of gas hydrates. Gas hydrate formation is similar to crystallization from liquid mixture, and gas-liquid system changes to liquid-solid or gas-solid systems. In general, it is known gas hydrate forms on gas-liquid interface, and thus the gas-liquid interfacial area, the driving force, and kinetic constant can affect hydrate formation. Therefore, an efficient way to increase these factors is necessary for continuously forming gas hydrate solid in gas-liquid system. For example, several efficient processes to increase the interfacial area for gas hydrate formation have been demonstrated, including a spray (Fukumoto et al., 2001) or jet reactor (Szymcek et al., 2008; Warzinski et al., 2008), and a bubble column (Luo et al, 2007; Hashemi et al., 2009)

besides general stirred tank. However, gas hydrate formation is very complicated by the presence of three phases (gas-liquid-solid) during gas hydrate formation; the formation of solid (gas hydrate) can occur on gas-liquid (water) interface.
Although many investigations about gas hydrate formation have been published, this chapter deals with gas hydrate formation kinetics with focusing on author's research with a semi-batch flow reactor equipped with static mixer. In the broad sense, this chapter will cover the multiple flow and pipe flow. The gas hydrate formation is composed of two main processes as well as crystallization; hydrate nucleation and hydrate growth processes. This chapter focuses attention on the overall gas hydrate formation process, and thus discusses the hydrate formation process based on the experimental data by varying thermodynamic, mechanical, and chemical conditions.

2. Semi-batch flow reactor with static mixer

In author's study, gas hydrate formation from gas-liquid fluids is carried out in Kenics static mixer. Static mixers are motionless mixing devices with fixed "mixing elements" arranged in a straight pipe. The Kenics static mixer experiments demonstrated that two fluids (drop/bubble and water) are efficiently agitated with the mixing elements and are subsequently converted to hydrate formed on the drop/bubble surface at specific temperature and pressure conditions (Tajima et al., 2004, 2007). Several structures of mixing element are designed for efficient agitation/mixing of fluids more than one. Compared with stirred tank type mixers, static mixers also generally provide continuous operational availability, small size and space requirements, flexibility in the process installation, and low power requirements (Godfrey, 1997).
Fig.1 shows the author's semi-batch flow reactor with static mixer for continuous gas hydrate formation system. Kenics-type mixing elements of a stainless steel static mixer are used. There are 24 mixing elements and these are inserted into a pyrex glass tube (455 mm, i.d. 11.0 mm) for low pressure conditions (< 0.5 MPa) or into a stainless steel tube (same size to glass tube) with a pyrex glass window for high pressure conditions (< 2.0 MPa). Static mixer can achieve the mixing performance depending on the gas and water flow rates. The target gas is injected with mass flow controller at the bottom of the reactor and the water flow rate is operated with the water supply pump either counter or co-current to the gas flow direction. At water flow rate of zero this system is regarded as a semi-batch system that only the gas go in and out of the reactor. The injected gas is converted to gas hydrate in the static mixer unit and unconverted gas is vented from at the top of the reactor. Transport of formed hydrate particles are carried out with the water fluid, and the hydrate particles are settled and separated at the recovery vessel. Water without large hydrate particle, therefore, is always supplied to the reactor. The recovery vessel is set up in a manner to prevent the gas hydrate blocking the gas supply nozzle or the reactor, and thus the continuous hydrate formation is achieved. Pressure and temperature conditions for target gas hydrate formation are selected according to gas-water-hydrate equilibrium condition in available literature data. The reactor, the recovery vessel, and the water supply pump are all placed in a low temperature thermostatic chamber to control the system temperature. Experimental pressure is controlled within ±0.01 MPa by a pressure-regulating valve installed on the downstream side of the reactor. Various gas hydrate formations are carried out under constant pressure and temperature conditions.

To calculate the hydrate formation rate, outlet gas flow rates are measured by a mass flow meter after the gas had passed through the reactor. Gas hydrate formation was confirmed by both visual observations and variations in outlet gas flow rates. The gas uptake rate into hydrate was determined using the difference between inlet and outlet gas flow rates, assuming that all the gas molecules are used to form hydrate. The gas uptake rate is equal to overall gas hydrate formation rate (r_{hy}).

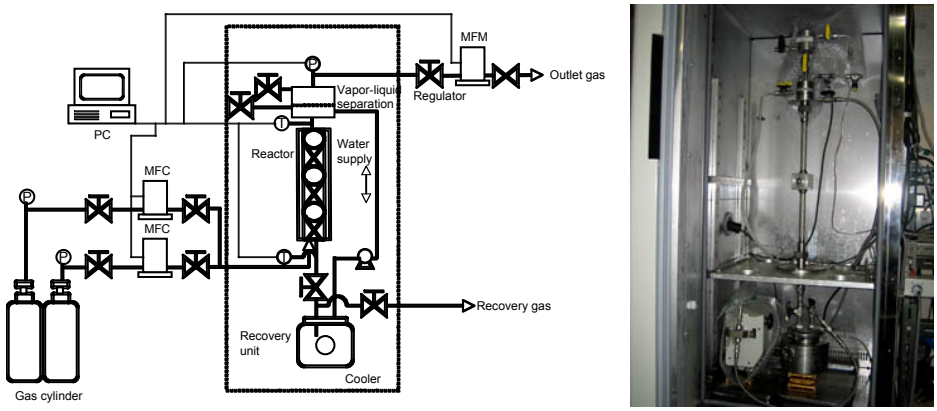

(a) Schematic drawing of the system (b) Appearance in the chamber

Fig. 1. Semi-batch flow reactor with static mixer for gas hydrate formation system

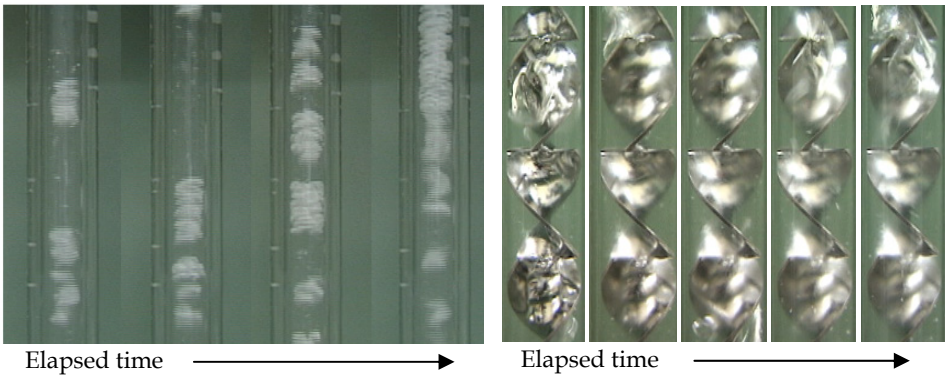

(a) no-mixing element (empty tube) (b) mixing element insert

Fig. 2. Static mixing effect on gas-water-hydrate fluids (CH_2FCF_3 gas-water system at 276K and 0.20 MPa with 200 mL/min of gas flow rate)

Fig.2 shows the static mixing effect on gas hydrate formation from CH_2FCF_3 gas-water system. When the gas hydrate formation is carried out in empty tube, bubble surface is covered with hydrate, and consequently the flow channel in the tube is blocked (Fig.2a). The insert of mixing elements can form hydrate slurry and prevent the tube blockage by mixing functions long time (Fig.2b). This result indicates that the mixing function of this mixing

element is important for the removal of hydrate film from bubble surface. The details of mixing function effect have been mentioned in previous literature for liquid CO_2-water system in the co-current flow reactor (Tajima et al., 2005). In the semi-batch flow reactor, the hydrate slurry formation is depending on not only mixing functions of the mixing elements but other conditions; operation pressure, operation temperature, gas and water flow rates, gas species, and so on. The relation between the hydrate formation pattern and these conditions will be discussed again later.

3. Hydrate formation rate analysis

There are many discussion about gas hydrate formation kinetics. With regard as this point, another book about natural gas hydate is available (Sloan and Koh, 2008). Although gas hydrate nucleation and growth processes have been investigated and discussed by many researchers, temperature difference, chemical potential difference, and fugacity difference are selected as the driving force. Here, let's say overall gas hydrate formation rate r_{hy} is expressed by the chemical potential difference between formation and equilibrium as the driving force (Englezos et al., 1987; Daimaru et al., 2007; Li et al., 2009; Tajima et al., 2010a).

$$r_{hy} = -\frac{\mathrm{d}n}{\mathrm{d}t} = aK^* \left(\mu_{\mathrm{g}} - \mu_{\mathrm{eq}} \right) \tag{1}$$

where n is the number of moles of target gas (guest gas) consumed in the gas phase, t is elapsed time, aK^* is the hydrate formation rate constant, a is the interfacial area, K^* is the overall kinetics constant, and μ_g and μ_{eq} are chemical potentials of guest gases in the gas phase and hydrate phase, respectively. The overall kinetics constant K^* will be expressed using the mass transfer coefficient k_L and the hydrate crystal growth constant k_f.

$$\frac{1}{K^*} = \frac{1}{k_L} + \frac{1}{k_f} \tag{2}$$

This idea is very similar to the treatment of crystal growth behavior of crystalization (the nucleation process is ignored because of crystal seed addition) and gas absorption with reaction in chemical engineering field.

$$r_{hy} = -\frac{\mathrm{d}n}{\mathrm{d}t} = aK^* \cdot RT \ln\left(\frac{f_g}{f_{eq}} \right) \tag{3}$$

Although Eq.(2) may have to take account of the hydrate nucleation actually, we omits the part of the nucleation here. Because the chemical potential terms can be reduced to the fugacity of the gas, Eq.(1) can be easily transformed to the form of Eq.(3). R is the gas constant, T is the operation temperature, and f_g and f_{eq} are the fugacities of the guest molecules in vapour phase and in hydrate phase, respectively. The fugacity f_{eq} is equal to that under equilibrium. Because the fugacity can be simply expressed by the pressure and fugacity coefficient ϕ (Eq.(4)), Eq.(3) will be appropriated by Eq.(5).

$$f = \phi \cdot P \tag{4}$$

$$r_{hy} = -\frac{\mathrm{d}n}{\mathrm{d}t} \approx aK^* \cdot RT\ln\left(\frac{P_g}{P_{eq}}\right) \tag{5}$$

where P_g and P_{eq} are the pressure in the gas phase and in equilibrium, respectively. Equation (5) was used to calculate the hydrate formation rate constant aK^* using the experimental overall gas hydrate formation rate r_{hy}, experimental gas phase pressure P_g, and available literature data for the gas-water-hydrate equilibrium pressure P_{eq} at the experimental temperature.

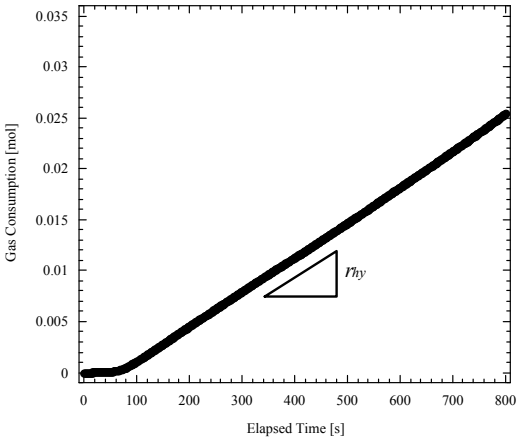

Fig. 3. Typical gas consumption line to calculate the overall hydrate formation rate (Tajima et al., 2010a).

Guest gas	aK^* [mol²/(s·J)]	P_g [MPa]	T [K]	Reactor	Reference
CH_2FCF_3	2.08 x 10^{-8}	0.20	276.2	Author's reactor	Tajima et al., 2010a
$CHClF_2$	4.40 x 10^{-8}	0.16	276.1	Author's reactor	Tajima et al., 2011a
Xe	1.2 x 10^{-8}	3.5	275	Stirred tank	Daimaru et al., 2007
CH_4	6.22 x 10^{-10}	6.0	275.15	Stirred tank	Daimaru et al., 2007
CO_2	1.33 x 10^{-7}	6.0	277.65	Stirred tank	Li et al., 2009
SF_6	4.26 x 10^{-9}	0.30	276.1	Author's reactor	Tajima et al., 2011b

Table 1. A type of gas hydrate formation rate constant of various guest gases.

Figure 3 shows typical gas consumption line in the semi-batch flow reactor. During the early stage of hydrate formation, the gas consumption is very small and unequable, which is parhaps because of the hydrate nucleation and unsteady state. The gas consumption becomes constant over time because the hydrate formation in the reactor reachs a steady state. Therefore, the overall hydrate formation rate can be calculated from the slope of the gas consumption line in the late stage. For instance, Table 1 summarizes the hydrate

formation rate constant from our studies and previous literatures in which hydrate formation rate is analysed with the similar equation. In the study using the stirred tank reactor, the hydrate formation rate constant have been calculated assuming that the gas-water sytem is sufficiently agitated, that is, $k_L >> k_f$. This assumption will be discussed later. The hydrate formation rate constant aK^* for freon gas hydrate (CH_2FCF_3, $CHClF_2$) are same order of magnitude as xenon hydrate, and two order of magnitude higher than that of CH_4 hydrate. The aK^* for SF_6 hydrate was one order of magnitude lower than above freon gas hydrate. The aK^* for CO_2 hydrate is highest among above other gas hydrates. It is guessed that the gas hydrate formation rate constant may be depending on the guest gas solubility in water, but further information and investigation are necessary to confirm this relationship.

4. Relation between hydrate formation and operation conditions

This section focuses on the relation between the gas hydrate formation and the operation conditions in the semi-batch flow reactor. The overall gas hydrate formation process is very affected by varying thermodynamic, mechanical, and chemical conditions. Thermodynamic conditions are operation pressure and temperature. The gas and water flow rate are defined as the mechanical conditions because the flow rates will vary the gas-water mixing state by mixing element in the semi-batch flow reactor. Here, it is regarded as the chemical conditions that the hydrate formation promoter is added in water phase, because the additives will vary the chemical potential of water phase and interfacial tension.

4.1 Thermodynamic conditions

In general, gas hydrate formation rate constant in stirred tank and agitation is analyzed assuming that $k_L >> k_f$, but this assumption requires careful attention. In the static mixing reactor, depending on the pressure and temperature conditions (thermodynamic conditions), a single non-hydrate and main two types of hydrate formation patterns are observed regardless of target gas species. Fig.4 shows typical gas hydrate formation patterns observed in the semi-batch flow reactor. In this case, the operation temperature is gradually decreased under constant pressure or P_g increases under constant T, constant gas and water flow rates. There is a gas-water system under outside pressure and temperature conditions of hydrate equilibrium curve (Fig.4a). Under near-equilibrium conditions, the hydrate formation is not occurred (Fig.4b). The non-hydrate formation condition is probably a meta-stable region. The two types of gas hydrate formation patterns, which are detailed below, are labelled “hydrate plug” (Fig.4d) and “hydrate slurry” (Fig.4c). The hydrate plug has a target gas hydrate “shell” formed on the surface of the bubbles. Whereas the hydrate slurry consists of very small target gas hydrate particles in water and a hydrate shell rarely formed on the bubble surface (Tajima et al., 2007). The observation results imply that the formed hydrate peels and sheds from the bubble surface. Three step mechanisms of hydrate film growth at gas-water interface have been reported (Sloan & Koh, 2008); (1) thin porous hydrate film formation, (2) thick porous hydrate film formation, and (3) nonporous hydrate film formation. Hydrate slurry pattern is perhaps formed by peering and shedding porous hydrate film at Steps 1 and 2. If nonporous hydrate formation is achieved due to higher hydrate growth rate, it is difficult to shed the film and hydrate plug formation will become dominant. Hydrate slurry turned into hydrate plug with an increase in operation pressure and a decrease in

operation temperature, which means the increase in the hydrate formation rate by increasing the driving force. Therefore, the assumption, $k_L >> k_f$, may be unsuitable depending on the hydrate formation patterns, and the hydrate shedding will be an important consideration for gas hydrate formation from gas-water system.

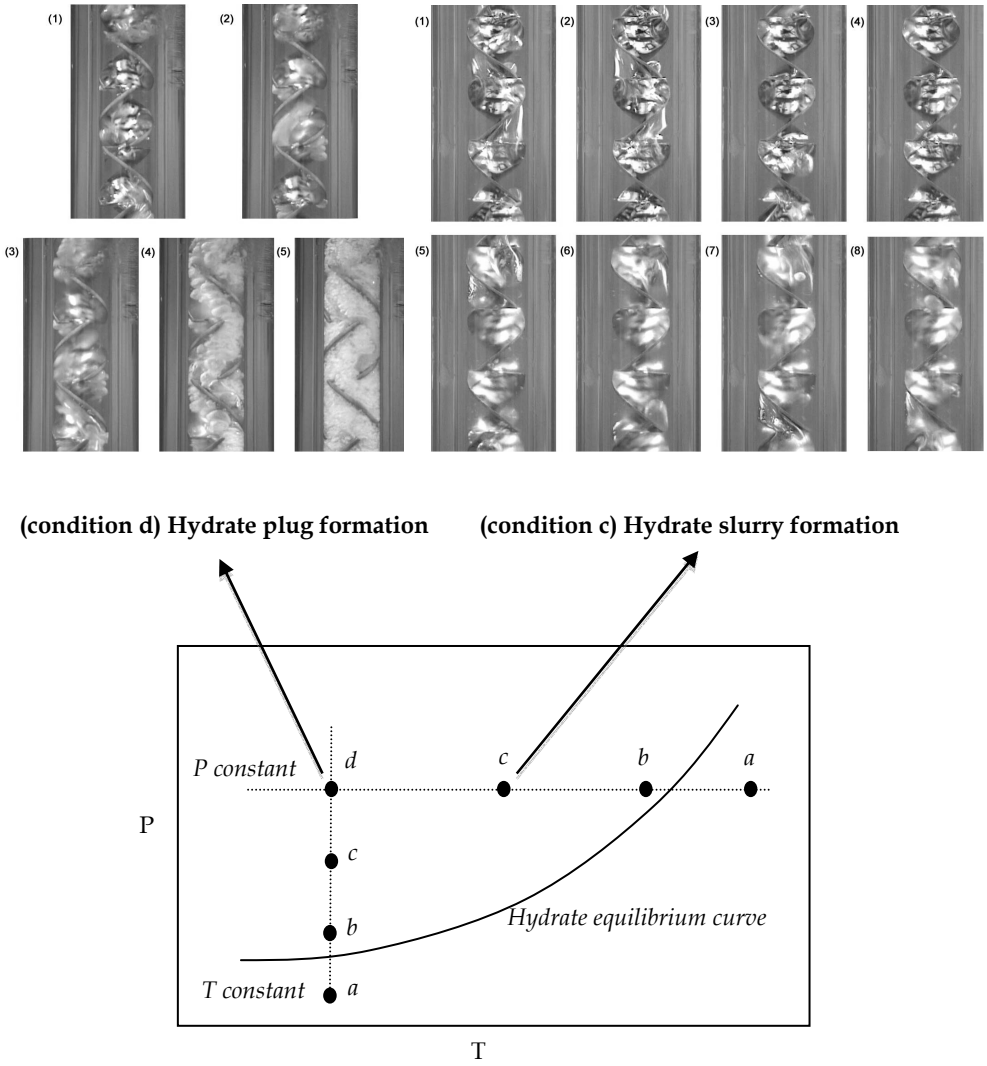

Fig. 4. Typical gas hydrate formation patterns in the semi-batch flow reactor. Conditions (*a*) and (*b*) are gas-water system, (*c*) and (*d*) are time-course in the hydrate formation, hydrate slurry and hydrate plug (Tajima et al., 2007)

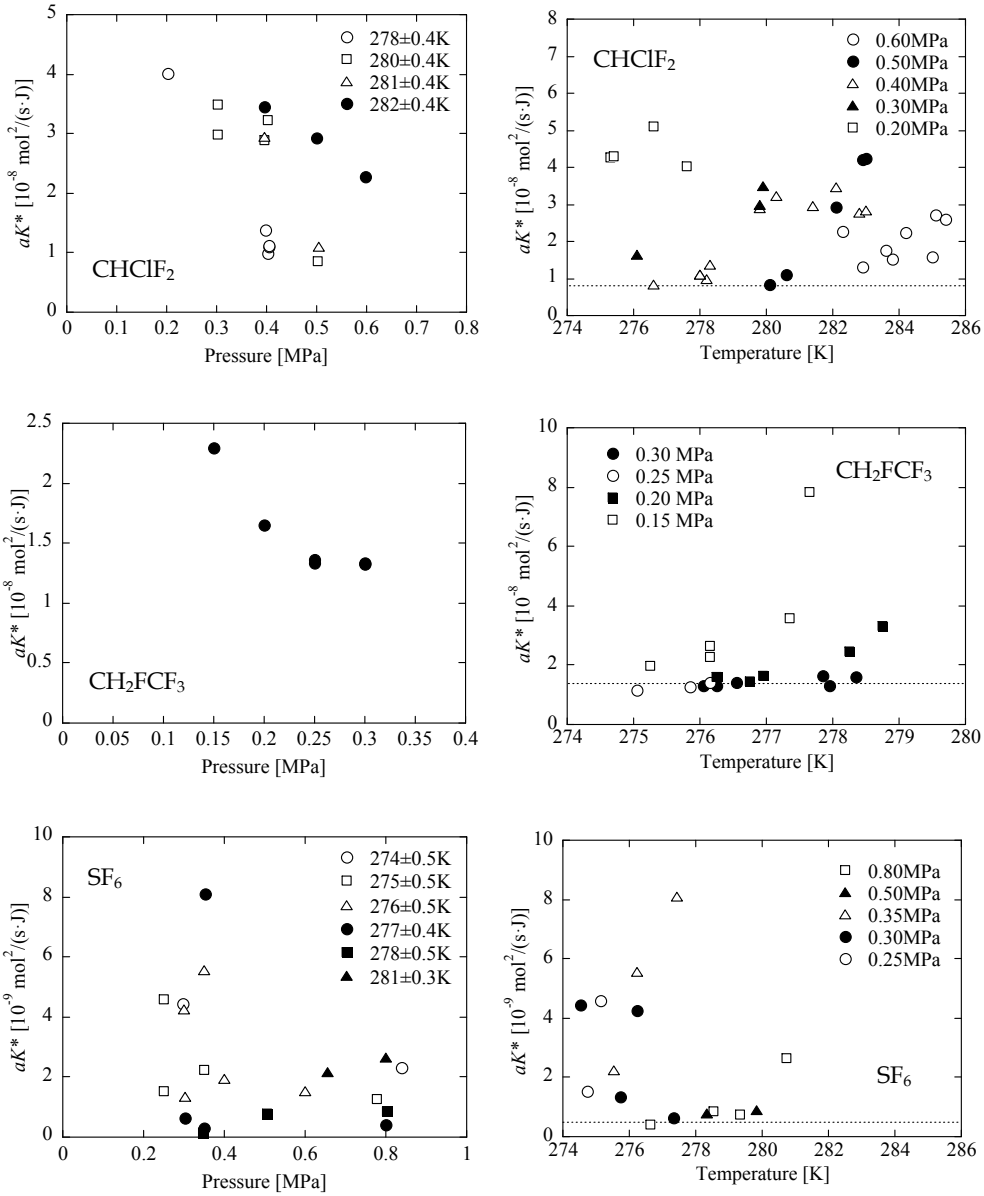

(a) operation pressure effect (b) operation temperature effect

Fig. 5. Effect of operation pressure and temperature on the aK^* value of various gas hydrate at constant another one (Tajima et al., 2010a, 2011b).

Fig.5 shows the effect of operation pressure on the aK^* value of various hydrates at constant temperature. Without respect to gas species the aK^* is decreased with an increase in the operation pressure but the data for SF_6 are scattered because of very small value. Although the hydrate formation rate may increase with operation pressure increase essentially, higher formation rate leads to form the strong hydrate shell on bubble surface. The formation of strong hydrate shell on bubble surface will prevent further hydrate formation, and thus reduce the aK^*. Fig.5 also shows the effect of operation temperature on the aK^* at constant operation pressure. These conditions are corresponding to the equilibrium pressure change. The aK^* value decreases and approaches a certain value with decreasing operation temperature at constant pressure. As well as operation pressure effect, hydrate shell formation will prevent further hydrate formation.

All present gas hydrate formation shows similar trend for thermodynamic condition change; the gas hydrate formation rate constant aK^* is decreased with the increase in operation pressure and decrease in temperature. These results indicate that the hydrate formation (nucleation and crystal growth) and mass transfer are largely inhibited by the formation of strong hydrate shell at bubble surface. The gas hydrate shell is easy to form on target gas bubble when no-mixing condition. Although the static mixing operation in the reactor can accelerate the hydrate shedding and thus keep the gas-water interfacial area (Tajima et al., 2005, 2010a), higher hydrate growth rate do not allow the strong hydrate shell to shed from bubble surface. The strong hydrate shell formation implies that the hydrate crystal growth rate is higher than the mass transfer rate (which includes the shedding rate of hydrate formed at the bubble surface). Therefore, in the higher pressure and lower temperature case, hydrate formation rate constant is apparently decreased. This trend is independent with hydrate structure, sI and sII (pure $CHClF_2$ gas forms sI hydrate, and pure CH_2FCF_3 and SF_6 gas are sII hydrate).

As presented above, this hydrate shell formation inhibits hydrate growth and is decreased the aK^* value because of two causal factors mainly; decrease in the interfacial area a, and resistance to mass transfer from gas to water phase k_L. Therefore, the peel of hydrate shell from bubble surface is a point well taken for a feasible hydrate formation mechanism.

4.2 Mechanical conditions

As discussed above, for gas hydrate formation, it is necessary to prevent hydrate growth inhibition by hydrate shell formation at the bubble surface. The author investigated varying both the flow rate and direction of water flow compared with gas flow in the reactor (Tajima et al., 2010a). When changing the mechanical condition, that is the change of water-flow rate like as gas adsorption equipment, water recycling in the hydrate reactor accelerates hydrate formation. With gas-water co-current flow, the interfacial area and mixing effect of the static mixer are expected to increase, although the residence time of bubbles in the reactor decreases because they rise faster with the water flow. In contrast, a counter-flow increases the residence time. The counter-flow will also result in easier peeling and shedding of the formed hydrate from the bubble surface because of an increase in the shear force on the gas-water interface. Both water flow directions can increase the hydrate formation rate.

Fig.6 shows the effect of water-flow rate (Q_L) on freon gas ($CHClF_2$ and CH_2FCF_3) hydrate formation rate constant. A positive water flow rate indicates co-current flow to the target gas, and a negative flow rate indicates counter flow. In the complete semi-batch system, the water flow rate is zero. The vertical axis is the ratio of aK^* to one at $Q_L = 0$. Despite holding

thermodynamic conditions (operation pressure and temperature) constant for each gas, the gas hydrate formation is accelerated. Hydrate slurry formation is observed for both water flow conditions even though the hydrate shell formation is observed at Q_L = 0. Without respect to gas species and hydrate structure, the water flow can avoid the hydrate shell formation. In the thermodynamic condition in which the hydrate slurry is formed at Q_L = 0 (0.15MPa for CH_2FCF_3), the aK^* value has low dependence on water flow rate. These results indicate that under mechanical mixing condition there are two important factors in acceleration of hydrate formation; the increase in the gas-water interfacial area from breaking up bubbles and a renewal of the gas-water interface. The increase in the gas-water interface occurs with breaking up the bubble covered with hydrate shell during water-gas cocurrent flow, and causes of the continued presence of a fresh interface in the counter flow by peeling hydrate formed on bubble surface. Under thermodynamic conditions formed hydrate slurry at Q_L = 0, the mechanical effect is low because they meet sufficient conditions (higher hydrate peeling and shedding rate than hydrate growth rate) necessary for avoidance of hydrate shell formation. The kinetic data indicates that the overall hydrate formation rate would be equal to the mass transfer rate including the rate of hydrate peeling from the gas bubble.

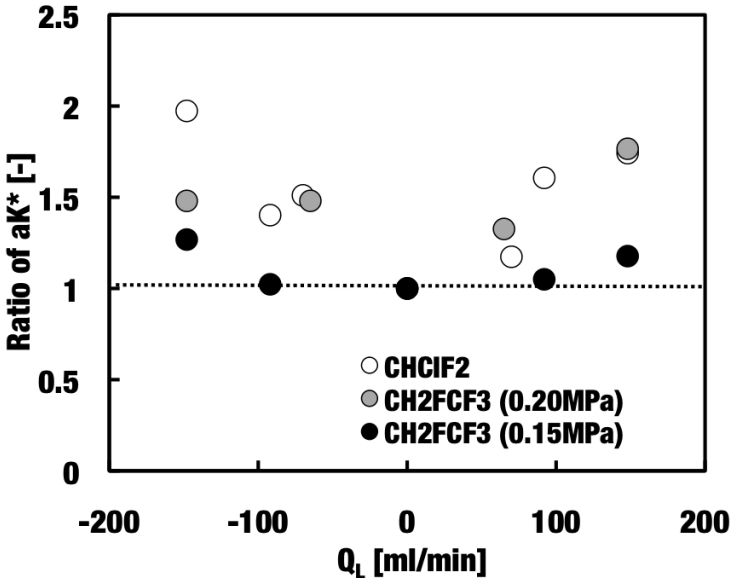

Fig. 6. Effect of water flow rate and direction on the aK^* at 275.8±0.3K for CH_2FCF_3 and 0.40MPa, 282.3±0.2K for $CHClF_2$ (Tajima et al., 2010a, 2011b).

4.3 Chemical conditions

A well-known promoter of gas hydrate is a surfactant, such as sodium dodecyl sulfate (SDS), of which the acceleration effect of the hydrate formation (Zhong & Rogers, 2000). Such surfactant additives, in the first place, have been used and investigated to prevent hydrate plug, namely hydrate inhibitor, in pipelines under certain pressure and temperature conditions because hydrate is a problem to the oil and gas industry (Huo et al., 2001). Effects

of surfactant such as SDS on gas hydrate formation have been widely investigated by many researchers, and the author has also investigated the ability of SDS to accelerate hydrate formation (Tajima et al., 2010b). Here focuses on the effect of SDS addition on the hydrate formation process under the SDS concentration below the critical micelle concentration (CMC). The surfactant additives do not shift the hydrate equilibrium condition and do not change hydrate structure, but these change the solution properties. Here the surfactant addition is defined as chemical condition for hydrate formation.

Fig.7 shows direct observation result of hydrate formation in SDS solution. From direct observation of hydrate formation, the hydrate shell is formed at the surface of bubbles in any SDS concentration, but the appearance of the hydrate shell and its behaviour are significantly changed with increasing the SDS concentration. Under the certain pressure and temperature conditions, $CHClF_2$ hydrate plug including bubble covered with the strong hydrate shell is formed (Fig.7a). Without SDS, smooth and homogenous hydrate film is formed at the surface of bubbles. Target gas is trapped in the rigid hydrate shell, and the bubbles are agglomerated each other to form a grape-like structure. Adding a small amount of SDS in water, hydrate shell formed is easily disappeared (Fig.7b). By the addition of SDS, the hydrate shell forms with rougher and heterogeneous surface; the hydrate shell seems to become loosely, and easily collapsed by the buoyant motion of target gas trapped in the shell.

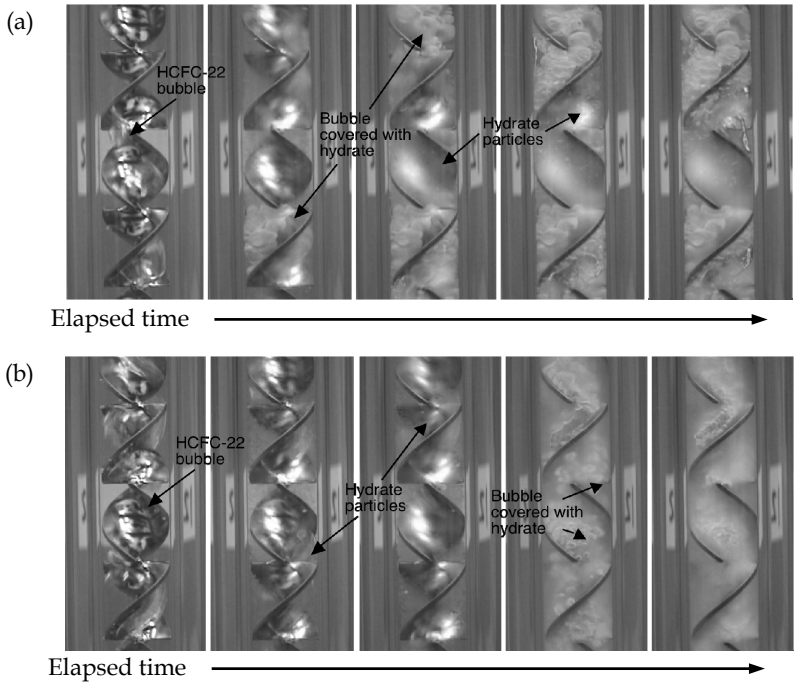

Fig. 7. $CHClF_2$ hydrate formation in water (a) and 400ppm SDS aqueous solution (b) at 0.40MPa, 283K (Tajima et al., 2010b).

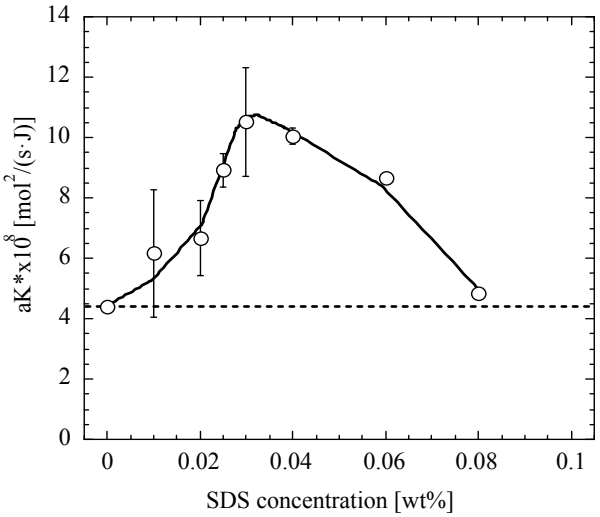

Fig. 8. Effect of SDS concentration on $CHClF_2$ hydrate formation rate constant. (Tajima et al., 2011a)

From point of view of hydrate formation kinetics, the promoting effect and the inhibition effect on gas hydrate formation emerged in each SDS concentration below CMC. Fig.8 shows the effect of SDS concentration on $CHClF_2$ hydrate formation rate constant. The value of aK^* is increased up to 0.03wt% SDS solution. The aK^* value at 0.03wt% SDS solution is 10.5 x 10^{-8} $mol^2/(s \cdot J)$, which is about 2.4 times larger than that in water (0wt% SDS). The aK^* value is gradually decreased as SDS concentration further increased. At 0.08wt% of SDS concentration, the aK^* value returns nearly to the level in water. There results have a similar trend to the experimental results using sodium alkylsulfonates (Daimaru et al., 2007) as promoting additive.

One of factors for promoting effect is the interfacial area, a, expansion came from the interfacial tension reduction. SDS addition in water is decreased in the surface tension of water, and thus gas bubble size before hydrate formation reduces with increasing additive concentration. In addition, SDS adsorption on bubble and hydrate surface would accelerate forming rough hydrate and peeling easily hydrate formed, that is, the increase in the overall kinetic constant, K^*. The SDS concentration range shown the promoting effect is close to that of the mono- and multi-layer adsorption of SDS on hydrate surface but the different guest molecule species (Zhang et al., 2008; Lo et al., 2008). SDS as a surfactant will promote not only the crystal growth but also the gas-liquid contact, mass transfer, with adsorption. Thus, the enhancement of the gas hydrate formation by the SDS addition can be attributed to the increase of both a and K^*.

Despite the a value is increased with increasing SDS concentration, the aK^* value is decreased with increase in SDS concentration, and furthermore, returns to the level in water. The aK^* value reduction implies that the decrease in the overall kinetic constant K^* counteracts the effect of the interfacial area expansion, which corresponds to inhibition of mass transfer or crystal growth. Although SDS cannot form own hydrate, the inhibition effect of SDS as anionic surfactant will come from their adsorption on bubbles and hydrate

particles. The previous researchers (Daimau et al., 2007) explained that the inhibition effect of the anionic surfactant is due to cover the gas-water interface with surfactant molecules. Recent research reported by zeta potential measurement that SDS adsorbs hydrate particle surface strongly and the SDS adsorption amount increases with increase in the SDS concentration (Zhang et al., 2008; Lo et al., 2008). Although zeta potential measurement for $CHClF_2$ hydrate in SDS solution cannot be carried out, the similar SDS adsorption will occur on $CHClF_2$ hydrate surface because of SDS adsorption via hydrogen bond. The author have observed the morphological change, from smooth and homogeneous to rougher and heterogeneous, of $CHClF_2$ hydrate surface that is more noticeable for the conditions with the SDS concentration higher than about 250 ppm (equal to 0.25 wt%) (Tajima et al., 2010b). The direct observation result implies that SDS molecules will absorb bubble and hydrate surface and produce a significant change in characteristic of the hydrate formed on the bubble surface for the SDS concentration. In higher SDS concentration, therefore, heavy adsorption of SDS molecules on bubbles/hydrate particles surface rather prevents $CHClF_2$ hydrate strongly from forming and growing despite the increased interfacial area with the decease in surface tension.

4.4 Feasible mechanism of hydrate formation in static mixing-type flow reactor

From aforementioned above, the hydrate formation process is greatly depending on the thermodynamic, mechanical, and chemical conditions; the condition effect is appeared with the appearance of hydrate formed. The data obtained for $CHClF_2$, CH_2FCF_3, and SF_6 appears to be necessary to explain the mechanism of hydrate formation in the static mixing-type flow reactor. Here, the author can estimate a feasible hydrate formation mechanism in the static mixing type flow reactor.

The hydrate formation rate is well known to consist of crystal growth rate and dissociation rate (mass transfer rate). In addition, the author requires consideration of the hydrate shedding rate to overall hydrate formation (Tajima et al., 2005, 2010b). Therefore, the hydrate formation rate will consist mainly of the hydrate formation rate (nucleation and crystal growth that is dependant on thermodynamic conditions) and the mass transfer rate (target gas dissociation in water and target gas hydrate shedding from bubble surface that is dependant on mechanical conditions).

Fig. 9 shows the speculated mechanisms for hydrate formation in static mixing-type flow reactor according to experimental results (Tajima et al., 2004, 2005, 2011b). The r_d, r_f, and r_s are rates of target gas dissociation to water, target gas hydrate nucleation and growth, and target gas hydrate particle/film shedding, respectively. The Case A-C situations are made due to the balance among the thermodynamic, mechanical, and chemical conditions in the reactor.

Case A is for gas hydrate slurry formation. In this case, the apparent interfacial area between water and target gas phases, a, is large enough to dissociate target gas from bubble to water phase because of $r_s > r_f$. As a result, the interfacial area keeps a constant nearly and the target gas dissociation is inhibited very little by porous hydrate formation. The overall hydrate formation rate r_{hy} depends on the K^* value (that is, k_L and k_f in Eq.(2)) mainly. Because continuous hydrate particle formation can be occurred, the overall hydrate formation rate constant aK^* is high. This situation is relation to mild thermodynamic conditions (lower pressure and higher temperature), high mechanical mixing conditions (high water flow rate), and lower additive concentration.

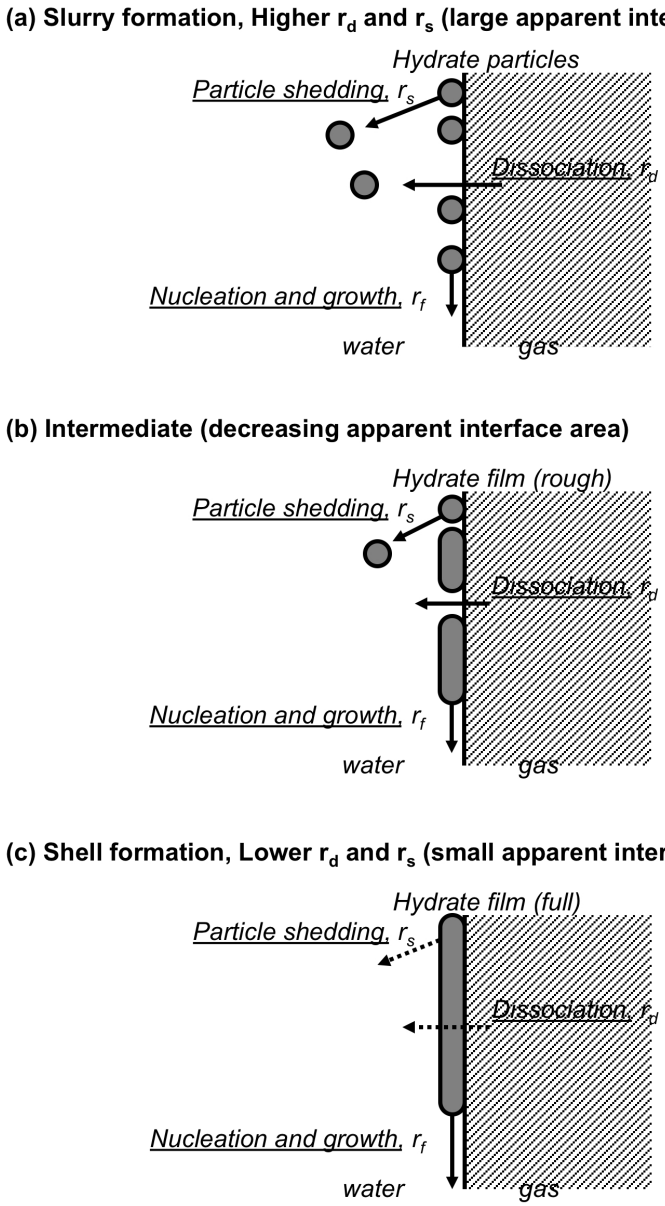

Fig. 9. Speculated mechanisms of hydrate formation in static-mixing type flow reactor (Tajima et al., 2011b)

Case C is for strong hydrate shell formation. In this case, the target gas bubbles are rapidly covered with strong hydrate shell because the hydrate formation rate r_f is relatively higher

than shedding rate r_s. The apparent interfacial area between gas and water, a, is considerably restricted and also the dissociation rate r_d is considerably decreased (for example, a similar situation have been observed in the case of CO_2 hydrate formation (Ogasawara et al., 2001)). As a result, there is little the further hydrate formation, and thus the overall hydrate formation rate constant aK^* is low depending on r_d and r_s. This hydrate formation occurs under hard thermodynamic conditions (higher pressure and lower temperature) and lower mechanical mixing conditions. Although the additive addition can prevent the strong hydrate shell, sufficient mechanical condition is necessary to form further hydrate with accelerating the hydrate shedding process.

Case B is for porous and rough hydrate particle/film formation and the intermediate case between Cases A and C. Hydrate particles and partial hydrate film are formed on bubble surface. The film pore and void channels allow target gas to diffuse into water phase (Sloan & Koh, 2008), and partial hydrate shedding is occurred on bubble surface. The apparent interfacial area between target gas and water, however, is decreased and the dissociation of target gas into water is limited by rough hydrate film formation. As a result, the aK^* value (not only a but also K^* values) is lower than that for Case A. In another case, higher concentration of additive in water phase will contribute to keep porous and rough hydrate film (Case B) with preventing hydrate growth (Tajima et al., 2010b). That is, additives (like as surfactants) adsorbing on bubble surface can keep the gas dissociation and the hydrate shedding rates.

If the solubility in water is very low, the dissociation rate (mass transfer rate) will be low. As a result, the overall formation rate is low. For example, relatively high solubility of CH_2FCF_3 and $CHClF_2$ (near CO_2 solubility in water) leads to higher dissociation rate and hydrate formation rate. On the other hand, lower solubility of SF_6 (near CH_4 solubility in water) cause lower dissociation rate. This trend is in agreement with the data obtained in this study (Table 1). The dissociation rate may be a rate-controlling step. Further investigation is necessary for hydrate formation rate equation.

5. Conclusion

The gas hydrate formation kinetics is investigated in the semi-batch flow reactor equipped with static mixer, and thus discusses the hydrate formation process based on the experimental data by varying thermodynamic, mechanical, and chemical conditions. In the flow reactor, there are multiple flows with gas-liquid-solid system, and the gas hydrate formation process is overly complicated. There are mainly two hydrate formation patterns in the reactor; hydrate slurry and hydrate plug. According to the experimental observation and results, the gas hydrate formation process consists of the hydrate nucleation, hydrate growth, hydrate shedding, and gas dissociation processes. Especially, the idea of the hydrate shedding from the interface is very important. The balance among these processes is altered under thermodynamic, mechanical, and chemical conditions. For the application of the gas hydrate technologies, it is necessary to not only convert sufficiently (mixture) gas to hydrate but also form hydrate appearance to transport and apply easy. Many researchers have investigated about the thermodynamic and chemical conditions in stirred tank, but the mechanical conditions have been less noticed. The static mixer in the flow reactor improves the mixing function in the reactor. Although it is perhaps difficult to find out the essential hydrate formation rate, the author expects that these results help the engineering application of gas hydrate.

6. Acknowledgment

The author is greatly thanks Professor Akihiro Yamasaki (Seikei University, Japan), Dr. Fumio Kiyono (AIST, Japan), and Professor Kazuaki Yamagiwa (Niigata University, Japan) for variable discussions. A part of this work was supported through the Grant-in-Aid for Young Scientists B (No.21710074), Japan, and Sasaki Environment Tec. Found, Japan. The author appreciates student's cooperation, Mr. Yasuhiro Oota, Mr. Hiroki Yoshida, Mr. Toshinao Furuta (graduated from Niigata University, Japan), Mr. Yosuke Nakajima (graduated from Kogakuin University, Japan), and Mr. Toru Nagata (finished Graduate School of University of Tsukuba, Japan).

7. References

Daimaru, T.; Yamasaki, A. & Yanagisawa, Y. (2007). Effect of Surfactant Carbon Chain Length on Hydrate Formation Kinetics, *Journal of Petroleum Science and Engineering*, Vol.56, No.1-3, (March 2007), pp.89-96, ISSN 0920-4105

Englezos, P.; Kalogerakisa, N.; Dholabhaia, P.D. & Bishnoi, P.R. (1987) Kinetics of Formation of Methane and Ethane Gas Hydrates, *Chemical Engineering Science*, Vol.42, No.11, (November 1987), pp.2647-2658, ISSN 0009-2509

Fukumoto, K.; Tobe, J.; Ohmura, R. & Mori, Y.H. (2001). Hydrate Formation Using Water Spraying in a Hydrophobic Gas: A Preliminary Study, *AIChE Journal*, Vol.47, No.8, (August 2001), pp.1899-1904, ISSN 0001-1541

Godfrey J. C. (1997). Static Mixer, In: *Mixing in the process industries*, Harnby, N.; Edwards, M. F.; Nienow, A. W. (Eds.), 225-249, Butterworth-Heinemann, ISBN 0-7506-3760-9, Oxford, UK.

Gudmundsson, J. S. & Børrehaug A. (1996). Frozen Hydrate for Transport of Natural Gas, *Proceedings of 2nd International Conference on Natural Gas Hydrates*, pp439-446, Toulouse, France, June2-6, 1996.

Hashemi, S.; Macchi, A. & Servio, P. (2009) Gas-Liquid Mass Transfer in a Slurry Bubble Column Operated at Gas Hydrate Forming Conditions. *Chemical Engineering Science*, Vol.64, No.19, (October 2009), pp.3709-3716, ISSN 0009-2509

Huo, Z.; Freer, E.; Lamar, M.; Sannigrahi, B. ; Knauss, D. M. & Sloan E. D. (2001). Hydrate Plug Prevention by Anti-Agglomeration, *Chemical Engineering Science*, Vol.56, No.17, (September 2001), pp.4979-4991, ISSN 0009-2509

Kang, S.-P. & Lee, H. (2000). Recovery of CO_2 from Flue Gas Hydrate: Thermodynamic Verification Through Phase Equilibrium Measurements, *Environmental Science and Technology*, Vol.34, No.20, (October 2000), pp.4397-4400, ISSN 0013-936X

Lee, H. ; Lee, J. W.; Kim, D. Y.; Park, J.; Seo, Y. T.; Zeng, H.; Moudrakovski, I. L.; Ratcliffe, C. I. & Ripmeester, J. A. (2005). Tuning Clathrate Hydrates for Hydrogen Storage, *Nature*, Vol.434, 7 April, (April 2005), pp.743-746, ISSN 0028-0836

Li, S.; Fan, S.; Wang, J.; Lang, X. & Liang, D. (2009). CO_2 Capture from Binary Mixture via Forming Hydrate with the Help of Tetra-n-Butyl Ammonium Bromide, *Journal of Natural Gas Chemistry*, Vol.18, No.1, (March 2009), pp.15-20, ISSN 1003-9953

Lo, C. ; Zhang, J.S.; Somasundaran, P.; Lu, S.; Couzis, A. & Lee, J.W. (2008). Adsorption of Surfactants on Two Different Hydrates, *Langmuir*, Vol.24, No.22, (November 2008), pp.12723-12726, ISSN 0743-7463

Luo, Y.-T.; Zhu, J.-H.; Fan, S.-S. & Chen, G.J. (2007). Study on the Kinetics of Hydrate Formation in a Bubble Column, *Chemical Engineering Science*, Vol.62, No.4, (February 2007), pp.1000-1009, ISSN 0009-2509

Nagata, T.; Tajima, H.; Yamasaki, A.; Kiyono, F. & Abe, Y. (2009). An Analysis of Gas Separation Processes of HFC-134a from Gaseous Mixtures with Nitrogen-Comparison of Two Types of Gas Separation Methods, Liquefaction and Hydrate-Based Methods, in Terms of the Equilibrium Recovery Ratio, *Separation and Purification Technology*, Vol.64, No.3, (January 2009), pp.351-356, ISSN 1383-5866

Ogasawara, K.; Yamasaki, A. & Teng, H. (2001). Mass transfer from CO_2 Drops Traveling in High-Pressure and Low-Temperature Water, *Energy & Fuels*, Vol.15, No.1, (January 2001), pp.147-150, ISSN 0887-0624

Sloan, E. D.; Koh, C. A. (2008). *Clathrate Hydrates of Natural Gases, 3rd Ed.,* CRC Press, ISBN 978-0-8493-9078-4, Boca Raton, Florida, USA.

Szymcek, P.; McCallum, S.D.; Taboada-Serrano, P. & Tsouris, C. (2008). A Pilot-Scale Continuous-Jet Hydrate Reactor, *Chemical Engineering Journal*, Vol.135, No.1-2, (January 2008), pp.71-77, ISSN 1385-8947

Tajima, H.; Yamasaki, A. & Kiyono, F. (2004). Continuous Formation of CO_2 Hydrate via a Kenics-type Static Mixer, *Energy & Fuels*, Vol.18, No.5, (September 2004), pp.1451-1456, ISSN 0887-0624

Tajima, H.; Yamasaki, A. & Kiyono, F. (2005). Effects of Mixing Functions of Static Mixers on the Formation of CO_2 Hydrate from the Two-Phase Flow of Liquid CO_2 and Water, *Energy & Fuels*, Vol.19, No.6, (November 2005), pp.2364-2370, ISSN 0887-0624

Tajima, H.; Nagata, T.; Yamasaki, A.; Kiyono, F. & Masuyama, T. (2007) Formation of HFC-134a Hydrate by Static Mixing, *Journal of Petroleum Science and Engineering*, Vol.56, No.1-3, (March 2007), pp.75-81, ISSN 0920-4105

Tajima, H.; Nagata, T.; Abe, Y.; Yamasaki, A.; Kiyono, F. & Yamagiwa, K. (2010a). HFC-134a Hydrate Formation Kinetics During Continuous Gas Hydrate Formation with a Kenics Static Mixer for Gas Separation, *Industrial and Engineering Chemistry Research*, Vol.49, No.5, (March 2010), pp.2525-2532, ISSN 0888-5885

Tajima, H.; Kiyono, F. & Yamasaki, A. (2010b). Direct Observation of the Effect of Sodium Dodecyl Sulfate (SDS) on the Gas Hydrate Formation Process in a Static Mixer, *Energy & Fuels*, Vol.24, No. 1, (January 2010), pp.432-438, ISSN 0887-0624

Tajima, H.; Oota, Y. & Yamagiwa, K. (2011a). Effects of "Promoter" on Structure I Hydrate Formation Kinetics, In: *Physics and Chemistry of Ice 2010*, Y. Furukawa, G. Sazaki, T. Uchida, N. Watanabe (Ed.), pp.253-259, Hokkaido University Press, ISBN 978-4-8329-0361-6, Sapporo, Japan.

Tajima, H.; Oota, Y.; Yoshida, H. & Yamagkiwa, K. (2001b). Experimental Study for Gas Hydrate Formation and Recovery of Fluorine-Containing Compound in Static Mixing-type Flow Reactor, *Proceedings of 7th International Conference on Gas Hydrate*, Edinburgh, Scotland,UK, July 17-22, 2011.

Warzinski, R. P.; Riestenberg, D.E.; Gabitto, J.; Haljasmaa, I.V.; Lynn, R.J. & Tsouris, C. (2008). Formation and Behavior of Composite CO_2 Hydrate Particles in a High-Pressure Water Tunnel Facility, *Chemical Engineering Science*, Vol.63, No.12, (June 2008), pp.3235-3248, ISSN 0009-2509

Zhang, J.S.; Lo, C.; Somasundaran, P.; Lu, S.; Couzis, A. & Lee, J.W. (2008). Adsorption of Sodium Dodecyl Sulfate at THF Hydrate/Liquid Interface, *Journal of Physical Chemistry C*, Vol.112, No.32, (August 2008), pp.12381-12385, ISSN 1932-7447

Zhong, Y. & Rogers, R. E. (2000). Surfactant effects on gas hydrate formation, *Chemical Engineering Science*, Vol. 55, No.19, (October 2000), pp. 4175-4187, ISSN 0009-2509

16

Study of the Mass Transport on Corrosion of Low Carbon Steel Immersed in Sour Solution Under Turbulent Flow Conditions

R. Galvan-Martinez[1], R. Orozco-Cruz[1],
J. Mendoza-Flores[2], A. Contreras[2] and J. Genesca[3]
[1]*Unidad Anticorrosión, Instituto de Ingeniería*
Universidad Veracruzana, Veracruz
[2]*Instituto Mexicano del Petróleo, San Bartolo Atepehuacan*
[3]*Departamento de Ingeniería Metalúrgica, Facultad de Química*
Universidad Nacional Autónoma de México
México

1. Introduction

A corrosion process can be influenced, in different ways, by the relative movement between the metal and the corroding environment. This relative movement can increase the heat and mass transfer of reactants towards and from the surface of the corroding metal, with a consequent increase in the corrosion rate. Also, if solid particles are present, removal of protective films, erosion and wear on the metallic surface can occur. The corrosion of the metallic structure under turbulent flow is complex, but this problem has been studied mainly in the oil industry (Garnica-Rodriguez et al., 2009; Genesca et al., 2010; Mora-Mendoza et al., 2002; Papavinasam et al., 1993; Poulson, 1993), where, the flow and some gases are very important in the behaviour of the phenomenon processes. This oil industry has processes that involve the movement of corrosive liquids in metallic structures, for example, the transport of mixtures of liquid hydrocarbons and gas with water through pipes. Therefore the influence of flow on the corrosion processes is an important issue to be considered in the design and operation of industrial equipment. This influence is complex and many variables are involved. Many observations of flow-accelerated corrosion problems have been documented (Dean, 1990; Garverick, 1994; Poulson, 1993). One aim that has been so much studied in the petroleum industry is the effect of flow and dissolved gases, such as hydrogen sulphide (H_2S) and carbon dioxide (CO_2).

The most common type of flow conditions found in industrial processes is turbulent and according to increasing of the necessity to describe the corrosion of metals in turbulent flow conditions some laboratory hydrodynamic systems have been used with different degrees of success (Poulson, 1983, 1993, 1994). Among these hydrodynamic systems, rotating cylinder electrodes (RCE), pipe segments, concentric pipe segments, submerged impinging jets and close-circuit loops have been used and have been important in the improvement of the

understanding of the corrosion process taking place in turbulent flow conditions (Liu et al., 1994; Lotz, 1990; Schmitt et al., 1991; Silverman, 1984, 1988, 1990).

The use of the RCE, as a laboratory hydrodynamic test system, has been gaining popularity in corrosion studies (Nesic et al., 1995, 2000). This popularity is due to its characteristics, such as, it operates mainly in turbulent flow conditions; it has a well understood mass transfer properties and it is relatively easy to construct and operate (Gabe, 1974; Schlichting & Gersten, 1979; Gabe & Walsh, 1983; Poulson, 1983). The critical Reynolds number, *Re*, for the transition from laminar to turbulent flow is 200 approximately, for a smooth surface laboratory RCE (Gabe, 1974; Gabe & Walsh, 1983; Poulson, 1983, 1993; Galvan-Martinez et al., 2010). This Reynolds value will be equivalent to a rotation rate ≈ 38 rpm, for a cylinder of 0.01 m of diameter immersed in a fluid of ν = 1.0E-06 m^2s^{-1} (e.g. pure water). When the RCE is immersed in a fluid and rotated at a very low rotation rate the fluid moves in concentric circles around the cylinder (laminar conditions). As the rotation rate of the cylinder increases the flow pattern is disrupted, cellular flow patterns, known as "Taylor vortices", appear and the turbulent condition develops. These vortices enhance the mass, momentum and heat transfer at the rotating electrode (Gabe, 1974; Gabe & Walsh, 1983). In 1954, some researchers published what it is now considered as the basic study on the mass transfer characteristics of the RCE (Eisenberg et al., 1954).

The Reynolds number for a RCE is given by the following expression

$$Re_{RCE} = \frac{u_{RCE} d_{RCE}}{\nu} = \frac{u_{RCE} d_{RCE} \rho}{\mu} \tag{1}$$

Where u_{RCE} is the peripheral velocity of the RCE, d_{RCE} is the diameter of the RCE, ρ and μ are the density and viscosity of the environment, respectively. It is clear from this equation that there is a linear relationship between the Reynolds number and the rotation rate of the electrode. Figure 1 shows the correlation between the rotation rate of the electrode and the equivalent Reynolds number.

The RCE in corrosion laboratory studies is an useful tool for the understanding of mass transfer processes, effects of surface films, inhibition phenomena, etc., (Galvan-Martinez et al., 2010; Mendoza-Flores et al., 2002) taking place in turbulent flow conditions. However, the use of the RCE has been questioned by some researchers (Efird et al., 1993), due to the differences found between the values of corrosion rates measured on pipe flow electrodes and on the RCE. The reasons for these differences are still not well understood. However, some works have provided ideas on the explanation of this apparent difference (Mendoza-Flores, 2002; Mendoza-Flores & Turgoose, 2002; Turgoose et al., 1995). One of the main objectives of using hydrodynamic test systems in laboratory studies of turbulent flow is to obtain a series of criteria, aimed to help in the explanation and prediction of real life situations. In order to attain this, the data measured in one hydrodynamic system has to be compared, somehow, with the data measured in other hydrodynamic systems or with data obtained in real life systems. It has been suggested that the comparison among the results obtained in different hydrodynamic systems can be made by means of the wall shear stress (τ_w). This suggestion considers that, when two hydrodynamic systems are at the same value of τ_w, at the same flow regime (turbulent or laminar), the same flow velocities near the surface and mass transfer conditions, prevail (Silverman, 1990).

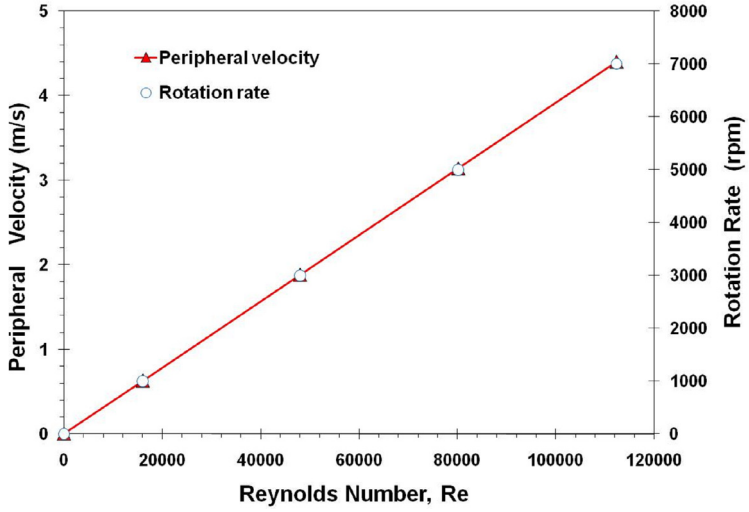

Fig. 1. Equivalence of rotation rate (rpm) and peripheral velocity (m/s) of the electrode and the calculated Reynolds number.

Dimensionless analysis using mass transfer concepts showed that the corrosion when controlled by diffusion of one of the species between the bulk fluid and the surface could be modelled completely by the rate of mass transfer of the rate limiting species and the Reynolds (*Re*), Sherwood (*Sh*) and Schmidt numbers (*Sc*) (Dean & Grab, 1984; Ellison & Schmeal, 1978; Ross et al., 1966). In general, the effect of flow can be used to determine if corrosion is under activation, diffusion or mixed control.

2. Experimental

2.1 Test environment

All experiments were carried out at 60°C, under static conditions (0 rpm) and turbulent flow conditions and, at the atmospheric pressure of Mexico City (0.7 bars). Two aqueous solutions were used as test environment: NACE brine (National Association of Corrosion Engineers, 1996) and a 3.5 % NaCl solution. These test environments were selected due to the fact that most of the H_2S corrosion laboratory tests are carried out in this solutions. The solutions were prepared using distilled water and reagent grade chemicals. In order to remove oxygen from the solution, N_2 gas (99.99%) was bubbled into the test solution for a period of 30 minutes before each experiment was carried out. After oxygen removal, H_2S gas (99.99%) was bubbled into the test solution until saturation was reached. H_2S bubbling was maintained during all the experimentation.

The measured saturation pH was 4.4 for the NACE brine and a pH of 4.5 for the 3.5% NaCl solution. In order to determine the purging time needed to remove all O_2 from the solution, a rotating cylindrical platinum electrode was cathodically polarized in a 1 M sodium sulphate solution, at room temperature and at different rotation rates. It was established that

the region associated to the mass transfer reduction of oxygen, on the cathodic polarization curve, disappeared after 30 minutes of purging time.

2.2 Experimental set up

All electrochemical measurements were carried out in an air-tight three-electrode electrochemical glass cell. Cylindrical working electrodes were used in all experiments. These cylinders were made of API X52 steel (American Petroleum Institute, 2004). The working electrode (WE) was machined from the parent material API X-52 and it had a diameter of 0.0012 m. The total exposed area of the working electrodes was 5.68E-04 m^2 and 3.4E-04 m^2 for static and dynamic conditions respectively. As reference electrode (RE) a saturated calomel electrode (SCE) was used and a sintered graphite rod was used as auxiliary electrode (AE). The experimental set up is schematically shown in Figure 2.

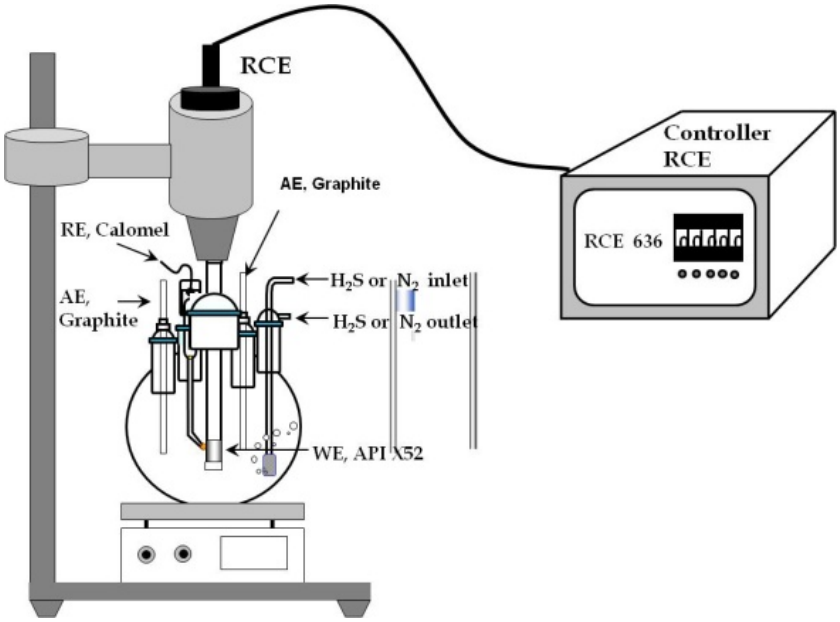

Fig. 2. Experimental set-up used in the electrochemical measurement.

Prior to each experiment, the steel working electrode was polished up to 600 grit SiC paper, cleaned in deionised water and degreased with acetone. All electrochemical tests were carried out on clean samples.

Hydrodynamic conditions were controlled using a Perking-Elmer EG&G Model 636 Rotating Cylinder Electrode system. In dynamic conditions or turbulent flow conditions, the

rotation rates tested were 1000, 3000, 5000 and 7000 rpm. It is important to point out that the electrochemical measurements were carried out also at static condition or 0 rpm.

2.3 Electrochemical measurements

A Potentiostat / Galvanostat was used in all the electrochemical tests. Potentiodynamic polarization curves were recorded at a sweep rate of 0.001 mVs^{-1}, starting the potential sweep at the rest potential or corrosion potential (E_{corr}) towards more cathodic potentials. It is important to mention that in order to get a better cathodic study, the cathodic polarization curve (CPC) and anodic polarization curve (APC) were made by separated.
The overpotential range used in the CPC was from +0.015 V to -0.5 V versus to corrosion potential (E_{corr}), on the other hand, the APC was recorded using an overpotential range between -0.015 to 0.5 V versus E_{corr}.
Laboratory tests indicated that, slower scan rates produced have not significant change on the measured current. In order to minimize the effect of the solution resistance a Lugging capillary was used. All the experiments were carried out by triplicate in order to check the reproducibility of the results. A plot of three representative measured plots is presented; this is due to the fact that it was found that the experimental variations of the measurements were negligible.

3. Experimental results and discussion

The corrosion of low carbon steel in brine solution containing H_2S has been investigated by several authors (Arzola et al., 2003; Galvan-Martinez et al., 2005; Vedage et al., 1993) using electrochemical techniques such as linear polarization resistance, electrochemical impedance spectroscopy and polarisation curves in quiescent systems. Even though it has been recognised for many years that hydrodynamic effects are often important in determining the rate of corrosive attack on metals, little attention has been paid to the influence of hydrodynamic factors on the analysis of the kinetics of materials degradation. Several approaches have been used to obtain some assessment of the magnitude of these hydrodynamic effects. Many hydrodynamic systems have been applied in the corrosion studies and one of these hydrodynamic systems is the RCE.
Researches about these hydrodynamic systems (Arzola, 2006; Galvan-Martinez, 2005, 2007) have shown that the corrosion mechanism for carbon steel exhibits a significant dependence on mass transfer. This has led various workers to suggest the use of dimensionless analysis as a means of relating laboratory- scale experiments to industrial-scale corrosion behaviour.
For an accurate study of the influence of flow velocity upon the corrosion rate of fluids in motion, the hydrodynamic conditions must be well-defined. The Reynolds number is a dimensionless number dependent on the fluid velocity or the electrode rotation rate according to the density and viscosity of the fluid. It is a characteristic dimension in order to define the type of flow. At low velocities, i.e. at low *Re*, a stable or laminar flow is encountered. Assuming the fluids under consideration to be Newtonian and incompressible in nature, the shear stress (τ) at any point in a laminar flow is given by:

$$\tau = \mu \frac{d\mathrm{u}}{dy} \tag{2}$$

If the velocity is increased, at a critical Reynolds number (Re_{crit}), the flow becomes turbulent and an additional mechanism of momentum mass transfer appears which is caused by rapid and random fluctuations of velocity about its average value. The Re_{crit} for the transition between laminar and turbulent flow will vary depending on the geometry and Re_{crit} for usual pipe flow has been experimentally found to be around 2100 (Rahmani & Strutt, 1992).

Figure 3 shows the measured values of corrosion potential (E_{corr}) as a function of Reynolds number. E_{corr} was obtained on the API X52 steel cylindrical samples immersed in NACE brine and 3.5% NaCl solution saturated with H_2S at different rotation rates (0, 1000, 3000, 5000 and 7000 rpm) and 60 °C. This figure shows that, for both solutions, E_{corr} has the general trend to increase with Re_{RCE}, with exception of the range 50000< Re_{RCE} <80000 approximately, where it decreases.

The measured E_{corr} corresponding to the 3.5% NaCl solution increased from values of –0.739 V to –0.714 V approximately, whereas in NACE brine increased from values of –0.734 to –0.719 V approximately.

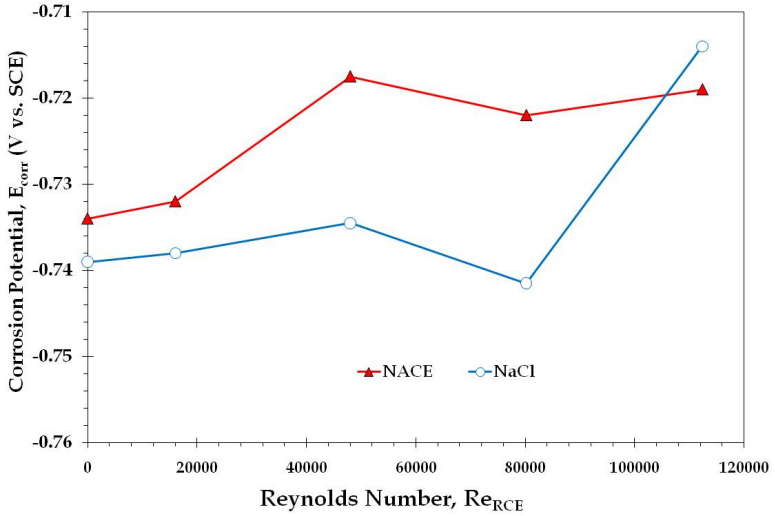

Fig. 3. E_{corr} as a function of different *Re* numbers of the cylindrical electrode in NACE brine and 3.5% NaCl solution at 60°C and 0.7 bars.

In order to obtain an estimation of the corrosion current densities (i_{corr}) for the API X52 steel immersed in both solutions containing H_2S, an extrapolation of the cathodic and anodic branches of the polarization curves was made for each case, in a region of ± 0.150 V of overpotential, approximately, with respect to the corresponding value of E_{corr}.

Figure 4 shows the estimated values of i_{corr} as a function of the calculated Re_{RCE}. According this figure, the i_{corr} values in both solutions increased and fell as the *Re* number increased. This figure demonstrates that the influence of flow on the measured corrosion is not a linear relationship.

Figures 5 and 6 show the cathodic polarization curves (CPC) obtained on API X52 steel cylindrical electrodes, in the NACE brine and 3.5 % NaCl solution saturated with H_2S at 60

°C and at 0.7 bars, as a function of the rotation rate. In these two figures are possible to see that all CPC (at all rotation rates) have a region where a diffusion process, taking place on the surface of the electrode, is influencing the overall cathodic current. It is to say, a region with well defined cathodic limiting current density, i_{lim} can be observed.

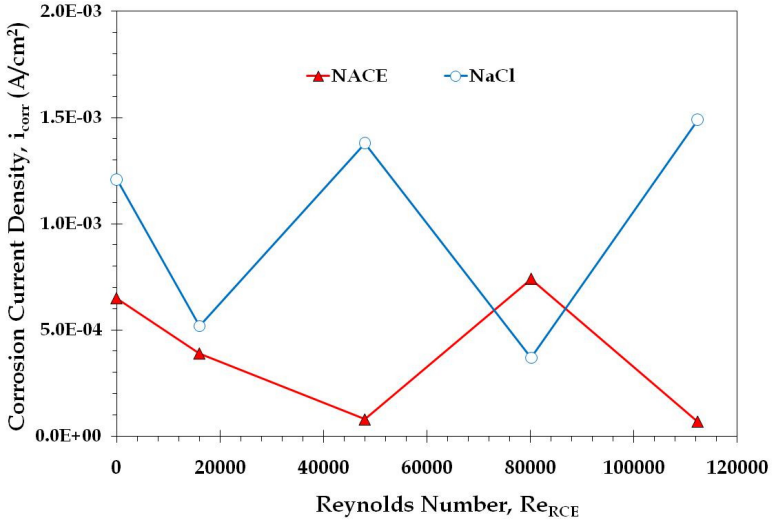

Fig. 4. Corrosion current density as a function of Re_{RCE}.

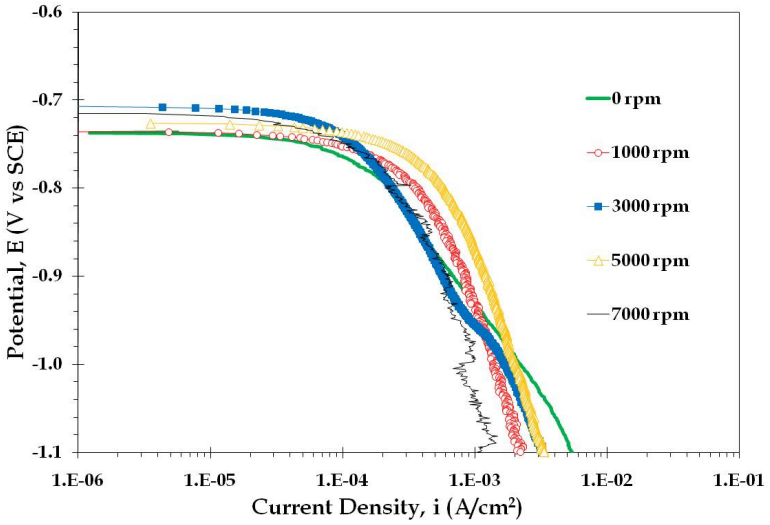

Fig. 5. Cathodic polarization curves as a function of the different rotation rate. API X52 steel immersed in NACE brine saturated with H_2S at 60°C.

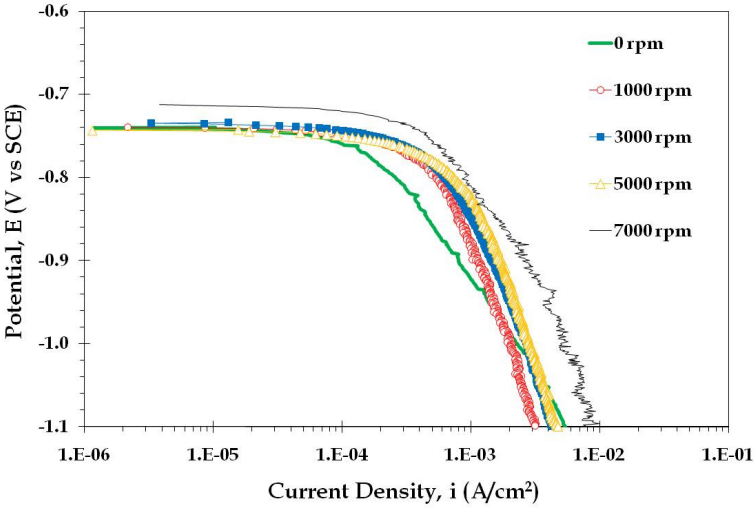

Fig. 6. Cathodic polarization curves as a function of the different rotation rate. API X52 steel immersed in 3.5% NaCl solution saturated with H_2S at 60°C.

In general, for these two hydrodynamic systems, only one plateau (i_{lim}) can be observed in the cathodic branches at each rotation rate. This behaviour could be attributed to the H^+ diffusing either, through the corrosion products layer or from the bulk of the solution towards to the surface of the electrode and the reduction of H_2S (Arzola, 2006; Galvan-Martinez, 2004). In both cases, the current plateau is controlled by mass transfer.

According to the analysis proposed by Schmitt (Schmitt & Rothmann, 1977) and Mendoza (Mendoza-Flores, 1997), it is possible to establish the different cathodic reactions involved in a system controlled by mass transfer under flow turbulent conditions.

Previous work about the steel corrosion in a sour solution say that, in a H_2S containing solution, in the absence of dissolved oxygen, the cathodic reaction of carbon steel, responsible for the corrosion of iron, may be attributed to hydrogen evolution produced by the reduction of hydrogen ions, where the hydrogen ions are supplied by dissociation of H_2S.

The hydrogen evolution can occur as follow:

$$H^+ + e^- \rightarrow H \tag{3}$$

It is important to note that in sour media, the source of the H^+, which promotes the hydrogen evolution, may be the H_2S or H_2O.

Some researchers like Shoesmith (Shoesmith et al., 1980) and Pound (Pound et al., 1985) propose that the cathodic reaction in the presence of H_2S, might be represented by the follow overall reaction:

$$2H_2S + 2e^- \rightarrow H_2 + 2HS^- \tag{4}$$

This reaction is limited by diffusion of H_2S to the electrode surface when the overpotential is far removed from the E_{corr} (Ogundele & White, 1986). It is important to point out that in this work, the measured experimental cathodic current should be a consequence of all the possible reduction reactions that can occur in the NACE and 3.5% NaCl solution saturated with H_2S. According to different researchers (Ogundele & White, 1986; Vedage et al., 1993), the main cathodic reactions in H_2S containing solutions in the absence of oxygen are:

$$2H^+ + 2e^- \rightarrow H_2 \tag{5}$$

$$H_2S + e^- \rightarrow H + HS^- \tag{6}$$

At a constant potential (E) value, as the rotation rate of the electrode increase the measured values of current density also increase. It is important to note that these features can suggest that a diffusion process is taking place on the surface of the cylindrical electrode.

According to previous cathodic analysis, it is important to define which process is controlling the cathodic reaction, the diffusion of the H^+ or H_2S. This fact can define the main reduction reaction.

With the equation proposed by Eisenberg et al., (Eisenberg et al., 1954) for the RCE is possible to calculate the cathodic current density or limiting cathodic current due to the reduction for a species i ($i_{lim,i}$). The equation is:

$$i_{\lim,i} = 0.0791 nFC_i d_{RCE}^{-0.3} \nu^{-0.344} D_i \mathrm{u}_{RCE}^{0.7} \tag{7}$$

Where the $i_{lim,i}$ is the limiting current density in turbulent conditions for species i (A/m^2), n is the number of electrons involved in the electrochemical reaction, F is the Faraday constant, C_i is the bulk concentration of the chemical species i (mol/m^3), d_{RCE} is the diameter of the rotating cylinder (m), ν is the kinematic viscosity of the solution (m^2/s), D_i is the diffusion coefficient of i (m^2/s) and u_{RCE} is the peripheral velocity of the RCE (m/s). This expression indicates a direct relationship of the calculated limiting current density ($i_{lim,H+}$) to the peripheral velocity of the RCE (u_{RCE}), to a power of 0.7.

If the concentration of dissolved O_2 is considered as negligible, then the species in solution capable of being reduced are H_2S and H^+. As the concentration of H_2O can be considered constant and the reduction rate of H^+ and H_2S slow and influenced by the diffusion of reactants, then it is possible to assume that in H_2S solution, both the H^+ ions and H_2S are reduced at the surface. According to these facts and at given flow rate, the total diffusion limited current $i_{lim,t,diff}$ for a H_2S solution could be described by the addition of two components.

$$i_{\lim,t,diff} = i_{\lim,H^+} + i_{\lim,H_2S} \tag{8}$$

Where i_{lim,H^+} and $i_{lim,H2S}$ are the limiting current densities for the H^+ and H_2S under turbulent flow condition.

In order to obtain the i_{lim,H^+} and $i_{lim,H2S}$ Mendoza and Schmitt (Mendoza-Flores, 1997; Schmitt & Rothmann, 1977) proposed that the theoretical i_{lim} for H_2S and H^+ reduction

could be compared with the experimentally measured i_{lim}, in order to obtain information about the predominant cathodic reaction (kinetics). In order to get the theoretical relationship between i_{lim} and u_{RCE} to a power of 0.7 for either H_2S or H^+, the values of density and kinematic viscosity were calculated according to the analysis proposed by Mendoza (Mendoza-Flores, 1997).

Figure 7 compares the different measured and calculated current densities as a function of u_{RCE} to a power of 0.7 in NACE brine. The values of cathodic current densities (i_c) were taken from the corresponding cathodic polarization curves in figure 5, at a constant potential of –0.860 V (SCE). The estimated values of corrosion current densities (i_{corr}) correspond to NACE brine were showed in figure 4. The values of calculated current densities, for the H^+ (a) and H_2S (b) reduction, were calculated with equation (7).

Figure 7(a) shows that the experimental cathodic current density increased and decreased as the rotation rate of the electrode at a power of 0.7 also increase. On the other hand, the corrosion current density has the same behaviour that the i_c. According to these facts are possible to conclude that the H^+ reduction reaction and iron oxidation reaction are no flow dependent. It is important to note that, although the i_c corresponding to H^+ reduction reaction has not a linear relationship with respect to the peripheral velocity of the RCE, it has a better adjust to the theoretical current obtained by the equation of Eisenberg et al., with respect to the i_c corresponding to the H_2S reduction reaction (see figure 7b). In general, the theoretical (i_{lim} obtained by equation of Eisenberg et al.) and experimental (i_c and i_{corr}) densities corresponding to the H^+ reduction have a fits better than the theoretical and experimental densities corresponding to the H_2S. According to this analysis, one conclusion should be obtained: the dominant cathodic reaction is the reduction of hydrogen ions.

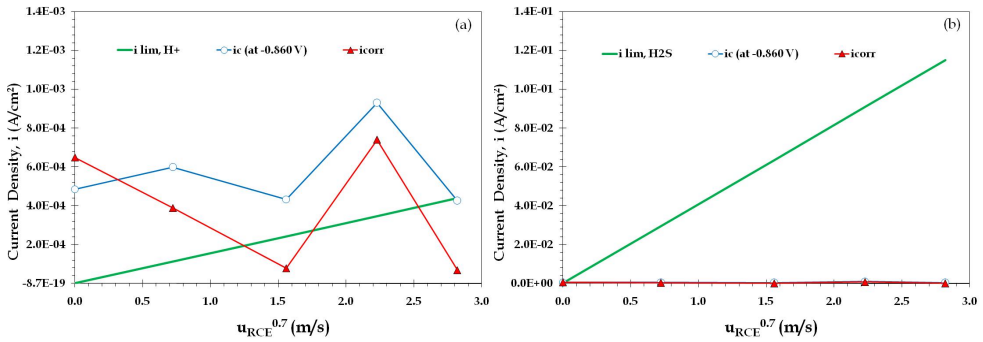

Fig. 7. i_{lim,H^+} (a) and $i_{lim,\ H2S}$ (b) as a function of u_{RCE} to a power of 0.7 in NACE brine.

In figure 8 is possible to see the comparison of the different measured and calculated current densities as a function of u_{RCE} to a power of 0.7 in 3.5% NaCl solution. The values of cathodic current densities (i_c) were taken from the corresponding cathodic polarization curves in figure 6, at a constant potential of –0.860 V (SCE). The estimated values of corrosion current densities (i_{corr}) correspond to NACE brine were showed in figure 4.

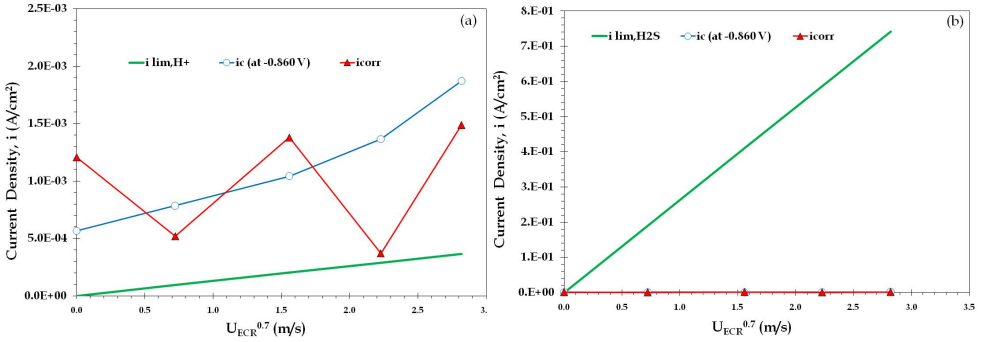

Fig. 8. $i_{lim,H+}$ (a) and $i_{lim,\ H2S}$ (b) as a function of u_{RCE} to a power of 0.7 in 3.5% NaCl solution.

From the figure 8a, it is possible to note the linear relationship between the experimental limiting current density of the H^+ reduction and the peripheral velocity of the RCE. This fact suggests that a mass transfer phenomenon can occurs in the cathodic reaction. According to this analysis is possible to say that the measured cathodic current is affected by flow and this current can be associated to the H^+ diffusing through the corrosion products layer, where they are reduced to H_2 gas. For that reason, the H^+ reduction is flow dependent. In figure 8b is possible to see that the comparison of the theoretical ($i_{lim,H2S}$) and experimental (i_c) current densities of the H_2S reduction have not good correlation. In general, the best fit of the theoretical and experimental current densities correspond to H^+ reduction. Finally and according to the analysis of the figure 8, is possible to say that in the corrosion of the steel immersed in 3.5% NaCl solution, the dominant cathodic reaction is the reduction of hydrogen ions (H^+). As a first approximation to the possible cathodic reaction mechanism prevailing under the experimental conditions studied, it was proposed by Mellor (Mellor, 1930):

$$H_2S_{gas} \leftrightarrow H_2S_{aq} \tag{9}$$

In aqueous solutions, H_2S is a weak acid (Widmer & Schwarzenbach, 1964):

$$H_2S_{aq} \leftrightarrow H^+_{aq} + HS^-_{aq} \tag{10}$$

$$HS^-_{aq} \leftrightarrow H^+_{aq} + S^-_{aq} \tag{11}$$

According to reactions predicted by equation (9) it is possible to get in containing dissolved H_2S, H^+ and HS^-. Under turbulent flow conditions, and as it has been experimentally demonstrated, the diffusion-limited reaction is a consequence of H^+ diffusion.
Silverman (Silverman, 1984) has suggested that the method of quantitatively relating the mass transfer relations must also ensure that the interaction between the alloy surface and the transfer of momentum is equivalent for both pipe and rotating cylinder geometries. Then, for the same alloy and environment, laboratory simulations allow duplicating the velocity- sensitivity mechanism found in the industrial geometry. The shear stress is a measure of the interaction between metallic surface and fluid. The shear stress at the wall can be estimated by the following equation (Bolmer, 1965):

$$\tau_{LAB} = \tau_{PLANT} \tag{12}$$

Then, for a given system, the mechanism by which fluid velocity affects corrosion rate in the industry is proposed to be identical to that which affects corrosion rate in the laboratory.
Figures 9 to 12 show current densities and the dimensionless number analysis as a function of the wall shear stress ($\tau_{W,RCE}$) and the Reynolds number (Re). In this analysis, the H^+ ions are considered to be the main active specie in the cathodic reaction in the environment. Figures 8 and 9 compare the measured cathodic current density (i_c) and the corrosion current density (i_{corr}) as a function of the wall shear stress ($\tau_{W,RCE}$) in NACE and 3.5% NaCl solution. The expression used in the calculation of $\tau_{W,RCT}$ for the RCE was (Denpo & Ogawa, 1993; Efird et al., 1993; Johnson et al., 1991):

$$\tau_{W,RCE} = 0.079 Re_{RCE}^{-0.3} \rho u_{RCE}^2 \tag{13}$$

Mass transfer and surface shear effects may have an important effect on the corrosion rate, either by modifying the rate of transport of chemical species to surface or from the surface, or by shear-stripping protective films from the metal/solution interface. So that, an accurate simulation of corrosion phenomena that occur in pipelines can be made in the laboratory only if the hydrodynamic effects are taken into account. For that reason, parameters such as the mass transfer coefficient, k_i, shear stress at the wall, $\tau_{W,RCE}$, and the Sherwood number, Sh, can be derived from these results.
Figure 9 shows i_c and i_{corr} as a function of $\tau_{W,RCE}$ in NACE brine. This figure shows that the measured i_c and i_{corr} increases and decreases as the $\tau_{W,RCE}$ increases. This behaviour suggests that the corrosion rate and the cathodic reaction are no dependent to the wall shear stress. This result confirms the behaviour presented in figure 7a, where the i_c and i_{corr} are no dependent of the flow.

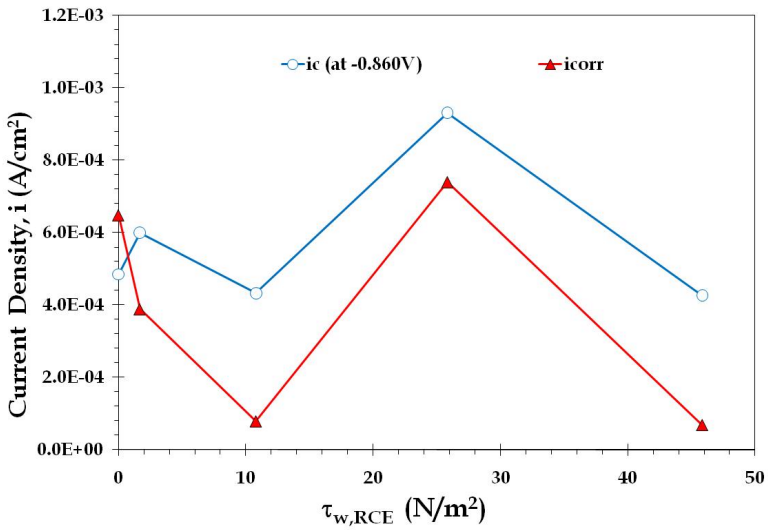

Fig. 9. Cathodic current density obtained at –0.860 V(versus SCE) on the CPC in figure 5 and corrosion current density as a function of $\tau_{W,RCE}$.

Figure 10 shows i_c and i_{corr} as a function of $\tau_{W,RCE}$ in 3.5% NaCl solution. In this figure, it is possible to see that as measured i_c increase the $\tau_{W,RCE}$ also increases. This result suggests that the cathodic reaction increased as the $\tau_{W,RCE}$ also increased. Mass transfer studies of electrochemical reactions are normally carried out under mass transfer limited current conditions. When limiting conditions prevail, the mass transfer coefficient for a given species H^+, k_{H+}, can be expressed as (Galvan-Martinez, 2004):

$$k_{H^+} = \frac{i_{\lim,H^+}}{nFC_{H^+}} \tag{14}$$

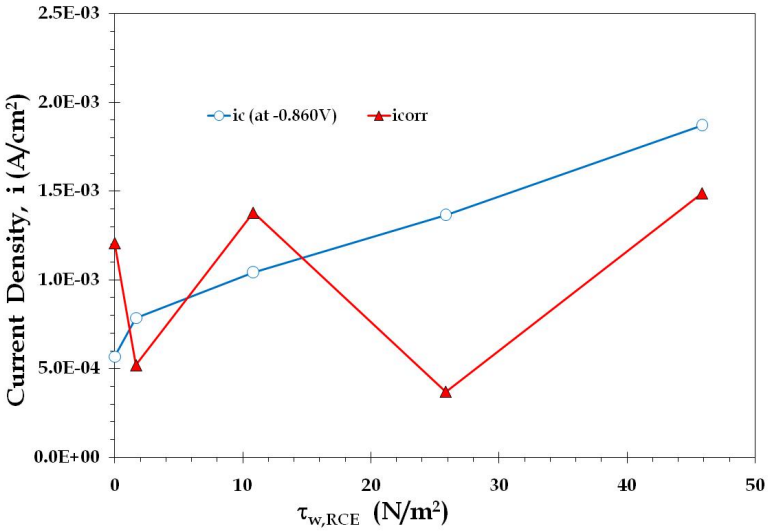

Fig. 10. Cathodic current density obtained at –0.860 V(versus SCE) on the CPC in figure 5 and corrosion current density as a function of $\tau_{W,\,RCE}$.

Where: i_{lim,H^+} is the mass transfer limited current for species H^+, F is the Faraday´s constant, n is the number of electrons involved in the reaction and C_{H+}, is the bulk concentration of the diffusing species H^+. It is important to mention that Silverman pointed out (Silverman, 2004) the measured mass-transfer coefficient could be converted to the Sherwood number and plotted as a function of the Reynolds number (Galvan-Martinez, 2004). The Sherwood number for the RCE (Sh_{H^+}) is given by the expression:

$$Sh_{H^+} = \frac{i_{\lim,H^+}\, d_{RCE}}{nF D_{H^+} C_{H^+}} \tag{15}$$

Where: d_{RCE} is the outside diameter of the rotating cylinder, D_{H^+} is the diffusion coefficient of specie H^+, it is the diffusivity of H^+ in the 3.5% NaCl solution -H_2S system (or NACE brine-H_2S system).
In figure 11, in the 3.5% NaCl solution is possible to see that the Sherwood number increases as the Reynolds number increases. This behaviour indicates that the cathodic reaction is controlled by the mass transport rate. Based on this study, the *Re* number dependence with the *Sh* number, appears to be proportional to a 0.7th power law. The coefficient of 0.7, which is the flow dependence of the *Sh* number, almost corresponds to the coefficients of the *Re* number, as indicated by the equation of Eisenberg et al., (Eisenberg et al., 1954) and, Chilton and Colburn analogy (Chilton & Colburn, 1934). Eisenberg et al. (Eisenberg et al., 1954) showed that in the range of 1.0E03 < *Re* > 1.0E05, the equation (7) is a straight line approximation.

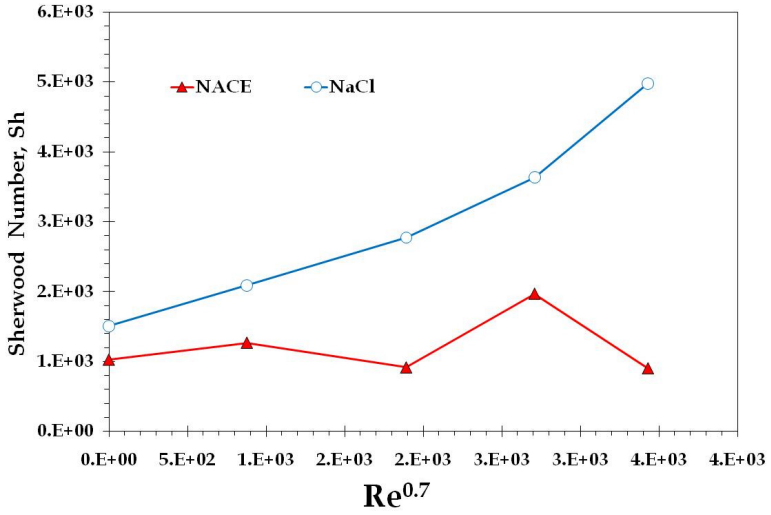

Fig. 11. Variation of dimensionless corrosion rate, expressed as the *Sh* number versus *Re* number to a power of 0.7.

Figure 12 shows the k_{H^+} as a function of *Re* number to a power of 0.7. On the 3.5% NaCl solution, the behaviour of the k_{H^+} is the same behaviour that showed the *Sh* number in figure 11 because the mass transfer coefficient increases when the Re_{RCE} also increases.
The behaviour shown in figures 11 and 12 can suggest that the mass transfer coefficient (Sh_{H^+} and k_{H^+}) is flow dependent, because it increases as the rotation rate also increases. In general, the behaviour presented by Sh_{H^+} and k_{H^+} indicates that the cathodic current is controlled by the mass transfer rate. On the other hand, the behaviour of Sh_{H^+} and k_{H^+}, in NACE brine, confirm the behaviour presented by the current densities, the cathodic process that happens in the corrosion of the steel immersed in NACE brine is not flow dependent. It is because the Sh_{H^+} and k_{H^+} increase and decrease as the *Re* number also increase.

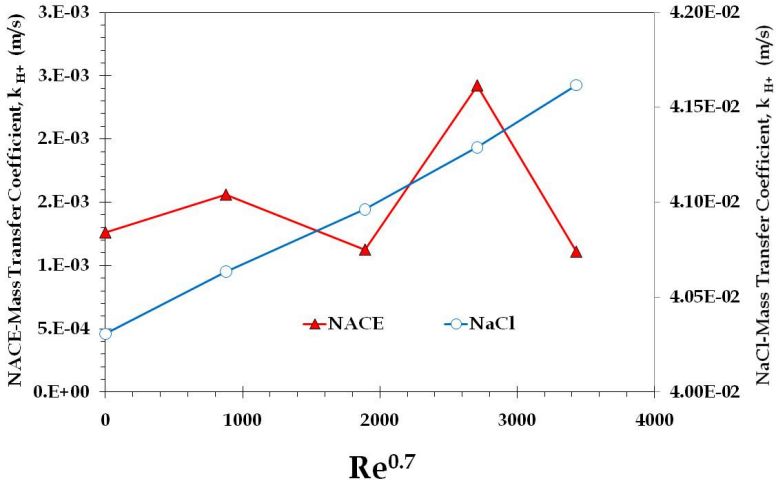

Fig. 12. Variation of mass transfer coefficient (k_{H^+}) versus *Re* number to a power of 0.7.

Figures 13 and 14 show the measured anodic polarization curves obtained on X52 steel cylindrical electrodes immersed in the NACE brine and 3.5% NaCl solution, respectively, saturated with H_2S at different rotation rates.

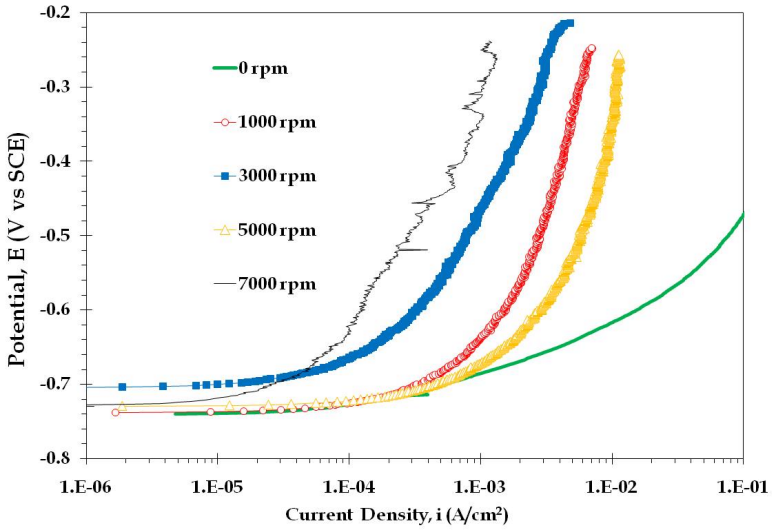

Fig. 13. Anodic polarization curves as a function of different rotation rates. X52 steel electrode immersed in NACE brine saturated with H_2S.

In both figures, it is possible to observe that the anodic Tafel slopes (b_a) are relatively high. This fact indicates a passivation process, taking place on the surface of the electrode. It is important to note that at 0 rpm the anodic polarization curve shows a b_a with values from 115 to 135 V vs. SCE approximately, where these values correspond to an activational or charge transfer process.

Figure 15 shows the estimated anodic Tafel slopes (b_a) as a function of Re_{RCE}, on cylindrical X52 steel electrodes immersed in NACE brine and 3.5% NaCl solution saturated with H_2S. The slopes were calculated on each anodic polarization curve, in the region from + 0.150 V of overpotential, to the corresponding E_{corr}. All the estimations of the Tafel slopes, in NACE brine and 3.5% NaCl solution, carried out from 1000 to 7000 rpm were higher than 0.250 V/decade. This fact can be suggested that a passivation process can be influence in the anodic reaction.

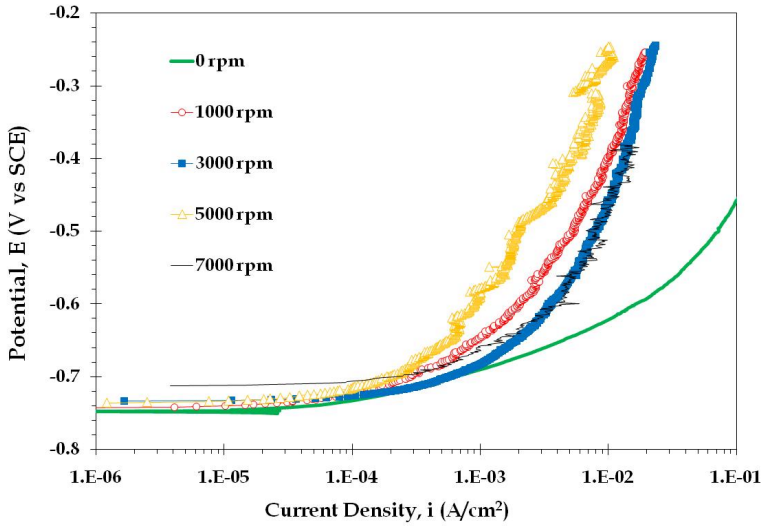

Fig. 14. Anodic polarization curves as a function of different rotation rates. X52 steel electrode immersed in 3.5% NaCl solution saturated with H_2S.

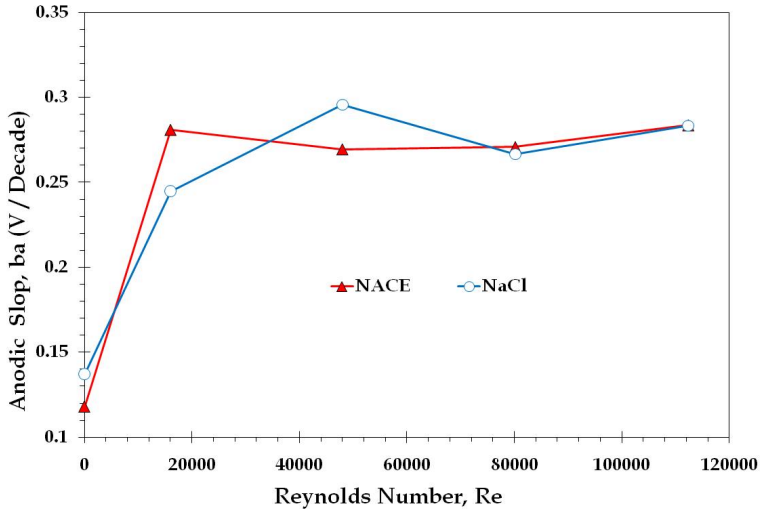

Fig. 15. Calculated anodic Tafel slopes as a function of Reynolds number. Cylindrical API X52 steel electrode immersed in NACE brine and 3.5% NaCl solution saturated with H_2S.

4. Conclusions

According to the experimental results is possible to conclude that the corrosion process of the X52 steel immersed in NACE brine and 3.5% NaCl solution at 60°C and turbulent flow condition, the main cathodic reaction correspond to the H^+ reduction.

$$H^+ + e^- \rightarrow H$$

All cathodic polarization curves, in 3.5% NaCl solution, were affected by the rotation rate of the cylindrical electrode because all CPC show a region that is influenced by a diffusion process, at all rotation rates. In general, when the rotation rate (or *Re* number) of the cylindrical electrode increases, the measured cathodic current density also increases. X52 steel in NACE brine, the cathodic polarization curves shows a region that is influenced by a diffusion process, at all rotation rates, but the current densities are not flow dependent.
In the corrosion process of the X52 steel immersed in 3.5% NaCl solution, the analysis of the current densities (i_c at 0.860 V vs. SCE and i_{lim,H^+}) and the mass transport (Sh_{H^+} number and mass transport coefficient ,k_{H^+}) can be assumed that the corrosion is being limited by the mass transfer rate. This is because the calculated slope of the straight line found in a plot of the measured data *Sh* vs *Re* number is 0.7. In addition, the above reaction can be assumed to be under complete control of mass transfer and, it is a flow dependent reaction. On the other hand, the corrosion process of the X52 steel immersed in NACE brine, the analysis of the current densities and the mass transport is can be assumed that the corrosion is being limited by the mass transfer rate, but the cathodic reaction is not flow dependent because the theoretical and experimental current densities and mass transport coefficients increased and decreased as the Re number also incremented.
All the estimations of the anodic Tafel slopes in NACE brine and 3.5% NaCl solution, carried out at flow condition (1000, 3000, 5000 and 7000 rpm), were higher than 0.250 V/decade. This fact can suggest that a passivation process can be influence in the anodic reaction.

5. Acknowledgment

The author, Mr. R. Galvan-Martinez, would like to thank the Mexican National Council of Science and Technology (CONACYT), the Mexican Petroleum Institute, the PROMEP Program (research project: 103.5 / 07 /2753) of the Ministry of Public Education from México and the Universidad Veracruzana for the support given to develop this work.

6. References

API Publication "API Specification for Line Pipe, API Specification 5L, 45th Edition, API, March-2004

Arzola-Peralta, S., Genesca-Llongueras, J., Mendoza-Flores, J., & Duran-Romero, R. (2003). Electrochemical Study on the Corrosion of X70 Pipeline Steel in H_2S Containing Solutions. *Proceedings of Conferences of NACE-Corrosion*, Paper 3401, Houston, USA, March 2003

Arzola-Peralta, S., Mendoza-Flores, J., Duran-Romero, R., & Genesca, J. (2006). Cathodic Kinetics of API X70 Pipeline Steel Corrosion in H_2S Containing Solutions to Under Turbulent Flow Conditions. *Corros. Eng. Sci. Technol.*, Vol. 41, Issue. 4, (2006) pp. 321-327, ISSN 1478-422x

Bolmer, P. W. (1965). Polarization of Iron in H_2S-NaHS Buffers. *Corrosion* Vol. 21, Issue 3, (March-1965), pp. 69-75, ISSN 0010-9312

Chilton, T. H., & Colburn, A. P. (1934). Mass Transfer (Absortion) Coefficients. *Ind. Eng. Chem*., Vol. 26, (1934), pp. 1183-1186, ISSN 0088-5885

Dean, S. W., & Grab, G. D. (1984). Corrosion of Carbon Steel by Concentrated Sulfuric Acid, *Proceedings of Conferences of NACE-Corrosion*, Paper 00147, Houston, USA, March 1984

Dean, S. W. (1990). Velocity Accelerated Corrosion Testing and Predictions, An Overview. *Mater. Perform*., Vol. 28 Issue 9, (September-1990), pp. 61-67, ISSN 0094-1492

Denpo, K., & Ogawa, H. (1993). Fluid Flow Effects on CO2 Corrosion Resistance of Oil Well Materials. *Corrosion,* Vol. 49, Issue 6, (1993) pp. 442-449. ISSN 0010-9312

Efird, K. D., Wright, E. J., Boros, J. A., & Hailey, T. G. (1993) Corrosion Control for Low-Cost Reliability. *Proceedings of 12th International Corrosion Congress*, Vol. 4, Houston, U.S.A. September-1993

Efird, K. D., Wright, E. J., Boros, J. A., & Hailey T. G. (1993). Correlation of Steel Corrosion in Pipe Flow with Jet Impingement and Rotating Cylinder Tests. *Corrosion*, Vol. 49, Issue 12, (December-1993), pp. 992-1003, ISSN 0010-9312

Eisenberg, M., Tobias, C.W., & Wilke, R. C. (1954). Ionic MassTransfer and Concentration Polarization at Rotating Electrode. *J. Electrochem.Soc*., Vol. 101, Issue 6, (June-1954), pp. 306-320, ISSN 0013-4651

Ellison, B. T., & Schmeal, W. R. (1978). Corrosión of Steel in Concentrated Sulfuric Acid. .*J. Electrochem. Soc*. Vol. 125, Issue 4, (April-1978), pp. 524-531, ISSN 0013-4651

Gabe, D.R., & Walsh, F.C. (1983). The Rotating Cylinder Electrode: A Review of Development. *J. Appl. Electrochem*, Vol. 13, Issue 1, (January-1983), pp. 3-22. ISSN 0021-891x

Gabe, D. R., (1974). The Rotating Cylinder Electrode. *J. Appl. Electrochem*., Vol. 4, Issue 2 (February-1974) pp. 91-108, ISSN 0021-891x

Galvan-Martinez, R. (2004). Influence Study of the Turbulent Flow on Carbon Steel Corrosion Immersed in H_2S Containing Solutions, PhD Thesis, UNAM, Mexico

Galvan-Martinez, R., Mendoza-Flores, J., Duran-Romero, R., & Genesca-Llongueras, J. (2005). Rotating Cylinder Electrode Study on the Influence of Turbulent Flow on the Anodic and Cathodic Kinetics of X52 Steel Corrosion in H_2S Containing Solutions. *Afinidad: Revista de Química Teórica y Aplicada,* Vol. LXII, Issue 519, (October 2005) pp. 448-454, ISSN 0001-9704

Galvan-Martinez, R., Mendoza-Flores, J., Duran-Romero, R., & Genesca-Llongueras, J. (2007). Effect of Turbulent Flow on the Anodic and Cathodic Kinetics of API X52 Steel Corrosion in H_2S Containing Solutions. A Rotating Cylinder Electrode Study. *Materials and Corrosion,* Vol. 58, Issue 7, (July-2007), pp. 514-521, ISSN 0947-5117

Galvan-Martinez, R., Orozco-Cruz, R., & Torres-Sanchez, R. (2010). Study of X52 Steel in Seawater with Biocides under Turbulent Flow Conditions. *Afinidad: Revista de Química Teórica y Aplicada,* Vol. LXVII, Issue 550, (November-2010) pp. 442-448, ISSN 0001-9704

Galvan-Martinez, R., Orozco-Cruz, R., Torres-Sanchez, R., & Martinez, E. A. (2010). Corrosion Study of the X52 Steel Immersed in Seawater with a Corrosion Inhibitor using a Rotating Cylinder Electrode. *Materials and Corrosion*, Vol. 61, Issue 10, (October-2010) pp. 872-876, ISSN 0947-5117

Garnica-Rodriguez, A., Genesca, J., Mendoza-Flores, J., & Duran-Romero, R. (2009). Electrochemical Evaluation of Aminotriazole Corrosion Inhibitor under Flow Conditions. *J. Appl. Electrochem.*, Vol. 39 Isuue 10 (October-2009) pp. 1809-1819, ISSN 0021-891x

Garverick, L. (1994). *Corrosion In The Petrochemical Industry - Essential Research*, ASM. International, ISBN 0871705052, Ohio, USA

Genesca, J., Olalde, R., Garnica, A., Balderas, N., Mendoza, J., & Duran-Romero R. (2010). Electrochemical Evaluation of Corrosion Inhibitors in CO_2 Containing Brines. A RCE and Flow-Loop Comparison, *Proceedings of Conferences of NACE-Corrosion*, Paper 00162, Houston, USA, March-2010

Johnson, B. V., Choi, H. J., & Green, A. S. (1991). Effects of Liquid Wall Shear Stress on CO_2 Corrosion of X52 Steel Simulated Oilfield Production Environments, *Proceedings of Conferences of NACE-Corrosion*, Paper 00573, Houston, USA, March-1991

Liu, G., Tree D.A., & High, M. S. (1994). Relationships Between Rotating Disk Corrosion Measurements and Corrosion in Pipe Flow. *Corrosion*, Vol. 50, Issue 8, (August-1994) pp. 584-593, ISSN 0010-9312

Lotz, U., (1990). Velocity Effect In Flow Induced Corrosion, *Proceedings of Conferences of NACE-Corrosion*, Paper 27, Houston, USA, March-1990.

Mellor, W. (1930). A Comprehensive Treatise on Inorganic and Theoretical Chemistry, Longmans, London, England

Mendoza-Flores, J. (1997). *Kinetic Studies of CO_2 Corrosion Processes Under Turbulent Flow*, PhD Thesis, University of Manchester, Manchester, UK

Mendoza-Flores, J., Duran-Romero, R., & Garcia-Ochoa, E. (2002). Effects of Turbulent Flow on The Efficiency of Triazole based Inhibitors. *Proceedings of Conferences of NACE-Corrosion*, Paper 02491, Houston, USA, March-2002

Mendoza-Flores, J., & Turgoose, S. (2002). Influence of Electrode Length on the Measurement of Cathodic Kinetics of Steel Corrosion In CO_2 Containing Solutions, under Turbulent Flow Conditions, *Proceedings of Conferences of NACE-Corrosion*, Paper 02490, Houston, USA, March-2002

Mora-Mendoza, J. L, Chacon-Nava, J. G, Zavala-Olivares, G., Gonzalez-Nunez, M. A, & Turgoose, S. (2002). Influence of Turbulent Flow on the Localized Corrosion Process of Mild Steel with Inhibited Aqueous Carbon Dioxide Systems. *Corrosion* Vol. 58, Issue 7, (July-2002) 608-619, ISSN 0010-9312

NACE Publication 1 D196, "Laboratory Test Methods for Evaluating Oilfield Corrosion Inhibitors" (Houston. TX: NACE, 1996)

Nesic, S., Solvi, G. T., & Enerhaug, J. (1995). Comparison of the Rotating Cylinder and Pipe Flow Tests for Flow-Sensitive Carbon Dioxide Corrosion. *Corrosion* Vol. 51, Issue 10, (October-1995) pp. 773-787, ISSN 0010-9312

Nesic, S., Bienkowski, J., Bremhorst, K., & Yang., K. S. (2000). Testing for Erosion-Corrosion Under Disturbed Flow Conditions Using a Rotating Cylinder with a Stepped Surface. *Corrosion* Vol. 56, Issue 10 (October-2000) pp. 1005-1014, ISSN 0010-9312

Ogundele, G. I., & White, W.E. (1986). Some Observations on the Corrosion of Carbon Steel in Sour Gas Environments: Effects of H_2S and $H_2S/CO_2/CH_4/C_3H_8$ Mixtures. *Corrosion* Vol. 42, Issue 7, (July-1986) pp. 398-408, ISSN 0010-9312

Papavinasam, S., Revie, R.W., Attard, M., Demoz, A., & Michaelian, K. (2003). Comparison of Laboratory Methodologies to Evaluate Corrosion Inhibitors for Oil and Gas Pipelines. *Corrosion,* Vol. 59, Issue 12, (December-2003) pp. 897-912, ISSN 0010-9312

Poulson, B. (1983). Electrochemical Measurement in Flowing Solution. *Corros. Sci.,* Vol. 23, Issue 4, (April-1983), pp. 391-430, ISSN 0010-938X

Poulson, B. (1993). Advances in Understanding Hydrodynamic Effect on Corrosion. *Corros. Sci.,* Vol. 35, Issue 1-4, (1993), pp. 655-665, ISSN 0010-938X

Poulson, B. (1994). A Submerged Impinging Gas Jet for Corrosion and Electrochemical Studies. *J. Appl. Electrochem*., Vol. 24, Issue 1, (January-1994), pp. l-7, ISSN 0021-891x

Pound, B. G., Abdurrahman, M. H., Glicina, M. P., Wright, G. A., & Sharp, R. M. (1985). The corrosion of Carbon Steel and Stainless Steel in Simulated Geothermal Media. *Aust. J. Chem*., Vol. 38 Issue 8(August-1985) pp. 1133-1140, ISSN 0004-9425

Rahmani, M. & Strutt, J. E. (1992). *Hydrodynamic Modeling of Corrosion of Carbon Steel and Cast Irons in Sulfuric Acid*, Published for the Materials Technology Institute of the Chemical Process Industries, Inc. By National Association of Corrosion Engineers, ISBN: 1-877914-40-1, United States of America.

Ross T. K., Wood G. C., & Mahmud, I. (1966). The Anodic behaviour of Iron-Carbon Alloys in Moving Acid Media. *J. Electrochem. Soc*., Vol. 113, Issue 4, (April-1966), pp. 334-345, ISSN 0013-4651

Schlichting, H. & Gersten, K. (1979). *Boundary Layer Theory. 8th Edition,* Springer, ISBN 3540662707, New York, USA

Schmitt, G., & Rothmann, B. (1977). Investigations into the Corrosion Mechanism of Unalloyed Steel in Oxygen-Free Carbonic Acid Solutions. Part I – Kinetics of Hydrogen Evolution. *Werkst. Korros*., Vol. 28, Issue 12, (December-1977) pp.816-822, ISSN 0947-5117

Schmitt, G., Bruckhoff, W., Faessler, K., & Blummel, G. (1991). Flow Loop vs Rotating Probes- Experimental Results and Service Application. *Mater. Perform*., Vol. 30, Issue 2, (February-1991), pp. 85-92, ISSN 0094-1492

Shoesmith, D. W., Taylor, P., Bailey, M. G., & Owen, D. (1980). The Formation of Ferrous Monosulfide Polymorphs During the Corrosion of Iron by Aqueous Hydrogen Sulfide at 21-Degrees-C. *J. Electrochem. Soc*., Vol. 127, Issue 5, (May-1980), pp. 1007-1015, ISSN 0013-4651

Silverman, D. C. (1984). Rotating Cylinder Electrode for Velocity Sensitivity Testing. *Corrosion*, Vol. 40, Issue 5 (May-1984). pp. 220-226, ISSN 0010-9312

Silverman, D.C. (1988). Rotating Cylinder Electrode- Geometry Relationships for Prediction of Velocity-Sensitive Corrosion. *Corrosion*, Vol. 44, Issue 1 (January-1988) pp. 42-49. ISSN 0010-9312

Silverman, D. C. (1990). Rotating Cylinder Electrode -An Approach For Predicting Velocity Sensitive Corrosion, *Proceedings of Conferences of NACE-Corrosion*, Paper 00013, Las Vegas, USA, March-1990

Silverman, D. C. (2004). The Rotating Cylinder Electrode for Velocity-Sensitive Corrosion – A Review, *Corrosion*, Vol. 60, Issue 11, (November-2004) pp. 1003-1023, ISSN 0010-9312

Turgoose, S., Dawson, J. L., Palmer, J. M., & Rizk, T., (1995). Boundary Layer Effects in Turbulent. Flow Testing. *Proceedings of Conferences of NACE-Corrosion*, Paper 95112, Houston, USA, March-1995

Vedage, H., Ramanarayanan, T. A., Mumford, J. D., & Smith, S. N. (1993). Electrochemical Growth of Iron Sulfide Films in H_2S-Saturated Chloride Media. *Corrosion*, Vol. 49, Issue 2, (February-1993) pp. 114-121. ISSN 0010-9312

Widmer M., Schwarzenbach G. (1964). Die Acidität des Hydrogensulfidions HS. *Helv. Chim. Acta,* Vol. 47, Issue 1, (1964), pp.266-271, ISNN 1522-2675

17

Mass Transfer Performance of a Water-Sparged Aerocyclone Reactor and Its Application in Wastewater Treatment

Xuejun Quan, Qinghua Zhao, Jinxin Xiang,
Zhiliang Cheng and Fuping Wang
College of Chemistry and Chemical Engineering
Chongqing University of Technology, Chongqing
P.R. China

1. Introduction

Ammonia is one of the most important contaminants impairing the quality of water resource. Ammonia is commonly present in municipal and industrial wastewater, such as landfill leachate, coke plant wastewater, and petrochemical and metallurgical wastewater. The accumulation of ammonia in water results in eutrophication and the depletion of oxygen due to nitrification (Tan et al., 2006). Moreover, wastewaters containing ammonia are often toxic, which makes their biological treatment unfeasible (Hung et al., 2003). Such adverse effects of ammonia promote the development of various techniques for its removal for instance, biological nitrification-denitrification (Calli et al., 2005; Dempsey et al., 2005), air stripping (Bonmati & Floatats, 2003; Basakcilardan-kabakci et al., 2007; Marttinen et al., 2002; Ozturk et al., 2003; Saracco & Genon, 1994), struvite precipitation (Jeong & Hwang, 2005; Lee et al., 2003; Uludag-Demirer et al., 2005; Rensburg et al., 2003), membrane separation (Tan et al., 2006), catalytic liquid-phase oxidation (Huang et al., 2003), and selective ion exchange (Jorgensen & Weatherley, 2003).

The air stripping process with relatively low cost and simple equipment is widely used in the removal of ammonia from wastewater, and high rates of ammonia removal can be achieved (Ozturk et al., 2003). In addition to this process, other processes like absorption can recover ammonia that is transferred from the liquid phase to the air stream (Bonmati & Floatats, 2003). Therefore, air stripping is a good method for the removal and recovery of valuable ammonia from wastewater. In order to get high process efficiency, air stripping is usually operated in a packed tower because it can provide a larger mass transfer area (Djebbar & Naraitz, 1998). However, in practice, air stripping in packed towers usually leads to scaling and fouling on packing because of reactions between CO_2 in air and some metal ions in wastewater. In order to reduce cost, slaked lime is usually used to adjust the pH value of wastewater, thus forming a suspension. But a packed tower is not suitable for the air stripping of this kind of suspension because of the presence of solid particles that are seen in the suspension. Additionally, air stripping is a time consuming process when using some traditional equipments, because of a lower mass transfer coefficient of ammonia from the liquid to gas phase.

In recent years, some new gas-liquid contactors, with high mass transfer rate but without packing, have been used for the gas-liquid operation (Bokotko et al., 2005). Because

ammonia is a soluble gas with a small Henry's law constant, the overall mass transfer resistance in the air stripping largely lies on the gas film side (Matter-Muller et al., 1981). Therefore, decreasing the gas film resistance and increasing the gas-liquid contact area will accelerate the mass transfer of ammonia from the liquid to gas phase. A newly designed gas-liquid contactor, water-sparged aerocyclone (WSA), was developed in this work. The WSA is suitable for the air stripping of wastewater with suspended solids and has a higher mass transfer rate than some traditional stripping equipment like packed towers and tanks.

The overall mass transfer performance of the WSA was investigated using the air stripping of ammonia from wastewater. Further, in order to reveal the mass transfer mechanism of this new mass transfer equipment, the effects of major parameters on the pressure drop of gas phase, liquid side mass transfer coefficient k_L and specific mass transfer area a were also investigated. As a new gas-liquid mass transfer equipment, the WSA was used to simultaneously remove NH_3-N, total P and COD from anaerobically digested piggery wastewater using cheap $Ca(OH)_2$ as the precipitant for PO_4^{3-} and some organic acids, and as pH adjuster for NH_3-N stripping.

2. Experimental setup and methods

2.1 Design of the WSA reactor

The WSA reactor is essential equipment for the air stripping of ammonia from water; its configuration is shown in Fig. 1. In operation, the wastewater containing ammonia is pumped into the water jacket and then sparged towards the centerline of the WSA through the porous section of the inner tube wall, thus forming a large gas-liquid contact area. The transfer of ammonia from liquid to air is high because of the very small amount of liquid.

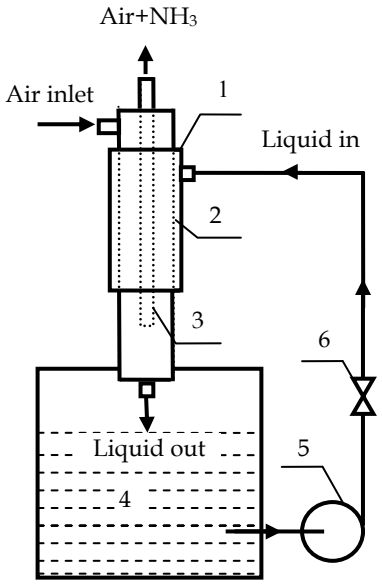

Fig. 1. The water-sparged aerocyclone reactor (WSA). 1-outer tube; 2-porous section of inner tube; 3-central gas tube; 4-water tank; 5-circulating pump; 6-valve.

The WSA reactor unit consists of two concentric right-vertical tubes and a conventional cyclone header at the top. The inner diameter of the inner tube is 0.09 m, which uses the upper section design as a porous structure for the jetting of water. 160 small holes with a diameter of 2 mm are arranged in axial symmetry on the porous section (8 holes per circle and 20 circles with an interval of 10 mm along each axial direction). The outer tube secures even distribution of water through the porous tube. The length of the porous tube section is 0.3 m and the overall length of the inner tube is 0.6 m. Wastewater is supplied through the porous section of the inner tube, and sprayed towards the centerline of the WSA. Compressed air is tangentially fed into the aerocyclone at the top header of the inner tube. Ammonia containing water is kept in the 100 l water tank, and circulated by a centrifugal pump. The water in the tank is heated by an electric heating element when needed, and its temperature is controlled by a thermocouple and measured accurately with a temperature meter. The pressure drop in the WSA is measured with a manometer. The valves located on the pipelines to the aerocyclone are used for the control of the gas and liquid phase flow rates.

2.2 Experimental setup design

The air stripping of ammonia from water is carried out in a specially designed system shown in Fig. 2.

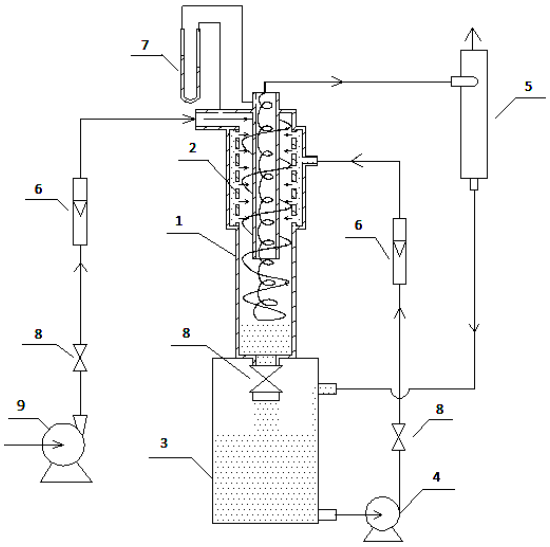

Fig. 2. The flow diagram of the experimental setup and the WSA configuration. 1- water-sparged aerocyclone; 2- porous section; 3- water tank; 4- circulating pump; 5- gas-liquid separator; 6- rotameters; 7-U type manometers; 8- valves; 9- air pump.

The primary unit is the WSA reactor, in which the separation of ammonia from water occurs. Compressed air is produced by an air compressor and tangentially introduced into the top header of the WSA, forming a strong rotating air flow field within it. Ammonia containing water is kept in a water tank, and pumped into the water jacket between the two

concentric tubes of the WSA by a circulating pump, and finally sprayed into the airflow field. Waste gas exits out through the center gas tube in the WSA and tangentially enters the gas-liquid separator, in which liquid droplets taken out by the waste gas are separated and flow back into the water tank. Volumetric flow rates are measured by means of rotameters, whereas manometers measured the pressure. Volumetric flow rates of air and water entering the WSA is adjusted by the means of valves. The cyclone header is a part of the inner tube and has a hight of 0.02 m over the porous inner tube. A rectangular gas inlet gap with 0.003 m width and 0.02 m length is tangentially connected with the cyclone header. The gas flow rate was controlled within 1.1~1.9 l/s, which was an equivalent of the gas inlet velocity of 18.3 ~ 31.7 m/s.

2.3 Experimental procedure

In all the experiments, 10 l fresh aqueous $Ca(OH)_2$ suspensions with different ammonia concentrations were prepared just before the experiment. Primary experiments indicate that a $Ca(OH)_2$ dosage of 4 g/l can be used for maintaining a constant pH value of the suspension, which is always 11~12; and lower than 2 g/l of dosage can not maintain a constant pH value, causing an unsteady air stripping process. The ammonia equilibrium in the aqueous solution is pH and temperature dependent, and the ratio of free ammonia to total ammonia can be calculated out (Bonmati & Floatats, 2003). When the pH value is 11~12, the ammonium nitrogen is almost all converted into molecular ammonia in an aqueous solution, ensuring the air stripping of ammonia. Under this condition, the overall performance of the WSA reactor is dependent on the mass transfer rate of ammonia from water to air.

The experiments were carried out in a batch mode. Each experiment was repeated to get experimental data with an error of less than 5 %, and the averaged value was used. Before each run, the water tank was filled with the 10 l fresh aqueous $Ca(OH)_2$ suspension. Then the compressed air was allowed to enter the aerocyclone at a prescribed flow rate. When the pressure reading reached a steady state, the circulation pump at a certain flow rate pumped the suspension in the tank into the WSA. During circulation, the total ammonia concentration in the suspension is continuously decreasing and is measured at an interval. The suspension samples were taken out from the water tank and centrifuged to get a supernatant for the determination of ammonia. The ammonia concentration was measured using the Nessler's Reagent ($HgCl_2$-KI-KOH) Spectrophotometry at 420 nm according to the Standards of the People's Republic of China (GB 7479-87).

In order to understand the overall performance, the effect of major process parameters on the air stripping efficiency and mass transfer coefficient of ammonia was investigated, including the flow rate of air and suspension, initial ammonia concentration, and the temperature of the suspension. At the same time, the scaling and fouling in the WSA was observed.

2.4 The overall mass transfer coefficient of ammonia stripping in the WSA

The efficiency of ammonia removal η is defined according to the measured results, as

$$\eta = \frac{C_{in} - C_t}{C_{in}} \tag{1}$$

Where C_{in} and C_t are the ammonia concentrations in the suspension at the beginning and at any time, respectively, mg/l.

For an air stripping system, the mass transfer rate of volatile compound A from water in a batch stripping unit has been derived by Matter-Muller et al (1981) and is shown as follows:

$$-\ln\frac{c_{A_t}}{c_{A_0}} = \frac{Q_G H_A}{V_L}[1-\exp(-\frac{K_L a V_L}{H_A Q_G})]t \tag{2}$$

where c_{A_t} and c_{A_0} are the liquid phase concentrations of compound A at any time t and at the beginning, g/m^3; H_A is the dimensionless Henry's constant; K_L is the overall liquid mass transfer coefficient, m/min; a is the interface area per unit volume of liquid, m^2/m^3; V_L is the total volume of liquid, l; Q_G is the gas flow rate, l/min and t is the stripping time, min.

When $\frac{K_L a V_L}{H_A Q_G} << 1$, equation (2) becomes:

$$-\ln\frac{c_{L,At}}{c_{L,A_0}} = K_L a \bullet t \tag{3}$$

This case happens when the exit stripping gas is far from saturation.

In the present work, ammonia is an easily soluble gas and the exit stripping gas is possibly far from saturation because of the very short residence time of the stripping gas in the WSA, so the calculation of the mass transfer coefficient of ammonia removal was tentatively made according to the Eq.(3).

2.5 The determination of liquid side film mass transfer coefficient k_L and specific mass transfer area a

It is a very important work to determine the mass transfer coefficient k_L and specific mass transfer area a for the further understanding of the mass transfer characteristics of the WSA.

Firstly, the determination method of specific mass transfer area has been well established using a chemical absorption of CO_2 by NaOH solution (Tsai et al., 2009). In this system, when the NaOH concentration is high enough, the reaction between CO_2 and NaOH could be seen as a rapid pseudo first order reaction with respect to CO_2, and the CO_2 concentration in the bulk solution could be regarded as zero approximately. Thus, the a could be calculated out from the following equations:

$$G_A = \beta k_L A C_i \tag{4}$$

Usually β is called chemical absorption strengthening factor; G_A is the absorption rate of CO_2, mol/s; A is the mass transfer area, m^2; C_i is the concentration of CO_2 on the gas-liquid interface in equilibrium with the CO_2 fractional pressure.

According to the related chemical absorption theory and the Henry's law,

$$\beta = k_L^{'} / k_L = \sqrt{1 + Dk_1 / k_L^2} = \sqrt{1+\gamma^2} \tag{5}$$

$$\text{And } C_i = Hp_i \tag{6}$$

And when γ>10, $\beta \approx \gamma$, thus, from the equations 4—6, $A = \frac{G_A}{Hp_i\sqrt{Dk_1}}$ and $a = A/V$, here V is the mass transfer volume in the WSA, i.e. the whole inner volume subtracted by that of the central gas tube in the WSA.

After the specific mass transfer area was obtained, the k_L could be determined by a CO_2 — H_2O absorption system. This is a physical absorption system; the mass transfer resistance mainly lies in the liquid side film, thus,

$$G_A = k_L a V C_i \tag{7}$$

The parameters a, V, C_i could be obtained through the above-mentioned process. Thus the k_L could be calculated from Eq. 7, and $a = G_A/(k_L V C_i)$.

2.6 The determination of the pressure drop of gas phase through the WSA

The pressure drop of gas phase through the WSA, i.e. the two points between the inlet and outlet of gas phase, was determined using a U-type manometer, as shown in Fig.2, with a water-air system as working medium. In order to know the interaction of the gas-liquid phases in the WSA, the liquid content ε_L in the gas phase at the gas outlet was also determined using a gas-liquid cyclone separator.

In the experimental process, the flow rate of the liquid phase should be larger than 1 m^3/h, which corresponds to the jet velocity of 0.381 m/s, so as to get an even jet distribution of the liquid phase in the jet area. The experimental operation process was similar with that for the air stripping of ammonia. In order to fully understand the characteristic of hydrodynamics in the WSA, the gas phase inlet velocity was controlled within 4—20 m/s, wider than that in a traditional cyclone.

3. Results and discussion

As mentioned above, the objective of this work is to develop new air stripping equipment of industrial interest for the removal of volatile substances such as ammonia. Firstly, to understand the overall performance of the WSA and how the major parameters affect the performance is very important. And a comparison between the WSA and some traditional air stripping equipment should be done to assess its performance. Then the effects of major process parameters on the mass transfer coefficient in liquid side film and specific mass transfer area were carried out, so as to reveal the mass transfer mechanism in the WSA. Thirdly, the pressure drop of gas phase which can reflect the momentum transfer in the WSA was also investigated, facilitating the understanding of the mass transfer process.

3.1 The mass transfer performance of the WSA

3.1.1 Effect of initial ammonia concentration on ammonia removal efficiency

The effect of the initial ammonia concentration on the air stripping efficiency of ammonia is shown in Fig. 3. It exhibits a very high air stripping efficiency of ammonia in a wide range of ammonia concentration (1200 ~ 5459 mg/l). Ammonia removal efficiency higher than 97 % was achieved just with 4 h of stripping time. However, using the same volume of the suspension, achieving this efficiency of ammonia removal in a traditional stripping tank needed more than 24 h. This also illustrates that the mass transfer rate of ammonia from the suspension to air in the WSA is very high compared with some traditional stripping processes.

In order to further understand the mass transfer of ammonia in the WSA, the mass transfer coefficients under different initial ammonia concentrations could be obtained using Eq. 3, i.e. plotting $-\ln(C_t/C_{in})$ vs. stripping time t and making a linear regression between –

$\ln(C_t/C_{in})$ and stripping time t could get the mass transfer coefficients K_La shown in Fig. 3 with a very good relative coefficient (R^2 =0.9975 ~ 0.9991). It clearly indicates that ammonia concentration has little effect on the mass transfer coefficients, i.e. the coefficients vary in 0.019 ~ 0.021 min^{-1} even though the ammonia concentration varies greatly (from 1200 to 5459 mg/l). The reasonable explanation for this phenomenon is that the process is surely controlled by the diffusion of ammonia through a gas film.

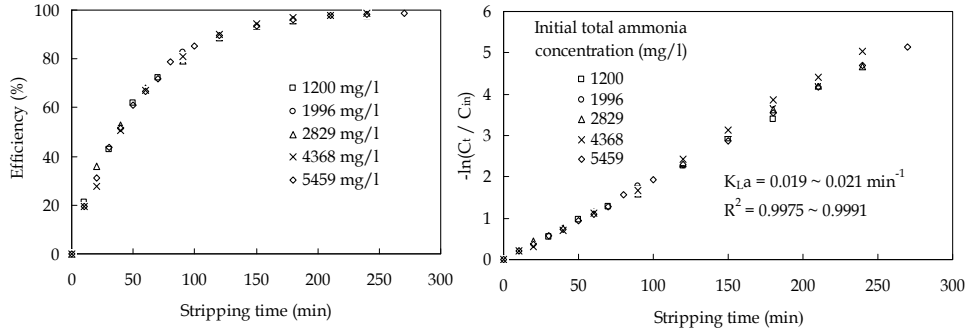

Fig. 3. Effect of initial ammonia concentration on ammonia removal efficiency (left) and mass transfer coefficients of ammonia (right) in the WSA reactor. Experimental conditions: V_L=10 l, U_L = 0.77 m/s, Q_g =1.9 l/s, Temperature 15 °C, Pressure drop 0.2-0.3 MPa.

As shown in Fig. 3, the air stripping efficiency of ammonia is almost independent of ammonia concentration. This could be further explained according to the analysis of the mass transfer process. From Eq. 3, the following equation could be easily obtained.

$$\ln(1-\eta) = -K_L a \bullet t \tag{8}$$

Applying Eq. 8 for the air stripping process of a higher and lower concentration of ammonia suspension, respectively, $\ln(1-\eta_L) = \ln(1-\eta_H)$, i.e. $\eta_L = \eta_H$ can be obtained within a same period of stripping time because of the almost constant mass transfer coefficients K_La. That is to say, the air stripping efficiency for a system controlled by diffusion through a gas film is theoretically independent of the concentration of volatile substances. The higher the concentration, the bigger the air stripping rate. Increasing ammonia concentration can increase the driving force of mass transfer, leading to a higher rate of ammonia removal.

3.1.2 Effect of jet velocity of the aqueous phase

Increase of flow rate of the suspension may result in the increase of jet velocity of the suspension, U_L, thus changing the gas-liquid contact time and area. So, the effect of jet velocity of the aqueous phase on air stripping efficiency and mass transfer coefficient of ammonia was investigated. The results are shown in Fig. 4.

It can be seen that jet velocity of the aqueous phase has little effect on ammonia removal efficiency, and that the double increase of the jet velocity did not result in an obvious increase of the mass transfer coefficient under the experimental conditions. This illustrates that the increase of the jet velocity can not obviously increase the contact area of the two phases and can not reduce the mass transfer resistance. In the WSA, the contact area of the two phases and mass transfer resistance may be mainly determined by the gas flow rate in such a strong aerocyclone reactor, which will be investigated in subsequent section.

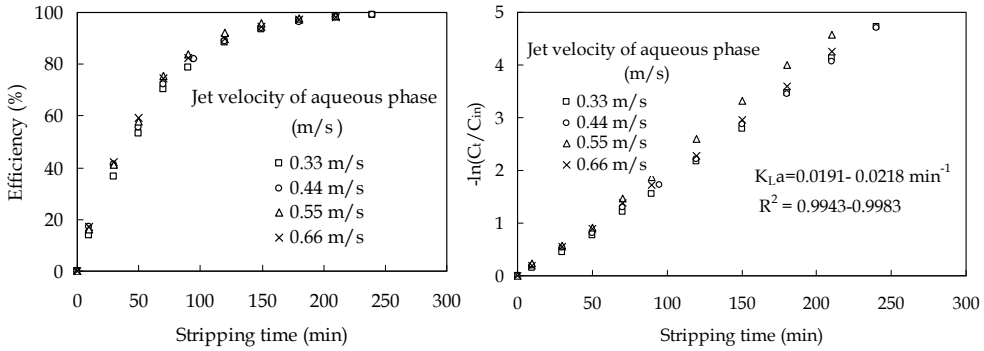

Fig. 4. Effect of jet velocity of aqueous phase on air stripping of ammonia (left) and mass transfer coefficient of ammonia removal (riht). Experimental conditions: V_L=10 l, Q_g=1.9 l/s, C_{in}=3812 mg/l, Pressure drop 0.2-0.3 MPa, Temperature 14 - 15℃.

3.1.3 Effect of air flow rate

The effect of air flow rate Q_g on air stripping efficiency and on the volumetric mass transfer coefficient of ammonia removal is shown in Fig. 5. It seems that there is a critical value for air flow rate, which is about 1.4 l/s under the corresponding experimental conditions. When air flow rate is below this value, it has less effect on both the efficiency and the mass transfer coefficient of ammonia removal; but when air flow rate is over this value, it can result in an obvious increase in the two values.

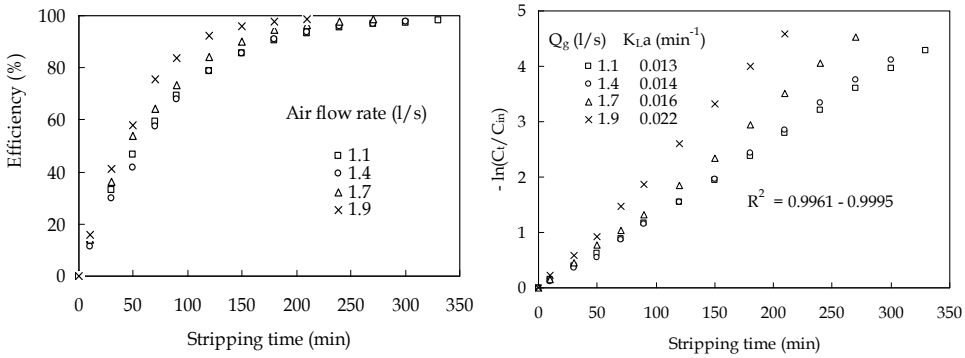

Fig. 5. Effect of air flow rate on air stripping of ammonia (left) and mass transfer coefficient of ammonia removal (right). Experimental conditions: V_L=10 l, U_L=0.55 m/s, C_{in}=2938 mg/l, Temperature 14 -15 ◦C, Pressure drop 0.12-0.3 MPa.

The phenomenon mentioned above is probably associated with the effect of the air flow on the interface of the gas-liquid phases. As mentioned above, the overall mass transfer resistance for ammonia removal is mainly present in the gas film side. The mass transfer resistance in the gas film side can be reduced by increasing the air flow rate. When the air flow rate is within a lower range (< 1.4 l/s in this work), the increase of the air flow rate has almost no effect on the mass transfer coefficient (from 0.013 to 0.014 min^{-1}) probably because

of the lower shear stress on the surface of the water droplets. Higher gas flow rate (>1.4 l/s in this work), produces larger shear stress on the droplet surface, thus clearly reducing the gas film resistance and increasing the mass transfer coefficient greatly (from 0.014 to 0.022 min^{-1}). On the other hand, a higher gas flow rate can produce larger shear stress, which exerts on the surface of the water droplets and along the porous tube surface, to cause the breakage of water drops into fine drops or even forming mist, thus leading to an obvious increase in mass transfer area. Therefore, the obvious increase in the $K_L a$ when the air flow rate was over 1.4 l/s may be caused by the combinational effect of this two reasons, showing clearly the effect of a highly rotating air field enhancing mass transfer between phases.

In fact, from the viewpoint of the dispersed and continuous phases, the gas-liquid mass transfer process in the WSA is similar with that in the impinging stream gas-liquid reactor (ISGLR), which enhances mass transfer using two opposite impinging streams (Wu et al., 2007). In the ISGLR, there is also a critical point of impinging velocity, 10 m/s. The effect of impinging velocity on the pressure drop increases rapidly before this critical point, and after that the effect becomes slower. The reason for this is not quite clear yet, but it is possible that a conversion of a flow pattern occurs at this point (Wu et al., 2007). Likely, the rapid increase of the mass transfer coefficient in the WSA after the critical point may be also caused by a conversion of flow patterns occurring at this point, but this needs to be further investigated.

Now there are two kinds of devices that can also enhance mass transfer very efficiently, i.e. ISGLR (Wu et al., 2007) and the rotating packed bed (RPB) (Chen et al.,1999; Munjal & Dudukovic, 1989a; Munjal & Dudukovic, 1989b). Making a comparison among these devices, the WSA, ISGLR and RPB, all have essentially the same ability of enhancing the mass transfer between the gas and liquid phases. WSA and ISGLR have no moving parts, whereas RPB is rotating at a considerably high speed, and needs a higher cost and maintenance fee, and possibly has a short lifetime (Wu et al., 2007). In addition, WSA has the advantage of a simple structure, easy operation, low cost and higher mass transfer efficiency.

3.1.4 Effect of aqueous phase temperature

Both ammonia removal efficiency and the mass transfer coefficient increase with the aqueous phase temperature, as shown in Fig. 6. Particularly, when the temperature increases over 25 ℃, the effect is more obvious. First, the increase of temperature will promote the molecular diffusion of ammonia in a gas film, resulting in the increase of the $K_L a$. On the other hand, the gas-liquid distribution ratio K is the function of pH and temperature, and can be expressed as the following equation (Saracco & Genon, 1994):

$$K = \frac{1.441 \times 10^5 \times e^{-3513/T}}{1 + 2.528 \times 10^{-pH} \times e^{6054/T}} \tag{9}$$

Calculation indicates that when ambient temperature exceeds 25 ℃, the increase of temperature will lead to a more obvious increase of the distribution ratio K. Provided the pH is high enough (such as 11), temperature strongly aids ammonia desorption from water. This makes the driving force of mass transfer increase largely. These two effects of temperature accelerate ammonia removal from water. If possible, the air stripping of ammonia should be operated at a higher temperature.

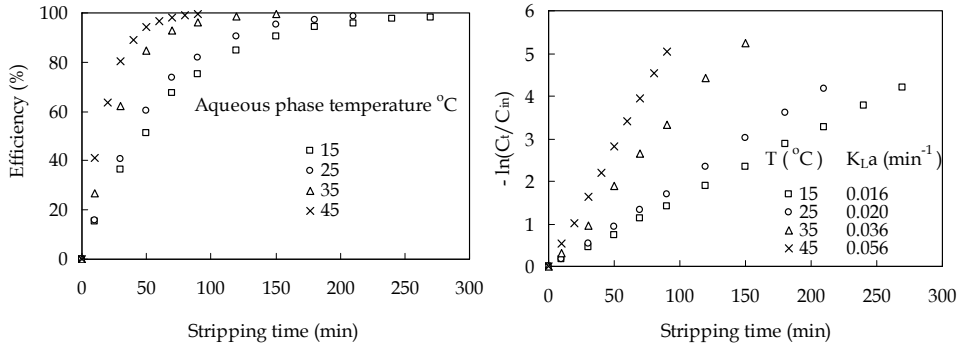

Fig. 6. Effect of aqueous phase temperature on air stripping of ammonia (left) and mass transfer coefficient of ammonia removal (right). Experimental conditions: V_L =10 l, U_L =0.55 m/s, Q_g =1.9 l/s, C_{in} =2910 mg/l, Pressure drop 0.2-0.3 MPa.

3.1.5 Comprehensive evaluation and comparison with other traditional equipments

As stated in the introduction, the main goal of the present work is to solve two problems in the air stripping of ammonia, i.e. improving process efficiency and avoiding scaling and fouling on a packing surface is usually used in packed towers. Compared with a traditionally used stirred tank and packed tower, the air stripping efficiency of ammonia in the newly developed WSA is very high because of the unique gas-liquid contact mode in the WSA. In operation of the WSA, the major parameters are air flow rate and aqueous phase temperature. In order to get a higher stripping efficiency, air stripping of ammonia should be operated at a higher air flow rate (> 1.4 l/s) and a higher ambient temperature (> 25 ℃). As for scaling and fouling, after many experiments, no scale and foul were observed in the inner structure of the WSA although there were $Ca(OH)_2$ particles suspended in the aqueous phase. The self cleaning effect of the WSA is probably caused by a strong turbulence of fluids in the WSA.

It is interesting to make a comparison between different air stripping processes of ammonia to understand the characteristics of the WSA. Air stripping of ammonia is generally carried out in stripping tanks and packed towers. The mass transfer coefficients of some typical stripping processes are compared in Table 1. At the same temperature, using the WSA to strip ammonia can get a higher mass transfer coefficient than using other traditional equipments; in addition, the air consumption is far less than that of the compared processes.

Equipments	Stripping conditions	Air consumption Q_G/V_L (l / l.s)	K_La (min^{-1})	References
WSA	V_L = 10 l , Q_G = 1.9 l/s, temperature 15 ℃	0.19	0.016	This work
Tank	V_L = 50 ml , Q_G = 0.08l/s, pH=12.0, temperature 16 ℃	1.60	0.008	Basakcilardan -kabakci, et al., 2007
Packed tower	V_L= 1000 l , Q_G =416.7l/s, pH=11.0,temperature15℃	0.42	0.007	Le et al., 2006

Table 1. The comparison of the air consumption and the mass transfer coefficients of the air stripping of ammonia in different equipments.

3.2 The mass transfer mechanism within the WSA

As discussed above, air flow rate is the major parameter affecting the volumetric mass transfer coefficient $K_L a$ in the WSA from the viewpoint of hydrodynamics. So the effects of the gas phase inlet velocity on k_L, a and $K_L a$ were all further investigated using a CO_2—NaOH rapid pseudo first order reaction system, to further elucidate the mass transfer mechanism within this new mass transfer equipment.

The results were shown in Fig. 7. It is known from Fig. 7(c) that the overall volumetric mass transfer coefficient increases almost linearly with the increasing of gas phase inlet velocity with a larger slope until the gas phase inlet velocity increases to about 10 m/s, and then almost linearly increases with a slightly lower slope, indicating that when U_g is higher than 10 m/s, the increasing rate of $K_L a$ with U_g was slowed down. From Fig. 7(a), it could be seen that the k_L increases very rapidly and linearly with the increase of U_g until it reaches about 8 m/s, and then the change of k_L with U_g has no remarkable behavior or even is leveled off. In contrast, the specific mass transfer area a increases proportionally with the increase of U_g almost in the whole experimental range of the gas phase inlet velocity, as shown in Fig. 7(b). Therefore, both k_L and a simultaneously contribute to the increase of the overall $K_L a$ before about 8 m/s of U_g making it increase rapidly; after that only a contributes to the increase of the $K_L a$, leading to the slowing down of its increase.

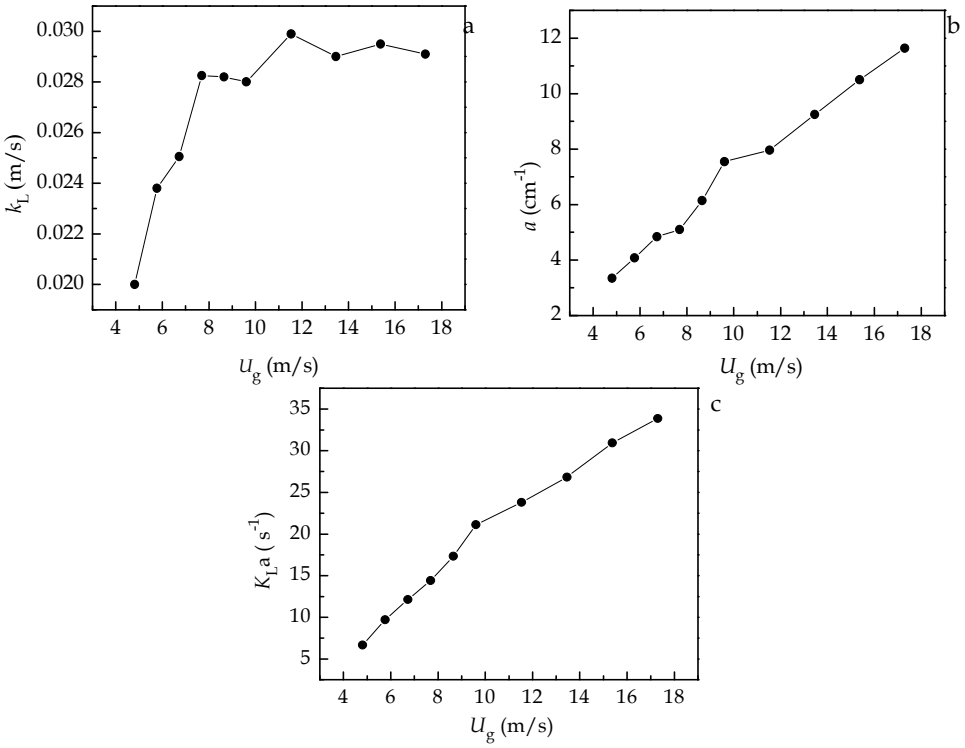

Fig. 7. Effect of gas phase velocity on the mass transfer coefficient in liquid side film (a), the specific mass transfer area (b)and the volumetric mass transfer coefficient (c) within the WSA for CO_2—NaOH system. Experimental conditions: U_L=0.33 m/s, Liquid phase temperature 27~29.7 ◦C.

As a result, it appears that the gas cyclone field in the WSA does intensify the mass transfer process between gas-liquid phases. There is a critical gas phase inlet velocity. When U_g is lower than this value, the increase of the inlet velocity has a double function of both intensifying k_L and increasing mass transfer area; whereas when U_g is larger than this value, the major function of U_g increase is to make the water drops in the WSA broken, mainly increasing the mass transfer area of gas-liquid phases. From the viewpoint of hydrodynamics, increasing the U_g will intensify the gas cyclone field in the WSA and increase the shear stress on the water drops, thus resulting in the thinning of the gaseous boundary layer around the water drops and facilitating the increase of k_L. However, when the thinning of the boundary layer is maximized by the increase of U_g, the change of k_L will become leveled off with increasing the U_g. So theoretically, there should be a critical value, as mentioned above, which could make the k_L maximized.

3.3 The pressure drop characteristic of gas phase through the WSA

The pressure drop of gas phase ΔP and the liquid content ε_L through the WSA were simultaneous measured in this work, so as to more clearly understand the transport process occurring in the WSA. The changes of ΔP and ε_L with U_g under different water jet conditions are shown in Fig. 8.

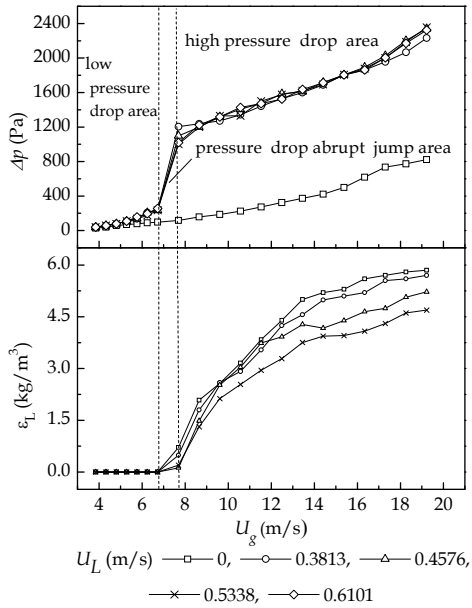

Fig. 8. Effect of inlet gas velocity on pressure drop and liquid holdup at different jet velocities.

It could be seen that when there was no liquid jet in the WSA, i.e. $U_L = 0$, the ΔP increased continuously with the increase of U_g, exhibiting the pressure drop characteristic of a traditional cyclone. Further it was observed that the data could fit the pressure drop formula, Eq.10 very well, and the resistance coefficient $\xi = 3.352$.

$$\Delta p = \xi \frac{U_g^2}{2} \rho_g \tag{10}$$

where ΔP—pressure drop, Pa; ξ—resistance coefficient; U_g —gas phase inlet velocity, m/s; ρ_g —gas phase density, kg/m^3.

Meanwhile, it could be also seen that when there was jet in the WSA, the change of the ΔP with U_g was obviously different from that for a traditional cyclone. When U_g<6.728 m/s, ε_L ≈0, the ΔP in this area was higher than that for a traditional cyclone; when U_g ≥7.690 m/s, ε_L increased rapidly with U_g, and ΔP also increased continuously with the increase of U_g but had an additional pressure drop value higher than that for a traditional cyclone under a certain U_g. Here it is worthy of noting that the gas inlet velocity for ε_L rapid increase (U_g ≥7.690 m/s) is very close to that for k_L maximization (about 8 m/s, as mentioned in section 3.2). So this again indirectly indicated that this value should be the critical gas inlet velocity at which water drops and jets were broken into a large number of small droplets or fog, simultaneously increasing ε_L and a. Interestingly, it can be seen that when U_g =6.728 ~ 7.690m/s, ε_L increased rapidly from zero and the ΔP jumped from a lower to a higher pressure area, the jumped height seems to equal the additional value as just stated before. It could be believed that the pressure drop jump was caused by the transformation of liquid flow pattern when the U_g increased to a critical value. And this could be justified by the abrupt increase of ε_L at U_g =6.728 m/s. Thus the pressure drop within the overall experimental range of U_g could be roughly divided into three areas, respectively called low pressure drop area, pressure drop jump area and high pressure drop area. In fact, the three pressure drop areas corresponded respectively to the observed three kinds of liquid flow pattern, here respectively called steady-state jet (U_g <6.728 m/s), deformed spiral jet (U_g = 6.728~7.690 m/s) and atomized spiral jet (U_g ≥7.690 m/s).

Further it could be seen from Fig. 8 that when U_g >6.728 m/s, the liquid jet velocity had little effect on the ΔP, thus indicating the dominant role of the gaseous cyclone field in the WSA. This is in agreement with the conclusion that the gas phase inlet velocity is the major process parameter, as stated above. From the experimental results and the related discussion mentioned above, the ΔP, $K_L a$ and ε_L all increased with the increase of U_g, this further indicated that the mass and momentum transfer processes in the WSA were closely interlinked and occurred simultaneously.

The major factors affecting the ΔP include gas density ρ_g, gas viscosity μ_g, gas inlet velocity U_g, liquid density ρ_L, liquid jet velocity U_L, the diameter of jet holes d, liquid surface tension σ_L, the inner diameter D. The following dimensionless equation could be obtained using dimensional analysis:

$$Eu_g = f(\mathrm{Re}_g, We_L, \frac{d}{D}) \tag{11}$$

Here, $Eu_g = \dfrac{\Delta p}{\rho_g U_g^2}$ is the Euler number; $\mathrm{Re}_g = \dfrac{\rho_g U_g d_0}{\mu_g}$ the Reynolds number of gas phase; $We_L = \dfrac{\rho_L U_L^2 d}{\sigma_L}$ the Weber number of liquid phase and dimensionless diameter, d/D.

Using the experimental data to fit Eq. 11 could obtain the following equations:

1. For the low pressure area: $Eu_g = 1.3685 \times 10^{-4}\, \mathrm{Re}_g^{1.2353}\, We_L^{0.0163}$, with R^2=0.98;
2. For the high pressure area: $Eu_g = 4.3131 \times 10^{5}\, \mathrm{Re}_g^{-1.2233}\, We_L^{0.0022}$, with R^2=0.99.

The dimensionless diameter d/D does not appear in the two equations because it was maintained at a constant value in the pressure drop experiments. But this will be further investigated in the near future to optimize the structure of the WSA. From these two equations, it could be seen that the power of the We_L number is too small to be neglected compared with other powers in the same equation, indicating that We_L has little effects on the ΔP. This is in agreement with the experimental result mentioned above that the jet velocity had little effect on the ΔP, and it was mainly controlled by gas inlet velocity. So ignoring the We_L in Eq.11 and using the experimental data to fit it again, the following equations could be obtained:

1. For the low pressure area: $Eu_g = 1.4111 \times 10^{-4}\, \mathrm{Re}_g^{1.2353}$, with R^2=0.98;
2. For the high pressure area: $Eu_g = 4.3371 \times 10^{5}\, \mathrm{Re}_g^{-1.2234}$, with R^2=0.99.

These equations apply for $\mathrm{Re}_g = 2.3 \times 10^3 \sim 11.7 \times 10^3$ and $We_L = 3.98 \sim 10.21$, and the relative deviation between the experimental and calculated values using the above equations, is less than 7.7 % in the whole range of experimental data, showing a satisfactory prediction, as shown in Fig. 9.

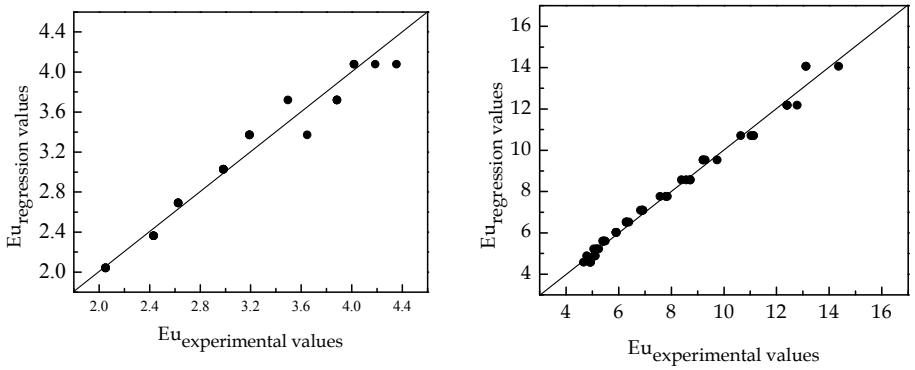

Fig. 9. Compares of regression values and experimental values, (left) low pressure drop area (right) high pressure drop area.

4. The application of the WSA in wastewater treatment

As a mixer and stripper, the WSA could be used for the precipitation of some hazardous materials and for the stripping of volatile substances in wastewaters. As an example, the WSA and the experimental setup as shown in Fig. 2, was used for the treatment of an anaerobically digested piggery wastewater (Quan et al., 2010).

Pig farms with hundreds to several thousands of animals are in operation in many countries without adequate systems for waste treatment and disposal (Nikolaeva et al., 2002). A large amount of piggery waste is discharged from the cages every day. This waste is a mixture of feces, urine and food wastage (Sanchez et al., 2001). Piggery waste is characterized by a high content of organic matter and pathogenic microorganisms. Anaerobic digestion could be considered as one of the most promising treatment alternatives for this kind of waste. In practice, many large scale pig farms in Chongqing area collect the liquid and solid fractions of piggery waste separately in pig cages to minimize the amount of piggery waste. This collection mode is a water-saving process and is beneficial to subsequent treatment. The solid fraction is directly transported to an anaerobic digester for fermentation to make organic fertilizer. The liquid fraction, a mixture of pig urine, manure leachate and washing wastewater, flows into an anaerobic digester after passing through a simple screen mesh. Practice illustrates that anaerobic digestion can greatly reduce the COD of piggery wastewater (Nikolaeva et al., 2002) . Practical operation of anaerobic digestion in many pig farms in Chongqing area can make the COD of piggery wastewater to be reduced to lower than 500 mg/l. But the anaerobically digested liquor usually still contains more than 160 mg/l of NH_3-N and more than 30 mg/l of total P. The national discharge standards of pollutants for livestock and poultry breeding stipulated that the COD, NH_3-N and total P must be lower than 400 mg/l, 80 mg/l and 8.0 mg/l, respectively (GB 18596-2001). So the anaerobically digested liquor of piggery wastewater needs to be further treated to make its COD, especially NH_3-N and total P to be decreased to lower than the required values stipulated by the national standards.

The further removal of NH_3-N and total P from anaerobically digested liquor can be conducted using air stripping (Bonmati & Floatats, 2003; Basakcilardan-kabakci et al., 2007; Marttinen et al., 2002; Ozturk et al., 2003; Saracco & Genon, 1994) and struvite precipitation (Jeong & Hwang, 2005; Lee et al., 2003). Similar with the struvite precipitation, it was reported that calcium ions can be also used as a precipitant to form $CaNH_4PO_4.4H_2O$ (Li et al., 2007). This work presented an efficient integrated process, which consists of chemical precipitation and air stripping, for the simultaneous removal of NH_3-N, total P and COD from anaerobically digested piggery wastewater. In the process, cheap $Ca(OH)_2$ was chosen as the precipitant for NH_4^+ and PO_4^{3-}, as pH adjuster for the air stripping of ammonia. The WSA was used to validate the large scale application possibility of the suggested simultaneous removal process.

The anaerobically digested liquor of piggery wastewater used in this experiment was taken from the effluent of the largest pig farm in Chongqing city, China. The pig farm is located in the Rongchang County, the modern animal husbandry area of China, about 100 km northwest of Chongqing city. The liquid and solid fractions of piggery waste are separately collected in the pig farm. The liquid fraction (a mixture of urine, leachate of manure and washing water) flows into an anaerobic digester after passing through a simple plastic screen. The effluent generally contains COD 150~500 mg/l, more than 160 mg/l of NH_3-N and more than 30 mg/l of total P and its pH is 7.3~8.0.

The simultaneous removal of N, P and COD from the anaerobically digested liquor was conducted in the new WSA, as shown in Fig. 2. For every run, 12 l of the digested liquor was poured into the water tank in the experimental setup and then added different dosages of $Ca(OH)_2$ powder under proper stirring to form a suspension with a pH higher than 11. Then

the air was pumped into the aerocyclone at a prescribed flow rate. When the pressure reading reached a steady state, the circulation pump at a certain flow rate pumped the suspension in the tank into the WSA. During circulation, the concentrations of NH_3-N, total P and COD in the suspension were continuously decreased because of the chemical precipitation reaction, air stripping of residual ammonia and adsorption. The suspension samples were taken out from the water tank and centrifuged to get supernatants for the determination of NH_3-N, total P and COD. All the experiments were carried out at ambient temperature (28~30℃). Each experiment was repeated to get experimental data with an error of less than 5 %, and the averaged value was used.

The effects of process parameters, including $Ca(OH)_2$ dosage, air inlet velocity (U_g) and jet velocity of liquid phase (U_L), on the simultaneous removal of NH_3-N, total P and COD were investigated for the optimization of operation conditions. All the results were shown in Figs. 10-13.

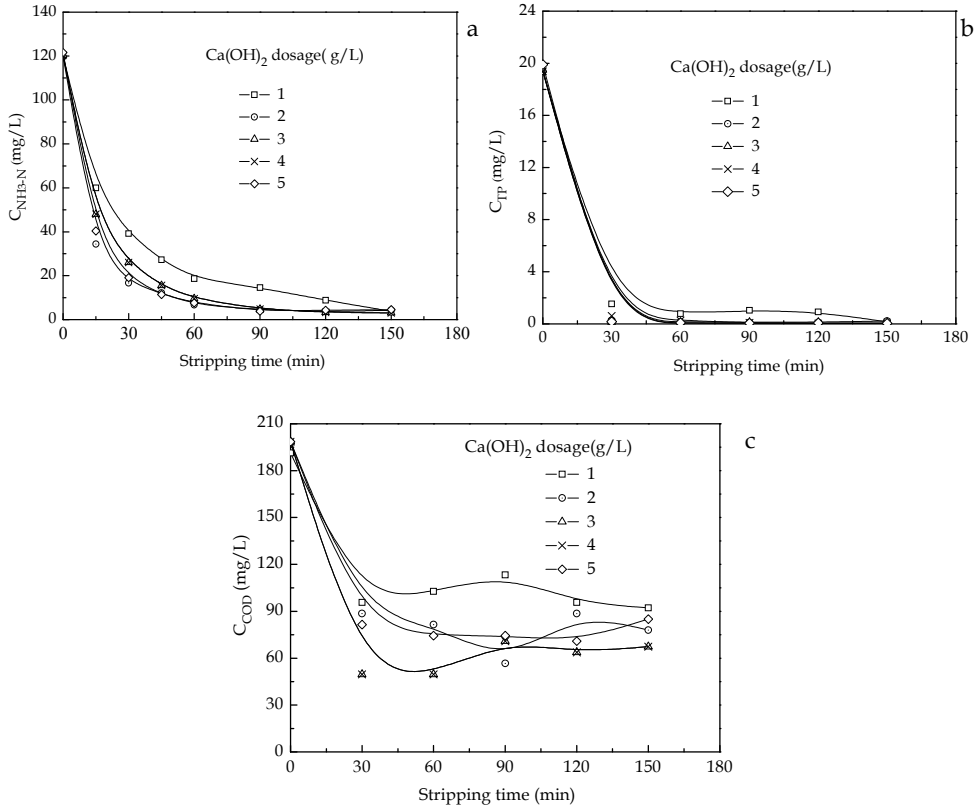

Fig. 10. The effects of $Ca(OH)_2$ dosage on NH_3-N (a), total P (b) and COD (c) removal. Experimental conditions: V_L =12 L, U_l = 0.37m/s, U_g = 4.81 m/s , Temperature: 28~30 ^oC.

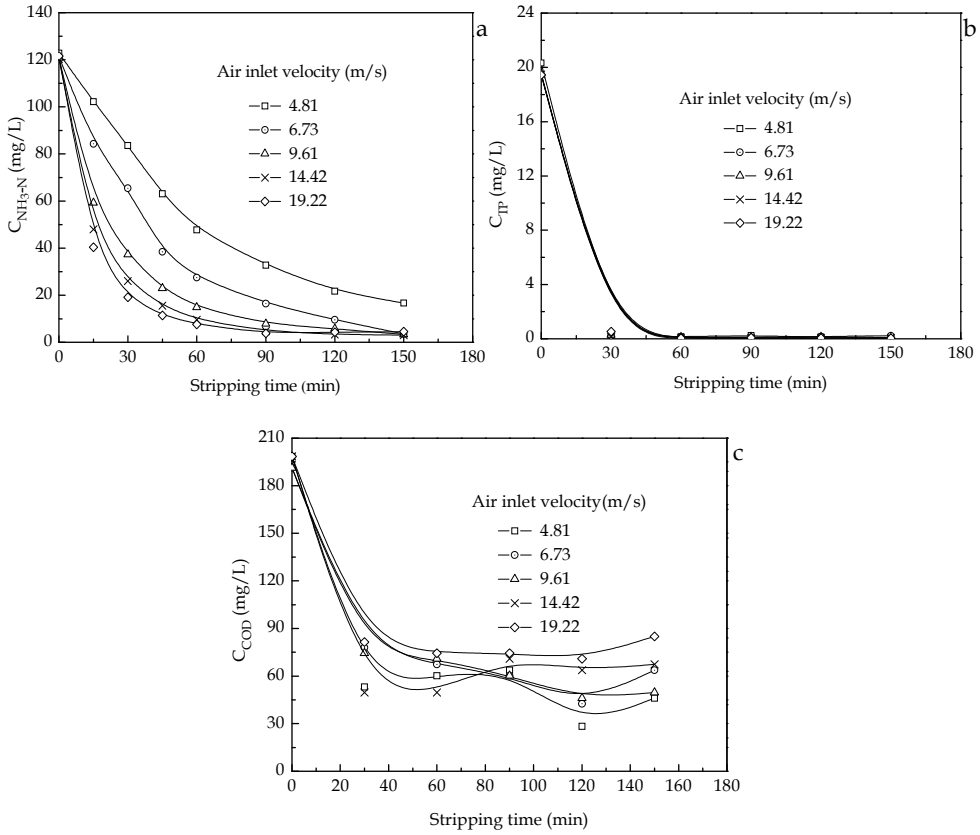

Fig. 11. The effects of air inlet velocity on NH_3-N (a), total P (b) and COD (c) removal. Experimental conditions: V_L =12 L, U_l = 0.37 m/s, $Ca(OH)_2$ dosage =3 g/l, Temperature 28~30 ºC.

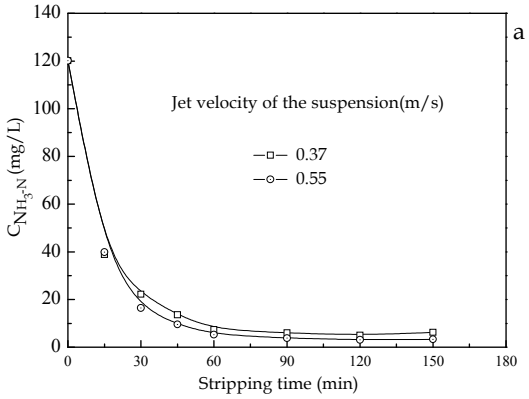

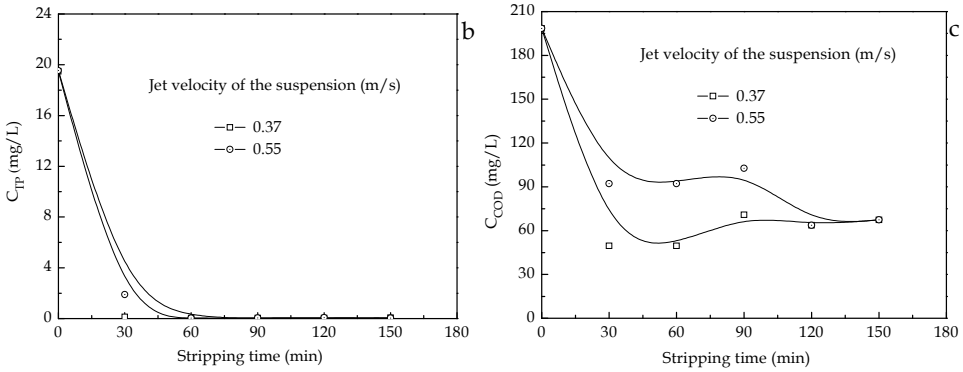

Fig. 12. The effects of jet velocity of the suspension on NH_3-N (a), total P (b) and COD removal (c). Experimental conditions: V_L =12 L, U_g = 4.81 m/s, $Ca(OH)_2$ dosage =3g/l, Temperature: 28~30 °C.

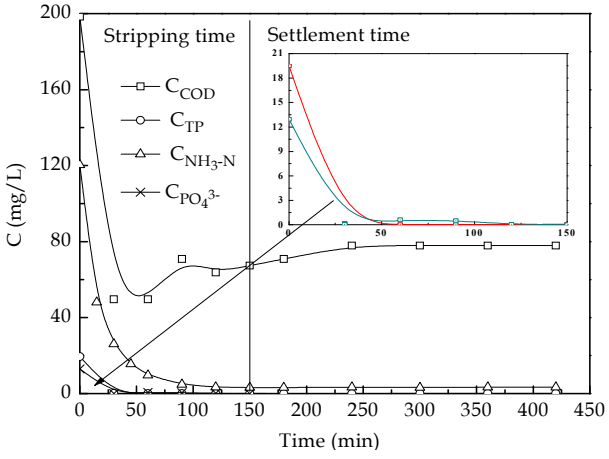

Fig. 13. The effects of stripping time and sedimentation time on NH_3-N, total P and COD, PO_4^{3-} removal. Experimental conditions: V_L =12 L, U_g = 4.81 m/s, U_l=0.37 m/s, $Ca(OH)_2$ dosage =3 g/l, Temperature: 28~30 °C.

It could be seen that the physicochemical process occurring in the gas-liquid-solid multiphase system in the integrated process could be conducted and operated very well in air stripping equipment without any packing. The WSA could be effectively used for the simultaneous removal of NH_3-N, total P and COD. 3 g/l of $Ca(OH)_2$ is a proper dosage for the simultaneous removal. A higher air inlet velocity is beneficial to the removal rate of NH_3-N. A higher jet velocity of the liquid phase results in a faster removal of the total P. Selecting the air inlet velocity and the liquid jet velocity is needed for a better simultaneous

removal of NH_3-N, total P and COD. Nevertheless, in all the cases, the removal efficiencies of the NH_3-N, total P and COD were over 91 %, 99.2 % and 52 % for NH_3-N, total P and COD, respectively.

5. Conclusions

Air stripping of ammonia is a widely used process for the pretreatment of wastewater. Traditionally, this process is carried out in stripping tanks or packed towers. In practice, scaling and fouling on a packing surface in packed towers and lower stripping efficiency are the two major problems in this process.

In order to enhance process efficiency and avoid scaling and fouling in long run operations, new equipment that is suitable for air stripping of wastewater with suspended solids was developed. Air stripping of ammonia from water with $Ca(OH)_2$ was performed in the newly designed gas-liquid contactor water-sparged aerocyclone (WSA). WSA exhibited a higher air stripping efficiency and an excellent mass transfer performance, and consumed less air compared with stripping tanks and packed towers. In addition, no scaling and fouling was observed in the inner structure of the WSA. The stripping efficiency and mass transfer coefficient in the WSA obviously increases with the liquid phase temperature and air flow rate. An efficient air stripping of ammonia should be conducted at a higher ambient temperature and a higher air flow rate.

In order to reveal the mechanism of the mass transfer process in the WSA, the effect of the major parameter—gas phase inlet velocity, on the liquid side film mass transfer coefficient k_L, and specific mass transfer area a was separately investigated using a CO_2—NaOH rapid pseudo first order reaction system. The results indicated that there is a critical gas phase inlet velocity. When U_g is lower than this value, the increase of the inlet velocity has a double function of both intensifying k_L and increasing mass transfer area; whereas when U_g is larger than this value, the major function of U_g increase is to make the water drops in the WSA broken, increasing the mass transfer area of gas-liquid phases.

The pressure drop of gas phase ΔP was also investigated in this work, so as to more clearly understand the transport process occurring in the WSA. It was observed that when there were jets in the WSA, the change of the ΔP with U_g was obviously different from that for a traditional cyclone. And the pressure drop within the overall experimental range of U_g could be roughly divided into three areas, which could be called low pressure drop area, pressure drop jump area and high pressure drop area, respectively. In fact, the three pressure drop areas corresponded respectively to the observed three kinds of liquid flow pattern, i.e. the so called steady-state jet (U_g < 6.728 m/s), deformed spiral jet (U_g = 6.728~7.690 m/s) and atomized spiral jet ($U_g \geq$ 7.690 m/s). The following equations,

$$Eu_g = 1.4111 \times 10^{-4}\,\mathrm{Re}_g^{\,1.2353} \quad \text{and} \quad Eu_g = 4.3371 \times 10^{5}\,\mathrm{Re}_g^{\,-1.2234},$$

could be used for the prediction of the gas phase pressure drop, respectively, for the low pressure area and for the high pressure area, with a satisfactory degree.

As an example, the WSA was used for the treatment of an anaerobically digested piggery wastewater. Practice showed that the WSA could be effectively used for the simultaneous removal of NH_3-N, total P and COD from the wastewater. 3 g/l of $Ca(OH)_2$ is a proper dosage for the simultaneous removal. A higher air inlet velocity is beneficial to the removal

rate of NH_3-N. A higher jet velocity of the liquid phase results in a faster removal of the total P. Selecting the air inlet velocity and the liquid jet velocity is needed for a better simultaneous removal of NH_3-N, total P and COD. In all the cases, the removal efficiencies of the NH_3-N, total P and COD exceeded 91 %, 99.2 % and 52 % for NH_3-N, total P and COD, respectively.

6. Acknowledgements

This work was financially supported by the Chongqing Science and Technology Committee under grant no. CSTC2005AC7107, CSTC2009AB1048, and by the key discipline construction project—"Chemical Engineering and Technology" in Chongqing University of Technology.

7. References

Basakcilardan-kabakci, S., Ipekoglu, A.N. & Talinli, I. (2007). Recovery of ammonia from human urine by stripping and absorption, Environmental Engineering Science Vol.24 (5): 615-624.

Bokotko, R.P., Hupka, J. & Miller J.D. (2005). Flue gas treatment for SO2 removal with air-sparged hydrocyclone technology, Environmental Science & Technology Vol.39: 1184-1189.

Bonmati, A. & Floatats X. (2003). Air stripping of ammonia from pig slurry: characterization and feasibility as a pre- or post-treatment to mesophilic anaerobic digestion, Waste Management Vol.23: 261-272.

Calli, B., Mertoglu, B. & Inanc, B. (2005). Lanfill leachates management in Istanbul: applications and alternatives, Chemosphere Vol.59: 819-829.

Chen, H., Deng, X., Zhang, J. & Zhang J. (1999). Measurements of the effective interface area and volumetric mass transfer coefficient in a multistage rotating packed bed with centrifugal atomizing by chemical adsorption, Chemical Reaction Engineering & Processing Vol.15 (1): 97-103 (in Chinese).

Dempsey, M.J., Lannigan, K.C. & Minall, R.J. (2005). Particulate-biofilm, expanded-bed technology for high-rate, low-cost wastewater treatment: Nitrification, Water Research Vol.39: 965-974.

Djebbar, Y. & Naraitz, R.M. (1998). Improved Onda correlations for mass transfer in packed towers, Water Science Technology Vol.38 (6): 295-302.

GB 18596-2001. The national standard of the People's Republic of China—discharge standard of pollutants for livestock and poultry breeding.

Hung, C.M., Lou, J.C. & Lin, C.H. (2003). Removal of ammonia solutions used in catalytic wet oxidation processes, Chemosphere Vol.52: 989-995.

Jeong ,Y.K. & Hwang, S.J. (2005). Optimum doses of Mg and P salts for precipitating ammonia into struvite crystals in aerobic composting, Bioresource Technology Vol. 96: 1-6.

Jorgensen, T.C. & Weatherley, L.R. (2003). Ammonia removal from wastewater by ion exchange in the presence of organic contaminants, Water Research Vol.37: 1723-1728.

Lee, S.I., Weon, S.Y., Lee, C.W. & Koopman, B. (2003). Removal of nitrogen and phosphate from wastewater by the addition of bittern, Chemosphere Vol.51: 265-271.

Le, L., Wang, H.W. & Lu, H.H. (2006). Nitrogen removal using an air stripping tower in an urban wastewater treatment plant, China Water & Wastewater Vol.17: 92-95 (in Chinese).

Li, Y.F., Yi, L.X., Ma, P.C. & Zhou, L.C (2007). Industrial wastewater treatment by the combination of chemical precipitation and immobilized microorganism technologies, Environmental Engineering Science Vol.24: 736-744.

Marttinen, S.K., Kettunen, R.H., Sormunen, K.M., Soimasuo, R.M. & Rintala, J.A. (2002). Screening of physical-chemical methods for removal of organic material, nitrogen and toxicity from low strength landfill leachates, Chemosphere Vol. 46: 851-858.

Matter-Muller, C., Gujer, W. & Giger, W. (1981). Transfer of volatile substances from water to the atmosphere, Water Research Vol.15: 1271-1279.

Munjal, S. & Dudukovic, P. (1989a). Mass transfer in rotating packed beds—I Development of gas—liquid and liquid—solid mass transfer correlations, Chemical Engineering Science, Vol.44 (10): 2245—2256.

Munjal, S. & Dudukovic, P. (1989b). Mass transfer in rotating packed beds—II Experimental results and comparison with theory and gravity flow, Chemical Engineering Science, Vol.44 (10): 2257—2267.

Nikolaeva, S., Sanchez, E., Borja, R., Travieso, L., Weiland, P. & Milan, Z. (2002). Treatment of piggery waste by anaerobic fixed bed reactor and zeolite bed filter in a tropical climate: a pilot scale study, Process Biochemistry Vol.38: 405-409.

Ozturk, I., Altinbas, M., Koyuncu, I., Arikan, O. & Gomec-Yangin C. (2003). Advanced physical-chemical treatment experiences on young municipal landfill leachates, Waste Management Vol. 23: 441-446.

Quan, X., Ye, C., Xiong, Y., Xiang, J. & Wang, F. (2010). Simultaneous removal of ammonia, P and COD from anaerobically digested piggery wastewater using an integrated process of chemical precipitation and air stripping, Journal of Hazardous Materials Vol.178: 326-332.

Rensburg, P., Musvoto, E.V., Wentzel, M.C. & Ekama G.A. (2003). Modelling multiple mineral precipitation in anaerobic digester liquor, Water Research Vol.37: 3087-3097.

Sanchez, E., Borja, R., Weiland, P. & Travieso, L. (2001). Effect of substrate concentration and temperature on the anaerobic digestion of piggery waste in tropical climates, Process Biochemistry Vol.37: 483-489.

Saracco, G. & Genon, G. (1994). High temperature ammonia stripping and recovery from process liquid wastes, Journal of Hazardous Materials Vol. 37: 191-206.

Tan, X.Y., Tan, S.P., Teo, W.K. & Li, K. (2006). Polyvinylidene fluoride (PVDF) hollow fibre membranes for ammonia removal from water, Journal Membrance Science Vol.271: 59-68.

Tsai, R.E., Seibert, A.F., Eldridge R.B. & Rochelle, G.T. (2009). Influence of viscosity and surface tension on the effective mass transfer area of structured packing, Energy Procedia Vol.1: 1197-1204.

Uludag-Demirer, S., Demirer, G.N. & Chen, S. (2005). Ammonia removal from anaerobically digested dairy manure by struvite precipitation, Process Biochemistry Vol.40: 3667-3674.

Wu, Y., Li, Q. & Li, F. (2007). Desulfurization in the gas-continuous impinging stream gas-liquid reactor, Chemical Engineering Science Vol.62: 1814-1824.

18

Hydrodynamical Simulation of Perspective Installations for Electrometallurgy of Aluminium

A. S. Filippov, A. A. Kanaev, V. I. Kondakov and I. A. Korotkin
Nuclear Safety Institute/Russian Academy of Sciences
Russian Federation

1. Introduction

Electrometallurgy is based on the electrolysis of fused chemical compounds of the metals. The process of electrolysis is not a simple chemical reaction of mix and match. As electricity is involved in this process, care is taken to understand and set up the apparatus as required. In view of this, basic requirements for theoretical, experimental understanding and following set up procedures are to be studied. The process inherent features, which define the hydrodynamics of the melt are:

- high-strength electric current, which generates a large amount of Joule heat; spatial distribution of the volumetric power may be nonuniform
- chemical reactions, which change the compound and generate a large amount of the gas bubbles; this may result in gradients of the melt density and current density
- bubble rising, which strongly defines the velocities at the melt.

The experimental explorations in the electrometallurgy are usually difficult or impossible because of the high temperature and hostile environment. For this reason electrometallurgical processes are the application field of CFD. The aim of this chapter – to demonstrate such application based on well developed and widely used methods of numerical analysis. The object of the development is an electrometallurgy of aluminium. The presented mathematical model of vertical electrode cell takes into account the electric field and current density, chemical composition, heating, natural convection, bubble flows. The integrated model of such kind may be used for the detailed 3D numerical simulations of the new installations.

1.1 Aluminium electrolysis as the task for electrochemical hydrodynamics

It should be noted that for today's aluminium electrolysis cells (AE) CFD modeling unlikely gives essentially new results. One obvious reason is that modern aluminium production technology exists already several decades. To explain the other reasons and the problem statement let's consider the typical multielectrode electrolytic cell for aluminium production. The advantages and disadvantages of the modern AE will be evident from this consideration.

The earth's crust contains about 9 percents of aluminium. But because of high chemical activity of this metal alumina (Al_2O_3) is highly stable and so cannot be reduced by conventional reducing agents like coke, carbon monoxide or hydrogen. To detach the metal from the oxygen the sodium aluminum fluoride is used, which is named cryolite (Na_3AlF_6). Actually the industrial electrolyte contains also the additions of aluminum, calcium,

magnesium fluorides (AlF_3, CaF_2, MgF_2), which allow to decrease the melting temperature (Borisoglebsky et al., 1999). For the sake of simplicity this composition in the electrolyte will also be referred as cryolite. Molten aluminium is deposited under a cryolite solution with 3-5% alumina.

The metal arises during the well known Hall-Heroult process (Grjotheim et al., 1982). The main products of the reactions are the aluminium and oxygen. The latter is generated at anode. Anodes of modern aluminium reduction cells consist mainly of the coal, which is inert with respect to cryolite. But oxygen joints the carbon, and carbon dioxide with small amount of carbon monoxide are the main gaseous reaction products. This results in the ecological problem involved with atmospheric pollution. The second technological problem is involved with the necessity of periodical changing of the spent electrodes because the coal anodes are consumed very quickly. While anode diminishes distance between the cathode and anode plates should be maintained constant. The only way to keep this distance is to make the working space horizontal as it is depicted at left in figure 1. Usually the aspect ratio of the horizontal working space has the order of 1/30. This horizontality causes the next two features. One is in the nonoptimal use of the area of the aluminium plant. The next feature is involved with so called anode effect: the rising of voltage, which can be caused by unsufficient rate of diffusion of alumina to the anode surfaces and also by accumulation of the generated gas in horizontal gap. This effect temporarily blocks the current and may result in stopping of the electrolysis in several cells.

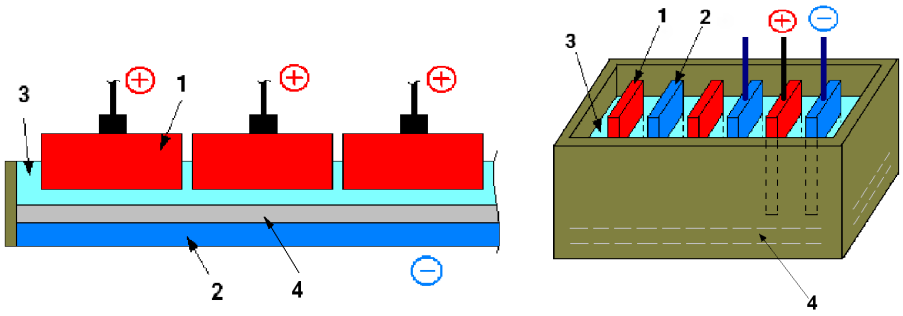

Fig. 1. Electrolytic cells with horizontal and vertical working spaces. 1– anode, 2– cathode, 3– electrolite, 4 – liquid aluminium.

The mathematical modeling of modern horizontal AEs is used mainly for the optimization of their thermal conditions and electricity consuming. This is done by solution of heat conduction equation and Laplace's equation for electric potential. In general CFD may be also used for the flow prediction and optimization of horizontal AE functioning. The flows in vertical gaps between the electrodes can be modeled successfully. But in the working space, the high gas content in combination with low velocities results in the conditions, which are beyond the application area of the commonly used multiphase models. The dynamics of the growth and coalescence of the large bubbles in the narrow horizontal interelectrode gap too much depends on the local conditions, which are not well known. The flow in working space is found too complex, and "physical" accuracy of the numerical model is a priory insufficient for the detailed numerical study. Nevertheless, that doesn't mean that we cannot to model anything in the horizontal electrolytic cells. There exists

many works on simulation in the electrometallurgy of Aluminium (see, for example, Purdie et al., 1992, Laszlo et al. 2005). One of the earlier works on numerical simulation by Fluent code was issued at 1993 (Purdie et al., 1992). But present-day AEs with horizontal working space are less predictable then those with vertical anode cells.

1.2 Perspective designs. Possibilities and aims of their numerical simulation

During the latest decades metallurgists tried to develop permanent anode for the AEs instead of the graphitic. It is also referenced as inert anode (La Camera et al., 1995, Dawless et al., 1999). The possibility of stable geometry of the working space allows vertical configuration of the anode and cathode plates as it is shown on right picture of fig.1. The above mentioned disadvantages of the existing AEs will be reduced to minimum. We don't concern here with the problem of chemical stability of inert anode, which is very complex, and consider the vertical AE as an object of application of computational fluid dynamics. In assumption of the anode's chemical stability the tasks of the numerical simulations of VAE conditions by the methods of the theory of continuous medium will be the following:

- Estimation and optimization of electric current distribution for effective use and uniform spending (through erosion) of the anodes.
- Estimation of spatial distribution of alumina concentration for effective functioning of VAE. The problem of alumina feeding of AE exists: alumina is more dense than the melt and tends to sink and be accumulated on the bottom; this requires the modeling of solution of alumina and its consumption in working space.
- Removal of volumetric Joule heating from the melt, which would be much more for vertical configuration. This heat is removed out through the installation's walls. The spatial temperature distribution and its extremes are the result of convectional heat removal to the installation's sidewall, and stationary temperature may be too large for electrochemical process.

These tasks demand the conjugated solution of the problems from different topics:

- Calculation of spatial distribution of electric potential and current density.
- Simulation of multicomponent chemistry in the melt (species transport and reactions) or development of well grounded simplifications about the melt composition and its properties.
- Heat transfer in solid structures and liquid electrolyte by heat conductivity and convective motion.
- Modeling of two–phase bubble flow: bubbles affect the spatial distribution of current density and strongly define the flow pattern and velocity.

The space and time requirements for industrial applications are:

- 3D model in realistic geometry.
- Modeling of steady states and transition regimes; modeling of unsteady physical processes (like alumina solution in a moving electrolyte).

In contrast to horizontal AEs the vertical electrolytic cells weren't widely used for aluminium production, there is no practical experience for them. Although the vertical configuration of the electrode plates is commonly used structure in electrolytic cells, the extreme parameters of aluminium production in VAEs demands intensive study. Due to complexities of the experimenting with new apparatus dealing with hostile environment at high temperatures such apparatus are the object of numerical investigation. The example of mathematical model of such kind, which can be realized in commercial code by means of user's defined functions is presented below.

2. Mathematical model

2.1 Identification of the phenomena to be modeled and choice of the approaches

Let's briefly outline the physics to be described (or in some cases – to be neglected). The elementary electrolytic cell is sketched in Fig.2. Due to applied electric field the current passes through the electrodes and cryolite–alumina solution. Because of finite conductivity and flatness of the electrodes the electric potential distribution and the current density may be nonuniform (terminal effect, Tobias and Wijsman, 1953). Electric current in the electrolyte is the ion's motion that results in the deposition of aluminium at the cathode and oxygen – at the anode. The oxygen forms bubbles that rise to upper surface where they eliminate from the electrolyte. The bubbles affect the electrolyte conductivity – greater the gas concentration (upper region), less – the electrolyte conductivity. The size of bubbles increases as them float to the surface (due to decreasing of hydrostatic pressure) and due to their coalescence. The bubble–liquid interaction results in volumetric forces (mainly – drag forces) that strongly affect the liquid motion. The volumetric Joule heating (mainly at the electrolyte) results in heat expansion, volumetric buoyancy forces and natural convection of the liquid. Tangent forces from wall friction and bubble motion make the flow turbulent. Since the alumina is spent at the electrodes and is injected at some distant place (feed point) the concentration of the solution is nonuniform that may affect the current density near electrode and, hence – bubble generation.

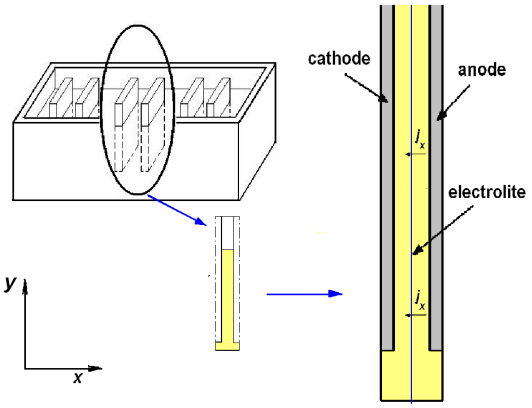

Fig. 2. Full and elementary calculation domains.

We see that even schematic representation of the alumina process requires conjugated modeling of several different phenomena, which occur in the flow. Each of them is described by its own equation(s). The mathematical model is based on the flow equations for multicomponent and multiphase medium with the specified particular terms, coefficients, boundary conditions, and model assumptions/simplifications. The electrolyte flow is partially a natural convection, and partially is a forced convection due to bubble driven forces. The flow is practically always turbulent. Hence, the equations describing heat transport, electric field, concentrations of electrolyte components, and turbulence are also necessary in the model. The energy equations and electricity equations are solved both in the melt and in a solid domains.

Note about electro–magnetic forces and possible magneto–hydrodynamics wave effects. These effects can really be observed in horizontal AEs at the free interface boundary of liquid aluminium and cryolite. In such conditions (see fig.1) the conducting medium having large sizes in two dimensions can be waved in electro–magnetic field like shallow water (Dupuis & Bojarevics 2005). In the case of vertical AE the accumulated liquid aluminium is practically outside the electric field, and due to electro–neutrality of the electrolyte (except the molecular double layer near electrode) the only possible electro–magnetic force may be the ponderomotive force in magnetic field of direct current, which may be shown to be sufficiently small and may be taken into account like a source term in the momentum equation.

The efficient computation may be achieved using the Eulerian two–fluid model with RANS turbulence model for simulation of the two-phase gas-liquid flow. In what follows k–ε model is used for the turbulence. Electrochemistry effects in the hydrodynamic model are taken into account by addition the convective diffusion equation(s) for scalar function(s) describing the composition of the melt, and source/sink terms for these scalar(s). The effects of magnetic field aren't taken into account in following formulations because they don't dominate in the flow dynamics. The material equations deal with the definite material models. The choice of them postulates definite properties and actually is one of the assumptions of the whole numerical model.

2.2 Media: Material models

The following types of materials with corresponding properties should be taken into consideration in simulation of AE:

- Solid structure materials – that of cathode, anode, walls and other solid structures of the facility. These materials don't move – the flow equations aren't solved for them. The material properties, which should be specified for solid material are: density, heat capacity, heat conductivity, electro–conductivity.
- Liquid material – electrolyte, which solidifies at temperature about 970^{o}C or lower depending on composition. It consists of several constituents, which can be schematized as two basic components: alumina and criolyte. The liquid is referred as a primary carrier phase in two-phase model, and gas – as a dispersed secondary phase, for which the bubble parameters are to be defined. The bubbles are assumed spherical. Both fluid and gas are modeled as incompressible liquid because the flow velocities are not greater than ~1m/s (the speed of sound u_s at the gas should be close to that of the air, u_{sg} ~330m/s, u_s for the dense electrolyte should be of the order of that of water i.e. u_{sf} ~1000m/s, hence Mach number for carrier flow is of the order of 10^{-3}–10^{-2}). Both liquids may be modeled as Newtonian and their material properties are: density, heat capacity, heat conductivity, viscosity, diffusivity (which actually is phenomenological coefficient for considered averaged mixtures), electro–conductivity.
- (optional) Melting/Solidification. It is usually described on the base of porous media model by introduction of effective sink terms for momentum and enthalpy within a solidus–liquidus temperature interval (Fluent Inc., 2005). The alternative way is in introducing the effective capacity and viscosity within a solidus–liquidus interval of a phase transfer. In such approaches the solidified material is modeled as liquid, i.e. the flow equations are solved for such material.

2.3 Two–phase flow equations

The continuity equation for gas phase:

$$\frac{\partial}{\partial t}\left(\alpha\rho_g\right)+\frac{\partial}{\partial x_i}\left(\alpha\rho_g u_i^{(g)}\right)=S_g \tag{1}$$

where the source term Sg describes the electrochemical gas generation, ρ_g – gas density. Momentum equation:

$$\begin{aligned}&\frac{\partial}{\partial t}\left(\alpha\rho_g u_i^{(g)}\right)+\frac{\partial}{\partial x_j}\left(\alpha\rho_g u_i^{(g)}u_j^{(g)}\right)=\\&=-\alpha\frac{\partial p}{\partial x_i}+\frac{\partial}{\partial x_i}\left(\alpha\rho_g\nu_g\frac{\partial}{\partial x_i}u_j^{(g)}\right)+\alpha\rho_g g_i+R_i^{fg}+\alpha\rho_g\left(F_i^{lift,g}+F_i^{W,g}+F_i^{vm,g}+F_i^{O,g}\right)\end{aligned} \tag{2}$$

Here g_i – components of gravity vector, R_i^{fg} models interfacial momentum transfer (drag force), $F_i^{lift,g}, F_i^{W,g}, F_i^{vm,g}, F_i^{O,g}$ are a lift force, wall force preventing from bubbles reattachment, virtual mass force, and other body forces, respectively.

The continuity equation for fluid:

$$\frac{\partial}{\partial t}\left((1-\alpha)\rho_f\right)+\frac{\partial}{\partial x_i}\left((1-\alpha)\rho_f u_i^{(f)}\right)=0 \tag{3}$$

Momentum equation for fluid:

$$\begin{aligned}&\frac{\partial}{\partial t}\left((1-\alpha)\rho_f u_i^{(f)}\right)+\frac{\partial}{\partial x_j}\left((1-\alpha)\rho_f u_i^{(f)}u_j^{(f)}\right)=\\&=-(1-\alpha)\frac{\partial p}{\partial x_i}+\frac{\partial}{\partial x_i}\left((1-\alpha)\rho_f\nu_f\frac{\partial}{\partial x_i}u_j^{(f)}\right)+(1-\alpha)\rho_f g_i+R_i^{gf}+(1-\alpha)\rho_f F_i^{O,f}\end{aligned} \tag{4}$$

where $\mu_f=\rho_f\nu_f$, vector R_i^{gf} models drag force, $F_i^{O,f}$ corresponds to other body forces. The main contribution to the viscosity coefficient is due to turbulent viscosity.

The equations (1)-(4) are closed by the definition of drag force R_i^{gf}. There exists a number of the closure equations (Loth, 2008), built for different conditions. The spherical particle (bubble) having the diameter d_p and moving relative to carrier flow with velocity u^{gf}, is characterized by the particle Reynolds number and particle relaxation time:

$$\mathrm{Re}_p=\frac{u^{gf}d_p}{\nu_f},\quad \tau_p=\frac{\rho_g d_p^2}{18\mu_f} \tag{5}$$

The drag force is written through the relative velocity:

$$R_i^{gf}=K^{gf}u^{gf} \tag{6}$$

where interaction coefficient K^{gf} is defined through the drag coefficient C_D:

$$K^{gf} = \frac{\alpha(1-\alpha)\rho_g}{\tau_p} C_D \mathrm{Re}_p \tag{7}$$

The common form of the drag coefficient of the deformable bubble may be taken as linear interpolation between the extreme cases as, in particular at (Filippov, Drobyshevsky et al., 2010):

$$C_D = C_D^{We_p \to 0} + \Delta C_D \left(C_D^{We_p \to \infty} - C_D^{We_p \to 0} \right) \tag{8}$$

where $C_D^{We \to 0}$ – drag coefficient of the spherical particle having almost zero Weber number, $C_D^{We_p \to \infty}$ – drag coefficient for large Weber numbers and $\Delta C_D = \Delta C_D(We_p, \mathrm{Re}_p)$ is some interpolation function. The forms of $C_D^{We_p \to 0}$, $C_D^{We_p \to \infty}$ and ΔC_D are defined for bubbles in contaminated liquid. The value of We is limited by $We<12$ that corresponds to the fragmentation of the bubbles.

One of the most commonly used relation for $C_D^{We_p \to 0}$ is Schiller–Naumann equation for spherical solid particle:

$$C_D^{We_p \to 0} = \begin{cases} \dfrac{24}{\mathrm{Re}_p}\left(1 + 0.15\mathrm{Re}_p^{0.687}\right) & Re_p \le 10^3 \\ 0.44 & \mathrm{Re}_p > 10^3 \end{cases} \tag{9}$$

The coefficient $C_D^{We \to \infty}$ is expressed as

$$C_D^{We_p \to \infty} = \frac{8}{3} + \frac{24}{Re_p} \tag{10}$$

being an interpolation between the solution for spherical segment and Stokes law for a sphere. For a contaminated liquid (that is the case for the electrolyte) coefficients $C_D^{We_p \to 0}$ and $C_D^{We_p \to \infty}$ are defined as for a solid spherical particle in accordance with eqs. (9) and (10).

The introduction of the expressions for the other forces ($F_i^{lift,g}, F_i^{W,g}, F_i^{vm,g}$) acting on the rising bubble is more complex because the influence of these forces is more complex. In particular, the lift force can depend strongly on bubble position and be oppositely directed in close points. All these forces require comprehensive experimental data for particular cases. Because of the natural convection and bubble rising the flow in working space of VAE should be directed upward and spatial distributions of gas volume fraction and vertical component of velocity may be close to that of rising bubbles injected from bottom into isothermal upward water flow in a vertical tube (see Figs.3-4). The near wall maximum of void fraction is the result of opposite action of lift force and wall force. Essential feature in the case of bubbles in VAE is the absence of the bottom gas injection and generation of gas in the vertical wall. That should result in not such deep minimum of volume fraction near the wall and its smaller values at the opposite side (i.e. near the cathode).

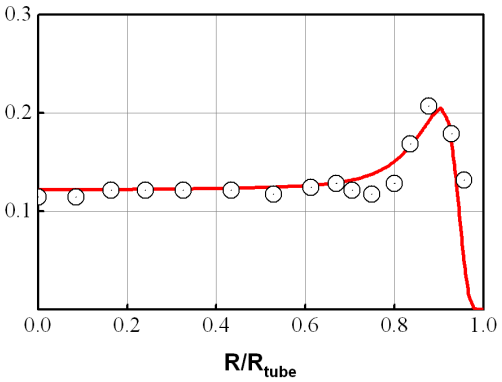

Fig. 3. Radial profiles of void fraction. Points – experiment (see Wang, 1987), line – simulation (Filippov, Drobyshevsky et al., 2010).

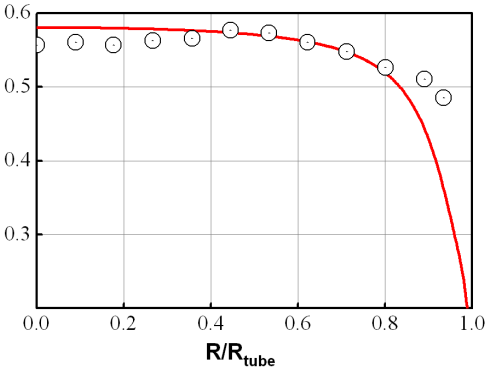

Fig. 4. Radial profiles of liquid velocity, m/s. Points – experiment (see Wang, 1987), line – simulation (Filippov, Drobyshevsky et al., 2010).

Note that the attempts to introduce the lift force and wall force in the full numerical model of VAE were based on the methodology outlined in (Filippov et al., 2010). As a whole these attempts didn't give a stable and robust algorithm in full model of VAE, although the separate tests on bubble motion with such model implemented in OpenFOAM® code were successfully performed (Filippov, Alipchenkov et al., 2010). Since the model of VAE is seemed to be overloaded by another physics, the simple phenomenology with effective horizontal force was introduced, which should integrally simulate the effect of $F_i^{lift,g}, F_i^{W,g}, F_i^{vm,g}$. The expression for such effective force and important question about the bubble size and polydispersity of secondary phase are discussed lower.

The boundary conditions for carrier flow are the common wall conditions for channel flows. No free surfaces are considered (that actually corresponds to crust formation at the upper boundary of electrolyte). The conditions for the secondary gas phase are stated as:

- the flux condition at the anode surface, in which gas is generated in accordance with the Faraday's low;
- the elimination conditions at the upper boundary: $\alpha = 0$;
- slip conditions at the other boundaries.

Note that in the case of crust of solid electrolyte situated atop the moving liquid the gas removal from the upper boundary of vertical working space meets with difficulties that may result in more wide area of bubbles expansion in the flow. In that case the simple condition of gas elimination $\alpha = 0$ may be substituted by more appropriate in accordance with the available empirical data.

2.4 Turbulence equations

For simulation of turbulent flows in multiple narrow gaps of working space of VAE only RANS models can be effectively used. The terms describing the generation of turbulence by buoyancy and bubble motion are better developed and tested for two–equation $k-\varepsilon$ model which is used by authors in all simulations. The equations for TKE and its dissipation rate (Pope,2000, Wilcox, 1994) in common form taken from Fluent's theory guide as follows:

$$\frac{\partial \rho k}{\partial t} + \frac{\partial \rho k u_k}{\partial x_k} = \frac{\partial}{\partial x_k}\left((\mu + \frac{\mu_T}{\sigma_T})\frac{\partial k}{\partial x_k} \right) + G_T + G_b - \rho\varepsilon + S_k \tag{11}$$

$$\frac{\partial \rho \varepsilon}{\partial t} + \frac{\partial \rho \varepsilon u_k}{\partial x_k} = \frac{\partial}{\partial x_k}\left((\mu + \frac{\mu_T}{\sigma_\varepsilon})\frac{\partial \varepsilon}{\partial x_k} \right) + C_{1\varepsilon}\frac{\varepsilon}{k}(G_k + C_{3\varepsilon}G_b) - C_{2\varepsilon}\rho\frac{\varepsilon^2}{k} + S_e \tag{12}$$

The turbulent viscosity –

$$\mu_T = \rho C_\mu \frac{k^2}{\varepsilon} \tag{13}$$

where C_μ is model constant. The density in these equations can be the density of mixture, the density of a carrier flow (dispersed turbulent model) or the density of a particular phase (if they are simulated as symmetric), dependently on the kind of the taken multiphase turbulent model.

The source terms G_T, G_b describe the production of k and ε due to velocity gradient and buoyancy, S_k, S_e stand for other possible production processes, $\sigma_\varepsilon, \sigma_T, C_{1\varepsilon}, C_{2\varepsilon}, C_{3\varepsilon}$ are the model constants.

Additional terms are introduced in modifications of $k-\varepsilon$ model for multiphase flows, which describe the effect of bubble presence, in particular, pseudo-turbulence induced by bubble wakes (van Wijngaarden, 1976). The question about effect of a turbulence even in the dispersed multiphase flows is even more complex matter than the above mentioned problem of modeling the body bubble forces. In absence of reliable experimental data the default data of the used commercial code are taken as the starting point.

2.5 Enthalpy equations

The enthalpy equations for primary and secondary phases include the balance of transport, diffusion, heat sources and (optionally) viscous heating:

$$\frac{\partial}{\partial t}\left(\alpha\rho_g h_g\right)+\frac{\partial}{\partial x_i}\left(\alpha\rho_g u_i h_g\right)=\frac{\partial}{\partial x_i}\left(\lambda_g\frac{\partial T}{\partial x_i}\right)+S_g+Q_{gf} \tag{14}$$

$$\frac{\partial}{\partial t}\left((1-\alpha)\rho_f h_f\right)+\frac{\partial}{\partial x_i}\left((1-\alpha)\rho_f u_i h_f\right)=\frac{\partial}{\partial x_i}\left(\lambda_f\frac{\partial T}{\partial x_i}\right)+S_f+Q_{fg} \tag{15}$$

The enthalpy h_s of s-th phase (where s=*f, g*) is:

$$h_s(T_s)=\int_{T_{ref}}^{T_s} c(T)dT \tag{16}$$

where T_s is the temperature, V_f is viscous heating, Q_{fg} is interphase heat exchange, S_f – other heat sources, $c(T)$ is constant pressure heat capacity. Heat conductivity coefficient λ_s takes into account turbulent heat transfer. The interphase heat exchange term Q_{fg} depends on the phase temperature difference. It is written through the heat transfer coefficient H_{fg}:

$$Q_{fg}=H_{fg}(T_f-T_g) \tag{17}$$

which for dispersed flows usually is calculated with the aid of the well known Ranz-Marshall correlation.

The temperature of the generated gas in AE should be equal to that of liquid and there is no reasons for these temperatures to be different in an incompressible liquid. Since there is no significant evaporation at the electrolyte, there is no significant interphase heat- and mass exchange between the primary and secondary phases. Therefore, interfacial heat-mass transfer doesn't play significant role in AEs.

Practically all generated gas erases from the system. It is interesting to compare the heat removal due to gas outlet with the total heat generation. The mass generated from 1 m² of the electrode plate is given by Faraday' lows:

$$\dot{m}_O=K_O\,j \tag{18}$$

where

$$K_O=\frac{1}{F}\cdot\frac{A_O}{Z_O} \tag{19}$$

and *j* is normal component of current density. The temperature of the generated gas is equal to that of its environment, hence, the rate of gas enthalpy generation can be estimated as:

$$\dot{H}=C_O(T_f-T_{ref})\dot{m}=C_O(T_f-T_{ref})K_O j \tag{20}$$

where reference temperature T_{ref} corresponds to room temperature, T_{ref}=300K.

Let the distance between the electrode plates is b. The Joule heat generation in working space per 1m² of electrode plates is

$$W=\frac{j^2}{\sigma}b \tag{21}$$

The ratio:

$$\frac{W}{\dot{H}} = \frac{j\ b\sigma}{C_O(T_f - T_{ref})K_O} \tag{22}$$

Substituting the typical values: $\sigma = 200Cm/m$, $j = 2{,}000 - 10{,}000A/m^2$, $b = 1/20m$, and constants for oxygen we obtain the ratio $W/\dot{H} \sim 10 - 50$. We see that for rough simulations in many cases the heat removal by the gas may be neglected and energy equation for the secondary phase – be omitted.

Boundary conditions for the enthalpy equations, which for incompressible flows are often solved for the temperatures, are the usual BCs for heat conduction equation. These BCs are set the same for both phases. On a coupled boundary between the solid and liquid materials the conjugation condition of continuous normal heat flux is stated. The same condition is stated on a boundary of different materials for electric potential equation considered below.

2.6 Electric field and current density

In conducting material the distribution of electric potential φ is related with current density by Ohm's low:

$$j_i = \sigma \frac{\partial \varphi}{\partial x_i} \tag{23}$$

Due to electro-neutrality of the all media $div\ \mathbf{j}=0$ or –

$$\frac{\partial}{\partial x_i}\sigma \frac{\partial \varphi}{\partial x_i} = 0 \tag{24}$$

This equation defines the spatial distribution of electric potential. The current density is used for calculation of the source term of volumetric Joule heating in the energy equation Eq. (15) for liquid phase.

The gas bubbles occupy the significant part of the volume that reduces correspondingly the cross-section of the interelectrode space, i.e. partially screens electric current. In the case of relatively small gas volume fractions (approximately α <0.2) the decrease of conductivity σ due to decreasing of effective conducting section depends on the bubble concentration through the Bruggeman's equation (Bruggeman, 1935):

$$\sigma = \sigma_0 (1 - \alpha)^{3/2} \tag{25}$$

where σ_0 is the conductivity of homogeneous electrolyte.

When gas volume fraction is close to 0.5 or larger the flow is poorly predictable. In such a case the equation (25) or similar to it may be used like phenomenology that gives right result in extreme case α =1.

The boundary conditions for potential equation (24) are specified in the places of current input/output, i.e. in a poles of the electric circuits. The values of current density at one pole P_- and electric potential at other pole P_+ are specified:

$$\sigma \frac{\partial \varphi}{\partial n} = j_n,\ x \in P_-\ ;\ \varphi = 0,\ x \in P_+ \tag{26}$$

At the coupled boundary of electrode and electrolyte the condition for normal component of current density is specified –

$$\sigma_S \frac{\partial \varphi_S}{\partial n}\bigg|_{\Omega_S} = \sigma_E \frac{\partial \varphi_E}{\partial n}\bigg|_{\Omega_E} \tag{27}$$

On the other boundaries – insulation condition (default BC):

$$\frac{d\varphi}{dn} = 0 \tag{28}$$

The overpotential effect (Newman & Thomas-Alyea, 2004) in the case of small potential drop along the electrodes may be taken uniform for all anode boundary and thus may be easily modeled. In general, the overpotential have to be determined for every definite installation with use of the detailed data on the electric resistance.

In calculation sequence of electrical part of full model Eq. (24) is solved first, then the current is defined from Eq. (23) and source term (15) for the enthalpy equation as well. Since the current density depends on spatial distribution $\alpha(x)$ of secondary phase, the common integration scheme for the full system with sequential solution of flow equations, energy equation and equations for field, concentration etc. will be explicit. But owing to slow change of $\alpha(x)$ obtaining of stable numerical solution is possible.

2.7 Electrolyte composition

The effect of nonuniform distribution of alumina concentration is of importance for consideration of the influence of the local deficiency of alumina on the current density and aluminium/gas generation. If the local concentration is greater than the definite minimum value (about 2%) the process is ruled by the electric potential and conductivity. The variations of electrolyte composition weakly influence the flow in comparison with the bubble motion (see below). But variations of the concentration of alumina can violate the electrolysis (the value of alumina concentration ξ <2% results in anode effect) and thus maintaining of ξ is of primary importance. From such point of view the modeling of electrolyte composition is important but somewhat separate problem, which may be solved with different levels of detailing. The zero level corresponds to neglect of electrolyte composition. A such model was outlined above. The following level of detailing is two–component model of composition and we will try to show that the possibility of such simplification really exists.

Actually the cryolite and alumina dissociate during their solution and form several charged ions. But this microscopic structure isn't exhibited macroscopically. The average distribution of concentration of the ions smoothly varies in space, except the very narrow double layer at anode surface, which cannot be modeled macroscopically (Borisoglebsky et al., 1999). In some extent the local stoichiometric composition depends on the dissolved alumina concentration only. It is important that having at the input of Hall-Heroult process one mole of Al_2O_3 we obtain two moles of Al and one and half moles of oxygen O_2 (or $1.5CO_2$), i.e. no new chemical compounds arises in the solution during the process of aluminium reduction. All that allows to consider the alumina electrolyte as the neutral idealized compound of alumina and cryolite only. The properties of such system (in particular, the density) will depend on its composition – the empirical data should be used. Note that electrolyte of

industrial AE can contain up to 10% of additions (Borisoglebsky et al., 1999). The generalizations of the idealized case of two–component mixture that is considered below depend on particular application of the numerical model. For example, we don't concern here the problem of alumina dissolution since this complex process depends on the details of technology and apparatus of alumina feeding.

The two components of the electrolyte are described by the alumina mass concentration ξ. Correspondingly, the criolyte concentration will be $1-\xi$. The transport equation for ξ is the equation of convective diffusion (Newman & Thomas-Alyea, 2004). In more or less general form this equation can be written as follows

$$\frac{\partial \rho\xi}{\partial t} + \frac{\partial}{\partial x_i}\left(\rho u_i \xi - D_M \frac{\partial \xi}{\partial x_j}\right) = S_A \tag{29}$$

Actually this is a balance equation for the alumina/cryolite masses, which are together form the primary phase. Since the gas density is negligible the density ρ in this equation may be the mean density of gas-liquid flow, which carries the concentration parameter ξ. The relation of actual density of electrolyte (primary phase) ρ_f with ξ should include the temperature and is taken from the empirical data. Note that here the diffusion coefficient D_M has the dimensionality of dynamical viscosity, Pa·s. It is equal to common diffusion coefficient D, multiplied by mean density. It includes the laminar and turbulent diffusion coefficients: $D_M = D_A + D_T$. D_T is calculated through the turbulent Schmidt number and turbulent viscosity (13): $D_T = Sc_T \mu_T$. For mixture gas jets $Sc_T = 0.5 - 0.7$ (Abramovitz, 1981).

The places of sources and sinks of alumina mass i.e. the sources and sinks of concentration for Eq. (29) are the alumina feed places and vertical working space of AE respectively. If we don't model the chemistry in electrolyte, the place of the sink of the averaged component (alumina) is not exactly positioned in the working space, and it is naturally to set this sink at the electrode surface. Both cathode and anode areas may be taken as the boundaries of concentration sinks, since due to intensive bubble motion the electrolyte composition should be effectively smoothed. The mass flux boundary condition describing the sink of alumina during the electrolysis at the boundary Γ_{out} is ruled by Faraday's lows, analogously to that of gas generation (18-19). The generation/elimination of $\xi(x,t)$ at every from the two electrode surfaces is defined as:

$$\dot{m}_{out}(x,t) = 0.5 D_M \left.\frac{\partial \xi}{\partial x_j}\right|_{x \in \Gamma_{out}} \tag{30}$$

where function $\dot{m}_{out}(x,t)$ is the given spatial distribution of alumina feed sources or is the sink at the electrode, which is calculated from the Faraday's lows using the calculated normal component of current density:

$$\dot{m}_{out}(x,t) = K j_n(x,t) \tag{31}$$

The source term of alumina feed may be specified both through the volumetric source S_A and the analogous flux boundary condition in a some part of the AE walls.

The velocity field $u_i(x)$ in the convective term is known from the flow equation. The transport of species in the liquid should be referred to the velocity $u_i^{(f)}(x)$ of a primary phase, which carries the species. Since the gas density is small, the velocity $u_i^{(f)}(x)$ is close to the centre of mass velocity in a mixture.

3. Further simplification, adaptation and verification of the integrated model

The equations presented above are well known and widely used. For real application of them to VAE the source/sink terms, coefficients, and boundary conditions should be specified. For the sake of effective solution of these conjugative equations some simplifications should be done. Some of them are discussed below. The possibilities of the simplifications are to be checked by verification and validation of the numerical models.

3.1 Some features of heat–mass transfer in horizontal and vertical AEs

The thermal regime of AE installations can be characterized by the averaged volumetric heat generation per unit volume $S_{fA} = W_{Ap} / V_{Ap}$, where W_{Ap} is the total heat generation in the cell, V_{Ap} is the estimated heated volume. As it was mentioned, vertical AEs may have the parameter S_{fA} some times greater than that of horizontal AEs. The reason is in their geometry as it can be seen from Fig.1: considerable volume of the horizontal AE is occupied by the electrodes and electrolyte lying out of working space. The heat scattering in horizontal AEs is successfully calculated with use of common heat conductivity equation, the areas of the electrolyte flow are taken into account in such a simulations through effective heat conductivity coefficients. Since the working space in horizontal AE is situated downward, the alumina granules being introduced in the electrolyte dissolute near the bottom and reach the working space without considerable problems.

In vertical AEs the S_{fA} parameter is larger since the working space occupies relatively larger volume. The dominant physical process in heat removal is the convection. Let's compare the mass flow rates resulting from the natural convection and from bubble driven forces. The cause of the motion in both cases may be characterized as an averaged density gradient in mixture. In case of natural convection in a single-phase liquid the gradient arises due to thermal expansion and nonuniform composition. The latter factor gives the relative density variation δ less than 10^{-2} (taking into account that variations of alumina concentration in working space are normally not much greater than 2%). Assumed temperature drops in working space shouldn't be greater than $\Delta T \sim 100K$, heat expansion coefficient $\beta \approx 0.5 \cdot 10^{-4}\ \mathrm{K}^{-1}$, thermal volumetric deformation: $\beta \Delta T \sim 10^{-2}$, the volumetric buoyancy force: $f_T \sim \rho_0 g(\beta \Delta T + \delta)$.

The averaged buoyancy force involved with presence of the gas bubbles is $f_G \sim \rho_0 g \alpha$. Usually gas volume fraction α has an order of 0.1, i.e. in that case we have $f_G >> f_T$. Hence, in working space bubble driven (drag) force should dominate and mainly defines the flow at the installation. This allows some roughness in determination of the density through the temperature and composition, but requires to pay larger attention to modeling of interfacial momentum exchange, namely to drag force.

3.2 Simplifications in multiphase model

The gas flow at the lowest part of vertical electrolytic cell consists of separate bubbles, gas volume fraction through the width of the gap is relatively small. The problem of description of a dispersed bubble flows in the vertical gap is satisfactory studied to this day for monodisperse bubble flow with $\alpha < 0.1 - 0.2$. There exists several models for polydisperse flows (see, for example (Krepper et al., 2007), (Silva & Lage, 2011), (Guan Heng Yeoh & Jiyuan Tu, 2010). Since the gas volume fraction in VAE may amount to the values of some tens percents, the bubble flow in the vertical working space may be really polydisperse due to various departure diameters and coalescence as it is sketched in Fig.5.

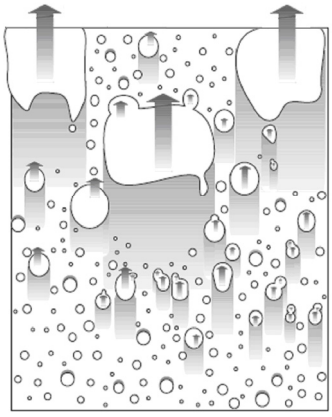

Fig. 5. Bubble accumulation and evolution.

The implementation of the model of polydispersity in the whole numerical model of VAE will result in the increasing of the number of equations, because several additional equations will be added, which describe the introduced size ranked groups of bubbles (usually – 3–4 or more). We should add the model of coalescence, probability density function (PDF) for bubble diameters. These equations and models require the experimental data, which for bubbles in cryolite are rather poor. The result of the such sophistication will be in an improvement of the model of dispersed bubble flow for the range of gas volume fraction of the order of 0.1-0.2. For higher volume fraction the applied MCFD methods will be essentially phenomenological, and here we have the common dilemma: before the implementation of a new improved approach the researcher should decide whether the improvement be really reached and what is the calculation cost of the work.

Because of complexity of the full numerical model of VAEs and the lack of the experimental data the models of polydispersity were not considered for them by authors. In all simulations the bubble size was taken as an averaged value, which may be varied during serial quality assurance calculations. The effects of the variable bubble size in a working space may be investigated numerically as a separate effects and be taken into account through the model coefficients.

Another important question to MCFD model concerns with the above mentioned body bubble forces. They influence the distribution of α across the vertical gap, that defines the cross profile of vertical component of a velocity and in somewhat may effect the mass flow

rate in the interelectrode gap. There exists several forms of equations for the lift force (see Antal et al., 1991, Legendre & Magnaudet, 1998), which were validated and used by many authors. The testing and identification of the models of the lift force and wall force (Antal et al., 1991, Lopez de Bertodano, 1994, Troshko & Hassan, 2001), which prevents from the bubbles reattachment, is usually performed in the bubble column with downward bubble injection. Air–water flows are commonly considered in such experiments. The analogous experiments for wall generation of the bubbles in fused cryolite are unknown to authors. The experience shows that implementation of new correlations in multiphase models always requires some fitting of the coefficients during the model verification. Since the using of lift force model in common form often reduces the stability of numerical calculations, more simple form of horizontal component force was taken for simulation of bubble motion across the gap. The robustness of simulations is an argument to develop and use the simplified "engineering level" models, which have to be tested and studied for prototypical conditions.

Another argument to use the simplified form for simulation of the bubble body force is in the above mentioned relatively small established range of the validity of disperse models. The experiments with bubble flows are conducted usually for air–water mixtures in conditions of clean and even walls of bubble columns and low gas volume fractions. In conditions of the aluminium reduction cell the wall roughness, the bubble size and gas volume fraction are usually relatively high, and the model validated on the water experiments may be incorrect in the conditions of VAE working space.

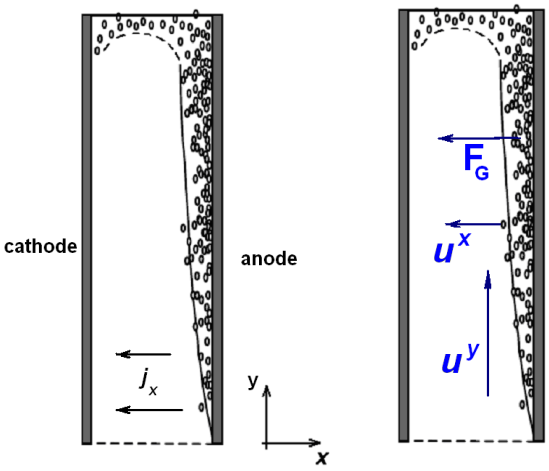

Fig. 6. To introduction of effective force.

In the experiments with vertical wall gas generations (see, for example, Cheung & Epstein, 1987, Ziegler & Evans, 1986) the average thickness of the near-wall bubble layer increases with the height. The proposed phenomenology takes into account only this fact. An effective body force is introduced for the gas phase, it acts in the secondary phase normally to wall, in which gas is generated (Fig. 6).

The simplified phenomenological forms of expressions for effective body force, acting on the bubbles in a narrow vertical channel and causing their horizontal drift, were introduced by

different authors in different forms. This approach was previously used to model vertical electrolysers in a 2D formulation, in particular, using discrete particle model of Fluent code (Mandin et al., 2006, Bech et al., 2003), where the horizontal drift of bubbles rising along the vertical wall was caused by additional effective force. Bech et al., (2003) considered such horizontal force as being a function of the distance to the vertical wall and expressed it via the force potential as

$$\psi(x) = -A\left[\frac{r_g}{x}\right]^n \tag{32}$$

where A and n are constants and $r_g = d_g/2$ is the bubble radius. The effective body force acting on the gas phase is as follows:

$$f(x) = -\nabla\psi = A \cdot r_g{}^n \cdot n \cdot x^{-n-1} \tag{33}$$

Mandin et al., (2006) assumed the horizontal force to be independent on the distance across the gap and to be such that its ratio to the drag force was equal to the assumed slope of the bubble trajectory.

A significant disadvantage of expressions (32) and (33) for the effective horizontal force is in their dependence on the domain geometry and the independence of the local gas concentration that can restrict applicability of this model for high gas content and leads to nonphysical effects. The effective force is better to be expressed only through local characteristics of a two-phase flow. During introducing this force it is natural to assume that the interaction between bubbles and turbulent flow, which is caused partially by other bubbles depends mainly on bubble's spacing and their average size. A simple assumption is that this force depends explicitly only on the gas volume fraction, while the dependence on the liquid velocity, viscosity, etc. can later be introduced via the corresponding multipliers. Then, it is also natural to introduce a gradient of α into the expression for the effective force, since, as it may be assumed, the gradient should be involved with the bubble repulsion direction in a case of high gas content. A simple expression for such an effective force is as follows:

$$\mathbf{f} = A\alpha^n \nabla\alpha / |\nabla\alpha| \tag{34}$$

where A and n are some constants. This formula takes into account the direction of the gradient of the gas volume fraction α. In the region of homogeneous α (which usually corresponds to the uniform distribution of bubble velocities), the effective force vanishes. At the edge of the bubbly region, the effective force (34) acting on the gas phase decreases with the concentration. The particle relaxation time (τ_p) and corresponding length (l_p) are small. For a bubble diameter of d = 3 mm, we obtain

$$\tau_p = \frac{\rho_g d_g^2}{18\mu_e} \sim 10^{-4}\text{s}, \quad l_p = u_g \tau_p \sim 10^{-5}\text{–}10^{-4}\text{m}. \tag{35}$$

Therefore, when a bubble leaves the two-phase zone, its motion related to the effective body force is rapidly terminated. In the region of small α, the motion of a gas phase is

determined only by their buoyancy and the carrier flow. The vertical component of gradient of α may be or may be not taken into account.

3.3 Numerical implementation and solver options

The modern CFD codes at parallel computers can solve all the equations presented above, on the meshes of the order of ten million cells even for transient problems. The minimal set of the equations includes usually the flow equations (1-4) with equations of turbulence model and energy equation (14-15) for all phases. The additional equations of convective diffusion type describing definite physical scalar values (such as concentration equation (29) or electric potential equation (24)) may be added together with their coefficients (user's defined scalar, UDS in Fluent code). Handling with coefficients of all equations is possible due to user's defined functions (UDF).

The particular attention should be paid to choice of solver's options since the numerical diffusion may distort the results. The problem of non-uniqueness of the obtained numerical solutions also exists. These issues lead authors to the following preferences in CFD code options which seem to be more or less general to all complex simulations of VAES:

- steady problems is commonly solved as transient by relaxation to steady state
- pressure-velocity coupling procedure uses SIMPLE (Versteeg & Malalasekera, 1995) algorithm for steady problems and PISO or Coupled (simultaneous solution of four flow equations for pressure and velocity components) solvers for really transient statements. The Coupled solver is preferable because of its better numerical stability
- second order spatial approximation in all solved PDEs
- realizable or RNG versions of $k-\varepsilon$ turbulence model.

3.4 Verification

The verification of the model was done for the separate phenomena, the modeling of which isn't included in standard possibilities of the used CFD code. For the models in consideration such verification set should include the tests concerning with:

- electro–conductivity problems
- natural convection of heat generating liquid
- rising of spherical bubbles generated at the vertical walls
- convective diffusion.

It is essential that the verification of two–phase procedures should be done in prototypical conditions, close to that of AEs as it was discussed above.

To this day the following problems were passed:

- electro–conductivity problems:
  a) simple simulative problem;
  b) the problem of terminal effect (Filippov, Korotkin, Urazov et al. 2008)
- natural convection of molten salt with solidification at cooled boundary (Filippov et al. 2009)
- conjugated simulation of effect of rising bubbles on the electrical conductivity (Filippov, Korotkin, Kanaev et al. 2008).

The verification and identification of the coefficients of the described model of effective body forces is not yet satisfactory performed because of luck of data on bubbles motion in vertical generating channels. One performed test concerned with CFD calculations is briefly outlined in what follows.

4. Simulation of elementary electrolytic cell

The elementary electrolytic cell (see Fig.7) was considered in 2D geometry: cross section by vertical plane, which is normal to the electrode plates was considered. Thermal boundary condition of third kind –

$$\lambda_m \frac{\partial T}{\partial n} = H(T - T_b) \tag{35}$$

was set on the top boundaries of the electrodes. Here the heat exchange coefficient $H = 200W/(m \cdot K)$ corresponded to the estimated heat removal. The bottom and vertical lateral boundaries were adiabatic that should be close to the condition in the elementary cell in the middle section of VAE. The potential difference was equal to 1V.
The results of two calculations are considered below, which were performed for the cases: (a) the absence of gas generation, and (b) the presence of gas generation.

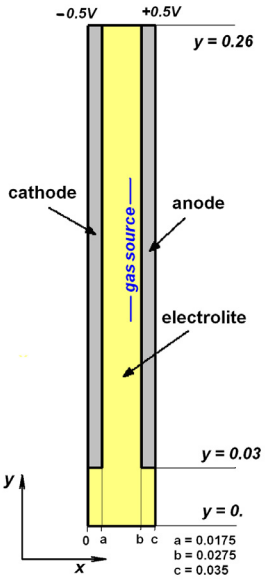

Fig. 7. To problem statement.

Figure 8 shows the vertical profiles of the current density, which were obtained numerically for problems (a) and (b) in comparison with the corresponding results of estimations using formulae presented in (Filippov, Korotkin, Urazov et al. 2008). In analytical solution the plates occupy all the height of the cell. The potential difference in analytical calculation was taken at a half-height of the electrode plates. Note that the partial screening of potential in the upper part of the working space promotes leveling of the current distribution along the vertical axis.
The effect of a gas phase in the flow is illustrated by Fig. 9, which shows the path lines for cases (a) and (b). Gas phase distribution is shown in Figs. 10 and 11. The introduction of the gas phase increases the maximum flow velocity (see Table 1) and changes the flow pattern.

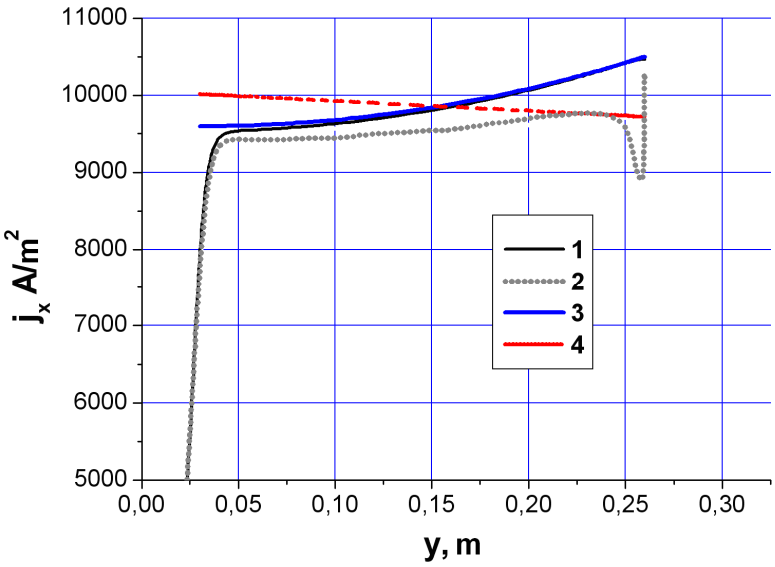

Fig. 8. Current density j_x profiles along the axis: 1– case (a), no gas deposition; 2– case (b) gas deposition; 3– case (a), analytical solution; 4– case (b), analytical solution.

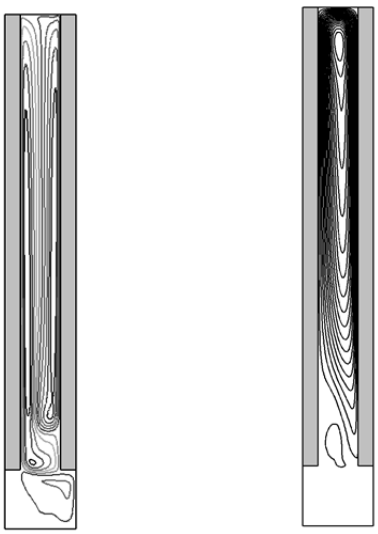

Fig. 9. Pathlines for cases (a) and (b).

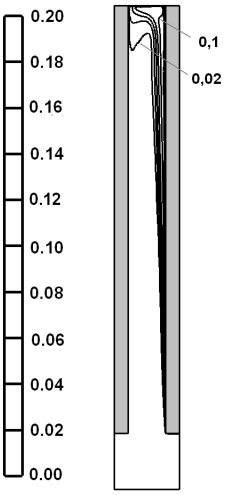

Fig. 10. Gas volume fraction

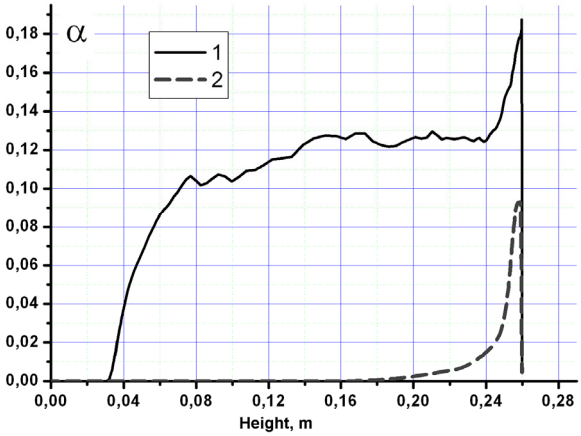

Fig. 11. Profiles of gas volume fraction: 1 – along the anode (distance=1mm), 2 – along axis of symmetry.

Table 1 presents some integral characteristics of the flow regime in the two cases under consideration. Here, the average gas volume fraction α_m was determined as the ratio of the volume occupied by the gas phase to the total volume of the calculation domain. The data of Table 1 show that both the maximum temperature and the temperature drop through the domain in case (b) are smaller that in case (a). This is related to a more intense motion of liquid and more intense heat exchange in the presence of the gas phase. Note that the temperature variation through the calculation domain is relatively small.

Case	T_{max}, K	$T_{max}-T_{min}$	u_{max}	α_m
a	1144,2	144,2	0,024	0
b	1087	87	0,16	0,014

Table 1. Mean values.

5. Conclusions

- The physical state of the media at the aluminium electrolysis may be described in terms of two-phase hydrodynamics, heat transfer, electric current, and convective diffusion with definite assumptions on chemical compositions.
- The uncertainties of models, material properties, boundary conditions and others limit the multiphase model's accuracy, therefore, in the integrated model of VAE including simulation of the bubble motion in cryolite, only the "engineering" level accuracy can be achieved. This means on the one hand that we shouldn't try to achieve the "excellent agreement" with the results of the precise air–water experiments. On the other hand this allows some simplifications in the integrated model for the sake of its robustness and effectivity. From such point of view –
- The integrated mathematical model of the processes in VAE was developed and realized on the base of Fluent code. Some reasons and the ways of simplifications were discussed in the chapter.
- The model was verified for the separate phenomena in simple geometrical configurations. The set of the tests includes heat transfer, natural convection, electric current distribution. The verification and identification of the introduced simple correlations for body forces defining the bubble's motion is required.
- Because of the simplifications made during the development, the validation of the full model on the integrated experiments with AE installations is required.
- The simulations carried out with the built integrated model demonstrated the robustness and efficiency of the calculations.

6. Nomenclature

A	Atomic mass, multiplier in equations
c_p	Heat capacity: J·kg^{-1}K^{-1}
d_p	Bubble diameter: m
D_M	"Dynamical" diffusion coefficient: Pa·s
f	Body force: N/m^3
F	Faraday's constant: F= 96500 C/mol
g	Gravity: m/s^2
H	Heat transfer coefficient: W·m^{-2}K^{-1}
I	Electric current, A
j	Electric current density: A·m^{-2}
k	turbulent kinetic energy: m^{2}s^{-2}
K	Electrochemical equivalent: kg/mol
m, M	Mass: kg
$\dot{m}$, $\dot{M}$	Mass generation: kg/s
p	Pressure: Pa
S	Volumetric source
T	Temperature: K
u	Velocity: m/s
x	Coordinates: m

Greek letters

α	Gas volume fraction
ε	Turbulence dissipation rate: m^{2}s^{-3}
λ	Thermal conductivity: W·m^{-1}K^{-1}
ν	Kinematic viscosity: m^{2}s^{-1}
μ	Dynamical viscosity: Pa·s
ρ	Density: kg/m^3
σ	Electric conductivity: Cm/m=1/(Ω·m)
τ_p	Particle relaxation time: s
φ	Electric potential: V
ξ	Alumina concentration
Ω	Calculation domain
$\partial\Omega$	Outer boundary of Ω

Subscripts

A	Alumina (source, mass etc.)
E	Electrolyte region
f	Fluid
g	Gaseous
i, j	Components of vectors, i,j =1,2,3
n	Normal direction
O	Oxygen
p	Particle

S Solid region (electrodes)
w Wall
0 Initial value

Abbreviations

AE Aluminium electrolysis cell
BC Boundary conditions
CFD Computational Fluid Dynamics
MCFD Multiphase CFD
VAE Vertical AE

7. References

Abramovitz, G.N. (1981) Theory of turbulent jets. Moscow 1981 (in Russian).

Antal S.P., Lahey R.T.Jr, Flaherty J.E. (1991). Analysis of phase distribution in fully developed laminar bubbly two-phase flow. Int. J. Multiphase Flow. Vol. 17. P. 635–652.

Bech, K., Johansen, S.T., Solheim, A., and Haarberg, T. (2003) Coupled current distribution and convection simulator for electrolysis cells, SINTEF, Materials Technology, N-7465 Trondheim, Norway, 2003.

Borisoglebsky, Yu.V. Galyevsky, G.V. Kulagin, N.M. Mincis, M.Ya. Sirazutdynov, G.A. (1999) *Metallurgy of aluminium* Hovosybirsk, Nauka, (in Russian).

Bruggemann, D.A.G. (1935) Ann. Phys. 24, 636 (1935).

Cheung, F.B., Epstein, M., (1987) Two-phase gas bubble-liquid boundary layer flow along vertical and inclined surfaces. Nuclear Engineering and Design 99, 83–100, (1987).

Dawless, R.K. et al. (1999), Molten Salt Bath Circulation Design for an Electrolytic Cell, US Patent 5,938,914, Aug 17 1999, Assignee: Alcoa.

Dupuis, M. and Bojarevics, V. (2005) Weakly coupled thermo-electric and MHD mathematical models of an aluminium electrolysis cell. Light Metals 2005

Filippov A. S., Korotkin I. A., Urazov I. O., Ushakova O. A., and Vasil'ev V. A. (2008) Thermo-Electrical Regime of a Vertical Electrolyzer: Estimates of the Effects of Electric Conductivity and Gas Evolution, J. Eng. Thermophys., 17, 3, 2008, p.218–226.

Filippov A.S., Strizhov V.Th., Tarasov O.V. (2009) Molten Pool Models Validation and Cross–Verification: CFD & SOCRAT Code, 17th Int. Conf. on Nucl. Eng., ICONE17, July 12-16, 2009, Brussels, Belgium

Filippov A. S., Korotkin I. A., Kanaev A. A., Kondakov V. V., Urazov I. O., Ushakova O. A., and Yakovlev P. G. (2008) Thermoelectrical Regime of a Vertical Electrolyzer. Part 2: Numerical Modeling of Two-Phase Electrolyte Convection, J. Eng. Thermophys., 17, 4, 2008, p.320–327.

Filippov, A.S. Drobyshevsky, N.I. Mukin, R.V. Mukina, L.A. Strizhov, V.F. Zaichik, L.I. (2010) Multiphase Model for Simulation Severe Accident Phenomena in NPP Primary Circuit and Containment. 7th Int. Conf. on Multiphase Flow, ICMF 2010, Tampa, FL USA, May 30-June 4, 2010

Filippov, A.S. Alipchenkov, V.M. Drobyshevsky, N.I. Mukin, R.V. Strizhov, V.F. Zaichik, L.I. (2010) CFD Application Of The Diffusion-Inertia Model To Bubble Flows And Boiling Water Problems, ASME Journal of Engineering for Gas Turbines and Power (2010) P. 122901-(1-7)

Fluent Inc. (2005), Fluent 6.2 User Guide, Fluent Inc., Lebanon, NH USA, 2005.

Guan Heng Yeoh, Jiyuan Tu (1991) Computational Technique for Multiphase Flows. Butterworth-Heinemann, 2010

Grjotheim, K. Krohn, C. Malinovsky, M. Matiasovsky, K. and Thonstad, J. (1982) *Aluminum Electrolysis (2nd Edition),* Aluminium-Verlag, Dusseldorf.

Krepper, E. Frank, Th. Lucas, D. Prasser, H.-M. and Zwart, P. J. (2007) "Inhomogeneous MUSIG model-a population balance approach for polydispersed bubbly flows," in Proceedings of the 6th International Conference on Multiphase Flow (ICMF '06), Leipzig, Germany, July 2007, paper no. 375

Laszlo I. Kiss, Sandor Poncsak, Jacques Antille (2005) Simulation of the bubble layer in aluminum electrolysis cells, Light Metals, P. 559-564.

La Camera et al., Process and Apparatus for Low Temperature Electrolysis of Oxides (1995), US Patent 5,415,742 May, Assignee: Alcoa.

Loth E. (2008) Quasi-steady shape and drag of deformable bubbles and drops. Int. J. Multiphase Flow 34 (2008) 523–546

Legendre, D. and Magnaudet, J.(1998) The lift force on a spherical bubble in a viscous linear shear flow, *J. Fluid Mech.* 368, pp. 81–126.

Lopez de Bertodano M., Lahey R.T.Jr, Jones O.C. (1994) Phase distribution in bubbly two-phase flow in vertical ducts. Int. J. Multiphase Flow. Vol. 20. N 5. P. 805–818.

Mandin, Ph., Anil Kumar, K.G., Hamburger, J. (2006) Biphasic Electrolysis Modelling: Coupling Between Phenomena And Scales. www.fluidyn.com/research%20papers/article_nafems_2006.pdf

Newman, J. Thomas-Alyea, Karen E. (2004) Electrochemical Systems, 3rd Edition, Wiley 2004.

Pope, S.B. (2000) Turbulent Flows. Cambridge University Press.

Purdie, J.M. BUek, M. Taylor, M.P. Zhang, W.D. Welch, B.J. and Chen, J.J. (1992) Impact of Anode Gas Evolution on Electrolyte Flow and Mixing in Aluminium Electrowinning Cells, Light Metals, P. 355-360.

Silva, L.F.L.R. Lage, P.L.C.(2011) Development and implementation of a polydispersed multiphase flow model in OpenFOAM. Computers and Chemical Engineering, 2011.

Tobias, C.W. and Wijsman, R. (1953) Theory of the Effect of Electrode Resistance on Current Density Distribution in Electrolytic. J. Electrochem. Soc. 100, p.450.

Troshko A.A, Hassan Y.A. (2001) A two-equation turbulence model of turbulent bubbly flow. Int. J. Multiphase Flow. Vol. 27. P. 1965–2000.

H.K.Versteeg and W.Malalasekera (1995) An introduction to computational fuid dynamics The finite volume method. Longman Group Ltd New York 1995.

Wang, S.K., Lee, S.J., Jones, O.C., Lahey, R.T., 1987. 3D turbulence structure and phase distribution measurements in bubbly two-phase flows. Int. J. Multiphase Flow 13, 327–343.

van Wijngaarden L. (1976) Hydrodynamic interactions between bubbles in liquid. J. Fluid Mech. Vol. 77. P. 27–44.

Wilcox, D. C. (1994) Turbulence Modeling for CFD, DCW Industries, Inc., California 1994.

Ziegler, D., Evans, J.W. (1986) Mathematical Modeling of Electrolyte Circulation in Cells with Planar Vertical Electrodes. I. Electrorefining Cells. J. Electrochem. Soc.: Electrochemical science and technology V. 133, No. 3, P.567–576 1986.